NASA/CP—2002-211212/VOL2

Sixth Microgravity Fluid Physics and Transport Phenomena Conference

Exposition Topical Areas 1–6

November 2002

The NASA STI Program Office . . . in Profile

Since its founding, NASA has been dedicated to the advancement of aeronautics and space science. The NASA Scientific and Technical Information (STI) Program Office plays a key part in helping NASA maintain this important role.

The NASA STI Program Office is operated by Langley Research Center, the Lead Center for NASA's scientific and technical information. The NASA STI Program Office provides access to the NASA STI Database, the largest collection of aeronautical and space science STI in the world. The Program Office is also NASA's institutional mechanism for disseminating the results of its research and development activities. These results are published by NASA in the NASA STI Report Series, which includes the following report types:

- TECHNICAL PUBLICATION. Reports of completed research or a major significant phase of research that present the results of NASA programs and include extensive data or theoretical analysis. Includes compilations of significant scientific and technical data and information deemed to be of continuing reference value. NASA's counterpart of peer-reviewed formal professional papers but has less stringent limitations on manuscript length and extent of graphic presentations.

- TECHNICAL MEMORANDUM. Scientific and technical findings that are preliminary or of specialized interest, e.g., quick release reports, working papers, and bibliographies that contain minimal annotation. Does not contain extensive analysis.

- CONTRACTOR REPORT. Scientific and technical findings by NASA-sponsored contractors and grantees.

- CONFERENCE PUBLICATION. Collected papers from scientific and technical conferences, symposia, seminars, or other meetings sponsored or cosponsored by NASA.

- SPECIAL PUBLICATION. Scientific, technical, or historical information from NASA programs, projects, and missions, often concerned with subjects having substantial public interest.

- TECHNICAL TRANSLATION. English-language translations of foreign scientific and technical material pertinent to NASA's mission.

Specialized services that complement the STI Program Office's diverse offerings include creating custom thesauri, building customized databases, organizing and publishing research results . . . even providing videos.

For more information about the NASA STI Program Office, see the following:

- Access the NASA STI Program Home Page at ***http://www.sti.nasa.gov***

- E-mail your question via the Internet to help@sti.nasa.gov

- Fax your question to the NASA Access Help Desk at 301–621–0134

- Telephone the NASA Access Help Desk at 301–621–0390

- Write to:
  NASA Access Help Desk
  NASA Center for AeroSpace Information
  7121 Standard Drive
  Hanover, MD 21076

NASA/CP—2002-211212/VOL2

Sixth Microgravity Fluid Physics and Transport Phenomena Conference

Exposition Topical Areas 1–6

Abstracts and presentations of a conference cosponsored by
the NASA Office of Life and Microgravity Sciences and Applications and
the Fluid Physics and Transport Phenomena Discipline Working Group
and hosted by NASA Glenn Research Center and
the National Center for Microgravity Research on Fluids and Combustion
Cleveland, Ohio, August 14–16, 2002

National Aeronautics and
Space Administration

Glenn Research Center

November 2002

Available from

NASA Center for Aerospace Information
7121 Standard Drive
Hanover, MD 21076

Available electronically at http://gltrs.grc.nasa.gov

PREFACE

The Sixth Microgravity Fluid Physics and Transport Phenomena Conference provides us with the opportunity to view the current scope of the Microgravity Fluid Physics and Transport Phenomena Program and conjecture about its future. The Microgravity Program has become part of the newly established Office of Biological and Physical Research (OBPR), NASA's fifth Enterprise.

Meanwhile, we commenced the long-awaited and exciting era of conducting Microgravity Fluid Physics experiments on the International Space Station (ISS). We successfully completed the Physics of Colloids in Space (PCS) experiment on ISS and launched the Investigating Structure of Paramagnetic Aggregates of Colloidal Emulsions (InSPACE) experiment that will be conducted later this year.

The excitement of utilizing ISS was tempered, however, by its cost problems that negatively impacted the research budget available for developing flight experiment facilities and hardware. As a result, the Microgravity Fluid Physics discipline took a significant budget reduction that caused deferral/discontinuation of a number of flight investigations that had successfully completed their peer-reviews and received their endorsement. The budget supporting the principal investigators was also negatively impacted, though to a smaller extent. On the positive side, the Fluids Integrated Rack (FIR) that supports much of fluid physics experiments survived these budget reductions. Also the subsequent support of the research community through letters to Congress and to NASA clearly showed how the research community values the Microgravity Fluid Physics and Transport Phenomena Program.

In March, NASA Administrator Sean O'Keefe created the Research Maximization And Prioritization (REMAP) Task Force to perform an independent review and assessment of research priorities for the entire scientific, technological, and commercial portfolio of the Agency's Office of Biological and Physical Research (OBPR) and to provide recommendations on how the office can achieve its research goals. The panel report was released on July 10, 2002. The recommendations of this panel placed almost all of the research content of the Microgravity Fluid Physics Program in Priority 1 or 2 putting the program in an advantageous position as NASA begins to implement the recommendations of the panel.

The program currently has a total of 106 ground-based and 16 candidate flight principal investigators. A look at the collection of abstracts in this document clearly shows both the high quality and the breadth of the ongoing research program. One can easily notice many established world-class scientists as well as investigators who are early in their career poised to achieve that stature. We hope that many of the participants in this conference will perceive microgravity fluid physics as an exciting and rewarding area of research and choose to participate in the NASA Research Announcement released in December 2001. Proposals submitted to the fluid physics research area are due December 2, 2002. More information can be found at the following Web site:
http://research.hq.nasa.gov/code_u/nra/current/NRA-01-OBPR-08/index.html

The content of the Microgravity Fluid Physics and Transport Phenomena Program is well aligned with OBPR's mission of "conducting basic and applied research to support human exploration of space and to take advantage of the space environment as a laboratory for scientific, technological, and commercial research." The fluid physics discipline has a major role in the Physical Sciences Division's goal of developing a rigorous, cross-disciplinary scientific capability, bridging physical sciences and biology to address NASA's human and robotic space exploration goals.

We have implemented a number of changes in the format of this conference based on the inputs received from the participants. We have expanded plenary sessions to include all presentations, eliminated parallel sessions and expanded the exposition session with poster presentations. We hope that this will allow the participants to get a better picture of the overall program through the plenary presentations and promote focused discussion/dialogue through poster presentations. The Discipline Working Group has provided the much-needed guidance in planning the content and the format of this conference. As in the past, we elected to go with a virtual proceedings of the presentation charts that will be available on the World Wide Web at http://www.ncmr.org/events/fluids2002.html. In this regard we acknowledge the support of our principal investigators who have provided us timely inputs of their charts and abstracts and accommodated our format requirements. This cooperation was critical in implementing this and is very much appreciated.

This conference has been organized and hosted by the National Center for Microgravity Research on Fluids and Combustion under the leadership of its Director, Professor Simon Ostrach. I would like to acknowledge the extensive efforts of Ms. Christine Gorecki and other members of the Center in planning, organizing, and hosting the conference and in preparing the proceedings and conference materials. Sincere appreciation is offered to the authors for providing the abstracts and presentation charts in a timely manner and to the members of the Microgravity Fluids Physics Branch of the NASA Glenn Research Center for their many contributions.

Finally, I would like to express my gratitude to all of the conference participants for their contributions to the success of this conference.

Dr. Bhim S. Singh
Fluid Physics Discipline Lead Scientist
NASA Glenn Research Center
21000 Brookpark Road
Cleveland, Ohio 44135
Phone: 216–433–5396
Fax: 216–433–8660
E-mail: bhim.s.singh@grc.nasa.gov

ACKNOWLEDGMENTS

This conference was made possible by the efforts of many people. We acknowledge the contributions of the following individuals:

Fluid Physics and Transport Phenomena Discipline Working Group
G. Paul Neitzel (chair), Georgia Institute of Technology
Bhim Singh (vice-chair), NASA Glenn Research Center
J. Iwan D. Alexander, Case Western Reserve University/National Center for Microgravity Research
Bradley Carpenter, NASA Headquarters
Francis Chiaramonte, NASA Headquarters
Stephen Davis, Northwestern University
Donald Gaver, Tulane University
Joel Koplik, City College of the City University of New York
G.P. Peterson, Rensselaer Polytechnic Institute
Matthew Tirrell, University of California Santa Barbara
David Weitz, Harvard University

Session Chairs
Plenary Sessions
J. Iwan D. Alexander, NCMR/Case Western Reserve University
Noel Clark, University of Colorado
Amir Faghri, University of Connecticut
Donald Gaver, Tulane University
R. Glynn Holt, Boston University
Gareth McKinley, Massachusetts Institute of Technology
Simon Ostrach, NCMR/Case Western Reserve University
Ramkumar Parthasarathy, The University of Oklahoma
Jack Salzman, Chief, Microgravity Science Division, NASA Glenn Research Center
Eric Shaqfeh, Stanford University
Mary Silber, Northwestern University
Paul Steen, Cornell University
Theo Theofanous, University of California, Santa Barbara
Eric Weeks, Emory University
David Weitz, Harvard University

National Center for Microgravity Research on Fluids and Combustion
Simon Ostrach, Director
Thomas Labus, Deputy Director
J. Iwan D. Alexander, Fluids Senior Scientist
Christine Gorecki, Conference Coordinator

Conference Team
J. Iwan D. Alexander
Christine Gorecki
Sandra Jones
Beatrix Norton
Cindy Rosenberger
Norman Weinberg
William Yanis

The Logistics and Technical Information Division and its support service contractors, particularly Kristen Easton, Caroline Rist, Lori Feher, Amy Fennell, Diane Furiga, Chris Sanyk, and Gayle DiBiasio.

TABLE OF CONTENTS

Exposition Session
Topical Area 1:
Colloids and Soft Condensed Matter

Nonlinear Theory of Void Formation in Colloidal Plasmas

A. Bhattacharjee
University of Iowa

A colloidal (or dusty) plasma is an electron-ion plasma containing a dispersed phase of micron-size solid particles. In typical plasma conditions, these particles usually acquire a large negative charge. As a result of the strong Coulomb coupling between the dust particles, a colloidal plasma may undergo phase transitions and exist in a liquid or a crystalline state. Recently, a number of colloidal plasma experiments, in laboratory as well as under microgravity conditions, have shown the spontaneous development of voids. A void is typically a small and stable centimeter-size region (within the plasma) that is completely free of dust particles and characterized by sharp boundaries. In the laboratory, the void is seen to develop from a uniform dust cloud as a consequence of an instability when the dust particle has grown to a sufficient size. The instability is first seen as a so-called filamentary mode, which exhibits a sudden onset. The filaments take the form of beam-like striations in the dust density and glow. The spectrum of the filamentary mode is observed to be broadband, with a peak at about 100 Hz. After onset, the filaments are seen to evolve rapidly (in about 10 ms) to a nonlinear saturated state containing a single void.

Theoretical analyses have confirmed that the ion drag force plays a crucial role in causing the initial instability. These analyses fall into two types: linear stability analyses that include the effect of ion drag, and nonlinear but steady-state analyses that yield void solutions. As yet, there appears to be no nonlinear time-dependent model that describes the spontaneous development of the linear instability and its subsequent saturation to produce a void.

In this paper we propose a basic, time-dependent, self-consistent nonlinear model for void formation in a dusty plasma. This basic model contains three elements: (a) an initial instability caused by the ion drag, (b) a nonlinear saturation mechanism for the instability, and (c) the void as one of the possible nonlinearly saturated states, dynamically accessible from the initially unstable equilibrium. For the initial instability we consider a simple variant of a zero-frequency mode, caused by the ion drag The saturation mechanism we adopt is relevant for collisional voids where ions achieve near-thermal velocities in the void region. In this regime, the ion drag force initially increases with the ion fluid velocity, attains a maximum when the ion fluid velocity equals the ion thermal velocity, and decreases when the ion fluid velocity exceeds the ion thermal velocity. As the linear instability grows, the ions are initially accelerated in the growing electric field, and the ion drag force initially increases. Eventually, as the ions are accelerated to speeds larger than the ion thermal speed, the ion drag force decreases to balance the electric field and thus saturate the instability. We demonstrate by analysis and numerical simulation that in the saturated state, a stable void is formed.

Prediction of Particle Clustering in Turbulent Aerosols

Jaehun Chun[1], *Aruj Ahluwalia*[2], *Donald Koch*[1] *and Lance R. Collins*[3]
[1]School of Chemical Engineering
Cornell University
Olin Hall
Ithaca, NY 14853
[2]Department of Chemical Engineering
Penn State University
102 Fenske Building
University Park, PA 16802
[3]Sibley School of Mechanical & Aerospace Engineering
Cornell University
246 Upson Hall
Ithaca, NY 14853

It has long been recognized that heavy particles in the micron size range embedded in a turbulent flow field are thrown out of regions of high vorticity and collect in regions of high strain. This particle clustering has a profound effect on processes such as collision, coalescence and evaporation/condensation. For example, recent work in the meteorology community suggests this effect may play an important role in the evolution of droplet nuclei in cumulus clouds. A recent study by Reade & Collins (2000) showed that the tendency of particles to cluster continues down to length scales much smaller than the Kolmogorov scale. Indeed, the particle pair correlation function was shown to increase as a power law of the inverse of the particle pair separation distance indefinitely (or at least until the finite particle size cuts it off). The traditional explanation of particle clustering based on the 'centrifuge' effect cannot explain this sub-Kolmogorov scale clustering. Motivated by this observation, we have developed an analytical theory for the pair correlation function for particles with a small but finite Stokes number. The theory treates the particle dynamics as a Markov process, in which a drift is generated by the tendency of particle pairs to occupy regions of higher strain than vorticity. This drift is opposed by turbulent diffusion, which turns out to be a nonlocal process due to the finite correlation length of the fluctuations. The theory predicts a power law for the pair correlation function that is in good agreement with direct numerical simulations and stochastic simulations of the velocity gradient following a particle trajectory. The theory does not predict the Reynolds number dependence of the pair correlation function directly (an important issue in the cloud physics problem), but relates it to the Reynolds number dependence of Lagrangian velocity statistics. These were studied over the limited range of Reynolds numbers that can be achieved in the direct numerical simulations; the results suggest a saturation of the effect at high Reynolds number, in agreement with recent high-Reynolds-number simulations of particle populations (Keswani & Collins 2002).

STUDIES OF ISLANDS ON FREELY SUSPENDED BUBBLES OF SMECTIC LIQUID CRYSTAL

A. Pattanaporkratana, B. Mavel, C. S. Park, J. E. Maclennan, and N. A. Clark

Department of Physics and Ferroelectric Liquid Crystal Materials Center, University of Colorado, Boulder, CO 80309 U.S.A.

We have constructed an optical system for observing the internal structure of freely suspended smectic liquid crystal bubbles using a reflected light microscope. Liquid crystal bubbles can have thicker circular regions (islands) which can easily be generated by shrinking the bubble diameter. The diameter of these islands is ~ 10 μm and they are typically up to five times thicker than the surrounding liquid crystal film (500 Å). In the Laboratory, the location of the islands is strongly influenced by gravity, which causes the majority of islands to migrate to the bottom half of the bubble.

We will describe the size and thickness distributions of islands and their time evolution, and also discuss two-dimensional hydrodynamics and turbulence of smectic bubbles, the shapes of islands and holes affected by bubble vibrations, and the interactions between islands, which we have probed using optical tweezers.

*This research is supported by NASA Grant NAG3-1846

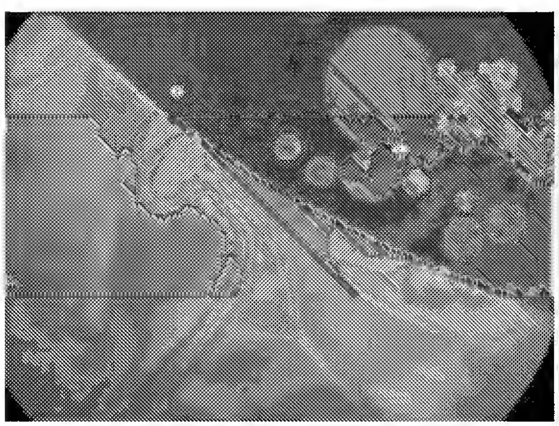

Figure. 1. Islands on Bubble Surface

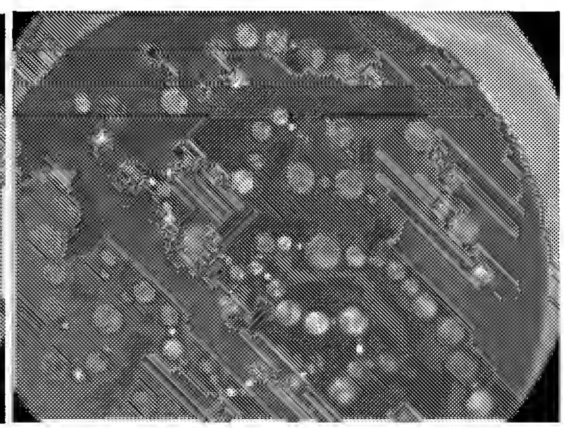

Figure 2. Large Aggregates: a long time after the sample preparation

PCS: The First Fluid Physics Payload on ISS

M. Doherty, NASA Glenn Research Center/ S. Sankaran
National Center for Microgravity Research

Abstract

The Physics of Colloids in Space (PCS) experiment was accommodated within International Space Station (ISS) EXpedite the PRocessing of Experiments to Space Station (EXPRESS) Rack 2 and was remotely operated from early June 2001 until February 2002 from NASA Glenn Research Center's Telescience Support Center in Cleveland, Ohio and from a remote site at Harvard University in Cambridge, Massachusetts. PCS is an experiment conceived by Professor David A. Weitz of Harvard University (the Principal Investigator), focusing on the behavior of three different classes of colloid mixtures. The sophisticated light scattering instrumentation comprising PCS is capable of color imaging, and dynamic and static light scattering from 11 to 169 degrees, Bragg scattering over the range from 10 to 60 degrees, and laser light scattering at low angles from 0.3 to 6.0 degrees. The PCS instrumentation performed remarkably well, demonstrating a flexibility that enabled experiments to be performed that had not been envisioned prior to launch.

While on-orbit, PCS accomplished 2400 hours of science operations, and was declared a resounding success. Each of the eight sample cells worked well and produced interesting and important results. Crystal nucleation and growth and the resulting structures of two binary colloidal crystal alloys were studied, with the long duration microgravity environment of the ISS facilitating extended studies on the growth and coarsening characteristics of the crystals. In another experiment run, the de-mixing of the colloid-polymer critical-point sample was studied as it phase-separates into two phases, one that resembles a gas and one that resembles a liquid. This process was studied over four decades of length scale, from 1 micron to 1 centimeter, behavior that cannot be observed in this sample on Earth because sedimentation would cause the colloids to fall to the bottom of the cell faster than the de-mixing process could occur. Similarly, the study of gelation and aging of another colloid-polymer sample, the colloid-polymer gel, also provided valuable information on gelation mechanisms, as did investigations on the extremely the low concentration silica and polystyrene fractal gel samples. In virtually all cases, the PI learned new and exciting things that have significantly enhanced his understanding of the science under investigation.

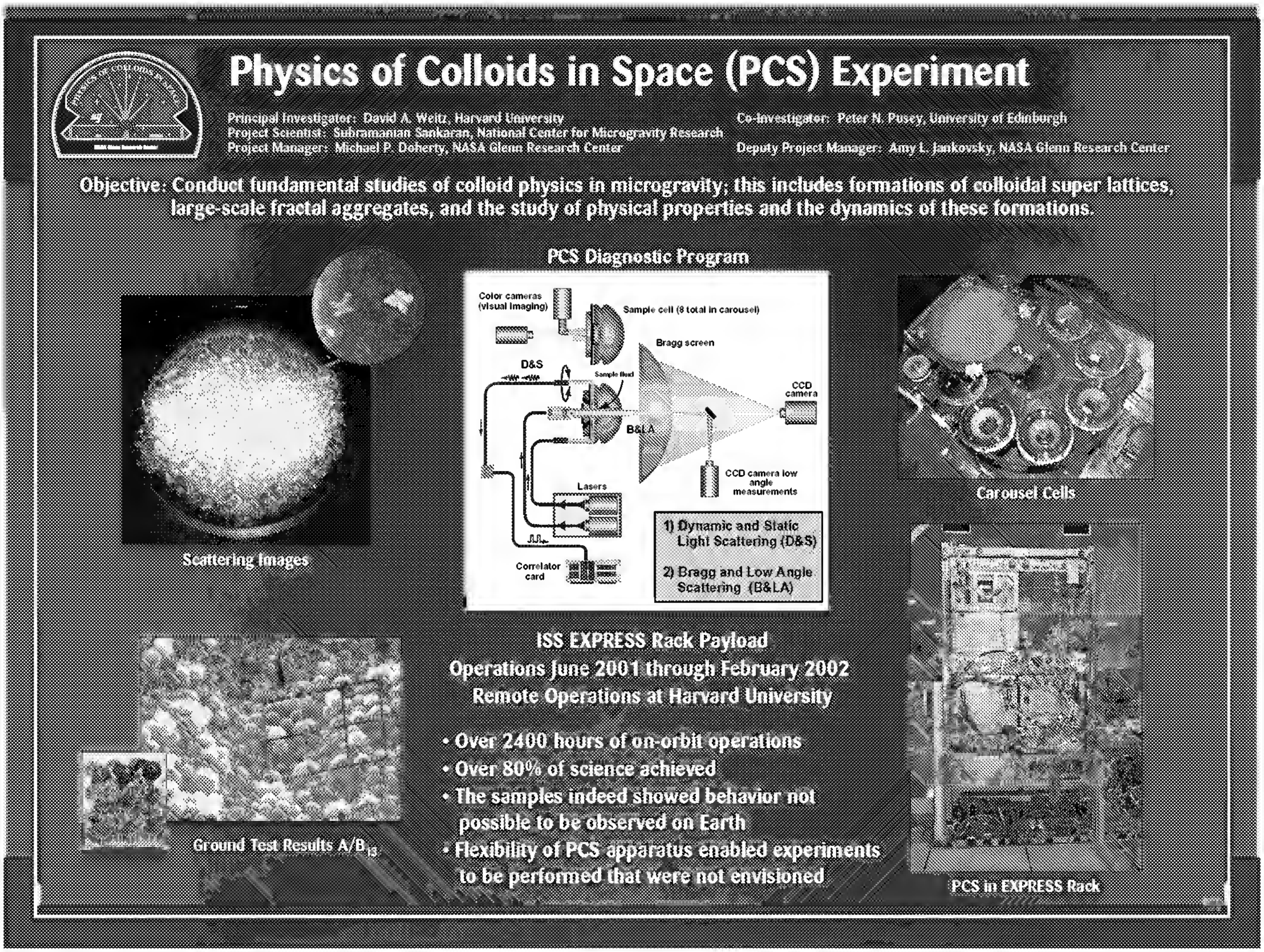
Physics of Colloids in Space (PCS) Experiment
Principal Investigator: David A. Weitz, Harvard University
Project Scientist: Subramanian Sankaran, National Center for Microgravity Research
Project Manager: Michael P. Doherty, NASA Glenn Research Center
Co-Investigator: Peter N. Pusey, University of Edinburgh
Deputy Project Manager: Amy L. Jankovsky, NASA Glenn Research Center
Objective: Conduct fundamental studies of colloid physics in microgravity; this includes formations of colloidal super lattices, large-scale fractal aggregates, and the study of physical properties and the dynamics of these formations.
Scattering Images
PCS Diagnostic Program
Color cameras (visual imaging)
Sample cell (8 total in carousel)
Bragg screen
D&S
CCD camera
B&LA
CCD camera low angle measurements
Lasers
Correlator card
1) Dynamic and Static Light Scattering (D&S)
2) Bragg and Low Angle Scattering (B&LA)
Carousel Cells
ISS EXPRESS Rack Payload
Operations June 2001 through February 2002
Remote Operations at Harvard University
• Over 2400 hours of on-orbit operations
• Over 80% of science achieved
• The samples indeed showed behavior not possible to be observed on Earth
• Flexibility of PCS apparatus enabled experiments to be performed that were not envisioned
Ground Test Results A/B13
PCS in EXPRESS Rack

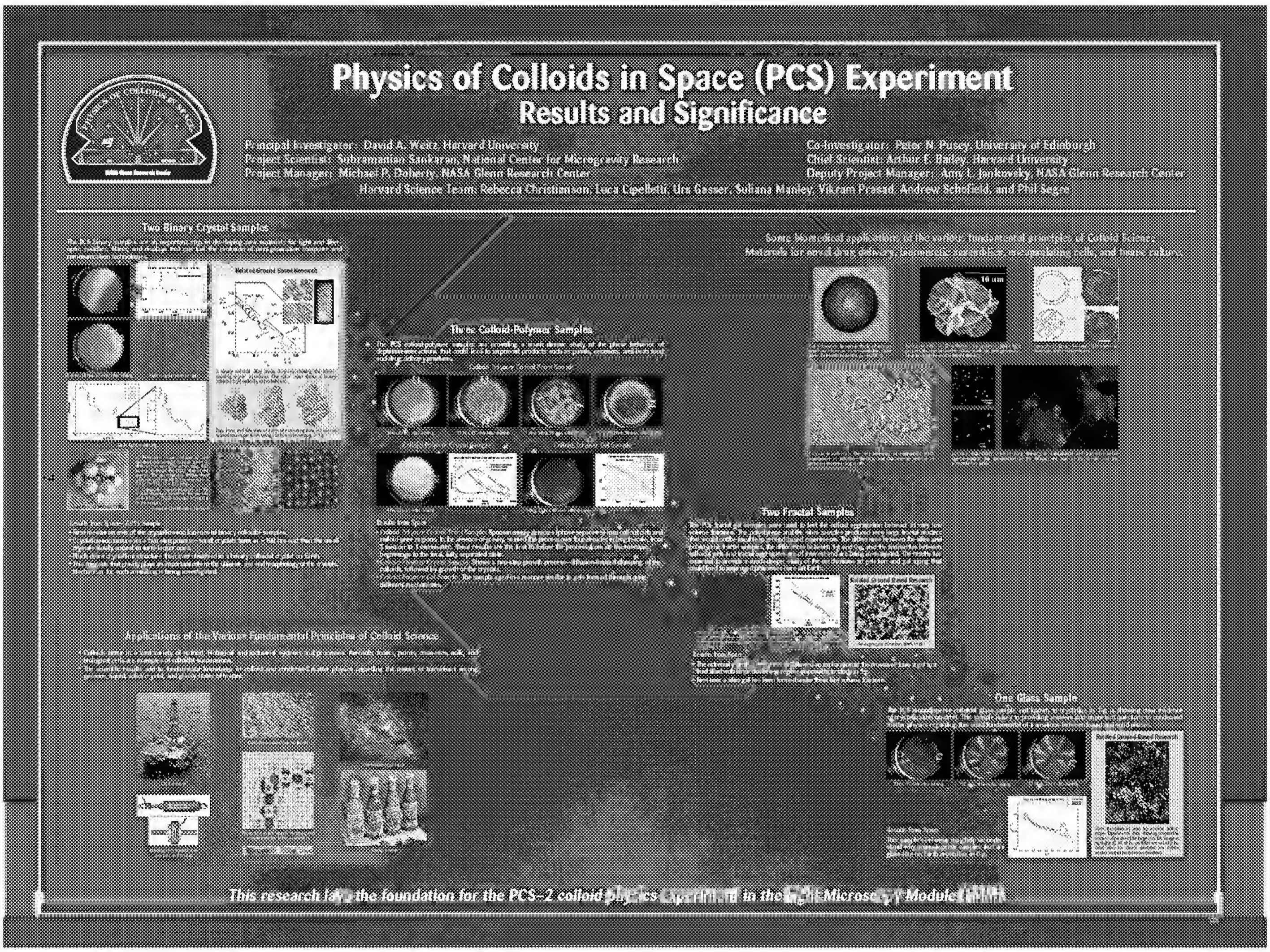
Physics of Colloids in Space (PCS) Experiment
Results and Significance
Principal Investigator: David A. Weitz, Harvard University
Project Scientist: Subramanian Sankaran, National Center for Microgravity Research
Project Manager: Michael P. Doherty, NASA Glenn Research Center
Co-Investigator: Peter N. Pusey, University of Edinburgh
Chief Scientist: Arthur E. Bailey, Harvard University
Deputy Project Manager: Amy L. Jankovsky, NASA Glenn Research Center
Harvard Science Team: Rebecca Christianson, Luca Cipelletti, Urs Gasser, Suliana Manley, Vikram Prasad, Andrew Schofield, and Phil Segre
Two Binary Crystal Samples
Three Colloid-Polymer Samples
Some biomedical applications of the various fundamental principles of Colloid Science:
Materials for novel drug delivery, biomimetic assemblies, encapsulating cells, and tissue cultures.
Two Fractal Samples
Applications of the Various Fundamental Principles of Colloid Science
One Glass Sample
Related Ground-Based Research
This research lays the foundation for the PCS-2 colloid physics experiment in the Light Microscopy Module

Compression of Paramagnetic Colloidal Chains

Daniel J. Smith
Department of Chemical Engineering
Massachusetts Institute of Technology
Cambridge, MA 02139

Alice P. Gast
Department of Chemical Engineering
Massachusetts Institute of Technology
Cambridge, MA 02139

Phone: (617) 253-1403
FAX: (617)-253-8388
Email: gast@mit.edu

Abstract

The electric or magnetic field-induced aggregation of polarizable particles produces a rapid rheological transition known as electrorheological (ER) or magnetorheological (MR) response. The ability to tune these interactions with an external field makes them attractive for feedback-controlled devices such as shock absorbers and suspension systems. In response to an applied magnetic field, paramagnetic colloidal suspensions aggregate into anisotropic microstructures that produce the bulk rheological response. The microstructure is composed of chains, columns of chains and chain networks. The deformation and rupturing of this microstructure leads to a finite yield stress for the suspension. In this work, we investigate the strengths and interactions of chains and columns of chains to compression parallel to the applied magnetic field with optical tweezers.

Optical trapping is used to manipulate the microstructure and to measure the forces resisting its distortion. The iron oxide present in the particles prevents us from trapping them directly, so we use a tether-handle system utilizing latex particles attached to the magnetic particles via the biotin-streptavidin binding reaction.

Using optical traps, we explore the response of single chains and columns of chains to compression. We find that chains bend and undergo reorganization processes before their ultimate failure due to rupture. We believe that these reorganization events are key mechanisms of stress reduction. Columns of chains exhibit the same mechanisms, but higher forces are required for both the rearrangements and column failure. This strengthening is caused by the enhanced local field due to additional magnetized particles and the additional strength of the column due to the multiple chain interactions. We show how these studies provide mechanistic explanations of magnetic suspension rheology. We model the microstructures and forces through numerical simulations.

DIFFUSIVE COARSENING OF LIQUID FOAMS IN MICROGRAVITY

Igor N. Veretennikov and James A. Glazier
Department of Physics, University of Notre Dame, Notre Dame, IN 46556

Our main goal is to simulate, to some extent, microgravity conditions in the presence of gravity, to check the stages of a proposed scenario for coarsening of "space" foams, and to determine relations between foam structure and wetness and rheological properties. Our current focus is on preliminary experiments needed for MRI studies of stabilized foam: optimization of the foam's composition, of imaging parameters and the investigation of foam stability against global convection.

To mimic foam behavior under microgravity, we stabilize the foam by supplying extra fluid on the top of the foam head. While this fluid increases the MRI signal, it also creates some extra problems. Although the Plateau borders have no breaks and are well resolved, the image is noisy and difficult to analyze. Noise sources include: 1) higher water content increases the signal from the membranes, which registers as noise since the membranes remain unresolved. 2) The extra flow in the membranes creates ghosts in the images due to phase errors. 3) The weak signal from the Plateau borders is averaged over a large voxel volume. To understand the relative importance of each noise source and to find an effective way to eliminate or reduce it, we conducted several series of experiments with solid gelatin-based foams. We make the foam from a heated gelatin-water solution and cool it immediately after foam generation.

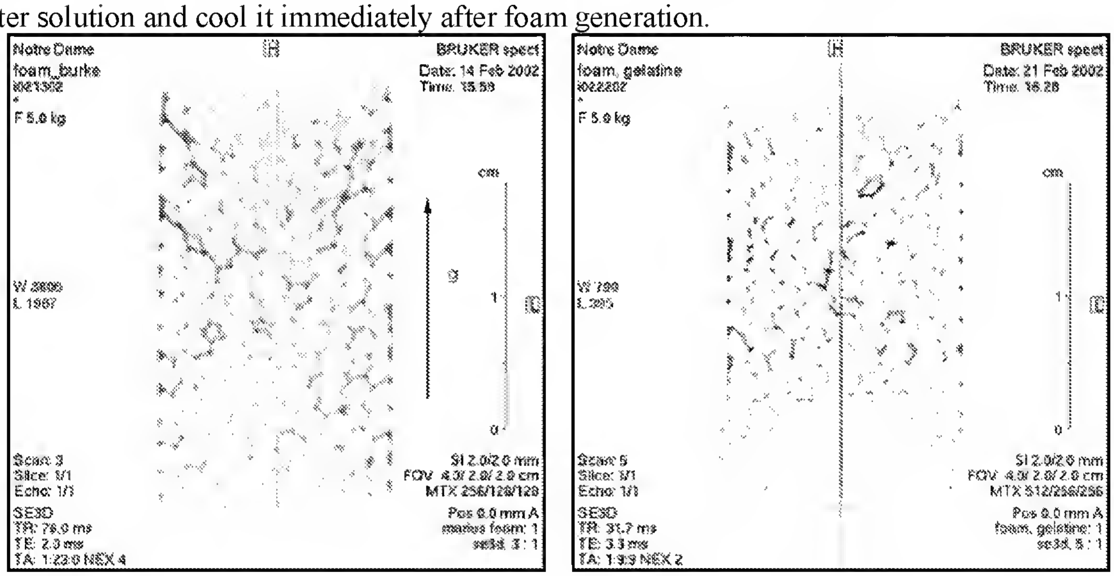

Then we image the resulting motionless foam using various imaging parameters. Figure 1a shows a sample central slice from a 256x128x128 MRI image. Some noise is still present, especially in the central part, where Plateau borders are thinner, suggesting that "partial volume" artifact is important. The 512x256x256 image of the same foam in Figure 1b has twice the spatial resolution (below 100 μm, which is below the Plateau border thickness) and is completely noise-free. We will use such clean images as real test data for our 3D data analysis algorithm.

Another interesting phenomenon in images of solidified foams (especially apparent in Figure 1a) is the presence of "lines" of increased gelatin content, inclined at about 45° from the vertical and directed from the tube axis to the wall. They seem to appear during solidification of the

gelatin and are related to the stress distribution in the solidifying foam. In liquid foams, we never see anything similar. Examining this effect in more detail may be important for solid foam production.

"Stabilized" foams are convectively unstable if the flow rate exceeds some critical value. We have carried out extensive experimental studies of these instabilities to avoid convection during MRI imaging. CMC-water solutions with different CMC concentrations and different surfactants were used as basic fluids. Foam was generated in a glass cylinder 50 cm long with an inner diameter of 45 mm. After foam equilibration, we increased the flow rate slowly in small increments until the foam began to move. We define the critical flow rate as the flow rate at which global convection, which affects every bubble, starts. The critical flow drops very fast with increasing viscosity, and remains almost constant when viscosity is higher than about 8 cPoise. It is almost independent of the chemical composition of the surfactant. Figure 2 shows the critical flow rate data. While the physical mechanism of these instabilities remains unclear, the most surprising result was our detection of a compression wave that precedes a melting wave. Foam melting occurs at a local wetness level well below the expected 35%. The flow through membranes is significant, not negligible.

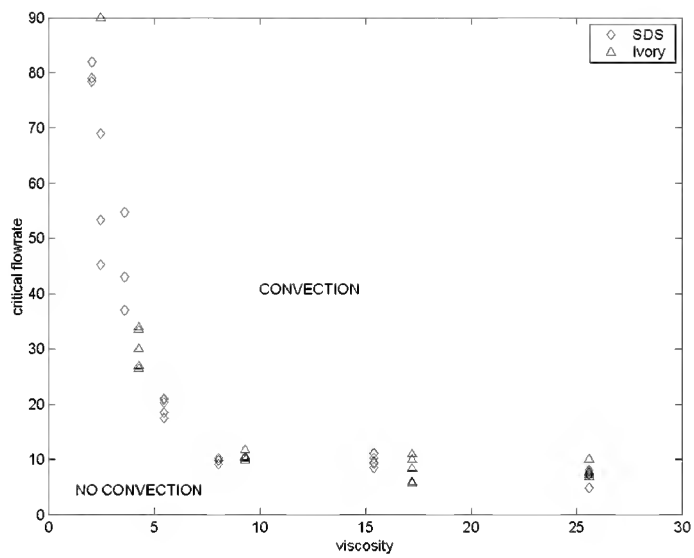

This convective instability may seriously affect our proposed scenario for the aging of "space foam." Our preliminary analysis of experimental data suggests that there are two critical parameters – the membrane thickness (which directly relates to the local foam wetness) and the shear rate (specified by the basic fluid viscosity, bubble size and transverse fluctuations in pressure) determining the instability onset. During the aging of "space foam," we expect both average bubble size and membrane thickness to increase. Hence, at some stage, the pressure fluctuations (caused, for example, by bubble disappearance) may induce global convection. The latter, in turn, should affect the bubble size distribution in a way similar to that observed in our earth-based experiments: strong convection leads to very homogeneous foam.

PI: Prof. James A. Glazier, 225 Nieuwland Science Hall, Department of Physics, University of Notre Dame, In 46556, email: jglazier@rameau.phys.nd.edu, fax: (574)-631-5952, phone: (574)-631-4010

KINETICS AND PERCOLATION IN DENSE PARTICULATE SYSTEMS

Chris Sorensen and Amit Chakrabarti
Department of Physics, Kansas State University, Manhattan, KS 66506-2601

ABSTRACT

Our work involves both experimentation and simulation of aggregating particle systems that form fractal aggregates that eventually fill space to form gels. Our experimental system is soot in diffusion flames. Our simulations model these flames as 3d, off lattice, Brownian motion systems, also known as diffusion limited cluster aggregation (DLCA). We observe in these systems the behavior of the kinetics, cluster size distribution, and cluster morphology as the system evolves from dilute to concentrated and finally to the gel.

With simulations, we find that the dynamical evolution of the system obeys typical DLCA type kinetics at early times when the system is dilute with a constant kinetic exponent z=1 and size distribution exponent λ=0. With increasing aggregation time crowding of clusters occurs and the kinetics can be described by continuously evolving exponents. Both exponents show universal behavior with aggregate volume fraction, independent of the initial volume fraction. Remarkably, the relationship between z and λ maintains it's mean-field nature i.e., mean field kinetics continue to hold when the system is crowded.

Small angle light scattering from heavily sooting flames shows submicron $D \simeq 1.8$ fractal aggregates early in the flame but later, as the soot growth continues, a new supermicron phase appears with a fractal dimension of ca. 2.7. Simulations show essentially the same behavior and allow us to determine that these superaggregates occur when the smaller, $D \simeq 1.8$ DLCA aggregates percolate. With this, we propose the following picture of the sol-to-gel transition: A dilute sol aggregates via DLCA or RLCA kinetics yielding aggregates with fractal dimensions of $D \simeq 1.8$ or 2.15, respectively. Because these aggregate fractal dimensions are less than the spatial dimension, the effective aggregate volume fraction (the occupied volume of the aggregates normalized by the system volume) approaches unity as the aggregation proceeds. Structure factor results for the largest cluster and the entire system imply that the fractal dimension of the aggregates remains 1.8 (or 2.15 for RLCA) right up to the ideal gel point. At the ideal gel point, the aggregates are so crowded that they percolate to form a $D \simeq 2.6$ *superaggregate* made up of $D \simeq 1.8$ (or 2.15 for RLCA) aggregates with an average size of $R_{g,G}$, the ideal gel point radius of gyration.

LOCAL PERTURBATIONS OF JAMMED COLLOIDS

Eric R. Weeks*, Piotr Habdas, David Schaar, and Andrew C. Levitt
Physics Department, Emory University, Atlanta, GA 30322

ABSTRACT

We use confocal microscopy to directly study the microscopic behavior of colloidal glasses and colloidal supercooled liquids. In particular we embed superparamagnetic particles into the system of non-magnetic PMMA colloids and then exert an external magnetic force on these particles to locally perturb the sample in a controlled manner. We investigate the range of these perturbations as a function of magnetic particle size, magnetic force, and colloidal particle concentration, in samples approaching the colloidal glass transition. The results of such studies address broader issues of both a universal description of the origin of the glass transition and also the flow of granular media studied by other groups.

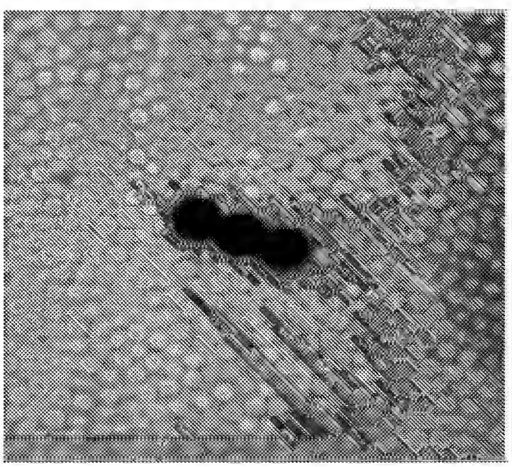

Three superparamagnetic particles stuck together, embedded in a sample of 2 micron diameter colloidal particles. The magnetic chain is rotated using an external magnetic field, and the motion of the other particles is examined. In these pictures, the chain is rotating at 1.25 rev/hr.

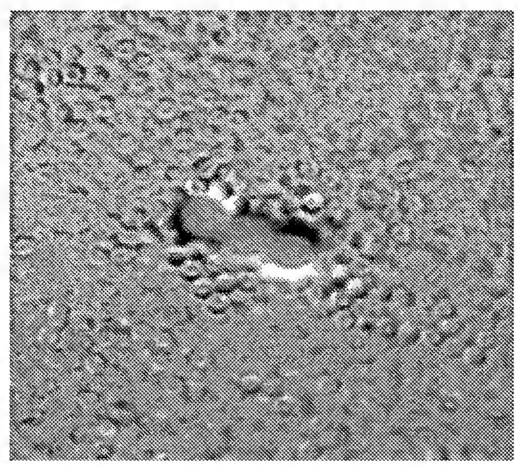

Two images are taken 1 min apart, and subtracted. Black or white regions indicate where the two pictures differ, highlighting the regions where particles are moving.

Movies can be seen at:
http://www.physics.emory.edu/~weeks/lab/

* weeks@physics.emory.edu, phone: 404-727-4479, fax: 404-727-0873

Exposition Session
Topical Area 2:
Fluid Physics of Interfaces

INSTABILITY OF MISCIBLE INTERFACES

R. Balasubramaniam, N. Rashidnia, M.J. Boggess, R.T. Schroer
National Center for Microgravity Research on Fluids and Combustion,
NASA Glenn Research Center, Cleveland, Ohio,
T. Maxworthy
University of Southern California, Los Angeles,
and
R.G. Wilson and J.I.D. Alexander
Case Western Reserve University, Cleveland, Ohio

Abstract

The dynamics of miscible displacements in a cylindrical tube is being studied experimentally and numerically, specifically when a more viscous fluid displaces a less viscous fluid. In the converse situation where a less viscous fluid displaces a more viscous fluid, a fingering instability is known to occur (Petitjeans and Maxworthy, 1996), and a flight experiment proposed by Maxworthy and Meiburg to investigate the interface dynamics in this case is currently being developed by NASA.

From the current theory of miscible displacements, developed for a porous medium satisfying Darcy's law (see review by Homsy, 1987), it can be shown that in the absence of gravity the interface between the fluids is destabilized and thus susceptible to fingering only when a more viscous fluid is displaced by a less viscous one. Therefore, the initial flat interface in the displacement of a less viscous fluid by a more viscous one ought to be stable. However, numerical simulations by Chen and Meiburg (1996) for such displacement in a cylindrical tube show that for a viscosity ratio equal to e, a finger of the more viscous fluid is indeed formed. These calculations were restricted to axisymmetric solutions of the Stokes equations that are valid for negligible values of the Reynolds number.

We report on the experiments that we have conducted to date when a more viscous fluid displaces a less viscous one in a vertical cylindrical tube. The experiments show that not only can a finger form in this instance but also that under certain conditions the advancing finger achieves a sinuous or snake-like spatial pattern. These experiments were performed using silicone oils in a vertical pipette of small diameter. The more viscous fluid also has a slightly larger density than the less viscous fluid. In the initial configuration, the fluids were under rest, and the interface was nominally flat. Both stably and unstably stratified initial configurations were studied. A dye was added to the more viscous fluid for ease of observation of the interface between the fluids. The flow was initiated by pumping the more viscous fluid into the less viscous one. The displacement velocity was such that the Reynolds number is small compared to one, and the Peclet number for mass transfer among the fluids is large compared to one. The gravitational effects are represented by the dimensionless parameter $F = \frac{g\Delta\rho d^2}{\mu U}$ where g is the acceleration due to gravity, $\Delta\rho$ is the density difference between the fluids, d is the tube diameter, μ is the viscosity of the more viscous fluid, and U is the displacement speed.

For the downward displacement of a more viscous fluid resting on the top of a less viscous fluid (*i.e.* an unstably stratified initial configuration), the experiments show that an axisymmetric finger is formed when the value of F is smaller than a critical value F_c. When $F > F_c$, the finger achieves a sinuous spatial pattern. The spatial pattern is not a helical three dimensional pattern, and appears to be two dimensional. Experiments are in progress to obtain F_c as a function of the viscosity ratio of the fluids.

For an upward displacement of the more viscous fluid from an initially stable configuration, only an axisymmetric finger is observed under all conditions. When F is small, the effect of gravity is small and the shape of the finger is qualitatively similar to that observed for downward displacement. For a larger value of F, the finger has a blunt shape. However, a needle shaped spike is seen to propagate from the main finger, similar to that observed by Petitjeans and Maxworthy (1996).

Numerical simulations of the miscible displacement process, starting from an initially flat interface, are in progress. The goal is to identify the conditions when the interface achieves a sinuous shape. When such a shape is computed, we will compare the onset condition and the post onset wavelength to experimental results. The computations will involve time accurate three dimensional simulations of the momentum and mass transport equations. Joseph and Renardy (1993) show that, in general, one must consider the following effects in the mixing region (i) a non-vanishing of the divergence of the velocity field caused by density changes of a fluid element due to diffusion (ii) Korteweg stresses, which accounts for forces in the fluids caused by concentration gradients. We will perform computations without and with these effects, for various values of the system parameters, chiefly the F parameter, the viscosity and density ratio, the Peclet number for mass transport and non-dimensional parameters associated with the Korteweg stresses. The Reynolds number will be small compared to one; however, we will retain the non-linear inertial terms in the momentum equations recognizing that they might be important in predicting the complex interface shapes.

References

Chen, C.H. and Meiburg, E. 1996. Miscible displacements in capillary tubes. Part 2. Numerical simulations. *J. Fluid Mech.,* **326**, 57-90.

Homsy, G.M. 1987 Viscous fingering in porous media. *Ann. Rev. Fluid Mech.,* **19**, 271.

Joseph, D.D. and Renardy, Y. 1993. Fundamentals of Two-Fluid Dynamics. Springer-Verlag.

Petitjeans, P. and Maxworthy, T. 1996. Miscible displacements in capillary tubes. Part 1. Experiments. *J. Fluid Mech.,* **326**, 37-56.

INSTABILITY OF MISCIBLE INTERFACES

R. Balasubramaniam, N. Rashidnia, R.T. Schroer

National Center for Microgravity Research on Fluids and Combustion,
NASA Glenn Research Center, Cleveland, Ohio

and

T. Maxworthy
University of Southern California, Los Angeles

Sixth Microgravity Fluid Physics and Transport Phenomena Conference, Cleveland, Ohio, August, 2002.

Objectives

Study the dynamics of miscible displacements experimentally and numerically

- in a cylindrical tube
- more viscous fluid displaces a less viscous fluid
- by numerical simulations, evaluate effects of (i) non-vanishing velocity divergence in the mixing region (ii) fluidstresses due to concentration gradients (Korteweg stresses)

Motivation

• Current theory (see Homsy, 1987) developed for Hele-Shaw flows (or a porous medium satisfying Darcy's law) shows that the interface is destabilized only when a less viscous fluid displaces a more viscous fluid. However, 3D effects are not included and the shape of the interface within the gap of the Hele-Shaw cell is unknown.

• Numerical simulations (axisymmetric) by Chen and Meiburg (1996) shows that for the displacement of a less viscous fluid by a more viscous one, a finger of the more viscous fluid is indeed formed.

• Our preliminary experiments have shown that not only can fingering occur when a more viscous fluid displaces a less viscous one in a cylindrical tube, but also that under certain conditions the advancing finger achieves a sinuous spatial pattern.

Experiments

- Silicone oils of various viscosites were used as the experimental fluids in vertical pipettes of diameter 1 and 3 mm. Dye was added to the upper fluid for observing the interface.

- The tube was surrounded by a square tube, and the interveing space was filled with the less viscous silicone oil, so that optical distortions are minimal.

- The flow was initiated by pumping from a syringe that is driven by a precisely controlled actuator.

- Experiments with both upward displacement and downward displacement were performed.

Experimental Results

- For downward displacement, for which the density stratification is unstable, a stable axisymmetric finger(Figure 1) as well as a finger with a sinuous shape have been observed (Figure 2).

- For upward displacement, for which the density stratificationis stable, a stable axisymmetric finger and an axisymmetric fingerwith a spike that forms from the main finger have been observed (Figure 3 and Figure 4).

- We therefore conclude that the unstable fingers with a sinuous shape are caused by a Rayleigh - Taylor instability. Figure 5 shows the instability in the absence of any displacement in the tube.

- Figure 6 shows a stability map for the transition between stable axisymmetric fingers and sinuous fingers for downward displacement, in which the dimensionless gravity parameter $F = \frac{g\Delta\rho d^2}{\mu U}$ is plotted versus the viscosity ratio. A similar stability map for the transition between stable axisymmetric fingers and fingers with spikes for upward displacement is in progress.

References

Homsy, G.M. 1987 Viscous fingering in porous media. *Ann. Rev. Fluid Mech.,* **19**, 271.

Chen, C.H. and Meiburg, E. 1996. Miscible displacements in capillary tubes. Part 2. Numerical simulations. *J. Fluid Mech.,* **326**, 57-90.

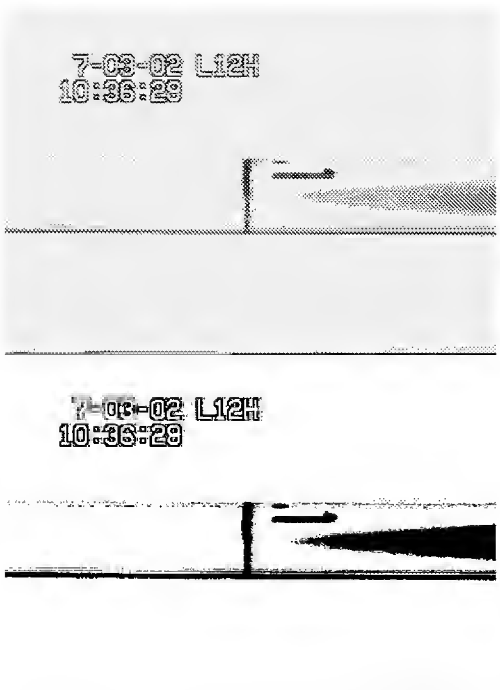

Figure 1
Stable Finger: 1000/500, V = 20 microns/s

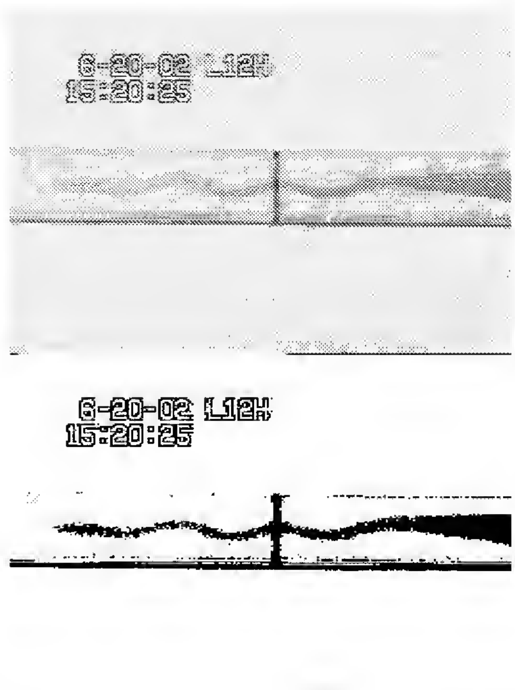

Figure 2
Sinusoidal Finger: 1000/50, V = 50 microns/s

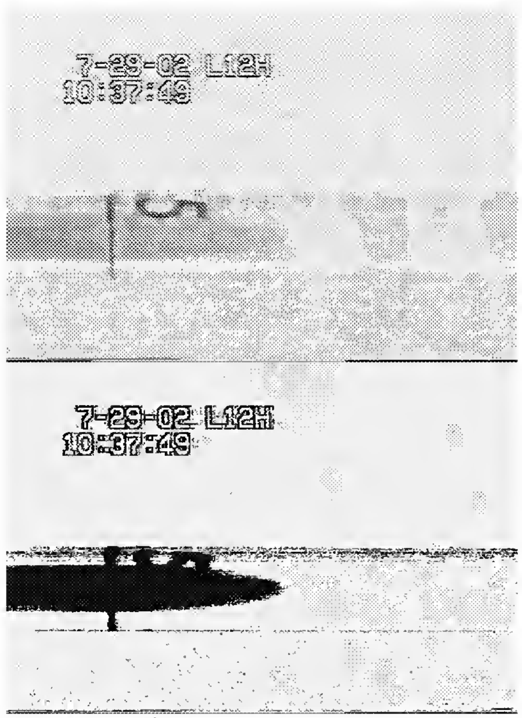

Figure 3
Axisymmetric Finger: 100/1000, V = 100 microns/s

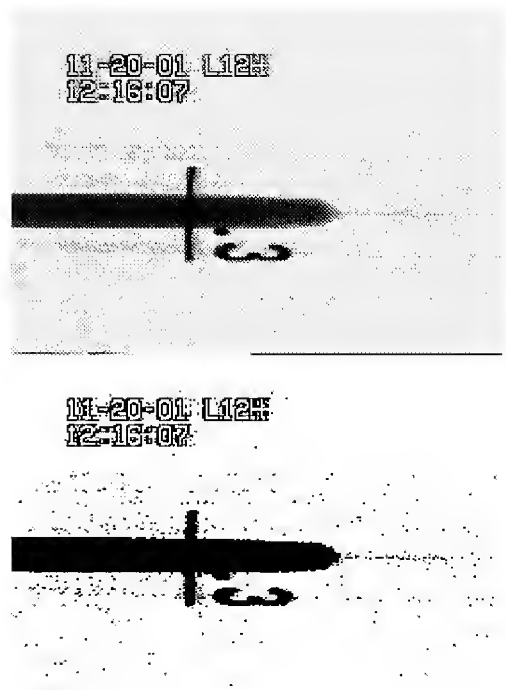

Figure 4
Spike: 100/1000, V = 20 microns/s

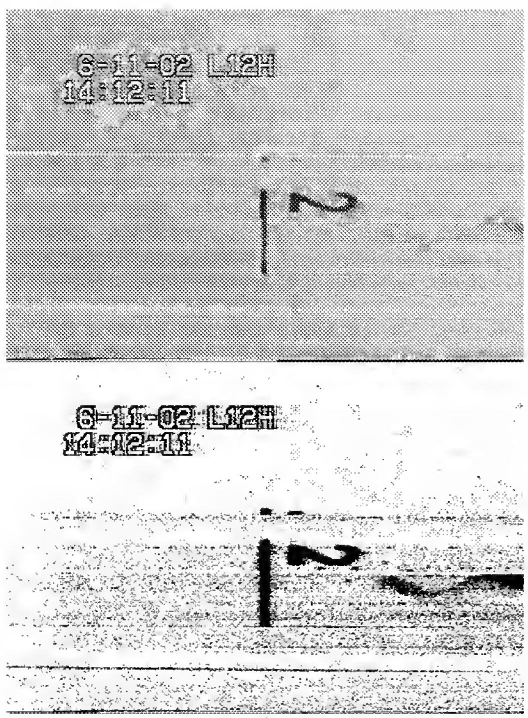

Figure 5
Sinusoidal Finger: 10000/1000, V = 0 microns/s

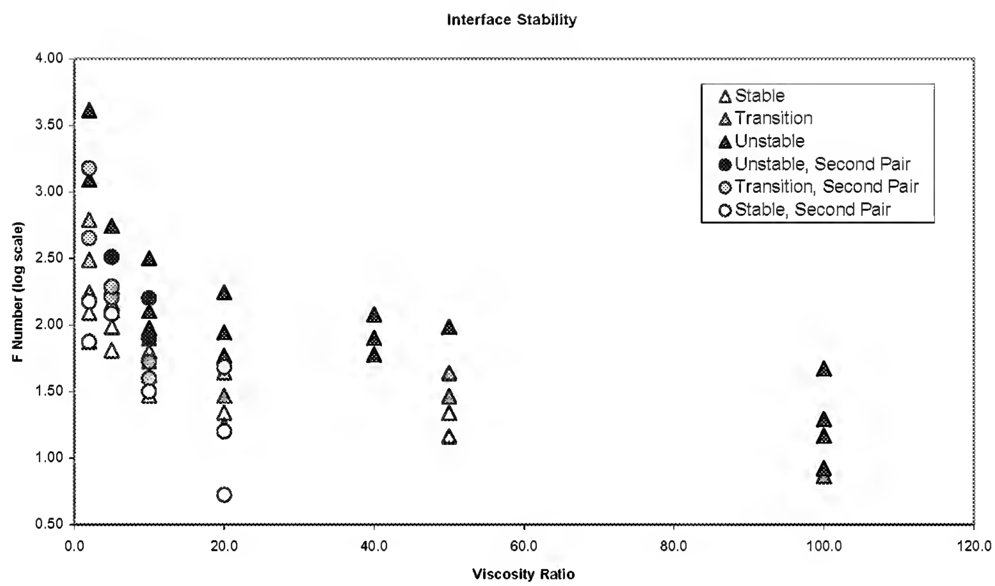

Figure 6
F vs. M Stability Map

The effect of flow on drop coalescence

Martin Nemer,[1] Xiaohui Chen,[1] Jerzy Bławzdziewicz,[2] and Michael Loewenberg[1]

[1] *Chemical Engineering, Yale University, New Haven, CT 06520*

[2] *Mechanical Engineering, Yale University, New Haven, CT 06520*

Drop coalescence is a complex process due to the nonlinear dynamics of a system with deformable interfaces. In earlier studies the effect of an external flow on near-contact motion of drops was assumed to be equivalent to an external body force [1–3]. Accordingly, the direct coupling between thin-film flow (in the near-contact region) and flow inside the drops was neglected. These assumptions have been used in calculations of collisional efficiencies [4] and analyses of experimental results [5–7].

Our investigations show that for drops with tangentially mobile interfaces the above assumptions do not hold. The velocity field produced inside the drops by the external flow couples to the film motion through tangential stress f_∞ acting on the film interface. For sufficiently thin films (e.g., long times), this stress qualitatively alters the dynamics of the lubrication region by arresting or enhancing film drainage.

Scaling analysis The effect of an external flow on drop motion can be understood by considering the magnitude of the stress f_∞. The external flow varies on the length scale of the drop diameter a and vanishes at the axis of symmetry of the film, thus

$$f_\infty \sim \mu\dot{\gamma}r_\infty/a. \tag{1}$$

Here μ is the drop viscosity, r_∞ is the lateral dimension of the thin film, and $\dot{\gamma}$ is the magnitude of the external flow. For given external flow and force, the pressure gradient in the film p' and lateral dimension r_∞ are nearly independent of film thickness h. It thus follows that

$$f_\infty \sim hp' \tag{2}$$

for sufficiently small h. Hence, external-flow-induced stress f_∞ affects the thin film behavior.

Numerical results These predictions are illustrated in Fig. 1, where results form axisymmetric boundary-integral simulations are shown for two drops with a constant interfacial tension σ. The drops are immersed in an external creeping flow field $\mathbf{u}_{\dot{\gamma}} = \dot{\gamma}(\frac{1}{2}r\hat{\mathbf{e}}_r - z\hat{\mathbf{e}}_z)$ or subjected to body forces $\mathbf{F}_i^{\mathrm{e}} = F_i^{\mathrm{e}}\hat{\mathbf{e}}_z$, where $i = 1, 2$.

For drops in straining flow, the flow-induced stress f_∞ is directed toward the symmetry axis; in this case, at long times a stationary film profile is attained. For drop motion driven by the external forces, f_∞ is directed away from the symmetry axis, and the film drains exponentially with time. In contrast to the above results, in the absence of flow-induced stresses ($f_\infty = 0$) the film has algebraic long-time behavior [8].

Asymptotic analysis For sufficiently weak external flow and force, drops are nearly spherical (except in the near-contact region), and the extent of the thin film is small. In this regime, the hydrodynamic forces F_i^{H} acting on the drops and the interfacial stress f_∞ were calculated by solving the outer problem of two tangential spherical drops in an external flow. The lubrication equations for the inner thin-film region, with boundary conditions

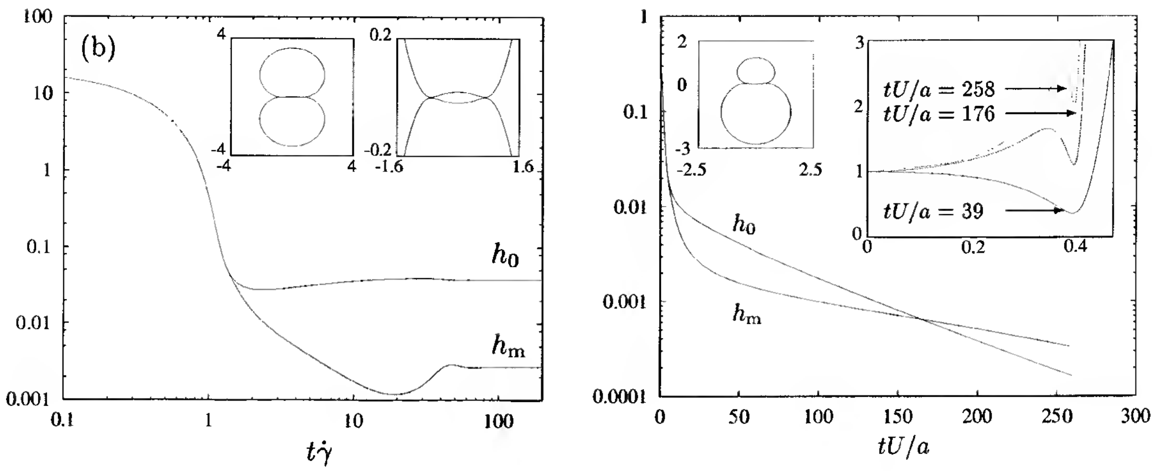

FIG. 1: Central and minimal gap versus time for (a) equal-size drops in straining flow with $\bar{\dot{\gamma}} = 0.02$ and no body force, and (b) drops with size ratio $k = 2$, driven by body forces $\bar{F}_1^e = \frac{1}{3}\pi$, $\bar{F}_2^e = \frac{4}{3}\pi$, and no external flow. Here $\bar{\dot{\gamma}} = \mu\dot{\gamma}a/\sigma$ and $\bar{F}_i^e = F_i^e/(\sigma a)$.

corresponding to the values of F_i^{H} and f_∞ calculated as described above, were solved by a matched-asymptotics method to obtain the long time stationary film profile. For two drops pushed together by an external flow, our asymptotic solution yields

$$h_0 \sim \bar{\dot{\gamma}}^{3/2}, \qquad h_{\mathrm{m}} \sim \bar{\dot{\gamma}}^3 \tag{3}$$

for the central and minimal stationary gaps.

Conclusions We have shown that external flow can arrest or enhance drainage of a thin film separating drops in near-contact motion. The effect of flow remains finite even for small capillary numbers, provided that the film thickness is sufficiently small. Therefore, this effect needs to be included in predictions of collisional efficiencies and interpretation of experimental data. Our analysis is also applicable to thin-film flows that involve Marangoni or thermocapillary stresses.

[1] A. F. Jones and S. D. R. Wilson, J. Fluid Mech. **87**, 263 (1978).
[2] S. G. Yiantsios and R. H. Davis, J. Colloid Interface Sci. **144**, 412 (1991).
[3] A. Saboni, C. Gourdon, and A. K. Chesters, J. Colloid Interface Sci. **175**, 27 (1995).
[4] M. A. Rother, A. Z. Zinchenko, and R. H. Davis, J. Fluid Mech. **346**, 117 (1997).
[5] X. Zhang, R. H. Davis, and M. F. Ruth, J. Fluid Mech. **249**, 227 (1993).
[6] M. Magna and H. A. Stone, J. Fluid Mech. **300**, 231 (1995).
[7] H. Yang, C. C. Park, Y. T. Hu, and L. G. Leal, Phys. Fluids **13**, 1087 (2001).
[8] M. B. Nemer, X. Chen, J. Bławzdziewicz, and M. Loewenberg, Bull. Am. Phys. Soc. **46**, 140 (2001).

Summary

We analyze drainage of a thin liquid film that separates two surfactant-free drops pressed together by external forces or flow. It is shown that the far-field tangential stress generated in the near-contact region by an outer flow qualitatively affects the film drainage dynamics. If this stress acts radially outward, exponential film drainage occurs. For a radially inward stress, film drainage is arrested at long times. The current theoretical models neglect the far-field stress and thus yield qualitatively incorrect predictions.

Drops in external flow

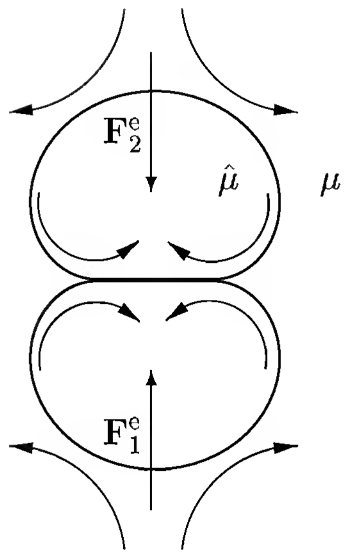

$$\mathbf{F}_i^{\mathrm{e}} = F_i^{\mathrm{e}} \hat{\mathbf{e}}_z, \qquad i = 1, 2$$

$$\mathbf{u}_{\dot{\gamma}} = \dot{\gamma}(\tfrac{1}{2} r \hat{\mathbf{e}}_r - z \hat{\mathbf{e}}_z)$$

Dimensionless parameters

$$\bar{F}_i^{\mathrm{e}} = F_i^{\mathrm{e}} / (\sigma a)$$

$$\bar{\dot{\gamma}} = \mu \dot{\gamma} a / \sigma$$

constant interfacial tension σ

thin film region

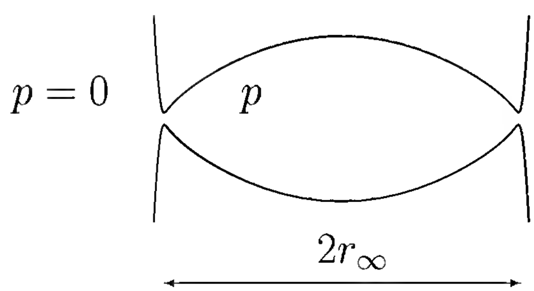

$$F_{\mathrm{c}} \simeq \pi r_\infty^2 p$$

$$p \simeq 2\sigma / a$$

Current models

flow $\quad \Longleftrightarrow \quad$ force $\qquad\qquad$ <u>*INCORRECT*</u>

Flow-induced traction

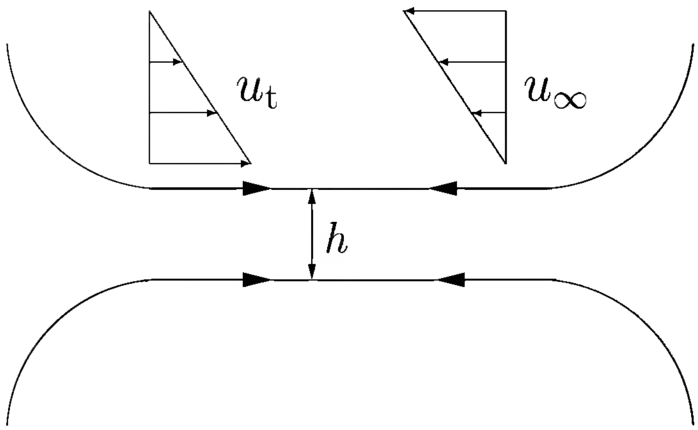

$$u = u_t + u_\infty$$

$$\Downarrow$$

$$f = f_t + f_\infty$$

$$f_t \sim \hat{\mu}\frac{u_t}{r_\infty} \qquad \text{local traction}$$

$$f_\infty \sim \hat{\mu}\dot{\gamma}_0 \qquad \text{far-field traction}$$

Stress balance

$$f \sim \frac{\Delta p}{r_\infty} h$$

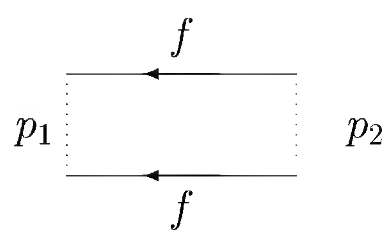

$$\Downarrow$$

$$f \sim f_\infty \qquad \text{for} \qquad h \sim \frac{\hat{\mu}\dot{\gamma}_0 a}{\sigma} r_\infty$$

Boundary-integral simulations

Film thickness at center h_0 and minimum h_{m}

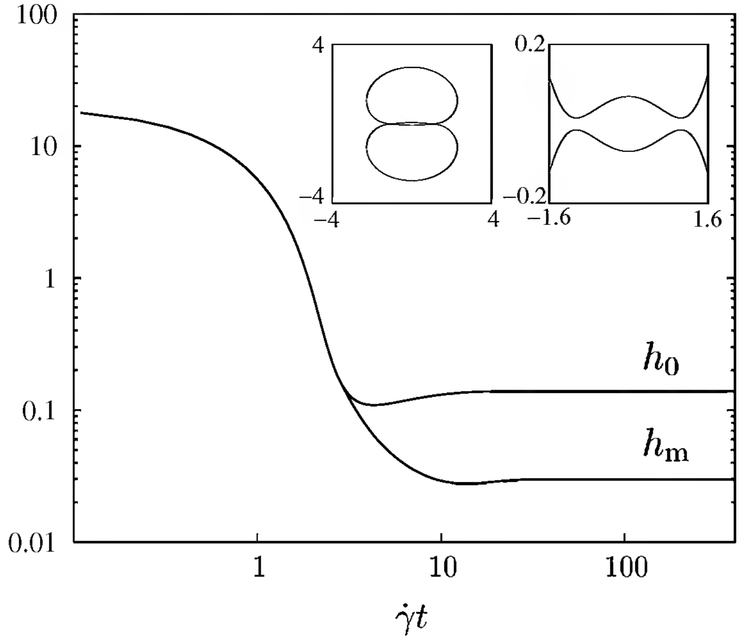

f_∞ inward

Fig. 1: Axisymmetric compressional flow with $\dot{\bar{\gamma}} = 0.05$.

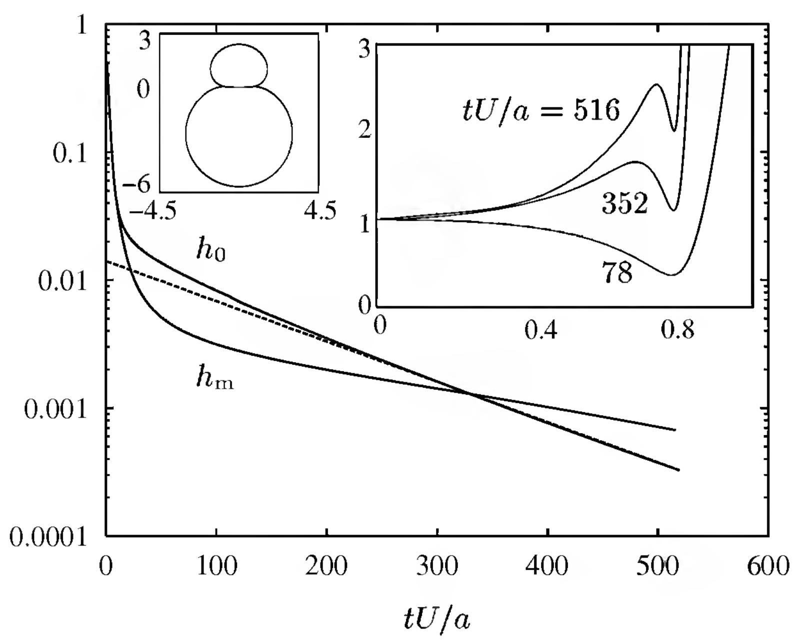

f_∞ outward

Fig. 2: Buoyancy motion with $\bar{F}_1^e = 4\pi$, $\bar{F}_2^e = \frac{1}{2}\pi$.

Stationary film thickness for $\dot{\bar{\gamma}} \ll 1$

Outer problem—tangent spheres

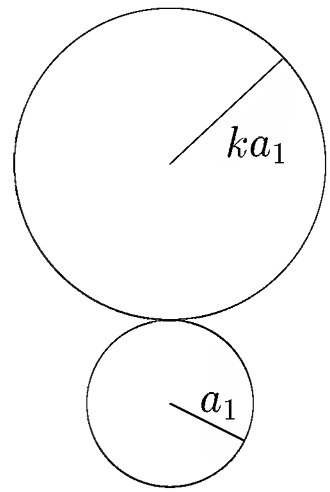

Resistance relation

$$F_{\pm}^{\mathrm{H}} = R_{\pm\bar{U}}\bar{U} + R_{\pm\dot{\bar{\gamma}}}\dot{\bar{\gamma}},$$

Force balance

$$F_{+}^{\mathrm{e}} + \bar{F}_{+}^{\mathrm{H}} = 0, \qquad \text{total}$$

$$F_{-}^{\mathrm{e}} + \bar{F}_{-}^{\mathrm{H}} = 2F_{\mathrm{c}}, \qquad \text{relative}$$

where $F_{\pm} = F_1 \pm F_2$.

Far-field stress

$$f_{\infty} = -rS, \qquad r\lambda \ll 1,$$

$$\lambda^{-1}S = \frac{(k-1)k}{4(1+k)^3}\bar{U} + \frac{4k-1-k^2}{2(1+k)^2}\dot{\bar{\gamma}}.$$

Inner problem

Stationary film equations

$$p = 1 - r^{-1} \left(r h'\right)' / 2$$

$$h p' = -2 r S$$

boundary conditions

$$h'(0) = 0, \qquad \lim_{r \to \infty} p(r) = 0$$

$$F_{\mathrm{c}} = 2\pi \int_0^\infty p r \mathrm{d} r$$

Dome Region

$$\bar{h}[\bar{r}^{-1}(\bar{r}\bar{h}')']' = B\bar{r} \qquad \text{film equation}$$

$$\bar{h}(0) = 1, \quad \bar{h}'(0) = 0, \quad \bar{h}'(1) = 0 \qquad \text{boundary conditions}$$

where

$$\bar{h} = h/h_0, \qquad \bar{r} = r/r_{\mathrm{m}}$$

$$B = 4 h_0^{-2} r_{\mathrm{m}}^4 S.$$

$$r_{\mathrm{m}} \simeq r_\infty = (F_{\mathrm{c}}/\pi)^{1/2}$$

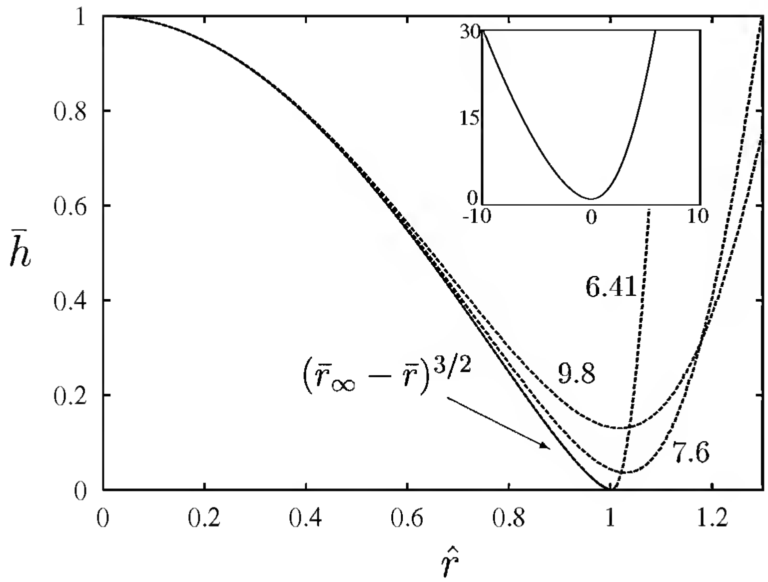

Fig. 3: Dome shapes for $B > B^*$ (dotted curves) and $B = B^*$ (solid curve); rim shape for $Q = Q^*$ (inset). Radial coordinate $\hat{r}$ is rescaled to match $\bar{h}''(0)$ for all values of B.

critical dome

$$B \to B^* = 6.39 \qquad \Longrightarrow \qquad h_{\mathrm{m}} \to 0$$

asymptotic solution

$$h(r) = h_0 \bar{h}^*(\bar{r}),$$

with

$$\bar{h}^*(\bar{r}) = \lim_{B \to B^*} \bar{h}(\bar{r}) \qquad \text{film profile}$$

$$h_0 = 2(\pi^2 B^*)^{-1/2} F_{\mathrm{c}} S^{1/2} \qquad \text{center thickness}$$

Rim region

$$\tilde{H}'''\tilde{H} = Q, \qquad \text{film equation}$$

$$\tilde{H}(0) = 1, \quad \tilde{H}'(0) = 0, \quad \lim_{\tilde{x}\to\infty} \tilde{H}''(\tilde{x}) = 2 \qquad \text{boundary conditions}$$

where

$$\tilde{H} = h/h_{\mathrm{m}} \quad \tilde{x} = (r - r_{\mathrm{m}})/h_{\mathrm{m}}^{1/2}$$

$$Q = 4h_{\mathrm{m}}^{-1/2} r_m S$$

matching conditions

$$\bar{h}^*(1+\bar{x}) = (\tfrac{8}{3}B^*)^{1/2}(-\bar{x})^{3/2}, \qquad \bar{x} \to 0^-$$

$$\Downarrow$$

$$\tilde{H}^*(\tilde{x}) = (\tfrac{8}{3}Q^*)^{1/2}(-\tilde{x})^{3/2}, \quad \tilde{x} \to -\infty$$

$$Q \to Q^* = 0.439$$

asymptotic solution

$$h(r) = h_{\mathrm{m}}\tilde{H}^*(\tilde{x})$$

with

$$\tilde{H}^*(\tilde{x}) = \lim_{Q\to Q^*} \tilde{H}(\tilde{x}) \qquad \text{film profile}$$

$$h_{\mathrm{m}} = 16(\pi^{1/2}Q^*)^{-2}S^2F_{\mathrm{c}} \qquad \text{center thickness}$$

Comparison with simulations

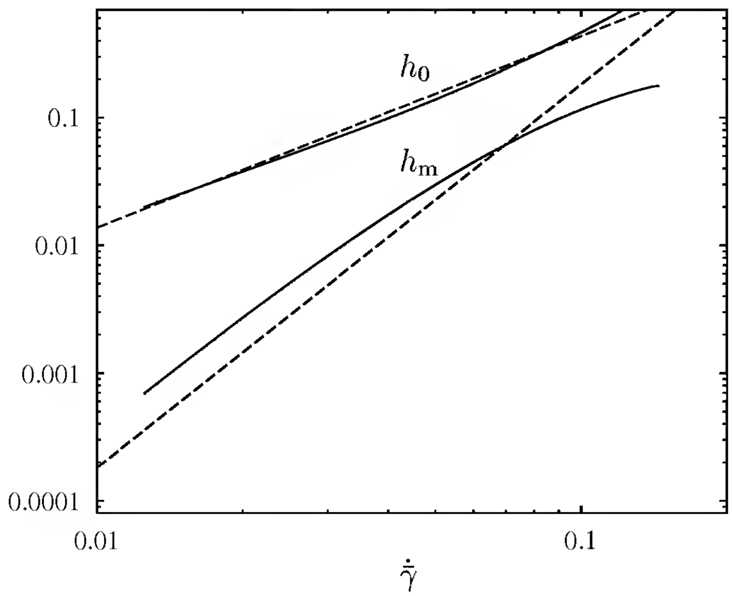

Fig. 4: Stationary center and minimum film thickness for equal-size drops in straining flow. Numerical simulations (solid lines); asymptotic results (dashed lines).

Van der Waals attraction

Modified rim equation

$$\tilde{H}\tilde{H}''' = Q^* - \tilde{A}\tilde{H}'\tilde{H}^{-3},$$

where

$$\tilde{A} = 4^{-6}\pi^2(Q^*)^6\sigma^{-1}a^{-2}AS^{-6}F_{\mathrm{c}}^{-3}$$ Hamaker constant A

Stable solution

$$\tilde{A} < \tilde{A}_{\mathrm{crit}}$$

$$\tilde{A}_{\mathrm{crit}} = 1.49$$

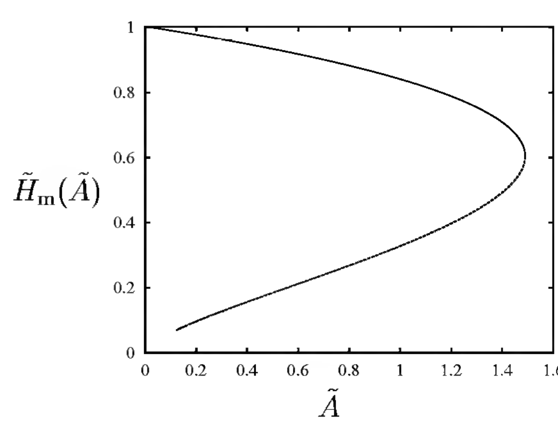

Dynamics of Surfactant-Laden Drops in a Hele-Shaw Cell

Nivedita R. Gupta[1], Ali Nadim[2], Hossein Haj-Hariri[3], Ali Borhan[4]

[1]Dept. of Chem. Eng., Univ. of New Hampshire, Durham, NH 03824
[2]Keck Graduate Inst. & Claremont Graduate Univ., Claremont, CA 91711
[3]Dept. of Mech. Eng., Univ. of Virginia, Charlottesville, VA 22903
[4]Dept. of Chem. Eng., Pennsylvania State Univ., University Park, PA 16802

Buoyancy-driven motion of a liquid drop in a Hele-Shaw cell filled with a second immiscible liquid is considered. In the absence of surfactants, a circle is an exact solution to the depth-averaged Hele-Shaw equations. A circular drop is shown to be linearly stable to infinitesimal shape perturbations provided the interfacial tension is finite. The evolution of the shape of a translating drop subject to finite initial shape deformations is studied by using the boundary integral method to solve the Hele-Shaw equations. Drops that are initially elongated in the direction of motion are found to revert to a circular shape for all Bond numbers considered. The stability of the shape of drops that are initially flattened (elongated normal to the direction of motion) depends on the extent of their initial deformation and the Bond number. Experimental observations of transient drop shapes show good qualitative agreement with the numerical predictions for both symmetric and asymmetric initial shape perturbations. In the presence of adsorbed surfactants, the interface separating the drop from the continuous liquid phase possesses its own distinct rheological properties. As the drop moves, the adsorbed surfactants are constantly redistributed along the interface by advection and diffusion, and give rise to non-uniformities in interfacial tension along the interface. This, in turn, affects the movement of the drop and its shape evolution. Dynamics of translating drops in the presence of bulk-insoluble surfactants are examined using the Langmuir adsorption framework in conjunction with a slip layer model derived for the depth-averaged tangential stress exerted on the two-phase interface. Given the initial shape of the drop and the buoyancy force acting on it, the interfacial distributions of velocity and surfactant concentration are computed, and the evolution of the drop shape is followed in time in order to identify the effect of interface contamination on the critical conditions for drop breakup.

DYNAMICS OF SURFACTANT-LADEN DROPS IN A HELE-SHAW CELL

Nivedita R. Gupta
University of New Hampshire, Durham, NH

Ali Nadim
Keck Graduate Institute, Claremont, CA

Hossein Haj-Hariri
University of Virginia, Charlottesville, VA

Ali Borhan
Pennsylvania State University, University Park, PA

BUOYANCY-DRIVEN MOTION

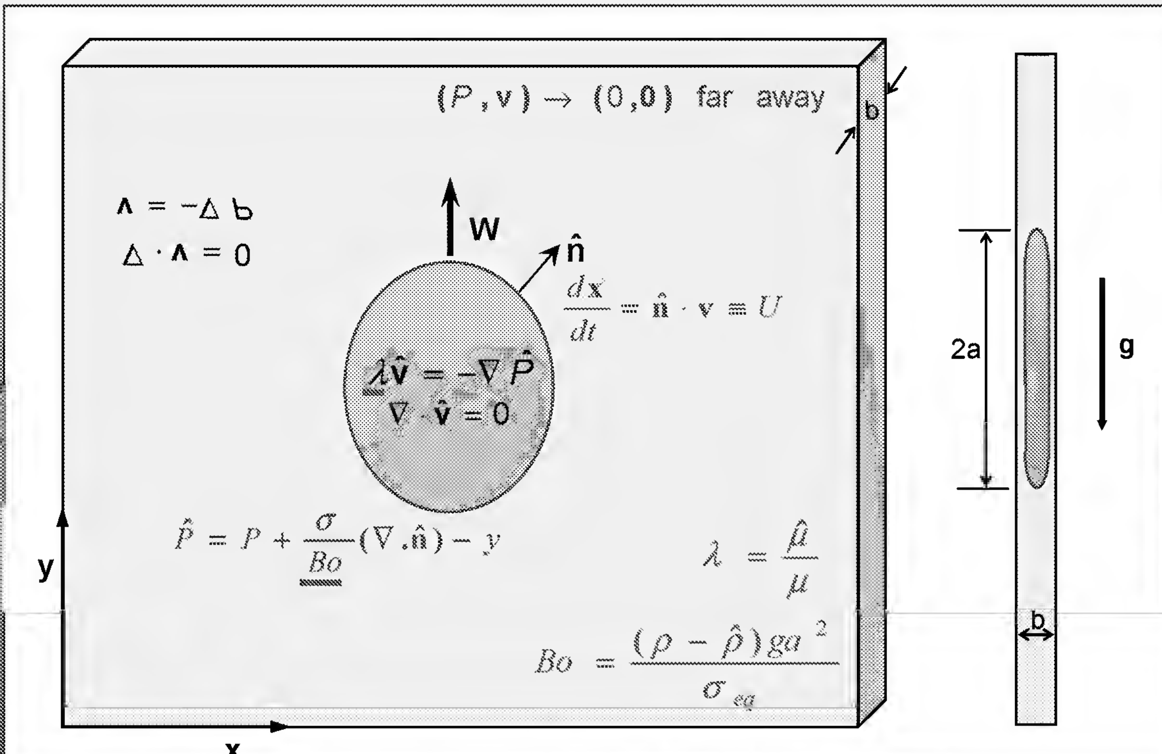

CLEAN DROPS

Linear Stability Analysis

Circle is a stable solution

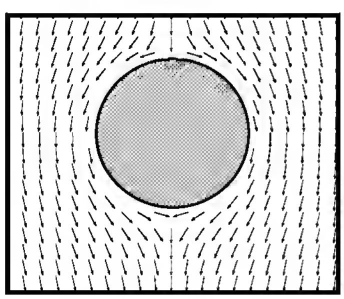

$\Delta = 0$

Non-linear Evolution of Axisymmetric Shape Perturbations

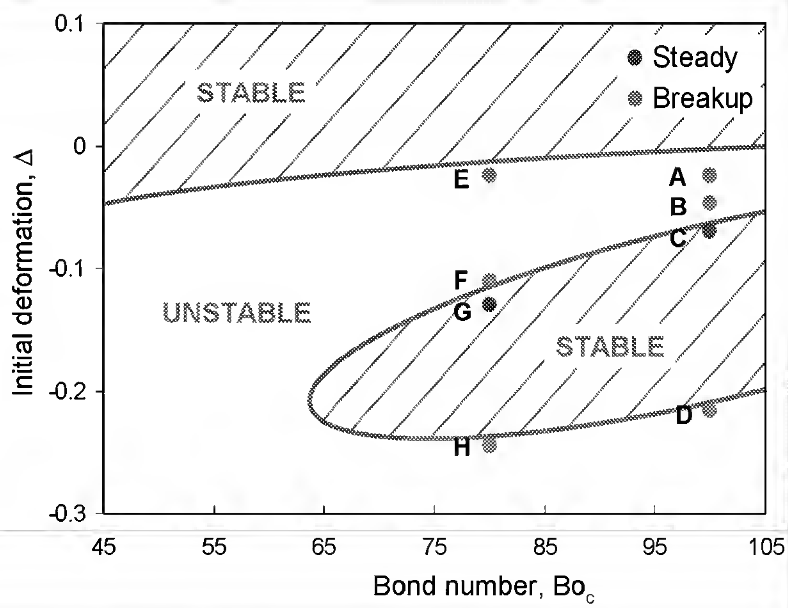

λ = 1, Bo = 100

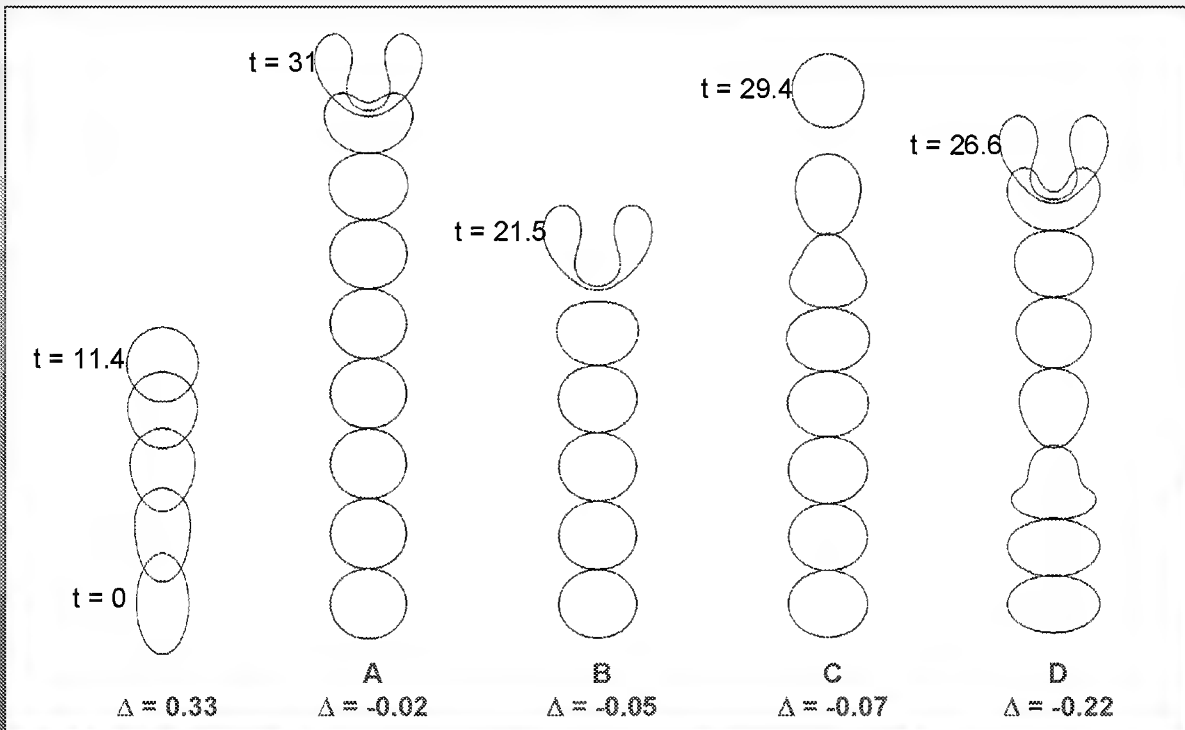

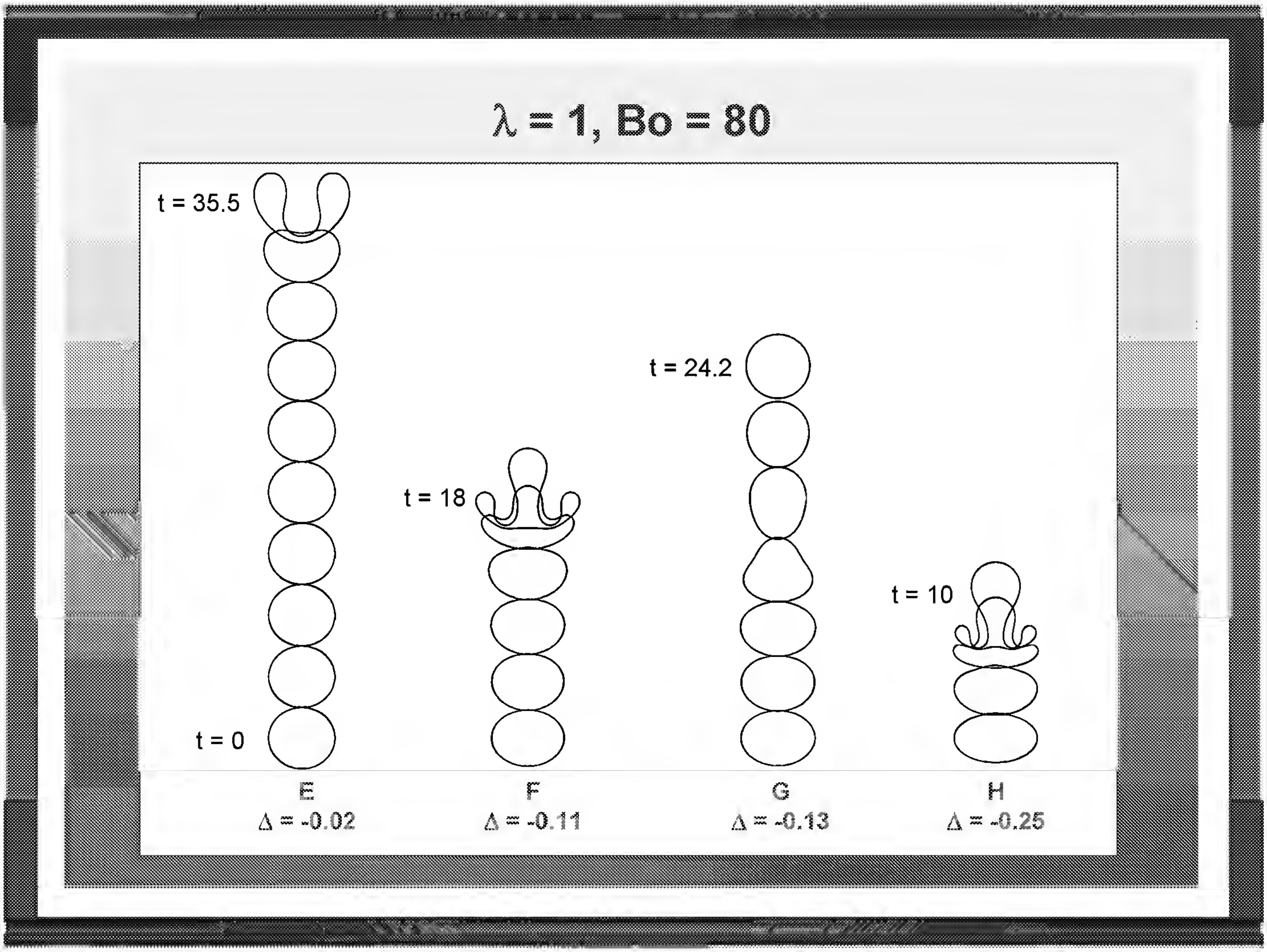
λ = 1, Bo = 80
t = 35.5
t = 0
t = 18
t = 24.2
t = 10
E
Δ = -0.02
F
Δ = -0.11
G
Δ = -0.13
H
Δ = -0.25

EFFECT OF VISCOSITY RATIO

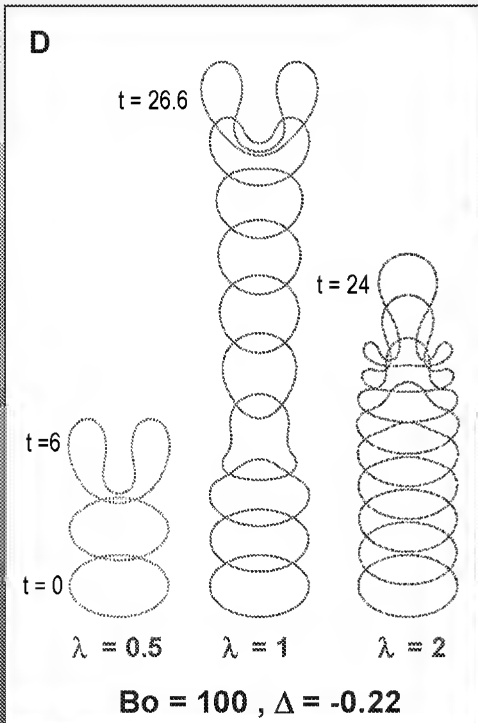

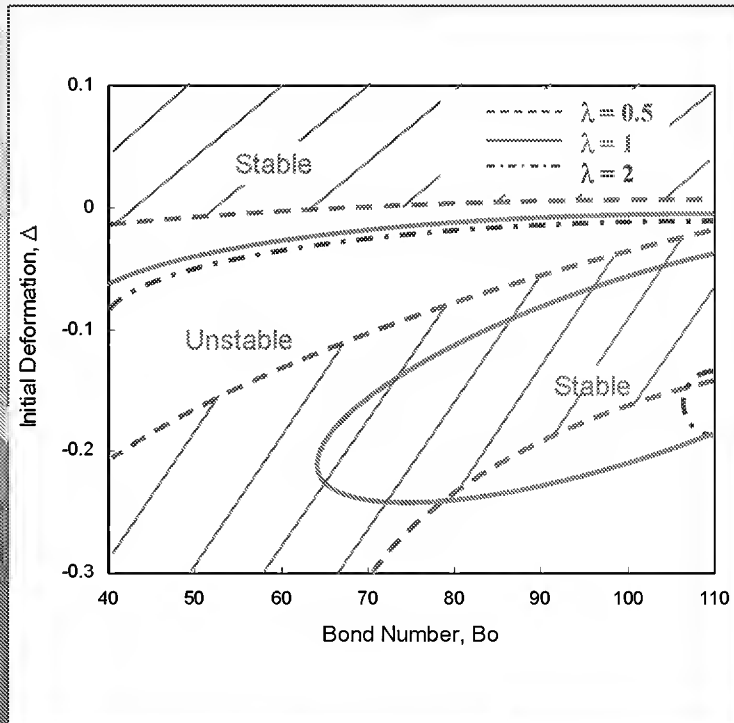

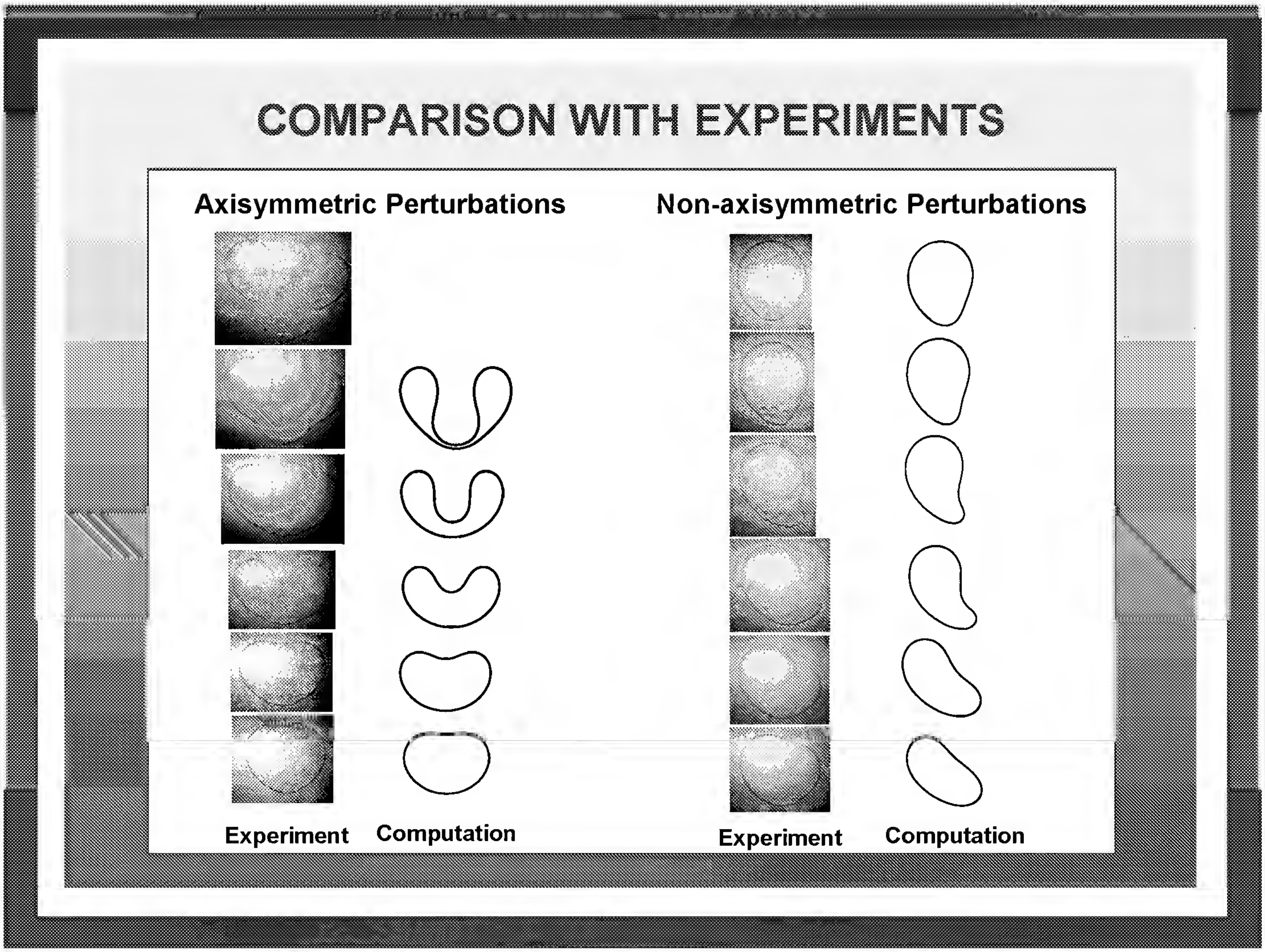
COMPARISON WITH EXPERIMENTS
Axisymmetric Perturbations
Non-axisymmetric Perturbations
Experiment
Computation
Experiment
Computation

SURFACTANT-LADEN DROPS

Depth-Averaged Tangential Stress Balance*

$$\frac{\partial}{\partial s}(\hat{P} + P) + (1 + \lambda)V_t^s = \frac{\delta}{Bo}\frac{\partial \sigma}{\partial s}$$

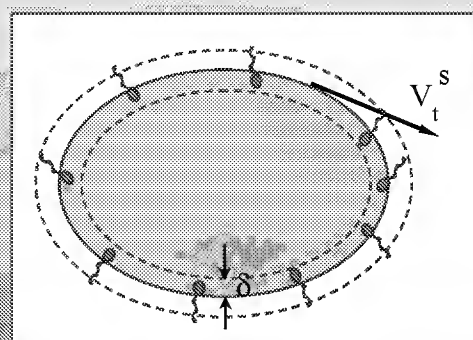

Surfactant Transport

$$\frac{D\Gamma}{Dt} + \Gamma\frac{\partial V_t^s}{\partial s} - \frac{1}{Pe}\frac{\partial^2 \Gamma}{\partial s^2} + \Gamma(\nabla . \hat{\mathbf{n}})U = 0$$

Surface Equation of State

$$\sigma = 1 + \beta \ln\left(\frac{1 - \chi_{eq}\Gamma}{1 - \chi_{eq}}\right)$$

Γ = Surfactant Concentration

χ_{eq} = Equilibrium Surface Coverage

V_t^s = Tangential Interface Velocity

* Nadim, A., Borhan, A. and Haj-Hariri, H., *J. Coll. Int. Sci.*, **181**, 159-164, 1996.

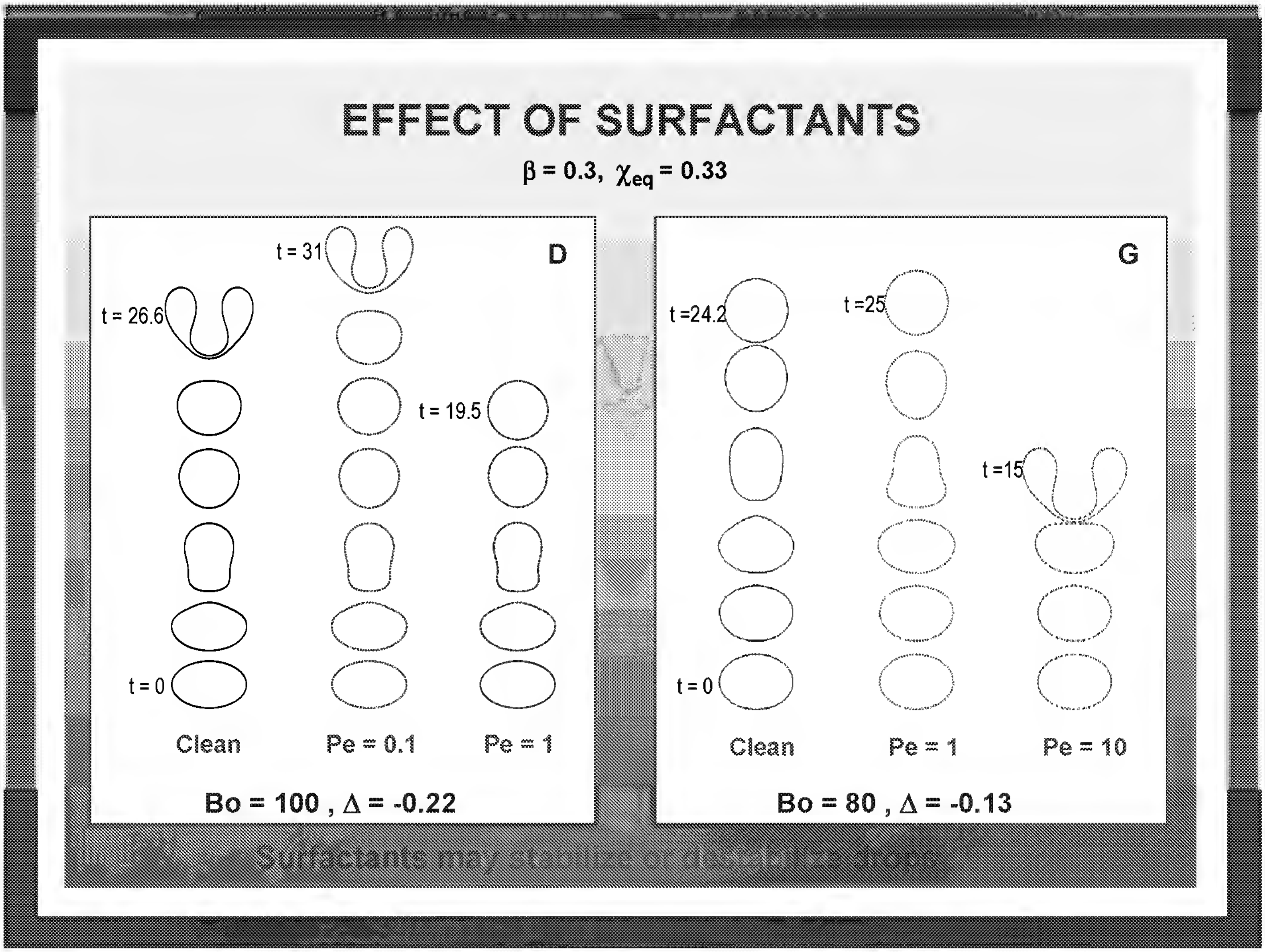
EFFECT OF SURFACTANTS
β = 0.3, χeq = 0.33
D
t = 31
t = 26.6
t = 19.5
t = 0
Clean
Pe = 0.1
Pe = 1
Bo = 100 , Δ = -0.22
G
t =24.2
t =25
t =15
t = 0
Clean
Pe = 1
Pe = 10
Bo = 80 , Δ = -0.13
Surfactants may stabilize or destabilize drops

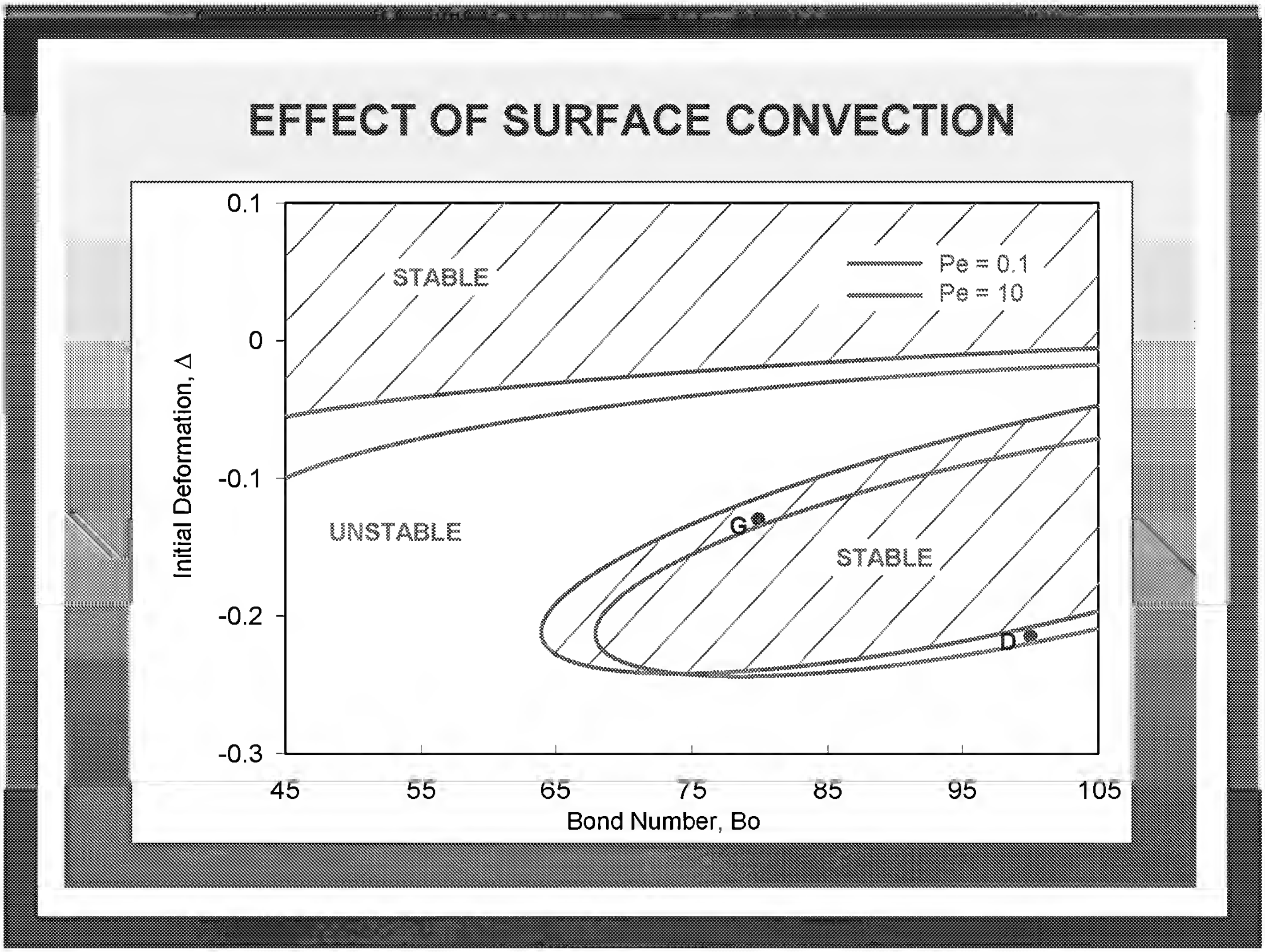
EFFECT OF SURFACE CONVECTION
STABLE
Pe = 0.1
Pe = 10
UNSTABLE
STABLE
G
D
Initial Deformation, Δ
0.1
0
-0.1
-0.2
-0.3
45
55
65
75
85
95
105
Bond Number, Bo

SURFACE COLLISIONS INVOLVING PARTICLES AND MOISTURE (SCIP'M)

Robert H. Davis, Dean A. Rager, Brian T. Good, and Advait Kantak
Department of Chemical Engineering
University of Colorado
Boulder, CO 80309-0424
phone: 303-492-7314; fax: 303-492-4341
email: robert.davis@colorado.edu

ABSTRACT

Collisions of small particles with other particles or surfaces play key roles in industrial and natural processes such as filtration, agglomeration, granular flow, sand blasting, pollen capture, planetary-ring dynamics, and clean-room applications. The surfaces are wet in many cases, which can cause the particles to stick or have reduced kinetic energy due to viscous losses.

Davis *et al.* (1986) first analyzed the problem of a particle colliding with a wet surface, which they called an *elastohydrodynamic collision*, by numerically solving the coupled lubrication equation for the fluid velocity and pressure and the solid-elasticity equation for the Hertzian deformation of the surfaces. They showed that the collision and rebound process is governed by two dimensionless parameters:

$$\text{Stokes number} \qquad St = mv_o \big/ \left(6\pi\mu a^2\right) \quad , \tag{1}$$

$$\text{elasticity parameter} \qquad \varepsilon = 4\theta\mu v_o a^{3/2} \big/ x_o^{5/2} \quad , \tag{2}$$

where $m = 4\pi a^3\rho_s/3$ is the mass of the ball, a is its radius, ρ_s is its density, μ is the fluid viscosity, v_o is the impact velocity starting at a separation x_o between the surfaces, $\theta = (1-\nu_1^2)/(\pi E_1) + (1-\nu_2^2)/(\pi E_2)$, and ν_i and E_i are Poisson's ratio and Young's modulus of elasticity for the ball (i = 1) and plane (i = 2). The same analysis applies for the collision of two spheres, with a and m then equal to the reduced radius and mass, respectively.

The analysis of Davis *et al.* (1986) predicts that no rebound will occur when the Stokes number is less than a critical value ($St < St_c$), due to viscous dissipation of the initial kinetic energy of the sphere. The value of the critical Stokes number for rebound is predicted to depend weakly on the elasticity parameter, increasing from $St_c \approx 1.5$ at $\varepsilon = 10^{-2}$ to $St_c \approx 8$ at $\varepsilon = 10^{-8}$. Rebound is predicted for $St > St_c$, and Davis *et al.* (2002) have used lubrication theory for undeformed spheres and scaling relations for elastic deformation to predict that the coefficient of restitution is then

$$v_r \big/ v_o \equiv e_{wet} = e_{dry}\left(1 - St_c \big/ St\right) \quad , \tag{3}$$

where v_r is the rebound velocity, e_{wet} is the coefficient of restitution for a wet surface, e_{dry} is the coefficient of restitution for a dry surface, and the critical Stokes number for smooth surfaces is

$$St_c = \frac{2}{5}\ln\left(\frac{4\sqrt{2}}{3\pi\varepsilon}\right) \quad . \tag{4}$$

To test the theory, experiments were performed to measure the rebound velocities of small plastic and metal spheres dropped from various heights onto a smooth quartz surface coated with a thin layer of viscous fluid. Similar experiments involving spheres fully immersed in a large body of fluid have been reported recently by Joseph *et al.* (2001) and Gondret *et al.* (2002). The spheres stick without rebounding for low impact velocities, due to viscous dissipation in the thin fluid layer (Figure 1). Above a critical impact velocity, however, the lubrication forces in the thin layer cause elastic deformation and rebound of the spheres. The apparent coefficient of restitution increases with the ratio of the Stokes number to its critical value for rebound (Figure 2). The experimental results show good agreement with the model, except that there is considerable scatter in the data (which may be due to surface roughness).

Additional work is underway on oblique collisions and on slow-speed collisions. The latter will require a low-gravity environment.

Davis, R. H., J.-M. Serayssol, and E. J. Hinch (1986) "The Elastohydrodynamic Collision of Two Spheres," *J. Fluid Mech.* **163**, 479-492.

Davis, R. H., D. A. Rager, and B. T. Good (2002) "Elastohydrodynamic Rebound of Spheres from Coated Surfaces," *J. Fluid Mech.* (in press).

Gondret, P., M. Lance, and L. Pettit (2002) "Bouncing Motion of Spherical Particles in Fluids," *Phys. Fluids* **14**, 643-652.

Joseph, G. G., R. Zenit, M. L. Hunt, and A. M. Rosenwinkel (2001) "Particle-wall Collisions in a Viscous Fluid," *J. Fluid Mech.* **433**, 329-346.

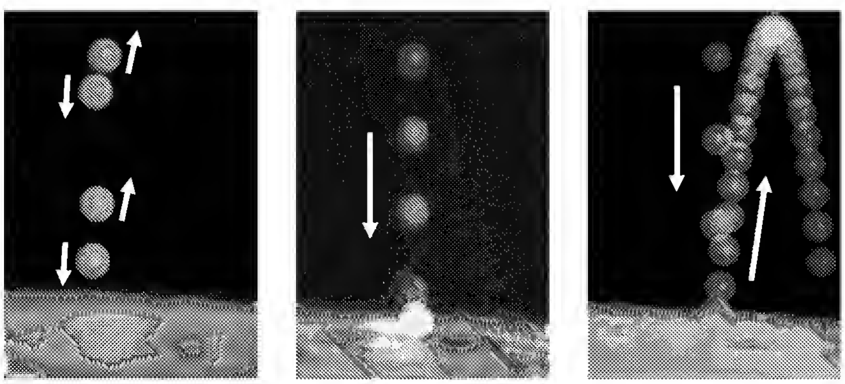

Figure 1. Strobed photographs of a nylon sphere of radius 0.32 cm dropped onto a dry quartz surface from a height of 20 cm (left panel), onto a quartz surface overlaid with a thin layer of fluid with 9.9 g/cm-s viscosity and 80 μm thickness from a height of 20 cm (middle panel), and onto the quartz surface with the same fluid layer from a height of 30 cm (right panel).

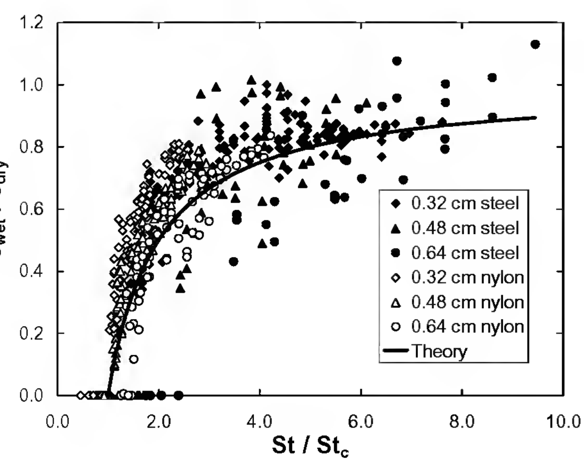

Figure 2. Coefficient of restitution for wet collisions, normalized by that for dry collisions, versus the ratio of the Stokes number to its critical value (determined from Eq. (4)) for nylon (open symbols) and steel (closed symbols) balls impacting a quartz surface overlaid with an 80-250 μm layer of fluid with 9.9 g/cm-s viscosity. The theoretical curve is from Eq. (3).

Surface Collisions Involving Particles and Moisture (SCIP'M)

Robert Davis, Brian Good, Advait Kantak and Dean Rager
Department of Chemical Engineering
University of Colorado

ABSTRACT

Collisions of particles with wet surfaces are important in filtration, agglomeration, wet granular flow, and pollen capture. Laboratory experiments involve dropping small plastic and metal balls onto a surface overlaid with a thin layer of a viscous fluid. Critical conditions for bouncing instead of sticking are determined with the aid of high-frequency strobotic photography. For bouncing, the rebound velocity, angle, and rotation are determined by image analysis. Bouncing increases with increasing ball size and impact speed, and with decreasing viscosity and thickness of the fluid layer. The results are interpreted using elastohydrodynamic theory, accounting for lubrication pressure in the thin viscous layer and elastic deformation of the solid ball and opposing surface.

The laboratory experiments are restricted to high impact velocities (~1 m/s, or higher), as otherwise gravitational acceleration obscures the rebound. As a result, relatively thick and viscous fluids layers on the surface are required to observe the transition between bouncing and sticking. Future experiments with lower impact speeds (~0.1 m/s, or lower) and surfaces wetted with water are planned for a low-gravity environment.

RESEARCH SCOPE

- Particle Collisions
  - wet surfaces
  - dry surfaces
  - stick or rebound

- Laboratory experiments
  - high velocities: 0.5 – 5 m/s
  - viscous fluids

- Parabolic flight experiments
  - low velocities: 1 – 10 cm/s
  - air & water

- Theory
  - lubrication
  - elasticity
  - solid contact and friction

LABORATORY EXPERIMENTS

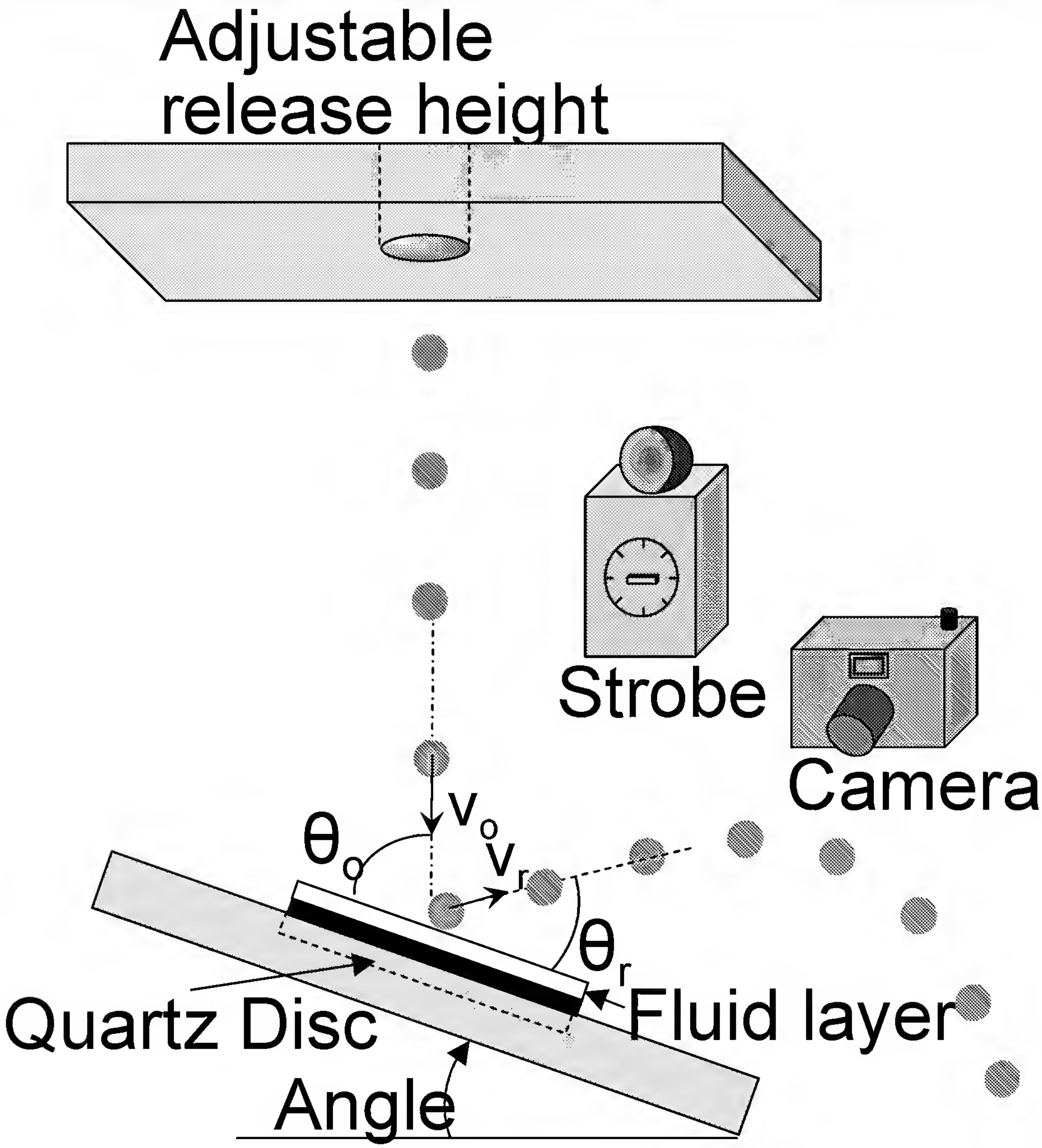

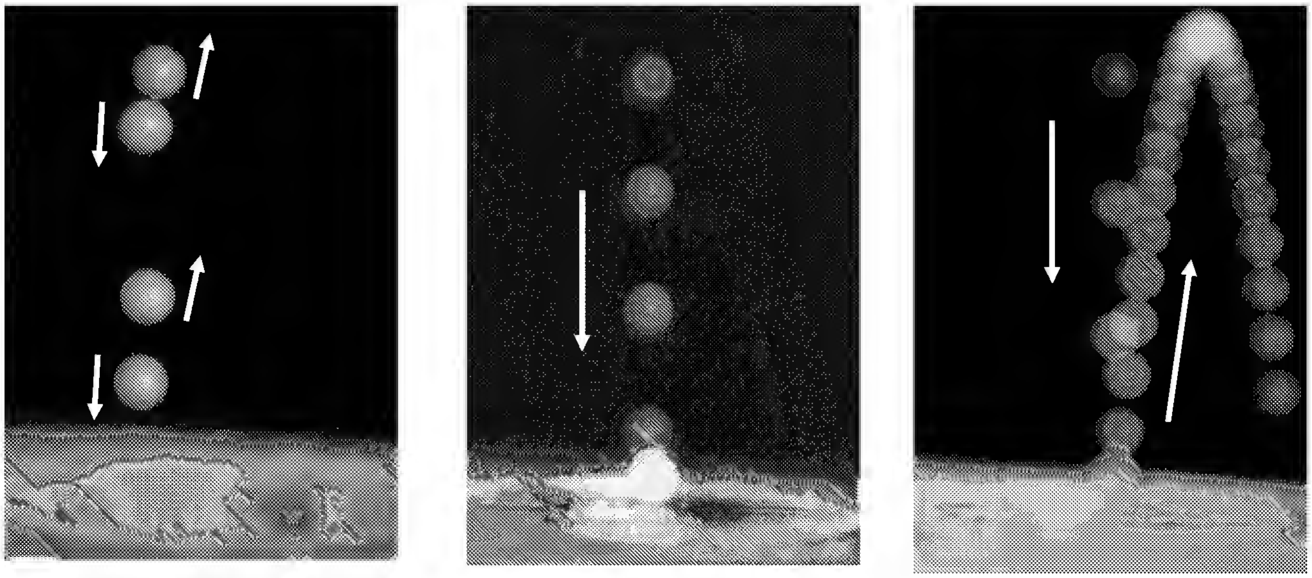

Dry, h = 20 cm   Wet, h = 20 cm   Wet, h = 30 cm

Nylon sphere of 0.32 cm radius dropped onto a dry quartz disk, and the same disk covered with 80 μm layer of oil with 9.9 g/cm-s viscosity

Nylon ball of 0.48 cm radius

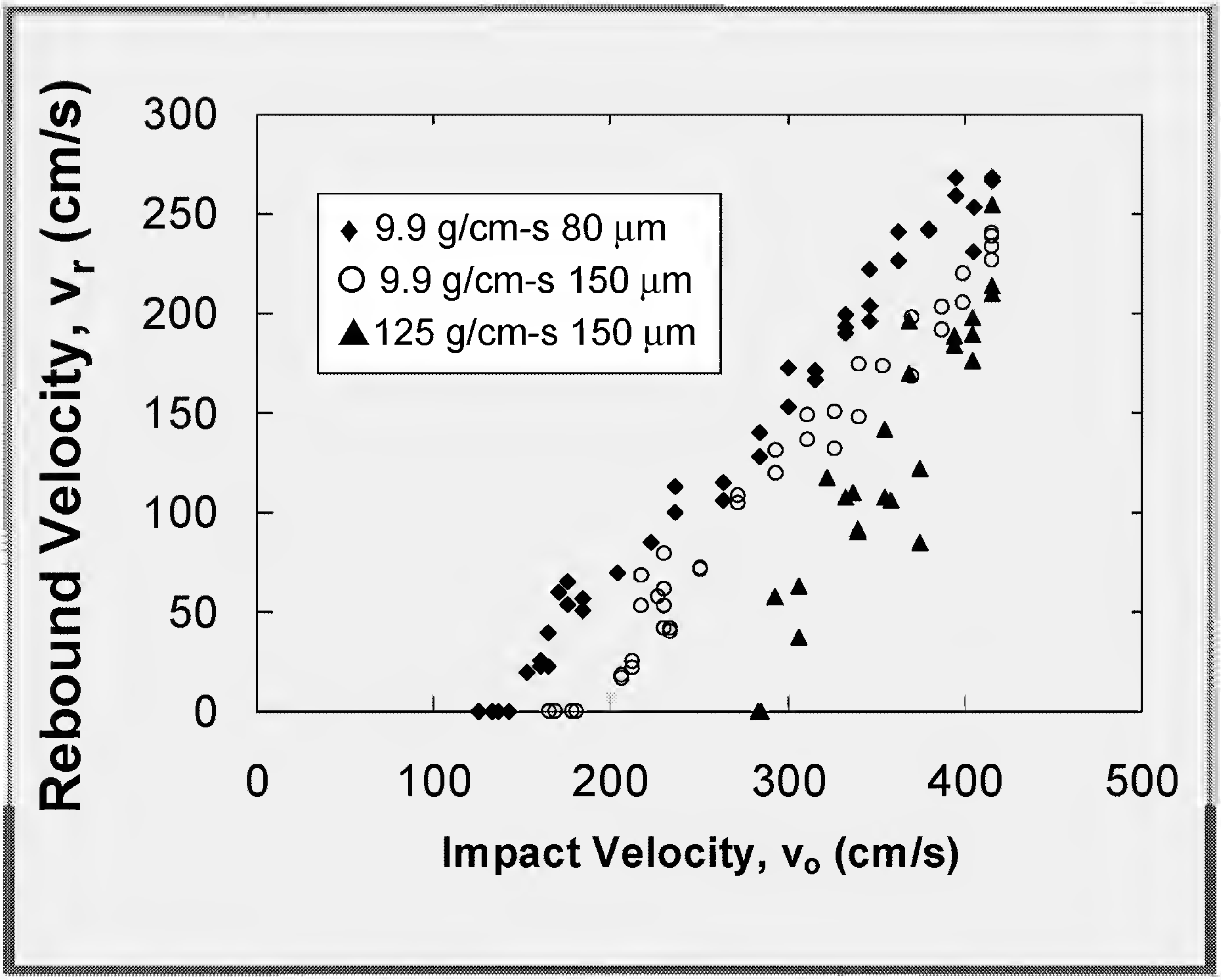

Nylon ball of 0.32 cm radius

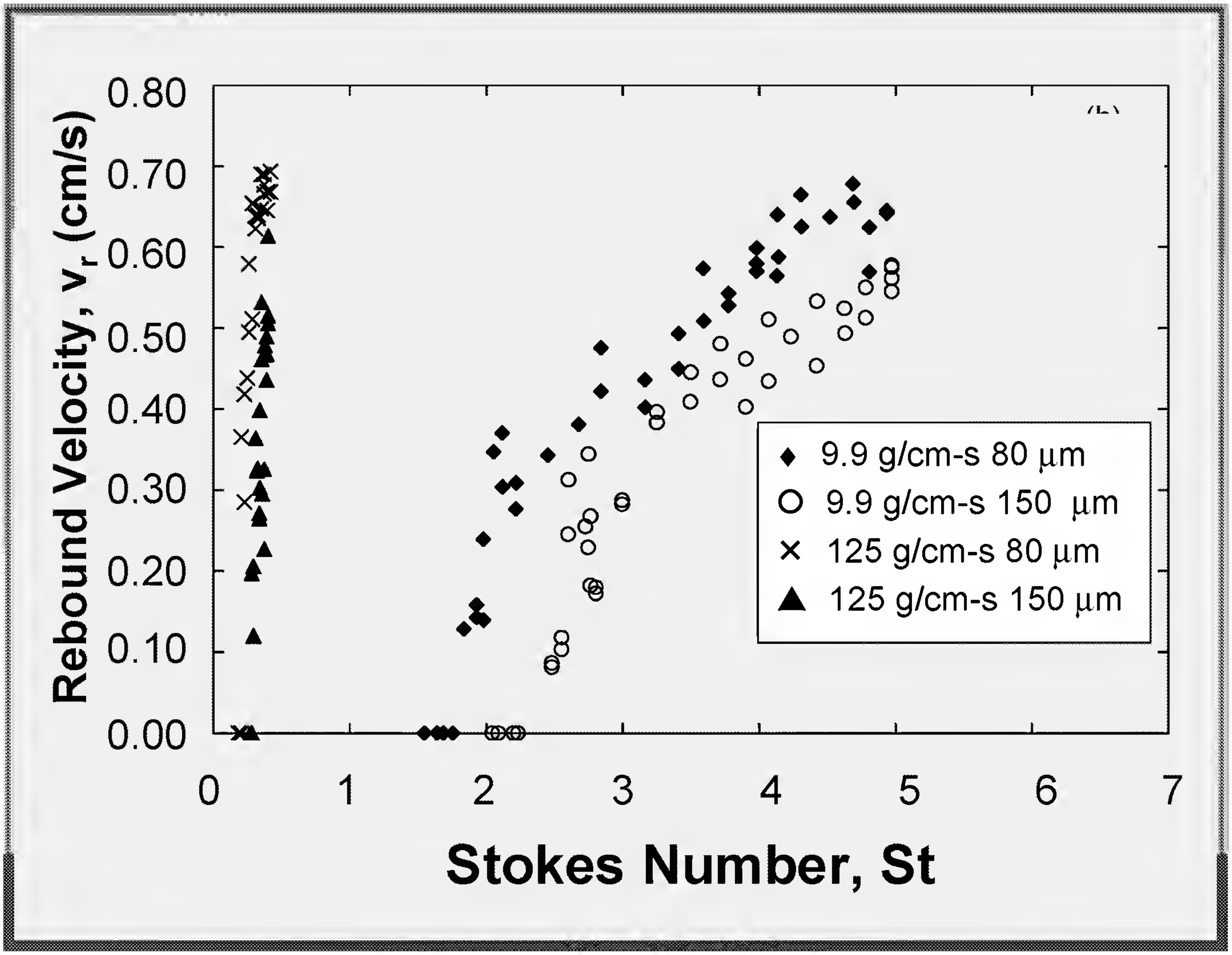

THEORY

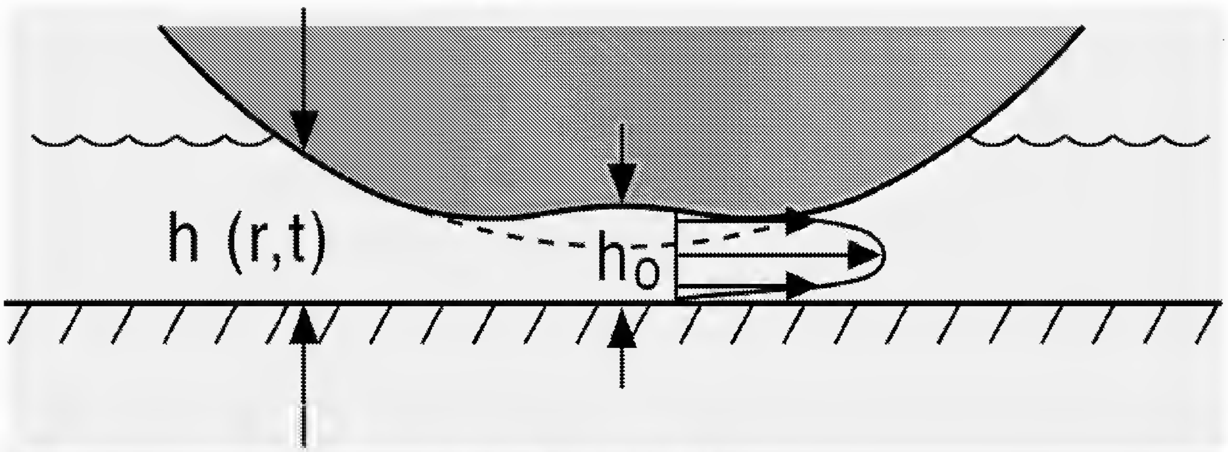

- Lubrication flow in thin gap
- Elastic deformation and rebound

$$e_{wet}/e_{dry} = 1 - St_c/St$$

$$St_c = 0.40 \ln\left(4\sqrt{2}/3\pi\varepsilon\right)$$

$$St = \frac{mv_o}{6\pi\mu a^2} \quad \text{Stokes number}$$

$$\varepsilon = \frac{4\theta\mu v_o a^{3/2}}{h_o^{5/2}} \quad \text{elasticity parameter}$$

Comparison of Theory and Experiment

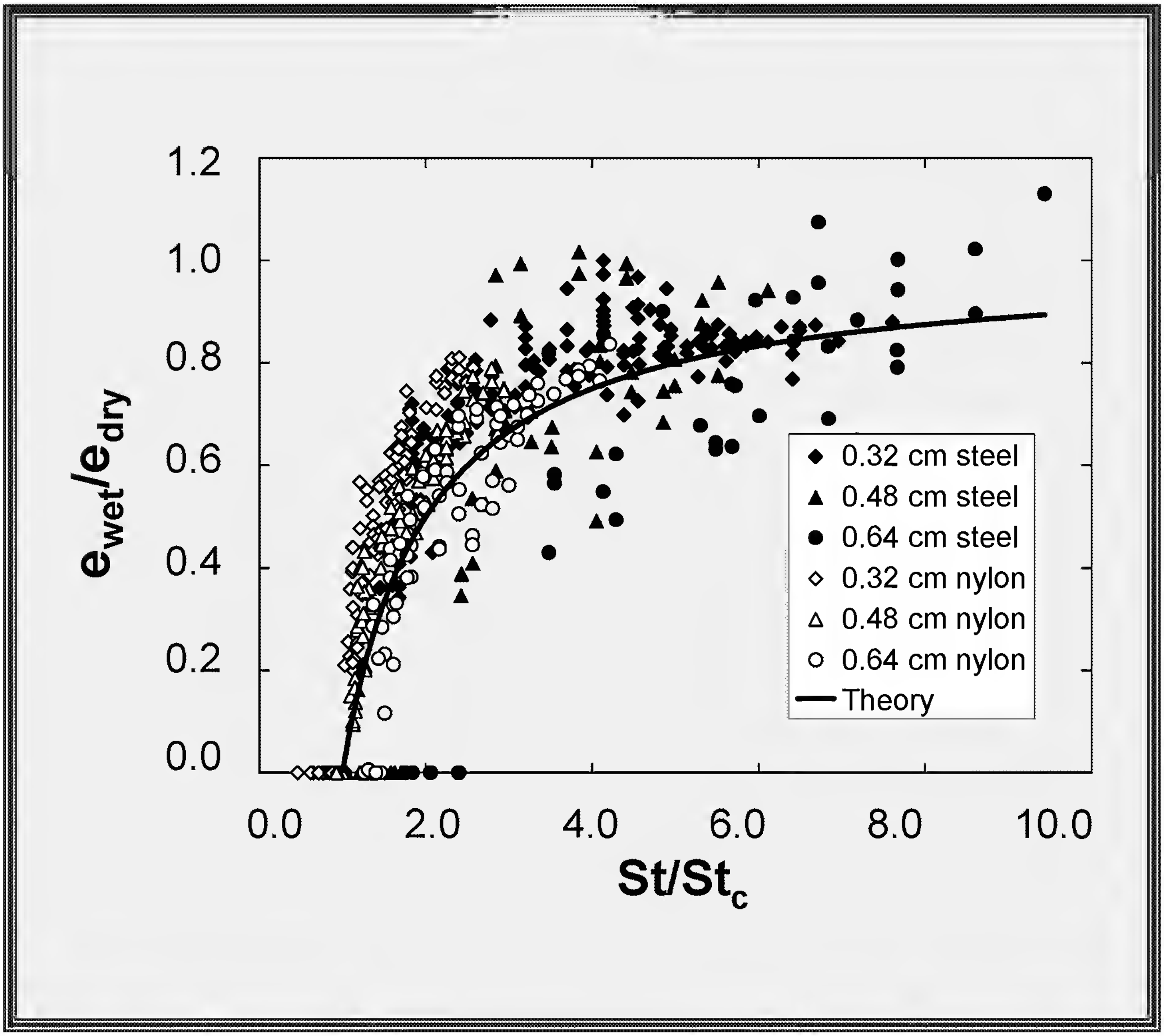

Collisions at Oblique Angles

Nylon ball of 0.64 cm radius
9.9 g/cm-s oil, 80 μm thick

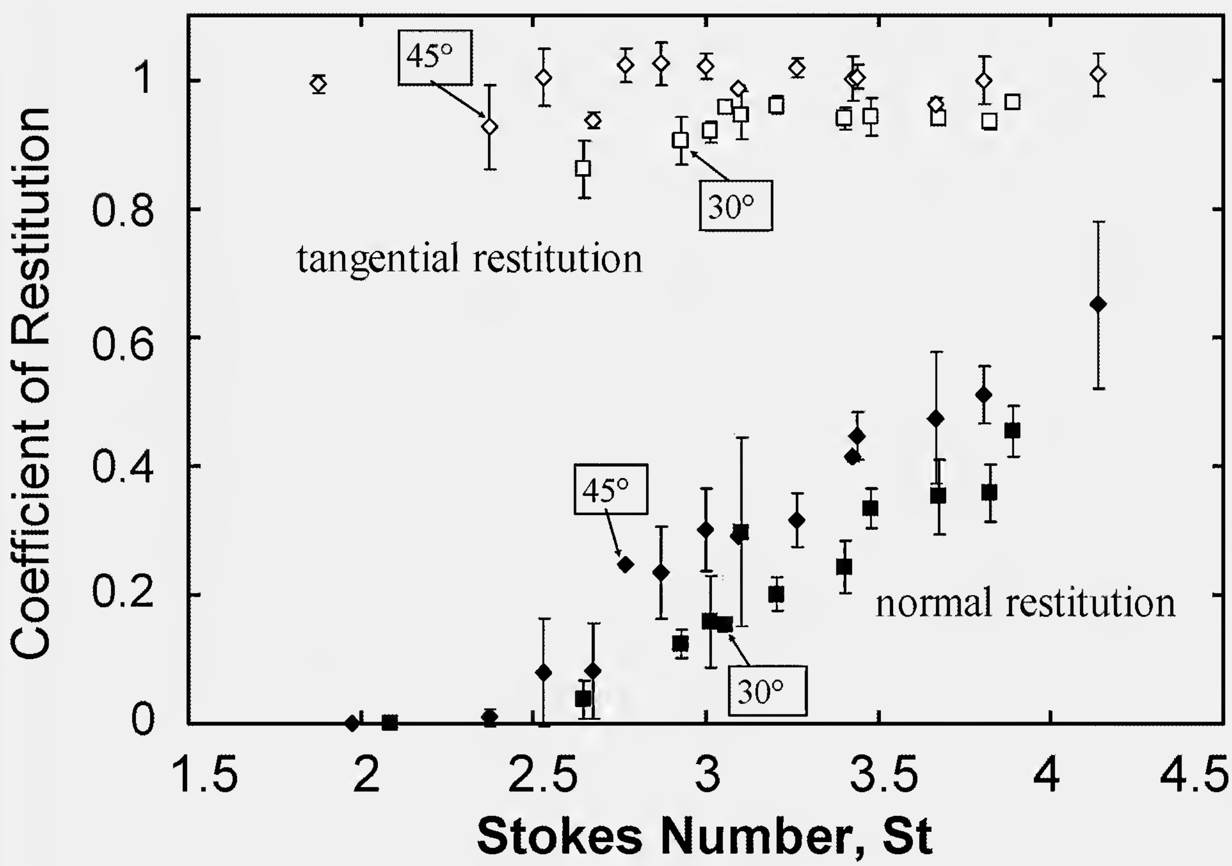

NEED FOR LOW GRAVITY

$$St = \frac{mv_o}{6\pi\mu a^2} = \frac{2a\rho_p v_o}{9\mu}$$

$St_c = 1 - 5$ for rebound

$V_o \approx 0.4 - 2$ cm/s for $a = 0.1$ cm

$\rho_p = 1.2$ g/cm^3

$\mu = 0.01$ g/cm-s

$V_r = ev_o$ e = coefficient of restitution ≈ 0.7

$H_{max} = v_r^2/2g < 1 \times 10^{-3}$ cm for $g = g_o$

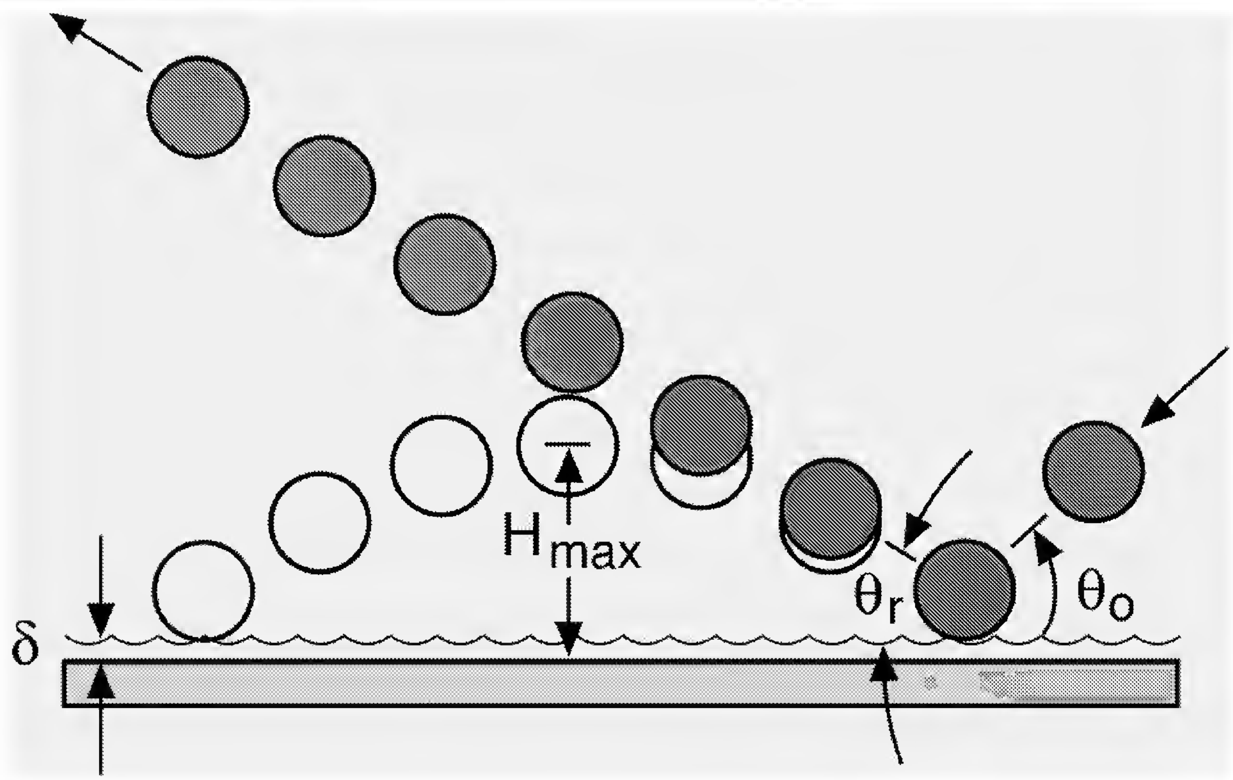

PARABOLIC FLIGHT EXPERIMENTS

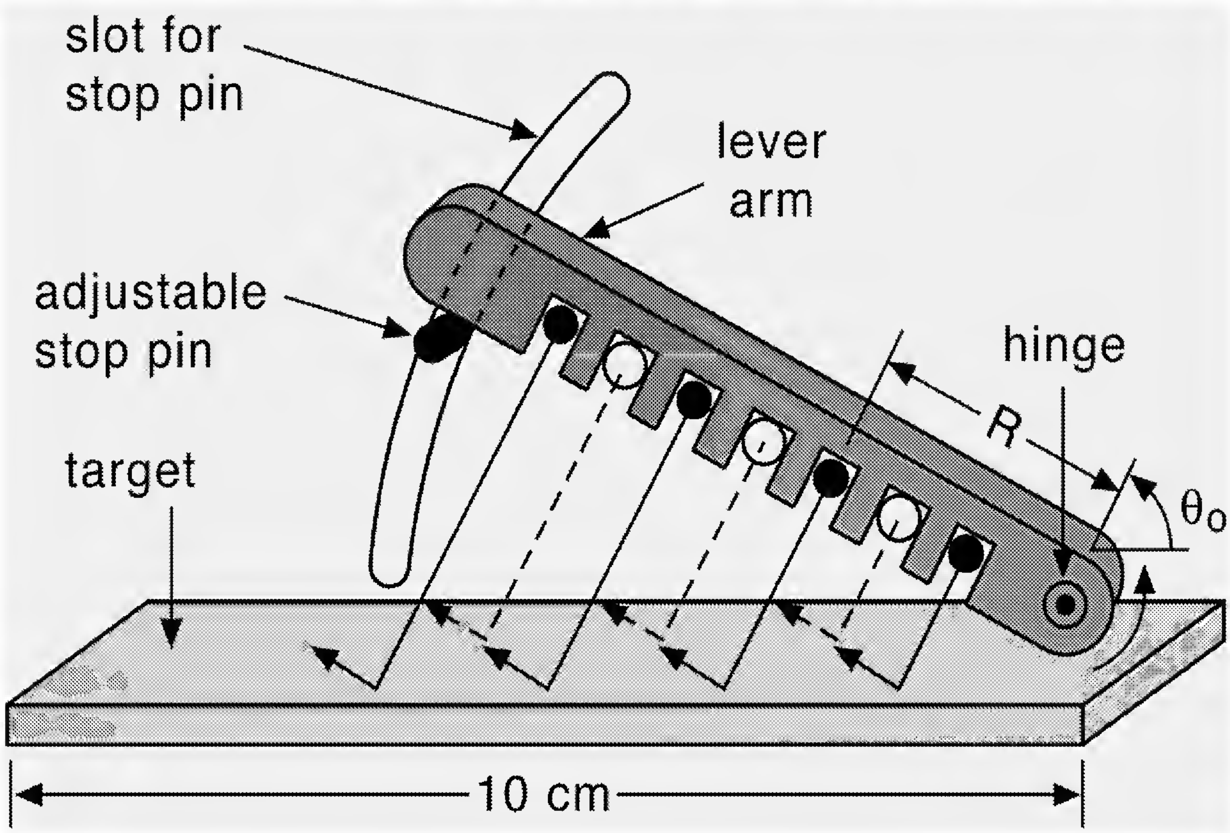

SCIP'M Apparatus

Diagnostics required:

- **Standard video for $v_o \leq 10$ cm/s**
- **High-speed video for v_o 10 cm/s**
- **Image-analysis software**

Conclusions

Particles bounce only if critical Stokes number is exceeded

- Normal coefficient of restitution increases with increased ball size and impact velocity, and with decreased fluid thickness and viscosity
- Tangential coefficient of restitution is near unity
- Low-gravity environment is needed for low-speed collisions

CRITICAL VELOCITIES IN OPEN CAPILLARY FLOWS

Antje Ohlhoff, Uwe Rosendahl, Michael E. Dreyer, Hans J. Rath

Center of Applied Space Technology and Microgravity (ZARM)
University of Bremen, Am Fallturm, D-28359 Bremen, Germany
e-mail: ohlhoff@zarm.uni-bremen.de, Fax: +49-421 218-2521, Phone: +49-421 218-4788

ABSTRACT

We consider a forced liquid flow in an open capillary channel with free liquid surfaces under low gravity. The channel consists of two parallel plates and is shown in Figure 1. The liquid flows along the x-axis from the inlet to the outlet and forms free surface at the sides between the plates. The flow is maintained by external pumps and the free surface deforms according to the pressure along the flow path. Since the free surface can only withstand a certain difference between the liquid pressure and the ambient pressure the flow rate in the channel is limited. The aim of the consideration is also to determine the shape of the free surface and to find the maximum flow rate without a collapse of the free surface. This critical flow rate depends on the geometry of the channel and the properties of the liquid, specified by the three dimensionless parameters, the OHNESORGE number $\mathrm{Oh} = (\rho\nu^2)/(2\sigma a)$, the aspect ratio $\Lambda = b/a$ and the dimensionless length $\tilde{l}$ (ρ is the density, ν the kinematic viscosity and σ the surface tension of the fluid). The right picture in Fig. 1 shows the cross section area A perpendicular to the flow direction. $k(x) = z(x, y = 0)$ is the observed and computed innermost line of the free surface, $Q^*_{\mathrm{crit}} = Q_{\mathrm{crit}}/A$ the critical volume flux.

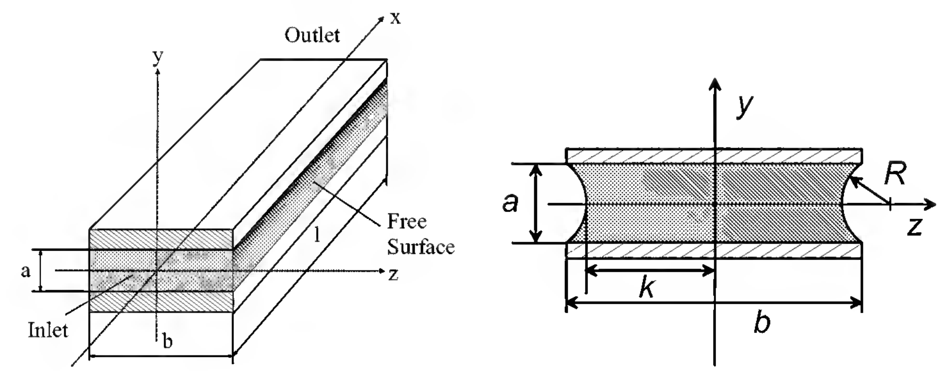

Figure 1: Schematic drawing of the flow channel consisting of two parallel plates. The right picture shows the cross section area A perpendicular to the flow direction.

The experimental investigations were performed in the drop tower Bremen and on board the sounding rocket TEXUS-37. In the TEXUS experiment the volume flux was increased in small steps up to the critical value (quasistatic approach) and the surface collapse was observed by video cameras. The main data are the positions of the liquid surfaces $k(x)$ as function of the adjusted volume flux and the critical flow rate. The results are discussed in [1], [2] and [3].

We developed a one dimensional, stationary mathematical model from the mass and momentum conservation equations. The model contains the pressure gradient caused by the shape of the free surface taking into account both radii of curvature, the convective acceleration due to the change in cross section and the friction losses in the channel. We

have to deal with an entrance flow problem, thus the velocity distribution does not obey a simple parabolic profile. The solution of the nonlinear differential system is obtained by a difference schemata (FDM) of second order and the Newton method. This yields the free surface, the mean velocity and the curvature, depending on the parameters. Furthermore we are able to anticipate the critical volume flux in a numerical sense. The numerical results for the free surface position and the critical volume flux shows a very good agreement with the experimental data [3].

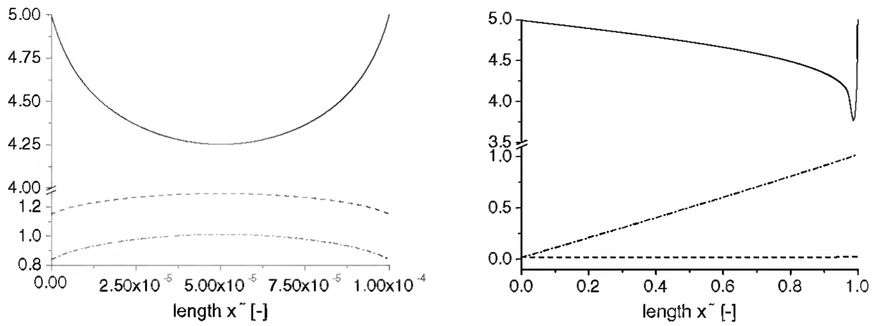

Figure 2: Typical results for convection dominated flow (left: $\mathrm{Oh} = 10^{-4}$, $\Lambda = 5.0$, $\tilde{l} = 10^{-4}$ $Q^* = 1.15$) and friction dominated flow (right: $\mathrm{Oh} = 10^{-2}$, $\Lambda = 5.0$, $\tilde{l} = 1.0$ $Q^* = 0.02$). The contour of the free surface is depicted with a solid line, the velocity with a dashed line and the mean curvature with a dashed-pointed line.

For the interpretation of the results the dimensionsless length $\tilde{l} = (\mathrm{Oh}l)/(4a)$ is very appropriate and provides physical insight into the dominant forces. Figure 2 shows typical results from the numerical calculation for the different parts, dominated by convection and dominated by friction. The computations are close to the critical volume flux. The left picture shows the case of low Ohnesorge number and short channel length. The smallest cross section is approximately in the middle of the channel. Especially the mean curvature at the inlet is approximately equal to the curvature at the outlet. The right picture shows the case of large Ohnesorge number and large channel length. The free surface has a strong slope to fit the boundary condition at the outlet. The mean curvature increases nearly linear and the difference between inlet and outlet is very high.

The integration of the momentum equation shows, that the curvature difference between inlet and outlet is a measure for the friction pressure loss in the channel. For small flow lengths $\tilde{l} \leq 10^{-3}$, the pressure loss between inlet and outlet is small, thus the flow is dominated by convective momentum transport. In the other extreme of a very long channel, $\tilde{l} \geq 10^{-1}$, the flow is dominated by viscous momentum transport and the curvature difference tends to unity. This limit can be taken to predict the maximal volume flux for a pure friction dominated flow by $Q^*_{\mathrm{crit}} = 1/(48\tilde{l})$.

1. M. E. Dreyer, U. Rosendahl, H. J. Rath, Experimental Investigation on Flow Rate Limitations in Open Capillary Vanes, AIAA 98–3165, 1998.

2. U. Rosendahl, A. Ohlhoff, M. E. Dreyer, H. J. Rath, Investigation of Forced Liquid Flows in Open Capillary Channels, to appear in Microgravity Sci. Technol.

3. U. Rosendahl, B. Motil, A. Ohlhoff, M. E. Dreyer, H. J. Rath, Critical Velocity in Open Capillary Channel Flows, AIAA-2001–5021, 2001.

Forced liquid flow in an open capillary channel

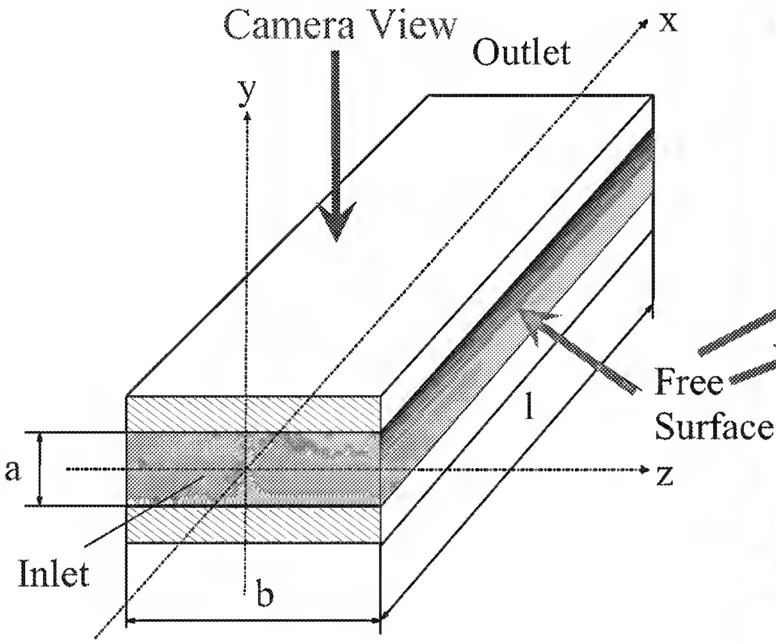

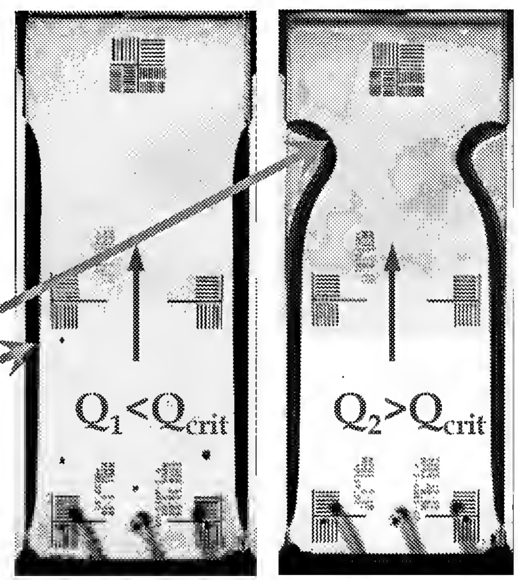

Stationary flow

Non-stationary flow
Gas ingestion at the sides

Capillary channel,
Liquid withdrawn at the outlet,
Liquid provided at the inlet

free surface can only withstand a certain capillary pressure
=> Flow rate is limited

Theoretical model

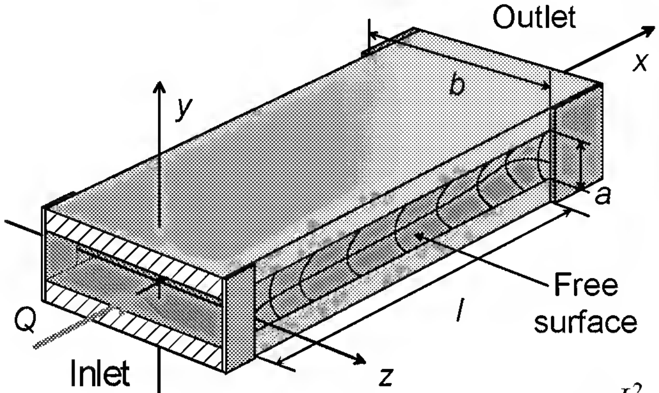

$$\mathrm{Bo} = \frac{\rho g L^2}{2\sigma} < 0.01$$

Cross section at x=constant:

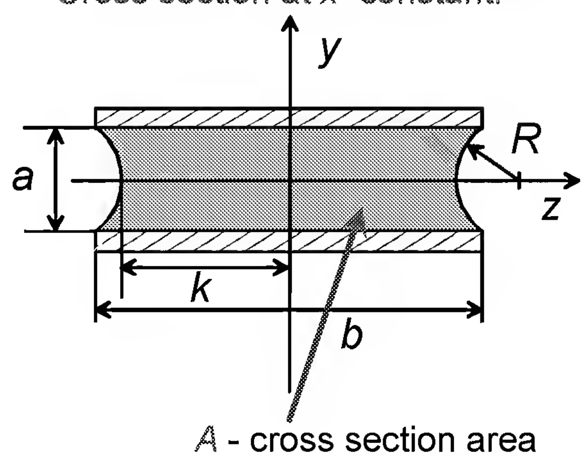

Bernoulli equation:

$$dp + \rho v dv + \cancel{g dx} - dw_f = 0$$

Convection Friction losses

Capillary pressure

Conservation of mass:

$$d(Av) = 0$$

+ Boundary conditions

Capillary pressure

Scaling: all length with a/2, velocity with $v_s = \sqrt{\frac{2}{\rho}\frac{\sigma}{a}}$

$$\longrightarrow \quad \boxed{\Lambda = \frac{a}{b},\ \mathrm{Oh} = \sqrt{\frac{\rho v^2}{\sigma D_h}},\ l}$$

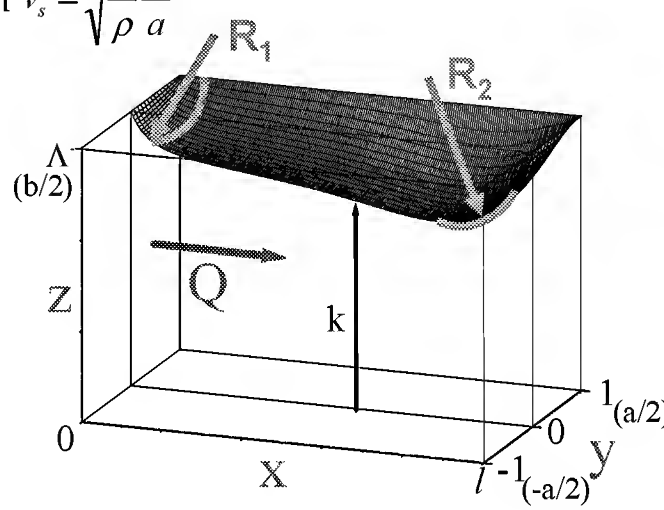

Gauss-Laplace equation:

$$\frac{p - p_a}{\sigma} = -2H = -\left(\frac{1}{R_1} + \frac{1}{R_2}\right)$$

$$dp = -2\sigma dH$$

Assumption: $\dfrac{\partial p}{\partial y} = \dfrac{\partial p}{\partial z} = 0, \quad z_y(y=0) = 0$

$$k(x) = z(x, y=0), \quad \gamma_s = 0$$

Capillary pressure:

$$2H(x, y=0) = \frac{k_{xx}}{(1+k_x^2)^{3/2}} + \frac{1}{R}\frac{1}{(1+k_x^2)^{1/2}}$$

$$R = \frac{1+(\Lambda - z)^2}{2(\Lambda - z)} \quad \text{for} \quad z \geq \Lambda - 1$$

$$R = 1 \quad \text{for} \quad z < \Lambda - 1$$

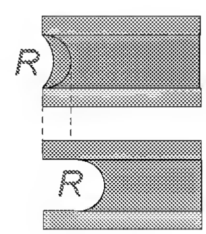

Pressure losses / Volume flux

Laminar viscous pressure loss:

$$dw_{f\_l} = 6\mathrm{Oh}\frac{Q}{A}dx$$

Hagen-Poiseuille

Convective acceleration:

$$vdv = -\frac{Q^2}{A^3}dA$$

Cross section area:

$$A(z) = 1 - \frac{1}{2\Lambda}R^2 \arcsin\frac{1}{R} + \frac{1}{2\Lambda}(R - \Lambda + z) \qquad \text{for} \quad z \geq \Lambda - 1$$

$$A(z) = \frac{1}{\Lambda}(z + 1 - \frac{\pi}{4}) \qquad \text{for} \quad z < \Lambda - 1$$

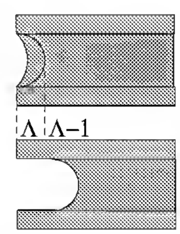

Volume flux: $Q = Av$

Entrance pressure loss

Entrance pressure loss:

(change of velocity profile)

Sparrow et al., Phys. Fluids 64

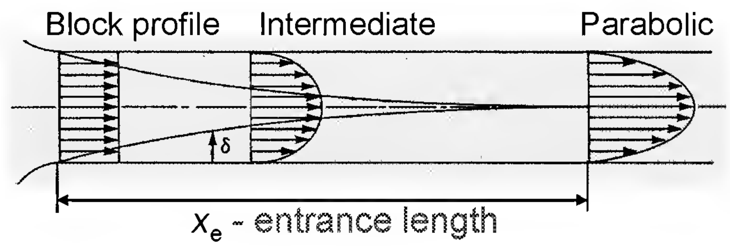

$$dw_{f\_s} = \frac{1}{D_h \mathrm{Re}_h} \frac{v^2}{2} \sum_{i=1}^{25} \left[192\, e^{-16\alpha_i^2 \tilde{x}_s} - 128\, e^{-32\alpha_i^2 \tilde{x}_s} \right] dx \qquad \tilde{x}_s = \frac{x_s}{D_h \mathrm{Re}_h}, \qquad \frac{x_e}{D_h \mathrm{Re}_h} = 0.0164$$

$$x_s = x + (1-\beta) x_e, 0 \le \beta \le 1$$

$\beta=0$ means "without Sparrow term"
(= laminar parabolic profile at the inlet)
$\beta=1$ means "full Sparrow term"
(= block profile at the inlet)

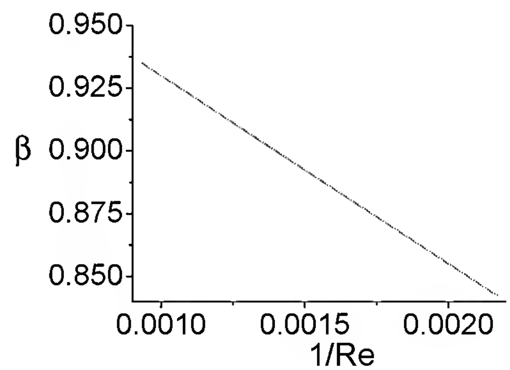

FIDAP (3D nozzle comp.):

$$\beta = L_1 + \frac{L_2}{\mathrm{Re}_h} \implies \beta = 1.0 - \frac{0.057}{Q}$$

Numerical solution

New variable: $h := 2H$ → more stable schema

Complete model:

$$\boxed{\begin{aligned} & k_{xx} + \frac{1}{R}\left(1 + k_x^{\,2}\right) - h\left(1 + k_x^{\,2}\right)^{1.5} = 0 \\ & h_x + \frac{Q^2}{A^3} A_z z_x - 6\mathrm{Oh}\frac{Q}{A} - dw_{f\_s} = 0 \end{aligned}}$$

Curvature

Bernoulli Equation

Boundary conditions:

$$k(x=0) = k(x=l) = \Lambda$$

$$h(x=0) = 2H_0$$

$$\gamma_s = 0 \qquad 2H_0 = -\frac{\Delta p_0 D_h}{4\sigma}$$

→

$$\Delta p_0 = -\left(K_{n1} + \frac{K_{n2}}{\mathrm{Re}_n}\right)\frac{\rho}{2} v^2$$

+ compensation tube

3D nozzle comp.(FIDAP):

$$K_{n1} = 1.4, K_{n2} = 312$$

Solution: Finite differences of second order (FDM) and Newton method

Error: $O(\Delta x^2)$

→

$$\boxed{\begin{aligned} & k(x) = f(\Lambda, \mathrm{Oh}, l, Q) \\ & Q_{crit} = g(\Lambda, \mathrm{Oh}, l) \end{aligned}}$$

Comparison with TEXUS-37 experiment

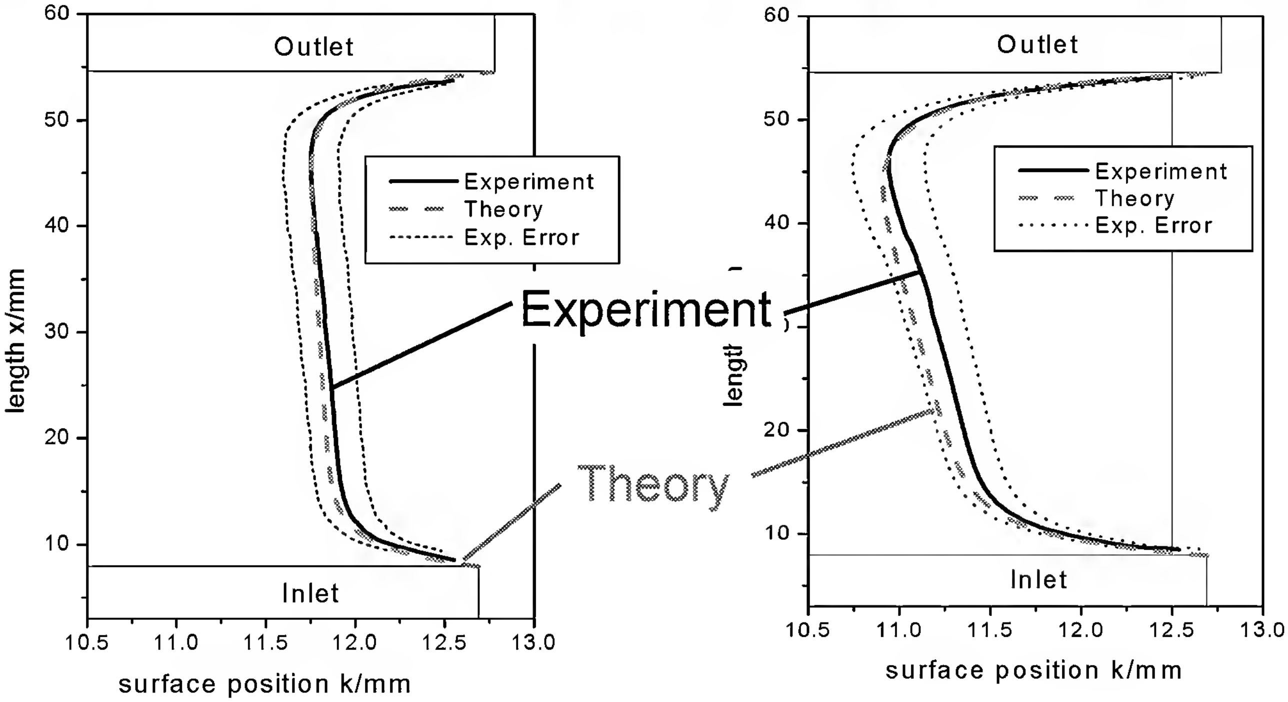

Q = 5.4 ml/s
$\mathrm{Re}_h = 626$

$\mathrm{Oh} = 1.5 \cdot 10^{-3}$
$\Lambda = 5$

Q = 8.2 ml/s
$\mathrm{Re}_h = 951$

Results and discussion

$\Lambda = 5$
$\mathrm{Oh} = 10^{-5}$
$\tilde{l} = 10^{-5}$

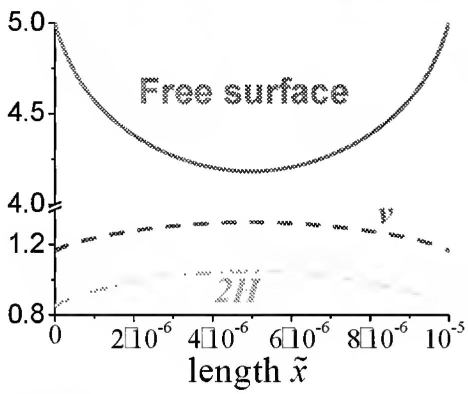

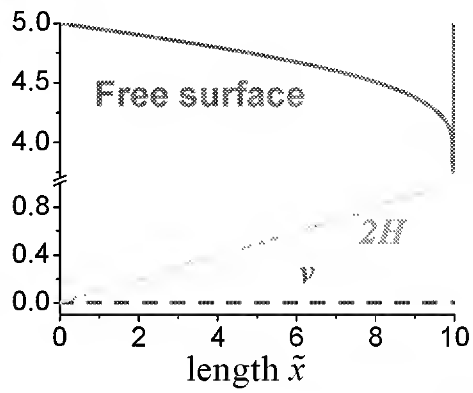

$\Lambda = 5$
$\mathrm{Oh} = 10^{-2}$
$\tilde{l} = 10$

Dominated by convection

Dominated by friction

$$\boxed{\tilde{l} = \frac{\mathrm{Oh}\, l}{2 D_h}}$$

$$\Delta h = h_{out} - h_{in} = -\frac{a}{2\sigma} w_{f\_out}$$

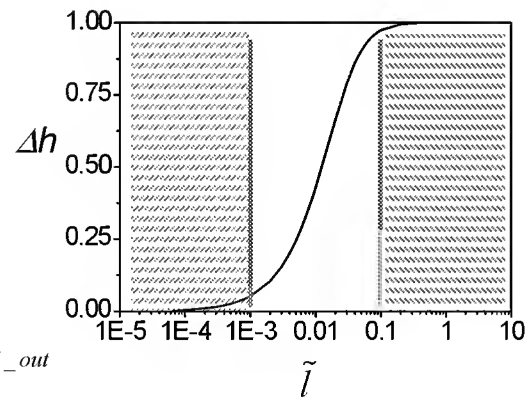

$$Q_{crit} = \frac{2}{K_{pf}\tilde{l}}$$

$$v_{crit} = \frac{2}{K_{pf}\tilde{l}}$$

Critical volume flux

Dominated by friction

$\Lambda = 2$

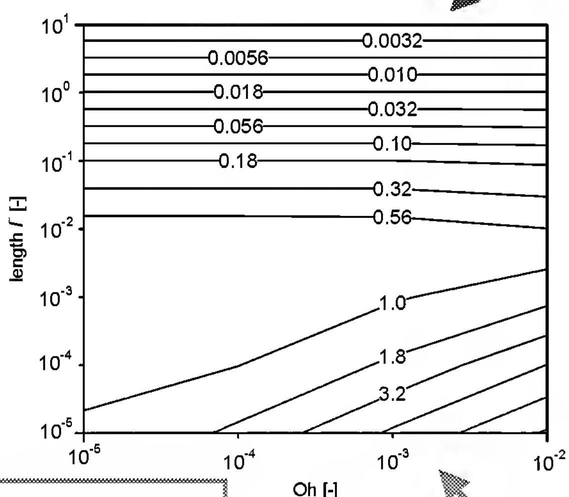

$\Lambda = 50$

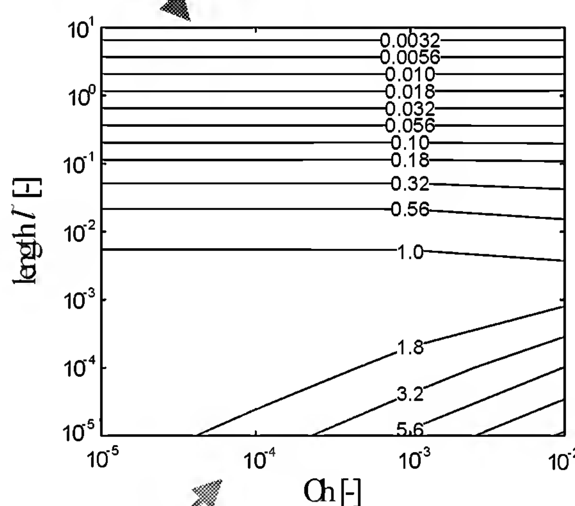

$$\boxed{\tilde{l} = \frac{\mathrm{Oh}\, l}{2 D_h}}$$

Dominated by convection

Critical Velocities in Open Capillary Flows

DaimlerChrysler Aerospace
Space Infrastructure

Antje Ohlhoff, Uwe Rosendahl,
Michael E. Dreyer,
Hans J. Rath

Center of Applied Space Technology and Microgravity (ZARM), University of Bremen

www.zarm.uni-bremen.de/interface_phenomena.html

Support for the research project by the German Aerospace Center (DLR) and the European Space Agency (ESA) is gratefully acknowledged

Microscale Investigation of Thermo-Fluid Transport In the Transition Film Region of an Evaporating Capillary Meniscus Using a Microgravity Environment

K.D. Kihm
Department of Mechanical Engineering, Texas A&M University
College Station, Texas 77843-3123
E-mail: ken-kihm@tamu.edu, Tel. 979-845-2143, Fax: 979-862-2418

J.S. Allen
National Center for Microgravity Research

K.P. Hallinan
University of Dayton

D.M. Pratt
Wright-Patterson Air Force Base

ABSTRACT

In low gravity, the solid-liquid inter-molecular surface forces are comparable to capillary and gravitational forces at significantly greater film thickness (1 ~ 10 microns), than is possible in earth's gravity (0.01 ~ 0.1 microns). Therefore, advanced microscale optical techniques to measure the film thickness, heat transport, and liquid velocity fields in the transition film region of an extended meniscus; probing, for the first the thermo-fluid transport inside this very important micro-scale region.

Since the project initiation in the beginning of 2002, a preliminary ground study has been done to implement a Molecular Fluorescence Tracking Velocimetry (MFTV) system (Fig. 1), utilizing caged fluorophores of approximately 10-nm in size as seeding particles, ultimately to measure the velocity profiles in the thin film region. Fizeau interferometry in conjunction with a microscope has been completed to measure the thin film slope and thickness variations.

Although the extension of the thin film dimensions under microgravity will be achieved by using a conical evaporator, a simpler and easy-to-fabricate evaporator has been designed and constructed for the ground test (Fig. 2). Note that the experimental setup is to maintain a constant liquid volume and liquid pressure in the capillary region of the evaporating meniscus so as to insure quasi-stationary conditions during measurements on the transition film region. In addition, the new Confocal Laser Scanning Microscopy (CLSM), available at Dr. Kihm's laboratory, has been tested for its optical sectioning capability allowing a depth-wise resolution for MFTV applications.

A micro-heater array has been fabricated using photo-lithography to etch and vapor deposit platinum films (Fig. 3). The heater array is packaged on a thin silicon substrate and then the upper face of the substrate is planarized to form a smooth contact surface. Individual heater elements (20-μm-wide and 20-mm long) are designed to maintain either a constant surface temperature or a controlled temperature variation. A Wheatstone bridge circuit controls each heater element with the temperature-dependent heater resistance value as a feedback signal.

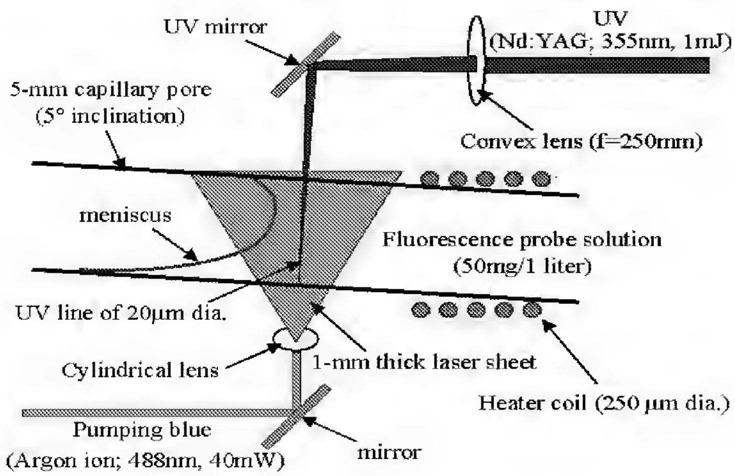

Fig. 1 Molecular Fluorescence Tagging Velocimetry (MFTV)

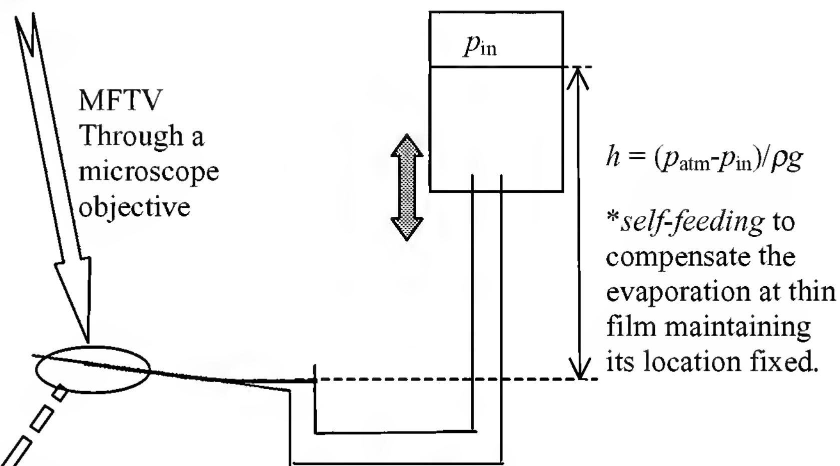

Fig. 2 Evaporating thin film generator

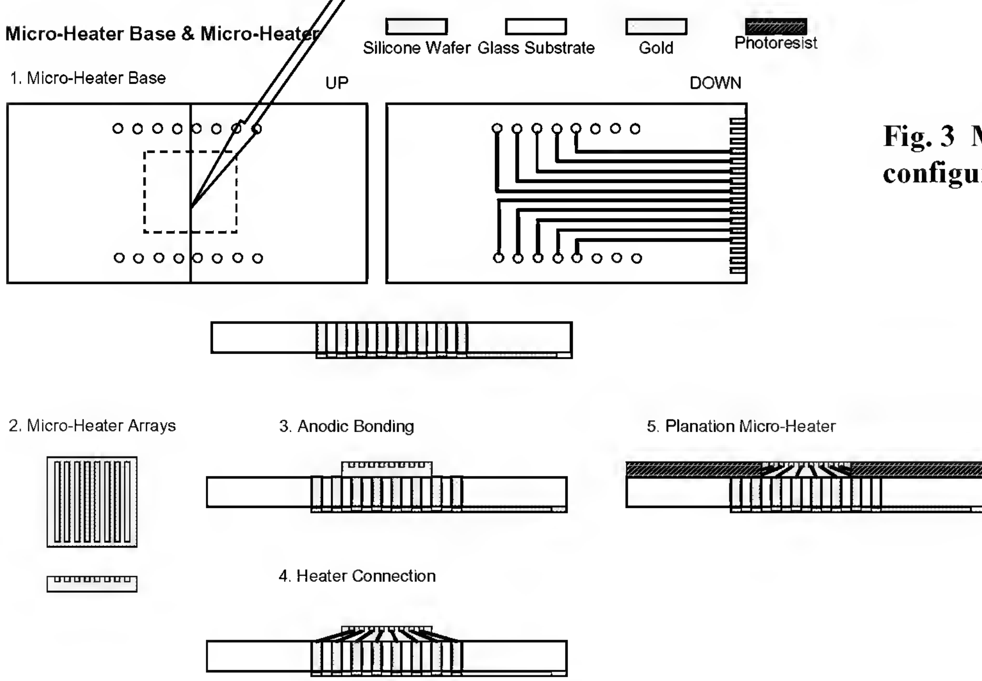

Fig. 3 Micro-heater configuration

DEVELOPMENT OF A NEW MEMBRANE CASTING APPARATUS FOR STUDYING MACROVOID DEFECTS IN LOW-G

Hanyong Lee, Sun-Tak Hwang and William B. Krantz
Department of Chemical Engineering, University of Cincinnati, Cincinnati, Ohio, 45221-0171

Alan R. Greenberg, Vivek Khare and Jeremiah Zartman
Department of Mechanical Engineering, University of Colorado, Boulder, Colorado 80309-0427

Paul W. Todd
Space Hardware Optimization Technology, Inc. Greenville, Indiana 47124-9515

ABSTRACT

A new membrane-casting apparatus is developed for studying macrovoid defects in polymeric membranes made by the wet- and dry-casting process in low-gravity. Macrovoids are large (10-50 μm), open cavities interspersed among the smaller pores in the substructure under the gelled skin surface layer of the cast membrane [1]. Although their occurrence is considered endemic to the wet- and dry-casting process since they can lead to compaction or skin rupture in the membrane process [2], recent studies suggest several useful applications such as transdermal and osmotic drug delivery systems [3,4], miniature bioreactors [5], etc. However, lack of knowledge about the macrovoid formation mechanism is an obstacle to further development of applications using them. An on-going debate is the role of the surface-tension-driven solutocapillary convection during macrovoid formation. The rapid growth of macrovoids within 1-5 seconds and the high polymer concentration in and near macrovoids make it difficult to explain the mechanism of macrovoid growth by diffusion alone, which is the widely accepted hypothesis proposed by Reuvers et al. [6]. The hypothesis advanced by our research group can explain this rapid growth via a mechanism that involves diffusion from the casting solution in the meta-stable region to the macrovoid enhanced by solutocapillary convection induced by the steep nonsolvent concentration gradient in the vicinity of the macrovoid.

Since macrovoid growth is hypothesized to be the interplay of a solutocapillary-induced driving force counteracted by viscous drag and buoyancy, eliminate the latter provides a means for testing this hypothesis. Moreover, free convection mass transfer in the nonsolvent immersion bath used to cause phase-separation in membrane casting complicates developing a model for both the wet-casting process and macrovoid growth. The low-g environment minimizes gravitationally induced free convection thereby permitting a tractable solution to the ternary diffusion equations that characterize membrane formation.

NASA's Parabolic Flight Research Aircraft provides a small window of low-g (~25 s) that can be used to study macrovoid development in both wet- and dry-cast membranes if an appropriate casting apparatus is used. This casting apparatus should be able to cast the membrane in both low- and high-g in a manner so that essential one-dimensional mass transfer conditions are achieved to insure lateral uniformity in the membrane. The apparatus used in previous research on membrane casting in low-gravity was operated with the plunger driven mechanism. The spring-loaded plunger pushes the bottom block containing the polymer casting solution well

directly under the absorbent chamber located in the upper stationary block [7]. However, membranes made via this casting apparatus often displayed lateral nonuniformities that precluded obtaining quantitative information on the macrovoid growth process. Thus, it was necessary to determine the reason for these structural irregularities observed in the low-g casting apparatus.

Both experimental as well as computer simulation studies of the low-g casting apparatus established that the impulsive action of the plunger caused the undesired structural nonuniformities. The simulation results showed that the width-to-depth aspect ratio of the shallow well that contains the casting solution in this apparatus was not an important factor in minimizing this problem. Even for a 40:1 (width : depth) aspect ratio, any convection induced by the horizontal motion of the interface of the casting solution will be damped out within 6.25×10^{-4} seconds. However, the experimental studies revealed that the impulsive motion of the plunger caused a "sloshing" of the casting solution that had to be eliminated. Therefore, the plunger-driven mechanism was changed to a cam-driven mechanism that did not cause any impulsive motion of the casting solution. Other refinements to this new membrane-casting apparatus include provision for removing the membranes from the casting wells in a less destructive manner. This was accomplished by using a slit geometry for the casting well that permitted disassembly for removal of the cast membrane. The materials used in the construction of this casting apparatus were chosen to insure wetting at the side walls and to maintain precise control of the thickness of the polymer solution in the casting well. An additional provision in this new casting apparatus is the ability to carry out both wet- as well as dry-casting. As such, this apparatus permitted the first studies of the wet-casting of polymeric membranes in low-g. Both wet- and dry-casting experiments on NASA's KC-135 research aircraft employing this new membrane-casting apparatus are scheduled in July 2002. The morphology of the resulting membranes will be characterized using an environmental scanning electron microscope (ESEM). The results of these low-g studies will be reported later.

[1] Konagurthu, S., "Macrovoids in dry-cast polymeric membranes: growth mechanisms, non-invasive detection, and effects on performance." Ph.D. Dissertation. University of Colorado, Boulder (1998)

[2] Kesting, R. E., *Synthetic Polymeric Membranes – A structural Perspective*, 2nd ed. Wiley, New York (1986).

[3] Herbig, S. H., Carinal, J. R., Korsmeyer, R. W. and Smith, K. L., "Asymmetric membrane tablet coating for osmotic drug delivery," J. Control. Release, **35** (1995) 127-136

[4] Smolder, C. A., Reuvers, A. J., Boom, R. M. and Wienk, I. M., "Microstructures in phase-inversion membranes. Part I. Formation of macrovoids," J. Mem. Sci., **73** (1992) 259-275

[5] Jacob, E. P. and Leukes, W. D., "Formation of an externally unskinned polysulfone capillary membrane." J. Mem. Sci., **121** (1996) 149-157

[6] Reuvers, A. J. "Membrane formation –diffusion induced demixing processes in ternary phase separation phenomena." Desalination, **32** (1980) 33-45

[7] Pekny, M. R., "Influence of solutocapillary convection on macrovoid defect formation in dry-cast polymeric membrane" M.S. Thesis. University of Colorado, Boulder (1996)

UNIVERSITY OF Cincinnati

Development of a New Membrane-Casting Apparatus for Studying Macrovoid Defects in Low-g

Hanyong Lee, William B. Krantz and Sun-Tak Hwang
Department of Chemical Engineering, University of Cincinnati
Cincinnati, Ohio, 45221-0171
Alan R. Greenberg, Vivek Khare and Jeremiah Zartman
Department of Mechanical Engineering, University of Colorado
Boulder, Colorado 80309-0427
Paul W. Todd
Space Hardware Optimization Technology, Inc.
Greenville, Indiana 47124-9515

GRANT NUMBER: NAG3-2451
TASK MONITOR: Dr. Chanthy Iek

I. Introduction

Polymeric Membrane Casting Methods

- Dry-Cast Process
  : Evaporation of Solvents from Casting solution
- Wet-Cast Process
  : Mass transfer between Solvents and Nonsolvents

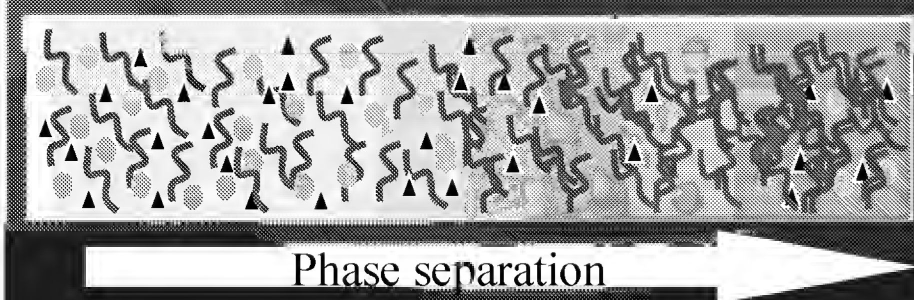

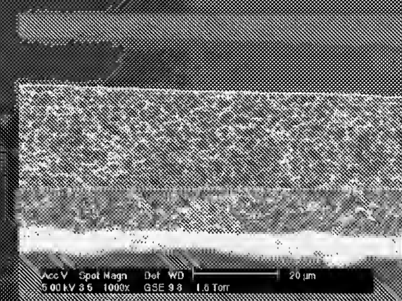

UNIVERSITY OF Cincinnati

I. Introduction

Macrovoids

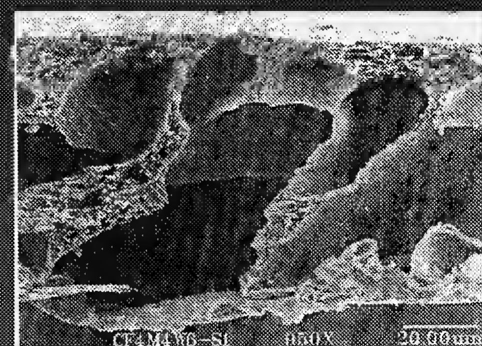

- Large bulbous pores (10~100 μm)
- Defects :
  decreasing selectivity and strength
- Applications :
  breathable clothing, tents, screen printing …
- Hypothesis for growing Mechanism :
  Smolders et al. – diffusion only
  Shojaie et al. - solutocapillary convection + diffusion
  (2-layer model)
  Pekny et al. – solutocapillary convection + diffusion
  (3-layer model)

UNIVERSITY OF Cincinnati

II. Objectives

Develop fundamental understanding of macrovoid pore growth process and means for controlling it

- Determine mechanism for macrovoid growth
- Utilize low-g to change body force
- Use surfactant to change surface forces
- Design & construct apparatus for casting membranes in low-g
- Extend low-g studies to wet-cast membranes
- Assess effective parameters on macrovoid growth

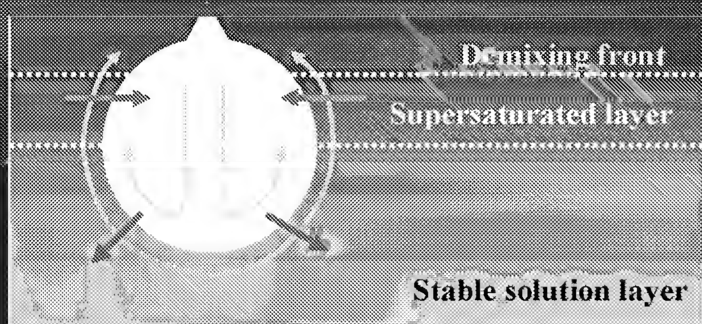

UNIVERSITY OF Cincinnati

III. Experimental Design & Construction

How to prevent "sloshing" problem in previous MCA?

Vertical velocity

Dimension		Velocity (cm/s)		Time(s)
Width	Depth	Convection	Diffusion	
1	2	1.7480E-10 <	1.2649E-07	6.25E-04
1	3	1.2350E-09 <	1.2649E-07	6.25E-04
40	1	1.8600E-08 <	1.2649E-07	6.25E-04
1	5	1.4120E-02 <	7.2595E-07	1.90E-05
7	1	6.9952E-04 <	4.3437E-07	5.30E-05

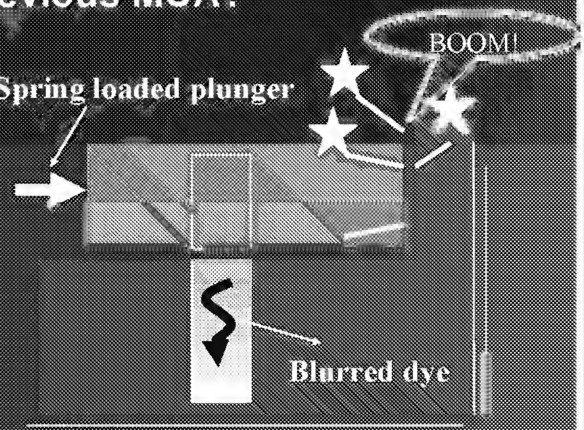

- Computer simulation results show that convective flow is very quickly damped out regardless of aspect ratio of casting well
- Experimental results show that spring-driven mechanism in previous membrane-casting apparatus (MCA) is a major cause of undesirable convection
- Cam-driven mechanism is more suitable for MCA than mechanism using spring-loaded plunger

UNIVERSITY OF Cincinnati

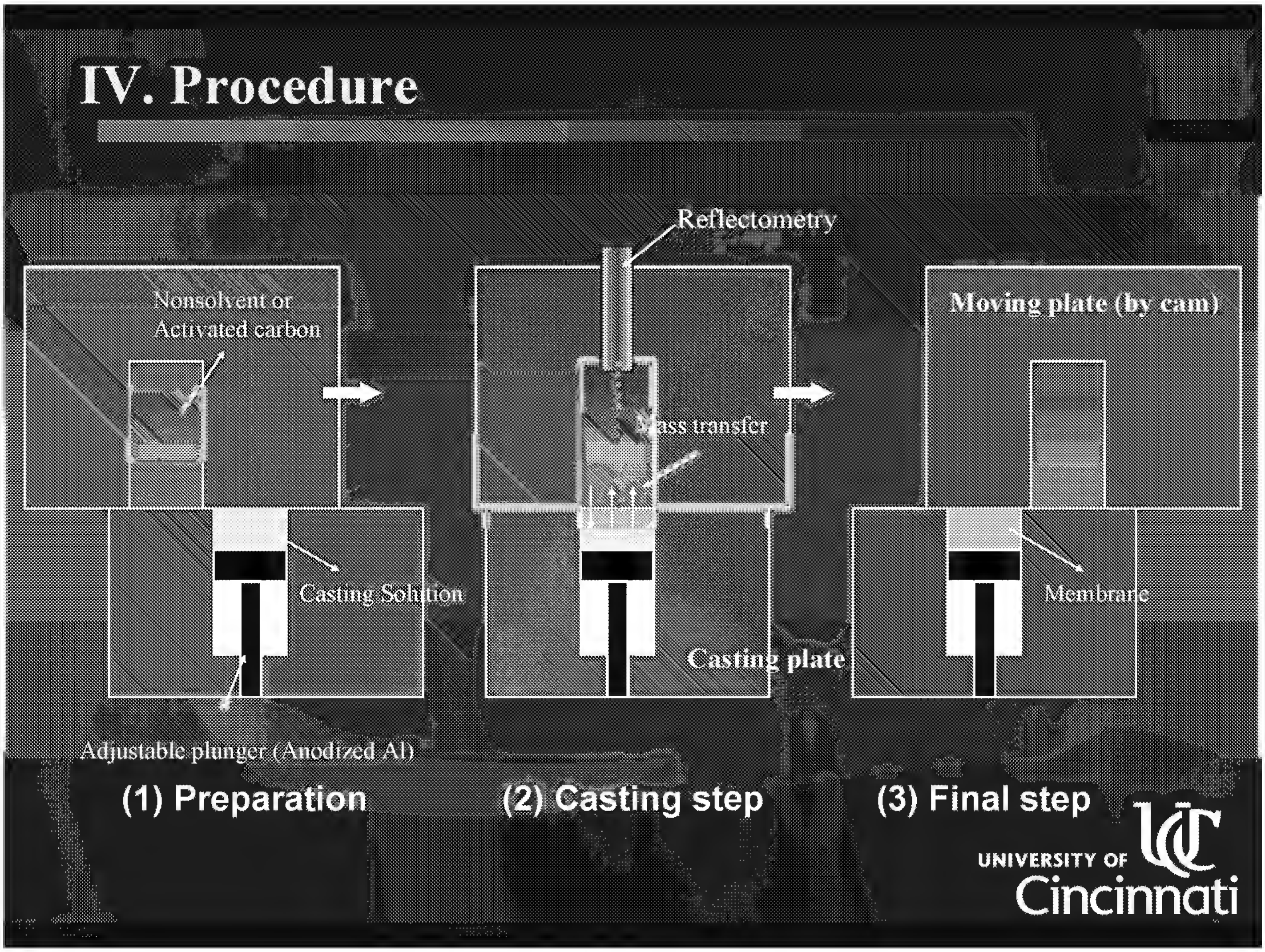
IV. Procedure
Reflectometry
Nonsolvent or
Activated carbon
Moving plate (by cam)
Mass transfer
Casting Solution
Membrane
Casting plate
Adjustable plunger (Anodized Al)
(1) Preparation
(2) Casting step
(3) Final step
UNIVERSITY OF
Cincinnati

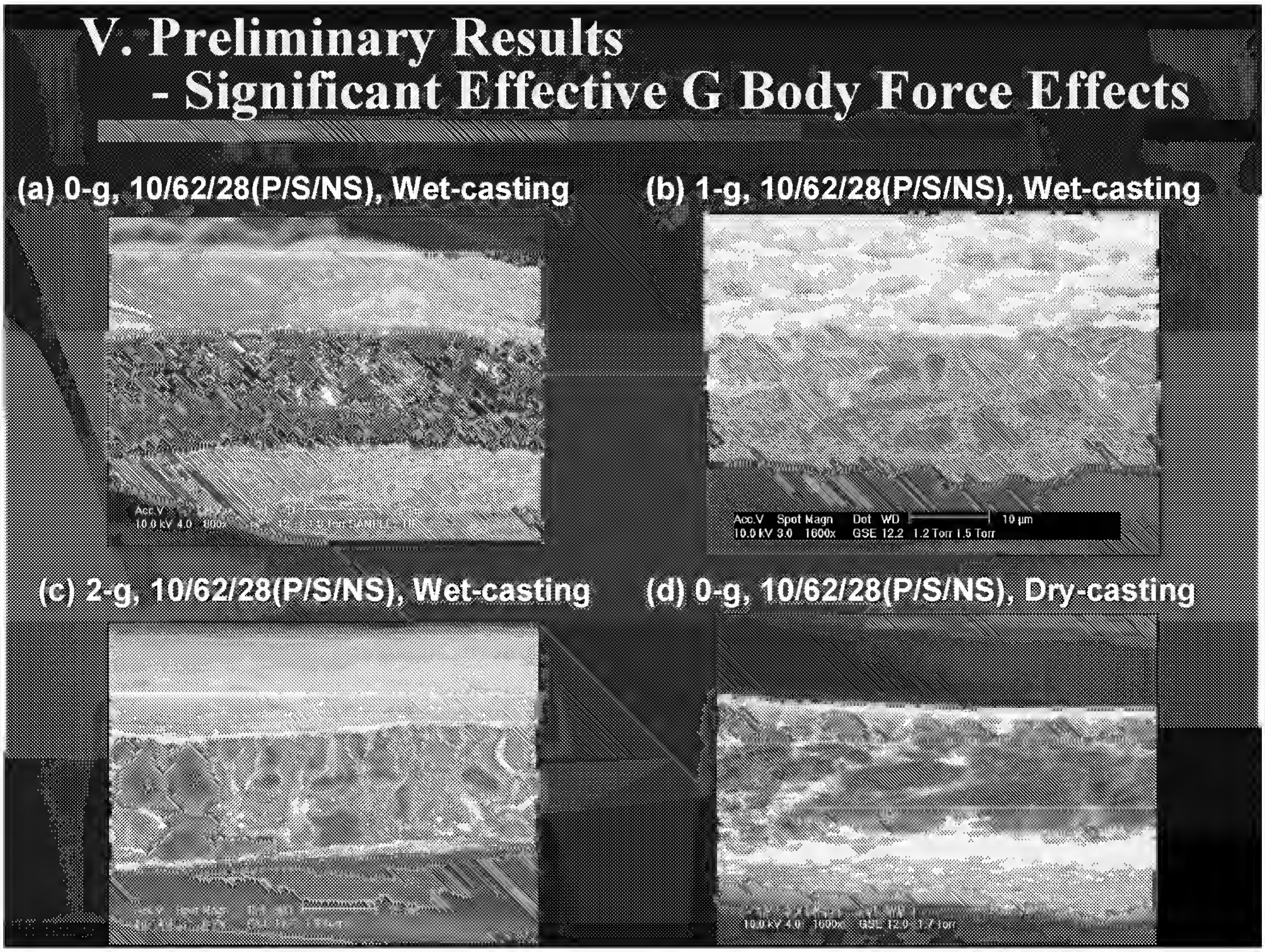
V. Preliminary Results
- Significant Effective G Body Force Effects
(a) 0-g, 10/62/28(P/S/NS), Wet-casting
(b) 1-g, 10/62/28(P/S/NS), Wet-casting
Acc.V Spot Magn Det WD 10 µm
10.0 kV 3.0 1600x GSE 12.2 1.2 Torr 1.5 Torr
(c) 2-g, 10/62/28(P/S/NS), Wet-casting
(d) 0-g, 10/62/28(P/S/NS), Dry-casting

VI. Preliminary Conclusions

- New MCA is successfully designed to make membranes via wet-casting as well as dry-casting processes
- Experimental results and simulation results show that spring-driven mechanism in previous MCA is a major reason for "sloshing" problem
- Anodized aluminum is better material for adjustable bottom plate of casting well because of ease of detaching the sample and improved light reflectometry measurement of phase inversion
- The optimal initial thickness of casting solution is 70 microns for 25 seconds in low-g
- As gravitational body force increases, macrovoids appear to penetrate more deeply through membrane
- The body force is one of factors that can affect the growth of macrovoids through its influence on coalescence that is identified as important factor during macrovoid growth

Using Nonlinearity and Contact Lines to Control Fluid Flow in Microgravity

M. Perlin, W.W. Schultz, X. Bian, and M. Agarwal, University of Michigan

Slug flows in a tube are affected by surface tension and contact lines, especially under microgravity. Numerical analyses and experiments are conducted of slug flows in small-diameter tubes with horizontal, inclined and vertical orientations. A PID-controlled, meter-long platform capable of following specified motions is used. An improved understanding of the contact line boundary condition for steady and unsteady contact-line motion is expected. Lastly, a direct fluid-handling method using nonlinear oscillatory motion of a tube is presented.

I. Quasi-static tube inclination with axial gravitational component

A. *Incipient motion*: Experiments were conducted on quasi-statically inclined, 3.7 mm diameter glass circular cylinders containing fluid slugs. Using a simple force balance, the governing equation is

$$\sin(\theta) = \frac{4\sigma}{\rho d \lg}\left[\cos\alpha - \cos\beta\right]$$

where θ = angle of the cylinder measured from horizontal, α = contact-line angle at the lower end of the slug for incipient motion, β = contact-line angle at the upper end of the slug for incipient motion, ρ = mass density of liquid (water), σ = air-water interfacial surface tension, and l = slug length. For a typical slug length of 5.08 cm, $\alpha = 53^0$ and $\beta = 25^0$. The theoretical value of θ was 2.75^0; the measured value of θ was 2.53^0. When the cylinder's inner surface is pre-wetted, α is closer to β, and θ is decreased significantly.

B. *Viscous drag on a fluid slug*: Constant motion of a fluid slug is achieved by inclining the tube. Video is used to capture the subsequent motion. When a constant slug velocity results, equilibrium presumably requires the driving force (i.e. pressure force due to gravity) to equal the sum of the viscous and the contact line forces. The liquid flow field is complicated by the deformation of the ends of the slug. For a slug with a large aspect ratio (length to diameter) and velocity U, the pressure decrease due to viscosity should be $p_v = \frac{8l\mu U}{R^2}$ neglecting the flow near the ends. As the retarding force due to the contact lines is vastly different for dry and pre-wetted surfaces, experiments under both conditions are conducted. Again, the contact line force for pre-wetted tubes is much smaller than for the dry tubes. Especially for long cylinders, the effect of air in the tube is considered with this friction comparable to the viscous effects directly on the slug.

II. Resonance analyses and experiments for fixed contact or stick-slip motion

As the eventual objective of this project is to control fluid flow in microgravity by nonlinearity, we investigated the natural frequency of the end surfaces of the slug. Presumably, the natural frequency of the confined slugs should create the largest disturbances of the end caps, thereby producing maximum net flow. The initial analytic solution was based on the simplest model, a

zero-dimension (0-D) approximation (i.e. a liquid slug where the center of mass shifts due to the oscillation of its ends). Here the end-cap surface is assumed spherical for the axisymmetric geometry, with the spherical segment set by the contact angle. To solve for the natural frequency and its mode shape, the potential flow problem for a fixed contact line condition is formulated as a generalized eigenvalue problem. The dynamic and kinematic boundary conditions are evaluated at the original equilibrium surface. The surface elevation $z = \eta(r,t)$ (relative to the unperturbed curved surface $z = \zeta(r)$) is expressed as a summation of basis functions (cosine series, Chebyshev polynomials, etc.) and the problem is solved accordingly. In figure 1 the numerical results for the 'slosh mode' are presented with direct comparison to the aforementioned 0-D approximation. Good agreement is observed. An experiment was conducted to verify the analysis. The measured slosh frequency is smaller than the analysis suggests. The deviation may be attributed to viscosity and possible contact line slip. The effect of partial slip was also evaluated by introducing a simple slip parameter γ, defined as a slip coefficient in the contact line stick-slip condition: $\eta + \gamma\eta_r = 0 \, (r = R)$. As $\gamma \to 0$, the frequencies converge to the pinned contact-line solution. When $\gamma \to \infty$, the contact line slips on the wall, and the frequency goes to zero as the restoring force of the meniscus vanishes.

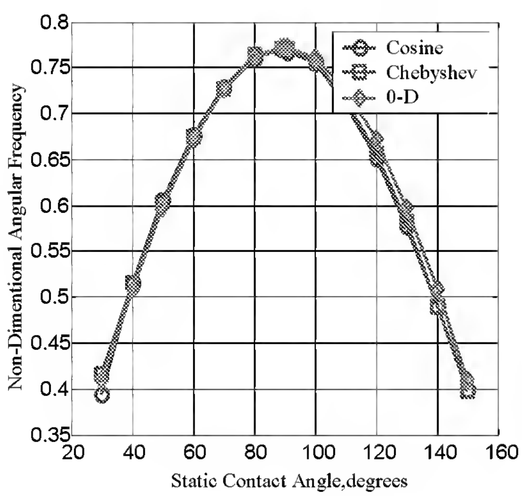

Figure 1. End cap resonance frequency versus static contact angle.

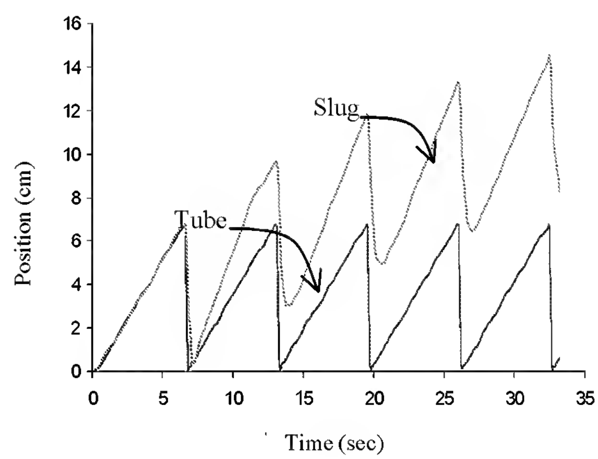

Figure 2. Motion of cylinder and slug showing mean motion generated.

III. Periodic horizontal motion to generate a mean flow

To experimentally achieve periodic motion, an infinite number of motion profiles can be tested. Presented in figure 2 is a cylinder position versus time graph that generates slug mean motion. To qualitatively study the mean motion, three segments of constant cylinder acceleration are chosen that forms a saw-tooth-like velocity profile over each cycle. As shown, a mean motion of the slug is generated with low frequency motion. Motions at higher frequencies will be presented also.

Using Nonlinearity and Contact Lines to Control Fluid Flow in Microgravity

M. Perlin, W.W. Schultz, X. Bian, and M. Agarwal

The University of Michigan

Supported by NASA
Award NAG3-2406

Summary

Numerical analyses and experiments are conducted on (finite Re) slug flows in small-diameter tubes for varying inclined orientations. An improved understanding of the contact line boundary condition for steady and unsteady contact-line motion is evolving. In addition, a direct fluid-handling method using nonlinear oscillatory motion of a tube is presented.

I. Quasi-static tube inclination with axial gravitational component

A. Incipient motion

Force balance: $$\sin(\theta) = \frac{4\sigma}{\rho d L g}(\cos\beta - \cos\alpha)$$

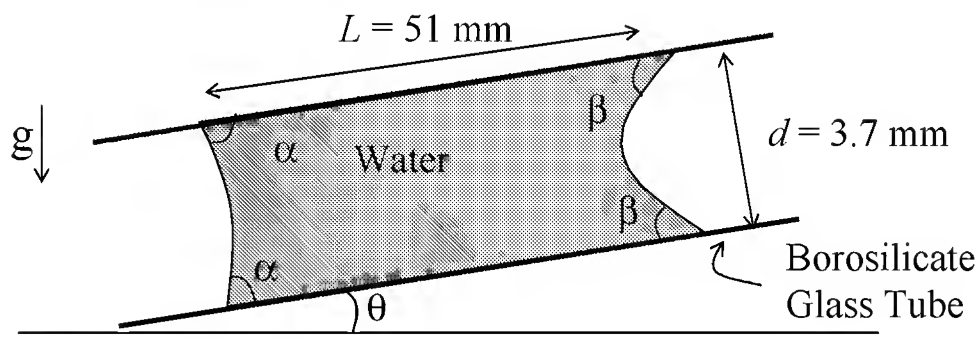

Fig. 1. Estimated θ = 2.7⁰; Measured θ =2.5⁰. For pre-wetted inner tube, α is closer to β, and θ is decreased significantly.

I. Quasi-static tube inclination with axial gravitational component (continued)

B. Viscous drag on a fluid slug with constant velocity

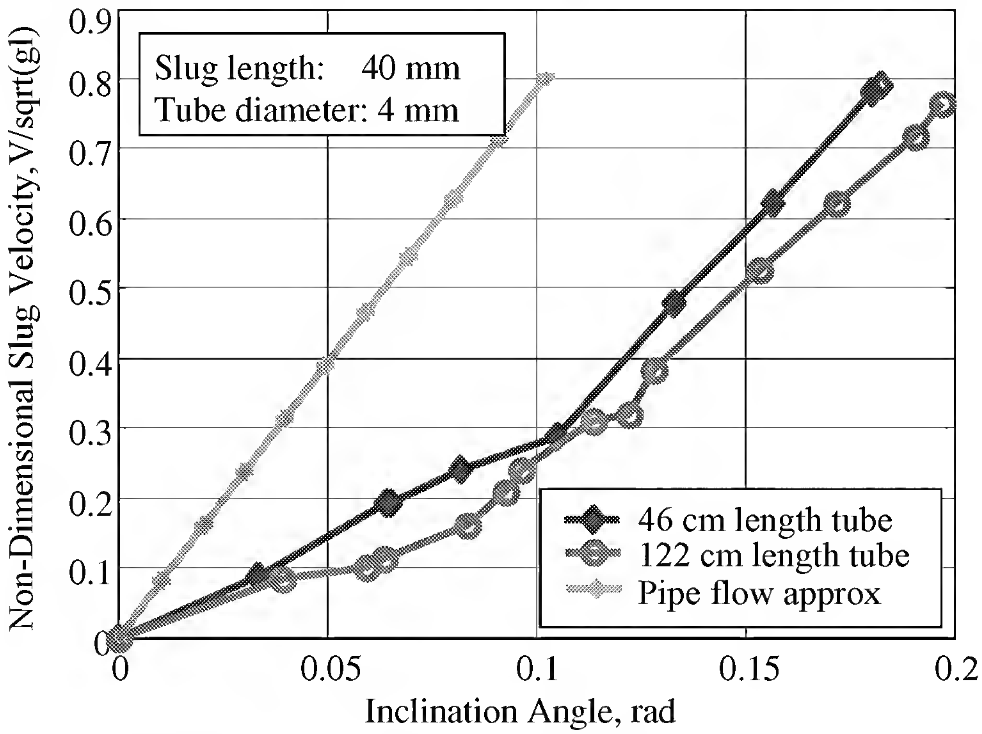

Fig. 2. Slug velocity versus inclination. As expected, the near menisci flow and the friction due to air are important to the total resistance. (Longer tube slows slug velocity.)

II. Resonance analyses & experiments for fixed contact line or stick-slip motion

We investigated the natural frequency of the end surfaces of the slug. A spectral method was used to solve the eigenvalue problem of the potential flow for originally spherical menisci.

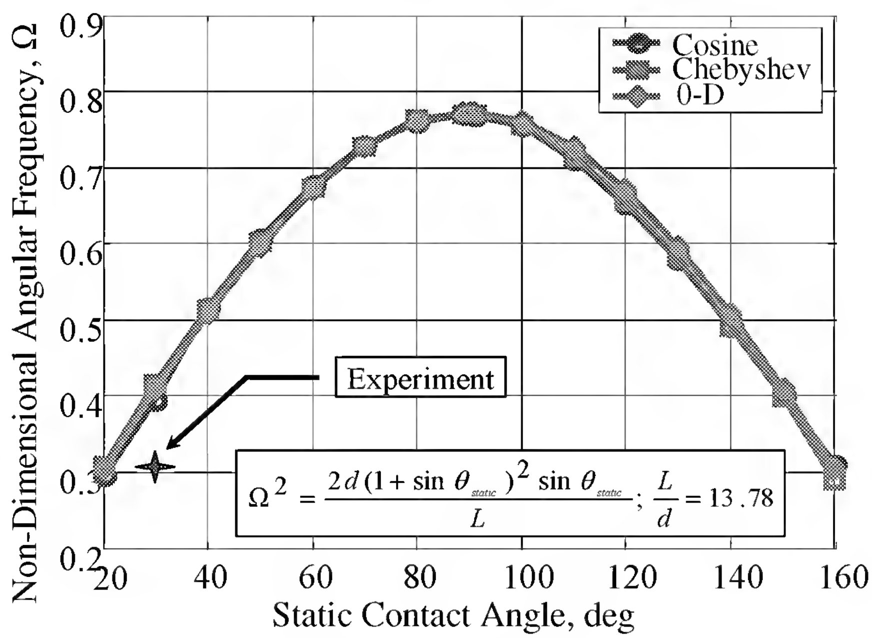

Fig. 3. End cap resonance frequency versus static contact angle. The lowest slosh frequency is surprisingly close to a simple zero-dimensional spring-mass approximation.

II. Resonance analyses & experiments for fixed contact line or stick-slip motion (continued)

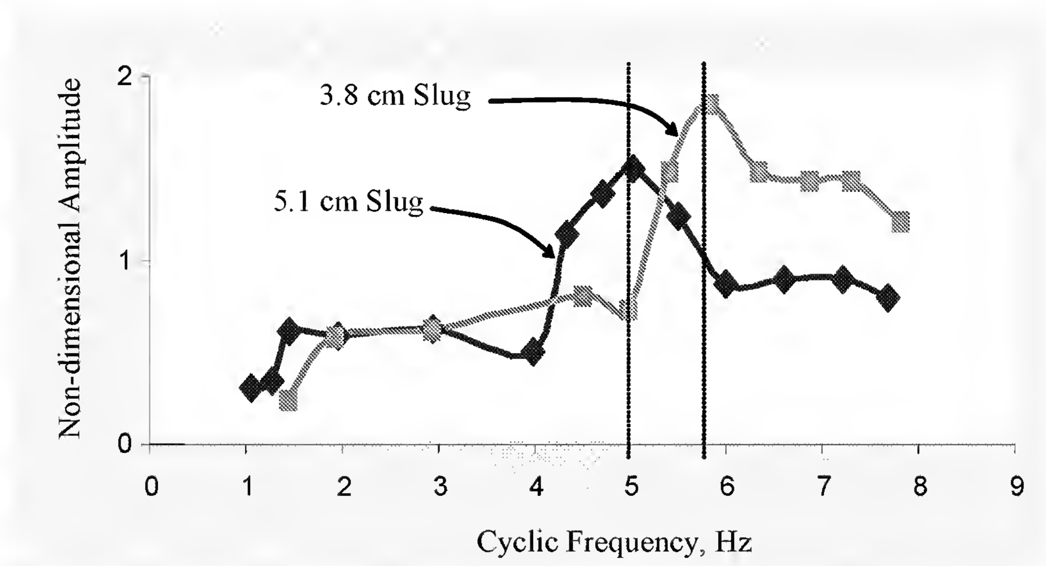

Fig. 4. Experimental results of end cap amplitude response for slugs of different lengths.

II. Resonance analyses & experiments for fixed contact line or stick-slip motion (continued)

Slip effects are evaluated by defining a stick-slip parameter, γ, where $\eta + \gamma\eta_r$=0, and η is the surface elevation

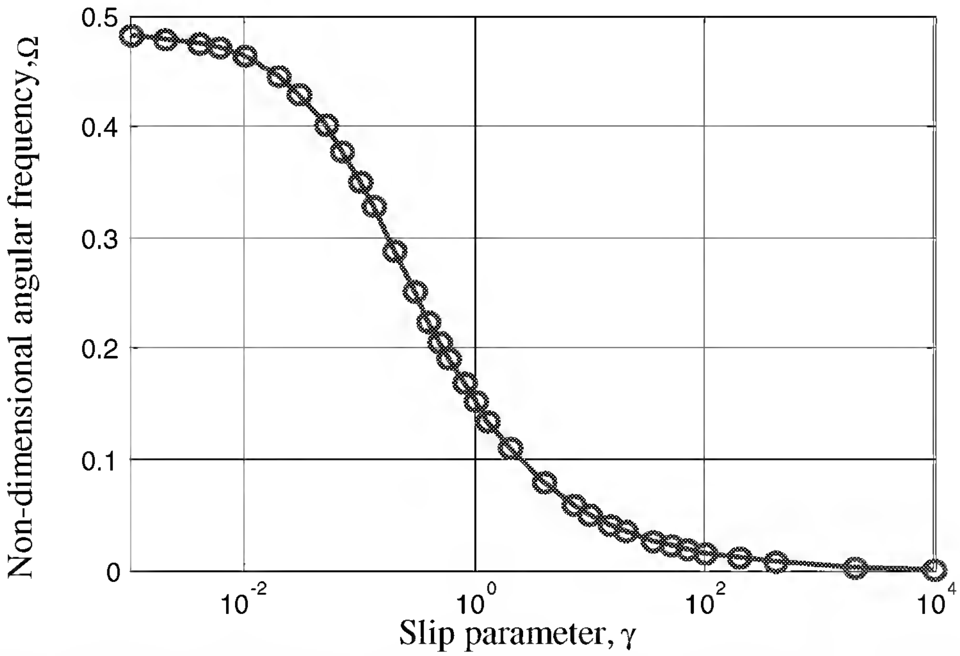

Fig. 5. Lowest slosh frequency versus the slip parameter, γ, for aspect ration L/D = 10 and contact angle θ = 30°. The frequency decreases monotonically when contact line slips.

III. Periodic horizontal motion to generate a mean flow

Slug mean flow is generated by oscillatory motion of a horizontally oriented tubes.

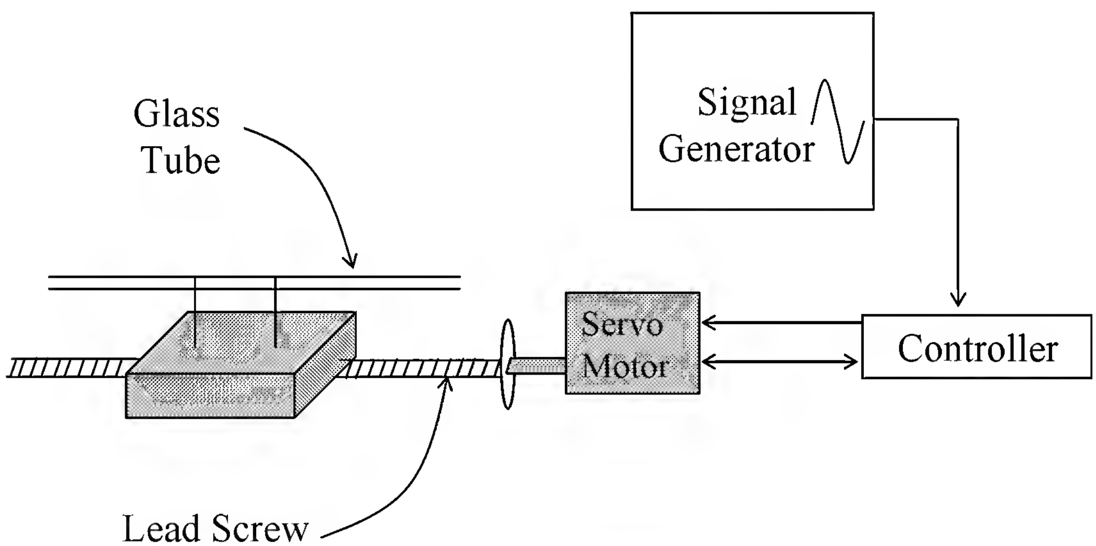

Fig. 6. A PID-controlled, meter-long platform capable of following specified motions is used for horizontal experiments.

III. Periodic horizontal motion to generate a mean flow (continued)

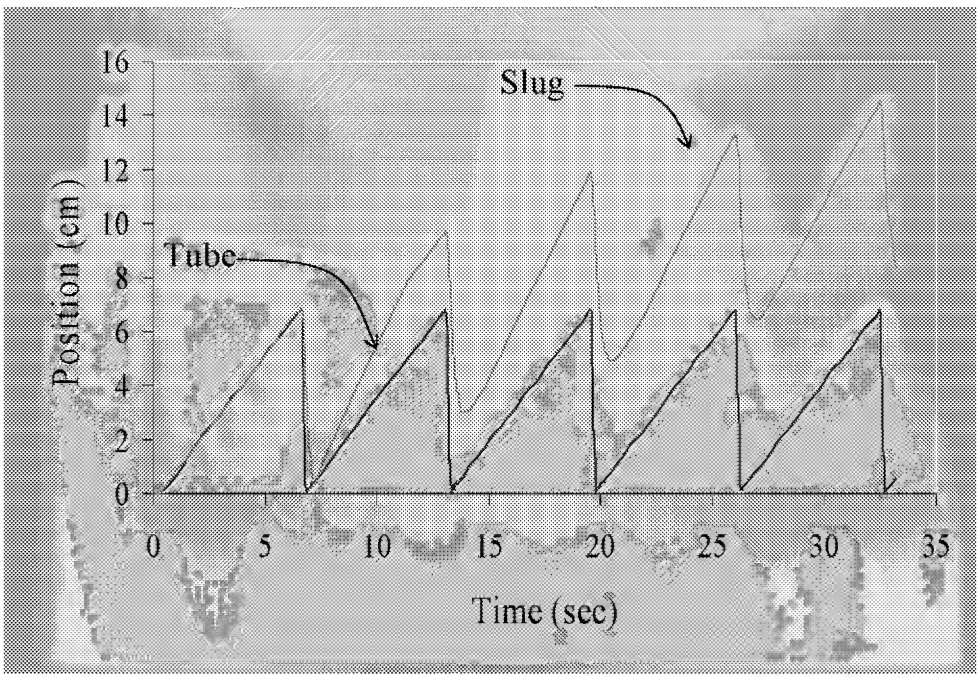

Fig. 7. Asymmetric tube motion generates net slug displacement.

Conclusions

- The difference in apparent contact angles accounts for incipient slug motion.
- Near menisci flow, wetting, and air resistance are important.
- Static apparent contact angle is important in primary mode of slug oscillation.
- Mean flow is achieved for very low frequency asymmetric motion.

OPTICAL MEASUREMENT OF MASS AND THERMAL DIFFUSION FLUIDS

By

Nasser Rashidnia

A robust instrument is developed to measure much needed crucial thermophysical properties such as diffusion coefficient of miscible fluids, concentration and thermal gradient fields with high precision.

Approach:

- **Use a very low power (< 0.1mW) laser light in combination with a polarization prism and a half-wave retarder to construct the common-path interferometer.**
- **Select and position the prism at a special orientation with respect to the direction of gradient orientation.**
- **Obtain interferograms in real time that contain index of refraction gradient field.**
- **Analyze the data to obtain diffusivity for mixing fluids, concentration and thermal gradient fields.**

Features & Advantages:

1. **Robust instrument; Easy to set up and align**
2. **Variable sensitivity (a feature lacking in all other standard interferometers)**
3. **High data-density thermal and mass diffusion real-time measurement capability.**
4. **No need for ultra optical quality test-cell windows.**

OPTICAL MEASUREMENT OF MASS AND THERMAL DIFFUSION IN FLUIDS

Schematic of the common-path shearing interferometer(CPI)

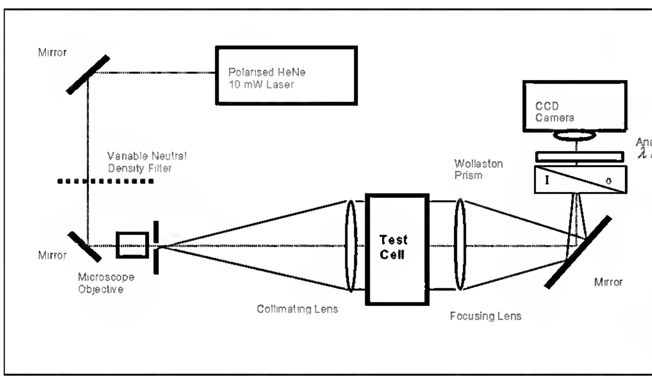

Bench Top Setup of the Instrument

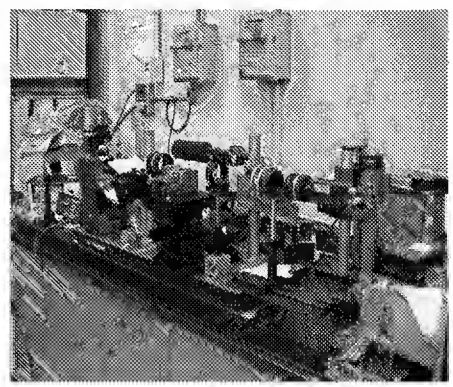

OPTICAL MEASUREMENT OF MASS AND THERMAL DIFFUSION IN FLUIDS

Application: Thermal diffusion

(a) Numerical predictions of the temperature field ($\Delta\ \theta = 0.025$) around a bubble under a heated surface, (b) numerical predictions of the fringe distribution ($\varphi_{min} = -0.50$, $\varphi_{max} = 1.0$), and (c) experimental interferograms for the case with Ma = 9.4×10^4, Ra = 1.4×10^4, Pr = 7.80, R_b = 0.115 cm, $Ma_m = 3.4 \times 10^3$, Bo = 3.42, and Ar_b = 0.78.

OPTICAL MEASUREMENT OF MASS AND THERMAL DIFFUSION IN FLUIDS

Application: Mass Diffusion

Table 1. Comparison of measured diffusivities

Silicone – Oil Fluid – Pairs	$D_{1-\frac{1}{e}}(cm^2/s)$	$D_{\frac{1}{e}}(cm^2/s)$	$D_{Wiener}(cm^2/s)$	*Technique*
1000 cs/100 cs	$(4.36 \pm 0.30) \times 10^{-8}$	$(4.79 \pm 0.22) \times 10^{-8}$	$(1.69 \pm 0.06) \times 10^{-8}$	WM
	$(5.11 \pm 0.73) \times 10^{-8}$	$(5.41 \pm 0.75) \times 10^{-8}$	-	CPI
1000 cs/10 cs	$(2.61 \pm 0.10) \times 10^{-7}$	$(2.47 \pm 0.10) \times 10^{-7}$	$(3.14 \pm 0.15) \times 10^{-7}$	WM
	$(2.83 \pm 0.72) \times 10^{-7}$	$(2.34 \pm 0.68) \times 10^{-7}$	-	CPI
1000 cs/1 cs	$(4.17 \pm 0.23) \times 10^{-6}$	$(2.48 \pm 0.21) \times 10^{-6}$	$(1.93 \pm 0.08) \times 10^{-6}$	WM
	$(2.65 \pm 0.32) \times 10^{-6}$	$(1.93 \pm 0.29) \times 10^{-6}$	-	CPI

WM – Wiener's method [8]
CPI – Common-path interferometer

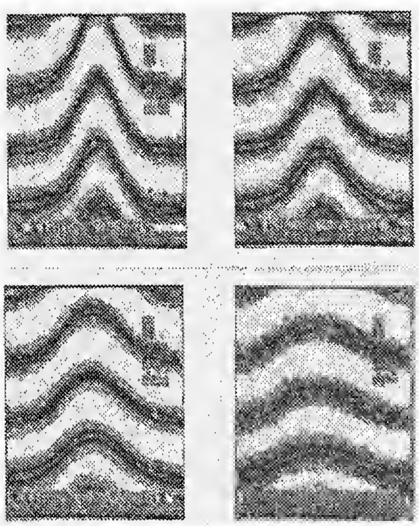

Interferogram images near the interface of 10 cSt and 1000 cSt silicone oils at (a) 160, (b) 280, (c) 460, and (d) 1000 minutes after the fluids came into contact.

Sixth Fluids Conference, NASA GRC, Cleveland, OH, August 2002
N. Rashidnia

NCMR
FLUIDS AND COMBUSTION

OPTICAL MEASUREMENT OF MASS AND THERMAL DIFFUSION IN FLUIDS

Application: Concentration dependent diffusivity

(A)

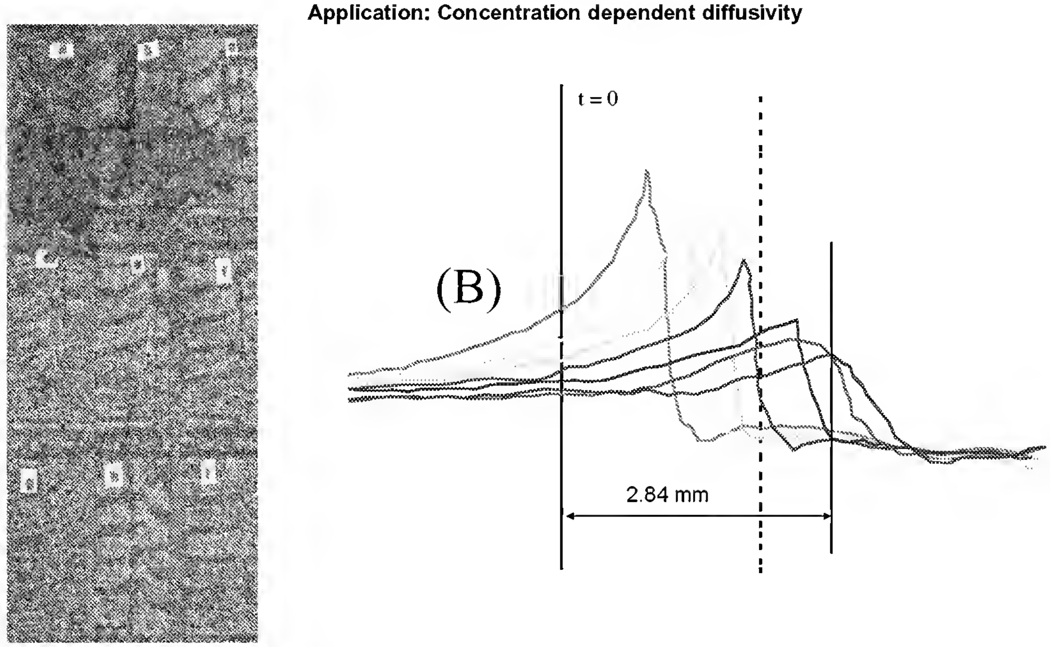

(A) Fringe images and (B) the traces of fringe two from the bottom of panels representing the evolution of the concentration gradient in water-glycerine system for (b) t=1 min, (c) to t=54 min, (d) t=86.5 min, (e) t=118 min, (f) t=145.5 min, (g) t=205.5 min, (h) t=265.5 min, (i) t=325.5 min.

OPTICAL MEASUREMENT OF MASS AND THERMAL DIFFUSION IN FLUIDS

Diffusivity of water-glycerine system

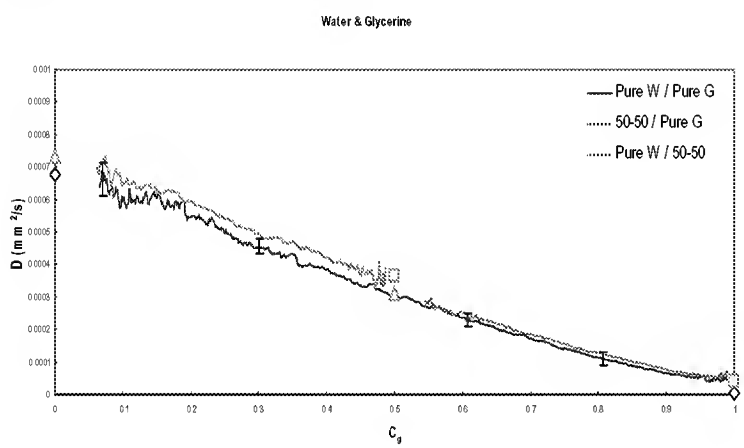

Comparison of local diffusivity

Cw	**D** **(mm²/s)** Present	**D** **(mm²/s)** Maxworthy (1996)
0	4.6E-5	1.7E-5
0.75	5E-4	3.5E-4

Sixth Fluids Conference, NASA GRC, Cleveland, OH, August 2002
N. Rashidnia

NCMR
FLUIDS AND COMBUSTION

OPTICAL MEASUREMENT OF MASS AND THERMAL DIFFUSION IN FLUIDS

Relevant Reference Publications

1. **N. Rashidnia & R. Balasubramaniam & M. Boggess, "Concentration dependent diffusivity of miscible liquids measured with interferometry," paper F0040, in *The 10th International Symposium on Flow Visualization (ISFV10)* Kyoto, Japan, 2002.**

2. **N. Rashidnia & R. Balasubramaniam, "Development of an interferometer for measurement of diffusion coefficient of miscible liquids," *Applied Optics*, 41: (4) 1337-1342-3195 March 1st 2002**

3. **N. Rashidnia, R. Balasubramaniam, J. Kuang, P. Petitjeans and T. Maxworthy, "Measurement of the diffusion coefficient of miscible fluids using both interferometry and Wiener's method," *International Journal of Thermophysics*, Vol. 22, No 2, pp. 547-555, March 2001.**

4. **N. Rashidnia and R. Balasubramaniam, "Optical measurement of concentration gradient near miscible interfaces," *Ann. N.Y. Acad. Sci.* 974: 1-8 (2002). Also paper UEF: MTP-01-22, the *United Engineering Foundation*, Microgravity Transport Processes in Fluid, Thermal, Biological and Materials Sciences II, pp. 140-144, Ed. S.S. Sadhal, 2001.**

5. **M. Kassemi and N. Rashidnia, "Steady and oscillatory thermocapillary convection generated by a bubble," *Physics of Fluids*, Vol. 12, No. 12, pp. 3133-3146, 2000.**

6. **N. Rashidnia, "Novel diffusivity measurement optical technique," *The 9th International Symposium on Flow Visualization*, Eds. G. M. Carlomango and I. Grant, pp. 451.1-451.8, 2000, ISBN 0 9533991 1 7.**

OPTICAL MEASUREMENT OF MASS AND THERMAL DIFFUSION IN FLUIDS

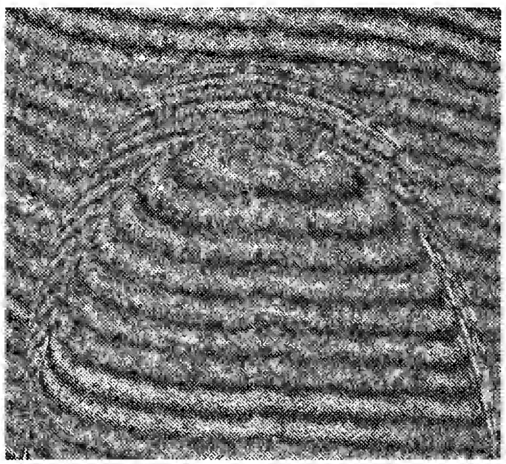

Current Application

Investigation of the concentration field near a moving and inter-diffusive interface of a low viscosity into a higher viscosity oil.

Future Application

Soap film thickness full-field measurement and particle detection in bio-fluids

Sixth Fluids Conference, NASA GRC, Cleveland, OH, August 2002
N. Rashidnia

MAGNETIC FLUID MANAGEMENT (MFM)

Dr. Eric Rice, Mr. Robert Gustafson, Dr. John Hochstein,
Mr. Jeff Marchetta, and Dr. Martin Chiaverini
Orbital Technologies Corporation (ORBITEC^{TM})

INTRODUCTION

The difficult problem of cryogenic fluid handling in many aerospace applications in low gravity environments can be solved by employing a new magnetic fluid technology called magnetic fluid management (MFM). The innovative MFM technology has the potential to provide significant advancements over other technologies such as screens, vanes, porous plugs, and no-vent fill processes. MFM technology utilizes the magnetic properties of cryogenic fluids for phase separation. This enables new processes which greatly simplify many critical tasks now encountered, such as gas-free liquid transfer between cryogenic containers, liquid-free gas venting during storage, liquid-free gas venting during tank refill, and use of a self-regulating control system to maintain tank pressure during liquid expulsion.

COMPUTATIONAL MAGNETIC FLUID DYNAMICS (CMFD) MODELING

The magnetic fluid dynamics of the MFM system is being modeled with a modified and enhanced version of the RIPPLE code, originally developed by Los Alamos National Laboratory for modeling the unsteady flow of incompressible, constant property, Newtonian fluids. The ability of the RIPPLE code and its variants to model flows with highly deforming free surfaces in which surface tension forces are significant has been well documented, as has been their fidelity in modeling the propellant reorientation process. Reorientation is determined by the magnet's ability to influence a reasonable portion of the propellant to traverse the tank wall and come in contact with the opposing tank head.

1-G LABORATORY TESTING

A series of ground-based experiments were designed to determine the effect of magnetic fields on ferrofluid and LOX in full gravity. Initial CMFD analyses of both LOX and ferrofluid motion in a cylindrical tank in a 1-g environment have been conducted to support the design of ground-based experiments. The goal of this work is to help identify a reasonable combination of magnetic field strength, tank radius, and ferrofluid volume and concentration that would result in observable fluid deformations in a laboratory environment.

REDUCED GRAVITY AIRCRAFT FLIGHT TESTING

The KC-135 flight testing will involve the construction of two dewar systems: one would be transparent and fully instrumented to be used with ferrofluid for preliminary testing; the other one would be an optimally designed cryogenic dewar that is instrumented as necessary to validate the

models. The flight testing will occur during two different weeks. Flight experiments would include:

First Test Series-Transparent Dewars - Ferrofluid
[Rare-Earth Magnet configuration (strong, medium, weak)]
- Acquisition and Stability Testing
- Liquid Expulsion Demonstration
- Liquid-Free, Gas Vent Demonstration
- Fluid Gauging Demonstration .

Second Test Series- Cryogenic Dewar - Liquid Oxygen
[Rare-Earth Magnet Configuration (strong, medium, weak)]
- Acquisition and Stability Testing
- Liquid Expulsion Demonstration
- Liquid-Free, Gas Vent Demonstration
- Fluid Gauging Demonstration
- Heating/Self-Regulating Pressurization.

The following types of measurements must be made to satisfy our scientific objectives: video images via cameras (perhaps with borescopes and light pipes), acceleration in the X-Y-Z axes of the experiment, temperature using cryogenic diodes and thermocouples, pressure in the vessels, fluid position, vent flow rates, liquid levels using cryogenic level sensors, time clock to link all the measurements to flight events, etc. The data would be collected and stored on a laptop PC for analysis.

CURRENT STATUS

The modified RIPPLE code has been enhanced to include fluid magnetic surface tension effects and increase the user friendliness. Ground experiments (performed in 1-g) are being developed and performed as a precursor to the KC-135 flight experiments. ORBITEC has obtained permission to use some of the MAPO (Magnetically Actuated Propellant Orientation) KC-135 flight hardware that was developed and tested by NASA Marshall Space Flight Center. New dewars are being designed for use with the MAPO experiment support structure on upcoming KC-135 flights.

PI CONTACT INFORMATION

Dr. Eric E. Rice
Orbital Technologies Corporation (ORBITEC™)
Space Center, 1212 Fourier Drive
Madison, WI 53717
(608) 827-5000
(608) 827-5050 *fax*
ricee@orbitec.com

MOTION OF DROPS ON SURFACES WITH WETTABILITY GRADIENTS

R. Shankar Subramanian*, John B. McLaughlin, Nadjoua Moumen, and Dongying Qian
Box 5705, Department of Chemical Engineering, Clarkson University, Potsdam New York 13699

ABSTRACT

A liquid drop present on a solid surface can move because of a gradient in wettability along the surface, as manifested by a gradient in the contact angle. The contact angle at a given point on the contact line between a solid and a liquid in a gaseous medium is the angle between the tangent planes to the liquid and the solid surfaces at that point and is measured within the liquid side, by convention. The motion of the drop occurs in the direction of increasing wettability. The cause of the motion is the net force exerted on the drop by the solid surface because of the variation of the contact angle around the periphery. This force causes acceleration of an initially stationary drop, and leads to its motion in the direction of decreasing contact angle. The nature of the motion is determined by the balance between the motivating force and the resisting hydrodynamic force from the solid surface and the surrounding gaseous medium.

A wettability gradient can be chemically induced as shown by Chaudhury and Whitesides (1992) who provided unambiguous experimental evidence that drops can move in such gradients. The phenomenon can be important in heat transfer applications in low gravity, such as when condensation occurs on a surface. Daniel et al. (2001) have demonstrated that the velocity of a drop on a surface due to a wettability gradient in the presence of condensation can be more than two orders of magnitude larger than that observed in the absence of condensation. In the present research program, we have begun to study the motion of a drop in a wettability gradient systematically using a model system. Our initial efforts will be restricted to a system in which no condensation occurs.

The experiments are performed as follows. First, a rectangular strip of approximate dimensions 10 x 20 mm is cut out of a silicon wafer. The strip is cleaned thoroughly and its surface is exposed to the vapor from an alkylchlorosilane for a period lasting between one and two minutes inside a desiccator. This is done using an approximate line source of the vapor in the form of a string soaked in the alkylchlorosilane. Ordinarily, many fluids, including water, wet the surface of silicon quite well. This means that the contact angle is small. But the silanized surface resists wetting, with contact angles that are as large as 100°. Therefore, a gradient of wettability is formed on the silicon surface. The region near the string is highly hydrophobic, and the contact angle decreases gradually toward a small value at the hydrophilic end away from this region. The change in wettability occurs over a distance of several mm.

* PI e-mail address: subramanian@clarkson.edu, fax: (315) 268-6654, phone: (315) 268-6648

The strip is placed on a platform within a Plexiglas cell. Drops of a suitable liquid are introduced on top of the strip near the hydrophobic end. An optical system attached to a video camera is trained on the drop so that images of the moving drop can be captured on videotape for subsequent analysis. We have performed preliminary experiments with water as well as ethylene glycol drops. Results from these experiments will be presented in the poster.

Future plans include the refinement of the experimental system so as to permit images to be recorded from the side as well as the top, and the conduct of a systematic study in which the drop size is varied over a good range. Experiments will be conducted with different fluids so as to obtain the largest possible range of suitably defined Reynolds and Capillary numbers. Also, an effort will be initiated on theoretical modeling of this motion. The challenges in the development of the theoretical description lie in the proper analysis of the region in the vicinity of the contact line, as well as in the free boundary nature of the problem. It is known that continuum models assuming the no slip condition all the way to the contact line fail by predicting that the stress on the solid surface becomes singular as the contact line is approached. One approach for dealing with this issue has been to relax the no-slip boundary condition using the Navier model (Dussan V., 1979). Molecular dynamics simulations of the contact line region show that for a non-polar liquid on a solid surface, the no-slip boundary condition is in fact incorrect near the contact line (Thompson et al., 1993). Furthermore, the same simulations also show that the usual relationship between stress and the rate of deformation breaks down in the vicinity of the contact line. In developing continuum theoretical models of the system, we shall accommodate this knowledge to the extent possible.

References

Chaudhury, M.K., and Whitesides, G.M. 1992 How to make water run uphill. Science **256**, 1539-1541.

Daniel, S., Chaudhury, M.K., and Chen, J.C. 2001 Fast drop movements resulting from the phase change on a gradient surface. Science **291**, 633-636.

Dussan V., E.B.. 1979 On the spreading of liquids on solid surfaces: static and dynamic contact lines. in Ann. Rev. Fluid Mech., ed. M. Van Dyke, J.V. Wehausen, and J.L. Lumley (vol. 11, pp. 371-400). Palo Alto, CA: Annual Reviews, Inc.

Thompson, P.A., Brinckerhoff, W.B., and Robbins, M.O. 1993 Microscopic studies of static and dynamic contact angles. J. Adhesion Sci. Technol. **7**, No. 6, 535-554.

Motion of Drops on Solid Surfaces with Wettability Gradients

By Nadjoua Moumen, Dongying Qian, R. Shankar Subramanian and John B. McLaughlin

Clarkson University,
Potsdam New York

Objectives

- Make experimental measurements of the velocity and shape of a drop moving on a surface because of a gradient in wettability along the surface to establish the scaling laws associated with this motion

- Compare the observed velocity and shape with predictions from numerical calculations as well as asymptotic analytical predictions

Background and Motivation

- A drop will move when placed on a surface on which the contact angle depends on position (Greenspan, J. Fluid Mech. 1978; Chaudhury and Whitesides, Science 1992)
- This motion can be useful in
  - Condensation heat transfer
  - Debris removal in ink jet printing
  - Moving drops in a laboratory on a chip

Parameters

- A force balance on the drop yields the characteristic velocity scale $U = \dfrac{R\,\sigma\,\nabla\theta_e}{\mu}$

- Using this velocity scale, Reynolds and Capillary numbers are defined as follows

$$\mathrm{Re} = \frac{UR}{\nu} \qquad Ca = \frac{\mu U}{\sigma}$$

- The scaled drop speed, $V = V^*/U$ will depend on the Reynolds and Capillary numbers as well as the Bond number, defined below.

$$Bo = \frac{\rho g R^2}{\sigma}$$

Experiments

- First, a surface with a wettability gradient is prepared
- Next, the surface is placed on a microscopy stage and drops are introduced; their motion is videotaped from the side as well as from above
- The dependence of the static contact angle on position is measured by holding drops fixed at different locations on the surface

Wettability Gradient Preparation

- A strip (10×20mm) is cut out of a silicon wafer
- The strip is cleaned thoroughly
- Its surface exposed to a vapor from an alkylchlorosilane for 1~2 min inside a desiccator.
- The surface close to the vapor develops high hydrophobicity (large contact angle), which decreases with distance from the source.

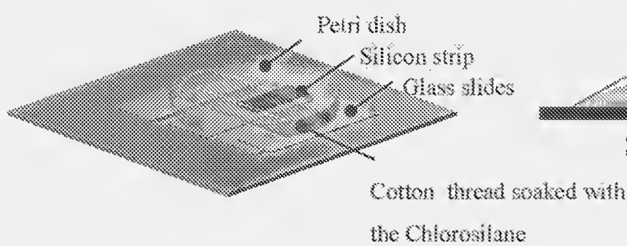

Experimental Apparatus

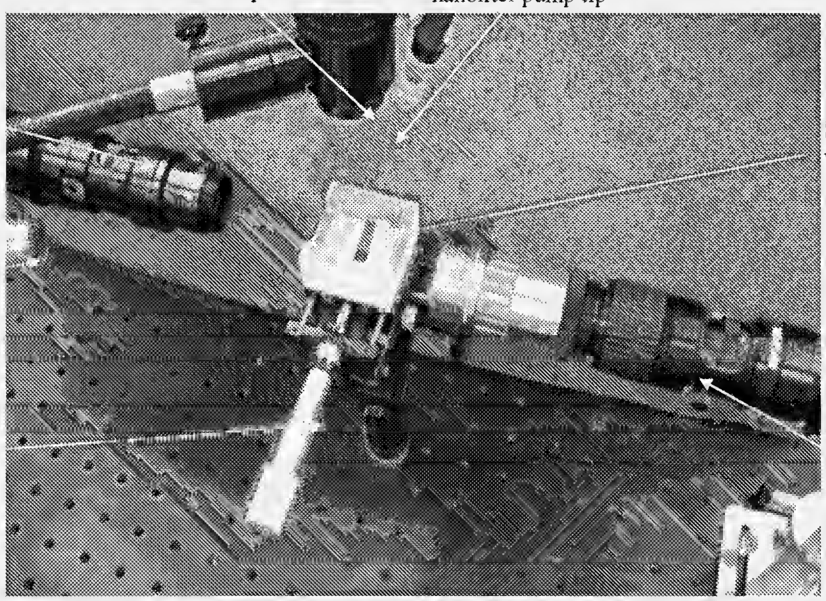

Preliminary Results

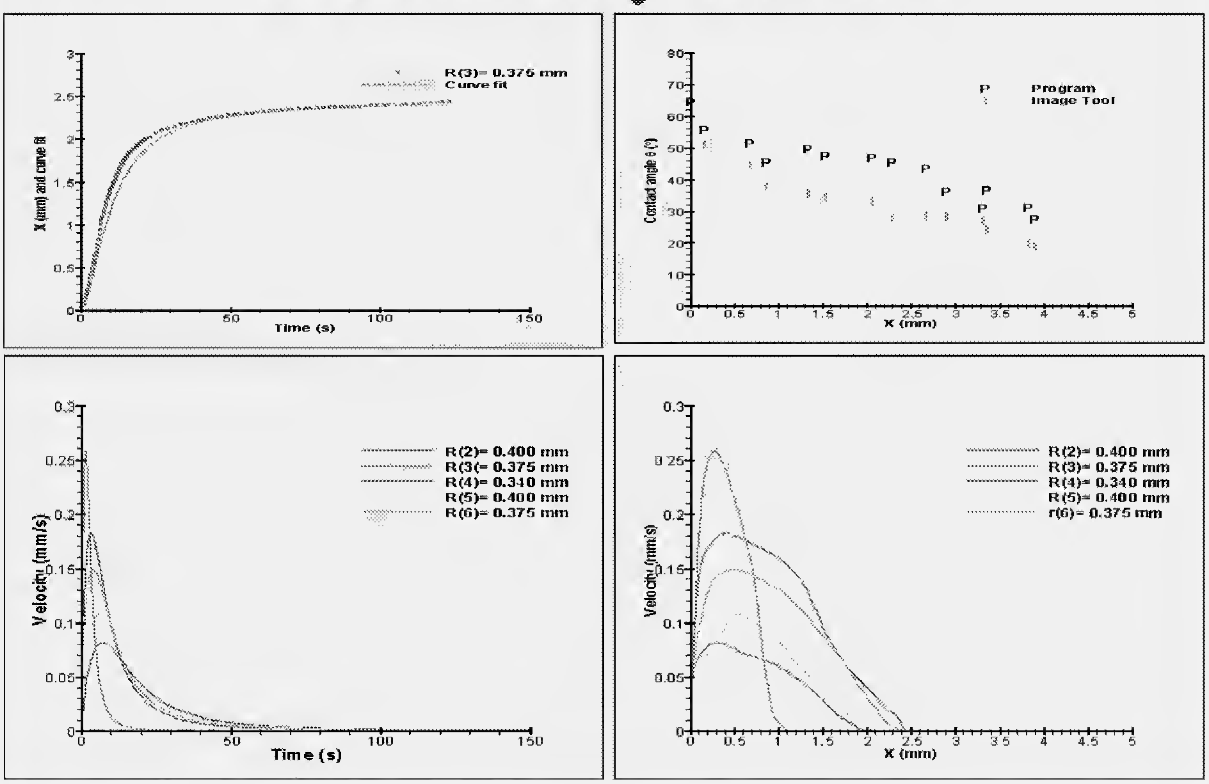

Preliminary Results

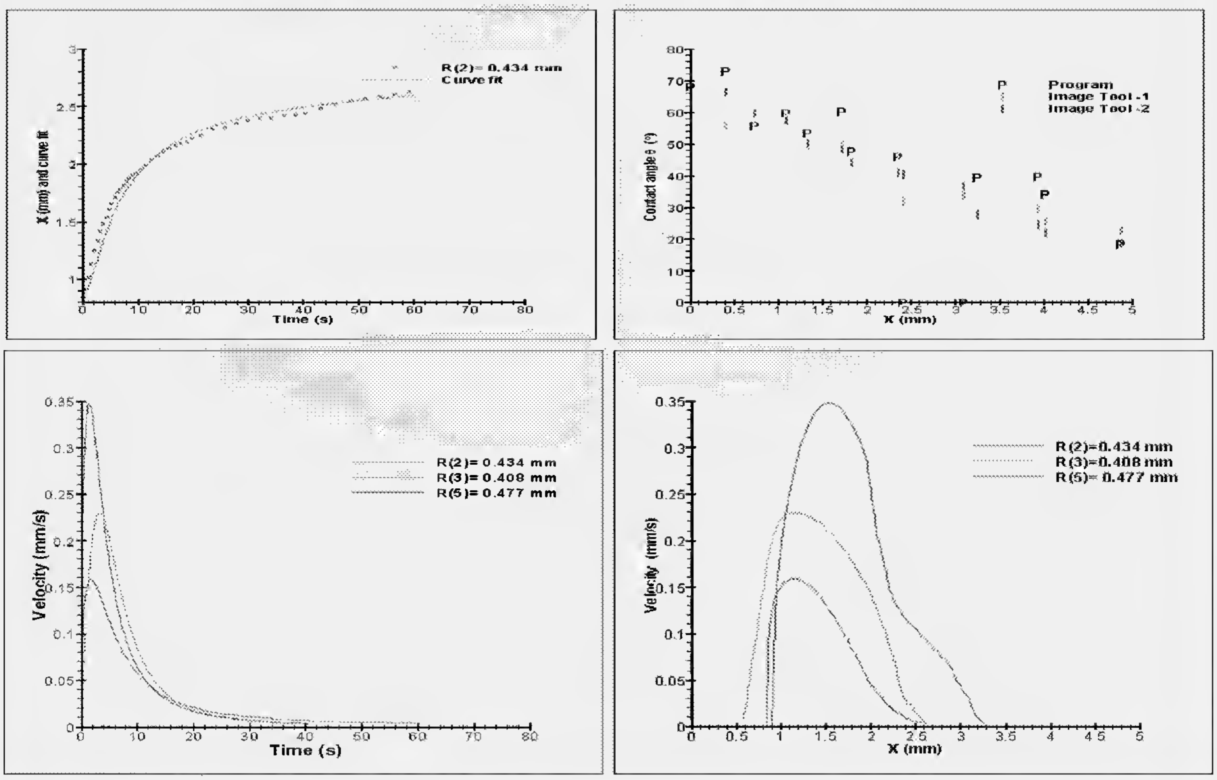

Plans for Future Work

- Perform experiments on different liquids to explore a good range of values of the Reynolds, Capillary, and Bond Numbers
- Obtain numerical solutions of the governing equations along with the associated boundary conditions, and predict the speed and shape of the drop as a function of the parameters
- Develop asymptotic analytical predictions for small values of the Capillary and Bond numbers and Stokes motion

Acknowledgments

- NASA for financial support
- Professor Manoj K. Chaudhury and Ms. Susan Daniel, Lehigh University for help with gradient preparation training
- Undergraduate students Mohammed Yusuf and Aaron Lyndaker from the McNair program for help in data analysis and gradient preparation

MICROCHANNEL PHASE SEPARATION AND PARTIAL CONDENSATION IN NORMAL AND REDUCED GRAVITY ENVIRONMENTS

Ward E. TeGrotenhuis and Victoria S. Stenkamp
Battelle Memorial Institute, Richland, Washington

ABSTRACT

Microtechnology was conceived as a means of shrinking the length scales of heat and mass transfer to 100 microns or less so that orders of magnitude increases in throughput can be realized in chemical processes. The subsequent reduction in size and mass lends itself well to space applications. Using proprietary sheet architecture, Battelle has created such devices with micro chemical and thermal systems (MicroCATS) for gas phase reactions, heat transfer and solvent extraction. Figure 1 depicts a device cross section with micrometer size channels used in such devices.

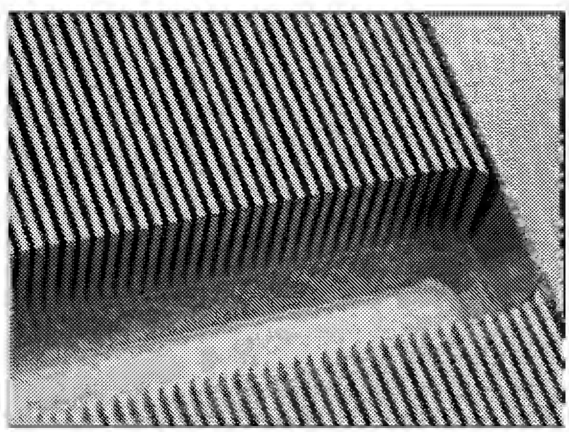

Figure 1. Cross section of microchannels

In this work, Battelle has extended the technology to include phase separation and partial condensation with phase separation in channels between 100 microns and a few millimeters at the smallest dimension. These length scale channels are advantageous for all reduced gravity applications involving two-phase flow since hydrodynamic, interfacial and capillary forces dominate over gravitational forces. By controlling the wettability and porosity of the materials within the device, separation occurs spontaneously thus allowing high throughputs and easy recovery from process upsets. Enhanced heat transfer in the case of condensation is obtained through reduction of the narrowest channel dimension. Scale up is achieved by simply increasing the number of layers. Potential space applications for phase separation and condensation include water management in environmental control and life support and thermal systems involving phase change (heat pipes, vapor compression cycles). These devices are also well suited for in-situ resource utilization or “living off the land” since they are compact and efficient. Applications include phase separation and condensation of water during in-situ propellant production.

The performance is reported for a single channel phase separator in both normal and microgravity environments and for a multi channel condenser in normal gravity. A schematic of a single channel device is presented in Figure 2. In the case of phase separation, a gas/liquid mixture is fed to the device and no cooling channel is present. Liquid is moved through the capture structure to the wicking or pore throat structure via capillary and hydrodynamic forces, then towards the appropriate outlet. The gas is allowed to move freely through the device and exit through its outlet. In the case of partial condensation with phase separation, vapor and non-condensable gas is fed to the device and a cooling channel is present. Vapor condenses on the wall nearest the cooling channel so that liquid must be moved to the liquid exit via capillary forces. A multichannel device consists merely of alternating layers of cooling and condensing channels.

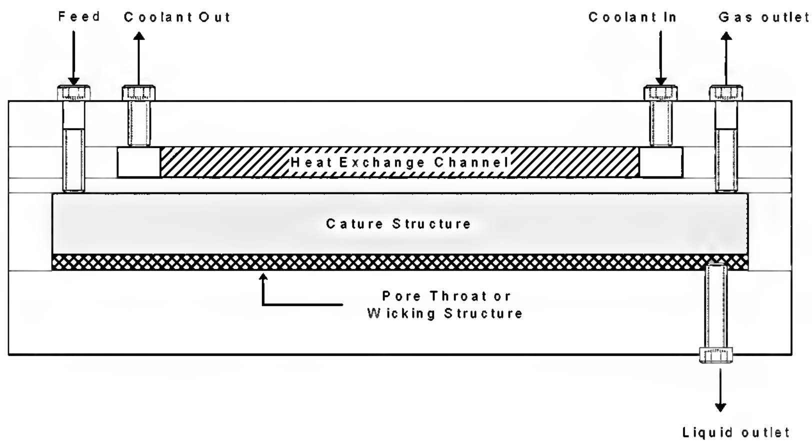

Figure 2. Single channel separator shown in co-current flow.

Complete separation has been obtained during phase separation in both normal and microgravity environments with gas residence times of hundredths of seconds. Liquid fractions tested ranged from 0.0005 to 0.14. In the case of condensation with phase separation, an air-cooled multi-channel device has been operated in normal gravity with complete separation of the gas and liquid phases. Water recovery was essentially 50%, with the difference accounted for by humidification of the air. The overall heat transfer coefficient has been calculated as high as 3300 $W/m^2.K$ with a specific power of over 1200 W/kg.

CAPILLARY FLOW IN INTERIOR CORNERS

Mark M. Weislogel
P.O. Box 751-ME, Portland State University, Portland, OR 97207
Email; mmw@cecs.pdx.edu, Fax; 503-725-4292, Ph; 503-725-8255,

ABSTRACT

Capillary flows in interior corners have an established place in fluids-handling operations in reduced gravity environments. A quantitative understanding of corner flows is essential for the myriad fluid management tasks in space including flows in liquid-fuel tanks, thermal control systems, and life-support systems. Though low-g fluid system designs are 'largely successful,' current techniques for predicting system performance are primarily limited to order of magnitude estimates, delicately guided by the experience of the designer, or direct numerical simulation which can be prohibitively time consuming. Highly reliable and quantitative design tools serving between these extremes are welcome contributions to the low-g fluids management community.

In this research effort, an asymptotic analysis developed and benchmarked for capillary flows in simplified containers possessing interior corners [1] is generalized and broadly applied to flows in containers and/or corner geometries of increasing complexity. Closed form solutions to important problems such as interior corner transient flow rates, local and global flow characteristics, interface profiles, and stability are determined for a variety of container types and boundary conditions. A partial list of problems addressed includes flows in corners of infinite extent [2], regular and irregular polygonal cylinders [3], and complex 'vaned' containers modeling propellant management devices in liquid fuel tanks [4]. Other complicating conditions such as nonplanar corners, out-of-plane corners, helical corners, background accelerations, heat and mass transfer, and interfacial shear are addressed. Applications of the results to low-g fluid system design and analysis are manifold and an excellent example is provided by way of a post-analysis of NASA's Vented Tank Resupply Experiment performed on the shuttle in 1996.

Extensive drop tower and low-g aircraft experiments are performed to guide and/or support the development and application of the most fundamental aspects of the theory. For the special case of steady capillary driven flow the analysis is readily extended to complex corner networks modeling macroscale flows within intricately vaned containers in space as well as microscale flows on rough surfaces on Earth.

References

[1] Weislogel, M.M., Lichter, S., Capillary Flow in Interior Corners, *J. Fluid Mech.*, 373:349-378, November 1998.

[2] Weislogel, M.M. Capillary Flow in Containers of Polygonal Section, *AIAA J.*, 39(12), 2320-2326, 2001.

[3] Weislogel, M.M. Capillary Flow in Interior Corners: the Infinite Corner, *Phys. of Fluids*, 13(11):3101-3107, Nov., 2001.

[4] M.M. Weislogel, S.H. Collicott, Analysis of Tank PMD Rewetting Following Thrust Resettling, 40th AIAA Meeting, AIAA 2002-0757, Reno, Jan. 14-17, 2002.

Two-Dimensional Turbulence in the Presence of a Polymer

Yonggun Jun and X.L. Wu
Department of Physics and Astronomy
University of Pittsburgh, Pittsburgh, PA 15260

Polymers of sufficient length are known to quench turbulence [1]. However, the fundamental mechanism of quenching, namely the interactions between the polymer and turbulence, is not well understood. In this experiment, we examine the effect of a polymer additive to turbulence in a freely suspended film. The experimental geometry is two-dimensional due to the fact that films are very thin, confining the flow velocity to the plane of the film. The turbulence in the film is created by electromagnetic convection as delineated in the figure below.

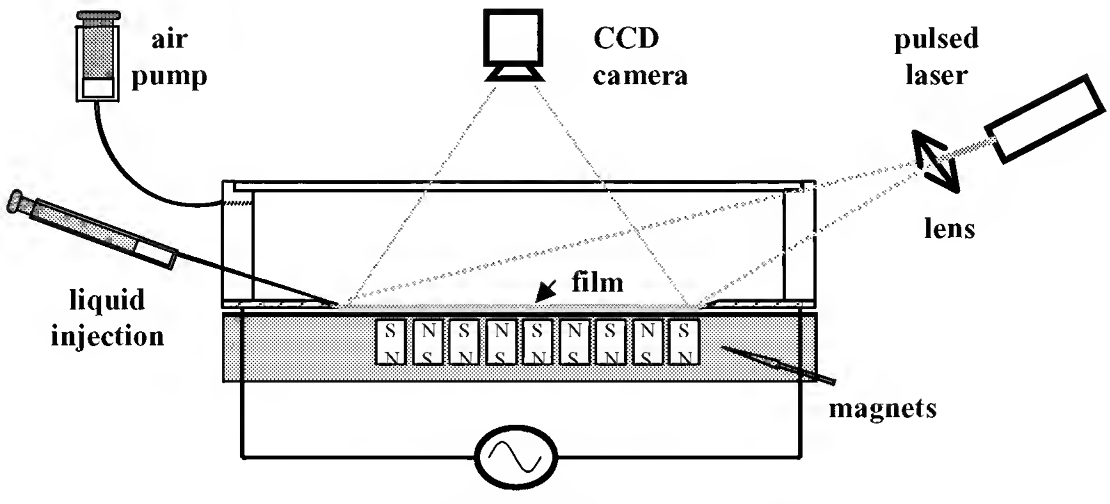

Here a uniform electric current is injected into a salt-doped film, and the ionic current in the film couples to an externally imposed magnetic field, giving rise to a set of vortices. Various convection states can be achieved depending on the magnitude of the current, but in this study we are interested in a large applied current so that flow in the film is spatiotemporally chaotic, or turbulent. The flow velocity field can be interrogated by a particle imaging velocimeter, which consists of a CCD camera and a pulsed laser. For more information on the experimental setup, see Ref. [2].

Since we are ultimately interested in studying polymer conformational fluctuations in the presence of turbulent velocity field, large λ-DNA molecules are used in the experiment. The λ-DNA has a contour length of 16 μm which folded into a globular form of radius ~1 μm in diameter. Preliminary observations show that there exist two different flow regimes depending on the DNA concentrations. For low DNA concentrations (<50 ppm), the 2D film is homogeneous and the turbulent velocity field is similar to those without polymers. For higher DNA concentrations, the film develops inhomogeneities when the turbulent intensity becomes large, with v_{rms}>10 cm/s. Tenuous

filaments spontaneously appear and are sometimes discernible to naked eyes. The thin filaments appears to be due to aggregation of DNA molecules, since no such aggregates are present in the bulk suspension, or in the absence of strong turbulence. It remains an intriguing possibility that quenching of turbulence may be a collective effect rather than due to single polymers as suggested by different theories [3,4]. Our current work concentrates on optical microscopy to visualize individual DNAs will put this question to rest.

References:

[1] J.L. Lumley and I. Kubo, The Influence of Polymer Additives on Velocity and Temperature Fields, ed. G. Gampert (Springer, Berlin, 1984).
[2] M. Rivera and X.L. Wu, External Dissipation in Driven Soap Film Turbulence, Phys. Rev. Letts., **85**, 976 (2000).
[3] M. Tabor and P.G. de Gennes, *A Cascade Theory of Drag Reduction*, Europhys. Lett., **2**, 519 (1986).
[4] M. Chertkov, et al., *Polymer Stretching by Turbulence*, Phys. Rev. Letts., **84**, 4761 (2000).

Exposition Session
Topical Area 3:
Complex Fluids

MICROGRAVITY IMPACT EXPERIMENTS: RESULTS FROM COLLIDE-2

Joshua E. Colwell, Larry W. Esposito, and Mihály Horányi
LASP, University of Colorado, Boulder CO 80309-0392, josh.colwell@lasp.colorado.edu,
303-492-6805, Fax: 303-492-6946

ABSTRACT

Protoplanetary disks, planetary rings, the Kuiper belt, and the asteroid belt are collisionally evolved systems. Although objects in each system may be bombarded by impactors at high interplanetary velocities (km/s or higher), they are also subject to repeated collisions at low velocities ($v \sim 1$-100 m/s). In some regions of Saturn's rings, for example, the typical collision velocity inferred from observations by the Voyager spacecraft and dynamical modeling is a fraction of a centimeter per second [1]. These interparticle collisions control the rate of energy dissipation in planetary rings and the rate of accretion in the early stages of planetesimal formation. Dust on the surface of planetary ring particles and small (1 cm – 10 m) planetesimals helps dissipate energy in the collision, but may also be knocked off, forming dust rings in the case of ring particles and slowing or inhibiting accretion in the case of planetesimals.

The Collisions Into Dust Experiment (COLLIDE) is a self-contained autonomous microgravity experiment that made its second flight in the payload bay of space shuttle Endeavour on flight STS-108 in December 2001. COLLIDE-2 (Figure 1) performed 6 impact experiments into powder in microgravity at speeds between 1.2 and 108 cm/s, simulating the collisions that occur in some astrophysical systems.

(a)

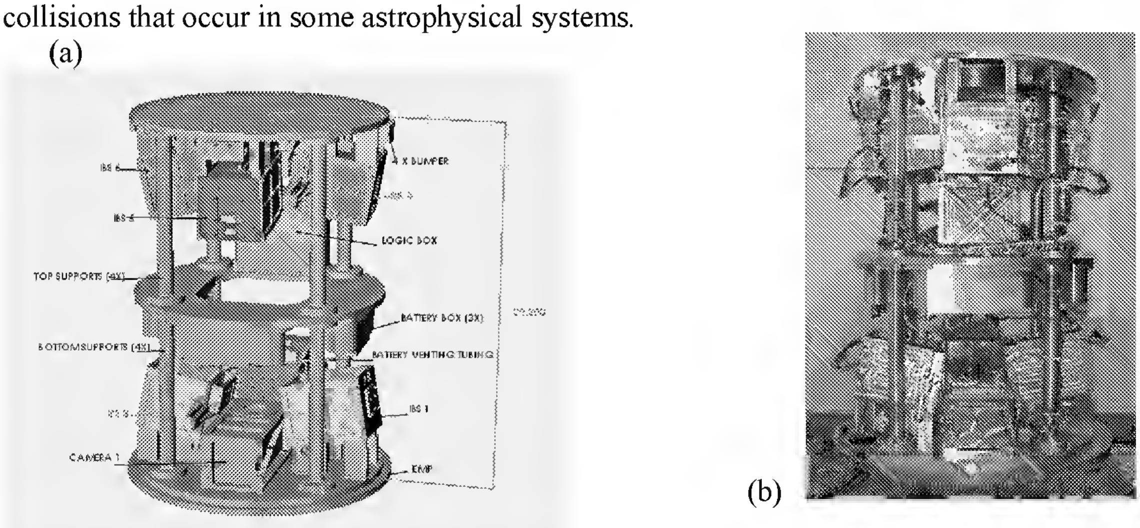

(b)

Figure 1: (a) Schematic of the COLLIDE-2 payload indicating major experiment components. Three impact experiment boxes are mounted to each end plate around a sealed camera container. The camera images the three boxes on the opposite end plate through a hole in the central plate which also serves as the mounting point for electronics and batteries. (b) Image of COLLIDE-2 prior to flight in a similar orientation to the schematic in (a).

Impactors were quartz spheres approximately 1.9 cm in diameter. The target material was quartz sand sieved to a size range of 75-250 μm in 5 of the 6 experiments and JSC-1, a ground

basaltic mineral sieved to the same size range in the sixth experiment. The experiment took place in an evacuated standard space shuttle Hitchhiker container fourteen hours after launch. The temperature of the samples at the time of the experiment was 17°C. Digital video recordings of the impacts were made using two consumer-grade camcorders, each one recording three impacts in sequence. Analysis of the video data provides an accurate measure of the impactor velocity before and after impact, velocity of the fastest ejecta produced (if any), and a qualitative measure of the amount of ejecta produced. A single video frame from one impact experiment is shown in Figure 2.

On the first flight of COLLIDE on STS-90 in 1998 experiment malfunctions prevented data from being returned for 3 of the 6 impact experiments. Those experiments used JSC-1 as a target material for all impacts, and included the sub-75 μm portion of the size distribution. Impacts at 15 cm/s and 17 cm/s resulted in virtually no ejecta, and rebound coefficients of restitution were <0.03. A similar coefficient of restitution was found for a third impact at 90 cm/s [2]. The broad size-distribution JSC-1 used in COLLIDE compacted during launch vibrations resulting in a cohesive surface and little or no ejecta production. The quartz sand used in COLLIDE-2 has rounder grains which do not interlock with each other as much as the semi-angular JSC-1 grains. On COLLIDE-2 we found significant ejecta produced at impact speeds above 20 cm/s and no rebound of the impactor at impact speeds below that level. A summary of the findings from COLLIDE-2 is shown in Table 1.

V (cm/s)	Target	Ejecta	Rebound
1.3	SiO_2 sand	0	No
3.9	SiO_2 sand	$M_{ej}<M_{imp}$	No
28	SiO_2 sand	$M_{ej}\geq M_{imp}$	Yes
81	SiO_2 sand	$M_{ej}>M_{imp}$	Yes
108	SiO_2 sand	$M_{ej}>M_{imp}$	Yes
12	JSC-1	$M_{ej}<M_{imp}$	No

Table 1: Summary of results from the 6 COLLIDE-2 impact experiments. A threshold for the boundary between accretion and erosion is between impact speeds of 12 and 28 cm/s for the conditions in this experiment.

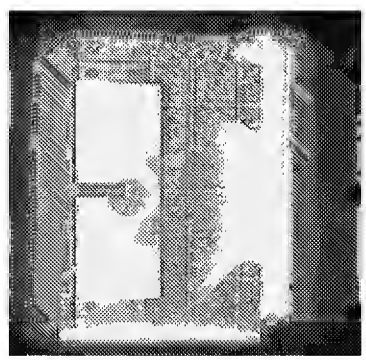

Figure 2: Video frame 0.06 seconds after impact into at 108 cm/s. The reflected image of the projectile is visible in the mirror at left, and the direction of motion of the projectile is left to right. Fiduciary lines are 2 cm apart.

The impact into JSC-1 on COLLIDE-2 was at a speed comparable to two impacts on COLLIDE, but with an impactor that was 9 times more massive. On COLLIDE-2 the impactor remained embedded in the target surface, in contrast to the slow rebound observed on COLLIDE. This difference in behavior is likely due to the absence of small particles in the COLLIDE-2 target, increasing the overall porosity of the target and allowing the surface to deform more in response to the collision.

REFERENCES

[1] Esposito, L. W., *Annu. Rev. Earth Planet. Sci.*, **21**, 487 (1993).
[2] Colwell, J. E., and M. Taylor, *Icarus*, **138**, 241 (1999).

Microgravity Impact Experiments: Results from COLLIDE-2

Joshua E. Colwell, Larry W. Esposito, and Mihály Horányi
Laboratory for Atmospheric and Space Physics, University of Colorado, Boulder CO.

Background

•In planetary rings and the early stages of planetesimal formation, collision velocities are typically much less than 10 m/s. Colliding particles are likely coated with or consist of smaller dust particles and have negligible surface gravitational accelerations.
•Dust in planetary rings is produced by a combination of interparticle collisions and direct meteoroid bombardment of the larger ring particles. The dynamics and mass distribution of larger ring particles can be inferred from observations of dust if the production of dust in low-velocity, microgravity impacts can be understood.
•Planetary rings spread through dissipation of energy in collisions. The amount of energy dissipated in low-velocity collisions in the presence of dust layers helps determine the age of planetary rings.
•Accretion of cm-sized agglomerates of dust particles in protoplanetary disks can be understood through surface electrostatic forces. Accretion of planetesimals larger than about 1 km is aided by gravity. Almost no data exist on the formation of km-sized planetesimals from cm-sized agglomerates.
•Previous and relevant experimental results are reported in the references below.

COLLIDE addresses these issues of origin and evolution of planetary rings and the formation of planetesimals in the origin of the solar system.

Experiment Description

•COLLIDE-2 is a Space Shuttle Hitchhiker payload that flew on the MACH-1 Hitchhiker bridge on STS-108 in December, 2001, in a 5.0 cubic foot evacuated standard Hitchhiker container.

•The payload performs six independent microgravity impact experiments in six Impactor Box Systems (IBS) and records the impacts on digital videotape at 30 frames per second using digital camcorders (Figure 1).

•Each IBS consists of a tray for the target regolith material, a launcher, LEDs for illumination for the cameras, and a mirror to provide an orthogonal view of the impact. The direct view of the camera is parallel to the target surface.

•The experiment is turned on by a baroswitch on ascent of the space shuttle, activating a 14-hour internal electronic timer. The experiment runs at the conclusion of the 14-hour timer during a time of minimal accelerations on the orbiter.

•Each IBS is operated in sequence: lights are turned on to provide illumination for the cameras, a door covering the target powder is opened, and a spring-release mechanism propels the projectile into the target surface at speeds between about 1 and 100 cm/s (Figure 3). The experiment is completed in 30 minutes.

•Data are stored on digital videotape (Figures 4-6).

Results

•All 6 IBSs on COLLIDE-2 functioned properly. Results on ejecta production and impactor rebound are summarized in Table 1.

•The experiment captured the transition from erosional to accretional impacts for the target and impactor materials used.

•Compared to COLLIDE-1, more ejecta was produced at similar impact speeds, but with a more massive projectile.

•Prior to each impact, target grains were levitated off the surface by electrostatic forces while the target tray door opened (Figure 7). This provides experimental data on the process of spoke formation in Saturn's rings.

•Limits have been placed on ejecta masses and velocities in the 6 COLLIDE-2 impacts, but final data analysis is not yet complete.

•Correlative analysis with additional microgravity impact experiments with the Physics of Regolith Impacts in Microgravity Experiment (PRIME) on the KC-135, and ground-based experiments at 1g is underway.

•These experiments suggest that for efficient accretion of planetesimals collision speeds must be below ~50 cm/s for objects smaller than a few cm in scale.

•Dust production in planetary rings from interparticle collisions similarly requires collision velocities above ~50 cm/s or ring particles significantly larger than the cm-sized particles used as impactors in these experiments. Otherwise dust production in rings is dominated by micrometeoroid bombardment of ring particles.

V_{impact}	Target	Ejecta	Rebound
1.3	SiO_2 sand	0	No
3.9	SiO_2 sand	$M_{ej}<M_{imp}$	No
28	SiO_2 sand	$M_{ej}\geq M_{imp}$	Yes
81	SiO_2 sand	$M_{ej}>M_{imp}$	Yes
108	SiO_2 sand	$M_{ej}>M_{imp}$	Yes
12	JSC-1	$M_{ej}<M_{imp}$	No

Table 1: Summary of results from COLLIDE-2. For the materials and impactor masses in COLLIDE-2 the transition from accretionary to erosional impacts occurs between impact speeds of 12 and 28 cm/s.

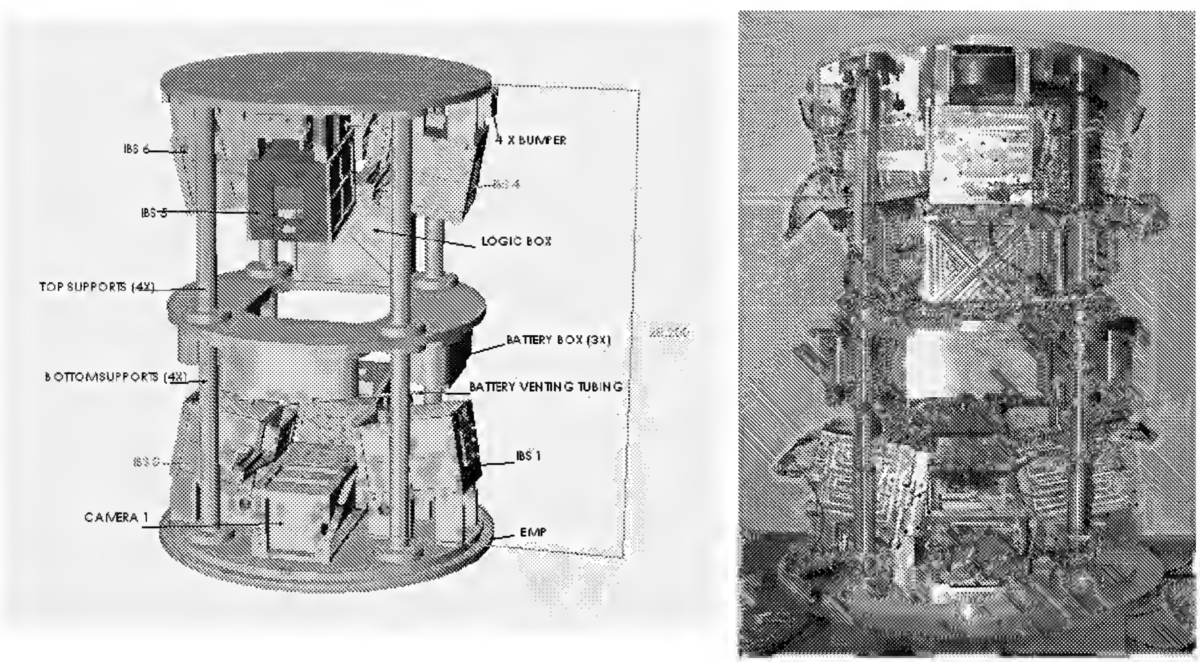

Figure 1: Schematic and photograph of the COLLIDE-2 experiment showing major experiment components. The support structure consists of 3 shelves connected by solid struts. Batteries and electronics are mounted on the central shelf which has a central opening to allow camera views from one end of the experiment to the other. Each end plate supports three Impactor Box Systems (IBS) and a sealed camera container for viewing the 3 IBSs on the opposite end plate.

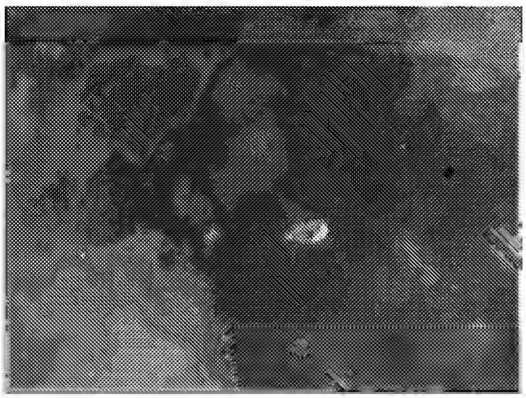

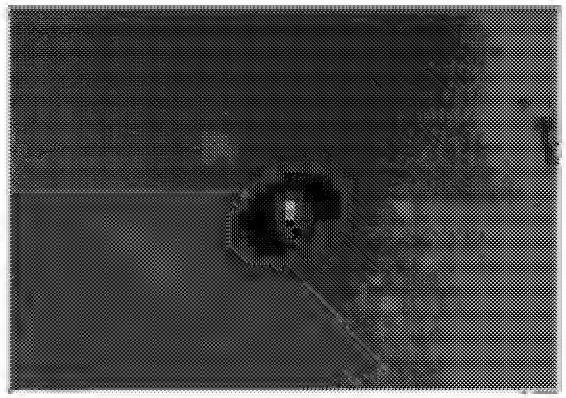

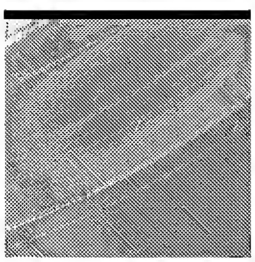

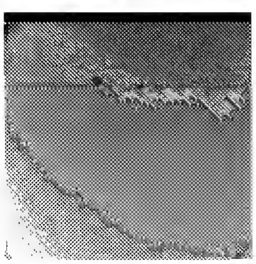

Figure 2. Top: Hubble Space Telescope images of circumstellar dust disks in the Orion nebula. These disks may be the sites of the first stages of planet formation where micron-sized grains accrete into cm-sized agglomerates and eventually km-sized planetesimals and planets.

Left: Two Voyager 2 images of the rings of Uranus seen at high phase angle (upper) highlighting dust in the ring system, and low phase angle (lower) showing only the macroscopic particles. Because dust particle lifetimes are short, the continued existence of narrow dust rings requires an ongoing, collisionally derived source of dust from the larger ring particles.

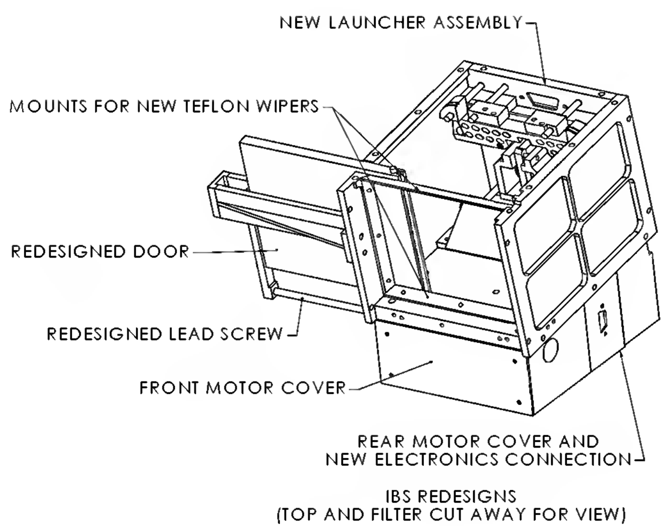

Figure 3. Schematic of a COLLIDE-2 IBS highlighting improvements made since the first flight of COLLIDE. The door holds the target powder in place until the experiment runs in microgravity. The back plate of the target tray is not shown. The motor that operates the door is mounted beneath the IBS. The launcher and lighting assembly faces the target tray, and the mirror is mounted at a 45 degree angle to the base.

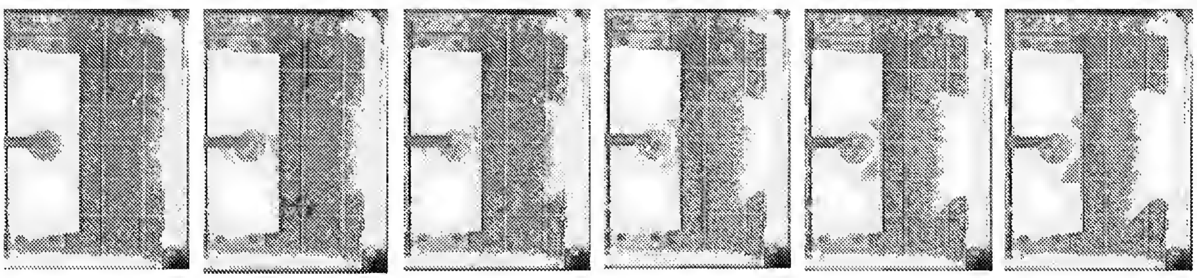

Figure 4. A series of frames from the IBS-1 impact experiment on COLLIDE-2, at 1/30th second time intervals, proceeding from left to right. The spacing of the grid lines in the background is 2 cm. The rectangle at left is a mirror showing the impactor on the target surface. The impactor is a 1.9-cm diameter quartz sphere and the target is quartz sand with a size distribution of 75-250 micrometers. The impact speed was 108 cm/s. The fastest ejecta is traveling at a speed of approximately 20 cm/s.

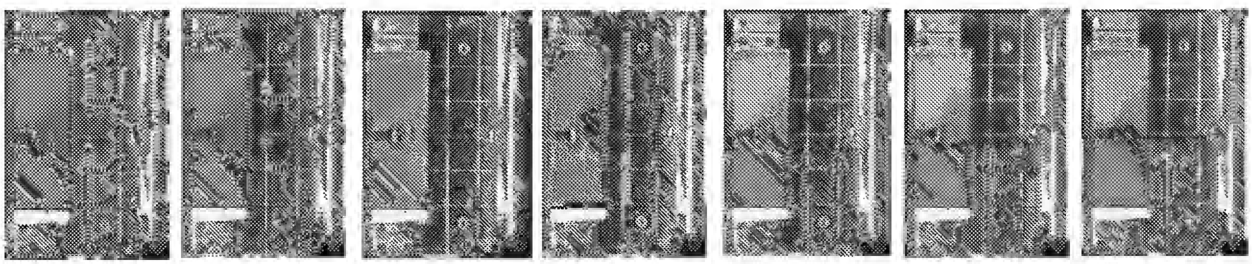

Figure 5. A series of frames from the IBS-5 impact into JSC-1 lunar regolith simulant at a speed of 12 cm/s. The relative timing of the frames, from left to right, is 0, 0.33, 0.67, 1, 1.5, 2, 2.5 seconds. The impactor was a 1.9-cm diameter quartz sphere. The JSC-1 in this experiment was sieved to a size range of 75-250 micrometers. Impacts at similar speeds into JSC-1 on the first flight of COLLIDE yielded no ejecta compared to tens of milligrams of ejecta on COLLIDE-2. The difference is due to the 10x more massive projectile and the absence of grains smaller than 75 microns on COLLIDE-2.

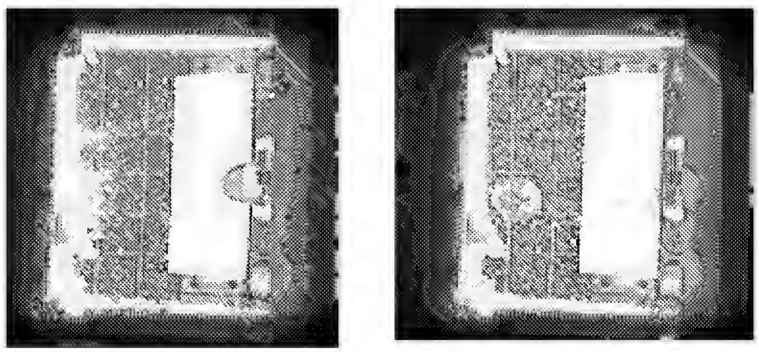

Figure 6. Two frames from the 1.3 cm/s impact in IBS-3 showing the projectile approaching the target surface at left. The frames are 5 seconds apart. The particles already off the surface were levitated by electrostatic forces. No further particles were liberated in this impact.

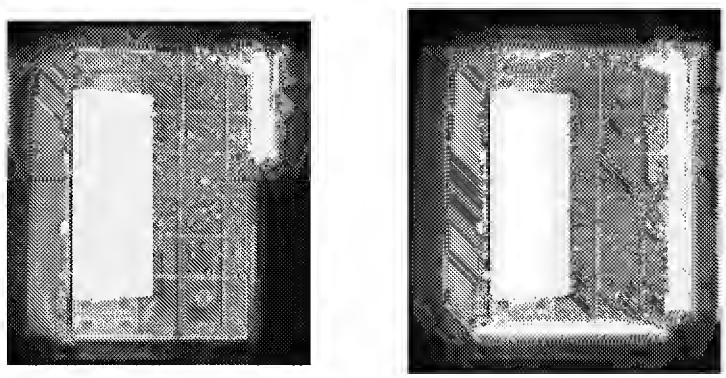

Figure 7. Two frames from the door-opening sequence of IBS-1 showing target grains (quartz sand) lifting off the target surface. This phenomenon is due to triboelectric charge on the grains causing them to move in a static electric field within the IBS. Grains moved to the walls of the IBS where they remained until the impact.

This levitation of dust in a low-gravity environment is believed to be responsible for the production of spokes in Saturn's rings, the dark radial smudges visible in the background image of this poster. Plasma generated by hypervelocity impacts onto large ring particles is accelerated outward over the rings by Saturn's corotational electric field where dust particles on the surface of the larger particles collect the charge and are electrostatically levitated to form the visible spokes.

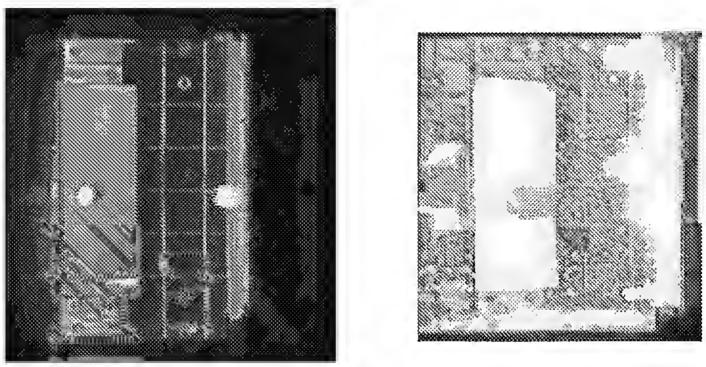

Figure 8: Comparison between COLLIDE-1 (left) and COLLIDE-2 (right). In the impact at left, the impactor is a 0.95-cm diameter Teflon sphere and the target is a broad size distribution JSC-1. The frame is at the moment of contact with the target surface. No ejecta was produced in this 15 cm/s impact. In the impact at right, the impactor is ~10x more massive and at a speed of 81 cm/s, and the target is quartz sand. The angular shape of the JSC-1 grains reduces ejecta production compared to the rounder and more equally sized quartz grain targets used in COLLIDE-2.

References

•Colwell, J. E., and L. W. Esposito 1990a. A numerical model of the Uranian dust rings. *Icarus* **86**, 530-560.

•Colwell, J. E., and L. W. Esposito 1990b. A model of dust production in the Neptune ring system. *Geophys. Res. Lett.* **17**, 1741-1744.

•Colwell, J. E., and M. Taylor 1999. Low Velocity Microgravity Impact Experiments into Simulated Regolith. *Icarus* **138**, 241-248.Dilley, J. P. 1993. Energy loss in collisions of icy spheres: Loss mechanism and size-mass dependence. *Icarus* **105**, 225-234.

•Dilley, J. P., and D. Crawford 1996. Mass dependence of energy loss in collisions of icy spheres: An experimental study. *J. Geophys. Res.* **101**, 9267-9270.

•Hartmann, W. K. 1978. Planet formation: Mechanism of early growth. *Icarus*, **33**, 50-62.

•Hartmann, W. K. 1985. Impact Experiments 1. Ejecta velocity distributions and related results from regolith targets. *Icarus*, **63**, 69-98.

•Wurm, G., J. Blum, and J. E. Colwell 2001. The Aerodynamical Sticking of Dust Aggregates. *Phys. Rev. E*, **64**, #046301.

•Wurm, G., J. Blum, and J. E. Colwell 2001. A New Mechanism for the Formation of Planetesimals in the Solar Nebula. *Icarus*, **151**, 318-321.

MICROGRAVITY IMPACT EXPERIMENTS: THE PRIME CAMPAIGN ON THE NASA KC-135

Joshua E. Colwell, Stein Sture, and Andreas R. Lemos
LASP, University of Colorado, Boulder CO 80309-0392, josh.colwell@lasp.colorado.edu, 303-492-6805, Fax: 303-492-6946

ABSTRACT

Low velocity collisions (v < 100 m/s) occur in a number of astrophysical contexts, including planetary rings, protoplanetary disks, the Kuiper belt of comets, and in secondary cratering events on asteroids and planetary satellites. In most of these situations the surface gravity of the target is less than a few per cent of 1 g. Asteroids and planetary satellites are observed to have a regolith consisting of loose, unconsolidated material. Planetary ring particles likely are also coated with dust based on observations of dust within ring systems [1]. The formation of planetesimals in protoplanetary disks begins with the accretion of dust particles. The response of the surface dust layer to collisions in the near absence of gravity is necessary for understanding the evolution of these systems.

The Collisions Into Dust Experiment (COLLIDE) performs six impact experiments into simulated regolith in microgravity conditions on the space shuttle [2]. The parameter space to be explored is quite large, including effects such as impactor mass and velocity, impact angle, target porosity, size distribution, and particle shape. We have developed an experiment, the Physics of Regolith Impacts in Microgravity Experiment (PRIME), that is analogous to COLLIDE that is optimized for flight on the NASA KC-135 reduced gravity aircraft. The KC-135 environment provides the advantage of more rapid turnover between experiments, allowing a broader range of parameters to be studied quickly, and more room for the experiment so that more impact experiments can be performed each flight. The acceleration environment of the KC-135 is not as stable and minimal as on the space shuttle, and this requires impact velocities to be higher than the minimum achievable with COLLIDE.

The experiment consists of an evacuated PRIME Impact Chamber (PIC) with an aluminum base plate and acrylic sides and top (Figure 1). A target tray, launcher, and mirror mount to the base plate. The launcher may be positioned to allow for impacts at angles of 30, 45, 60, and 90 degrees with respect to the target surface. The target material is contained in a 10 cm by 10 cm by 2 cm tray with a rotating door that is opened via a mechanical feed-through on the base plate. A spring-loaded inner door provides uniform compression on the target material prior to operation of the experiment to keep the material from settling or locking up during vibrations prior to the experiment. Data is recorded with the NASA high speed video camera. Frame rates are selected according to the impact parameters. The direct camera view is orthogonal to the projectile line of motion, and the mirrors within the PIC provide a view normal to the target surface. The spring-loaded launchers allow for projectile speeds between 10 cm/s and 500 cm/s with a variety of impactor sizes and densities. On each flight 8 PICs will be used, each one with a different set of impact parameters.

(a) (b)

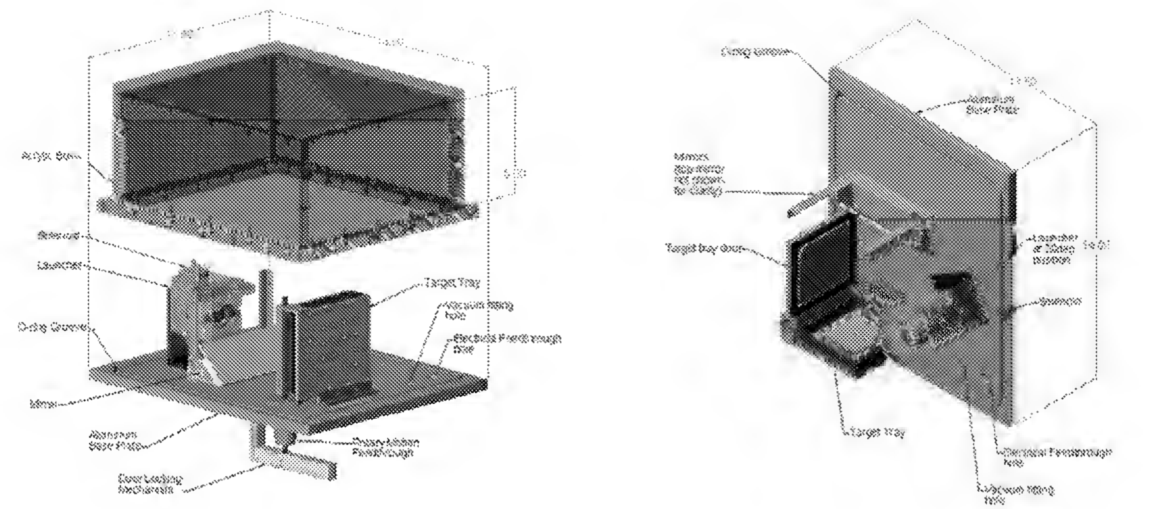

Figure 1: Schematic of PRIME Impact Chamber. (a) The closed target tray at right has vent holes to allow evacuation of pore spaces in the target material. The launcher is positioned for a normal impact onto the target surface. The handle for opening the target tray door is visible below the base plate. (b) The PIC in flight orientation with the target tray door open and the launcher positioned for a 30 degree impact. The acrylic top is not shown for clarity.

The target tray mechanism was tested on the KC-135 in July 2001, and the launchers follow the design of the COLLIDE launchers. The first flight of PRIME is scheduled for the week of July 8, 2002, with repeated flights throughout the year. The anticipated data include the normal and tangential coefficients of restitution for the impactor, the velocity distribution and mass of the ejecta, and the dependence of these quantities on the following parameters: impactor velocity, impactor mass, impactor density, and target particle properties. Initial experiments will be conducted at conditions as close to zero-g as possible, while subsequent experiments will explore the effects of increasing the acceleration to lunar and Martian levels. The range of impact velocities to be studied is 10 cm/s to 500 cm/s. This overlaps the range of impact velocities in the COLLIDE experiment (1 cm/s to 100 cm/s) as well as concurrent ground-based experiments at impact speeds above 100 cm/s [3].

Preliminary results from COLLIDE-2 and ground-based experiments suggest that PRIME will be able to explore the transition regime between accretional impacts (where the impactor sticks to the target and there is little or no ejecta) and erosional impacts (where the impactor rebounds and/or significant ejecta is produced). Results from PRIME will be combined with results from COLLIDE, ground-based experiments at 1 g, and numerical simulations employing discrete element models to develop parameterized models for the outcomes of low velocity collisions in various astrophysical contexts. These models will then be applied to models of planetesimal formation, the evolution of planetary rings, and the production of regolith on asteroids and planetary satellites.

REFERENCES

[1] Esposito, L. W., *Annu. Rev. Earth Planet. Sci.*, **21**, 487 (1993).
[2] Colwell, J. E., and M. Taylor, *Icarus*, **138**, 241 (1999).
[3] Colwell, J. E., and M. T. Mellon, *33rd Lunar Planet. Sci. Conf.*, Abs. #1757 (2002).

Microgravity Impact Experiments: The PRIME Campaign on the NASA KC-135

Joshua E. Colwell, Stein Sture[1], and Andreas Lemos
Laboratory for Atmospheric and Space Physics, University of Colorado, Boulder CO.
1 Dept. of Civil Engineering, University of Colorado, Boulder CO.

Background

•The scientific objectives of the Physics of Regolith Impacts in Microgravity Experiment (PRIME) are identical to those of the COLLIDE space shuttle experiment: to understand the energy dissipation, ejecta production, and mechanical response of regolith in low-gravity environments to low-velocity impacts. These impacts are common in several astrophysical environments including planetary rings and protoplanetary disks (background image of this poster) and in secondary cratering in asteroids (Figure 1).

•The COLLIDE payload provides 6 microgravity impact experiments at speeds between 1 and 100 cm/s. PRIME has been optimized for flights on the KC-135 where the gravity levels are not as stable as on the space shuttle. The KC-135 allows for more experiments to be run and more data to be collected permitting more of the broad parameter space to be experimentally explored.

•The limited duration of low-gravity periods on the KC-135 restricts the impact velocities to greater than about 10-15 cm/s, while the NASA high speed NAC video camera permits frame rates up to 1000 frames per second and a corresponding higher maximum impact velocity of 500 cm/s.

•The impact velocity range for PRIME (10-500 cm/s) overlaps that of COLLIDE (1-100 cm/s) and concurrent ground-based experiments (100-250 cm/s).

Related Experiments

•PRIME is based on the COLLIDE space shuttle experiment (Figure 2). Results of the first flight are in Colwell and Taylor (1999) and the second flight results are discussed in a companion poster.

•Ground-based experiments have been conducted in a small vacuum chamber at LASP, University of Colorado (Figure 2). These impact experiments provide a complementary data set to the microgravity impacts: ejecta masses at different velocities are measured accurately through the use of collector rings in conjunction with direct video imaging. This allows us to measure the dependence of ejecta mass and velocity distributions on impact parameters.

•Other low-velocity impact experiments, including impacts into regolith and low-velocity impacts using ice targets with pendulums are listed in the references below.

Experiment Description

•PRIME consists of a set of PRIME Impact Chambers (PIC). Each of these PICs performs one impact experiment during a single parabola on a flight of the KC-135. Each PIC is reset between flights.

•The PIC consists of an Aluminum baseplate and acrylic sides and top to allow video recording of the impact from outside the box. The interior is evacuated to simulate space conditions. A launcher, target tray, and mirror assembly are mounted to the baseplate (Figure 4).

•The target tray door contains the granular target material prior to the low-gravity period when the impact experiment is performed. It is opened via a manual feed-through in the base plate. The target tray door contains an inner, spring-loaded compression plate that prevents the target material from settling prior to the impact experiment.

•Projectiles are spheres up to 2 cm in diameter in a variety of materials, and are launched by a compression spring with a spring constant designed to provide the desired impact speed between 10 and 500 cm/s. The launcher is activated by a rotary solenoid and has two restraining doors to minimize spin of the projectile prior to launch. The launcher can be mounted to provide impact angles of 30, 45, 60, and 90 degrees with the target surface (Figure 4).

•Two mirrors provide additional views of the projectile striking the target surface and of ejecta particles for ejecta velocity determination (Figure 4).

•The PICs are loaded into a storage rack on the KC-135 and are swapped into an experiment mounting rack which has illumination for the high speed camera and is aligned with the camera prior to a run of the experiment (Figure 7).

First Results and Future Work

- The first set of flights of PRIME were conducted in July, 2002. Some preliminary data are shown in Figure 8. Flights are scheduled for August and September 2002 and will continue in 2003.
- Preliminary analysis of the first PRIME data indicate that results are consistent with results from COLLIDE-2 on the transition between accretion and erosion in these types of impacts: little or no ejecta is produced at impact speeds below 50 cm/s, while significant ejecta is produced at higher speeds, with the ejecta mass exceeding the projectile mass.
- The flexibility of the PRIME payload will allow us to map this transition region across many parameters, including impactor mass, impactor density, impact angle, and target material properties.
- Experiments with identical parameters to those performed in the lab (Figure 3) and on COLLIDE-1 and COLLIDE-2 are planned.
- Planned upgrades to the experiment include a free-floating version that will eliminate effects of residual accelerations of the KC-135 that may affect the lowest velocity impacts, a drop-tower version for impact speeds below 10 cm/s, and a strobed laser sheet for better tracking of ejecta.
- Experiments will also be run with non-realistic, large (mm-sized) spherical target particles for direct comparison with numerical simulations and direct velocity measurements of each ejecta particle.

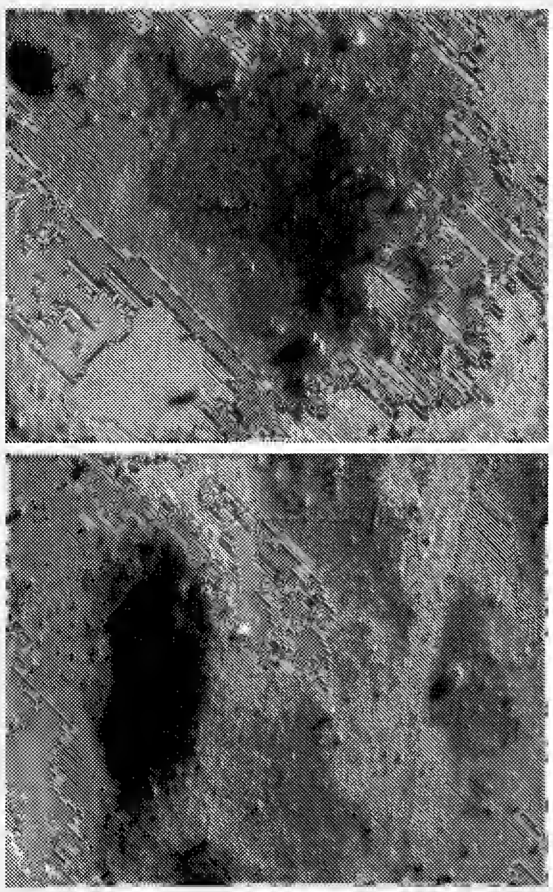

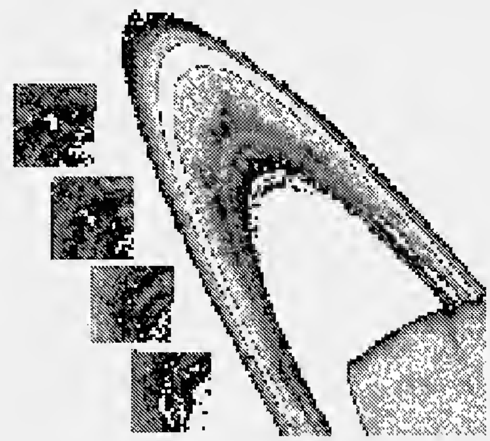

Figure 1: Images of the surface of 433 Eros from the NEAR spacecraft. Left: blocks and boulders are visible buried at various depths in a fine-grained regolith. These blocks are ejecta from energetic impacts elsewhere on the asteroid. Top: Images of Saturn's rings showing dark, radial "spokes" composed of dust particles lifted off the surface of larger ring particles.

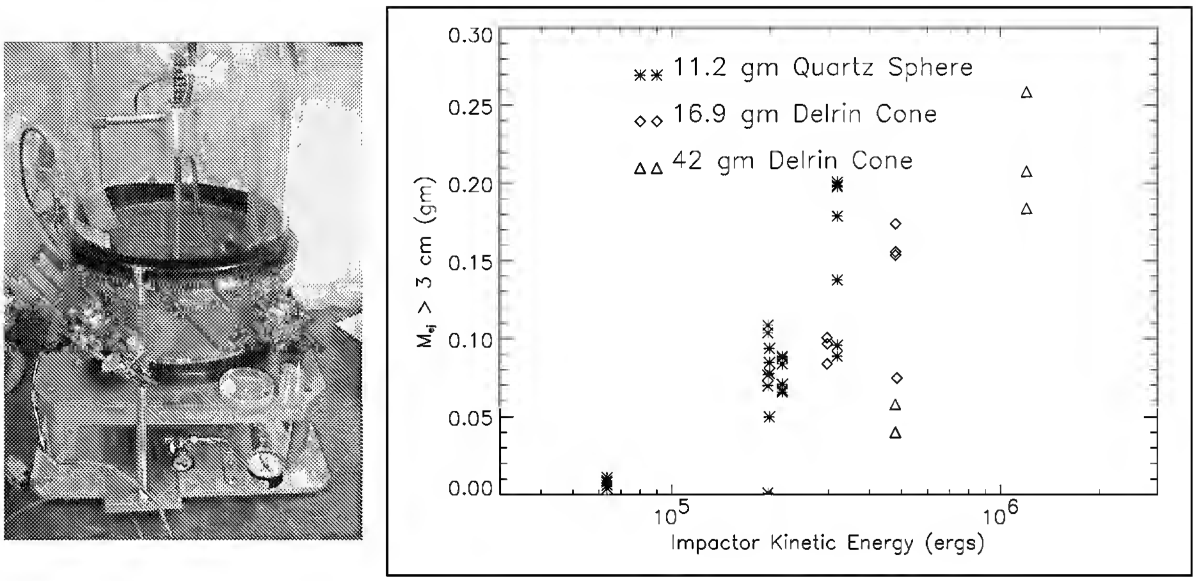

Figure 2: Left: Experimental apparatus for ground-based low-velocity impact experiments. A strobed laser is used for imaging ejecta, which is collected on a series of concentric rings to measure ejecta mass and velocities. Right: Ejecta mass as a function of impact energy. Different amounts of ejecta are produced at the same impact energy with different mass impactors indicating that the outcome of an impact is not a simple function of kinetic energy.

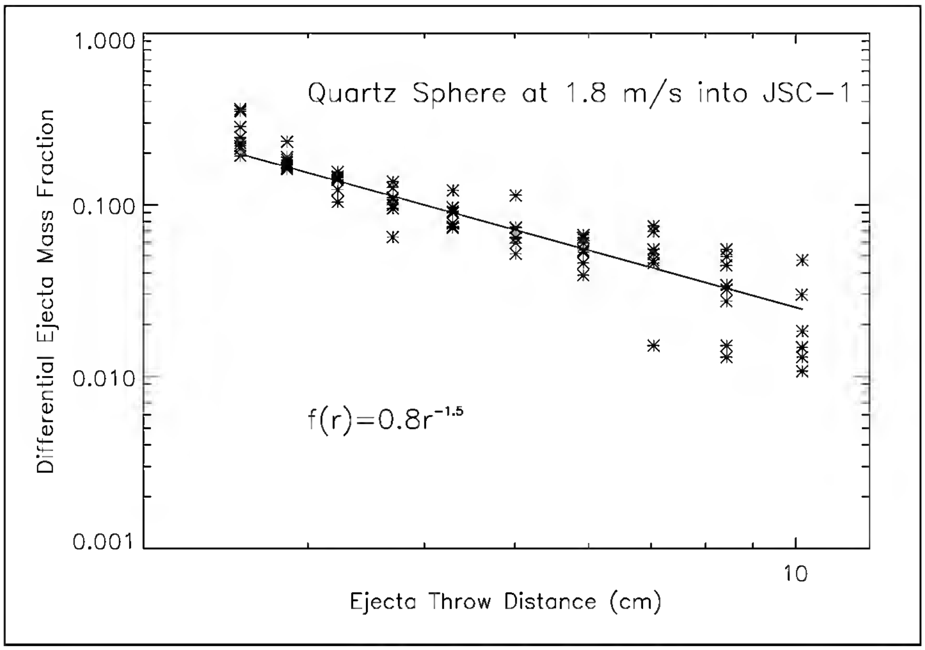

Figure 3: Ejecta velocity distribution derived for a ground-based impact at 1.8 m/s into quartz sand, making use of collector rings. Straight line is a best-fit power-law to data from six experiments at the same impact velocity. Direct imaging of ejecta in PRIME provides velocities of individual particles, crater formation, and coefficients of restitution. A stobed laser sheet will be added to PRIME to derive data similar to these. Only normal incidence low-velocity impacts can be performed in the lab.

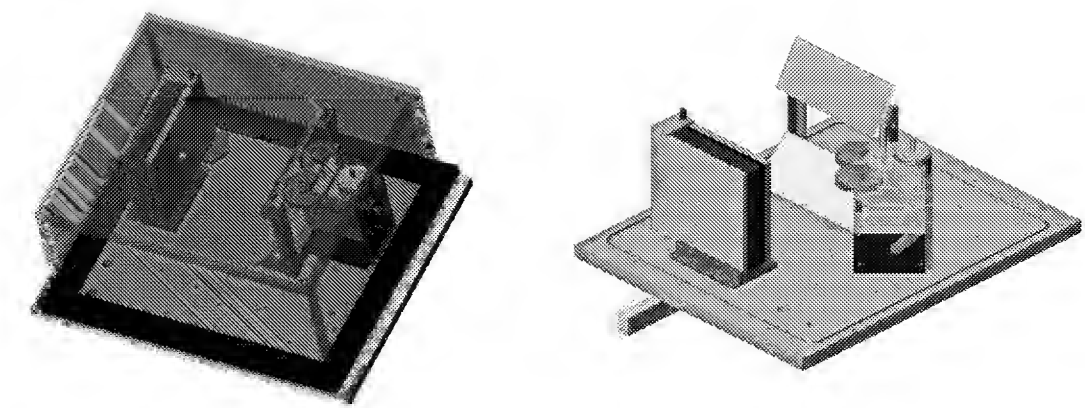

Figure 4: Two schematic drawings of the PRIME Impact Chamber (PIC). Left: the target tray is to the left and the launcher is positioned for a normal (90 degree) incidence impact. The projectile fires between the two mirrors. Right: the acrylic top and sides are not shown for clarity. The launcher is positioned for a 45 degree incidence impact. The handle for opening the target tray door is visible in yellow beneath the baseplate. An o-ring maintains pressure at levels below 0.1 mbar.

Figure 5: The 8 PRIME Impact Chambers daisy-chained together for evacuation prior to flight, with Andreas Lemos, at NASA Glenn Research Center.

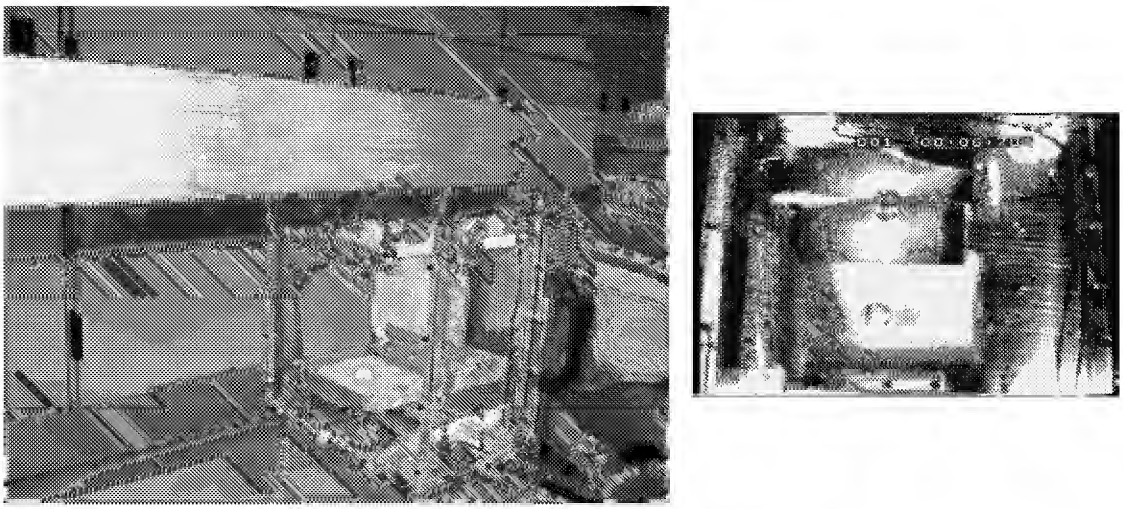

Figure 6: Left: ground testing of PRIME showing one PIC mounted in the experiment rack (Figure 7), with the target tray door open and a projectile resting in the target powder. Right: the view of the NASA high speed video camera. The target is at the bottom, and the launcher is at the top for this experiment. The open door is at left, and two mirrors at the top provide a view of the projectile striking the surface and an orthogonal view of the target surface to the direct, edge-on view. A 2-cm diameter projectile is on its way to the target surface.

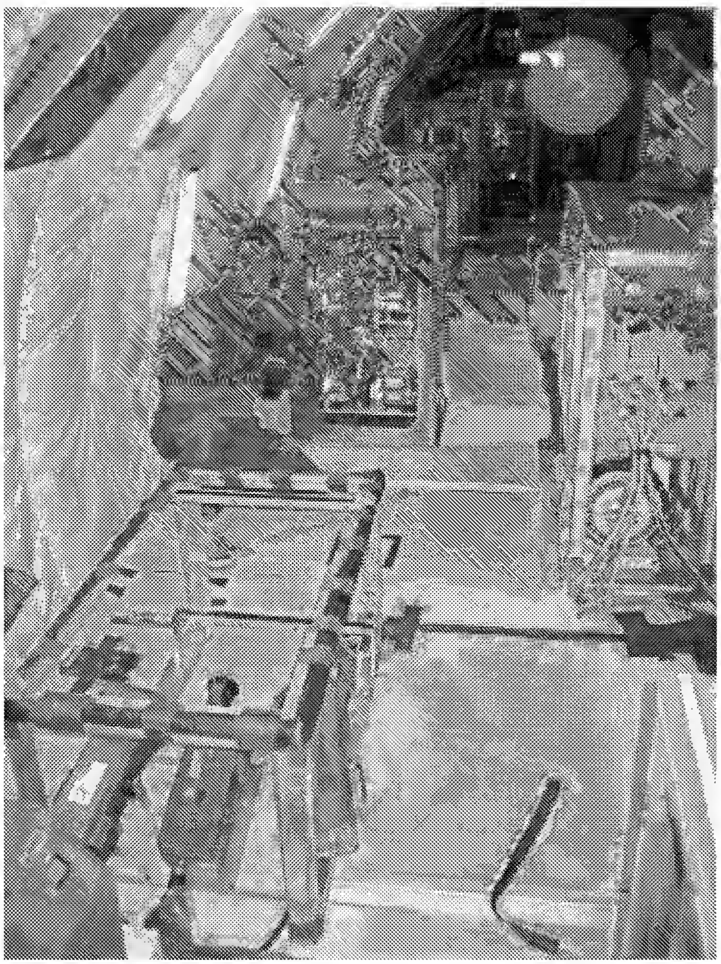

Figure 7:
The experiment mounted in the KC-135 for its first flight, July 9, 2002. In the foreground is the high-speed camera (blue), and the experiment mounting rack. Behind student Matt Kanter, the PRIME storage rack is loaded with 8 PRIME Impact Chambers (PICs).

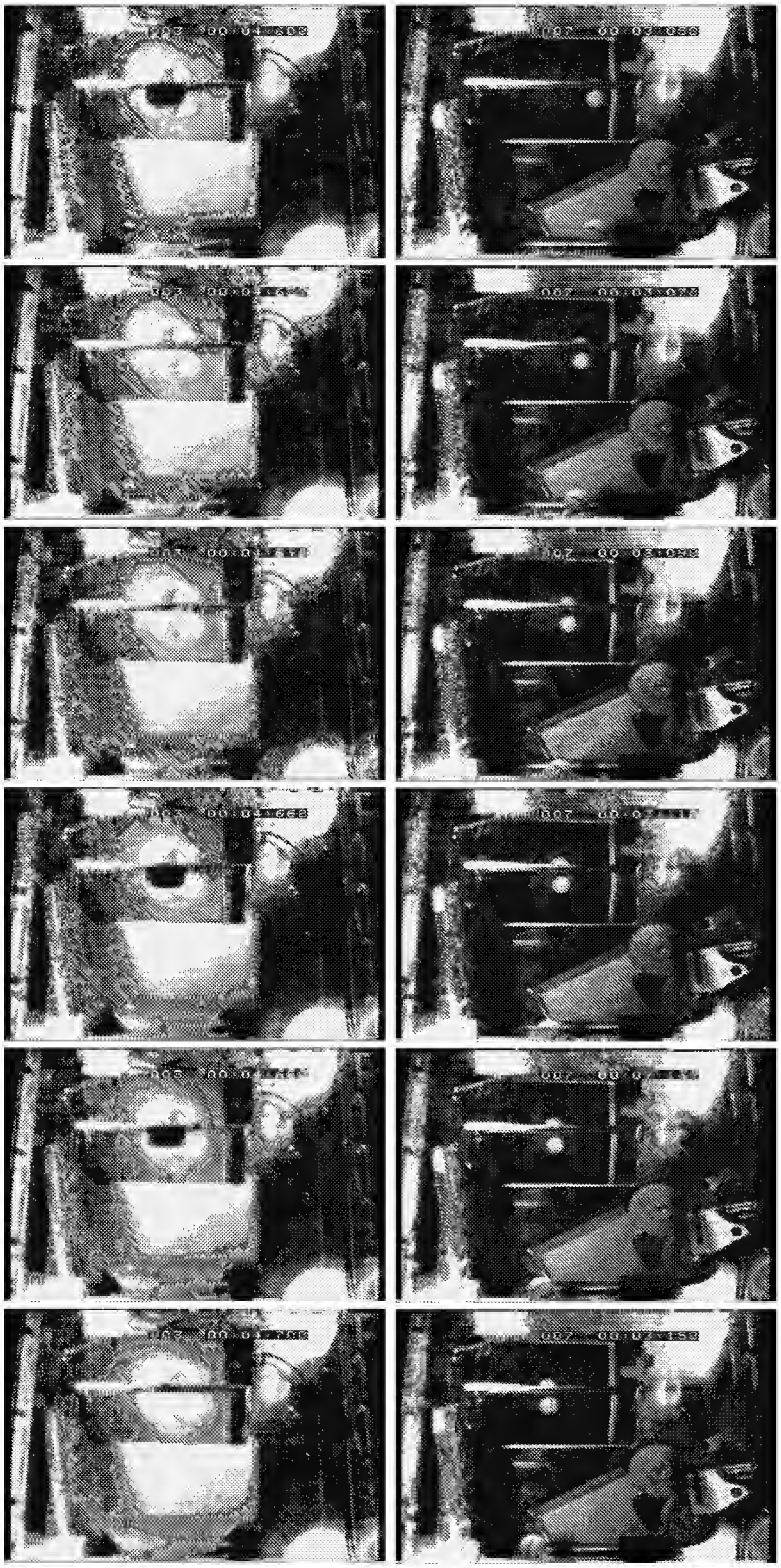

Figure 8: Still images from two impact experiments in the first set of runs of PRIME, July 11, 2002. Both sets run from top to bottom and cover 0.1 seconds at 0.02 second intervals. The layout of the frame is identical to that in Figure 6. Left: impact into quartz sand showing the development of the ejecta curtain. Ejecta velocities and crater formation are measured from the direct view and the reflected views in the mirrors. Right: an oblique impact into JSC-1. In the first three frames, prior to contact with the surface, there is almost no rotation of the projectile, while the last three frames show that the projectile is rotating. These data will provide the tangential as well as normal coefficients of restitution.

References

•Colwell, J. E., and L. W. Esposito 1990a. A numerical model of the Uranian dust rings. *Icarus* **86**, 530-560.

•Colwell, J. E., and L. W. Esposito 1990b. A model of dust production in the Neptune ring system. *Geophys. Res. Lett.* **17**, 1741-1744.

•Colwell, J. E., and M. Taylor 1999. Low Velocity Microgravity Impact Experiments into Simulated Regolith. *Icarus* **138**, 241-248.Dilley, J. P. 1993. Energy loss in collisions of icy spheres: Loss mechanism and size-mass dependence. *Icarus* **105**, 225-234.

•Dilley, J. P., and D. Crawford 1996. Mass dependence of energy loss in collisions of icy spheres: An experimental study. *J. Geophys. Res.* **101**, 9267-9270.

•Hartmann, W. K. 1978. Planet formation: Mechanism of early growth. *Icarus*, **33**, 50-62.

•Hartmann, W. K. 1985. Impact Experiments 1. Ejecta velocity distributions and related results from regolith targets. *Icarus*, **63**, 69-98.

•Hatzes, A. P., F. G. Bridges, and D. N. C. Lin 1988. Collisional properties of ice spheres at low impact velocities. *Mon. Not. R. Astr. Soc.* **231**, 1091-1115.

•Supulver, K. D., F. G. Bridges, and D. N. C. Lin 1995. The coefficient of restitution of ice particles in glancing collisions: Experimental results for unfrosted surfaces. *Icarus* **113**, 188-199.

•Wurm, G., J. Blum, and J. E. Colwell 2001. The Aerodynamical Sticking of Dust Aggregates. *Phys. Rev. E*, **64**, #046301.

•Wurm, G., J. Blum, and J. E. Colwell 2001. A New Mechanism for the Formation of Planetesimals in the Solar Nebula. *Icarus*, **151**, 318-321.

MULTIPLE LIGHT SCATTERING USING 3RD ORDER CORRELATION FUNCTIONS

A. S. Gittings, P. A. Lemieux and D. J. Durian*
Department of Physics and Astronomy, University of California, Los Angeles, CA 90095-1547

ABSTRACT

Multiple light scattering provides a non-invasive method for probing the structure of optically opaque materials such as aqueous foam, colloids and sand. Diffusion-wave spectroscopy (DWS) [1-3] examines the intensity fluctuations of the speckle pattern to extract dynamical information about the scattering sites. When many, uncorrelated scattering sites are present, the electric field is a random Gaussian variable, and the dynamics are easily determined from the second order intensity correlation function $g^{(2)}$.

$$g^{(2)}(\tau) = 1 + \beta|\langle E(0)E^*(\tau)\rangle|^2/|\langle EE^*\rangle|^2 \qquad \ldots(1)$$

$$g^{(2)}(\tau) = 1 + \beta|\gamma(\tau)|^2 \qquad \ldots(2)$$

This crucial relation relates the measured $g^{(2)}$ with the electric field auto-correlation function $\gamma(\tau)$, which can then be expressed in terms of the scattering site dynamics.

It is not possible, however, to tell whether the Gaussian approximation is valid by inspection of $g^{(2)}$ alone. Recently, a method has been developed to test whether the scattering is Gaussian by measuring higher order intensity correlation functions [3]. In this experiment we measured the third order intensity correlation function $g^{(3)}$ for aqueous foam (Gillette Foamy Regular) and compared it with the Gaussian prediction for $g^{(3)}$.

$$g^{(3)}(\tau_1, \tau_2) = 1 + \beta_1(|\gamma_{01}|^2 |\gamma_{02}|^2 |\gamma_{12}|^2) + 2\beta_2 \mathrm{Re}(\gamma_{01}\gamma_{12}\gamma_{20}) \quad \ldots(3)$$

Preliminary data indicate that the scattering is Gaussian to sixth order in the electric field.

REFERENCES

[1] D. Weitz and D. Pine, "Diffusing-wave spectroscopy," *in dynamic light scattering: The Method and Some Applications*, W. Brown, ed. (Clarendon, Oxford, UK, 1993, pp. 652-720.
[2] G. Maret, "Diffusing-wave spectroscopy," Curr. Opin. Colloid Interface Sci. **2**, 251-257 (1997).
[3] P. A. Lemieux and D. J. Durian. "Investigating non-Gaussian scattering processes by using nth-order intensity correlation functions." *Journal Optical Society of America A*, **16**(7):1651-64, (1999).

* P.I. , 2-240A Knudsen Hall, Department of Physics and Astronomy, University of California Los Angeles, CA 90095-1547, USA. E-mail:durian@physics.ucla.edu, FAX: 310-206-5668, Phone: 310-206-2645.

ABSORPTION OPTICS OF AQUEOUS FOAMS

Ranjini Bandyopadhyay, Alex Gittings and D. J. Durian*
Department of Physics and Astronomy, University of California,
Los Angeles, CA 90095-1547

ABSTRACT

Aqueous foams are composed of gas bubbles packed together in a small volume of soapy water. The large number of gas-liquid interfaces in foams results in very strong scattering of light, which explains the opaque nature of conventional aqueous foams such as shaving foams and mousse. For dry foams, the interfaces can take the following three forms : the soap films where two bubbles meet, the triangular plateau borders where three soap films meet and the vertices where four plateau borders meet [1]. Previous experiments have shown that most of the scattering occurs from the plateau borders [2,3] and the transport mean free path of light (l*), the bubble radius (R) and the liquid fraction of foam (ε) is related through the relation $l^*=R/\varepsilon^{0.5}$ [2].

To understand the reflection and scattering of light at the gas-bubble interfaces, we study the absorption of photons in the liquid network as a function of the foam absorptivity. We do this to confirm if the time spent by the photons in the liquid phase is proportional to the liquid fraction of the foam. Our results indicate that for a specific range of liquid fractions ($0.05 < \varepsilon < 0.1$), the photons seem to get *trapped* in the liquid network. This result is independent of the absorptivity of the foam and leads us to conclude that under appropriate conditions, an aqueous foam behaves very much like an optical fiber network.

Aqueous foam is generated in the lab by the method of turbulent mixing [4] of N_2 gas with a jet of alpha-olefin-sulfonate (AOS) solution. The foam has been made absorbing by dissolving small quantities of rhodamine dye ([R] = 0.005 g/l, [R] = 0.01 g/l and [R] = 0.0124 g/l) in the AOS solution. The transmission of photons through the foams of liquid fractions $0.0297 < \varepsilon < 0.35$ has been studied using Diffuse Transmission Spectroscopy (DTS). For each liquid fraction, the transport mean free path l* (the length over which the photon travels before it gets completely randomized) has been estimated from DTS experiments on foams with [R] = 0.0 g/l. The absorption length of foams (l_a^{foam}) of various absorptivities has been estimated by fitting the transmission *vs*. thickness data to the formula [5]

$$T_d = \frac{1+z_e}{[1+(D_o^2+z_e^2)\mu_a'/D_o)\sinh(L'\sqrt{\alpha})/\sqrt{\alpha}+2z_e\cosh(L'\sqrt{\alpha})]} \qquad \dots(1)$$

In Eqn. (1), z_e is the extrapolation length ratio (distance outside the sample, in units of l*, where the photon flux extrapolates to 0), D_o = 0.33 is the dimensionless diffusion coefficient, $\mu_a'=l^*/l_a^{foam}$, $L' = L/l^*$ (L is the thickness of the sample) and $\alpha = \mu_a'\,(1/D_0+\mu_a')$.

Fig. 1 shows a plot of the ratio l_a^{foam}/l_a^{soln} for the liquid fraction range investigated, for all three rhodamine concentrations. l_a^{soln} is the absorption length of the pure rhodamine solution estimated using transmission measurements. In the liquid fraction range $0.05 < \varepsilon < 0.1$, the ratio is found to be lower than the theoretical prediction ($l_a^{foam}/l_a^{soln} \sim 1/\varepsilon$, shown by solid line in Fig. 1). The deviation of the experimental estimates of l_a^{foam}/l_a^{soln} from the solid line leads us to conclude that at $0.05 < \varepsilon < 0.1$, the foam behaves like an optical fiber network with the photons getting trapped in and then channeled through the plateau borders. We believe that our results may be explained quantitatively by relating the reflectance of light at liquid-gas and gas-liquid interfaces to the average angles of incidence at these interfaces.

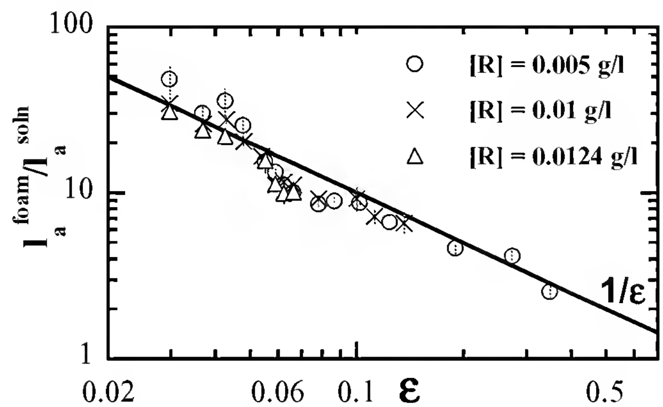

Fig. 1 : Ratio of absorption length of foam to that of the pure rhodamine solution for the liquid fraction range $0.05< \varepsilon < 0.1$ and [R] = 0.005 g/l (circles), 0.01 g/l (crosses) and 0.0124 g/l (triangles). The solid line ($y = 1/\varepsilon$) is the theoretical prediction assuming that the time spent by the photon in the liquid network is proportional to ε.

REFERENCES

* P.I. , 2-240A Knudsen Hall, Department of Physics and Astronomy, University of California Los Angeles, CA 90095-1547, USA. E-mail:durian@physics.ucla.edu, FAX: 310-206-5668, Phone: 310-206-2645.

[1] D. Weaire and S. Hutzler, *The Physics of Foams* (Oxford University Press, New York, 1999).

[2] M. U. Vera, A. Saint-Jalmes and D. J. Durian, Applied Optics **40**, 4179 (2001).

[3] D. J. Durian, D. A. Weitz and D. J. Pine, Science (USA) **252**, 686 (1991).

[4] A. Saint-Jalmes, M. U. Vera and D. J. Durian, European Physical Jl. B **12**, 67 (1999).

[5] A. Cox and D. J. Durian, Applied Optics **40**, 4228 (2001).

Phase-Shifting Liquid Crystal Interferometers for Microgravity Fluid Physics

DeVon W. Griffin
Microgravity Fluid Physics Branch
NASA Glenn Research Center
21000 Brookpark Road
Cleveland, OH 44135

Kenneth L. Marshall
Laboratory for Laser Energetics
University of Rochester
250 East River Rd
Rochester, NY 14623

Fluid physics investigations frequently need to measure the density of fluids and gases. Ground laboratories typically use interferometry for such measurements. However, interferometry can be difficult to employ in reduced gravity laboratories due to both the path lengths that are typically required and effects of parasitic vibrational noise. While older common path interferometers are relatively compact and are more immune to vibration, thus overcoming these problems, they have not been capable of phase-shifting, which is required for the most accurate data. Recent work demonstrated phase-shifting common-path interferometers based on liquid crystal devices.[1] However, initial interferometers did not operate at video frame rates and suffered from variations in optical density with applied voltage. The initial focus of this project was to eliminate both of these problems in the Liquid Crystal Point-Diffraction Interferometer (LCPDI). Progress toward that goal will be described, along with the demonstration of a phase shifting Liquid Crystal Shearing Interferometer (LCSI) that was developed as part of this work.

Mercer, Creath and Rashidnia[2] demonstrated that the liquid crystal point diffraction interferometer produced data as accurate as that generated using a Mach Zehnder interferometer. While accurate, this device could not operate at video frame rates, presented alignment difficulties due to the large number of microspheres used as spacers and suffered from voltage-dependent fluctuations in optical density.

Figure 1 is a photograph of the latest LCPDI. Other than a lens to focus the light from a test section onto a diffracting microsphere within the interferometer and a collimated laser for illumination, the pink region contained within the glass plates on the rod-mounted platform is the complete interferometer. The total width is approximately 1.5 inches with 0.25 inches on each side for bonding the electrical leads. It is 1 inch high and there are only four diffracting microspheres within the interferometer. As a result, it is very easy to align, achieving the first goal.

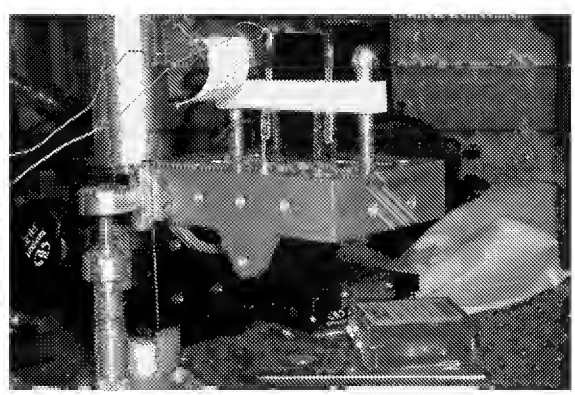

Figure 1 LCPDI

The liquid crystal electro-optical response time is a function of layer thickness, with thinner devices switching faster due to a reduction in long-range viscoelastic forces

between the LC molecules. The LCPDI in Figure 1 has a liquid crystal layer thickness of 10 microns, which is controlled by plastic or glass microspheres embedded in epoxy "pads" at the corners of the device. The diffracting spheres are composed of polystyrene/divinyl benzene polymer with an initial diameter of 15 microns. The spheres deform slightly when the interferometer is assembled to conform to the spacing produced by the microsphere-filled epoxy spacer pads. While the speed of this interferometer has not yet been tested, previous LCPDIs fabricated at the Laboratory for Laser Energetics switched at a rate of approximately 3.3 Hz, a factor of 10 slower than desired. We anticipate better performance when the speed of these interferometers is tested since they are approximately three times thinner.

Phase shifting in these devices is a function of the AC voltage level applied to the liquid crystal. As the voltage increases, the dye in the liquid crystal tends to become more transparent, thus introducing a rather large amount of error into the phase-shifting measurement. While that error can be greatly reduced by normalization, we prefer eliminating the source of the error. To that end, we have pursued development of a "blend" of custom dyes that will not exhibit these properties. That goal has not yet been fully achieved as is illustrated by the set of five interferograms in Figure 2. Guardalben, et al, presented a similar set of interferograms in a paper partially funded by this grant.[3]

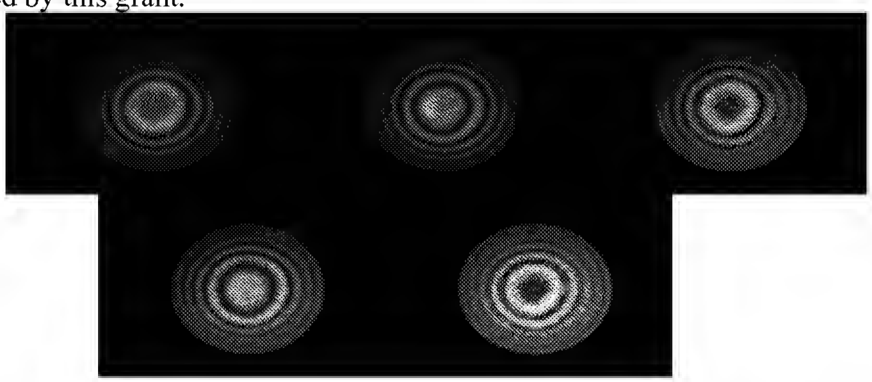

Figure 2 Set of five interferograms shifted by 90 degrees between each image

Shearing interferometers are a second class of common path interferometers. Typically they consist of a thick glass plate optimized for equal reflection from the front and back surface. While not part of the original thrust of the project, through the course of laboratory work, we demonstrated a prototype of a shearing interferometer capable of phase shifting using a commercial liquid crystal retardation plate.[4] A schematic of this liquid crystal shearing interferometer (LCSI) and a sample set of interferograms are in the reference.

This work was also supported by the U.S. Department of Energy Office of Inertial Confinement Fusion under Cooperative Agreement No. DE-FC03-92SF19460, the University of Rochester, and the New York State Energy Research and Development Authority. The support of DOE does not constitute an endorsement by DOE of the views expressed in this article.

References:

1. Mercer, C.R., Creath, K. , "Liquid-crystal point-diffraction interferometer for wave-front measurements," Applied Optics, **35**, 1633-1642 (1996).
2. Mercer, C.R., Rashidnia, N. and Creath, K., "High data density temperature measurement for quasi steady-state flows," Experiments in Fluids, **21**, 11-16 (1996).
3. Guardalben, M.J., Ning, L., Jain, N., Battaglia, D.J. and Marshall, K.L., "Experimental comparison of a liquid-crystal point-diffraction interferometer (LCPDI) and a commercial phase-shifting interferometer and methods to improve LCPDI accuracy," Applied Optics, **41**, 1535-1365 (2002).
4. Griffin, D.W., "Phase-shifting shearing interferometer," Optics Letters, **26**,140-141 (2001).

Phase-Shifting Liquid Crystal Point-Diffraction Interferometer for Microgravity Fluid Physics

DeVon W. Griffin[1] Kenneth L. Marshall[2] Carolyn R. Mercer[1]

[1]NASA Glenn Research Center [2]Laboratory for Laser Energetics, University of Rochester

Goals and Path of Research

GOAL:

Develop a phase-shifting LCPDI that can operate at least at NTSC video frame rates and can be easily commercialized.

ACCOMPLISHMENTS:

- Development of repeatable fabrication methods for cells with a thickness of 10 µm and four widely-separated spherical plastic spacers. The spacers are the diffraction objects.
- Design of negative dichroic dyes to prevent voltage-dependent changes in optical density
- Identified error sources in phase-shifted interferograms generated using a LCPDI[1]
- Demonstrated a phase-shifting shearing interferometer based on liquid crystal technology[2]
- Demonstrated 3.3 Hz switching in an LCPDI

1. Guardalben, M.J., Ning, L., Nieraj, J. Battaglia, D.J. and Marshall, K.L., "Experimental comparison of a liquid-crystal point-diffraction interferometer (LCPDI) and a commercial phase-shifting interferometer and methods to improve LCPDI accuracy" Applied Optics, 41, 1353-1365, (2002).
2. Griffin, D.W., "Phase-shifting shearing interferometer," Optics Letters, 26, 140-141 (2001).

Phase-Shifting Interferometry

- Historically, interferometric data was analyzed by using various algorithms to trace out the center of the bright and dark fringes. Though widely used, this technique had limited accuracy.
- With the advent of CCDs, various researchers realized that accuracy could be greatly improved by shifting the optical path of one interferometer arm by fractions of a wavelength and recording the intensity in the plane of the interferogram as a function of the shift. When processed using a suitable algorithm, this shifting of phase produces results accurate to one-thousandth of the wavelength of light used.
- Phase-shifting interferometry is now the industry standard for optical testing with the five-step algorithm generally regarded as the most accurate.

Phase-Shifted Set of Interferograms taken with LCPDI

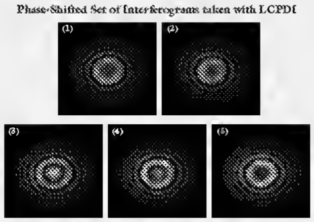

Developing the Technology

- Dyes equalize the intensity between the reference and diffracted beams. Applying voltage changes the optical density of the dye used, which must be compatible with the liquid crystal. Since no commercial dyes are available to balance this effect, the LLE group recently designed and has begun to synthesize a group of new dyes to correct this problem. Additionally, purification techniques will be employed to remove by-products that cause a scattering texture which increases with voltage.
- Switching speed has been increased by an order of magnitude. Device size is now 1.25 inches by 1 inch with a total thickness of less than 0.25 inches.
- The LLE group has developed an extensive protocol for device fabrication that includes techniques to position and isolate the diffracting spheres, as well as filling protocols. Forward-looking concepts include fabricating the diffracting elements using thin film deposition techniques.

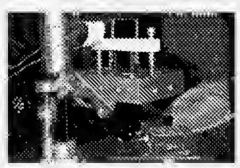

LCPDI in the laboratory.

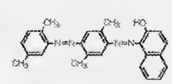

Commercial dye
(positive dichroism)

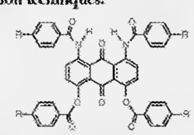

Synthesized dye
(negative dichroism)

Traditional Interferometers

- Mach-Zehnder (shown), Twyman-Green, and most other traditional interferometers have the test and reference beams physically separated.
- Given the separate beam paths, small relative motion of the two interferometer arms causes rapid shifting or complete washout of the interference fringes.
- The separate beam paths enable phase-shifting interferometry, which provides much greater accuracy than simply following interference fringes.

Mach-Zehnder Interferometer

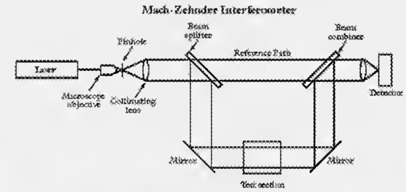

Point-Diffraction Interferometers

- In this interferometer, only one beam passes through the test section. A decollimating lens focuses this light on a small diffracting object. Much of the light passes undiffracted but the portion is diffracted off the object and forms a perfect reference beam that interferes with the undiffracted light.
- The common path of the test and reference beams make this interferometer much less sensitive to mechanical vibration.
- Lack of separation between the test and reference beams previously prohibited the use of phase-shifting techniques with point-diffraction interferometers.

Point-Diffraction Interferometer

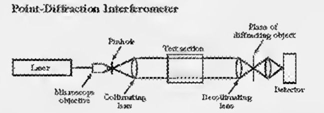

RHEOLOGY OF FOAM NEAR THE ORDER-DISORDER PHASE TRANSITION

R. Glynn Holt (rgholt@bu.edu) and J. Gregory McDaniel (jgm@bu.edu), Boston University, Dept. of Aerospace and Mechanical Engineering, 110 Cummington St, Boston, MA 02215

INTRODUCTION AND MOTIVATION

Foams are extremely important in a variety of industrial applications. They are widely used in firefighting applications, in flow applications such as enhanced oil recovery, and as trapping, transport and separation agents. The most important quality of a foam in many of these industrial processes is its response to imposed strain, or its *rheological* behavior. There exists little experimental data on the rheological properties of real 3D foams, even though such knowledge would likely enhance the efficacy of current applications and suggest other unique applications. The lack of 3D data is due in large part to the earth-based requirements for contact containment, and to the fact that gravity-induced drainage quickly destroys all but the "driest" foams, those with a very high gas volume fraction α_g. We introduce a unique method to provide non-contact control and manipulation of foam samples. The development of this technique will provide the ability to carry out a set of benchmark experiments in **0g** allowing determination of a foam's yield stress, bulk shear and dilatational moduli and viscosities as a continuous function of gas volume (or 'void') fraction α_g from the dry limit ($\alpha_g \approx 1$) through the order-disorder phase transition to the wet limit ($\alpha_g \ll 1$) of a bubbly liquid.

OBJECTIVES

The goal of the investigation is the determination of the mechanical and rheological properties of foams, utilizing the microgravity environment to explore foam rheology for foams that cannot exist, or only exist for a short time, in **1g**. *The specific objectives of the investigation are:*

1) To refine and utilize a novel, non-contact acoustic technique for experimentally measuring the stress-response of small samples of foam ("foam drops") subjected to both static and time-varying acoustic strain.
2) To experimentally measure the stress-response of foam drops subjected to both static and time-varying strain.
3) To model the response of foam drops to static and time-varying modulation of the acoustic field to extract rheological properties.
4) To define experiments that can be performed in the μg environment, where the effects of drainage, buoyancy and high acoustic fields can be avoided, and α_g can be varied smoothly through the order-disorder transition.

RESULTS

Our ground-based investigations have concentrated on the investigation and analysis of normal-mode oscillations of foam drops. We can organize the presentation of our results to date by void fraction:

Dry limit, effective medium model. In the limit of dry foams (void fraction greater than the critical value, and approaching unity) and small deformations from equilibrium, we model foam as an effective elastic solid medium. In [1] we present a model for the normal modes of oscillation of an effective elastic sphere. By specifying (via measurement) the natural frequency of a specific mode we may infer the effective shear elastic modulus G of the foam via the formula

$$G = \rho \left(\frac{\omega R}{\xi} \right)^2 \frac{1-2v}{2(1-v)} \qquad \textbf{(1)}$$

where ρ is the effective density of the foam, ω is the measured modal frequency, R is the measured drop radius, ξ is the computed dimensionless modal frequency from the model, and ν is Poisson's ratio for the foam.

Results for a drop with void fraction of 0.8 yielded a shear modulus $G = 75 \pm 3$ Pa, which is of the same order as several estimates of the shear modulus of foams reported in the literature using contact-based techniques. Importantly, this result was insensitive to the foam's Poisson ratio, which is difficult to independently measure.

Wet limit, bubble dynamics model. In the limit of 'low' void fractions (roughly 0.5 and below) we model foam as a bubbly liquid. In [2] we develop a model for the dynamics of a spherical drop of such a foam which retains fully nonlinear behavior of individual bubbles. The primary advantage of this bubble-based model is that it has predictive power.

In the limit of linear, inviscid motion we obtain approximate analytic expressions for the normal mode frequencies of a spherical foam drop of equilibrium radius R_0 as a function of the equilibrium void fraction α_{g0}:

$$\omega_n^2 \approx \frac{\sigma n(n-1)(n+2)}{\rho_l(1-\alpha_{g0})R_0^3} = \omega_{n,pureliquid}^2 \cdot \frac{1}{(1-\alpha_{g0})} \qquad \omega_0^2 \approx \frac{\omega_{SB}^2}{\frac{3R_0^2}{\pi^2 a_0^2}\alpha_{g0}\ (1-\alpha_{g0}) + 1 - \alpha_{g0}^{1/3}} \quad \mathbf{(2)}$$

The shape mode frequencies ω_n of mode number $n \geq 2$ (after a Legendre polynomial expansion) are approximately the mass-corrected Lamb frequencies for a pure liquid drop, where σ is the surface tension, and ρ_l is the liquid component density. The breathing mode frequency ω_0 depends on the frequency ω_{sb} of the individual bubble constituents of radius a_0 as well as the void fraction.

MICROGRAVITY RELEVANCE AND SIGNIFICANCE

All but the driest foams drain in gravity. The liquid component will flow downward, and the bubbles will rise until a pool of liquid with a dry foam cap will form. Gravity will thus prevent the measurement of foam properties as the gas volume fraction is decreased towards the order-disorder transition, because the foam will be destroyed. There is very little experimental data on the rheological properties of 3D foams, primarily because potential experiments are severely hindered by the requirement for contact containment, and draining and thinning due to gravity.

Our experimental technique can provide non-contact control and manipulation of multicomponent and multiphase drops. In comparison with existing experimental techniques for rheological measurements, our technique offers at least four advantages. First, it is a non-contact technique that can nevertheless provide stable positioning and straining manipulation of a sample. Second, we can easily levitate and strain samples of arbitrary void fraction continuously from 0 to 1. Third, we can test small samples of foam with variable number and size of bubbles to investigate limiting cases. Finally, we can simultaneously measure shear and compressional parameters, whereas traditional techniques are restricted to either of these.

REFERENCES

[1] J. Gregory McDaniel and R. Glynn Holt, "Measurement of aqueous foam rheology by acoustic levitation", Phys. Rev. E **61**, 2204 (2000).

[2] J. Gregory McDaniel, Iskander Akhatov, and R. Glynn Holt, "Inviscid dynamics of a wet foam drop with monodisperse bubble size distribution", Phys Fluids **14**, 1886-1894 (2002).

GRANULAR MATERIAL FLOWS WITH INTERSTITIAL FLUID EFFECTS

M. L. Hunt[1] and C. E. Brennen
California Institute of Technology, Pasadena, CA 91125

C.S. Campbell
University of Southern California, Los Angeles, CA

ABSTRACT

In 1954, R.A. Bagnold published his seminal findings on the rheological properties of liquid-solid flows. Over the last fifty years, this work has been cited extensively in studies of granular and debris flows, sedimentation, suspensions, magma flows, sand transport and a range of other multiphase flow processes. We recently completed an extensive reevaluation of Bagnold's work (Hunt, et al. 2002) and our analysis and simulations indicate that the rheological measurements of Bagnold were affected significantly by secondary flows within the experimental apparatus. The concentric cylinder rheometer was designed by Bagnold to measure simultaneously the shear and normal forces for a wide range for solid concentrations, fluid viscosities and shear rates. As presented by Bagnold, the shear and normal forces depended linearly on the shear rate in the `macroviscous' regime. As the grain-to-grain interactions increased in the `grain inertia' regime, the stresses depended on the square of the shear rate and were independent of the fluid viscosity. These results, however, appear to be dictated by the design of the experimental facility. In Bagnold's experiments, the height (h) of the rheometer was relatively short compared to the spacing (t) between the rotating outer and stationary inner cylinder (h/t=4.6). Since the top and bottom end plates rotated with the outer cylinder, the flow contained two axisymmetric counter-rotating cells in which flow moved outward along the end plates and inward at the midheight of the annulus. These cells contribute significantly to the measured torque, and obscured any accurate measurements of the shear or normal stresses.

Before doing the reevaluation of Bagnold's work, our research objective was to examine the effects of the interstitial fluid for flows in which the densities of the two phases were different. In Bagnold's original work, only neutrally buoyant spheres were used. Because of the questions that we have raised regarding Bagnold's measurements, the scope of our work can be expanded because issues associated with neutrally buoyant particles as well as flows of dissimilar densities are of considerable scientific interest and there appears to be no corresponding experimental measurements. The reduced-gravity environment on the KC135 aircraft will enable the measurements of particles of mismatched without having a separation of the two phases.

[1]Division of Engineering and Applied Science, Caltech, Pasadena, CA 91125; phone (626) 395-4231; fax (626) 568-2719; hunt@caltech.edu

After reevaluating Bagnold's work, we redesigned our experimental facility to minimize secondary flow effects. Like Bagnold's facility, we use a concentric cylinder rheometer with a rotating outer wall. The inner cylinder also is able to rotate slightly but will also be restrained by flexible supports; the torque is measured from the deformation of the flexures. The normal force is measured using piezoelectric transducers that record both impacts with the surface and fluid pressure variations resulting from particle collisions. Unlike Bagnold's apparatus, the top and bottom plates of the annulus will not rotate, and the torque measurement will be measured only in the center region of the inner annulus; these changes will minimize the secondary flow effects.

The experiments will cover a range of particle sizes (from d = 1.5 to 4 mm), particle concentrations (up to 55% solids concentration by volume), shear rates (γ = 10-160 sec^{-1}) and solid-to-fluid densities (ρ_p = 1.2 to 8). During one flight of the KC-135 we will change two parameters: the rotational speed and the fluid viscosity (μ). At one time during a flight, we plan to withdraw some of the fluid (water for example) within the annulus while injecting some fluid of a different viscosity (water-glycerin mixture). Hence, the experiments will cover flows where the particle inertia dominates the fluid effects (granular flows) to flows in which the fluid inertia dominates that of the particles (dilute suspension). The range of Stokes numbers ($St=d^2\gamma\rho_p/\mu$) will be from about 5 to 3000.

Currently, the experimental facility has just been completed. We have calibrated the normal impact measurements using carefully controlled single particle impacts with the transducers. The torque measurements have also been calibrated by mounting the inner cylinder in such a way that we could impose a known load on the drum. We use reluctance transducers to measure the motion and deformation of the flexures and calibrate the device with the imposed load. Measurements will also be made of the fluid temperature, acceleration and rotational speed of the outer drum.

The poster will overview the current status of our experiment and the planned experimental program.

REFERENCES

R.A. Bagnold, Experiments on a Gravity-Free Dispersion of Large Solid Spheres in a Newtonian fluid under Shear, ***Proc. R. Soc. London*** **225**, 49-63 (1954).

M.L. Hunt, R. Zenit, C.S. Campbell and C.E. Brennen, Revisiting the 1954 Suspension Experiments by R.A. Bagnold, ***J. Fluid Mechanics***, **452**, 1-24 (2002).

Investigators: Melany L. Hunt & Christopher E. Brennen, Caltech; Charles S. Campbell, USC

- ## Research Focus:

To experimentally document the transition from a suspension to a granular flow

- ## Research Accomplishments:

Demonstrated that the highly cited experiments by R.A. Bagnold (1954) on the suspension to granular flow transition are actually the result of secondary flows within the experiment and are not due to collisional interactions.[1]

Designed and built a concentric cylinder shear-cell to measure both shear and normal forces for a range of shear rates, particle sizes and densities, and fluid viscosities. Measurements for flows with collisional, inertial and viscous effects.

Preparing for upcoming flight experiments on the KC-135 aircraft.

Proposed a computational technique for liquid-solid flows that combines the discrete element method and smoothed-particle hydrodynamics.[2]

1. M.L. Hunt, R. Zenit, C.S. Campbell and C.E. Brennen, Revisiting the 1954 suspension experiments of R.A. Bagnold, **J. Fluid Mechanics**, 452, pp. 1-24 (2002).

2. V. Potapov, M.L. Hunt and C.S. Campbell, Liquid-Solid Flows Using Smoothed Particle-Hydrodynamics and the Discrete Element Method, **Particle Technology**, 116, pp. 204-213 (2001).

A Microgravity Experiment

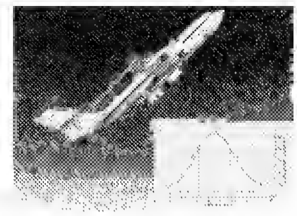

The microgravity environment will allow the liquid-solid flow experiments to be performed without sedimentation of the particles.

The Experiment:

- A concentric cylinder rheometer with rotation of only the outer cylinder that is controlled with a variable speed motor.
- The upper and lower guard cylinders are used to isolate end effects. Inner test cylinder is constrained by 3 instrumented flexures (differential variable reluctance transducers) to measure displacement and, hence, the torque.
- The collisional normal stress is measured using piezoelectric transducers mounted on the guard cylinders.
- The apparatus also includes a fluidization system to aid the dispersal of particle after the high gravity portion.
- A sight glass is mounted outside the cell.

NASA/CP—2002-211212/VOL2

Coaxial Rheometer

Apparatus cross-section

Dimensions:

outer radius 19 cm; gap 3.16 cm

total height 36.9 cm

test cylinder height 11.2 cm

Assembly sketch

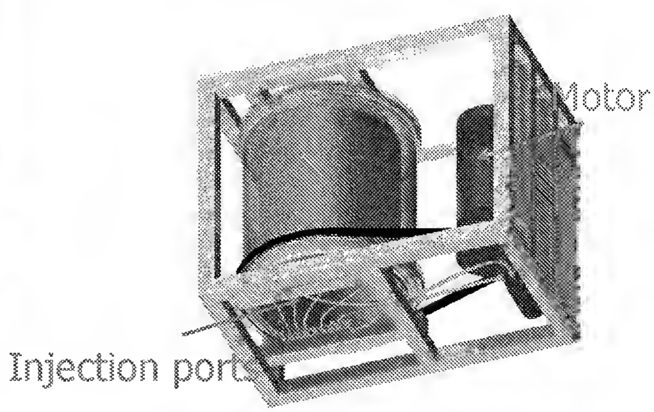

Parameters and Instrumentation

- Particles: 1.8 mm steel; 1.8 & 3 mm glass
- Fluids: water-glycerol mixtures
- Rotational speeds: 20-300 rpm
- Shear rate γ = 10-158 sec^{-1}
- Particle Stokes number:
  St =$\rho_p \gamma\, d^2/\mu$ from 10 to 4000

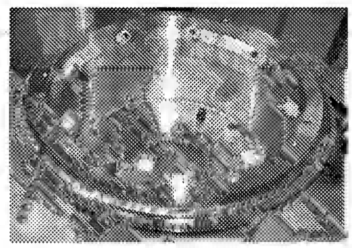

Fluid injection ports

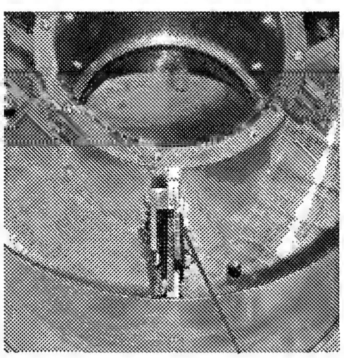

Flexures with stops and DVRT sensor

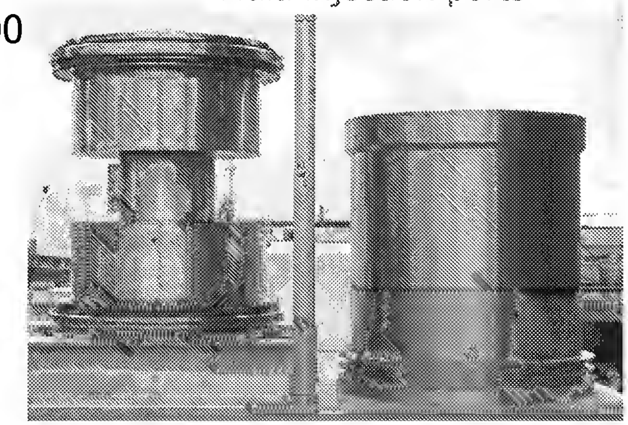

Both drums (minus test piece); bearings; seals; port for piezoelectric transducer; belt grooves

Current status

- Completed experimental apparatus; it seals and rotates; test stand is not yet completed
- Calibrated torque measurements on inner drum; the displacement of the flexures are measured for a range of torques from 0.4 to 27 Nm; range of flexures from 0.006 to 0.025 in; measurements in air and water
- Tested piezoelectric transducers for different types of particles in water and in glycerin-water mixtures
- Data acquisition is ready
- Sight glass and fluid injection system are ready

Revisiting Bagnold's Experiments (1954)

Proc. Royal Soc. London, A., 225, pp. 49-63, 1954

- Shear cell with neutrally buoyant particles
- Although widely cited, results have not been verified experimentally or computationally
- Measured averaged shear and normal forces; presented net results
- Introduction of the Bagnold number, $N=\rho d^2 \gamma \lambda^{1/2}/\mu$

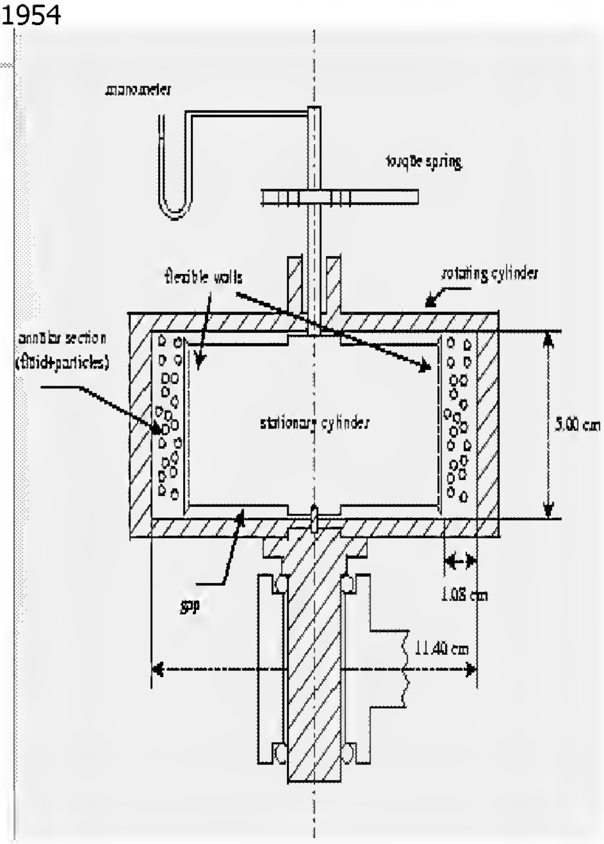

Questions with Bagnold's data

- Bagnold's shear stress data shows a dependence on shear rate to the 1.5 power and not the 2nd power
- Pure fluid results are significantly greater than found in comparable studies
- Height of annulus is 4.6 times the gap
- Rotation of upper and lower plates
- Counter rotating vortices
- Contribution to torque is due to shear flow across gap ($\tau \propto \gamma$) plus spin of end walls ($\tau \propto \gamma^{1.5}$)
- Can estimate shear stress results using an effective viscosity, $\mu' = \mu f(\phi)$

Bagnold's data with effective viscosity

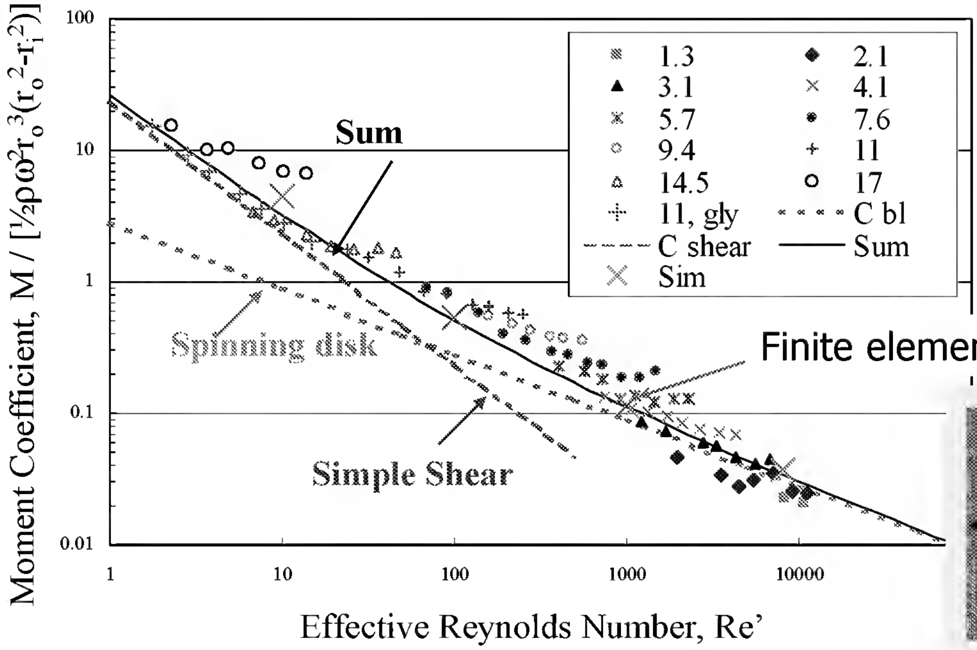

Finite element simulations

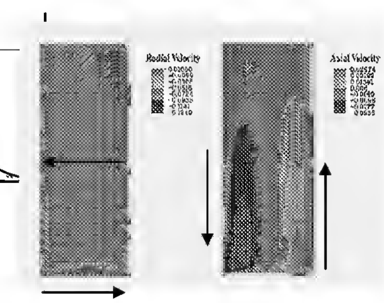

$Re' = \rho\omega R_o(R_o - R_i)/\mu'$ with $\mu' = \mu f(\phi)$

PHASE TRANSITION IN DUSTY PLASMAS:

A MICROPHYSICAL DESCRIPTION*

Glenn Joyce, Gurudas Ganguli, and Martin Lampe

Plasma Physics Division, Naval Research Laboratory, Washington, DC 20375-5346

ABSTRACT

Dust grains immersed in plasma discharges acquire a large negative charge and settle into a dust cloud at the edge of the sheath. In this region, the plasma ions stream toward the electrode at a velocity $\mathbf{u} \sim c_s=(T_e/m_i)^{1/2}$. Experimentally at sufficiently high gas pressure P, the random kinetic energy of the grains is damped by gas friction, and the grains are strongly coupled and self-organize into a crystalline configuration [1-3]. For lower pressures despite the dissipation of grain kinetic energy to gas friction, the dust grains reach a steady-state kinetic temperature T_d which is much larger than the temperature of any other component in the plasma. T_d is so large that the dust acts like a fluid [1-3]. We have used the dynamically shielded dust (DSD) model [4] to simulate these physical processes. We find that the known experimental features are nicely reproduced in the simulations, and that additional features are revealed. In the figure we plot the variation of T_d as P is continuously varied in a DSD code run. A marked difference is evident between the critical pressure P_m for the melting transition as P is decreased, and the critical pressure P_c for the condensation transition as P is increased. For $P_m < P < P_c$, mixed phase states are seen. This hysteresis occurs because the instability which triggers melting is different from the instability that heats the dust in the fluid phase and inhibits freezing.

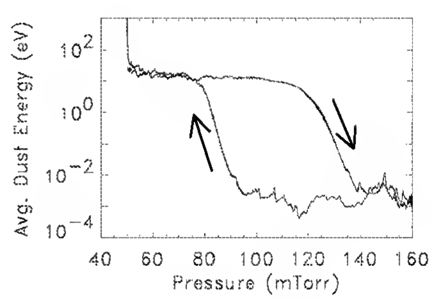

CONDENSATION: At low pressure, the dust is subject to a two-stream instability with the ions. This instability is responsible for the high temperature of the dust at low pressure. For further details we refer the reader to Ref [4].

MELTING: The basic physics underlying the melting transition has been elucidated in a series of papers [2,5,6]. In Refs [2,5] a phenomenological model for the asymmetric interaction between grains is constructed. We are developing a first-principles analytic approach to the melting transition, which embodies the same physics that is present in the DSD code. The inter-grain potential is the dynamically shielded Coulomb interaction, given in k-space by

$$\phi(k) = \sum \frac{Z_i e}{2\pi^2 k^2 D(k, -\mathbf{k} \cdot \mathbf{u} + i\nu_i)}, \tag{2}$$

where $D(k,\omega)$ is the linear plasma response function defined in Refs [4,7].

Crystal instabilities can be represented at various levels of detail. Experiments and DSD simulations indicate that the mode which initiates the melting process is a shear mode with propagation vector $\mathbf{k}$ parallel to the ion streaming. In the linear stage of this mode, the equation

of motion of a grain in the j^{th} layer, due to the forces exerted by the grains directly above and directly below, is

$$m\Delta\ddot{x}_j = C^+(\Delta x_{j+1} - \Delta x_j) + C^-(\Delta x_{j-1} - \Delta x_j) - m\nu_d \Delta\dot{x}_j \tag{3}$$

where

$$C^{\pm} \equiv \left[\frac{\partial^2 Ze\phi(\Delta x, z = \mp d)}{\partial(\Delta x)^2}\right]_{\Delta x=0}, \tag{4}$$

$\phi(x,z)$ is the Fourier transform of Eq. (2), d is the separation between grain layers, and Δx is the displacement of the grain from its equilibrium position in the x direction (transverse to the propagation direction z). Unlike the situation in ordinary crystals, the force constants $C^{\pm}$ are such that $C^+ \neq C^-$. For a transverse mode in an infinite crystal, $\Delta x_j \sim \exp[i(jkd-\omega t)]$, Eq. (3) leads to a dispersion relation

$$\omega = -\frac{i\nu_d}{2}\left\{1 \mp \sqrt{1 - \frac{4}{m\nu_d^2}\left[(C^+ + C^-)(1 - \cos kd) - i(C^+ - C^-)\sin kd\right]}\right\}. \tag{5}$$

Eq. (5) is similar to the dispersion relation for phonons in an ordinary crystal, except that here instability occurs because $C^+ \neq C^-$. The instability can be stabilized at high pressure due to the dust collisionality ν_d and/or the ion collisionality ν_i, which appears as damping of the attractive wake force C^- through the dielectric D in Eq. (2). The phonon streaming instability is similar to the two-stream instability that occurs in the fluid-dust phase. However, the stabilization pressure P_m for the phonon instability is lower than the critical pressure P_c for Buneman instability (i.e. for freezing), as indicated by the DSD code results. There is a range of pressures where both the solid and fluid phases of the dust are stable, which allows a mixed-phase system to exist, as observed [2].

REFERENCES

1. Melzer, A., et al, Phys. Rev. E54, R46, 1996; Phys. Rev. E **53**, 2757 (1996); Phys. Lett. A **191**, 301 (1994); Phys. Rev. E54, R46, 1996; Phys. Rev. E **53**, 2757 (1996); Phys. Lett. A **191**, 301 (1994)
2. Thomas, H,. *et al*, Phys. Rev. Lett. **73**, 652 (1994); Nature (London) **379**, 806 (1996); J. Vac. Sci. Technol. A **14**, 501 (1996); Phys. Rev. Lett. **73**, 652 (1994).
3. Chu, J. H. and Lin I, Phys. Rev. Lett. **72**, 4009 (1994).
4. Joyce, G., Lampe, M., and Ganguli, G., Phys. Rev. Lett., 88, 095006-1, 2002
5. Schweigert, V. A., *et al.*, Phys. Rev. E **54**, 4155 (1996); Phys. Rev. Lett. **80**, 5345 (1998).
6. Melandso, F., Phys. Rev. E **55**, 7495 (1997).
7. Lampe, M., Joyce, G., and Ganguli, G., Phys. Scripta T89, 106 (2001); IEEE Trans. Plasma Science **29**, 238 (2001); Proceedings ISSS, 2002 (to appear).

*This work was supported by NASA and ONR.

Glenn Joyce, Code 6790, Naval Research Laboratory, 20375
Phone(202)767-6785. Fax (202)767-0631. joyce@ppd.nrl.navy.mil

Experimental study of turbulence-induced coalescence in aerosols

Paul Duru, Luying Wang, Claude Cohen and Donald L. Koch

School of Chemical Engineering, Cornell University, Ithaca N   14853, USA.

Abstract

An aerosol consists of a dispersion of liquid particles in a gas. Coalescence occurs when Brownian motion, di erential sedimentation or turbulent gas ow drive two drops into contact and the drops form a larger drop. Coalescence modi es the size distribution of an aerosol which in turn a ects its main properties. For instance, raindrop coalescence play an important role in cloud dynamics, precipitation and the scavenging of pollutants by precipitation.

The rate of coalescence depends on the forces driving the relative motion of the particles. A good fundamental understanding of the mechanisms of coalescence leading to quantitative predictions of coalescence rates has been achieved for colloidal particles suspended in liquids. This achievement is largely attributable to the ability of researchers to isolate each of the driving forces in turn by judicious use of the density matching of the uid and particles and adjustment of the uid viscosity. In contrast, the current understanding of aerosol coalescence is rudimentary. Moreover, in experimental conditions on Earth, one is likely to observe mixed e ects of Brownian motion, sedimentation and turbulence on coalescence making a critical test of theory di cult.

We present an experimental ground-based study of aerosol coalescence due to turbulence. It will provide the necessary background to plan a microgravity experiment on aerosol coalescence.

An initially nearly monodisperse aerosol with high particle number density (typically 10 particles/cm^3) is produced using a Condensation Monodisperse Aerosol Generator (TSI 3475). It ows continuously through a plexiglass cell where it experiences a turbulent ow eld generated by an oscillating grid (see Figure 1). The initial size distribution is then modi ed due to turbulence-induced coalescence. Using droplets with an initial mean diameter of 3 m, we maximize the importance of turbulence on coalescence relative to Brownian motion (important for smaller particles) and sedimentation (important for larger particles).

To be able to compare experimental data on turbulence-induced coagulation with theory, a precise description of the turbulent ow eld is necessary. It has been characterized by measuring the velocity uctuations using a laser Doppler velocimetry technique (a typical result is shown in Figure 2). The turbulent kinetic energy is found to be constant in the central region of the cell (within a distance away from the grid mean position equal to half the stroke of the grid displacement) and then to decay away from the grid. Our results are similar to which one expects, based on previous experiments in liquids. In order to characterize the coalescence, the particle size distribution is measured *in situ* using a Particle Dynamics Analyser. This technique is based on the analysis of the light scattered by the particles as they cross a volume of measurement de ned by the intersection of two laser beams. The

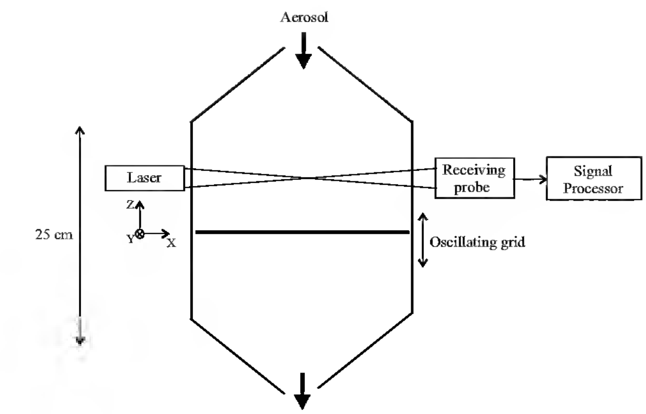

Figure 1: Sketch of the experimental setup.

size distribution being known, the particle number density can be measured using a light attenuation technique.

As already mentioned, the extent to which we can isolate turbulence from the other mechanisms that may lead to coagulation is limited and this forms the motivation for the future microgravity experiments. Under microgravity, we will be able to use substantially larger particles and eliminate Brownian motion without introducing e ects of sedimentation. However, this ground-based experiment will demonstrate the validity of our experimental methods to characterize the coalescence.

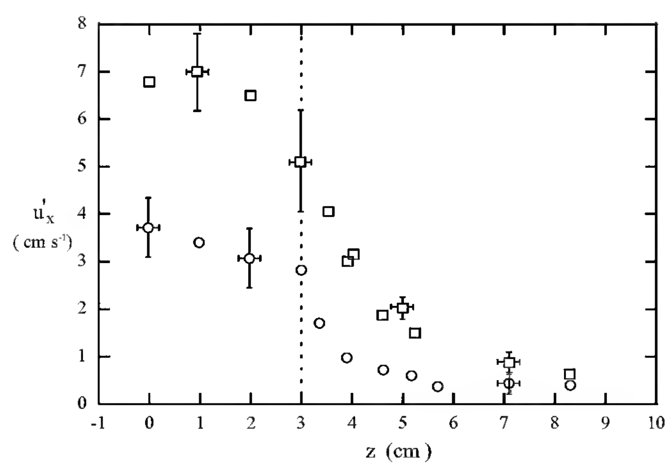

Figure 2: Velocity uctuation of the x-component of the velocity, $'_x$, as a function of the distance z to the grid mean position. The grid is oscillating around the position $z = 0$ with a 6 cm stroke, at a frequency $= 2\,\mathrm{Hz}$ (circle), $= 4\,\mathrm{Hz}$ (square). At a given z, the value of the velocity uctuations is obtained by averaging over several positions in the x y plane.

NON STEADY STATE GRANULAR SHEAR FLOWS

Wolfgang Losert[1], Gene Kwon
Department of Physics, IPST, and IREAP, University of Maryland, College Park, MD 20742

ABSTRACT

We experimentally investigate the shear flow of granular matter in a cylindrical Couette cell. Since granular flows dissipate energy, they must be continuously driven to remain in a flowing state. Previous experiments on steady state shear flows have found that velocity gradients are confined to a thin shear band, and that the shear force is roughly independent of shear rate if the material is allowed to dilate[1,2]. Our experiments in a Couette geometry focus on two related questions about non-steady state flows:

1) How does a granular shear flow start?[3]
2) How does a granular system respond to oscillatory shear?

In particular, we investigate the role of boundary conditions, which we expect to be of particular importance, since granular flows must be continuously driven (in general from a boundary) in order to be sustained. In our Couette cell a shear flow is generated by moving either the inner cylinder or the outer cylinder or both cylinders.

The motion of grains on the top surface is measured directly with fast imaging and particle tracking techniques. Previous studies have indicated that the velocity profile on the top surface is very similar to the velocity profile within the bulk. Measurements of the corresponding shear forces are in progress.

Initial experiments determined the steady state flow profiles under different driving conditions, with either inner, outer or both cylinders moving. In steady state, velocity gradients are confined to a roughly exponential shearband several particle diameters wide. The shear band is always located at the inner cylinder. A probable reason for this observation is the slightly smaller surface area of the inner cylinder compared to the outer cylinder. Since shear forces are transmitted from one cylinder to the other, the smaller surface area of the inner cylinder leads to larger shear stresses. Shear flow confined to regions of high stress can be reproduced in continuum mechanics models which include plastic flow, non-Newtonian fluid models, or locally Newtonian hydrodynamic models that include a strong density dependence of viscosity.

Most of these models are isotropic with respect to the shear direction. However, anisotropies manifest themselves in two distinct flow transients, when rotation of one of the cylinders is started. When the cylinder had been rotated in the same direction before, the thin shear band immediately forms. When the previous motion of the cylinder had been in the opposite direction, particles far from the moving cylinder are initially more mobile. After an extra displacement of up to six particle diameters, a thin shearband forms again in steady state. The extra displacement of particles far from the shear surface does not strongly depend on the shear rate prior or after the stop, solely on the direction of prior shear. This indicates that the static configuration of grains

[1]Additional PI information: wlosert@glue.umd.edu , Fax: 301-405-1678 , phone: 301-405-6759

after a shear flow exhibits anisotropies. The flow transient, at least, can then no longer be modeled with the isotropic form of the models described above.

Finally, we investigate oscillatory shear flow. During small amplitude oscillations the shear flow is confined to a thin shear band. In addition, a gradual compaction and strengthening of the granular material is observed. For sufficiently large oscillation amplitudes, the flow resembles a sequence of shear reversals. In oscillatory flows driven by the outer cylinder, coexistence of shearbands at the outer and inner cylinder can be found.

In summary, we have elucidated important properties of granular shear flows from non-steady state flow measurements: First, shear bands form preferentially near the inner cylinder, even when the outer cylinder is sheared. Transiently a shear band can also form near the outer cylinder during oscillatory driving. These observations should help refine models of granular shear flow.

One challenge in improving models of granular shear flow is the observation that the initial flow transient contains "memory" of the direction of previously applied shear. In order to incorporate this observation into flow models, the nature of the anisotropy requires further study. Currently we are investigating the three dimensional configuration of grains during the start of shear flow using confocal microscopy.

---

[1] W. Losert, L. Bocquet, T.C. Lubensky, and J.P. Gollub, "Particle dynamics in sheared granular matter," *Phys. Rev. Lett* 85, 1428 (2000).

[2] L. Bocquet, W. Losert, T.C. Lubensky, and J.P. Gollub, "Granular Shear dynamics and forces: Experiments and continuum theory," Phys. Rev. E **65**, 011307 (2002).

[3] W. Losert and G Kwon, "Transient and steady state dynamics of granular shear flows", to appear in Advances in Complex systems (2002).

Granular Flow Instabilities: Avalanching, aging, and segregation dynamics

NASA/CP—2002-211212/VOL2

Wolfgang Losert, Department of Physics, IPST, and IREAP, University of Maryland

J. Friedman (Geology), S. Van der Meer (Twente), M. Toiya, M. Newey, G. Kwon, R. Pizzaro

Funding: NASA

Additional Equipment Funding: ONR

How do grains start to flow?

Shear Flow Transients

How do grains segregate?

Segregation Transients

How do avalanches run out?

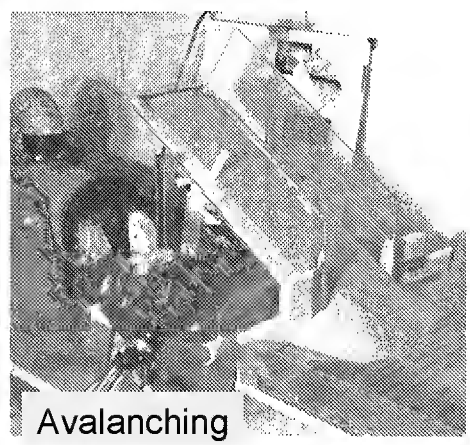

Avalanching

Email: wlosert@glue.umd.edu

Web: www.ireap.umd.edu/granular/

Abstract

The aim of this project is an interdisciplinary study of granular flow instabilities, involving laboratory experiments, and approaches and data sets from geology.

For granular matter, (Dia > 1 μm), collisions between particles dissipate kinetic energy. The equilibrium state of granular matter is therefore at rest, while during motion the material is far from equilibrium. Still, stable steady state flows are reachable in driven systems. However, steady flows can be unstable, which leads to dramatic effects such as avalanching, jamming, aging, and segregation.

Technological Relevance: The sudden jamming of grains in confined geometries, e.g. in a hopper, is a significant problem for food, mining, and raw materials processing industries. The slow creep and gradual strengthening of a quasi-stationary granular pile under stress can lead to structural damage of storage containers. The gradual segregation of poly-disperse mixtures of granular matter during shear is especially dangerous in the pharmaceutical industries, where active ingredients for drugs need to be uniformly mixed in powder form.

- Role of Gravity: Gravity often provides the only force that confines an assembly of non-cohesive grains in a compact configuration. It provides the driving force for avalanches. It also plays a key role for segregation dynamics, where some models and experiments find that gravity lets small grains fall down through cracks between large grains, leaving only large grains on top. The role of gravity may also be important for aging, e.g. for the slow strengthening of granular matter under stress. Better understanding and control of strengthening and flow instabilities may contribute to efficient handling and safe storage of powders and grains in a low gravity environment.

Proposed Research

*The proposed research will provide experimental data and test theoretical models to address **open questions** about granular flow instabilities:*

(A) Start and stop of shear flow: Granular matter can exhibit a sudden transition from a solid-like state to a flowing state and vice versa, e.g. during shear flow. What timescales and spatial scales best describe such a transition? Since granular flows are of a non-equilibrium nature and thus do not obey known minimization principles, could more than one stable steady flowing state be achieved? At what point in the solid to fluid transition can models of granular flow describe the flow?

(A) Dynamics of aging: Even an apparently stationary granular assembly slowly rearranges (aging). This causes changes in material properties, such as the gradual increase in yield strength. How do particles rearrange in a granular assembly during the aging process? How does an increase in yield strength relate to changes in the network of particle contacts? Does gravity contribute to aging?

(B) Dynamics of segregation: Grains of different size or shape will segregate under some conditions in a driven granular material. While models for segregation exist, several fundamental issues warrant further study. We investigate segregation of a mixture of three and more particle sizes.

(C) Long Runout Avalanching: Under certain confitions, avalanches can flow for extraordinarily long distances. We will investigate underr which conditions the system may tend to exhibit long runout.

(A): Granular shear flow

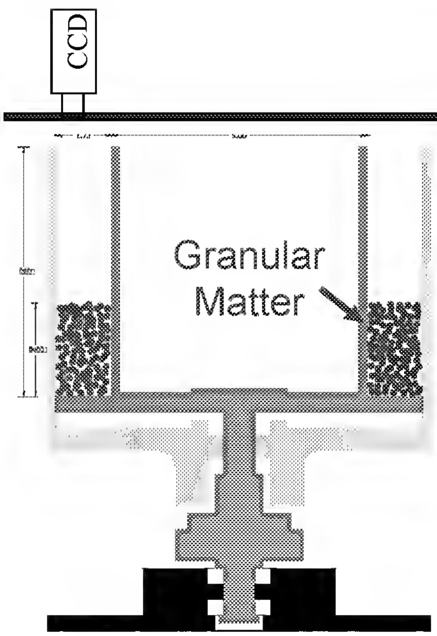

- 50 mm wide shearcell with movable outer and inner cylinder.
- Bottom wall movable with outer or inner cylinder.
- Particle motion measured on top surface using fast camera.
- Average density determined from height of granular column.

Imaging of Particle motion (top surface)

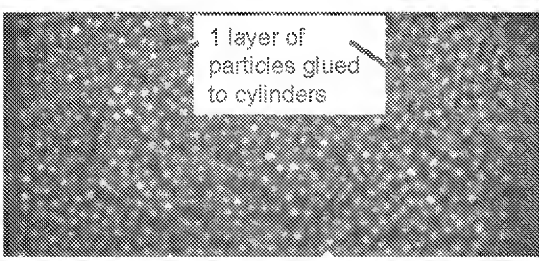

1mm Dia glass beads

~5o mm

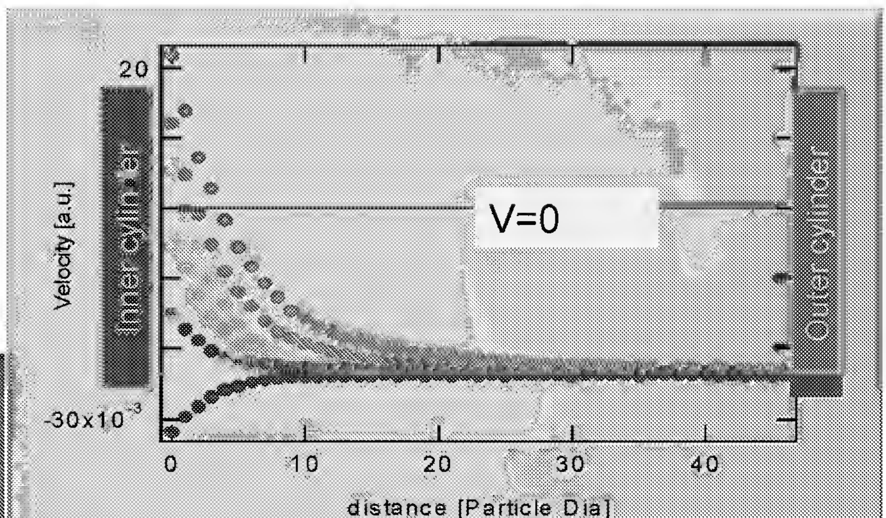

- Velocity gradients are concentrated in a shear band several particle diameters wide.
- In steady state, the shear band is always near the inner cylinder.

Preliminary Results A: Memory of Prior Shear

Start in same direction

Start in opposite direction

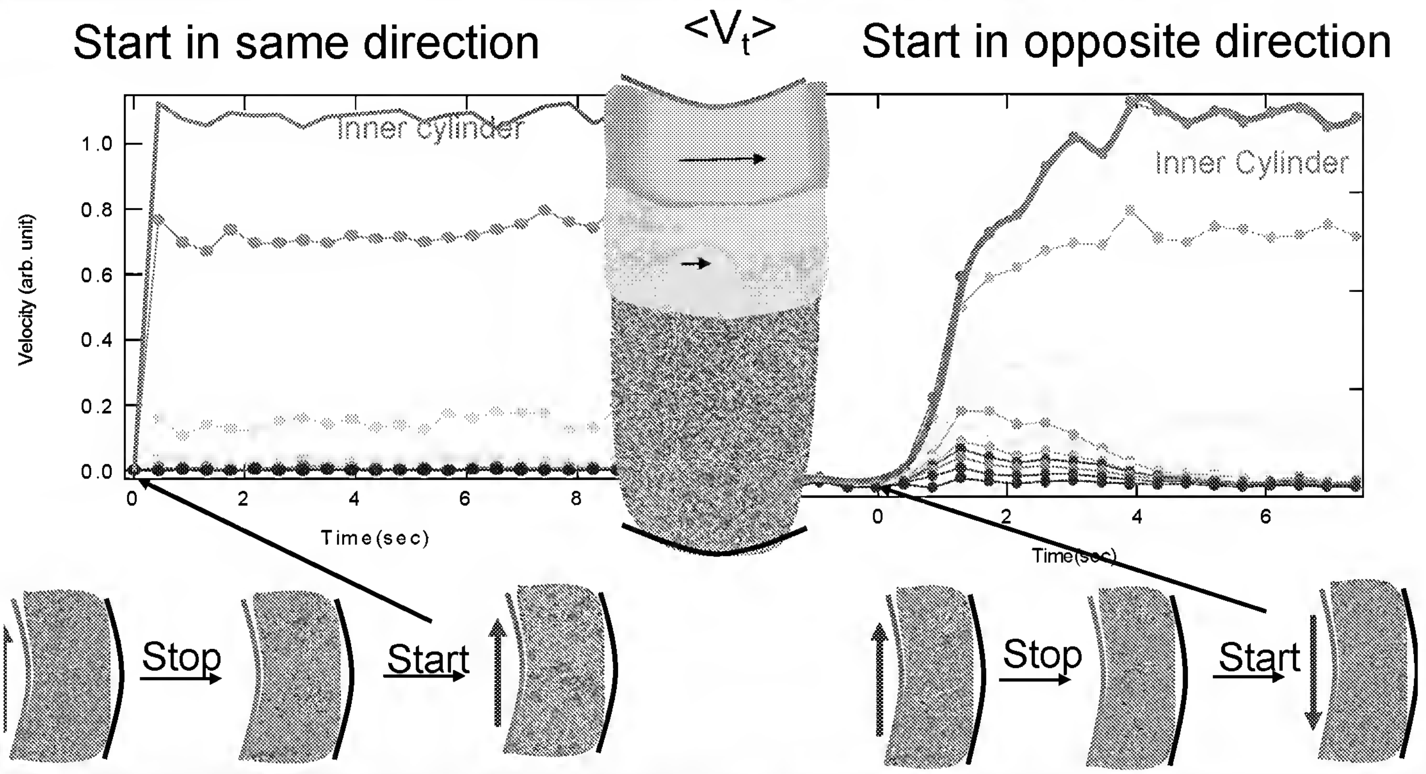

➢Steady state is reached "instantaneously"

➢Slower start (I.e. more shear force needed)

➢ Particles far from sheared surface move significantly during transient.

NASA 2002

Preliminary Results A: Compaction and Dilation

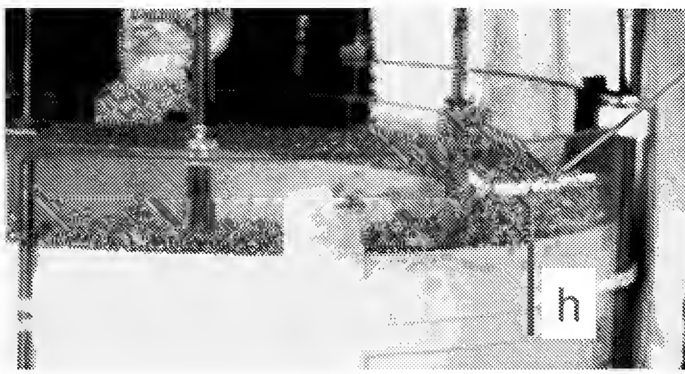

"Line" of light

line position h ~
Height of surface

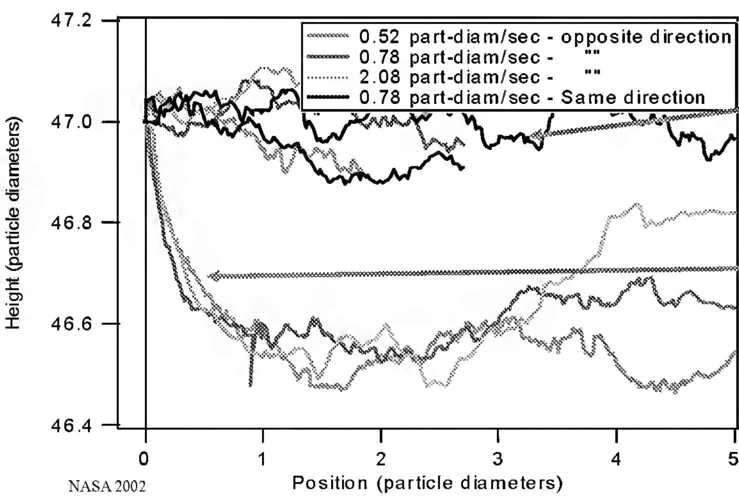

<u>Restart in same direction</u>

No compaction or dilation

<u>Restart in opposite direction</u>

Compaction over a characteristic distance proportional to the particle size, independent of shear speed, and gradual dilation.

Preliminary Results A: Imaging of 3D structure

Confocal microscopy of Granular matter

Cross section through glass beads coated with fluorescent dye

Currently imaging up to 10 particle diameters deep

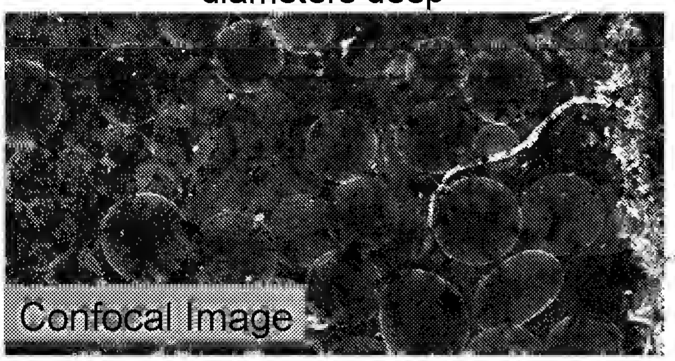

Confocal Image

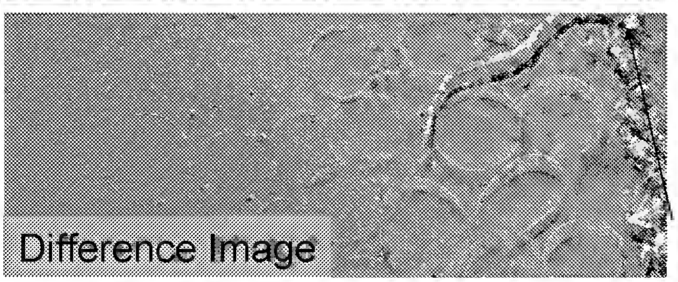

Difference Image

- Confocal microscopy permits long term measurements of individual particle rearrangements during aging.
- System exhibits anisotropic behavior on the macroscopic scale: should be reflected in microscopic arrangement
- Granular material immersed in fluid: Possible qualitative differences to dry granular flows.
- Measures (see Edwards and Grinev, Physica A):
  - Tensorial: Anisotropy of the contact network (difficult to determine accurately).
  - Topological: Anisotropy of the voronoi cell shape (in collaboration with J. Douglas, NIST).
  - Probabilistic: Velocity correlations during rearrangement. Correlations in particle position…

Shear Surface

(B): Axial Segregation in a Tumbler

- Mixture of glass beads of three or more sizes in a horizontally rotating cylinder
- Investigate flow transients that lead to a segregated/mixed state

Bands within bands form for a mixture of three sizes

0.5mm green

1mm blue

2mm clear (light blue)

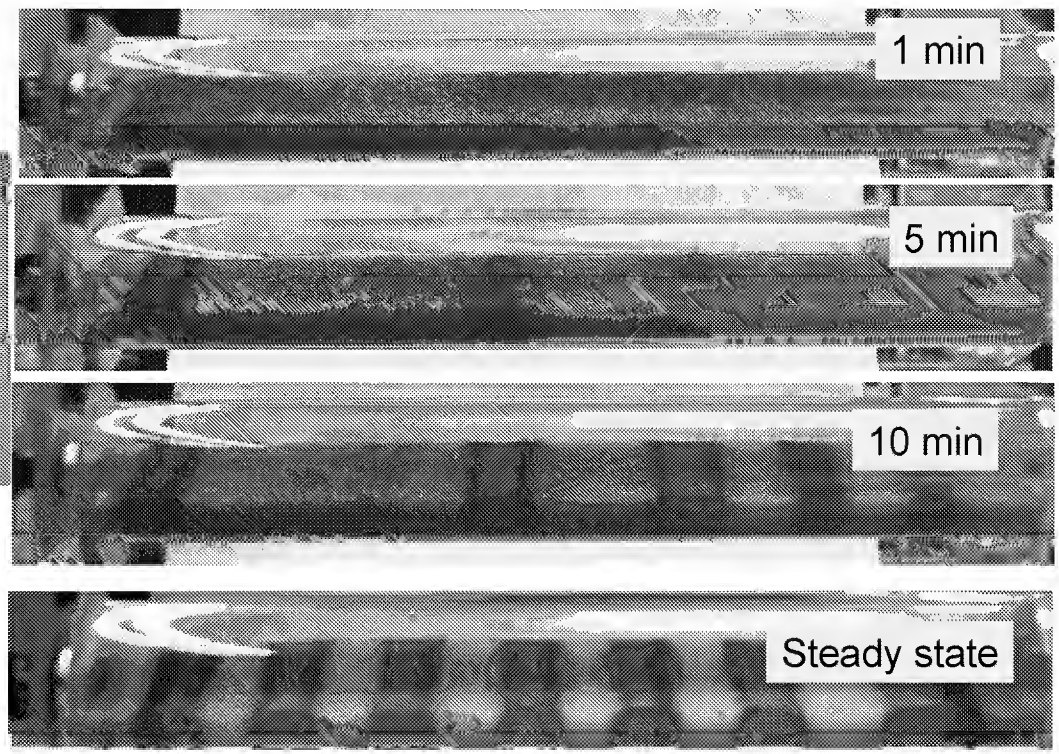

(C): Long Run-out Avalanche Experiment

Long Runout Avalanches in Nature

Mars rock avalanche. The landslide fell 5 miles and ran out 65 miles.

Laboratory Experiment

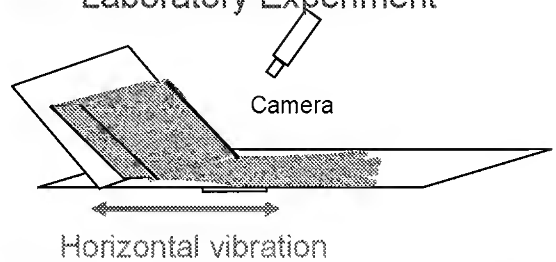

Horizontal Shaking to fluidize the granular material

Variation of Topology, material, vibration parameters

High speed imaging of **morphology** and **particle motion**

Measurement of height profiles across the flow with a 9 line laser sheet

Measurement of height profiles along the flow front with a laser line

IMPERMANENCE OF STATIC CHARGES ON GRANULAR MATERIALS: IMPLICATIONS FOR MICROGRAVITY EXPERIMENTS

John Marshall
jmarshall@seti.org; Ph 650-960-4535; Fax 650-961-7099
SETI Institute
2035 Landings Drive, Mountain View, CA 94043

The role of triboelectrostatic charges on granular materials was tested on USML-1 and USML-2, as well as on several KC-135 flights /1/. The goal of these experiments was to determine how static electricity affects the aggregation of particles in natural settings such as volcanic eruptions, dust storms on earth and Mars, and protoplanetary nebulae /2/. Knowledge so gained would also have relevance to industrial processing of a wide variety of granular materials (powdered coal, cement, grain, pharmaceuticals, etc.). The USML flights repeatedly demonstrated the existence of electrostatic polarizing forces that universally created filamentary aggregates from tribocharged (dielectric) grains released into a microgravity chamber. This polarizing force is considered to be an electrostatic dipole created by the random distribution of both positive and negative charges on each grain /3/. A discrete dipole moment on a grain is not to the exclusion of net charge (an imbalance of the charge mixture). In microgravity, the dipoles are able to rotate the grains so that they are always in a mutually attractive orientation with respect to their nearest neighbor grains; the result is the end-to-end stacking of grains that forms chains or filaments (ranging between 2 and 20 grains per chain for grains of about 400 microns diameter). Tribocharging of the grains in the USML experiments was accomplished by a forceful compressed air pulse injection into the experiment chambers, thereby permitting aggregation to occur while the grains were still mobile. After grain motion ceased, aggregation continued only for a few minutes, and then reached a stable inactive equilibrium phase lasting for the remainder of the experiment duration of up to 30 minutes.

These USML data formed the basis for proceeding to the Space Station experiment "Electrostatics of Granular Materials" (EGM), originally slated for a 2004 deployment, but now in stasis, with the exception of ground based studies that continue to hone our understanding of electrostatic phenomena. EGM would attempt to provide unequivocal proof of the dipoles while quantifying their properties. As part of EGM development, laboratory investigations were conducted on the tribocharging of various candidate flight samples. The goal of the tests was to determine the extent of net charging in granular populations as an indicator of the charge levels that would need to be measured on Space Station. It was also important to determine if tribocharging could be achieved with a "conservation of charge" within a given tribocharging apparatus. This conservation idea derives from a modeled concept in which positive charges are created on one surface as a result of transferring electrons to an adjacent surface: charge exchange should theoretically generate an equal number of positive and negative charges so that the system as a whole remains neutral (dipoles would be present, even with net neutrality of the grain population).

The laboratory device used for tribological experiments consisted of a cylindrical glass vessel with an air jet impinging upon particles within the vessel. Particulate material was caused to continually circulate while the impelling air escaped through a diffuser/screen system. Typical circulation/collision speeds of grains were mm/sec to several m/s. Electrostatic charge in the system was determined from a hand-held electrometer (ACL Model 300B) positioned ~ 2 cm from the vessel's outer wall at 90 degrees orthogonally from the air jet. The electrometer was designed for detecting patch charges on surfaces in clean rooms. The analog readout is calibrated for fixed distances from surfaces, and it is assumed that the meter was reading the electrical field emanating from a surface charge that has a magnitude equal to the reading, presumably with respect to ground. The charge registered near the vessel includes contributions from both vessel walls and grains inside the vessel. If the system had a charge balance --i.e. the grain charging was equal and opposite to that of the vessel, the measured charge would sum to zero. This was not the case --large net charges were observed, but the cause is undetermined. Positive charge could have leaked through the vessel support structure, via leakage to air, or in some cases, via transport on comminution fines vented from the system.

Quartz, glass, and plastic grains have been tested. These are candidate materials for EGM, although for convenience, larger grain sizes than those planned for EGM (~300 micron) were used in the lab tests. All samples being agitated by the air resulted in negative charge readings where the electrometer was located near the base of the vessel, with the grains charging positive in some cases, negative in others (as measured by inserting the electrometer into the vessel). With all materials, and all grain sizes (ranging from several hundred microns to several millimeters),

the electrometer registered several thousand volts (negative) in its external position. Glass spheres of 4 mm diameter generated in excess of - 8 kV for example. More important than the actual magnitude of this charging was the fact that the charge very rapidly dissipated as soon as the agitating air jet was turned off (this must have included discharge of the grains). Within seconds or minutes, the charge level would drop an order of magnitude to a few tens or hundreds of volts, particularly for the silicate materials. The appearance of a continuous high charge level during grain agitation and its subsequent almost immediate dissipation is attributed to grains acquiring very high voltage pulses of charge developed at grain contact points, but these charge patches are probably at or above the Gaussian limit locally, and rapidly decay by leakage or corona discharge to air, by discharge to other grains with opposite charge patches, by surface conductivity resulting from the high voltages, and by removal of charges attached to comminution particles carried away in the air stream. Thus, charge patches on one collision spot are degenerating as fast as they are being made by another collision. With so many grains creating tens of thousands of collisions per second, the dynamic equilibrium set up by the system gives the appearance of a stable charge. Thus, the charge ordinarily measured by electrometry on static piles of granular material is probably but a fraction of the charge produced during the causative tribological event.

The implications of these results are twofold. First, it means that electrostatic forces in dynamic granular systems are probably orders of magnitude higher than in static systems. Dust storms on planetary surfaces, volcanic eruption plumes, and mobilized industrial powders will be highly affected by charging and this may be manifest as rapid aggregation /4/ or enhanced Coulombic friction in the granular flow /5/. In the dispersed systems such as eruption clouds, the grain-to-grain interactions will be driven by both net charge and dipole moments on individual grains. In the non-dispersed granular flow systems (as in fluidized beds or grain piles), net charge will again be important, but the dipole coupling will be across grain boundaries rather than discretely contained within a grain itself, and the dipole will be unable to affect grain orientation because of grain-boundary interlocking. Ironically, the more dispersed a system is, the more effective the dipole and monopole effects become (especially in low or zero gravity environments) because grain orientation is facilitated, but at the same time, the dispersion leads to fewer contacts per unit time, thus reducing the magnitude of the charges (recalling the rapidity of charge decay during the interval between tribological contacts).

Secondly, the discovery of charge behavior in relation to tribological action adds a new and very significant enhancement to EGM science. Since charge decay can be very rapid with rates being highly material-dependent, charge cannot be regarded as a constant, and it is obviously a variable warranting investigation. We have added some new procedures to EGM --with very little additional effort, we will be able to shed light on the "non-static" nature of static electricity. It will be especially important to see how these high net charges relate to the dipole, and what their relative decay rates are. The fact that grains were "always attractive" in USML (during the same period when high tribological net charges were being actively developed) suggests that the dipole is commensurably powerful with the monopole. It will also be instructive to ascertain these measurements in a microgravity environment where grains are suspended, and thus unable to lose charge by contact with other grains, or via the vessel walls.

References: (1) Marshall. NASA CP 3272, 717-732 (1994). (2) Marshall & Cuzzi. Proc. LPSC, Houston (2001). (3) Abrahamson & Marshall. J. Electrostatics 55/1, 43-63 (2002). (4) Marshall et al. NASA TM 1998-208697 (1997). (5) Marshall et al. LPSC XXIX, 1135 (1998).

AN INTERFEROMETRIC INVESTIGATION OF MOVING CONTACT LINE DYNAMIC IN SPREADING POLYMER LIQUIDS

Pirouz Kavehpour, Gareth H. McKinley
Hatsopoulos Microfluids Laboratory, Department of Mechanical Engineering
Massachusetts Institute of Technology, Cambridge, MA

Ben Ovryn
Department of Biomedical Engineering, Case Western Reserve University,
Cleveland, OH

ABSTRACT

Studies of dynamic wetting phenomena and contact angle measurements frequently involve either visual or mathematical extrapolations of the macroscopic interfaces due to the difficulties inherent in quantitatively measuring the microscopic fluid physics that arise near the moving contact line. We have developed a phase-shifted laser feedback interferometer (psLFI) that can be used to rapidly and non-invasively measure the interfacial profile in the vicinity of moving contact lines of simple Newtonian and complex fluids [1-2].

The test fluids used in the present study are constant-viscosity silicone oils (Gelest Inc.) which perfectly wet the smooth silicon substrate. The viscosities are varied from $7 \leq \mu \leq 10^4$ cSt in order to explore a wide range of capillary numbers, $Ca = \mu U/\sigma$ (here σ is the surface tension and U is the steady spreading velocity). For wetting systems (in which the liquid spreads spontaneously to give a nominally zero contact angle) a precursor or primary film moves ahead of the main body of liquid [3]. When the disjoining pressures are large and the viscosity small, the precursor films may spread quite rapidly for significant distances ahead of the bulk fluid. A simplifying feature of wetting via a precursor film is that the motion of the bulk liquid is decoupled from the wetting line, hence the liquid may be considered to spread across a pre-wetted surface. The hydrodynamic equations yield a velocity dependence of the apparent contact angle that follows a simple power law for Ca <<1 given by $\theta_a \sim Ca^{1/3}$ (Tanner's law) [4]. Here θ_a is the apparent dynamic contact angle.

A syringe pump delivers a precise volume of liquid onto a clean silicon substrate. During the spreading process, the psLFI system is focused on the substrate in front of the moving wetting line as shown in the Fig. 1 and the spreading film flows past the approximately 1 μm diameter spot focused by the high numerical aperature objective lens. In order to estimate the optical path length (OPL) and interference fringe visibility, the intensity of the laser is monitored in real-time and discrete phase shifts are introduced using an electro-optic modulator (EOM); this process is automated using Labview. From the OPL data we can follow the evolution of the local thickness of the drop, $h(x)$, as a function of time. In Fig. 2 we show an example of the psLFI oresponse close to the wetting line. The left vertical axis shows the drop profile $h(x)$ [in nm] as a function of the lateral position x [in μm]. The right-hand axis shows the interference fringe visibility, m. The polished silicon substrate has a high visibility (m ~0.095) however this drops suddenly about 100 μm *before* the apparent or macroscopic contact line passes the measurement

point. In this offset region a very thin liquid film (~100 nm) can be detected in front of the contact line. The length of this precursor film, L_P, is measured from the position where the visibility drops to the position where the drop thickness starts to increase rapidly. A series of measurements over a wide range of (Newtonian) fluid viscosities and spreading velocities are shown in Fig. 3. The lateral extent of this precursor layer varies inversely with Ca and is in excellent agreement with the theoretical prediction, $L_P = \sqrt{SA/6\pi\sigma^2}\,Ca^{-1}$ where S is the spreading coefficient and A is the Hamaker constant [4]. We are currently using this technique to image the spatio-temporal evolution of the shape of the 'foot' in more complex fluids such as Xanthan gum (a rigid rod polymer), flexible polymer solutions and also highly entangled polymer melts.

BIBLIOGRAPHY:

1. Ovryn, B., et al., *Phase-shifted, real-time laser feedback interferometry.* SPIE, 1996. **2860**: p. 263-275.
2. Ovryn, B. and J.H. Andrews, *Phase-shifted laser feedback interferometry.* Opt. Lett., 1998. **23**(14): p. 1078-1080.
3. Bascom, W.D., R.L. Cottington, and C.R. Singleterry, in *Contact Angle, Wettability and Adhesion*, F.M. Fowkes, Editor. 1964, ACS: Washington, DC. p. 335-379.
4. de Gennes, P.G., *Wetting: Statics and Dynamics.* Rev. Mod. Phys., 1985. **57**: p. 827-863.

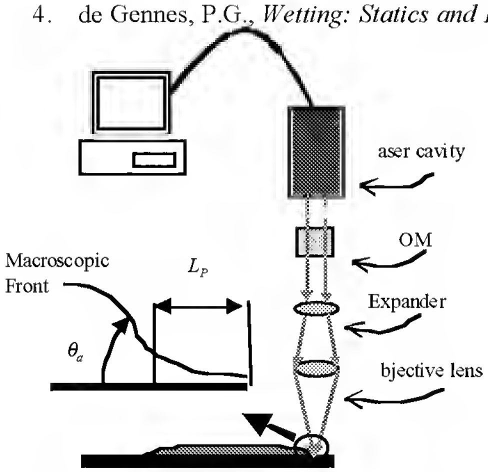

Fig. 1 Schematic of the psLFI instrument setup and (inset) spreading drop in the vicinity of the wetting line.

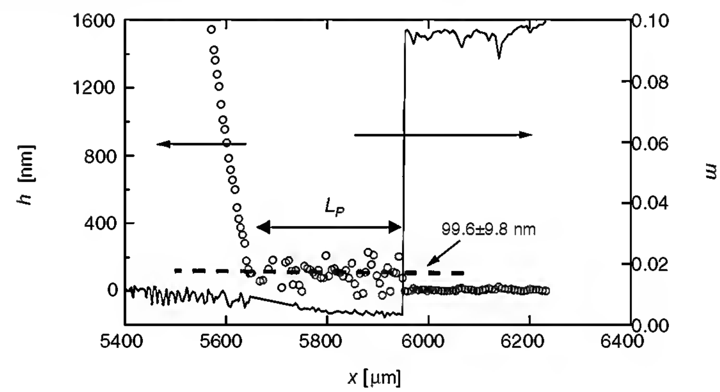

Fig. 2 Evolution in the profile of a silicone oil drop spreads on a silicon substrate. Circles (O) show the local thickness of the drop [in nanometers] and solid line is the visibility of the interference fringes, m.

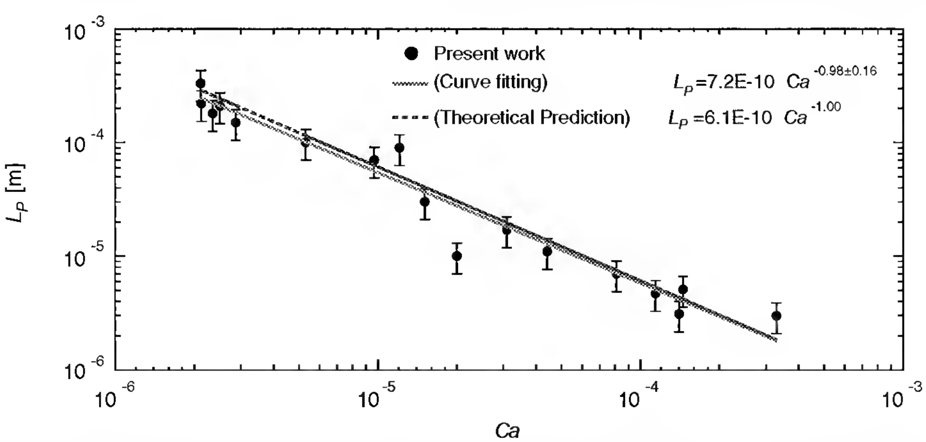

Fig. 3 Length of the precursor film, L_P, as a function of capillary number. Solid line (—) is the regression to the experimental results (●) and the dashed line (---) is the theoretical prediction.

NASA/CP—2002-211212/VOL2

Spreading of Fluids and Precursor Layer

- Hardy (1919) reported the existence of a very thin film in front of moving wetting line.
- Cottington et al. (1964) used ellipsometry to observe precursor film.
- Hervet & de Gennes (1984) theory on 1-D thin spreading edge.
- Existence of large extrapolation length for velocity field of polymeric liquids near a smooth surface predicted by de Gennes (1985).
- Huppert (1982) and Goodwin & Homsy (1991) studies of gravity currents and spreading of viscous drops on inclined plates.

<u>Project Goal:</u> [illegible]

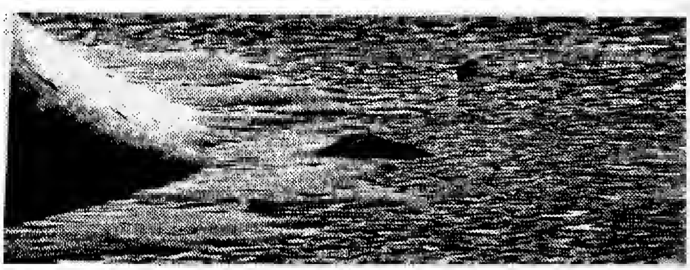

(Adamson & Gast, Physical chemistry of surfaces, 1997)

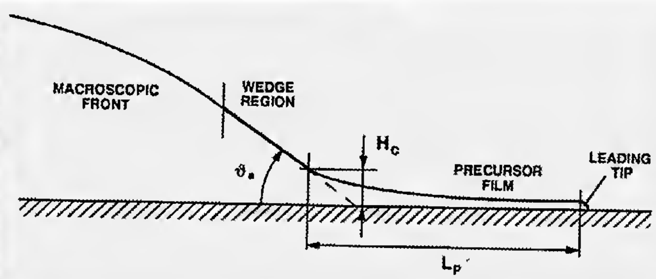

(Kistler, Hydrodynamics of wetting, 1993)

Phase-shifted Laser Feedback Interferometer(psLFI)

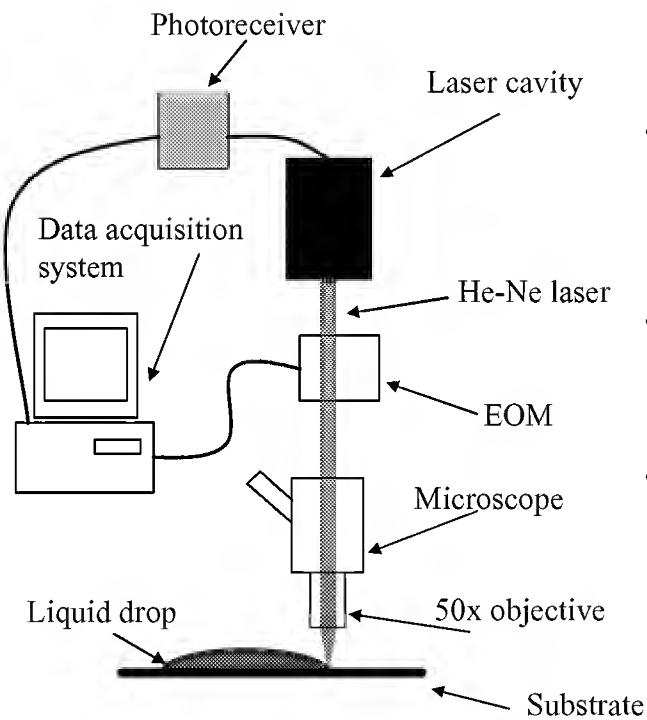

- Feedback into the laser eliminates the need for a beam splitter and separate reference arm.
- Electro-optical modulator (EOM) is used to impose a series of controlled phase changes.
- Vertical spatial resolution of 10 nm is achieved using phase-shifting algorithm.
- Diffraction-limited lateral resolution achieved using high N.A. objectives.

(Ovryn & Andrews, *Appl. Opt.*, 1999)

PSLFI in The Vicinity of Contact Line

- Resolve the precursor layer film in front of a spreading drop by observing drop in fringe visibility, *m*, and variation of drop height, *h*.
- Spreading of viscous Newtonian silicone oil on silicon substrate.

drop in fringe visibility, *m*, at beginning of the precursor layer

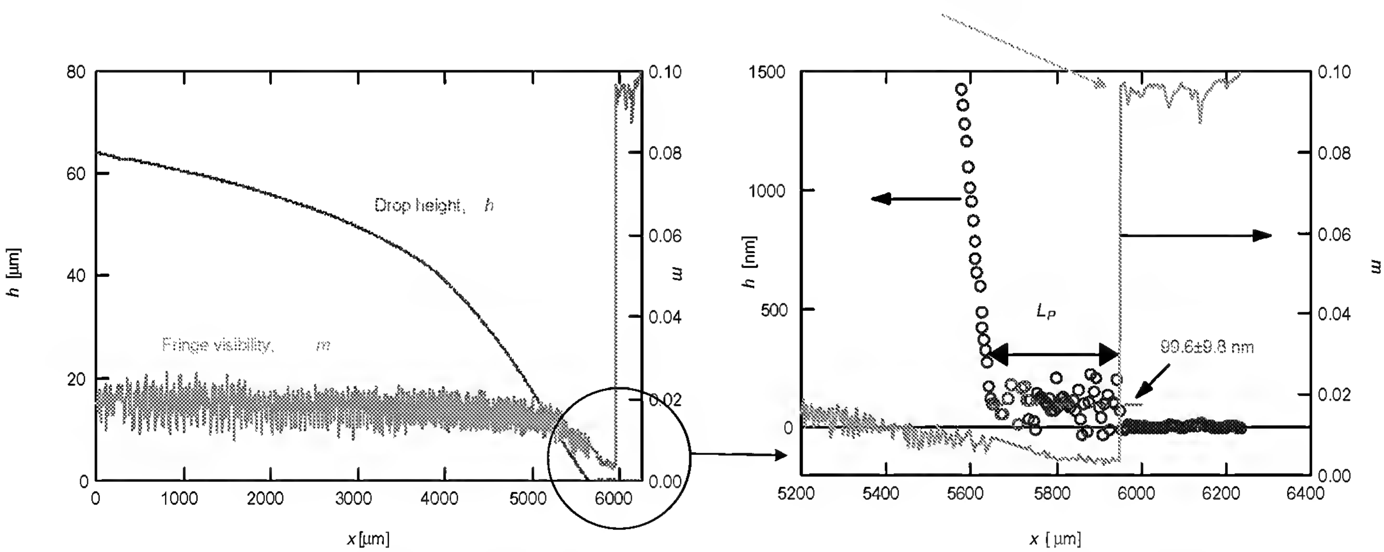

Dynamic Contact Angle, θ_a

$$\theta_a = \tan^{-1}\left((dh/dx)_{\max}\right)$$

- Local slope is calculated by numerical differentiation of drop profile.
- Dynamic contact angle, θ_a , corresponds to maximum value of slope.

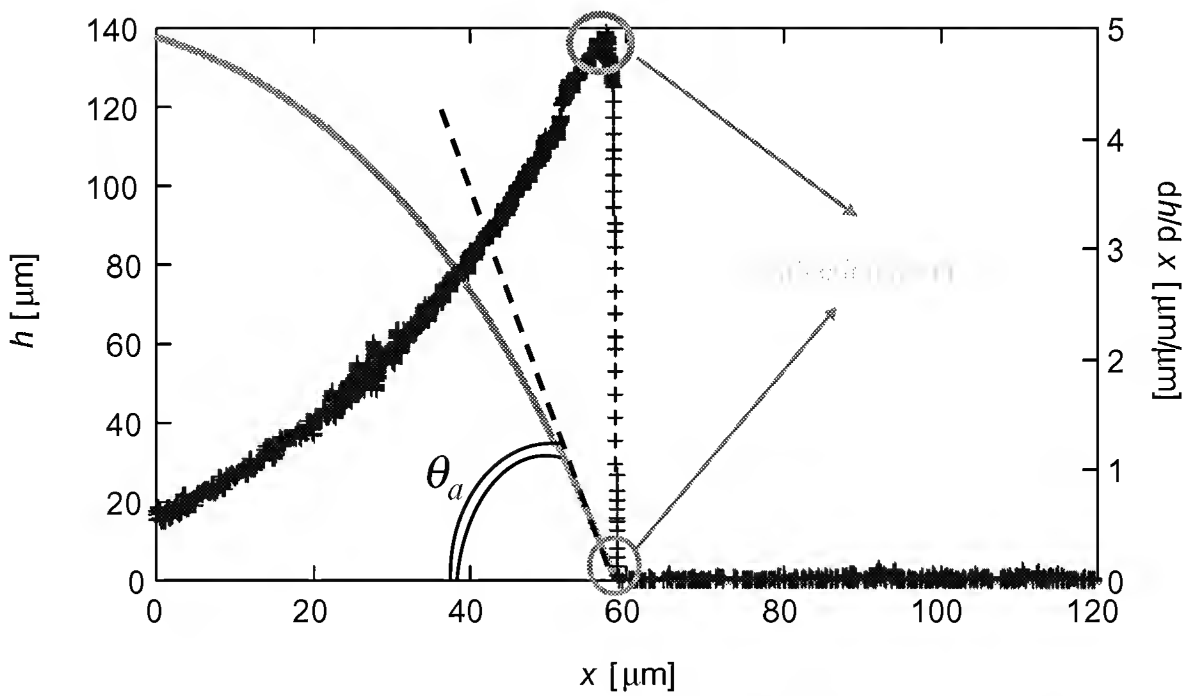

Confirmation of Tanner's Law

- Vary spreading velocity by using several different silicone oils.
- Dynamic contact angle is proportional to the capillary number, $Ca^{1/3}$. (Tanner, 1979)

For perfectly wetting fluids:

$$\theta_a \sim Ca^{1/3}$$

$$Ca = \frac{\eta U}{\sigma}$$

η : viscosity
U : Spreading velocity
σ : surface tension

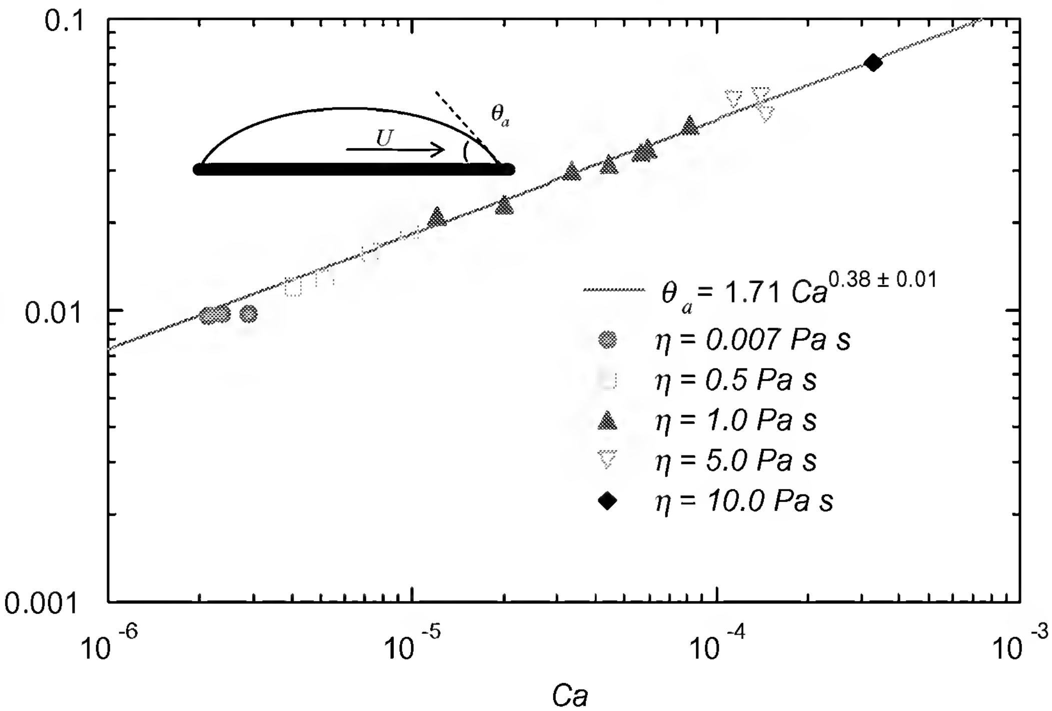

Precursor Layer Length, L_P

- L_P is determined by comparing spatial variation of visibility and drop heights.
- Theoretical prediction: $L_P \sim (SA/6\pi\sigma^2)^{1/2} / Ca$ (De Gennes, 1985).

$$\frac{L_P}{\sqrt{SA/6\pi\sigma^2}} \sim \frac{1}{Ca}$$

where:
A: Hamaker constant [J]
S: Spreading coefficient [N/m]

For our experiment:
$(SA/6\pi\sigma^2)^{1/2} = 6.1\times10^{-10}$ m

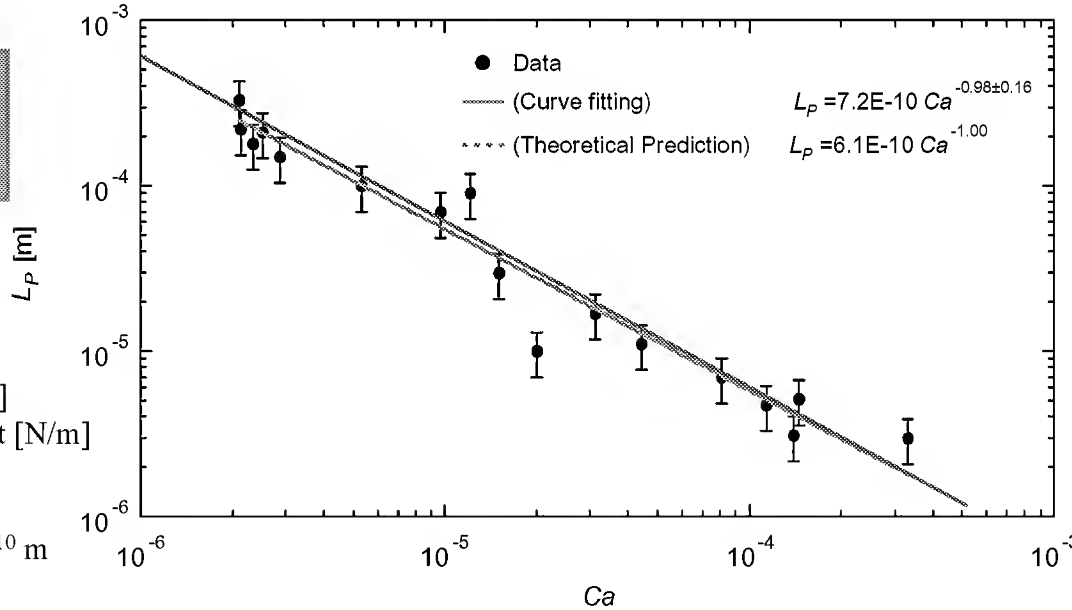

Gravity Current on an Inclined Plate

- Spreading of viscous drops on an inclined plate under gravitational body force.
- Measure droplet profile and and compare with self-similar profile predicted by Huppert (1982)
- Shift data so that $\xi = 0$ corresponds to inflection point of profile.
  - Dimensionless coordinates: $H = h/h_N$, $\xi = (x_N - x)/(\sigma h_N/\rho g \sin\alpha)^{1/3}$
- Close to contact line similarity solution predicts: $H \approx (16/15)^{1/4}\xi^{3/4}$

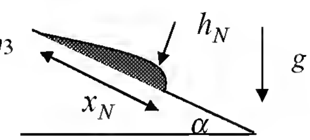

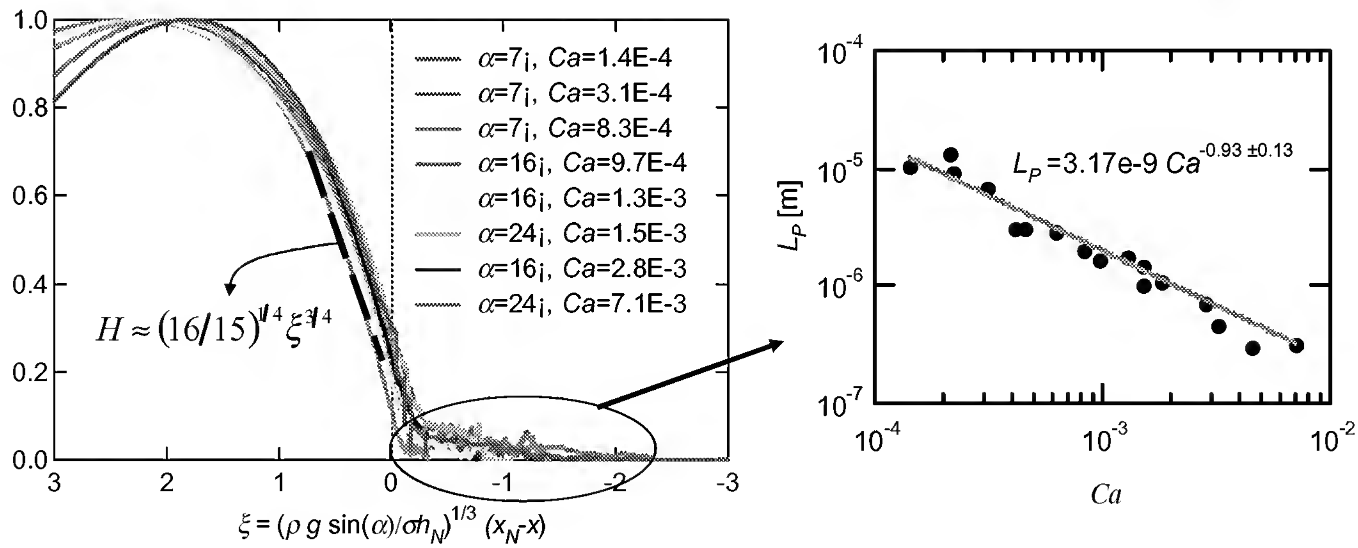

Power-laws for Spreading Drops on Inclined Plates

- For small inclination angles($\alpha \to 0$), lubrication theory remains valid.
- For $\alpha \to 0$ and for $Ca \ll 1$ Tanner's law recovered:

$$\boxed{\theta_a \sim \quad ^{1/3}}$$

- On "steeply inclined" plates, lubrication theory is not valid, $Bo \sim O(1)$ (Goodwin & Homsy, 1991; Hocking, 1983).
- Spreading is driven by a quasi-steady static balance, hence: $Ca \equiv Bo = \rho g h^2 \sin\alpha / \sigma$

$$\boxed{\theta_a \sim Ca^{1/2}}$$

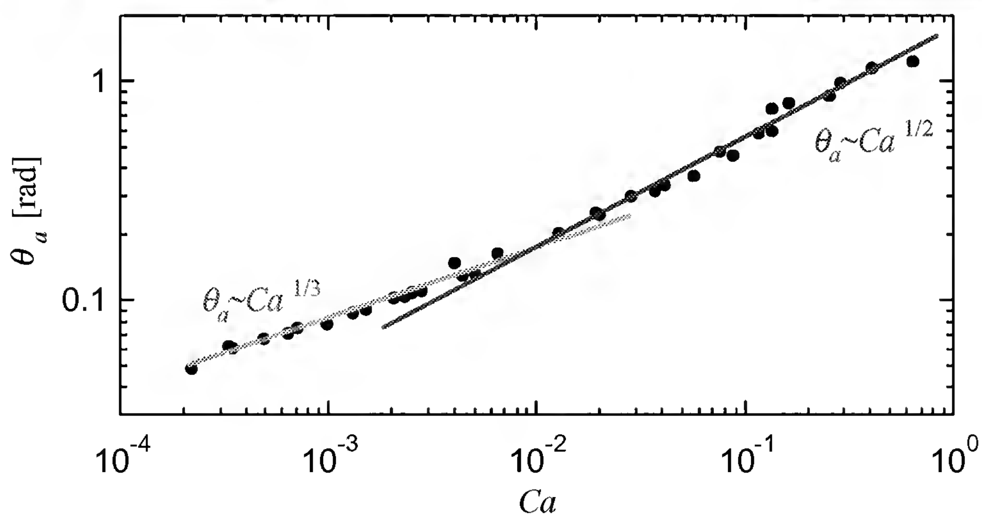

Conclusions

- Non-invasive optical technique has been used to investigate dynamical evolution at the vicinity of the dynamic contact line of spreading droplets.
- Existence of an “inflection point” close to the contact line is confirmed.
  - Macroscopic spreading is of form predicted by “Tanner’s Law”: $\theta_a \sim Ca^{1/3}$.
- Length of precursor layer, L_P, is determined by comparing spatial variation of visibility and drop heights.
  - L_P, is inversely proportional to the capillary number of the spreading drop as theory predicted.
- Shape of spreading drop on inclined plate close to the contact line follows the similarity solution given by Huppert (1982).
  - For $Bo \sim O(1)$, dynamic contact angle follows a new regime: $\theta_a \sim Ca^{1/2}$.
  - For $Bo << 1$, regardless of the slop of plate, $\theta_a \sim Ca^{1/3}$.

DROPLET FORMATION PROCESSES IN SOLIDS-LADEN LIQUIDS

Roy J. Furbank & Jeffrey F. Morris
Georgia Institute of Technology, Atlanta, GA 30332

ABSTRACT

The formation of droplets is an important phenomenon in many industrial applications as well as an interesting and challenging physical problem. Many of these processes involve the formation of droplets from particle-laden liquids including ink-jet printing technology, fuel combustion, and spray drying operations. This work investigates how the presence of solid particles in a suspending liquid affects the droplet formation process.

Droplet formation from pure liquids has been extensively studied both experimentally and numerically and is fairly well understood. However, little information is available concerning the process for solid-liquid suspensions. Experiments to date have investigated the formation of pendant drops of suspensions of varying particle volume fraction (φ) into both a second immiscible liquid and into ambient air. For each case the thread length achieved at pinch-off and the resulting drop size are measured and the effect of increasing φ observed.

The results of these experiments which illustrate the particle effects most clearly are the qualitative characteristics of the structure developed during the necking and subsequent pinch-off of the drop. For low particle concentration (typically up to $\varphi \approx 0.10$) the structure observed near pinch-off is the asymmetrical "needle-sphere" combination described by Peregrine *et al* (*JFM* **212**, 25 (1990)) for pure fluids. At larger particle fractions the structure observed near pinch-off becomes significantly different and the forming droplet has a less spherical, pear-like shape. This shape is similar to that observed by Shi *et al* (*Science* **265**, 219 (1994)) for increasingly viscous pure fluids and can lead to pinch-off occurring in a more variable manner at a location away from the edge of the forming drop. Simple rheological arguments based on the effective viscosity increase with φ fail to explain these qualitative changes in the drop structure

In addition to studying the case where purely pendant drops are formed at the orifice exit, this work also seeks to understand how particles affect the process after jetting has occurred. Understanding the flow behavior in this regime is critical to any practical application involving the use of particle-laden liquids. With this aim, experiments are in progress to investigate the transition from pendant to jetting droplet formation behavior, focusing on how the presence of solid particles in the liquid affect this transition. Future work will continue these efforts with a focus on expanding these initial experiments towards smaller scales, seeking to determine the generality of the influence of suspended particles.

AVALANCHE DYNAMICS AND STABILITY IN WET GRANULAR MEDIA

Peter Schiffer
Department of Physics and Materials Research Institute, Pennsylvania State University, University Park PA 16802

Pal Tegzes and Tamas Vicsek
Department of Biological Physics, Eötvös Loránd University, 1A Pázmány stny., Budapest, Hungary 1117

ABSTRACT

Avalanches and landslides are among the most dramatic of natural catastrophes, and they also provide an evocative metaphor for a wide range of propagating breakdown phenomena. On the other hand, the existence of avalanches, i.e. the sudden collapse of the system previously frozen into a high energy state, is a fundamental manifestation of the metastable nature of granular materials. Studies of avalanches and surface flows in granular media have largely focused on dry grains. By wetting such media, however, one introduces controllable adhesive forces between the grains which lead to qualitatively new behavior. In our previous work, we identified three fundamental regimes for the repose angle of wet granular materials as a function of the liquid content. The granular regime at very low liquid contents is dominated by the motion of individual grains; in the correlated regime corresponding to intermediate liquid contents, a rough surface is formed by the flow of separated clumps; and the repose angle of very wet samples results from cohesive flow with viscoplastic properties.

Here we report investigations of the avalanche dynamics and flow properties of wet granular materials, employing a rotating drum apparatus (a cylindrical chamber partly filled with a granular medium and rotated around a horizontal axis). At low rotation rates, the medium remains at rest relative to the drum while its surface angle is slowly increased by rotation, up to a critical angle θ_{max} where an avalanche occurs, thus decreasing the surface angle to the repose angle θ_r. The flow becomes continuous at high rotation rates, but the transition between avalanching and continuous flow is hysteretic in rotation rate in dry media. Previous studies of cohesive granular media in a rotating drum have focused on the surface angles of the medium before and after avalanches. In our measurements, we focus instead on characterizing the *dynamics* of cohesive flow. We quantitatively investigate the flow dynamics during avalanches at different liquid contents by analyzing the time evolution of the averaged surface profile obtained from hundreds of avalanche events, and we also measure surface velocities during continuous flow. In particular, we explore the nature of the viscoplastic flow, (observed at the highest liquid contents) in which there are lasting contacts during flow, leading to coherence across the entire sample. This coherence leads to a velocity independent flow depth at high rotation rates and novel robust pattern formation in the granular surface.

REFERENCES: Nature **387**, 765 (1997); Physical Review E **56**, R6271 (1997); Physical Review E **60**, 5823 (1999); cond-mat/0204399.

DYNAMICS AND CORRELATIONS IN WET GRANULAR MEDIA

P. TEGZES, A.-L. BARABÁSI, T. VISCEK, P. SCHIFFER

Penn State University - University of Notre Dame
Eötvös University

By wetting granular media, one introduces controllable adhesive forces between the grains which lead to qualitatively new behavior. We have identified three fundamental regimes of surface flow as a function of the liquid content. The granular regime at very low liquid contents is dominated by the motion of individual grains; in the correlated regime corresponding to intermediate liquid contents, a rough surface is formed by the flow of separated clumps; and very wet samples exhibit cohesive flow with viscoplastic properties. We investigated the avalanche dynamics and flow properties of wet granular materials, employing a rotating drum apparatus (a cylindrical chamber partly filled with a granular medium and rotated around a horizontal axis). We quantitatively investigate the flow dynamics during avalanches at different liquid contents by analyzing the time evolution of the averaged surface profile obtained from hundreds of avalanche events, and we also measure surface velocities during continuous flow. In particular, we explore the nature of the viscoplastic flow in which there are lasting contacts during flow, leading to coherence across the entire sample.

REFERENCES: Nature **387**, 765 (1997); Physical Review E **56**, R6271 (1997); Physical Review E **60**, 5823 (1999); cond-mat/0204399 (Physical Review Letters, in press); cond-mat/0207731.

Wet Granular Media

Small quantities of liquid added uniformly to grains
→ liquid at every grain-grain contact

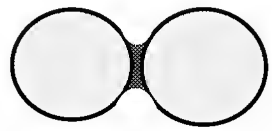

Adds new dimension to granular physics

- **capillary forces – attractive force, cohesion**
- **lubrication – decrease of static friction**
- **viscous forces**

In ambient atmosphere always some interstitial liquid from humidity

- **Impact on Physics**
- **Big Impact in Applications**

Our Experiments

- **glass beads -- ~1 mm diameter**
- **add oil -- low vapor pressure**
- **vary liquid content – 0.001% – 5%**

Draining Crater Studies: Three Regimes of Behavior

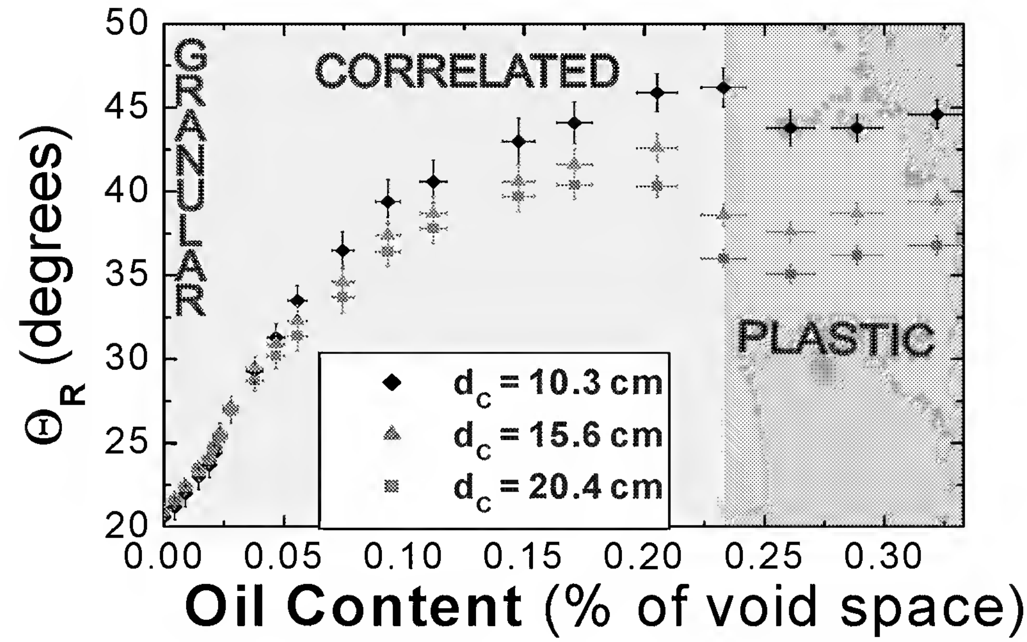

Granular Regime	**Individual grains flow down surface** **Theory: Albert *et al.***
Correlated Regime	**Correlated clumps flow down surface** **Theory: Halsey *et al.***
Viscoplastic Regime	**Coherent surface flow** **Θ_R drops with added oil**

Measurements of wet grains in a rotating drum

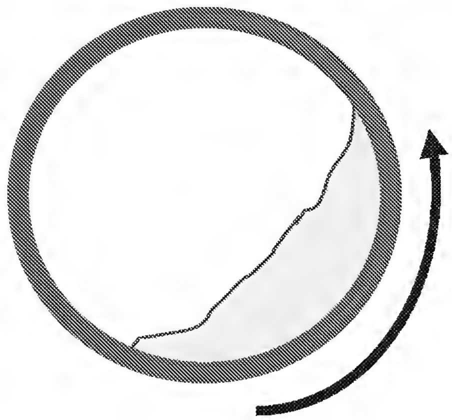

Can video to obtain <u>dynamic</u> information about wet granular flow down the surface

- Study process of avalanching
- Obtain surface topology and velocity
- Measure granular flux down slope

Background illumination needed due to beads sticking to the walls

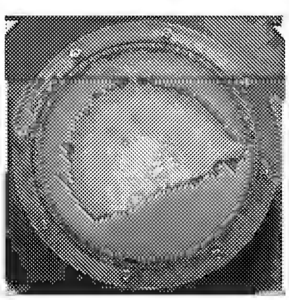

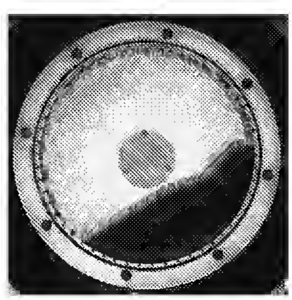

Continuous flow (higher rotation rates)

Granular | **Visco-plastic**

0.0025%
6 rpm

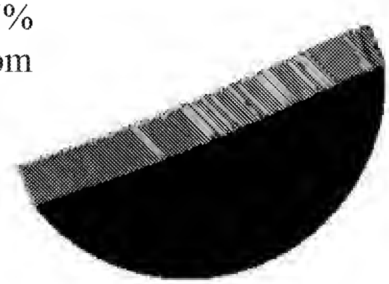

0.625%
6 rpm

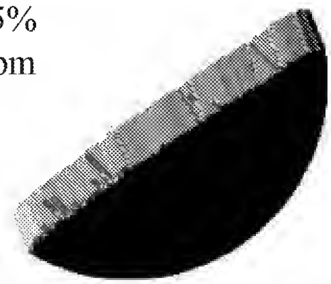

Brightness indicates local slope

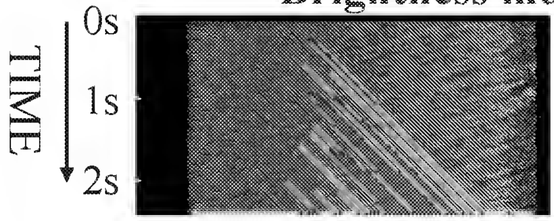

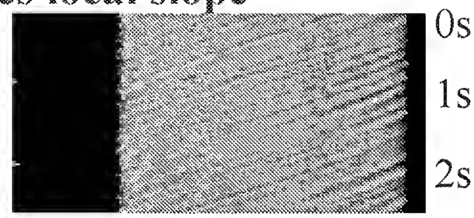

Individual grains rolling
Fast (25cm/s) and shallow

Lasting contacts in flowing layer
Slow (13cm/s) and deep

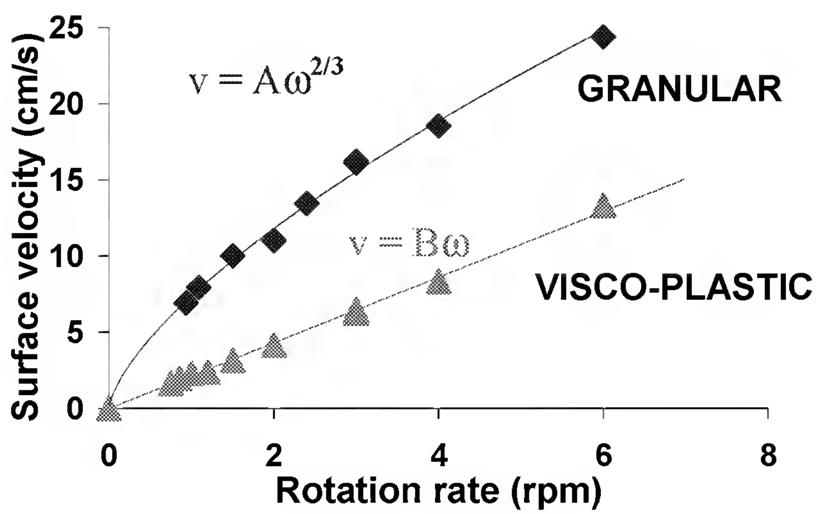

Avalanche flow (lower rotation rates)

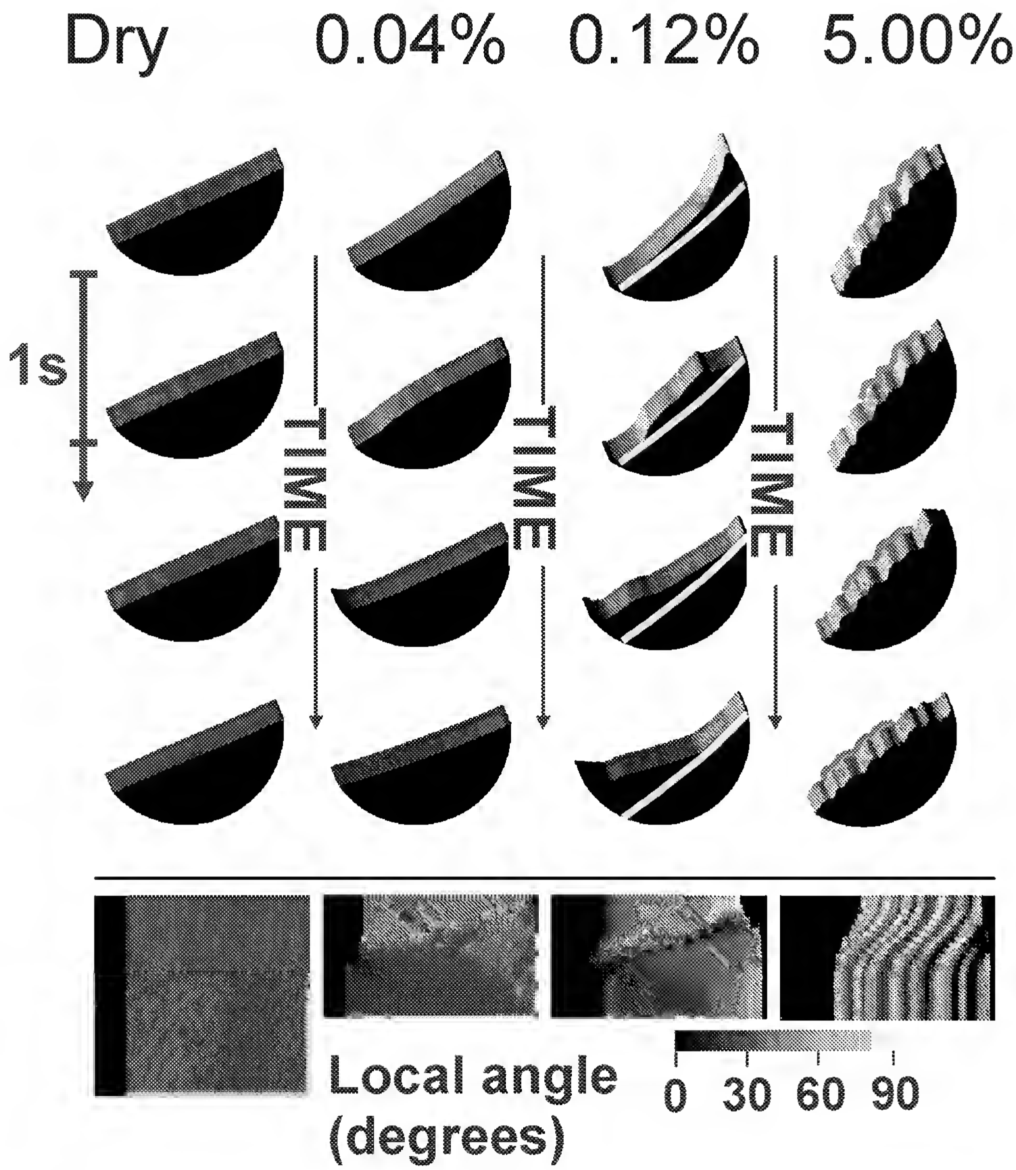

Can quantify the dynamics during avalanches

Model for Geological Events?

Landslide **Mudflow**

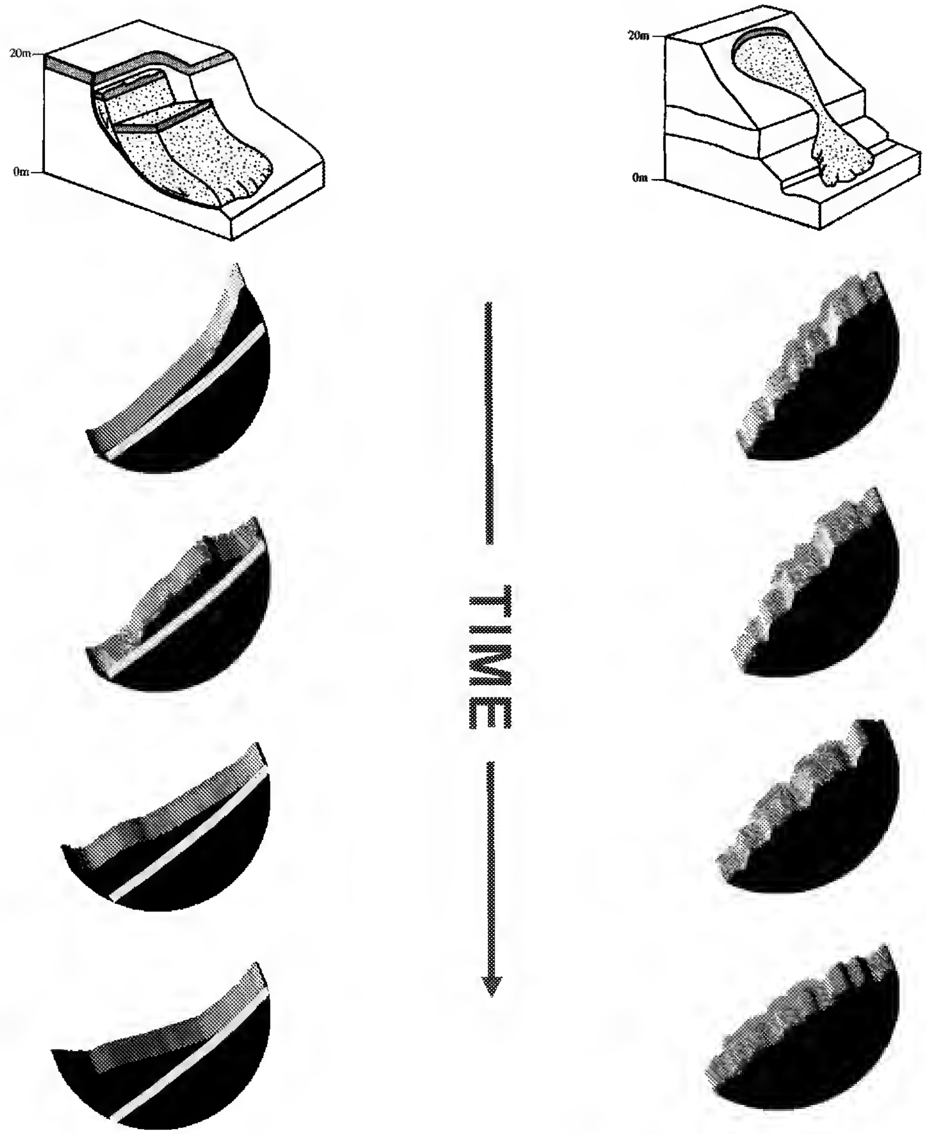

Illustration from: Landslide Recognition
ed. Dikau, Brunsden, Schrott, & Ibsen

Average over many avalanche events to obtain robust behavior

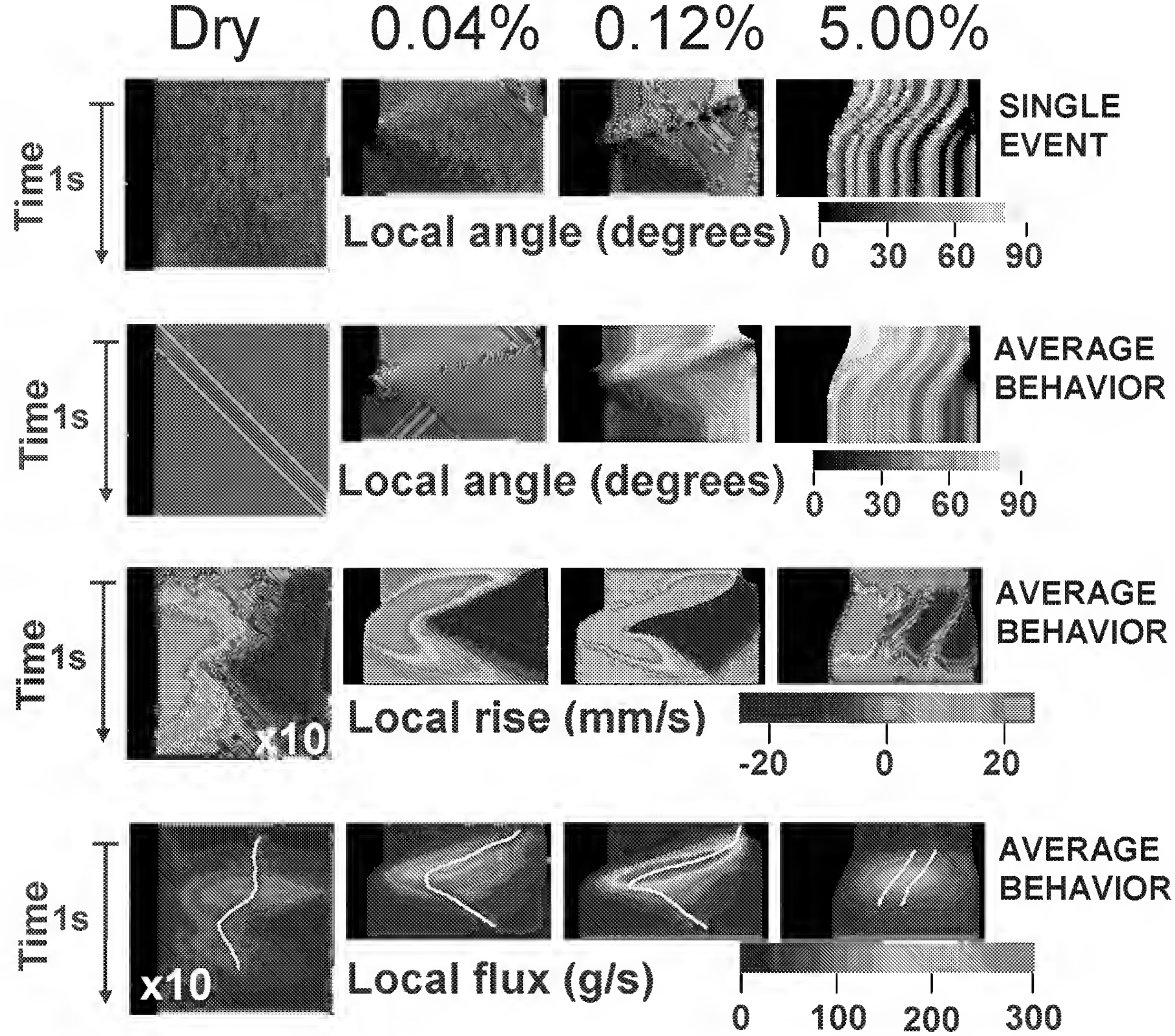

See upward-travelling kink at low liquid contents

See robust spontaneous pattern formation at large liquid content

DRAG FORCE AND PENETRATION IN GRANULAR MEDIA

Peter Schiffer and Yeekin Tsui
Department of Physics and Materials Research Institute, Pennsylvania State University, University Park PA 16802

Istvan Albert and Albert-Laszlo Barabási
Department of Physics, University of Notre Dame, Notre Dame, IN 46556

ABSTRACT

The motion of a solid object being pulled slowly through a granular medium is resisted by jamming of the grains, resulting in a drag force which differs dramatically from viscous drag in a fluid both in its average properties and in having large fluctuations with distinct characteristics. The drag process thus provides an excellent test-bed for the strength of locally jammed states among the grains and the effects of confinement on the jamming.

We have studied the drag force as a function of the velocity, the depth in the medium, the grain size and morphology for a vertical cylinder. The data agree well with theory for spherical media, but show an anomalously strong depth dependence for non-spherical grains. We also study the drag force on discrete objects with circular cross section moving slowly through a spherical granular medium. Variations in the geometry of the dragged object change the drag force only by a small fraction relative to shape effects in fluid drag. The drag force depends quadratically on the object's diameter as expected. We do observe, however, a deviation above the expected linear depth dependence, and the magnitude of the deviation is apparently controlled by geometrical factors.

We also have studied fluctuations in the drag force experienced by a vertical moving through a granular medium. The successive formation and collapse of jammed states give a stick-slip nature to the fluctuations which are periodic at small depths but become "stepped" at large depths, a transition which we interpret as a consequence of the long-range nature of the force chains and the finite size of our experiment. Another important finding is that the mean force and the fluctuations appear to be independent of the properties of the contact surface between the grains and the dragged object. These results imply that the drag force originates in the bulk properties of the granular sample.

Very recent work has focused on the effects of solid barriers within the grains on penetration of a granular medium. We have studied the force required to insert an object vertically into a granular medium, with particular attention to the effect of the bottom boundary. We find that, despite the long range nature of the force chains, the existence of the solid bottom of the granular container only affects the force when the inserted object is within a short range of the bottom, and that the roughness of the bottom surface has a strong effect on the force's depth profile.

REFERENCES: Physical Review Letters **82**, 205 (1999); Physical Review E **60**, 5823 (1999); Physical Review Letters **84** 5122 (2000); Physical Review E **64**, 031307 and **64**, 061303 and **64**, 061303 (2001).

Penetration, drag force, and local jamming in granular media

Y. K. TSUI, I. ALBERT, P. TEGZES, A.-L. BARABÁSI, T. VISCEK, P. SCHIFFER

Penn State University - University of Notre Dame - Eötvös University

The motion of a solid object being pulled slowly through a granular medium is resisted by jamming of the grains, resulting in a drag force which differs dramatically from viscous drag in a fluid both in its average properties and in having large fluctuations. We have studied the drag force and its fluctuations as a function of the velocity, the depth in the medium, the geometry of the dragged object, and the grain size and morphology. The drag process provides an excellent test-bed for the strength of locally jammed states among the grains and the effects of confinement on the jamming. Recent work has focused on the effects of solid barriers within the grains on penetration of a granular medium. We find that the surface texture of the solid barrier impacts the depth dependence of the resistance.

Physical Review Letters **82**, 205 (1999); Physical Review Letters **84** 5122 (2000); Physical Review E **64**, 031307 and **64**, 051303 and **64**, 061303 (2001).

Measure drag force in circular flow

Slowly Rotating Bucket of Grains, Cylinder Dipped In

Measure Force to <u>Keep Cylinder Fixed</u>

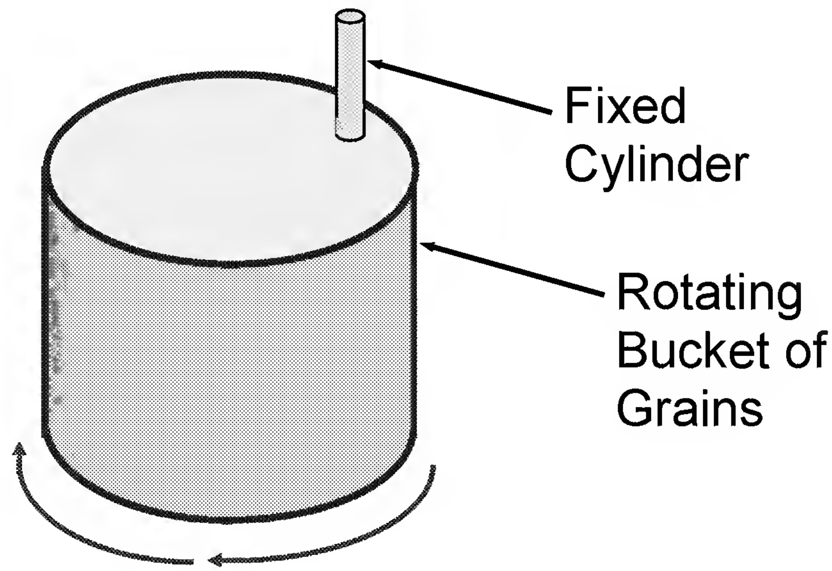

No variation in net drag force with bucket diameter (25 cm vs. 10 cm)

Average drag on cylinder has expected behavior

$$F_{drag} = \eta g \rho d_c H^2$$

independent of velocity and grain size

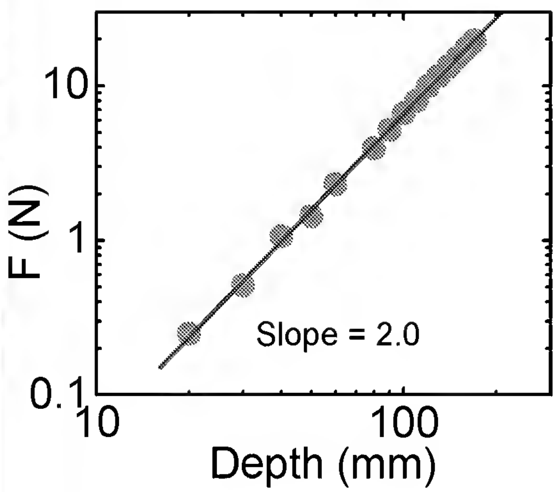

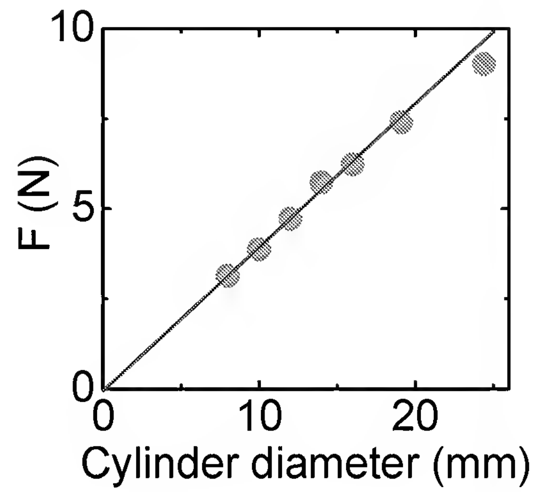

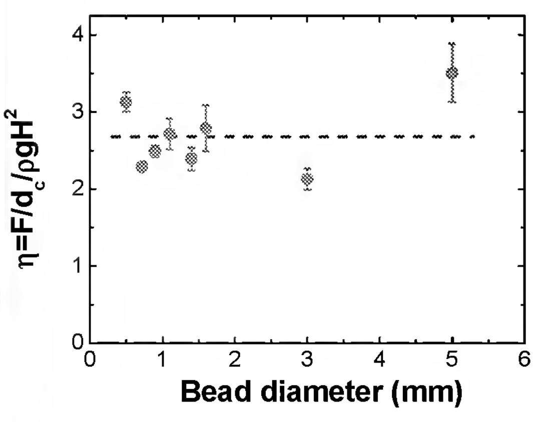

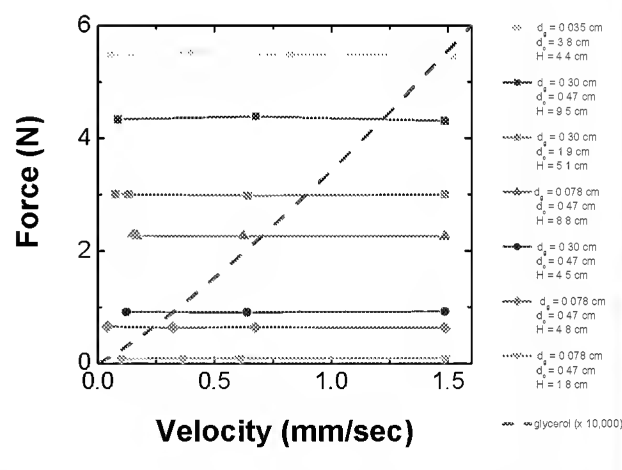

Fluctuations in drag illustrate collapse of jammed grains

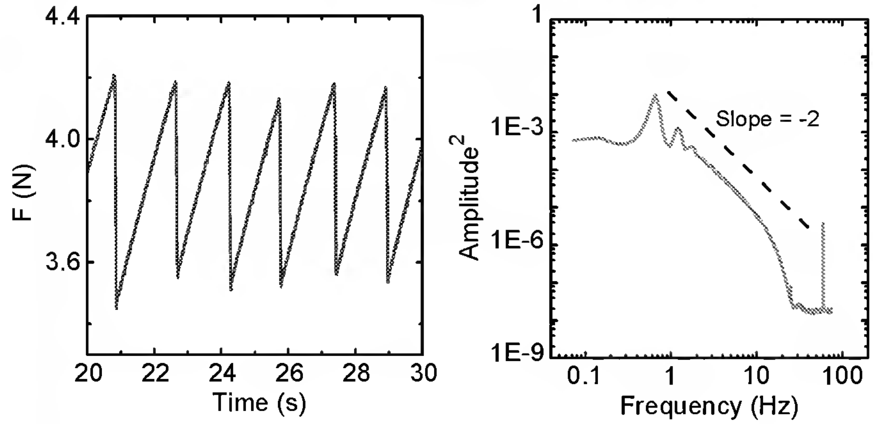

Fluctuations do not depend on rod shape or surface friction:

They result from bulk failure of the jammed grains

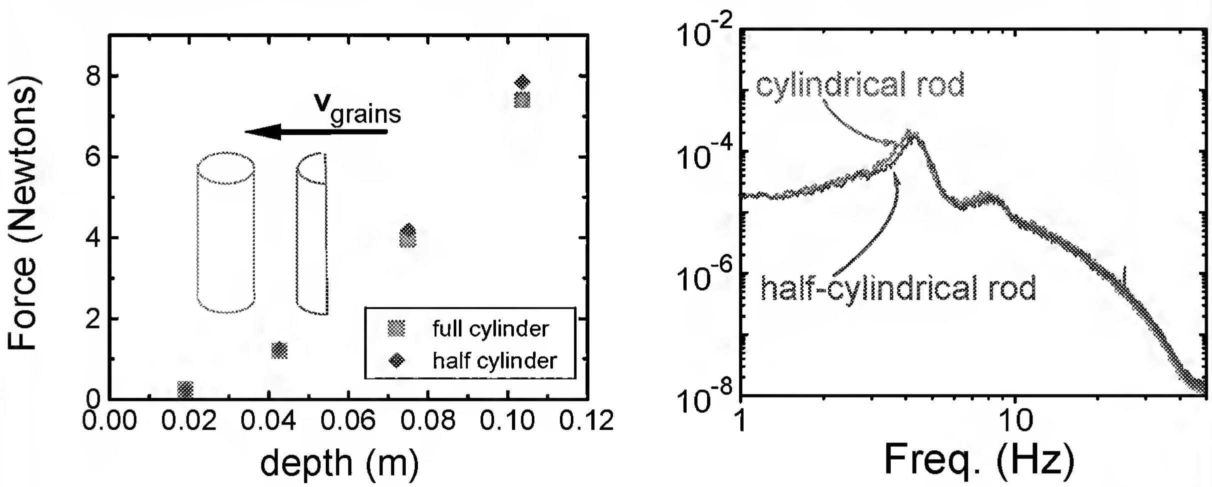

Fluctuations change in character with depth of insertion: finite size effect

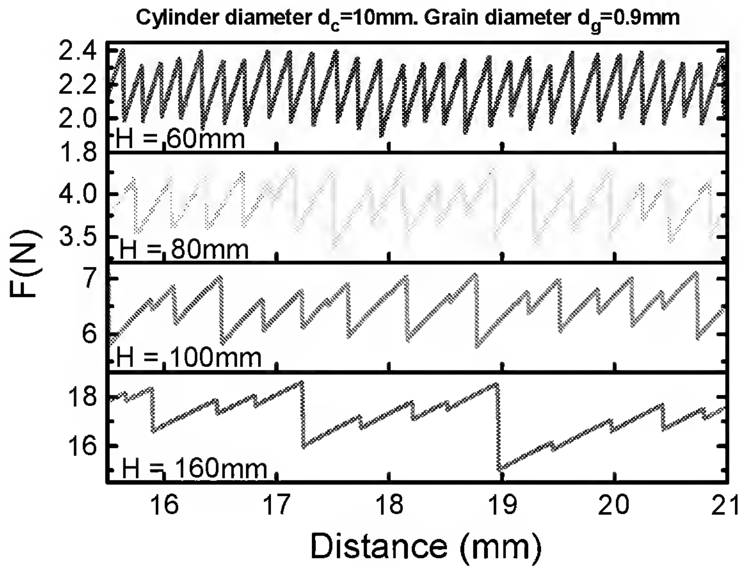

Transition to “stepped” stick-slip motion

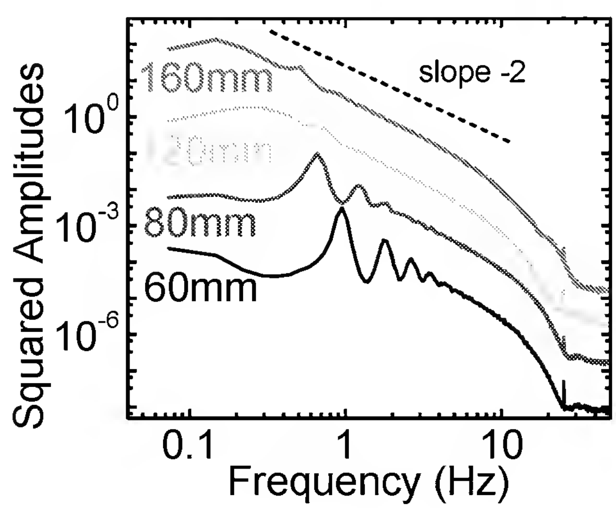

Study penetration of plate to boundary of granular sample

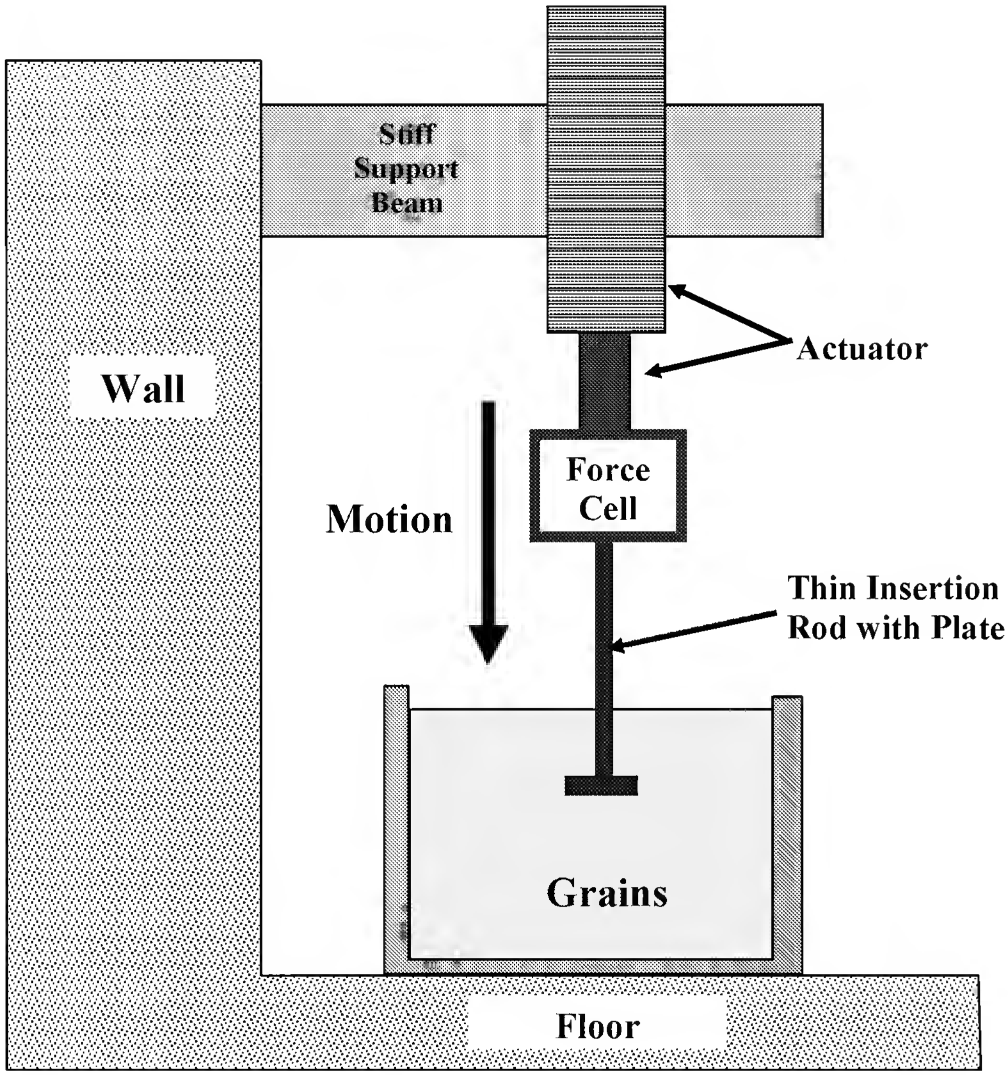

Study Glass Spheres (0.5 mm diam and larger)
Low velocities
Typical plate is 1.2 cm diameter

Raw Penetration Data: Force vs. Depth

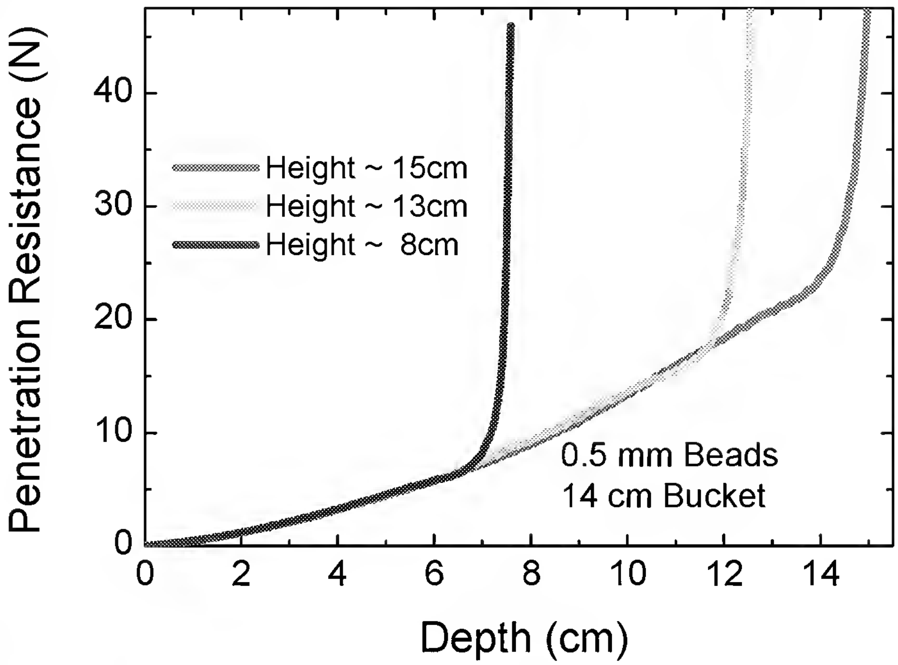

Results are independent of:

- **speed (low speeds)**
- **support rod diameter (d_{rod} < 0.5 cm)**
- **container size ($d_{container}$ > 10 cm)**

Large fluctuations with flat power spectrum

Length scale for "feeling" bucket bottom is quite short

Results are reproducible across range of grain sizes and "real" sand

Smooth bottom produces a dip in penetration resistance, rough does not

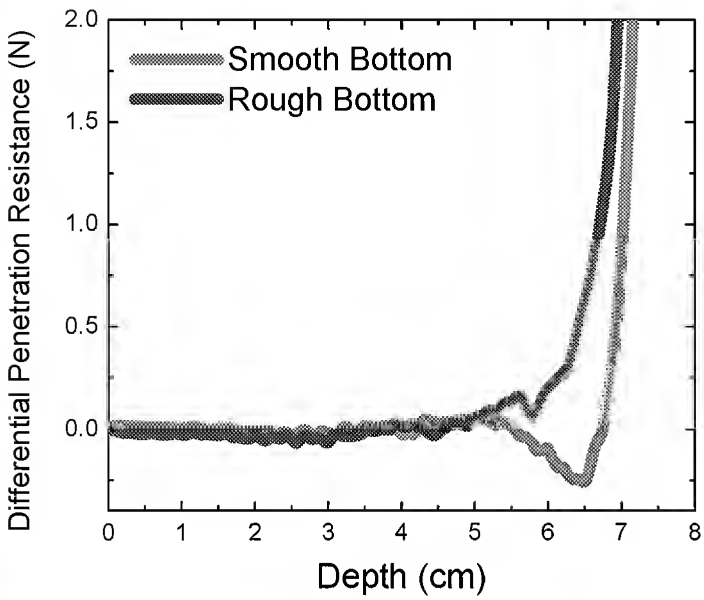

Take difference between F(z) for runs with different depths

Resistance dip comes from sliding on the bottom?

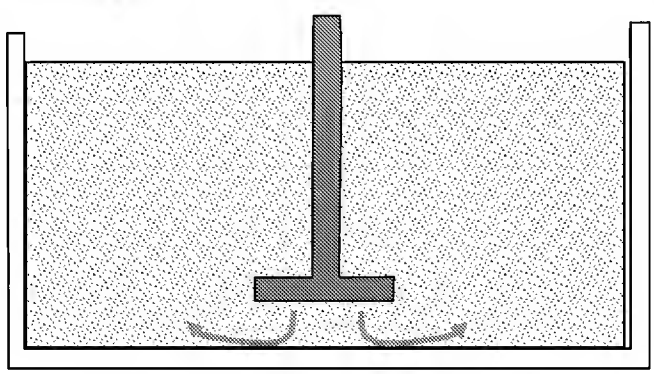

Further studies are ongoing…

CONSTITUTIVE RELATION IN TRANSITIONAL GRANULAR FLOWS

Hayley H. Shen
Dept. Civil & Env. Eng., Clarkson University, Potsdam, NY 13699-5710

Daniel M. Hanes
Dept. Civil & Coastal Eng., Univ. Florida, Gainesville, FL 32611

James T. Jenkins
Dept. Theoretical & Applied Mech., Cornell Univ., Ithaca, NY 14853

ABSTRACT

The behavior of granular materials spans the whole range from an elastic solid to a non-linear viscous fluid. The constitutive relation depends not only on the material composition, but also on the deformation and the rate of deformation. The key reason for this behavior is that granular materials are not only defined by the properties of the individual grains, but also by the structure of the aggregate. In a very dilute granular flow, the structure of the aggregate is simply defined by a uniform random distribution. As the concentration increases, the internal structure becomes complex. It evolves dynamically with the macroscopic deformation and is an integral part of the constitutive relation. The complexity and importance of the internal structure increase with the concentration. In a gravity field, the weight of a granular material naturally compacts it to produce a concentration gradient. To study the constitutive behavior of granular materials, the presence of gravity is therefore detrimental. Although empirical relations have been obtained for engineering designs to control granular flows on Earth, it is not known how well these Earth-bound relations can be used in another gravity field. Fundamental understanding must be derived to reliably design for granular flows in space exploration.

There are two extremes of granular flows of which significant amount of knowledge is available. One deals with a dense and quasi-static situation where the deformation rate nearly vanishes. The other deals with dilute and rapidly fluctuating grain velocities where particle inertia dominates. In near stationary granular flows the internal normal stress overwhelms the gravity effect. The concentration gradient due to gravity is negligible. In inertia dominant flows the only type of internal structure is the uniform random distribution of grains. As long as the concentration is low, its gradient does not affect this internal structure. However, under most natural conditions, a flowing granular material falls in between these two extremes. It is in this transitional regime that internal structure is sensitive to the concentration variation. This project, funded by the NASA Microgravity Fluid Physics Program, aims to study this transitional regime via physical experiments and computer simulations. A conceptual model has been established as described below.

There are two natural time scales in a granular flow. One is the travel time between two consecutive collisions and the other is the duration of a collision contact. At a very low shear-rate, the shear-induced particle velocity is low. Hence the travel time between collisions is longer than the contact time between colliding particles. Binary collisions prevail. As the shear-rate increases, the traveling time between collisions reduces and the probability of multiple collisions

goes up. These particle groups disperse shortly after and new groups form. When shear-rate is further increased, clusters grow in size due to an increasing chance for free particles to join before groups have the time to disperse. The maximum cluster size may depend on the global concentration and material properties. As the solid concentration approaches zero, the cluster size goes to one particle diameter. The maximum possible cluster size under any condition is the container size, provided that the shear flow is inside a container. The critical shear-rates that dictate the initiation of the multiple contacts, and the size and lifetime of the collision clusters, are functions of the concentration also. A "regime" theory has been proposed in Babic et al. (*J. Fluid Mech.* 219:81-118,1990). This theory suggested that both the solid concentration, C, and the non-dimensional shear-rate, B, are important in determining the regimes of the granular constitutive law, as shown in the figure.

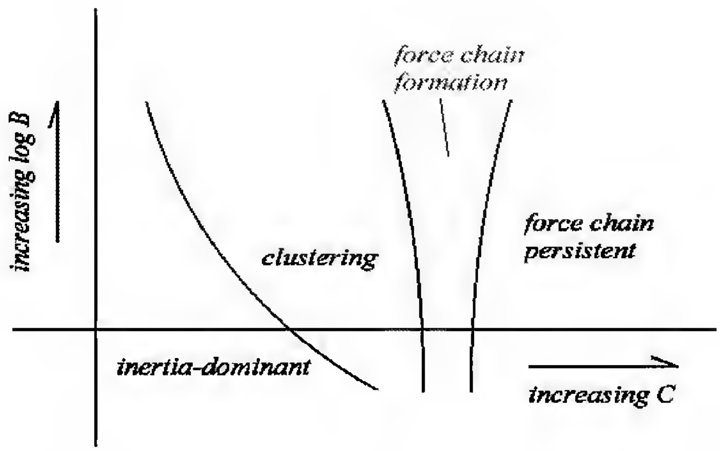

In the coming years, both physical and computer experiments will be conducted. These experiments will determine the stress and strain-rate relation while the microstructure of the granular material dynamically changes. Data obtained from these experiments will be used to link the microstructure of the granular material to the resulting constitutive relations. The above regime theory will be quantified. This poster gives a brief overview of the physical experiment, the computer simulation, and how these two will be integrated.

Granular Shear Flows – Constitutive Relations and Internal Structures

Hayley Shen, Dept. Civil & Env. Eng.
Clarkson University
Dan Hanes, Dept. Coastal Eng., University of Florida
James T. Jenkins, Dept. Theoretical & Applied Mechanics, Cornell University

NASA Microgravity Fluid Physics: NAG3-2717

Scientific Objectives

- Determine the onset of each of the regimes from grain-inertia to quasi-static.
- Obtain data to study the constitutive relation in each of the regimes.
- Test the effect of contact force models on macro-mechanics of granular assemblies.

The purpose of this study is to lay the foundation for modeling behaviors of ground materials on other planets where gravity differs from that on Earth. By understanding the fundamentals of granular materials, engineering work dealing with such materials on Earth can also be improved.

We learned from computer simulations as well as physical experiments that granular materials exhibits different rheological behavior under different shearing conditions. The constitutive relation is not only a material property, but also a flow property, as shown in the following figure.

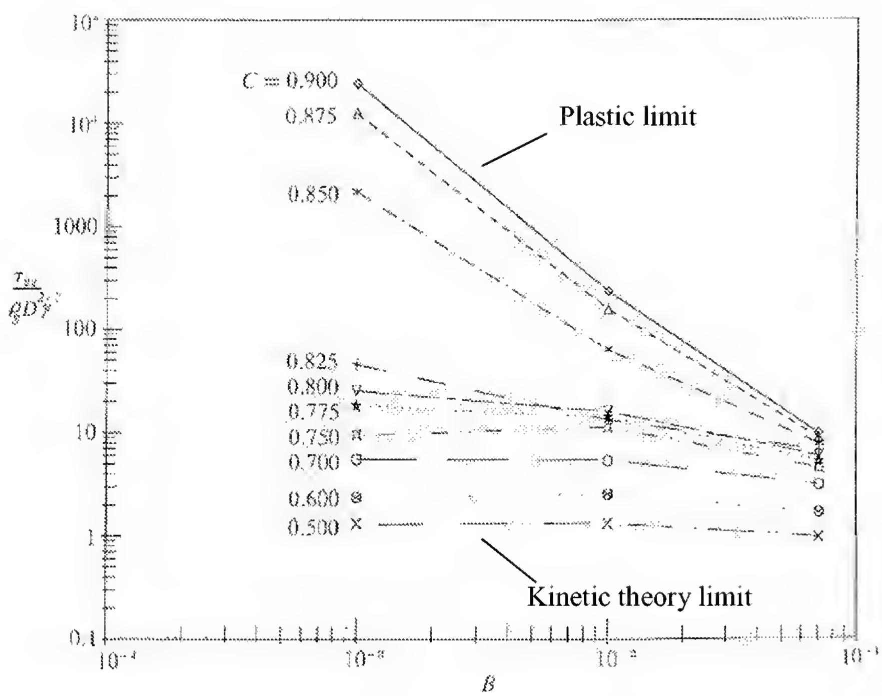

$$B = \dot{\gamma}\sqrt{\frac{\rho_s D^3}{k}}$$

= dimensionless strain rate

C = solid concentration

$$\frac{\tau}{\rho_s D^2 \dot{\gamma}^2} =$$

dimensionless stress

Babic, M. et al. 1990. The stress tensor in granular shear flows of uniform, deformable disks at high solids concentrations. *J. Fluid Mech.* 219:81-118.

There are four recognized regimes of a granular flow. From left to right, as the concentration increases and fixing the shear rate, the granular material gradually evolves from a non-Newtonian viscous material to completely plastic. This transition results from the change of internal structures.

A Regime Map

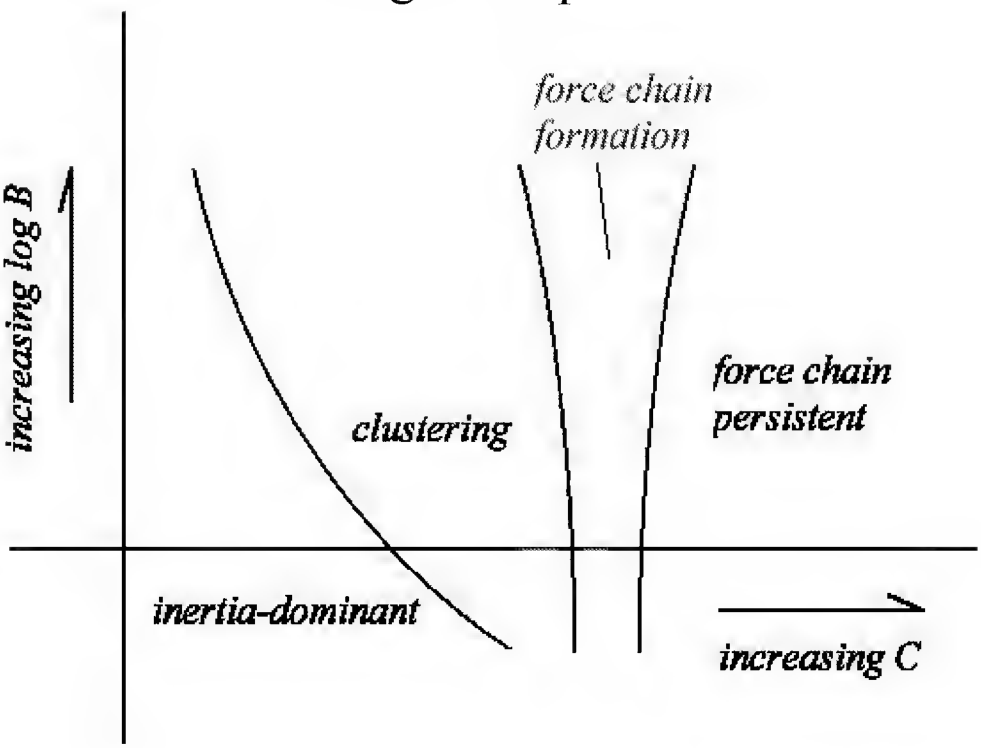
force chain
formation
increasing log B
clustering
force chain
persistent
inertia-dominant
increasing C

The formation of internal structure is explained below. When the time scale for binary collision is shorter than free-flight time scale, inertia-dominant constitutive relation is valid. As the free-flight time scale reduces, either through increasing *B* or increasing *C*, multiple collision and internal structure begin to alter the constitutive relation.

Two time scales: $t_{collision} \propto \sqrt{\dfrac{\rho_S D^3}{k(1-\zeta^2)}}$

$$t_{free-flight} \propto \dot{\gamma}^{-1} F(C), \;\; F(C) \uparrow C \downarrow$$

The transition of regimes due to internal structure is illustrated in the following picture. From left to right, the shear rate increases while keeping the concentration constant. From top to bottom, the shear rate is fixed but the concentration increases.

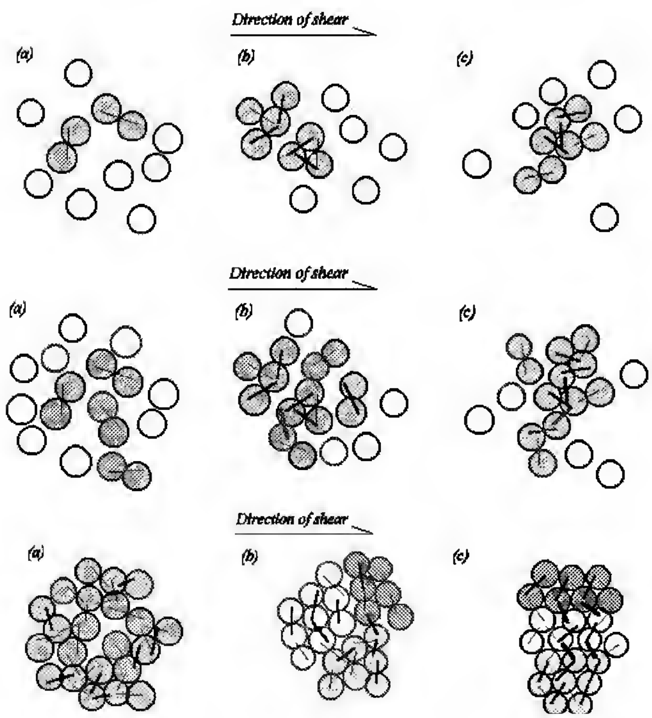

$C<C_r$ binary collision only

$C_r<C<C_{pc}$ multiple collision prevails, clusters form and break

$C_{pc}<C<C_{qs}$ multiple collision persists, force chains form and break

$C_{qs}<C$ force chains persist, true plastic flow

Recent computer simulations demonstrate the multiple collision phenomenon. The simulation uses 3000 disk particles. The following results are for frictionless particles with restitution coefficient of 0.1. The first set of panels are for C=0.3 and the second set of panels are for C=0.8.

In these animations, clustering is evident, but actual contacts cannot be detected visually, especially when C is high.

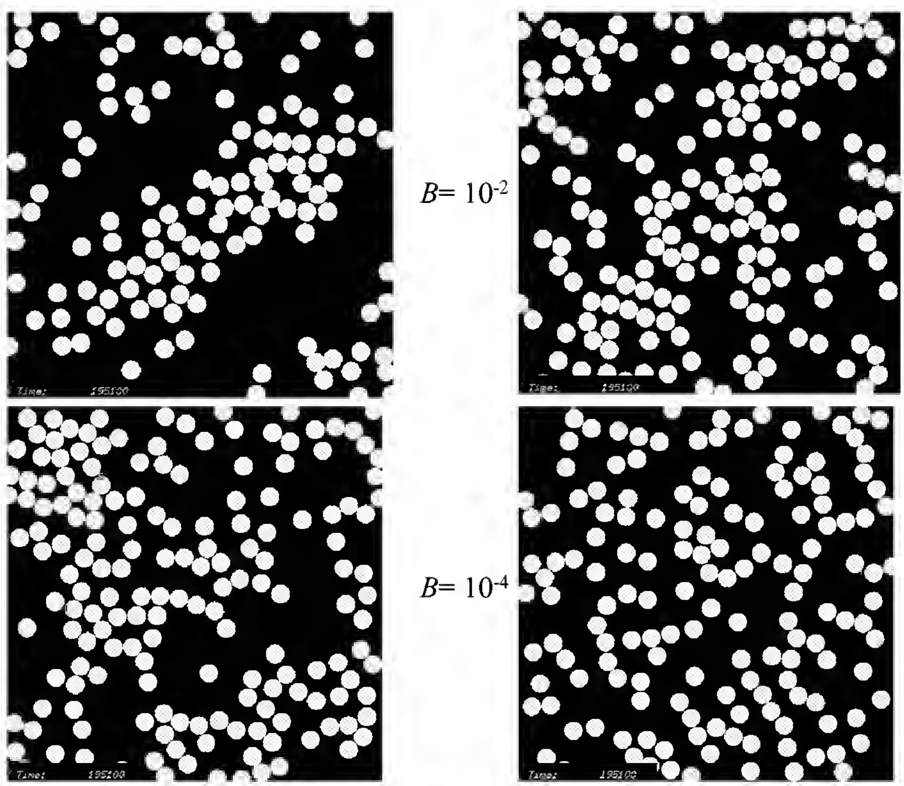

$B = 10^{-1}$

$B = 10^{-2}$

$B = 10^{-3}$

$B = 10^{-4}$

$B = 10^{-1}$

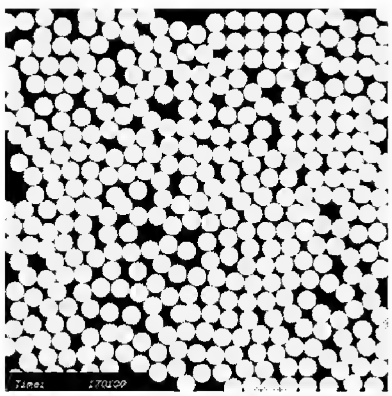

$B = 10^{-2}$

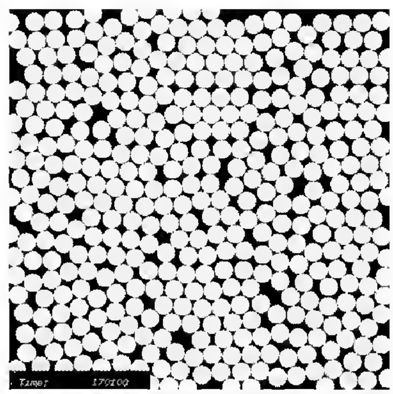

$B = 10^{-3}$

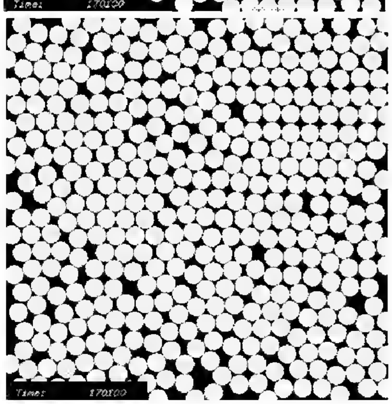

$B = 10^{-4}$

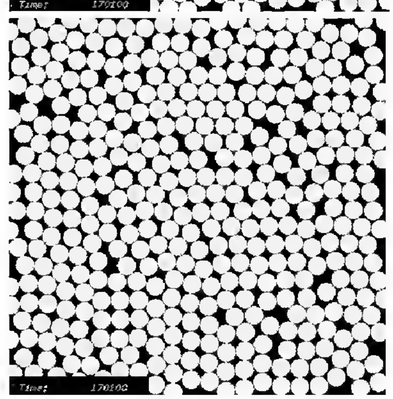

The actual contact and the size of groups with simultaneous contacts are extracted from the simulation. The following results show drastic change of the size of groups as *C* increases. Similarly, increasing *B* has the same effect.

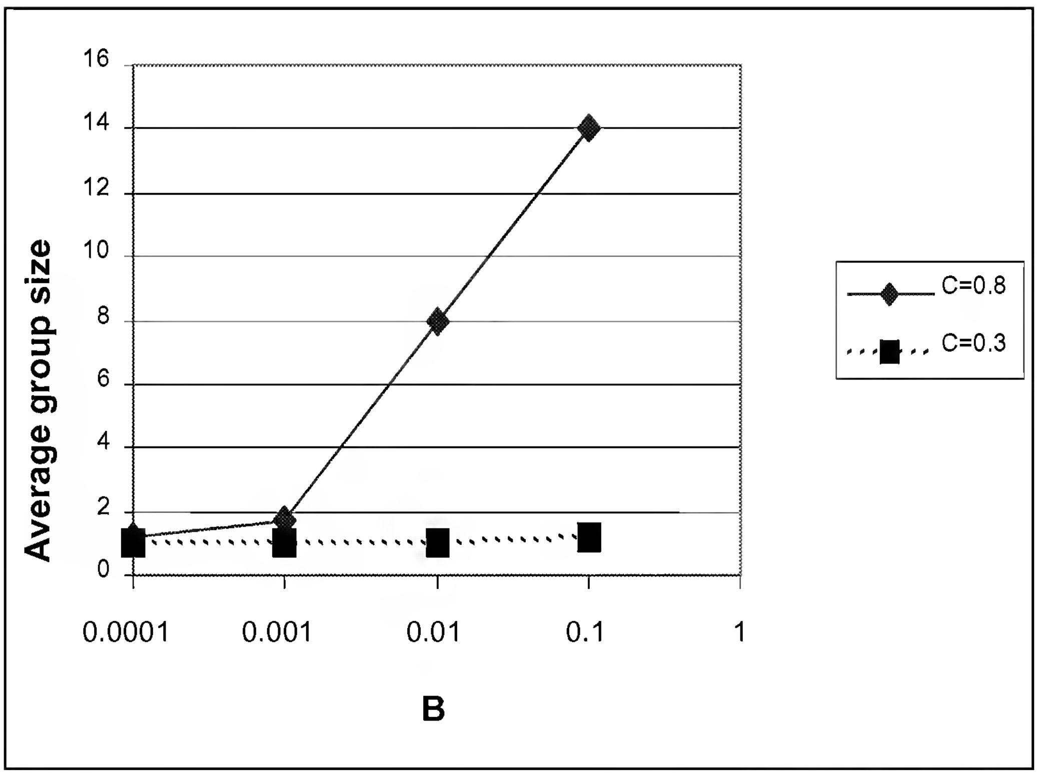
16
14
12
10
8
6
4
2
0
Average group size
0.0001
0.001
0.01
0.1
1
B
C=0.8
C=0.3

Physical experiments will be conducted to validate the computer simulation, and to prepare for micro-gravity experiments to directly measure the stress and strain rate under different concentration and shear rate, as well as different material properties. The equipment to be used for the ground based experiments is shown in the following figure.

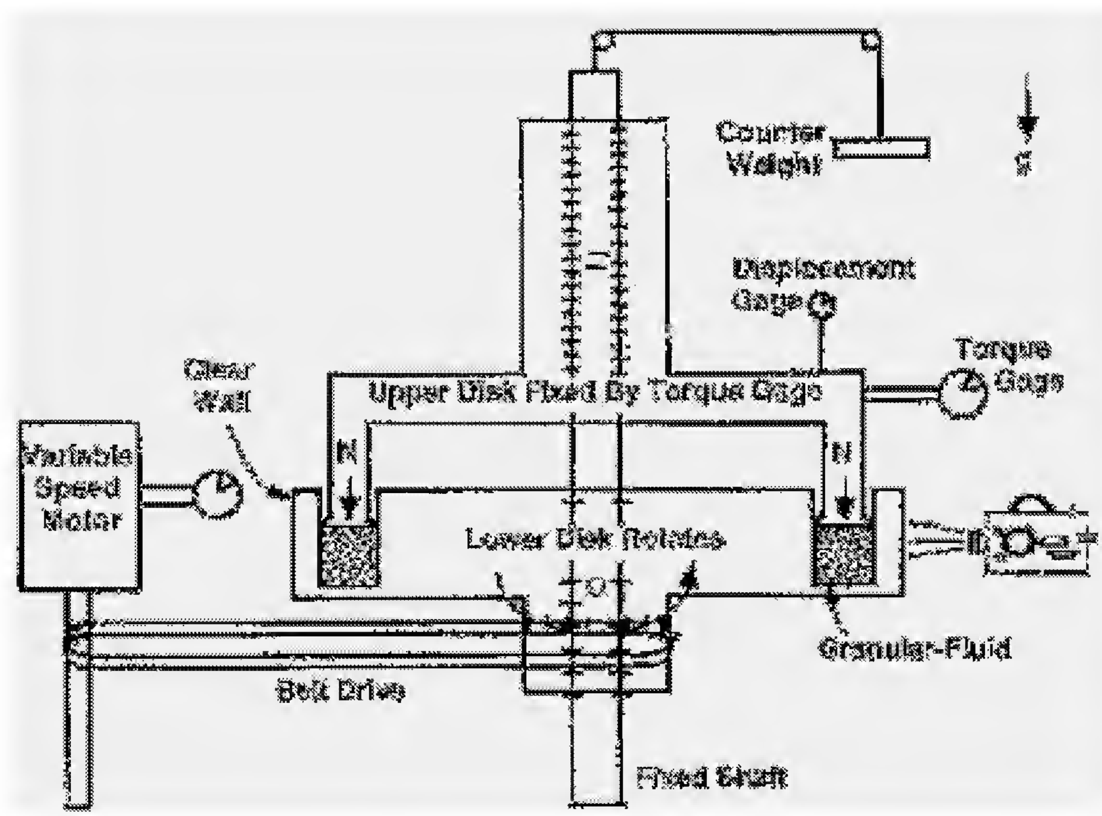
Counter Weight
g
Displacement Gage
Torque Gage
Clear Wall
Upper Disk Fixed By Torque Gage
N
N
Variable Speed Motor
Lower Disk Rotates
Ω
Granular-Fluid
Belt Drive
Fixed Shaft

An example of the shear cell in operation: 3 mm glass spheres, looking down at top surface following quasi-static shearing. Black spheres were originally at the screw location. Upper layers sheared while lower layers remained in place.

Study Plan

- **Physical Tests:** Because of the gravity effect, ground-based experiments will not be directly usable for rheological properties of granular material. However, these experiments are indispensable for testing the equipment and data acquisition techniques before space experiments. They also provide crucial data for validating computer simulation results.
- **Computer Simulations** : Computer simulations, inherently simplified versions of the reality, may not capture all real phenomena. A combination of physical and computer experiments is the best tool. We will simulate the shear cell with identical conditions to be used in the shear cell. These simulation results will be validated by adding gravity effect to the simulation, and compare the results with ground-based physical experiments. This computer simulation will also be used to guide the design as well as to choose the operating parameters for future microgravity experiments.
- **Constitutive Relation Modeling** : Both physical experiments and computer simulations will generate data required to determine the onset and the evolution of the transitional regions in a granular flow. We will relate the stress state to the evolution of the internal structures. Fabric and void tensors will be adopted in the geometric description of the internal structures.

AGGREGATION AND GELATION OF ANISOMETRIC COLLOIDAL PARTICLES

Ali Mohraz and Michael J. Solomon
Department of Chemical Engineering, University of Michigan Ann Arbor MI 48109-2136.
(mjsolo@umich.edu)

ABSTRACT

The quiescent and flow-induced structure and dynamics of colloidal aggregates and gels of anisometric particles are studied by means of static and dynamic light scattering. Ground-based studies of weak gels are possible due to the submicron size of the boehmite rod suspensions investigated; however, microgravity conditions would be required for more general studies. The properties of colloidal rod suspensions are compared to typical properties of spherical particle gels to understand the role of anisotropic excluded volume on gel structure and dynamics.

The structure and dynamics of colloidal aggregates and gels have long been of scientific and technological interest; however, most research has focused on suspensions of spherical particles. Yet, aggregates and gels of anisometric particles - colloidal rods and platelets - may exhibit structure and dynamics that are quite different from spherical colloids. For example, suspensions of colloidal rods gel at extremely low volume fractions and form birefringent sediments (A.P. Philipse, A.-M. Nechifor and C. Pathmamanoharan, Langmuir **10**, 4451 (1994)). The rheology of solutions and gels of colloidal rods and platelets differs dramatically from that of colloidal spheres (M.J. Solomon and D.V. Boger, J. Rheology **42**, 929 (1998)). Scientifically, studies with anisometric particles offer the opportunity to assess the role of anisotropic excluded volume and particle orientation in aggregates and gels. Technologically, anisometric colloids find use in a wide range of materials such as ceramics, polymer nanocomposites, well-bore drilling fluids and magnetic storage media.

Model colloidal boehmite rods of approximately monodisperse dimension and aspect ratio have been synthesized according to the method of Philipse and coworkers. In aqueous solution, these materials undergo gelation upon the addition of divalent salt. By means of a novel grafting reaction and procedure for solvent refractive index matching, the rods have also been dispersed in mixed organic solvents. In this case, gelation is induced by means of depletion interaction.

We report the effect of particle shape and anisotropic excluded volume on the structure, rheology, and internal dynamics of colloidal gels. The quiescent structure of these gels is characterized over two decades in the scattering vector, q, by combined small and wide-angle light scattering. The effect of particle aspect ratio on the gel microstructure is studied in particular. Light scattering studies conducted as shear deformation is applied to the material quantify how colloidal aggregates are oriented and deformed by flow. The internal dynamics of the gels are quantified by means of photon correlation spectroscopy.

SPLASHING DROPLETS

Randall L. Vander Wal*, John Patrick Kizito, Gordon M. Berger
National Center for Microgravity Research

J. Iwan D. Alexander
Case Western Reserve University and
National Center for Microgravity Research

Grétar Tryggvason
Worcester Polytechnic Institute

ABSTRACT

Current data on droplet breakup is scarce for the sizes and velocities typical of practical applications such as in spray combustion processes and coating processes. While much more representative of practical applications, the small spatial scales and rapid time-scales prevent detailed measurement of the internal fluid dynamics and liquid property gradients produced by impinging upon surfaces. Realized through the extended spatial and temporal scales afforded by a microgravity environment, an improved understanding of drop breakup dynamics is sought to understand and ultimately control the impingement dynamics of droplets upon surfaces in practical situations.

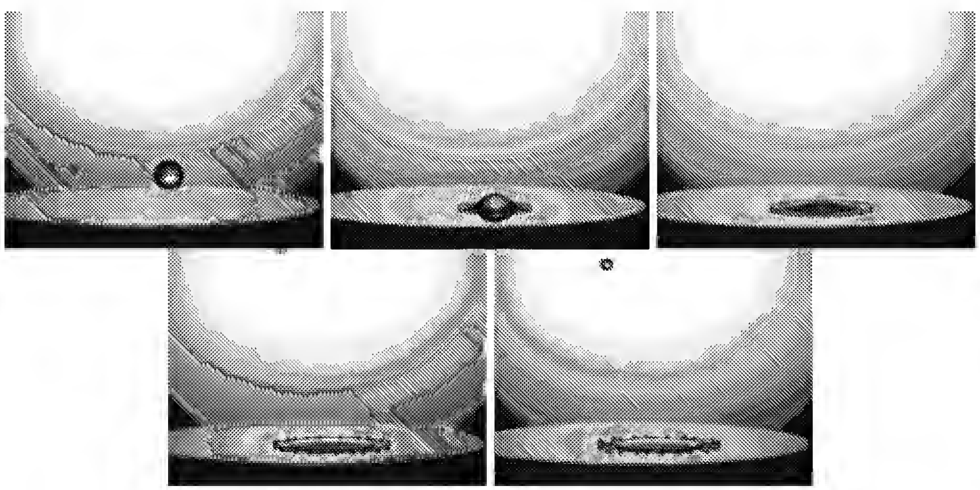

Figure 1: Experimental images of a sequences showing the spreading of a single droplet after impact and ensuing finger instabilities. (We=386, Re=370).

The primary objective of this research will be to mark the onset of different "splashing modes" and to determine their temperature, pressure and angle dependence for impinging droplets representative of practical fluids. In addition, we are modeling the evolution of droplets that do not initially splash but rather undergo a "fingering" evolution observed on the spreading fluid front and the transformation of these fingers into splashed products. An example of our experimental data is presented below. These images are of Isopar V impacting a mirror-polished surface. They were acquired using a high-speed

camera at 1000 frames per second. They show the spreading of a single droplet after impact and ensuing finger instabilities.

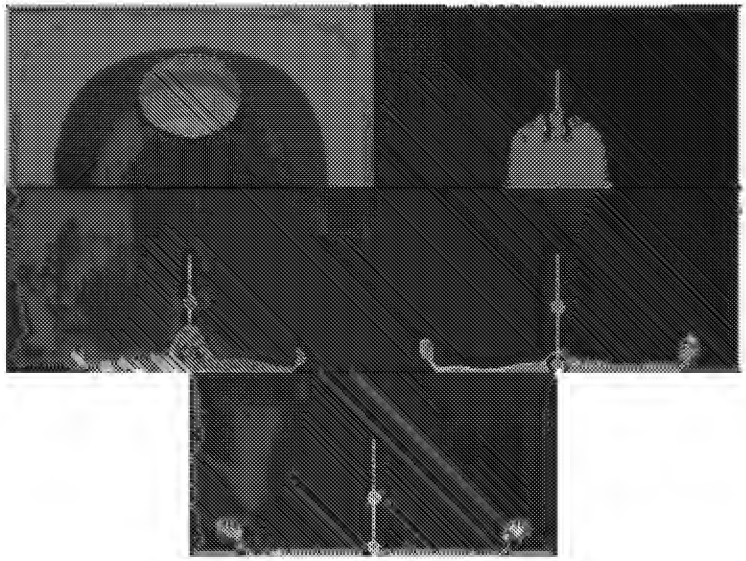

Figure 2: Numerical images sequence showing, axisymmetrically, the spreading of a single droplet after impact (same We, Re).

Normal gravity experimental data such as this will guide low gravity measurements in the 2.2 second drop tower and KC-135 aircraft as available. Presently we are in the process of comparing the experimental data of droplet shape evolution to numerical models, which can also capture the internal fluid dynamics and liquid property gradients such as produced by impingement upon a heated surface.

To-date isothermal numerical data has been modeled using direct numerical simulations of representative splashing droplets. The process involves using fluid front-tracking methods. These numerical methods are based on writing and simultaneously solving a set of basic equations for the whole computational domain using two grids systems to track a single droplet as it interacts with and spreads along a solid wall. The momentum transport equations are solved by a conventional finite volume method on a fixed, structured grid and the interface is tracked explicitly. The fluid-tracking algorithm determines the advections and distribution of the fluid properties such as viscosity and density. The surface tension is implemented as a source term in the momentum equation. At the splashing wall, fluid wall interactions are described by slip boundary conditions. We are in the process of adding contract line hydrodynamics.

The data obtained so far indicates that the present model describes well the droplet wall interactions to a point in time just before splash. We will present a comparison of our experimental data to representative numerical cases. We are also updating the code to take into account multiple tracking of the droplets after splash. As time permits we will present this data also.

*Contact information:

email: Randy.VanderWal@grc.nasa.gov

phone: 216-433-9065

fax: 216-433-3793

Splashing Droplets

Randall L. Vander Wal*, **John Patrick Kizito, Gordon M. Berger**
National Center for Microgravity Research
J. Iwan D. Alexander
Case Western Reserve University
Gretar Tryggvason
Worcester Polytechnic Institute

Acknowledgements NASA Contract # 3-544
Premal Patel, Matt Pierce and David Hiltner

*Contact information:
email: Randy.VanderWal@grc.nasa.gov
phone: 216-433-9065
fax: 216-433-3793

Motivation

- Improved understanding of drop breakup dynamics is needed to optimize the desired behavior of impinging drops in practical situations
  - Spray combustion as diesel engines
  - Rocket engines
  - Agricultural and medical sprays
  - Painting sprays
  - Printed circuit manufacturing
  - Aircraft icing
  - Spray cooling

Progress

- Mapped splash regimes
- Resolved spatial and temporal scales
- Simulated and predicted physical behavior
- Investigated a wide parametric range of Reynolds, Weber, and Ohnesorge numbers
- Defined the effects of substrate surface finish (contact angle)
- Studied temperature effects

Objectives

- The primary objective of the proposed work is to investigate on a fundamental level the mechanism(s) for droplet breakup and the effects of relative droplet-surface temperature, ambient pressure and impingement angle.

- The second objective is to develop a numerical model, benchmarked against experimental data capable of predicting droplet-surface breakup dynamics.

Role of Gravity

Droplet sizes in practical applications range from 10 - 100 microns with velocities extending from 1 to beyond 10 m/s. These small spatial scales and short temporal scales prohibit detailed study of the internal fluid dynamics and temperature profiles during droplet-surface interaction

- A low-gravity environment provides enhanced spatial and temporal scales while allowing similar non-dimensional parameter groupings of Ohnesorge, Weber and Reynolds numbers typical of practical applications.

- With well-defined initial conditions uninfluenced by gravity, insights into parameters governing droplet breakup behavior will be realized

Scaling Parameters

$$\mathrm{Re} = \frac{\rho U D}{\mu} \qquad We = \frac{\rho U^2 D}{\sigma} \qquad Oh = \frac{\sqrt{We}}{\mathrm{Re}}$$

ρ Density of the fluid

U Impact velocity

D Droplet diameter

μ Viscosity

σ Surface tension

Experimental Setup

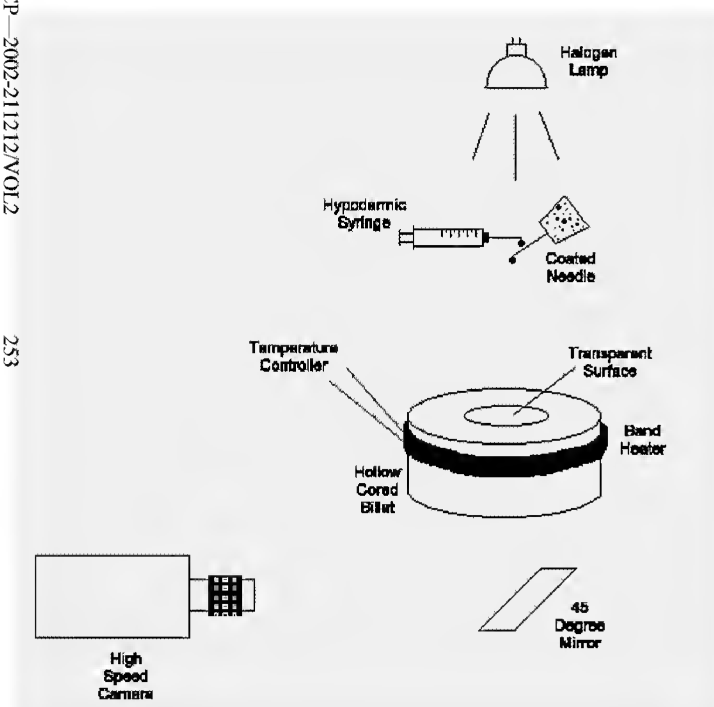

view from below

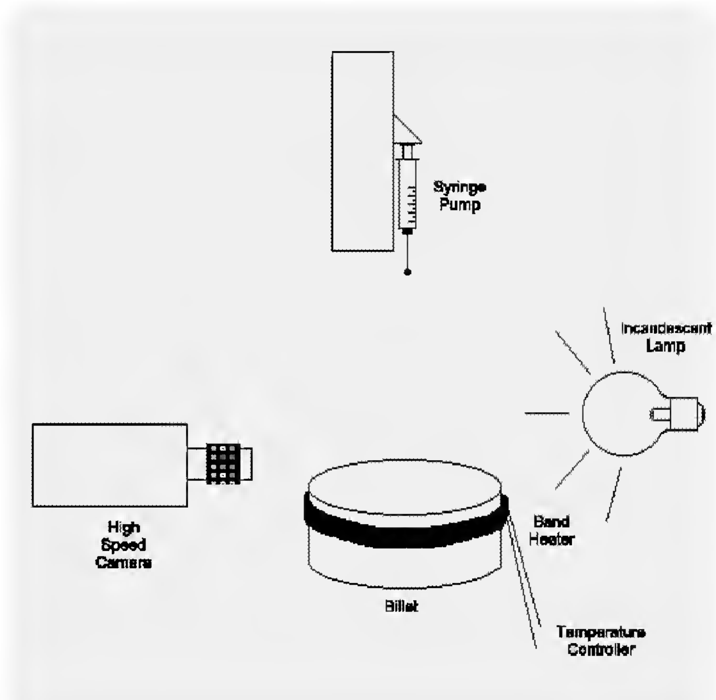

view from the side

Theory and Numerical Simulation

Methodology

- Our approach involves treating the liquid boundary surface as an imbedded interface by adding the appropriate source terms to the conservation laws. These source terms are in the form of delta functions localized at the interface and are selected in such a way so as to satisfy the correct matching conditions at the phase boundary

$$\frac{\partial(\rho\mathbf{u})}{\partial t} + \nabla \cdot (\rho\mathbf{u}\mathbf{u}) = -\nabla P - \rho\mathbf{g} + \nabla \cdot \mu\left(\nabla\mathbf{u} + \nabla\mathbf{u}^{T}\right) + \int_f F_s \delta\left(\mathbf{x} - \mathbf{x}_f\right) \cdot da$$

$$\nabla\rho\mathbf{u} = \int_f \Delta\rho \cdot (d\mathbf{x}_f / dt) \cdot \mathbf{n}\delta\left(\mathbf{x} - \mathbf{x}_f\right) \cdot da$$

- The model includes local grid refinement captures the draining of the film between the drop and the solid surface, the energy equation to compute the temperature distribution, temperature dependent surface tension, and mass transfer from the surface due to evaporation.

Strategy

- By carrying out a parametric study we examine the sensitivity of the results to changes in the relationship between the surface tension, viscosity and the droplet-surface interactions, it will be possible to determine what forces are important during the collision of drop with a surface and in the evolution of splashed products.

Experimental Results

Splash Regime (Red)

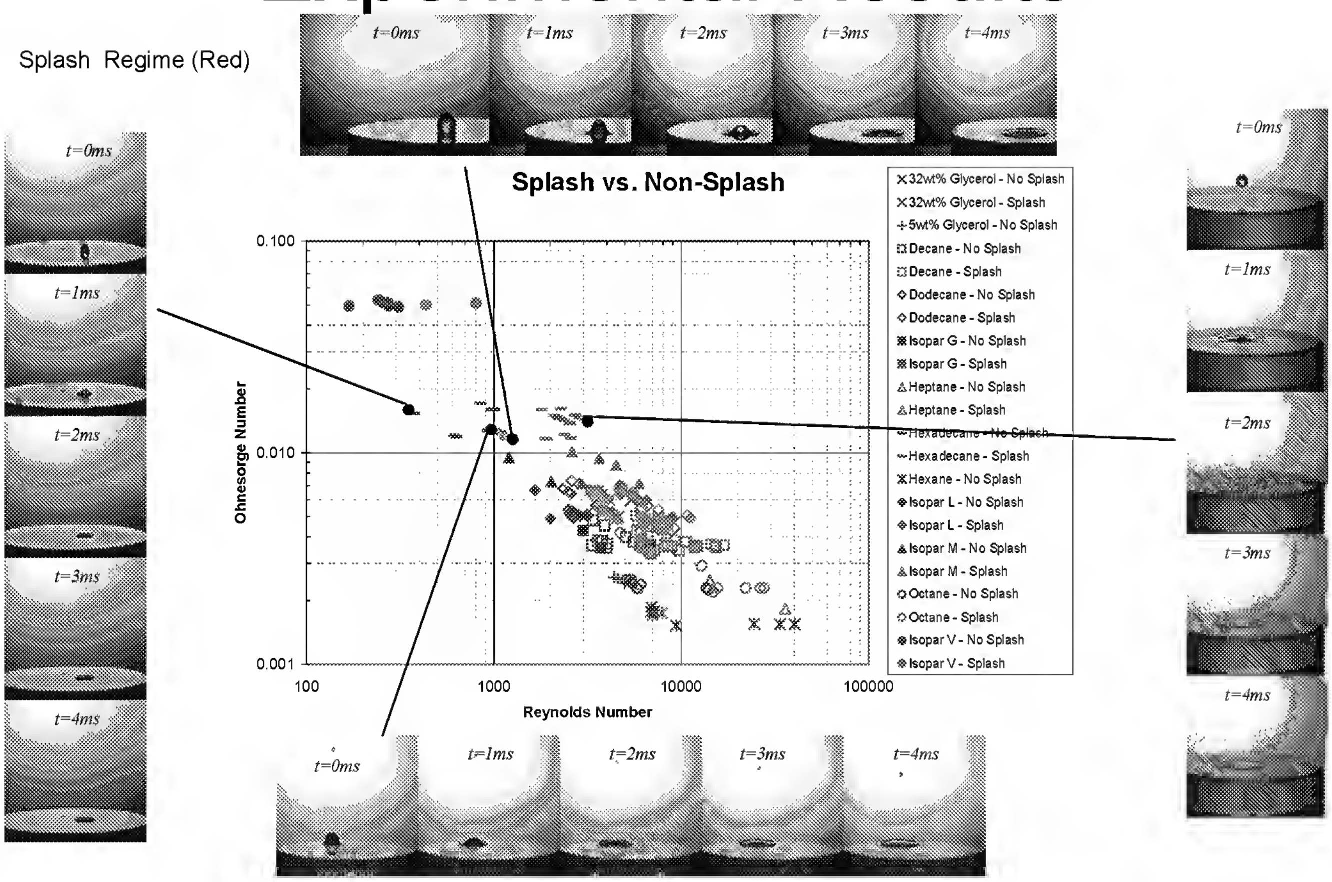

Finger Instabilities

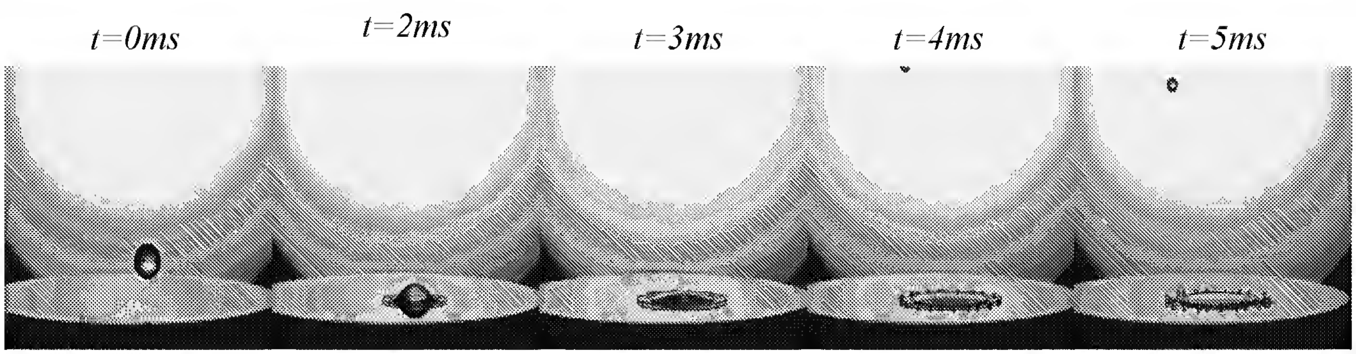

Spreading of a single droplet after impact and ensuing finger instabilities. (Oh= 0.053, Re=370)

Rebound

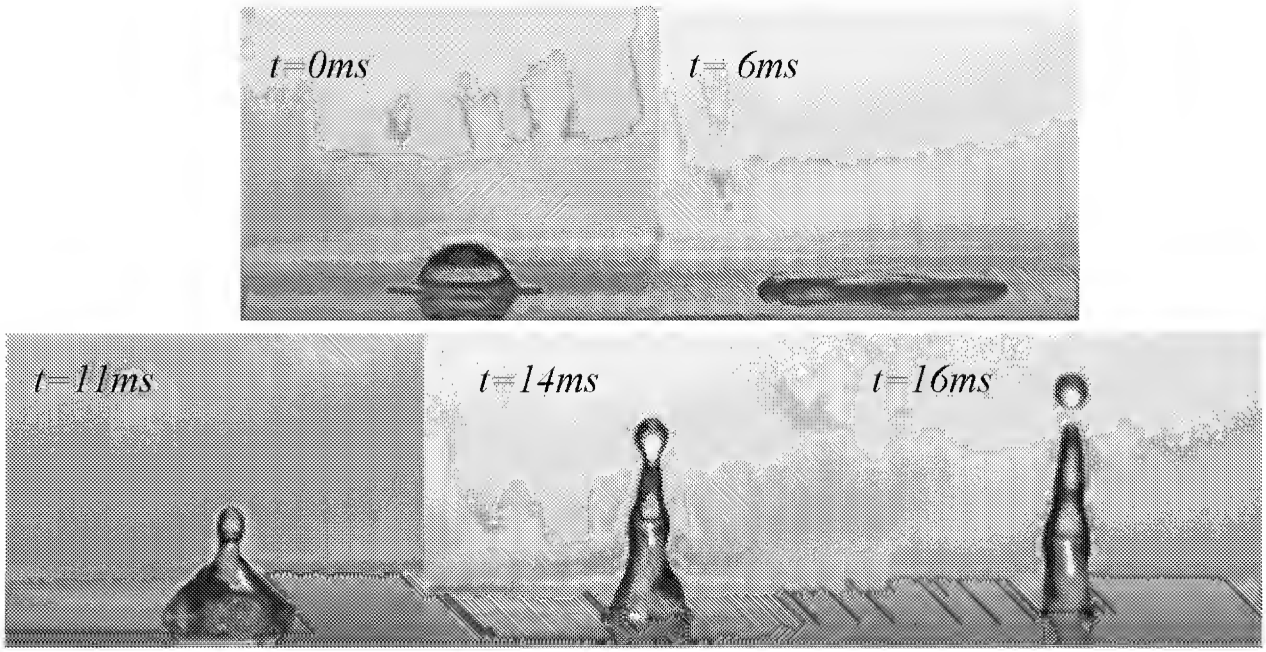

Oh=0.002, Re=5283

Numerical Results

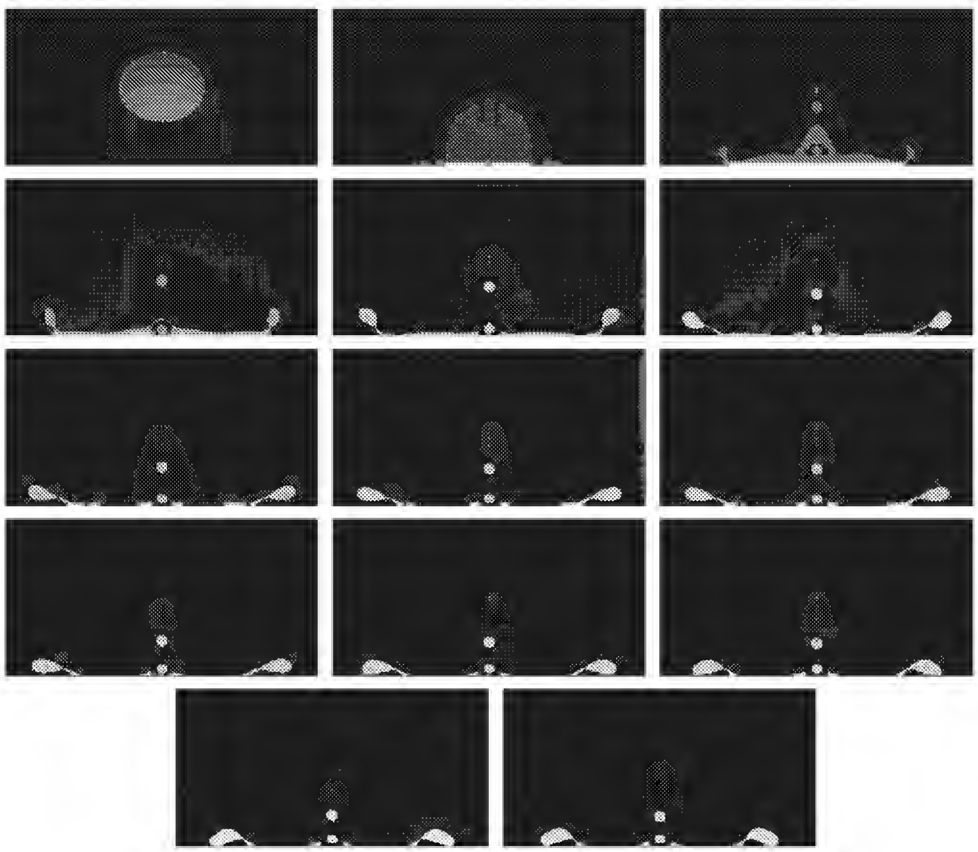

Oh=0.008, Re=2500, time lapse = 1ms

NASA/CP—2002-21212/VOL2

Interior fluid dynamics

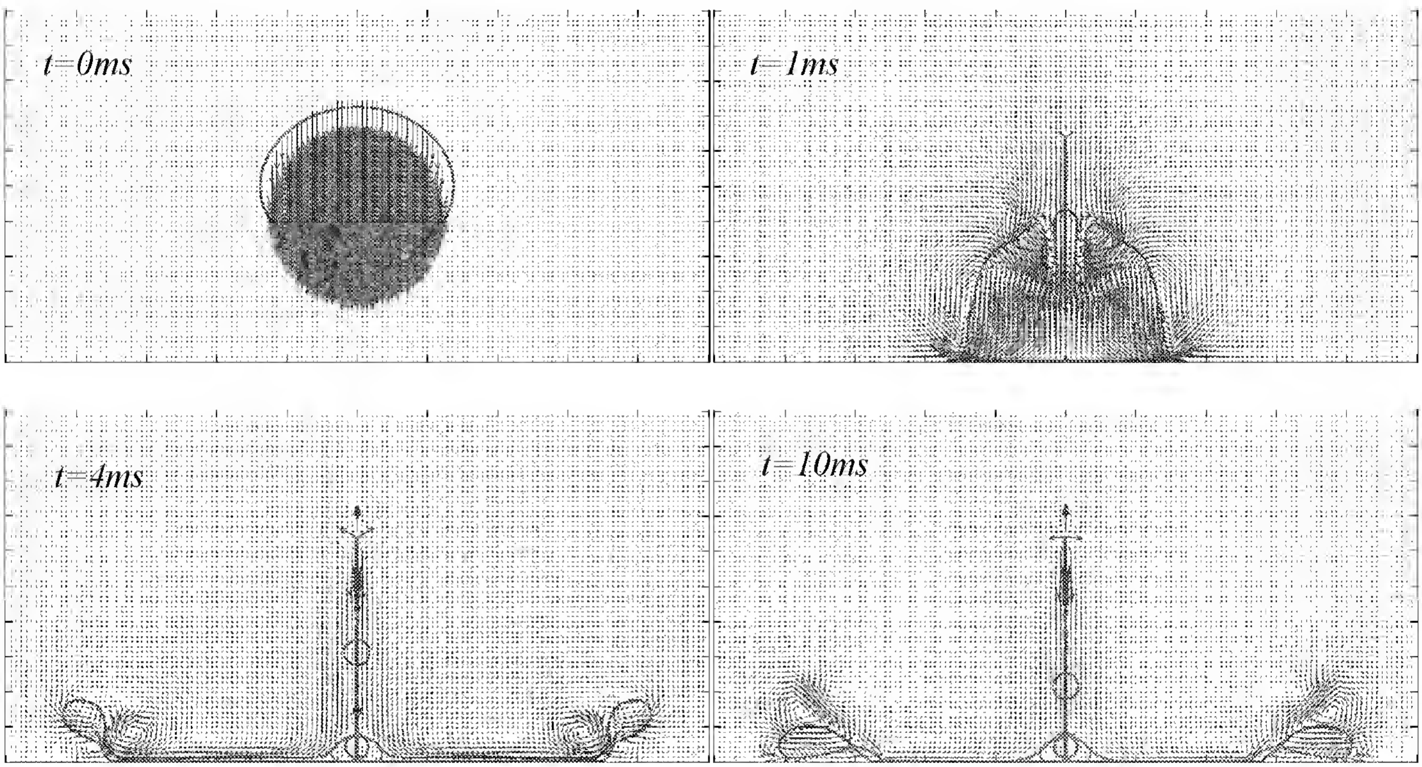

Oh=0.008, *Re*=2500

Summary

- A splashing map has been obtained for :
  - (1) Isothermal and Non isothermal surfaces,
  - (2) Different surface finishes
  - (3) Different fluids

Future Work

- Drop tower rig experimental will extend the parametric range
- Numerical code development will account for splash products

Flow around a cylinder immersed in a dense granular flow

D. Chehata, R. Zenit
Instituto de Investigaciones en Materiales,
Universidad Nacional Autónoma de México, Apdo. Postal 70-360,
Ciudad Universitaria, Coyoacán D.F. 04510, México

C. R. Wassgren
School of Mechanical Engineering,
Purdue University, West Lafayette IN 47907-1288, USA

The flow around a fixed cylinder immersed in a uniform granular flow is studied experimentally. Experiments are performed in a tall vertical chute that produces a quasi two-dimensional granular flow. A storage bin at the top of the chute feeds glass particles into the channel while the mean velocity of the flow is controlled by varying the width of a hopper located at the channel exit. Measurements of the drag force acting on a fixed cylinder are made using a strain gauge force measurement system. The flow velocity field is measured through a transparent wall using particle image velocimetry analyses of high speed video recordings of the flow. Experiments are performed for a range of upstream particle velocities, cylinder diameters, and two diameters of glass particles.

For the range of velocities studied, the drag force acting on the cylinder is independent of the mean flow velocity, contrary to what is expected from any ordinary fluid. The drag force scales with the asymptotic static stress state in a tall granular bed. The drag coefficient, defined in terms of a dynamic pressure, scales with the flow Froude number and a length scale parameter that accounts for the effective cylinder size.

Although the drag force on the cylinder does not change with the upstream flow velocity, the flow streamlines do, in fact, change with velocity. A large stagnation zone forms at the leading edge of the cylinder while at the trailing edge an empty wake is observed. The wake size increases with flow velocity.

Collisional granular flow around an immersed cylinder

C.R. Wassgren
School of Mechanical Engineering, Purdue University

R. Zenit
Instituto de Investigaciones en Materiales,
Universidad Nacional Autónoma de México

A. Karion
Carderock Division, Naval Surface Warfare Center

A two-dimensional collisional granular flow past an immersed cylinder is investigated using discrete element computer simulations. The drag force acting on the cylinder, F_d, is proportional to the upstream bulk density, $\rho\nu_\infty$, where ρ is the upstream particle mass density and ν_∞ is the upstream solid fraction, the square of the upstream velocity, U_∞, and the sum of the cylinder diameter, D, and surrounding particle diameter, d. The drag coefficient, defined as $C_d = (2F_d)/(\rho\nu_\infty U_\infty^2(D+d))$ has a strong dependence on the flow Knudsen number and a secondary weak dependence on the Mach number. The drag coefficient decreases slightly with decreasing coefficient of restitution and is relatively insensitive to the inter-particle friction coefficient. Bow shock structures and expansion fans similar to those observed in compressible fluid flows are also observed.

Exposition Session
Topical Area 4:
Multiphase Flow and Phase Change

FUNDAMENTAL STUDIES ON TWO-PHASE GAS-LIQUID FLOWS THROUGH PACKED BEDS IN MICROGRAVITY

Vemuri Balakotaiah
University of Houston

Mark J. McCready
University of Notre Dame

Brian J. Motil
NASA Glenn Research Center

ABSTRACT

In the typical operation of a packed-bed reactor, gas and liquid flow simultaneously through a fixed bed of solid particles. Depending on the application, the particles can be of various shapes and sizes and provide for intimate contact and high rates of transport between the phases needed to sustain chemical or biological reactions. The packing may also serve as either a catalyst or as a support for growing biological material. NASA has flown two of these packed-bed systems in a microgravity environment with limited or no success (Motil et al. [1]). The goal of this research is to develop models (with scale-up capability) needed for the design of the physicochemical equipment to carry out these unit operations in microgravity. New insight will also lead to improvements in normal gravity operations.

Our initial experiment was flown using an existing KC-135 two-phase flow rig with a modified test section. The test section is a clear polycarbonate rectangular column with a depth of 2.54 cm, a width of 5.08 cm, and 60 cm long. The column was randomly packed with spherical glass beads by slowly dropping the beads into the bed. Even though care was taken in handling the column after it was filled with packing, the alternating high and low gravity cycles with each parabola created a slightly tighter packed bed than is typically reported for this type. By the usual method of comparing the weight difference of a completely dry column versus a column filled with water, the void fraction was found to be .345 for both sizes of beads used. Five flush mounted differential pressure transducers are spaced at even intervals with the first location 4 cm from the inlet port and the subsequent pressure transducers spaced at 13 cm intervals along the column. Differential pressure data was acquired at 1000 Hz to adequately observe pulse formation and characteristics. Visual images of the flow were recorded using a high-speed SVHS system at 500 frames per second. Over 250 different test conditions were evaluated along with a companion set of tests in normal gravity. The flow rates, fluid properties and packing properties were selected to provide a range of several orders-of-magnitude for the important dimensionless parameters.

The well known Ergun equation for single phase flow through porous media is written by superposing the pressure drop expression for purely viscous (Blake-Kozeny) and purely inertial losses (Burke-Plummer):

$$\frac{-\Delta P}{Z} = 150\frac{(1-\varepsilon)^2}{\varepsilon^3}\frac{\mu U}{D_p^2} + 1.75\frac{(1-\varepsilon)}{\varepsilon^3}\frac{(\rho U)U}{D_p} \quad \text{where}$$

ε = void fraction, U = fluid superficial velocity, D_P = packing diameter, and Z = column length.

For two-phase flow in the microgravity environment, the measured pressure drop is the true frictional pressure drop since the hydrostatic head is nearly zero. Through dimensional arguments (neglecting gravity and the bed inclination), the non-dimensional form of the pressure drop is:

$$\frac{-\Delta P}{Z}\frac{D_P}{\rho_L U_{LS}^2} = f\left[\varepsilon,\ Re_{GS},\ \frac{1}{Re_{LS}},\ \frac{1}{We_{LS}},\ \frac{\rho_G}{\rho_L},\ \frac{\mu_G}{\mu_L}\right]$$

The pressure drop may be assumed to be a weak function of the last two ratios (density and viscosity) as they are small and do not vary significantly. Rearranging into a dimensionless form and adding an expression for the gas Reynolds number and liquid Weber number, the form of the modified Ergun equation becomes:

$$\frac{-\Delta P}{Z}\frac{D_P}{\rho_L U_{LS}^2} = \frac{150(1-\varepsilon)}{Re_{LS}} + \beta\left(\frac{Re_{GS}}{(1-\varepsilon)}\right)^{a}\left(\frac{(1-\varepsilon)}{Re_{LS}}\right)^{b}\left(\frac{1}{We_{LS}}\right)^{c} + 1.75$$

Determining the parameters by regression, we find that a=1/2, b=1/3, c=2/3 and β =0.8. Recognizing that $\frac{1}{Ca_{LS}} = \frac{Re_{LS}}{(1-\varepsilon)We_{LS}}$, the final form of the modified Ergun equation is:

$$f = \frac{-\Delta P}{Z}\frac{D_P}{\rho_L U_{LS}^2} = \frac{(1-\varepsilon)}{Re_{LS}}\left[150 + 0.8\left(\frac{Re_{GS}}{(1-\varepsilon)}\right)^{\frac{1}{2}}\left(\frac{1}{Ca_{LS}}\right)^{\frac{2}{3}}\right] + 1.75$$

The figure below shows two examples of the experimental data and the corresponding modified Ergun equation. Each plot represents a specific Suratman number indicated in the legend: $\left(Su = \frac{Re_{LS}}{Ca_{LS}(1-\varepsilon)} = \frac{\rho_L D_P \sigma}{\mu_L^2(1-\varepsilon)}\right)$

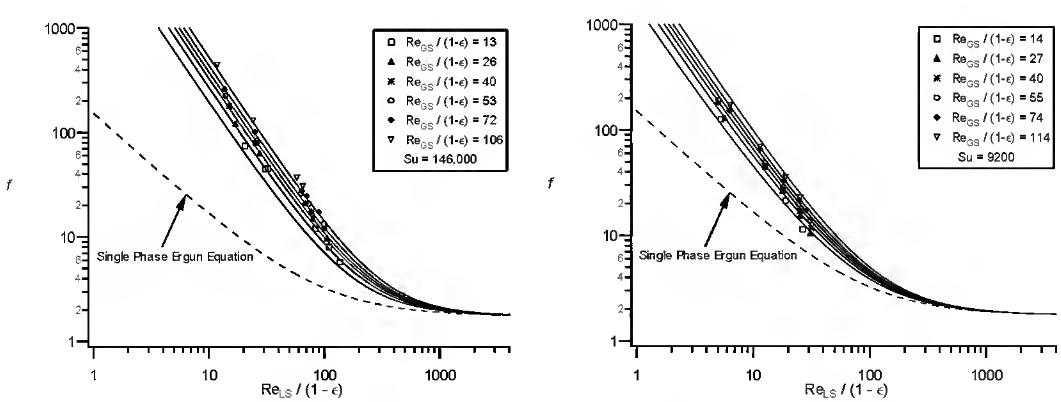

Plot of modified Ergun equation for two Suratman numbers.

[1] Motil, B. J., Balakotaiah, V., Kamotani, Y., "Effects of Gravity on Cocurrent Two-Phase Gas-Liquid Flows Through Packed Columns," AIAA-2001-0767 (2001).

Principal Investigator: Vemuri Balakotaiah, University of Houston

Co-Investigators: Mark J. McCready, University of Notre Dame
Brian J. Motil, NASA Glenn Research Center

Our goal is to develop a fundamental understanding of the role of gravity on two-phase gas-liquid flow through a fixed bed of solid particles by:

- Determining the flow patterns and transition boundaries in microgravity and testing the validity of flow regimes maps based on data in 1-g.
- Measuring the true frictional pressure drop for co-current gas-liquid flow through packed-beds and testing the validity of pressure drop correlations based on 1-g data.
- Studying the influence of gravity on pulse frequency and amplitude.

Experimental Setup for KC-135 Aircraft

- 8 flights - over 250 test conditions flown on NASA KC-135 aircraft (20 sec/run)
- Duplicated conditions for 1-g
- Rectangular cross section
  2.5 cm x 5 cm x 60 cm long
- 5 differential pressure trans. (1000 Hz)
- 2 cm and 5 cm spherical glass beads
- High speed video (500 fps)
- Air and Water-Glycerin (1 to 20 cP)
- $0.03 < G < 0.8$ kg/(s m^2)
- $3 < L < 50$ kg/(s m^2)
- $0.18 < Re_{LS} < 100$
- $4 \times 10^{-4} < We_{LS} < 0.2$
- $900 < Su_L < 365{,}000$

Why Packed Bed Reactors in Microgravity?

- Considered an “enabling technology” for NASA
  - Water processing (catalytic beds)
  - Reduce expendables (biological reactors)

- Two systems flown in microgravity environment with limited or no success
  - Volatile Removal Assembly Flight Experiment (VRAFE) STS-89
  - Biological Reactor tests on KC-135

- Better understanding of the role of gravity can lead to improved models for terrestrial reactors

Flow Regime Transition in Microgravity

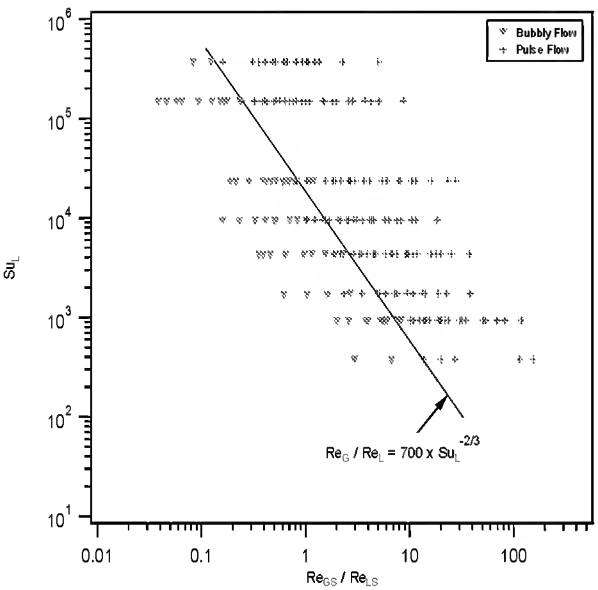

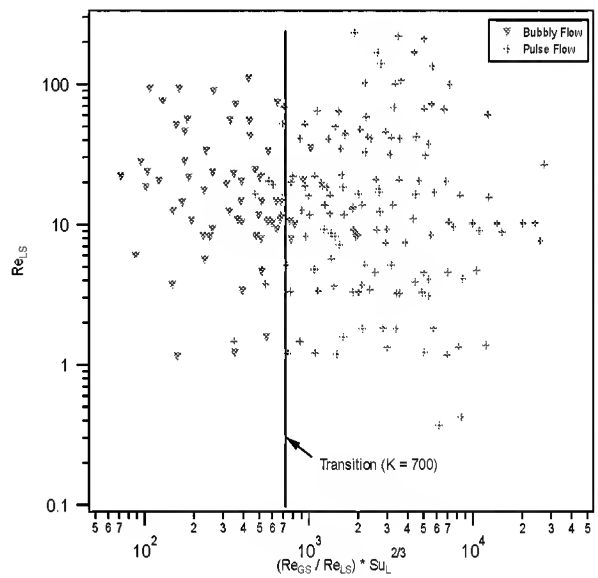

- Bubble-Pulse transition is a function of gas and liquid Reynolds numbers and the liquid Suratman number, where:

$$Su_L = \frac{Re_{LS}}{Ca_{LS}} = \frac{Re_{LS}^2}{We_{LS}} = \frac{d_P \rho_L \sigma}{\mu_L^2}$$

Effects of Gravity on Pulse Characteristics and Pressure Drop

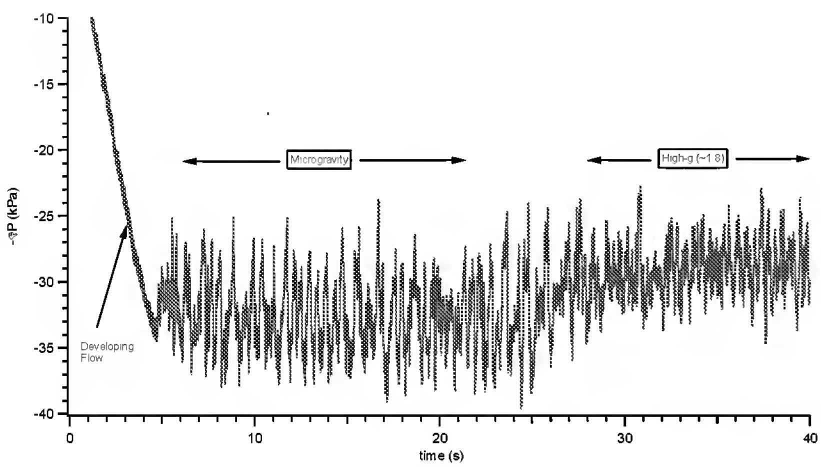

- With increasing gravity:
  - Pulse amplitude decreases
  - Pulse frequency increases

- As gas flow is increased, the average pressure drop difference between normal and microgravity decreases.

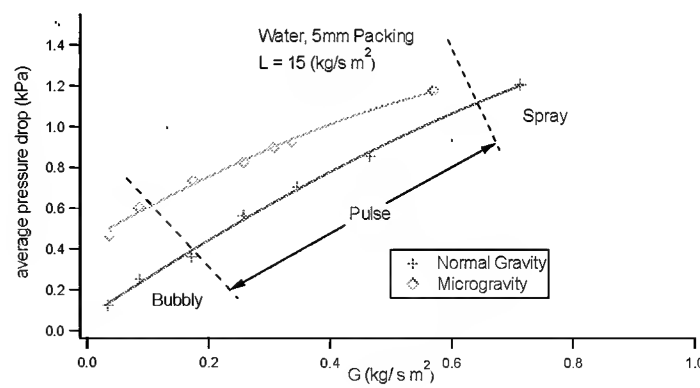

Lockhart-Martinelli Correlation

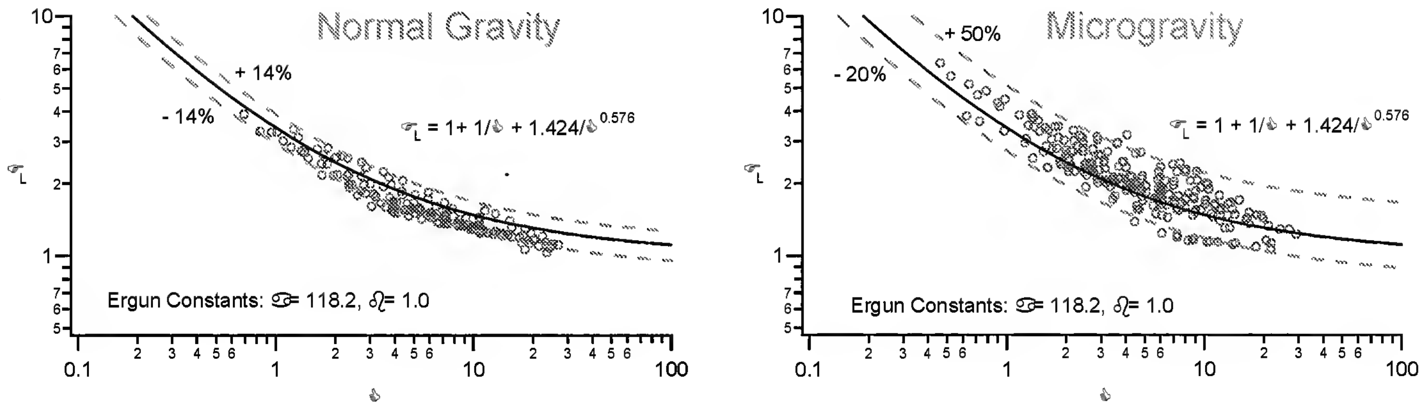

- Scatter is increased in the microgravity environment, an indication of the degree to which the capillary or surface tension effects are masked by hydrostatic head.

Frictional Pressure Drop in Microgravity

- Using Buckingham-Pi theorem, the dimensionless two-phase pressure drop can be written as:

$$\frac{-\Delta P}{Z}\frac{d_P}{\rho_L U_{LS}^2} = \mathrm{f}\left[\frac{Su_L}{Re_{LS}^2}, \frac{1}{Re_{LS}}, Re_{GS}, \varepsilon\right]$$

- Apply limiting cases
  1. In limit of zero interfacial tension between fluids, reduces to single phase.
  2. In the limit of zero gas flow, reduces to single phase.
  3. In the inertia dominated limit, the friction factor should be independent of the interfacial and viscous terms.

$$f_{\mathrm{TP}} - f_{\mathrm{SP}} = \gamma\left(\frac{Re_{GS}}{1-\varepsilon}\right)^a \left(\frac{1-\varepsilon}{Re_{LS}}\right)^b \left(\frac{(1-\varepsilon)^2 Su_L}{Re_{LS}^2}\right)$$

- Determining parameters by regression, reduces to:

$$f_{\mathrm{TP}} = \frac{-\Delta P}{Z}\frac{d_P}{\rho_L U_{LS}^2}\frac{\varepsilon^3}{1-\varepsilon} = \frac{1-\varepsilon}{Re_{LS}}\left[180 + 0.8\left(\frac{Re_{GS}}{1-\varepsilon}\right)^{\frac{1}{2}}\left(\frac{Su_L(1-\varepsilon)}{Re_{LS}}\right)^{\frac{2}{3}}\right] + 1.8$$

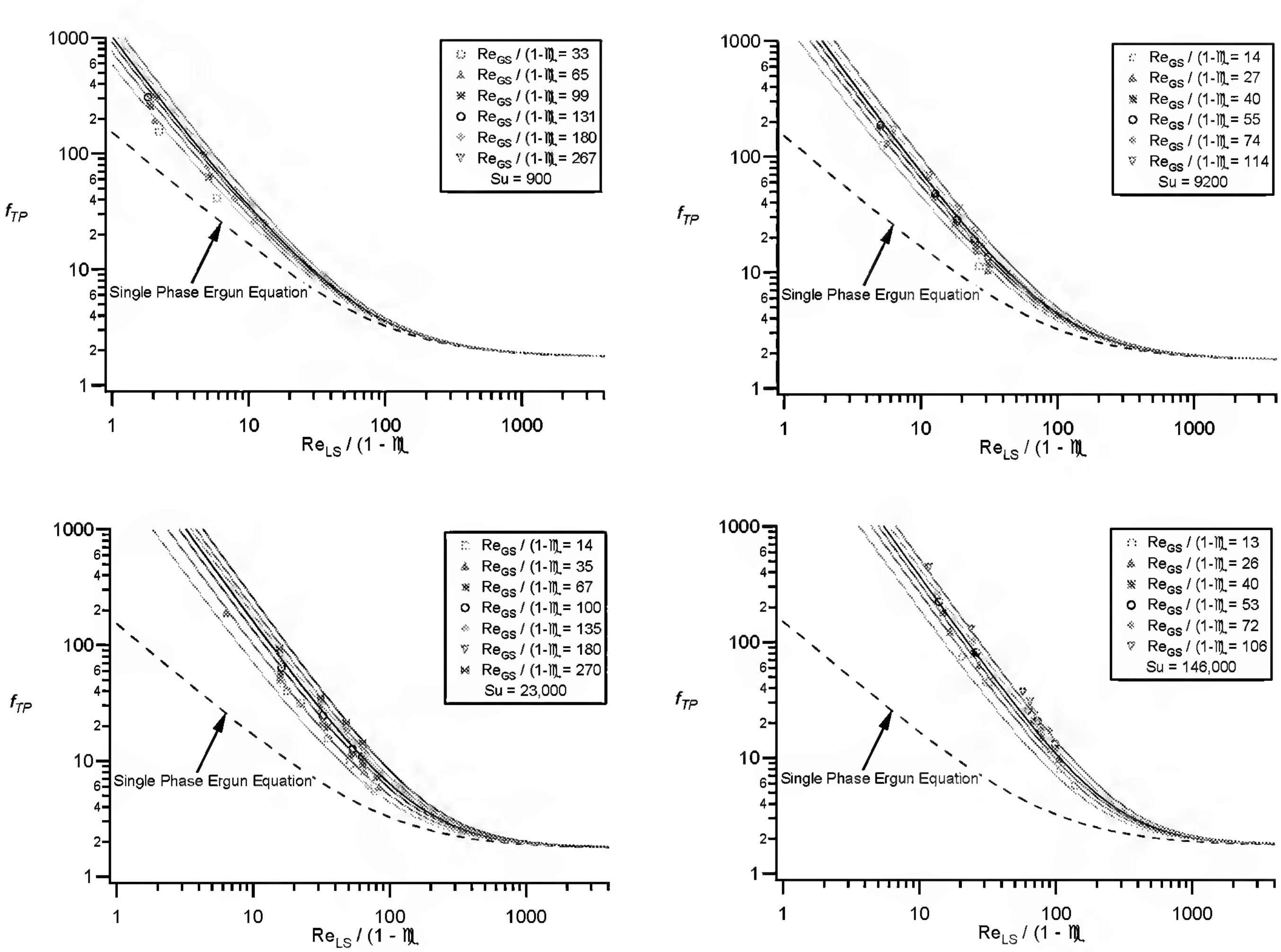

Re_GS / (1-η_L) = 33
Re_GS / (1-η_L) = 65
Re_GS / (1-η_L) = 99
Re_GS / (1-η_L) = 131
Re_GS / (1-η_L) = 180
Re_GS / (1-η_L) = 267
Su = 900
Single Phase Ergun Equation
f_TP
Re_LS / (1 - η_L)
Re_GS / (1-η_L) = 14
Re_GS / (1-η_L) = 27
Re_GS / (1-η_L) = 40
Re_GS / (1-η_L) = 55
Re_GS / (1-η_L) = 74
Re_GS / (1-η_L) = 114
Su = 9200
Re_GS / (1-η_L) = 14
Re_GS / (1-η_L) = 35
Re_GS / (1-η_L) = 67
Re_GS / (1-η_L) = 100
Re_GS / (1-η_L) = 135
Re_GS / (1-η_L) = 180
Re_GS / (1-η_L) = 270
Su = 23,000
Re_GS / (1-η_L) = 13
Re_GS / (1-η_L) = 26
Re_GS / (1-η_L) = 40
Re_GS / (1-η_L) = 53
Re_GS / (1-η_L) = 72
Re_GS / (1-η_L) = 106
Su = 146,000

Preliminary Conclusions

- Pulse flow exists in a wider range of gas and liquid flow rates compared to normal gravity.

- 1-g flow regime maps (with Fr number set to zero) were found to be not valid for predicting microgravity flow regime transitions.

- Interfacial effects were found to increase the pressure drop by as much as 300% compared to that predicted by single-phase Ergun equation.

- Lockhart-Martinelli correlation gives much larger errors in microgravity and is not reliable in predicting the pressure drop either in the bubble or pulse flow regimes.

- Pulse amplitude depends strongly on gravity level (with high gravity levels suppressing pulse formation).

Phase-Field Methods for Structure Evolution in Sheared Multiphase Systems

Vittorio Badalassi*, Hector Ceniceros**, Sanjoy Banerjee*
Department of Chemical Engineering
Department of Mathematics
University of California, Santa Barbara

A homogeneous disordered phase separates into ordered structures when quenched into a broken-symmetry phase. The competition of broken-symmetry phases to select an equilibrium state may be studied in terms of coarse-grained order parameters described by a suitable Landau free-energy function. A network of equilibrium-phase domains develops on quenching and coarsens with time with a topology that may be controlled by shear. We use three-dimensional simulations, in which time-dependent models for conserved–order parameters coupled to Navier-Stokes fluid models are solved, to investigate the evolution of such domains, e.g. spinodal decompositions of polymeric materials under shear. The numerical problems are formidable because of the strong nonlinearities inherent in the coupled model, and these are amongst the first 3D calculations undertaken.

In linear shear fields we find stable nanostrings, also recently seen in experiments. The affinity of the ordered phases to boundaries plays a role in the form of the structures that develop, with stacked plate-like phase distributions emerging under certain conditions. Such methods appear quite promising for design and analysis of multiphase and complex fluid formulations. The behavior of foams in such conditions is of particular interest in microgravity environments.

Phase-field Methods for Structure Evolution in Sheared Multiphase Systems

V. E. Badalassi[1], H. D. Ceniceros[2], S. Banerjee[1]

Dept. of [1]Chemical Engineering & Dept. of [2]Mathematics, University of California – Santa Barbara

Financial Support: [1]NASA – Contract No. NAG3-2414, [2]Academic Senate Junior Faculty Research Award

Phase fields models (e.g. the coupled Cahn-Hilliard/Navier-Stokes system, also called Model H) offer a systematic physical approach for investigating complex multiphase systems such as near-critical interfacial behavior, phase separation under shear, and microstructure evolution during solidification, but the models involve multiple scales and are nonlinear. Therefore, they are difficult to solve. We present here the first 3D continuum simulation of Model H that shows formation of string and plate-like structures.

Phase Field Theory

We consider as free energy of an inhomogeneous system $A[C]=\int_\Omega \left\{\beta\psi(C)+\frac{1}{2}\alpha|\nabla C|^2\right\}$

ψ is the homogeneous free energy (double well pot.), $|\nabla C|^2$ is the gradient free energy.
At equilibrium we expect the functional $A[C]$ to be a minimum with respect to variations of the function C: $\mu(C)=\frac{\delta A}{\delta C}=\beta\psi'(C)-\alpha\nabla^2 C=0$ with $\sigma\propto\sqrt{\alpha\beta}$ and $\xi\propto\sqrt{\alpha/\beta}$

Model B (Cahn-Hilliard, (1959))

$$\frac{\partial C}{\partial t}=\nabla\cdot\chi\nabla\mu$$

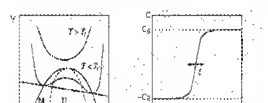

Schematic picture of the homogeneous specific free energy ψ as a function of C (left) and the equilibrium interface profile (right).

Model H (Hohenberg, Halperin, (1977))

Cahn Hilliard + phase field modified Navier-Stokes eqs.:

$$\frac{\partial C}{\partial t}+\vec{v}\cdot\nabla C=\frac{1}{Pe}\nabla\cdot\chi\nabla\mu$$

$$Re\left[\frac{\partial\vec{v}}{\partial t}+\left(\vec{v}\cdot\vec{\nabla}\right)\vec{v}\right]=-\vec{\nabla}p+\vec{\nabla}\cdot\left(\vartheta\left(\vec{\nabla}\vec{v}+\vec{\nabla}\vec{v}^T\right)\right)+\frac{1}{Ca}\mu\vec{\nabla}C$$

$\rho,\eta,\sigma,\vartheta,\chi$ are density, viscosity, surface tension, normalized viscosity and mobility

$$Re=\frac{\rho U_0 L_0}{\eta},\ Ca=\frac{2\eta U_0}{3\sigma},\ Pe=\frac{U_0 L_0}{M_0\beta}.$$

The Numerical Method

(1) Solve C-H eq. with a semi-implicit method and spectral spatial discretization to obtain C^{n+1}:

$$\frac{C^{n+1}-C^n}{\Delta t}+\vec{v}^n\cdot\nabla C^n=\frac{1}{Pe}\left[a\nabla^2\mu^{n+1}+\nabla\cdot\chi^n\nabla\mu^n-a\nabla^2\mu^n\right]$$

If $a\geq\frac{1}{2}\max\chi$ the method is unconditionally stable. For the nonlinear term $\psi'(C)$ in μ^{n+1} we write $\nabla^2\psi'(C)=\nabla(\psi''\nabla C)$ and let $a=\frac{1}{2}\max(\psi''(C))=\frac{1}{2}\psi''(\pm 1)=1$

(2) Using C^{n+1} compute the surface force and solve the modified N-S eqs. with a projection method to obtain $\vec{v}^{n+1}$. The variable viscosity term is also treated semi-implicitly. The spatial discretization is spectral in the stream-wise and span-wise directions and a combination of spectral and "spectral-like" compact finite difference in the wall normal direction.

To achieve higher accuracy and damp high frequency components (from non-linearities) we embed the Euler time advancements in each step in a third order T.V.D. Runge-Kutta Method.

Scaling of Coarsening Process in 2D Phase Separation

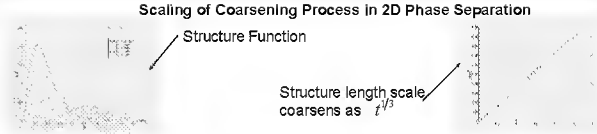

2D Phase Separation in a Channel under Shear

$Pe=7.5,\ Re=0.1,\ Ca=0.5$

$Pe=37.5,\ Re=0.5,\ Ca=2.5$
(5 X previous shear rate)

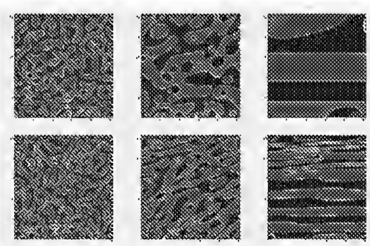

3D Phase Separation

$\chi=1$

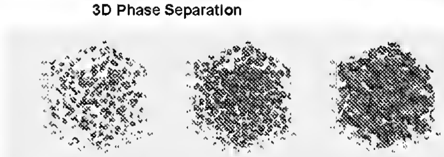

3D Phase Separation in a Channel under Shear forms Plates and Strings

$Pe=5,\ Re=0.12,\ Ca=20$

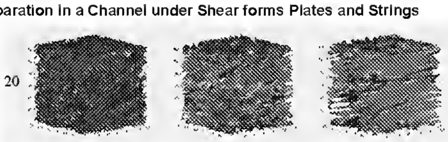

Conclusions

- Numerical scheme effectively handles thin interfaces, viscosity contrast, and inertial effects
- Scaling behavior is predicted by Lifshitz-Slyozov theory (1961)
- Similar structures are found in experiments by Hashimoto (1995), and Onuki (1997)

Computational Techniques for Multiphase Flow and Transport in Microgravity Environments

Ravi Chella, Chemical Engineering, Florida State University, Tallahassee, FL 32310

A mesoscopic approach is taken for modeling flow in multiphase systems, with the system characterized by a coarse-grained conserved order parameter that takes characteristic values in the bulk phases and varies continuously in a narrow interfacial region). This approach (Chella, R. and Vinals, J, "Mixing of a two-phase fluid by cavity flow", Phys. Rev. E 53 , 3832 (1996)) provides significant computational advantages over classical continuum approaches. This formulation has been extended to incorporate interactions with solid boundaries through modification of free energy functionals to include short-range and long range interactions with the walls. This approach has been implemented using a lattice-Boltzmann approach.

Development of Parallel MPI program

To facilitate application of the the lattice-Boltzmann method for immiscible transport to three-dimensional and irregular geometries, a parallel version of the program was developed using MPI (Message Passing Interface) . Both three-dimensional and one-dimensional domain decompositions were tested. Superlinear speedup was observed. This is expected to be due to the large memory requirements for the lattice Boltzmann method in three-dimensions which results in extensive memory paging for all but the smallest systems.

Evolution of microstructure and rheology in complex fluids under externally applied flows

The influence of shear and extensional flows in retarding phase separation and stabilizing certain morphologies was investigated. In particular, the interplay between interfacial tension and viscosity differences between phases are examined. Specific applications are to binary fluids undergoing spinodal decomposition, and the nucleation and growth of droplets. In binary liquid mixtures, the morphology of the phase separating domain varies from interconnected domains (bicontinuous patterns) to droplets, depending on composition and quench depth. Hydrodynamics significantly influences the dynamics of phase separation. For sufficiently strong flows, a non-equilibrium morphology can be stabilized. Results of a simulation of two-dimensional spinodal decomposition under shear is shown. The steady state lamellar morphology developed for three cases corresponding to a Capillary number Ca=0.1, and dimensionless shear-rates of 0.05, 0.075 and 0.1,respectively, are shown below in Fig. 1. Scaling relationships for the structure factor

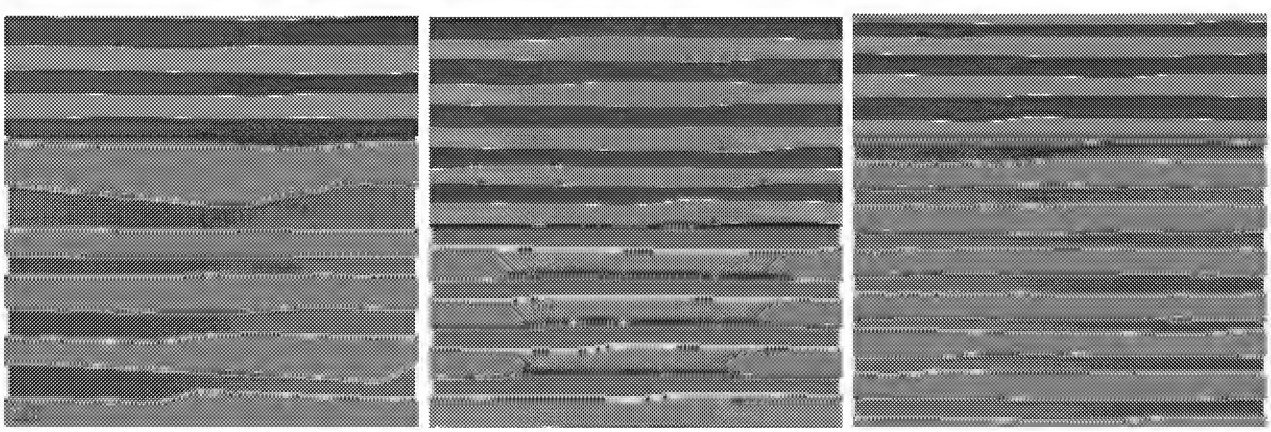

Figure 1: Steady state morphology for shear rates: (a) 0.05, (b)0.075, (c) 0.1

and the growth law of the characteristic domain size length scale were verified for spinodal decomposition in two and three-dimensions for the case of no externally imposed flow. For spinodal decomposition under shear, the system is no longer isotropic, and a useful measure of the morphology of the system is given by:

$$\mathbf{A} = \frac{< \nabla\phi\nabla\phi >}{< |\nabla\phi|^2 >}$$

As the order parameter ϕ varies rapidly in the interfacial region, $\nabla\phi$ is in the direction normal to the interface. Under shear, the off-diagonal components of $\mathbf{A}$ tend to zero at long times because of the alignment of the interfaces along the flow direction. In two-dimensions, for a lamellar structure $A_{xx} \rightarrow 0, A_{yy} \rightarrow constant$, where x is the flow-direction and y the shear direction. For $S \geq 0.05$, a stable lamellar morphology is obtained. In two dimensions, it is relatively easy to directly measure the interfacial length, and the proportionality of $< |\nabla\phi|^2 >$ to the surface to volume ratio is verified. In three-dimensional simulations, it is difficult to directly measure the interfacial area, but $|\nabla\phi|^2$ is readily calculated. The off-diagonal terms of $\mathbf{A}$ tend to zero for long times, and examination of the diagonal terms allow the steady state morphology to be characterized.

Simulations have been carried out both for spinodal decomposition and nucleation and growth under shear. Both cyclic (Lee's) and solid boundary conditions are used. At long times both lamellar and tubular structures are observed depending on the capillary number, shear rate, and the volume fraction of the two phases. Work is underway both theoretically using stability considerations, and computationally to relate the morphology to the shear rate, interfacial tension and viscosity ratio.

The evolution of the scattering pattern in planes parallel to the flow direction were determined and found to be in good qualitative agreement with experimental light scattering measurements on phase separation under shear by Professor Beysen's group, reported in the literature. Contributions of the domains to the excess viscosity $\delta\eta$ and the normal stresses W_1 and W_2 in the weak-shear regime [Onuki, A, Phys. Rev. A, 35, 5149 (1987)]: were calculated for different fluid properties and processing conditions.

Spinodal Decomposition in Confined Geometries

In phase separation in confined geometries, bicontinuous, capsule, or plug configurations have been experimentally observed depending depending on the relative strength of the interfacial to wetting forces. The influence of solid surfaces on the dynamics of phase separation in confined geometries in three-dimensions was investigated. The influence of both long range and short range surface forces are of interest. Results of a simulation that show the transition from from plug to continuous configurations with increasing magnitude of surface forces are shown in Fig. . In larger channels an intermediate capsule regime is also observed.

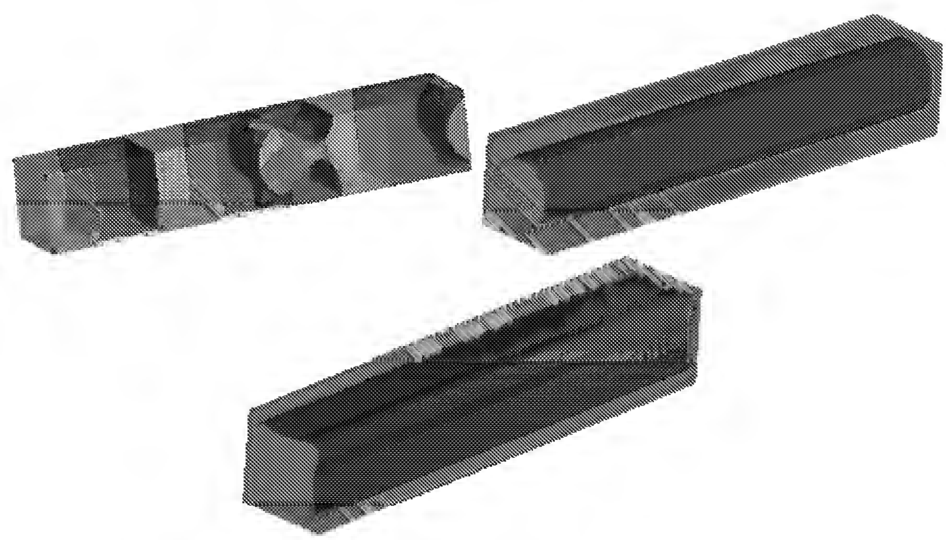

Figure 2

EXPERIMENTS ON HYDRODYNAMIC AND THERMAL BEHAVIORS OF THIN LIQUID FILMS FLOWING OVER A ROTATING DISK INCLUDING NUCLEATE BOILING

Basar Ozar, Baki M. Cetegen and Amir Faghri *
Mechanical Engineering Department
University of Connecticut, Storrs, CT 06269-3139

ABSTRACT

Experiments on characterization of thin liquid films over stationary and rotating disks are described in this study. The thin liquid film is created by controlled liquid impingement by introducing deionized water from a flow collar at the center of an aluminum disk at a known initial film thickness with uniform radial velocity. Experiments were performed for a range of Reynolds numbers based on the liquid inlet gap height and velocity and (flow rates) between 238 (3.0 lpm) and 1188 (15.0 lpm). The angular speed of the disk was varied from 0 rpm to 300 rpm. Radial film thickness distribution was measured using a non-intrusive laser light reflection technique that enabled the measurement of the instantaneous film thickness over a finite segment of the disk. When the disk was stationary, a circular hydraulic jump was present. The liquid film thickness in the subcritical region (downstream of the hydraulic jump) was an order of magnitude greater than that in the supercritical region (upstream of the hydraulic jump) which was of the order of 0.3 mm. As the Reynolds number increased, the hydraulic jump migrated toward the edge of the disk. In case of rotation, the liquid film thickness exhibited a maximum on the disk surface. The liquid film inertia and friction influenced the inner region where the film thickness progressively increased. The outer region where the film thickness decreased was primarily affected by the centrifugal forces. A flow visualization study of the thin film was also performed to determine the characteristics of the waves on the free surface. At high rotational speeds, radial waves were observed on the liquid film. It was also found that the tangent of the waves present on the liquid surface was a function of the ratio of local radial velocity and local azimuthal velocity. Radial temperature distribution was measured using an amplified thermocouple/slip ring arrangement. Local Nusselt number was seen to increase with flow rate and angular velocity. The inertia forces rather than rotation was found to have more significance on the Nusselt number at the inner parts of the disk. Semi-empirical correlations were presented in this study for the local and average Nusselt numbers. For nucleate boiling experiments, temperature profile over the disk was measured using the same amplified thermocouple/slip ring arrangement. Laser light reflection technique was utilized to measure the bubble size, its growth and motion. The bubbles were found to grow to diameters that were larger than the film thickness. The dynamics of bubble motion was characterized as a function of rotational speed of the disk, liquid flowrate over the disk as well as the overheat level.

* Principal Investigator. Phone: (860) 486-2221, Fax: (860) 486-0318,
E-mail: faghri@engr.uconn.edu

MELTING PROCESSES FOR UNFIXED PHASE CHANGE MATERIAL IN THE PRESENCE OF ELECTROMAGNETIC FIELD – SIMULATION OF LOW GRAVITY ENVIRONMENT –

Eduardo Gonçalves and **Mohammad Faghri**
Department of Mechanical Engineering
University of Rhode Island, Kingston, Rhode Island, USA

Yutaka Asako
Department of Mechanical Engineering
Tokyo Metropolitan University, Tokyo, Japan

Majid Charmchi
Department of Mechanical Engineering
University of Massachusetts, Lowell, Massachusetts, USA

ABSTRACT

Electromagnetic simulation of low-gravity environment has been numerically investigated to study the transport phenomena associated with melting of an electrically conducting Phase Change Material (PCM) inside a rectangular enclosure. Electromagnetic fields are configured in such a way that the resulting Lorentz force can be used to damp and/or counteract the natural convection as well as the flow induced by sedimentation and/or floatation, and thereby simulating the low gravity environment of outer space. Computational experiments are conducted for unfixed (top-wall heated) gallium as shown in Fig. 1. The governing equations are discretized using a control-volume-based finite difference scheme. Numerical solutions are obtained for true low-gravity environment as well as for the simulated-low-gravity. The result shows that when the Lorentz force is caused by the presence of magnetic field alone, the low-gravity condition is simulated by the damping effect, which is shown to have a profound effect on the flow field (see Fig. 2(c)). On the other hand, it is shown that under electromagnetic field simulation, where the Lorentz force is caused by the transverse electric and magnetic fields, it is possible to minimize the flow field distortion caused by the high magnetic field and therefore achieving a much better simulation of low-gravity. See Figs. 2(b) and 3.

Fig. 3 illustrate the effects of actual and simulated low-gravity on the major melting characteristics such as the Solid velocity, Melt thickness and Melt rate. As seen here, low-gravity simulated by the electromagnetic field (or electric low-gravity), show good agreement with those of actual low gravity whereas the magnetically simulated cases, show some discrepancies. Among these discrepancies are the fact that the melt rate under some ranges magnetic low-gravity (i.e., $g_B \geq g_0 10^{-3}$) are higher than those of electric low-gravity, See Fig. 3 (c). This suggests that these higher melt rate cannot be attributed to the effects of Joule heating, which would otherwise favor the electric field simulation, therefore the damping effect must be the cause. Also, the "no transient regions" on the solid velocities, suggests that the solid velocity under magnetic low-gravity respond directly to the magnetic forces, which respond much faster than the momentum diffusion associated with the melting evolution.

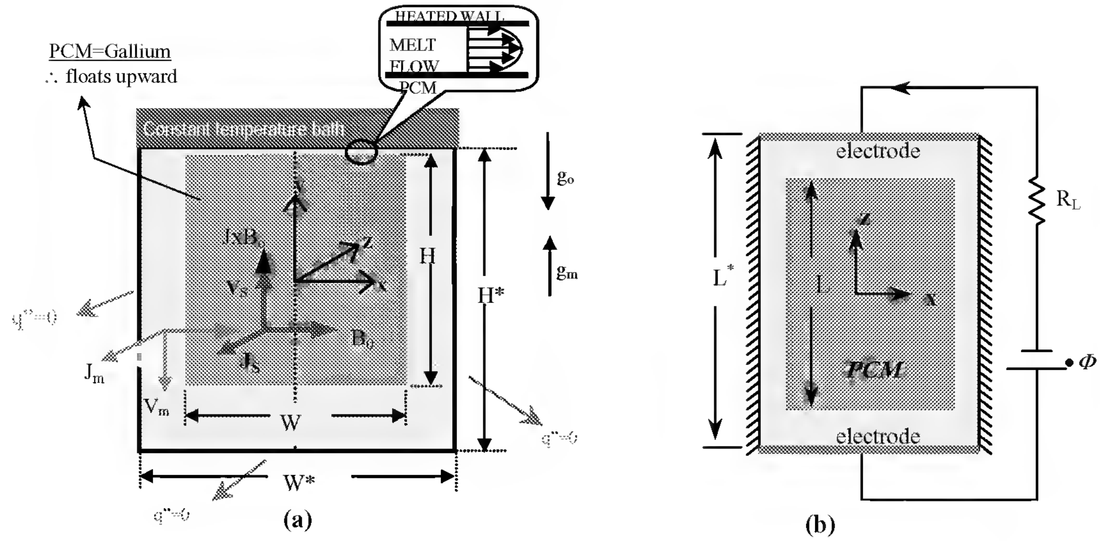

Figure 1: schematic setup of the problem:. (a) flow Configuration and (b) external circuit

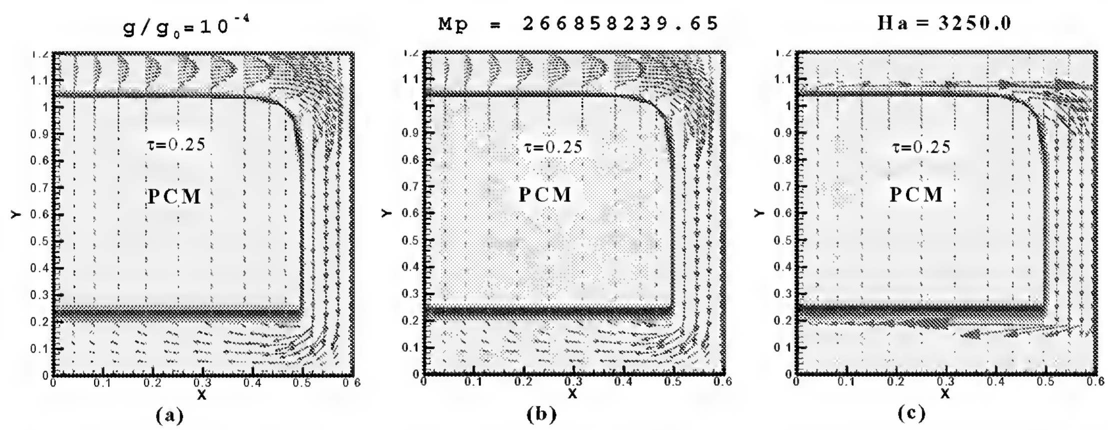

Figure 2: Effects of actual and simulated low-gravity on the melt flow structure; (a) actual low-g, (b) low-g simulation by electromagnetic field and (c) low-g simulation by magnetic field

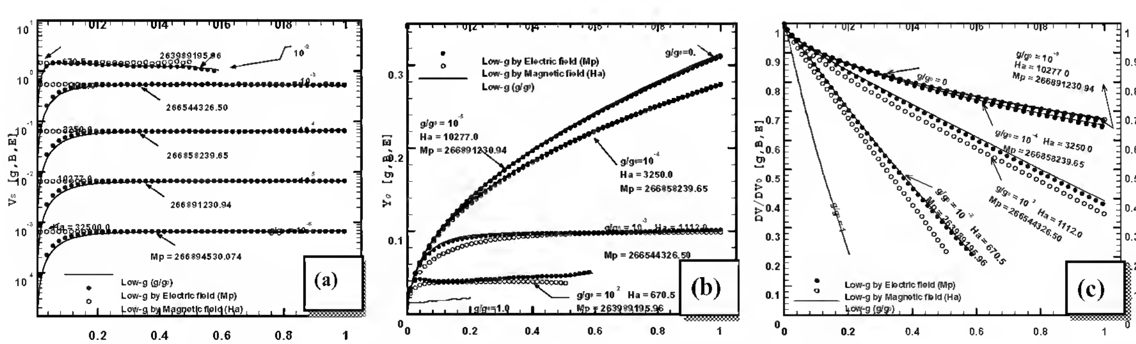

Figure 3: Effects of actual and simulated low-gravity on; (a) Solid velocity, (b) Melt thickness (c) Melt rate
Solid line = actual low-g ⇔ solid circles = electric low-g ⇔ hollow circles = magnetic low-g

INSTABILITIES AND THE DEVELOPMENT OF DENSITY WAVES IN GAS-PARTICLE AND GRANULAR FLOWS

Benjamin J. Glasser, Elizabeth D. Liss, Stephen L. Conway and Jayati Johri
Department of Chemical and Biochemical Engineering
Rutgers University
Piscataway, New Jersey 08854
Email: bglasser@sol.rutgers.edu, Tel: 732-445-4243, Fax: 732-445-2581

ABSTRACT

The dynamics of gas-particle and granular flows impact numerous technologies related to the local utilization of Lunar and Martian soils and the Martian atmosphere. On earth, such flows occur in a large number of industries including the chemical, pharmaceutical, materials, mining and food industries.

DENSITY WAVES IN GRAVITY-DRIVEN GRANULAR FLOW

A particle dynamic computer simulation is used to examine rapid granular flow in a vertical channel. Flow in the channel leads to an inhomogeneous distribution of the particles and two distinct types of density waves are identified: an S-shaped wave and a clump. The density waves are further characterized by quantifying their temporal evolution using Fourier methods and examining local and global flow properties of the system, including velocities, mass fluxes, granular temperatures and stresses. A parametric study is used to characterize the effect of the system parameters on the density waves. In particular we are able to show that the dynamics of large systems are often qualitatively and quantitatively different from those of small systems. Finally, the types of density waves and dominant Fourier modes observed in our work are compared to those that are predicted using a linear stability analysis of equations of motion for rapid granular flow.

CONNECTIONS BETWEEN DENSITY WAVES IN GAS-PARTICLE FLOWS AND COMPRESSIBLE FLOWS

It is shown that under certain simplifying assumptions, model equations of motion and continuity for the particles in a fluidized bed can be related to those of a compressible fluid acted upon by a density dependent force. A linear stability analysis shows that the

base state of the compressible flow equations can lose stability in the form of plane density waves. The plane waves emerge through a Hopf bifurcation and propagate through the bed as traveling waves. Through a bifurcation analysis coupled with parameter continuation we compute the solution structure of the fully-developed plane waves. It is found that as the amplitudes of the plane waves increase, they lose stability in the lateral direction. A comparison of these results with previous work on gas-fluidized beds shows that the salient features of the instability of a gas-fluidized bed are captured by the basic physics of compressible flows.

NASA/CP—2002-211212/VOL2

285

Instabilities and the Development of Density Waves in Gas-Particle and Granular Flows

August 2002

Benjamin J. Glasser, Elizabeth D. Liss,

Stephen L . Conway and Jayati Johri

Department of Chemical and Biochemical Engineering
Rutgers University
Piscataway, New Jersey

THE STATE UNIVERSITY OF NEW JERSEY
RUTGERS

Motivation

- The dynamics of gas-particle and granular flows impact numerous technologies related to the local utilization of Lunar and Martian soils and the Martian atmosphere.
- On earth such flows occur in a large number of industries including the chemical, pharmaceutical, materials, mining and food industries.
- Density waves are often seen in these systems, for example, the occurrence of bubbles and clusters in gas-particle flows, and clustering in granular flows.
- Density waves can have a dramatic effect on local flow properties like stresses and thus impact processing issues like attrition of particles.
- In chemical reactors, density waves can affect reactor conversion, yield and selectivity. They also lead to difficulties with scale-up which typically necessitate pilot plants and empiricism.

Bubble in fluidized bed

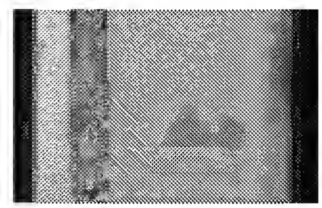

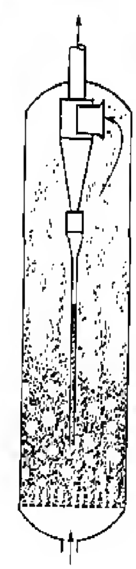

Fluidized Bed Reactor
- Kunii and Levenspiel (1991)

Density Waves in Gravity Driven Granular Flow

- Fully developed flow structures observed for each L/W variation:
  - *Total energy eventually plateaus.*
  - *Intermediate, unstable states.*
  - *Dependent on system parameters.*

Narrow pipe W/d=33.3 | Wide pipe W/d=66

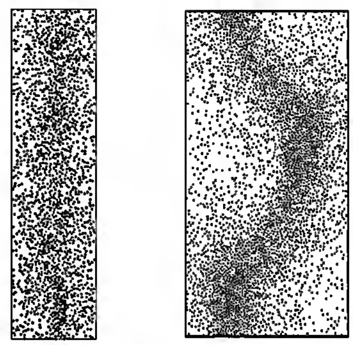

Parameters:
e_p=0.95
e_w=0.97
ν=0.31

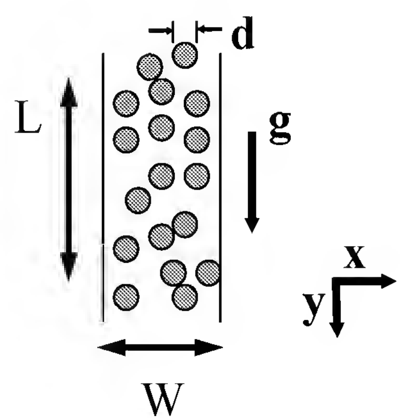

Effect of Length:

Parameters:
e_p = 0.85
e_w=0.97
ν =0.31
W/d=33.3

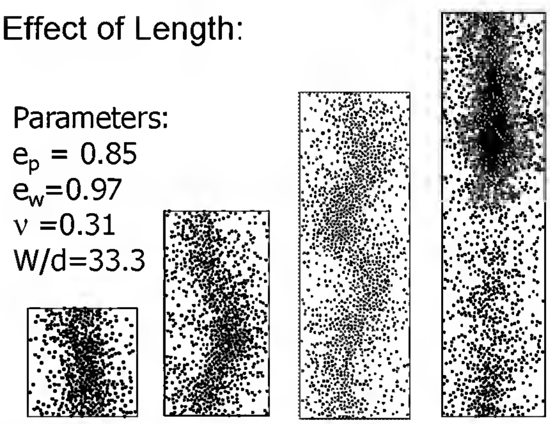

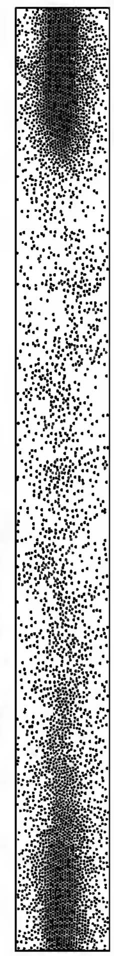

L/W = 1 | 2 | 3 | 4 | 10

Quantitative Characterization

- Depending on system parameters each of the three characteristic structures may appear at a given length to width ratio.

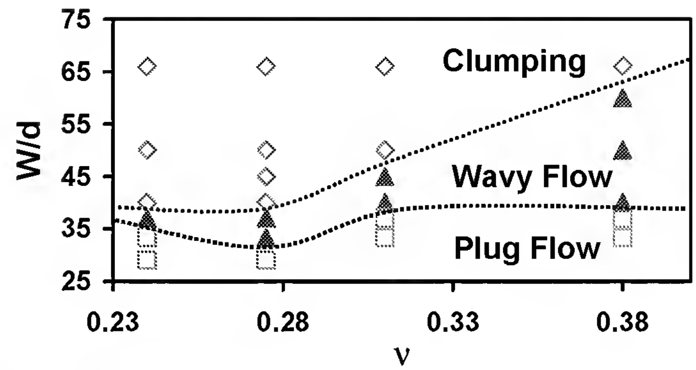

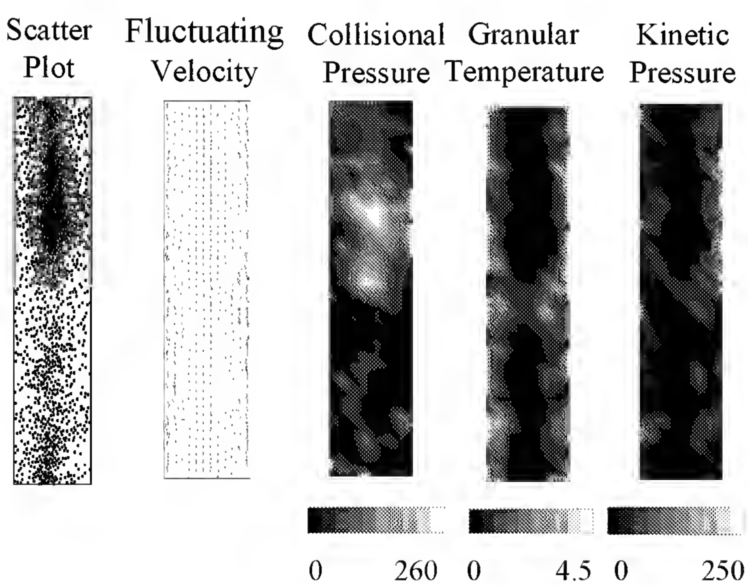

- Local flow properties can vary significantly when structure is present.
- To appropriately describe the system being examined, the correct density waves must be identified.

Density Wave Evolution

- Temporal development characterized using Fourier methods.
  - *General agreement in comparison with continuum approaches and linear stability analysis.*
    - *Wang and Tong (1998, 2001)*

Wavenumber Power Profiles

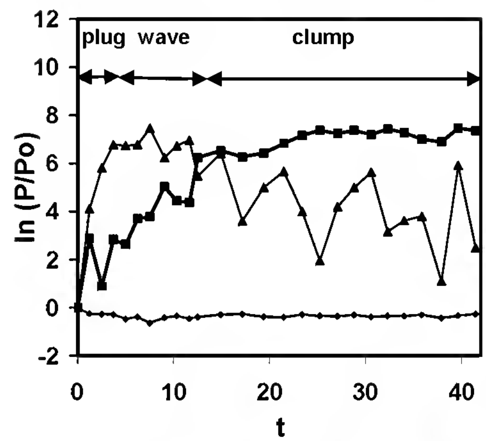

Wavenumber Power Spectra

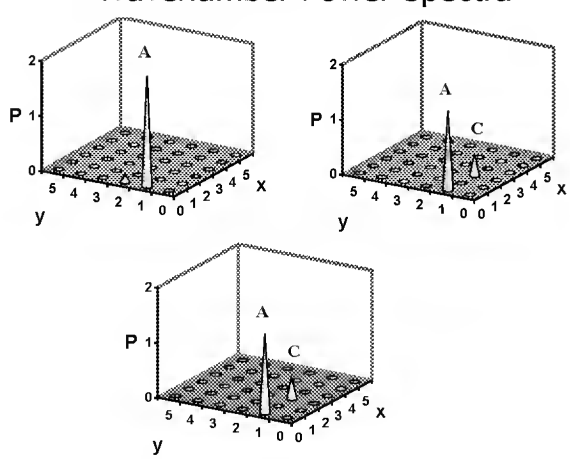

Eigenfunction Approximations

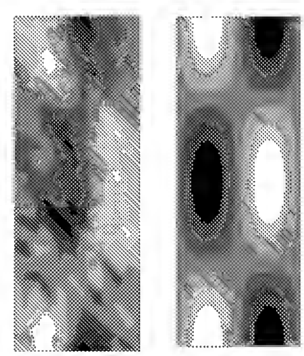

Summary of Gravity-Driven Granular Flow

- Density waves have been observed experimentally, but were attributed to the presence of interstitial fluid
  - *Poschel(1994), Horikawa* et al.*(1996), Raafat, Hulin & Herrmann (1996), Moriyama* et al. *(1998) , Aider* et al. *(1999) and Hua & Wang (1999)*
- Here, density waves are found to develop in a gravity driven granular flow in the absence of air.
- Three distinct forms of inhomogeneities have been characterized by energy, wavenumber and dependency on W/d, L/W, average solids fraction, coefficient of restitution, and friction.
- Large enough systems must be simulated to accurately capture the effects of microstructure formation on the system flow properties. The critical system size is dependent on the type of density waves present.
- Macroscopic flow properties of gravity driven flow (stress, granular temperature, etc.) are strongly affected by inhomogeneities.

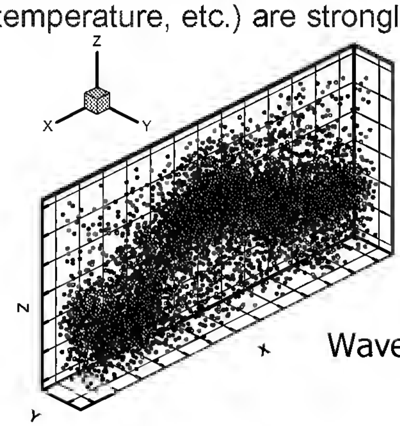

Wave in 3D system

- E. D. Liss, S. L. Conway, B. J. Glasser, "Density waves in gravity-driven flow through a channel", Physics of Fluids, Vol 14, No. 9, (2002)

Connections between Density Waves in Gas-Particle Flows and Compressible Flows

$$\frac{\partial \varepsilon}{\partial t} + \nabla .(\varepsilon \mathbf{u}) = 0$$

$$\frac{\partial}{\partial t}(1 - \varepsilon) + \nabla .[(1 - \varepsilon)\mathbf{v}] = 0$$

$$\rho_g \varepsilon \frac{D_g \mathbf{u}}{Dt} = \nabla .\mathbf{E}_g - \mathbf{f} + \varepsilon \rho_g \mathbf{g}$$

$$\rho_s (1 - \varepsilon) \frac{D_s \mathbf{v}}{Dt} = \nabla .\mathbf{E}_s + \mathbf{f} + (1 - \varepsilon) \rho_s \mathbf{g}$$

Density or voidage waves
Anderson and Jackson (1967)
Homsy et al., (1980),
Batchelor (1993) and many others

- Two phase models: complicated forms. Physical understanding of density wave formation difficult.
- Do density waves occur due to the nonlinear coupling between gas and solid phases? Or could they occur due to the solids flow itself? What is the role of gravity?

Model Equations

- Neglect terms on the order of the gas density and viscosity
- Assuming constant slip velocity between the two phases, the gas phase equations in the 2 phase model can be decoupled from the solid phase
  - Exactly true at uniform fluidization

Single phase compressible flow, $\rho=(1-\varepsilon)\,\rho_s$ **but** with density dependent force

$$\frac{\partial \rho}{\partial \mathrm{t}} + \nabla \bullet (\rho \mathbf{v}) = 0$$

$$\rho\left[\frac{\partial \mathbf{v}}{\partial \mathrm{t}} + \mathbf{v} \bullet \nabla \mathbf{v}\right] = \mathbf{F} - \nabla P + \nabla \bullet \boldsymbol{\sigma}_d + \rho \mathbf{g}$$

$$\boldsymbol{\sigma}_d = \mu[\nabla \mathbf{v} + \nabla(\mathbf{v})^T - \frac{2}{3}(\nabla \bullet \mathbf{v})\mathbf{I}]$$

Assumptions:
- P = P (r) only (analogous to an isothermal gas)
- **F**(r) arises from drag force and is an increasing function of density

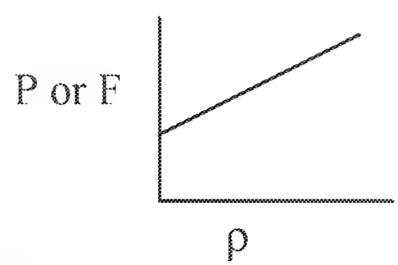

*Johri, J., and **Glasser, B.J.**, Connections between Density Waves in Fluidized Beds and Compressible Flows, AIChE J., **48**, 1645-1664, (2002).*

Instabilities and the Evolution of Density Waves

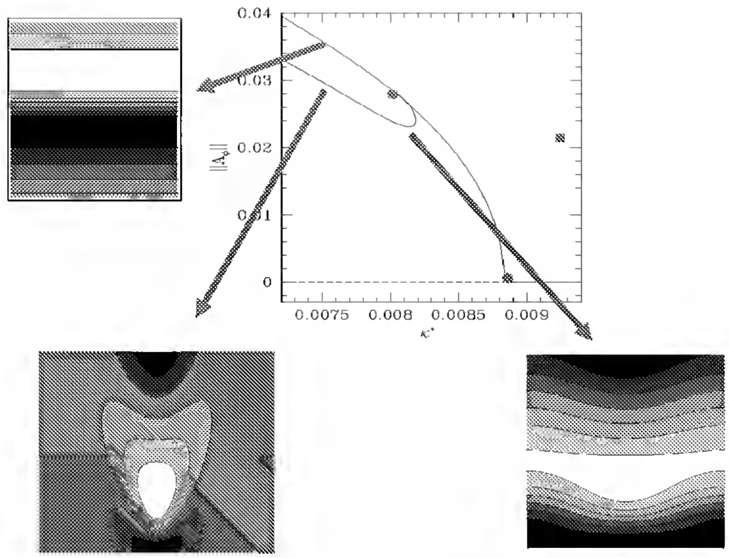

- The salient features of instability formation predicted by the two phase model are captured using a much simpler model involving a single phase of variable density.
- The main role of the gas is to provide a drag force to suspend the particles. Varying the closure for the drag does not affect the solution shape. Its main effect is to vary the point at which fluidization occurs.
- Shape and properties of the non-uniform structures are governed by solid phase. The wavespeed of the structures is set by the compressibility. More work is needed on measuring the solid phase stress.

Bubble formation and detachment in reduced gravity under the influence of electric fields

Cila Herman, Estelle Iacona and Shinan Chang

Department of Mechanical Engineering, The Johns Hopkins University, 3400 N. Charles Street, Baltimore, MD 21218, USA

Objectives

The objective of the study is to investigate the behavior of individual air bubbles injected through an orifice into an electrically insulating liquid under the influence of a static electric field (Figure 1a). Both uniform and nonuniform electric field configurations were considered. Bubble formation and detachment were recorded and visualized in reduced gravity (corresponding to gravity levels on Mars, on the Moon as well as microgravity) using a high-speed video camera. Bubble volume, dimensions and contact angle at detachment were measured. In addition to the experimental studies, a simple model, predicting bubble characteristics at detachment was developed. The model, based on thermodynamic considerations, accounts for the level of gravity as well as the magnitude of the uniform electric field. Measured data and model predictions show good agreement and indicate that the level of gravity and the electric field magnitude significantly affect bubble shape, volume and dimensions.

Experimental setup

The experimental setup designed for this study is arranged in three racks. The experimental rack carries the test cell and the measurement and actuation equipment. The personal computer rack carries the

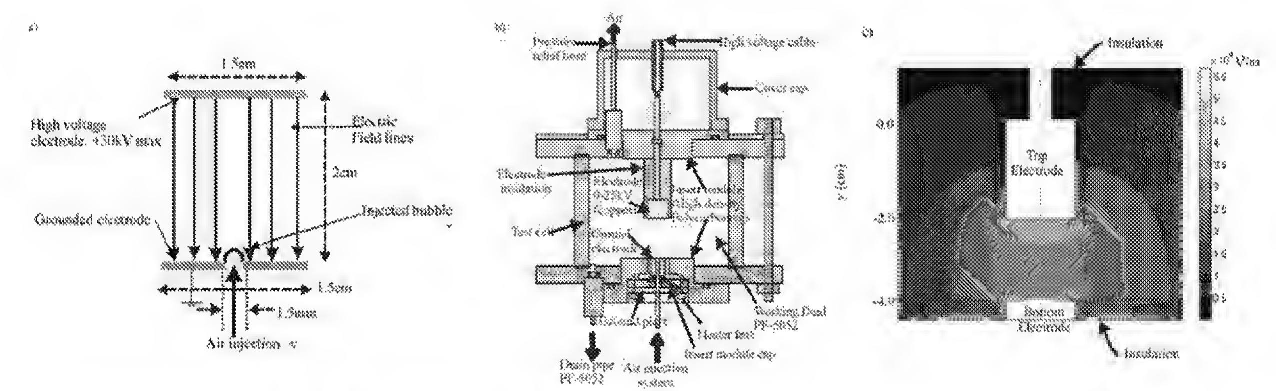

Fig. 1. a) Schematic of the investigated physical situation b) test cell and c) magnitude of the electric field in the test cell for potential difference between the electrodes determined numerically.

computer, monitor, data acquisition and control hardware and power backup units. The camera rack with the high-speed video recorder is connected to the camera head on the experimental rack through the umbilical. A triaxial accelerometer measures the components of the acceleration vector. The NEC 500 high-speed video recorder (provided by NASA GRC) allows visualization of the bubble formation process. The test cell is a rectangular vessel (Figure 1b). Its four walls are manufactured of 12.5mm thick, clear Polycarbonate to allow visualization experiments. The volume of the test cell is 9cmx9cmx10cm. A static electric field E (0-15.5kV/cm) is formed between the bottom electrode and a parallel top electrode, spaced 20mm apart. The bottom electrode is a 15mm diameter, electrically grounded copper cylinder. Air is injected into the test cell (at constant flow rate through a 1.5mm diameter orifice in the bottom electrode) with a syringe, driven by a linear translation stage. The working fluid, PF5052, is chemically inert and electrically insulating. Its relative permittivity is 1.73. In order to better understand the structure of the electric field in the test cell, the electric field distribution was computed assuming a 2D configuration, using the commercial finite element code, FEMLAB 2.0 (Figure 1c).

Results

The reduced gravity environment was realized during parabolic flights in NASA's KC-135 aircraft. A period of about 20s of low gravity was available per parabola. Experiments were carried out in bolted-down and free-floating configurations. Bubbles shown in this section represent typical behavior of injected bubbles at detachment for a particular set of experimental conditions. When the detachment of the bubble occurred after a regular and periodic formation behavior, key bubble dimensions (volume V_{dm}, major axis a_m, minor axis b_m, aspect ratio a_m / b_m and contact angle ϕ_m) were measured in the selected image sequences. Shapes of injected air bubbles recorded at the moment of detachment and their key dimensions for electric field magnitudes of $E = 0$, 2.5, 5, 7.5 and 10kV/cm are presented in Figure 2.

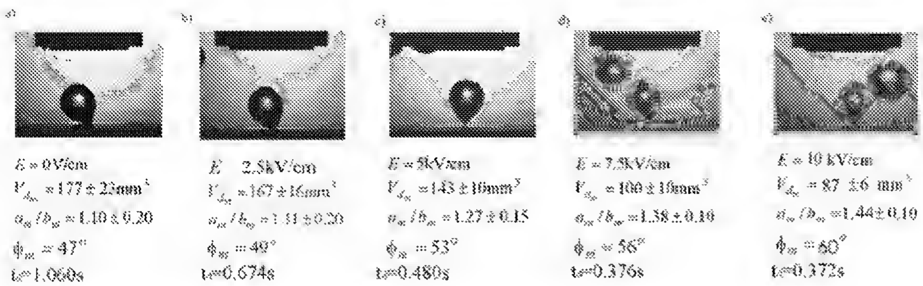

Fig 2. Experimentally visualized bubble shapes at detachment in microgravity for a) $E = 0$V/cm, b) 2.5kV/cm, c) 5kV/cm, d) 7.5kV/cm and e) 10kV/cm.

Without the electric field, the bubble in Fig. 2a is almost spherical (aspect ratio of 1.1) and slightly tilted due to small, residual, lateral acceleration components. Based on Figs. 2c-e it can be concluded that the bubble is increasingly elongated in the direction parallel to the applied electric field and the bubble axis is vertical. This behavior indicates that a uniform electric field affects bubble detachment and defines the preferential direction of the bubble axis. As a result of shape changes, the aspect ratio and the contact angle increase by 27% and 32%, respectively, when increasing the electric field magnitude from 0 to 10kV/cm. Under the same conditions, the volume at detachment is also affected by the presence of the electric field and it decreases by 51%. The period of bubble formation t_d (the time between bubble apparition and its detachment) decreases 50%. The influence of gravity level on bubble shape at detachment is illustrated in Figure 3. As expected, in the investigated range of gravity levels and electric field magnitudes, the influence of gravity level is more pronounced than that of the electric field.

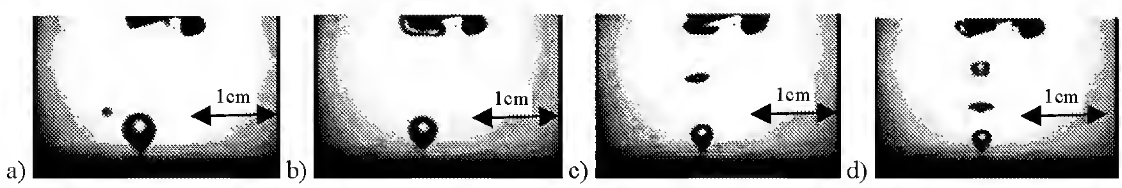

Fig 3. Bubble at detachment for U=10kV and different gravity levels
a) A_Z =-0.006 g V_d=32.483mm^3, b) A_Z =0.085 g V_d=18.851mm^3, c) A_Z =0.134 g V_d=10.964mm^3 and d) A_Z =0.374 g V_d=6.648mm^3

Acknowledgments

The research reported in this paper was supported by NASA research grant NAG3-1815. Support for Estelle Iacona was provided by the ESA postdoctoral fellowship. Support for Shinan Chang is provided by China Scholarship Council. The experiments in the KC-135 aircraft were carried out by Cila Herman, Gorkem Suner, Steven Marra and Ed Scheinerman. The support by the KC-135 crew and by NASA Glenn Research Center was invaluable for the successful completion of the experiments.

Electric field effects on an injected air bubble at detachment in a low gravity environment

Cila Herman, Estelle Iacona, Shinan Chang

The Johns Hopkins University
Heat Transfer Laboratory

Cila Herman

Introduction

Motivation: enhance boiling heat transfer in the low gravity environment.

Why: In terrestrial conditions, boiling is an efficient way to remove heat from a heated surface (cooling of electronic equipment, heat exchangers….)
In microgravity: boiling bubbles grow very large, coalesce and form a vapor film at the heated surface ⇒ burn-out of the surface.

Electrohydrodynamics (EHD) = Explore the possibility of substituting the buoyancy force with a force induced by the electric field

Objectives:
Experimental investigation of the behavior of a single injected air bubble into an electrically insulating liquid.
Analysis of the bubble development and detachment under the influence of a static electric field in the microgravity environment.

The Johns Hopkins University
Heat Transfer Laboratory

Cila Herman

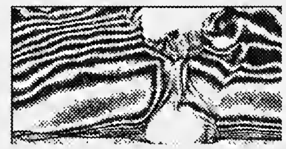

Test cell

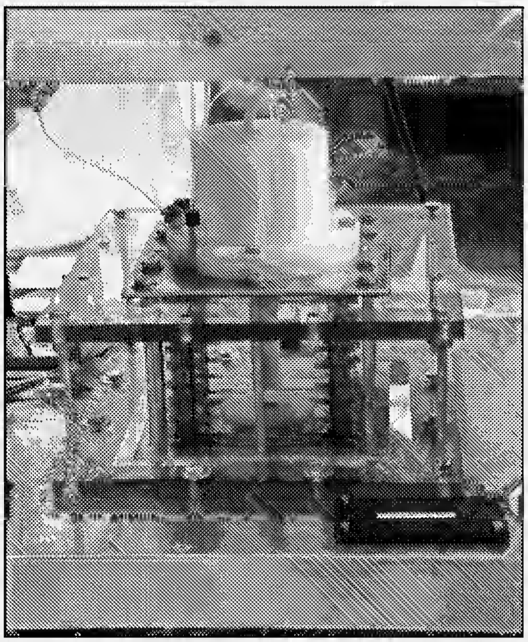

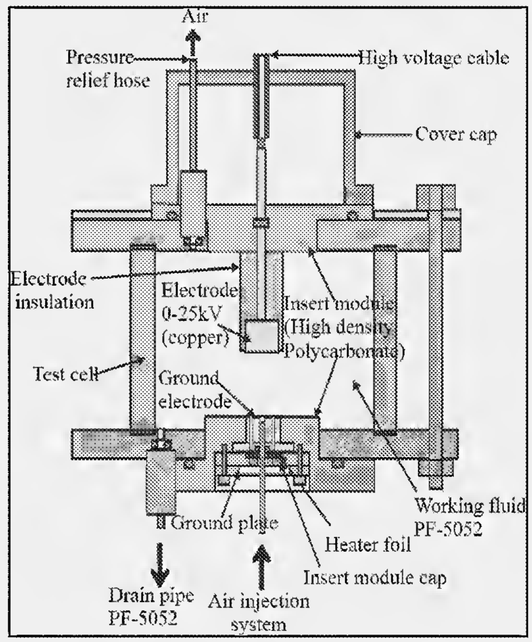

•Rectangular test cell (9x9x10cm)
•Four walls of 2cm thick clear Polycarbonate
•Air bubble injected into PF5052

•Bubble exposed to a static electric field (0-30kV potential difference) formed between the bottom and top copper electrodes

Experimental hardware

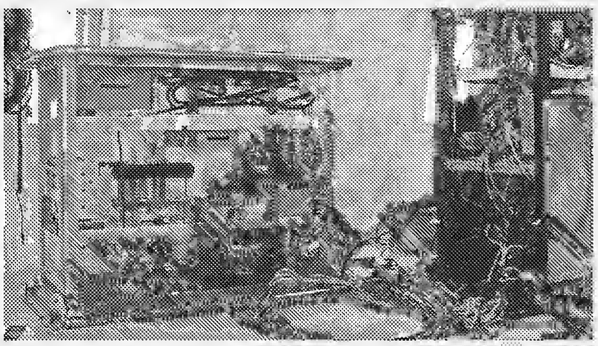

Experimental rack
attached to the airplane frame

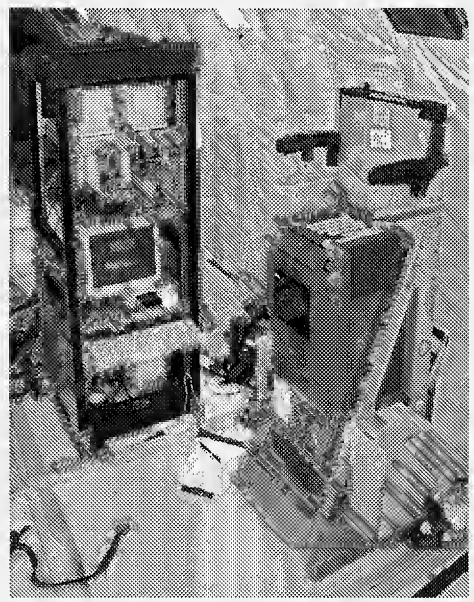

Computer rack

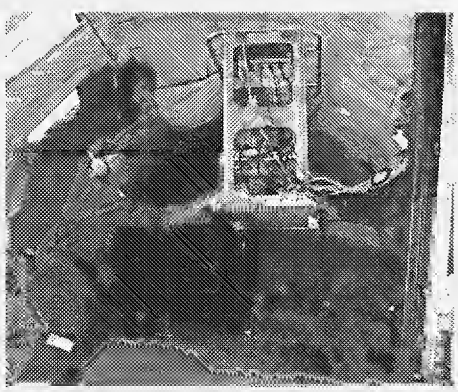

Experimental rack
free-floating

NASA/CP—2002-211212/VOL2

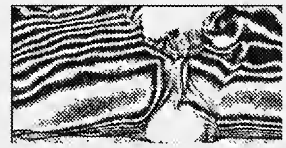

Image processing

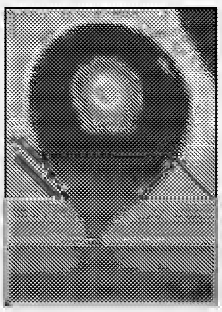

Bubble image
after digitization

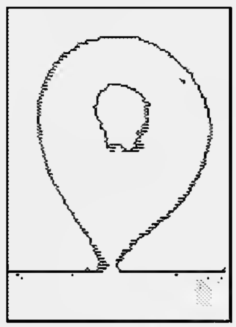

Bubble interface
after edge recognition

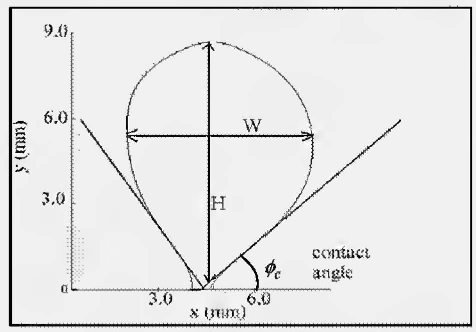

Bubble contour represented through the fifth
order polynomial fit

Bubble visualization in terrestrial conditions

Detachment information (no electric field):

V_d= 9.5 mm^3 H = 3.7 mm W = 2.6 mm H/W = 1.4

t=0.0s t=0.024s

Effect of the electric field magnitude in microgravity: uniform electric field

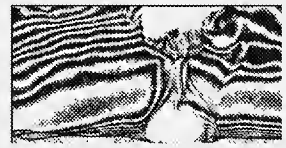

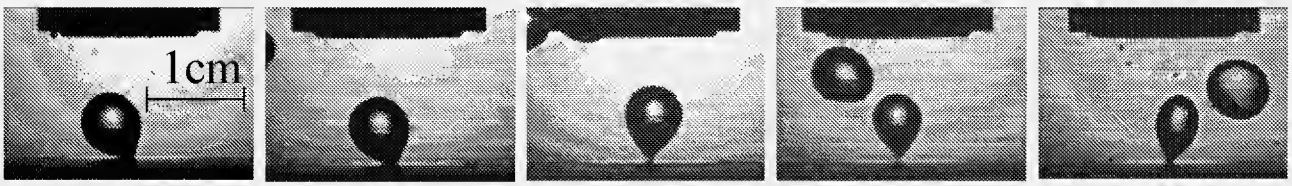

U = 0V	U = 5kV	U = 10 kV	U =15 kV	U = 20 kV
t_d = 1.060 s	t_d = 0.774 s	t_d = 0.432 s	t_d = 0.376 s	t_d = 0.300 s
V_d = 177 mm^3	V_d = 167 mm^3	V_d = 143 mm^3	V_d = 100 mm^3	V_d = 87 mm^3

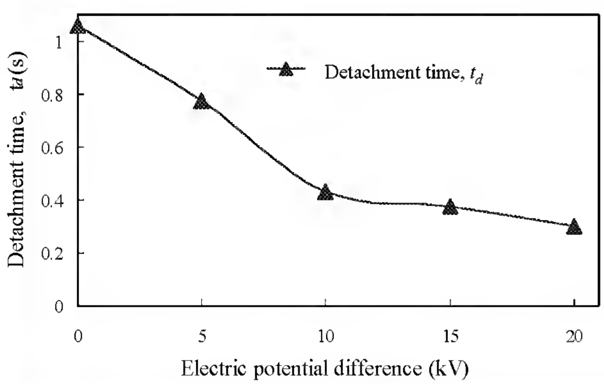

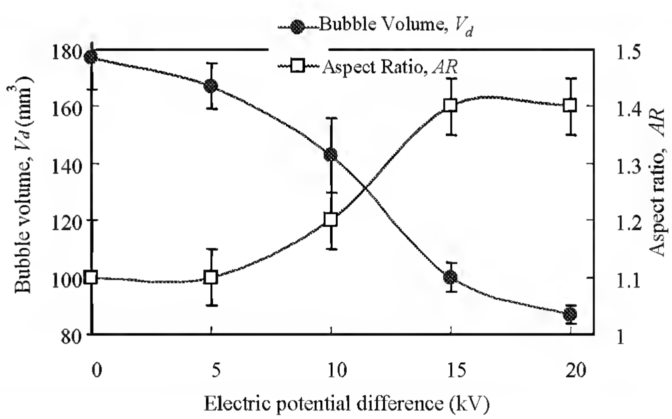

NASA/CP—2002-211212/VOL2

Effect of gravity on bubble detachment

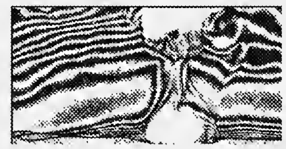

Bubble at detachment for U=10kV (non-uniform electric field) and different gravity levels

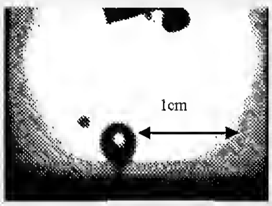

A_z=0.006g

V_d=32.4mm^3

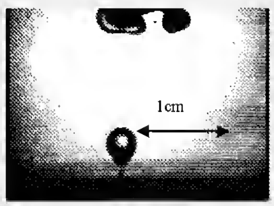

A_z= 0.085g

V_d =18.8mm^3

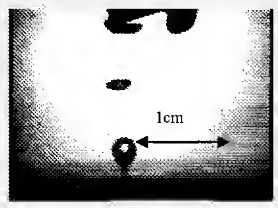

A_z= 0.134g

V_d =10.9mm^3

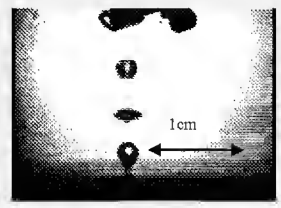

A_z= 0.374g

V_d =6.6mm^3

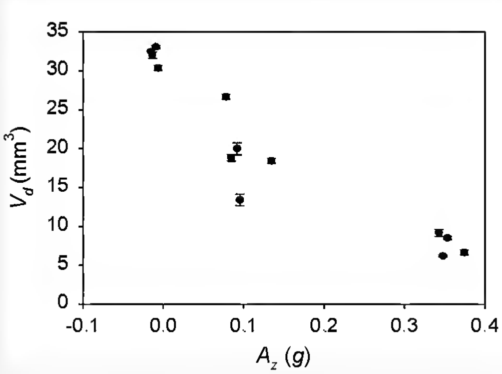

Measured bubble volume

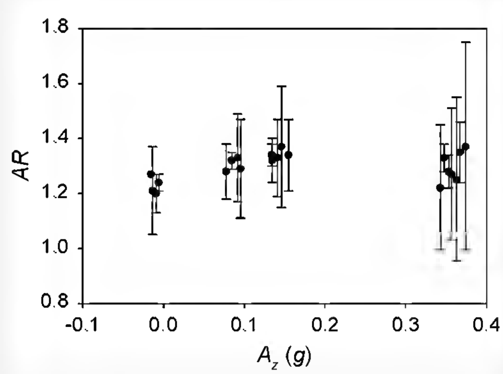

Aspect ratio

Bubble formation in terrestrial gravity under non-uniform electric field

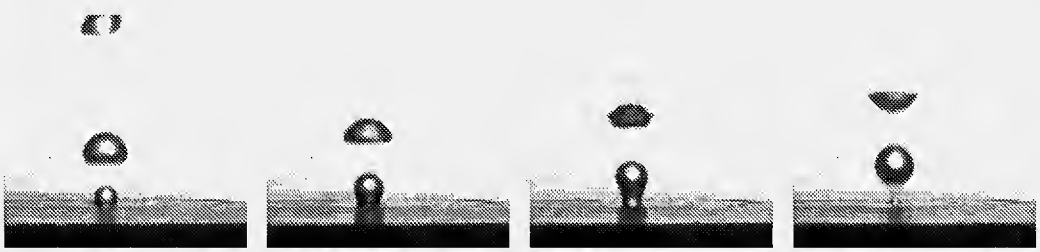

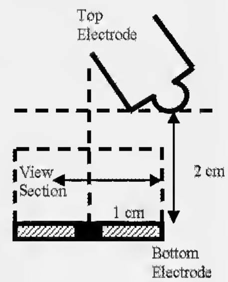

Bubble cycle life in terrestrial condition with no electric field

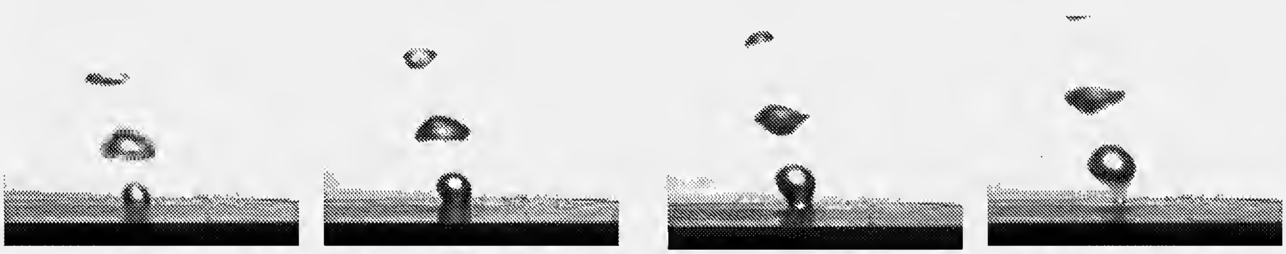

Bubble cycle life in terrestrial condition under the influence of an electric field
E=12.5kV/cm

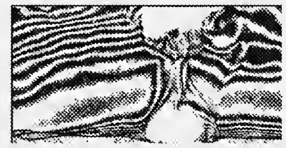

Acknowledgements

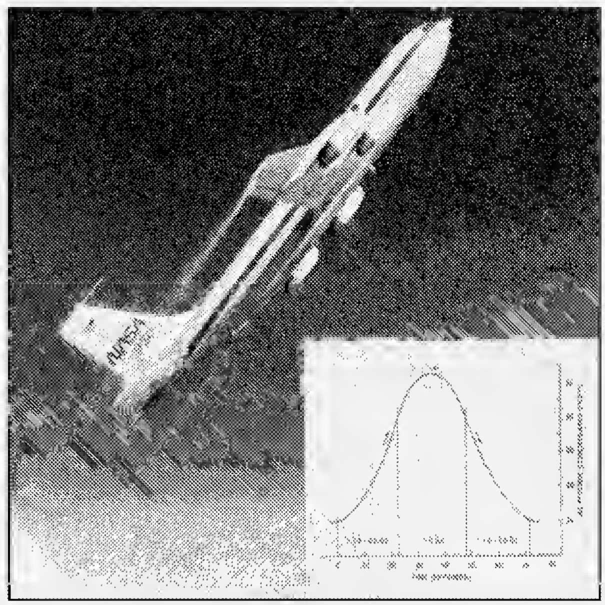

- The research was supported by NASA research grant NAG3-1815 and NAG-32726
- Support for Shinan Chang was provided by China Scholarship Council.
- Support for Estelle Iacona was provided by the ESA postdoctoral fellowship.
- The experiments in the KC-135 aircraft were carried out by Cila Herman, Gorkem Suner, Steven Marra and Ed Scheinerman.
- The support by the KC-135 crew and by NASA Glenn Research Center was invaluable for the successful completion of the experiments.

The Johns Hopkins University
Heat Transfer Laboratory

Cila Herman

Conclusions

Investigation of the effect of an applied static electric field on the behavior of an injected air bubble

Experiments carried out

- for gravity levels of earth (1g), Mars (≈0.3g), Lunar (≈0.1g , 0.2g) and microgravity
- with initially uniform and non-uniform electric fields from 0V/cm to 12.5kV/cm.

Measurement of characteristic bubble key parameters at detachment

⇒ Bubble shape, volume, aspect ratio, contact angle and period of growth significantly affected by gravity level and electric field magnitude

The Johns Hopkins University
Heat Transfer Laboratory

Cila Herman

Stability and Heat Transfer Characteristics of Condensing Films

J.C. Hermanson,* P.C. Pedersen,† J.S. Allen,‡ M.A. Shear,†
Z.Q. Chen,* A.N. Alexandrou,° and W.W. Durgin*

*Mechanical Engineering Department, Worcester Polytechnic Institute, Worcester, MA 01609; †Electrical and Computer Engineering Department, Worcester Polytechnic Institute, Worcester, MA 01609; ‡National Center for Microgravity Research, Cleveland, OH 44135; °Department of Mechanical and Manufacturing Engineering, University of Cyprus, 1678 Nicosia, Cyprus; Corresponding author: jherm@wpi.edu

The overall objective of this research is to investigate the fundamental physics of film condensation in reduced gravity. The condensation of vapor on a cool surface is important in many engineering problems,[1,2] including spacecraft thermal control and also the behavior of condensate films that may form on the interior surfaces of spacecraft.

To examine the effects of body force on condensing films, two different geometries have been tested in the laboratory: 1) a stabilizing gravitational body force (+1g, or condensing surface facing "upwards"), and 2) de-stabilizing gravitational body force (-1g, or "downwards"). For each geometry, different fluid configurations are employed to help isolate the fluid mechanical and thermal mechanisms operative in condensing films. The fluid configurations are a) a condensing film, and b) a non-condensing film with film growth by mass addition by through the plate surface.

Condensation experiments are conducted in a test cell containing a cooled copper or brass plate with an exposed diameter of 12.7 cm. The metal surface is polished to allow for double-pass shadowgraph imaging, and the test surface is instrumented with imbedded heat transfer gauges and thermocouples. Representative shadowgraph images of a condensing, unstable (-1g) n-pentane film are shown in Fig. 1a-b. The interfacial disturbances associated with the de-stabilizing body force leading to droplet formation and break-off can be clearly seen in Fig. 1b. The heat transfer coefficient associated with the condensing film is shown in Fig. 2. The heat transfer coefficient is seen to initially decrease, consistent with the increased thermal resistance due to layer growth. For sufficiently long time, a steady value of heat transfer is observed, accompanied by continuous droplet formation and break-off.[1,2]

The non-condensing cell consists of a stack of thin stainless steel disks 10 cm in diameter mounted in a brass enclosure. The disks are perforated with a regular pattern of 361 holes each 0.25 mm in diameter. Non-condensing experiments in -1g have employed 50 cSt and 125 cSt silicone oil pumped through the perforated disks at a specified rate by a syringe micropump. The time to droplet break-off and the disturbance wavelengths appear to decrease with increasing pumping rate.

The ability to reliably perform multi-point, ultrasonic measurements of the film thickness has been demonstrated. A linear array of eight transducers of 6 mm diameter (with a beam footprint of comparable size) are pulsed with a square-wave signal at a frequency of 5 MHz and a pulse duration of approximately 0.3 μs. For thin films (60 μm to 2-3 mm in thickness) the layer thickness is determined by frequency analysis, where the received ultrasound pulse is Fourier transformed and the spacing between the peaks in the frequency spectrum is analyzed.[3] For thicker layers (up to at least 1 cm in thickness), time-domain analysis is performed of the received ultrasound pulses to generate directly the layer thickness.

A time-trace of the film thickness at a point using a single transducer in the linear array is shown in Fig. 3 for the case of an unstable (-1g) n-pentane film. The oscillations in film thickness are evidently due to the passage and/or shedding of droplets from the cooled plate surface. The entire transducer array was used to measure the changes in film thickness resulting from the passage of gravity waves generated either by an oscillating wall or the impact of a single droplet on the free surface of a film. The enclosure in both cases was 14 cm square and the transducer spacing was 12 mm. Best results were obtained using as test fluid a mixture of 50% glycerol and 50% water with a fluid layer thickness of 3-5 mm. In both cases the measured wavelengths and wave propagation

speeds using the ultrasound technique compared reasonably well with those observed by optical imaging.

The authors acknowledge the assistance of Ms. L.A. Deluca and Ms. K.A. Hufnagle. This research is supported by NASA under Cooperative Agreement NAG3-2395.

References

[1]Gerstmann, J. and Griffith, P., "Laminar film Condensation on the Underside of Horizontal and Inclined Surfaces," *Int. J. Heat Mass Transfer*, Vol. 10, 567-580, 1967.

[2]Yanadori, M., Hijikata, K., Mori, Y. and Uchida, M., "Fundamental study of laminar film condensation heat transfer on a downward horizontal surface," *Int. J. Heat Mass Transfer* Vol. 28, No. 10, 1937-1944, 1985.

[3]Pedersen, P.C., Cakareski, Z., and Hermanson, J.C., "Ultrasonic Monitoring of Film Condensation," *Ultrasonics* **38**, 486-490, 2000.

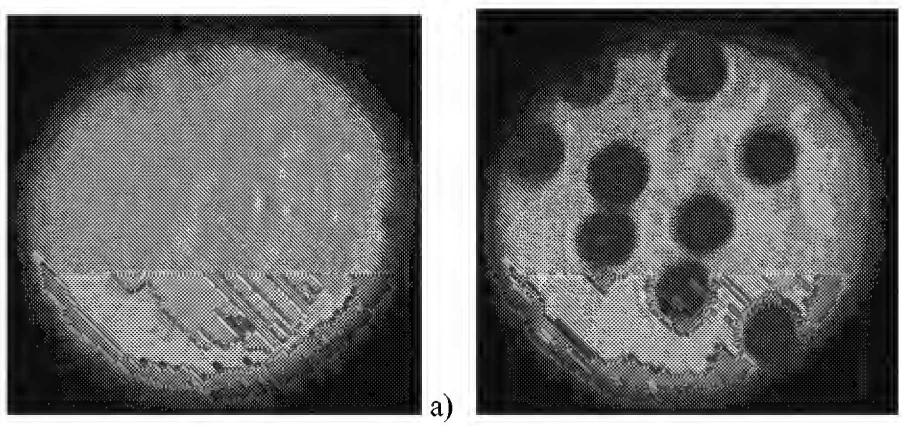

a) b)

Fig. 1a-b Condensing n-pentane film in unstable (-1g) configuration. a) 30 s after start of condensation, T_{wall} = 13.9 C, T_{sat} = 18.1 C; b) 40 s after start of condensation, T_{wall} = 13.9 C, T_{sat} = 21.3 C.

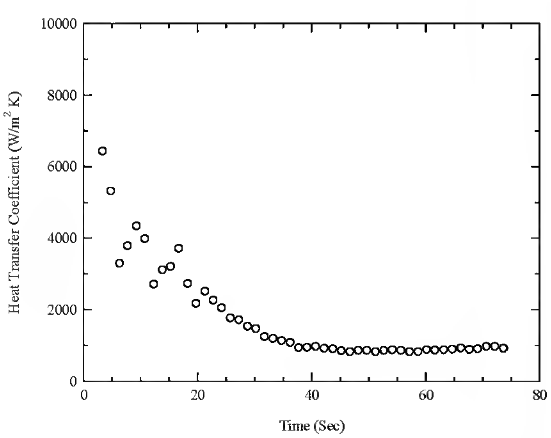

Fig. 2 Time evolution of heat transfer coefficient for unstable (-1g), condensing n-pentane film.

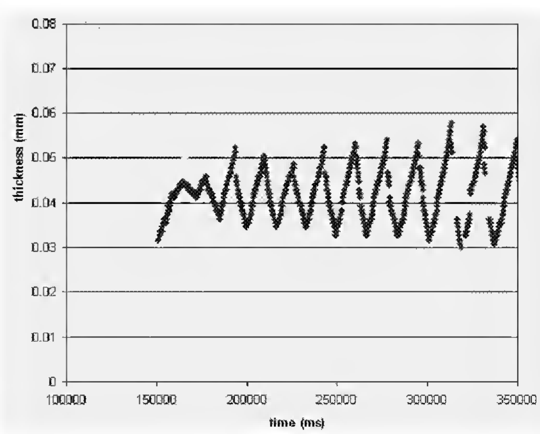

Fig. 3 Ultrasound point measurements of film thickness for unstable (-1g) condensing n-pentane film.

TWO-PHASE FLOW IN MICROCHANNELS WITH NON-CIRCULAR CROSS SECTION

Chris A. Eckett and Hal J. Strumpf
Honeywell International

ABSTRACT

Two-phase flow in microchannels is of practical importance in several microgravity space technology applications. These include evaporative and condensing heat exchangers for thermal management systems and vapor cycle systems, phase separators, and bioreactors. The flow passages in these devices typically have a rectangular cross-section or some other non-circular cross-section; may include complex flow paths with branches, merges and bends; and may involve channel walls of different wettability. However, previous experimental and analytical investigations of two-phase flow in reduced gravity have focussed on straight, circular tubes. This study is an effort to determine two-phase flow behavior, both with and without heat transfer, in microchannel configurations other than straight, circular tubes. The goals are to investigate the geometrical effects on flow pattern, pressure drop and liquid holdup, as well as to determine the relative importance of capillary, surface tension, inertial, and gravitational forces in such geometries.

An evaporative heat exchanger for microgravity thermal management systems has been selected as the target technology in this investigation. Although such a heat exchanger has never been developed at Honeywell, a preliminary sizing has been performed based on knowledge of such devices in normal gravity environments. Fin shapes considered include plain rectangular, offset rectangular, and wavy fin configurations. Each of these fin passages represents a microchannel of non-circular cross section. The pans at the inlet and outlet of the heat exchanger are flow branches and merges, with up to 90-deg bends. R-134a has been used as the refrigerant fluid, although ammonia may well be used in the eventual application.

The experimental portion of the program consists of two phases:

1. Ground laboratory testing of various microchannels in normal gravity
2. KC-135 reduced gravity testing of selected channels

The first phase of the program is in progress. Ground testing is being conducted in the Morrin-Martineli-Gier Memorial Heat Transfer Laboratory at UCLA. This experiment is an investigation of two-phase flow in small rectangular channels, without heat transfer. For simplicity, nitrogen and water are used as the working fluids. The experimental setup consists of a gas-pushed liquid feeding system, a nitrogen feeding system, the test section, a differential pressure drop measurement, still frame and video flow visualization via CCD camera, a nitrogen flow meter, and a liquid exit collection with precision scale for liquid flow rate measurement. The setup has been completed and preliminary experiments have been conducted to verify the measurements and visualization. Initial experiments have been performed on a set of three channels, each with a rectangular cross section of 0.04 in. width and 0.02 in. height. The first channel is straight, the second has a 45-deg corner, and the third has a 90-deg corner. A second

set of three test sections to be investigated involves straight rectangular channels of various cross-sectional dimensions. A later set will involve channels of different sizes and geometries, to be determined on the basis of the results from the first two sets.

The ground experiments are intended to model the flow in a single fin passage of a plain fin heat exchanger. In the absence of phase change, the relative mass flow rates of the gas and liquid are chosen to model various different refrigerant vapor qualities between 0 and 1 in the real application. A scaling analysis has been performed to match the liquid and gas superficial Reynolds numbers in the nitrogen-water experiments with those in the proposed R-134a evaporative heat exchanger. Typical Reynolds numbers are on the order of 10^2 for the liquid and 10^3 for the gas. The ground experiment test section sizes have been chosen to cover a range of Bond numbers and Suratman numbers representative of the proposed evaporative heat exchanger at normal gravity and at KC-135 reduced gravity.

One feature of the proposed evaporative heat exchanger in reduced gravity is that the Bond number is very low, on the order of 10^{-2} (for the KC-135) to 10^{-4} (for space-based applications), while the Suratman number is quite high, greater than 10^5. Thus, the two-phase flow is expected to be gravity independent, and surface tension forces are expected to dominate viscous forces. Such a combination of Bond number and Suratman number cannot be obtained in a 1-g experiment within the realm of practical working fluids. This is the justification for flight experiments.

The second phase of the program involves future experiments performed on the NASA KC-135 aircraft. The working fluid will be R-134a. Test section sizes and shapes will be selected on the basis of the findings from the ground experiment. Initial flights are expected to be adiabatic experiments with fixed qualities. A second set of flights is expected to incorporate a heating element and investigate the effect of phase change on the two-phase flow.

Principal Investigator:
Dr. Hal J. Strumpf
Chief Engineer, Heat Transfer
Airframe Systems
Honeywell International
2525 W. 190th St.
M/S 36-1-93010
Torrance, CA 90504
hal.strumpf@honeywell.com
Phone: (310) 512-3359
FAX: (310) 512-3432

Two-Phase Flow in Multi-Channels – Liquid Holdup and Capillary Flow

Chris A. Eckett, Hal J. Strumpf
Honeywell International Inc.
Airframe Systems
Torrance, CA

Ivan Catton, Jinliang Wang, Erik Merilo
University of California Los Angeles

Jeffrey Allen
National Center for Microgravity Research

Supported by NASA NRA-HEDS-98-03

Introduction

- **Background**
  - Two phase flow in microchannels occurs in many microgravity space technology applications
  - Practical devices involve
    - rectangular and other non-circular channel cross sections
    - complex flow paths (bends, branches, merges)
    - channel walls of differing wettability
  - Previous research has focussed on straight circular channels
- **Goal**
  - Experimental study of microgravity two phase flow in non-circular microchannels, with and without heat transfer
  - Examine flow patterns, pressure drop, liquid holdup
  - Determine relative importance of surface tension, inertial, viscous and gravitational forces

Honeywell

Target Technology

EVAPORATOR FOR THERMAL MANAGEMENT SYSTEM

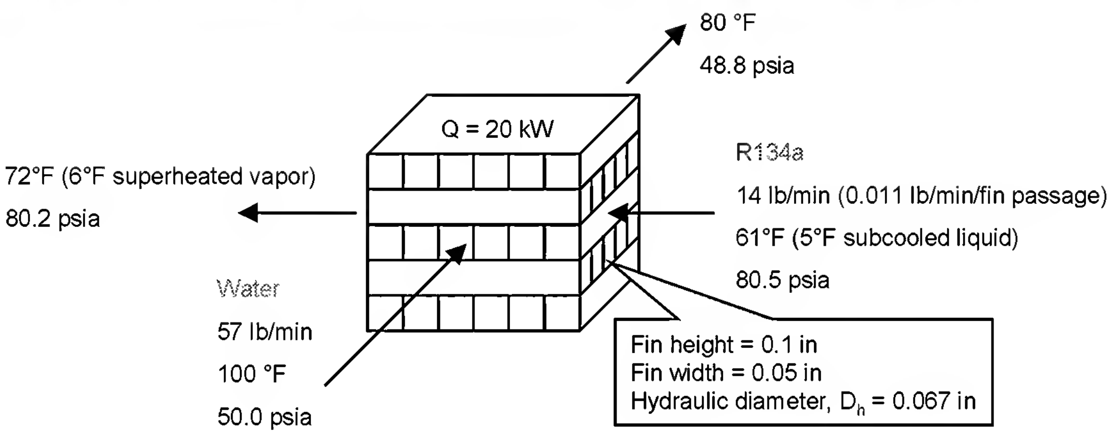

Saturated R134a in single fin passage:

Superficial liquid Reynolds number, Re_{LS} = 200 at 0% quality

Superficial vapor Reynolds number, Re_{VS} = 3800 at 100% quality

Suratman number, $Su = \frac{\rho_L D_h \sigma}{\mu_L^2} = 4 \times 10^5$ $\Rightarrow$ surface tension dominated

$$\text{Bond number, } Bo = \frac{(\rho_L - \rho_V) g D_h^2}{\sigma} = \begin{cases} 4, & \text{at 1g} \quad \Rightarrow \text{gravity dependent (?)} \\ 0.04, & \text{at 0.01g (KC-135)} \quad \Rightarrow \text{gravity independent} \end{cases}$$

Honeywell

Laboratory Experiment

SCALING ANALYSIS

- Laboratory tests performed in rectangular channels with nitrogen-water (adiabatic)
  - Different mixtures of nitrogen and water used to model fixed qualities in evaporative system
- Similarity assumptions for scaling:
  - Maintain channel aspect ratio
  - Select channel sizes to match Bond number of evaporative system at either 1g or 0.01g
  - Select flow rates to match liquid and vapor superficial Reynolds numbers Re_{LS} and Re_{VS}
- Resultant channel sizes and Suratman numbers:
  - 1g matched: 0.15 in x 0.3 in
    - $\Rightarrow$ Su = 4×10^5 (surface tension dominated)
  - 0.01g matched: 0.015 in x 0.03 in
    - $\Rightarrow$ Su = 4×10^4 (viscous dominated)

Honeywell

Laboratory Experiment

EXPERIMENTAL SETUP

- **Morrin-Martineli-Gier Memorial Heat Transfer Laboratory at UCLA**

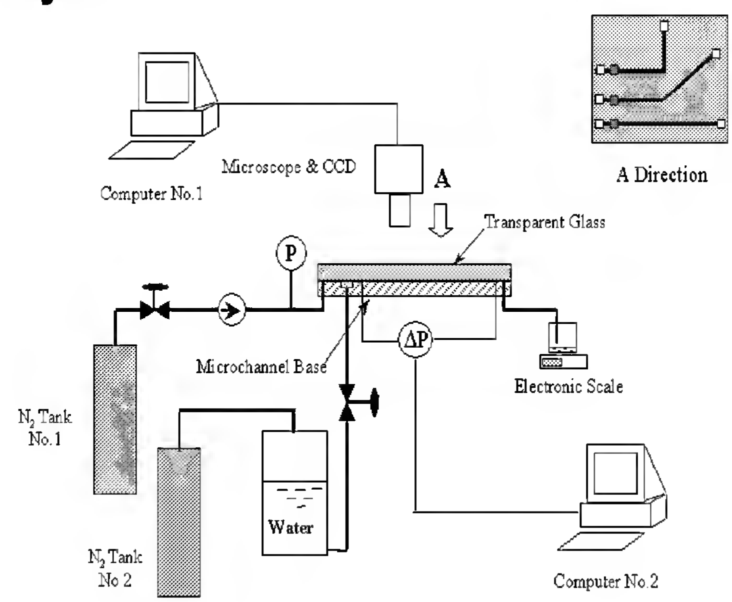

Honeywell

Laboratory Experiment

PRELIMINARY RESULTS

- Slug and annular flows observed
- Small pressure fluctuations observed during slug flow
- In some cases, liquid holdup observed in channel corners with high liquid flow rate and low gas flow rate (slug flow)
- Large pressure fluctuations observed during holdup

Honeywell

Laboratory Experiment

PRELIMINARY RESULTS

- **Channel dimension: 0.02 in. height, 0.04 in. width**
- **Slug flow:**

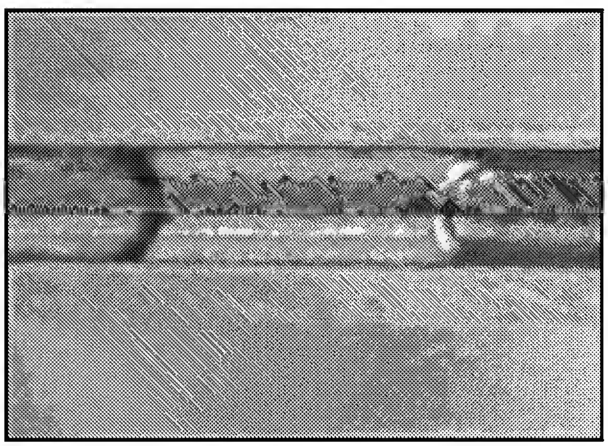

- **Annular flow:**

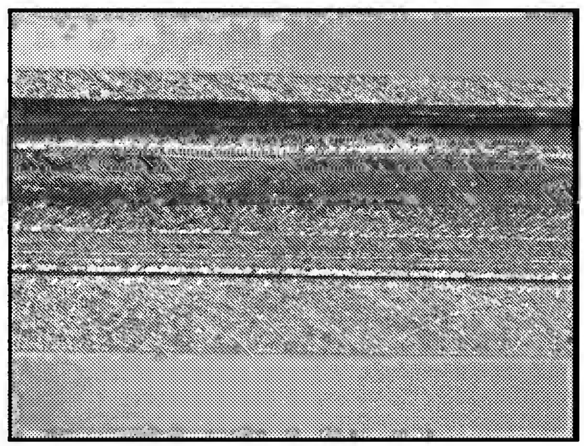

Honeywell

Future Experiments

- **Laboratory Experiment (2002)**
  - Examine range of flows around target Reynolds numbers to determine flow pattern maps
  - New geometries
    - bends/branches/merges
    - different sized channels: 0.05 in x 0.1 in, 0.125 in x 0.25 in, 0.1 in x 0.05 in
- **KC-135 Experiment (2003)**
  - Select channel geometry and flow rates of most interest from laboratory experiment
    - scale up to one complete layer of heat exchanger fins
  - Working fluid: R134a refrigerant, entering at various liquid-vapor qualities between 0 and 1
  - Two flights
    - adiabatic - fixed quality
    - non-adiabatic - heating element ⇒ small increase in quality

Honeywell

KC-135 Experiment

EXPERIMENTAL SETUP

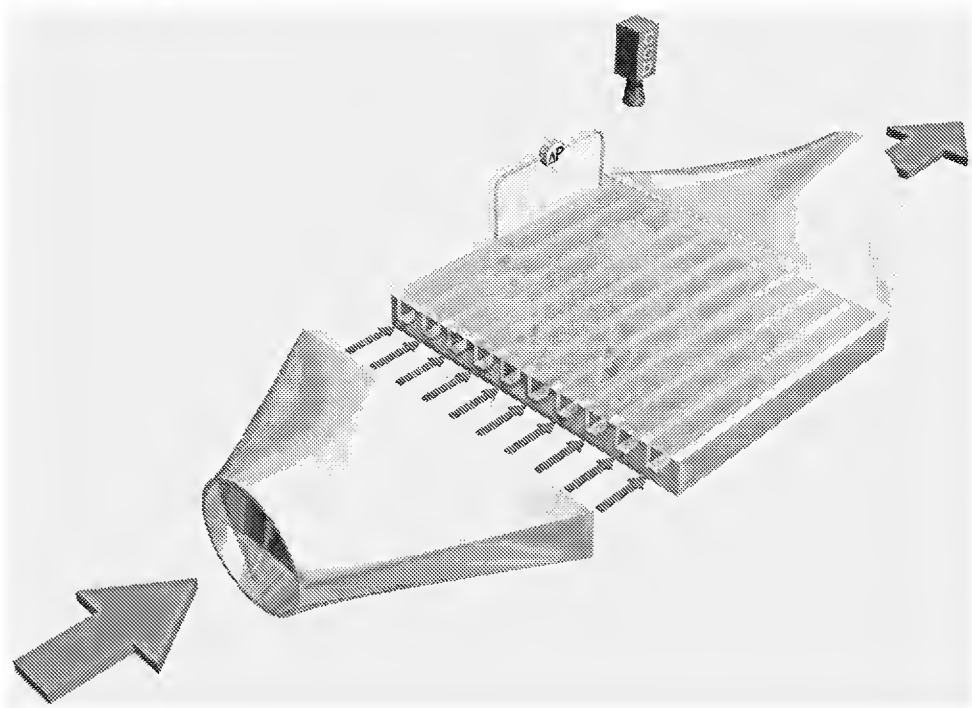

Honeywell

GAS EVOLUTION IN ROTATING ELECTROCHEMICAL SYSTEMS UNDER MICROGRAVITY CONDITION

Yasuhiro Kamotani and Thaveesak Boonpongmane
Department of Mechanical and Aerospace Engineering
Case Western Reserve University
Cleveland, Ohio 44106

ABSTRACT

The effect of gas evolution on mass and heat transfer in rotating electrochemical cells is being investigated experimentally, both in 1-g and in reduced gravity. This work is motivated by the need of efficient electrochemical cells in microgravity. In microgravity, gas bubbles that are generated in an electrochemical cell must be removed from the electrode surface. In the present work, we investigate a means to enhance heat and mass transfer and, at the same time, to remove gas bubbles effectively for electrochemical systems.

Currently, we are investigating the effect of gas evolution on heat transfer. A cylindrical enclosure is rotated around its axis on a rotating table. The container diameter is 0.15 m and the depth is 0.05 m. The top wall is heated and the bottom wall is cooled. The container is filled with water. Without gas evolution, the flow in the cell is driven mainly by the centrifugal buoyancy, which generates radially outward flow along the bottom wall and inward flow along the top wall. In the present experiment, the Ekman number (Ek) is very small ($1 \times 10^{-5} < Ek < 4 \times 10^{-5}$). Consequently, the radial flow is confined to relatively thin Ekman layers along the top and bottom walls. The fluid is mainly in solid-body rotation with the enclosure, but the radial flow induces additional azimuthal flow through the Coriolis force. As a result, the azimuthal flow is slower (faster) than the container rotation near the cold (hot) wall. In the present heat transfer experiment, we are in the so-called Ekman suction regime, where the centrifugal buoyancy is mainly balanced by the Coriolis force, so that the radial flow is very much suppressed. The main quantity of interest in the present experiment is the overall heat transfer rate from the hot to cold walls, non-dimensionalized as the average Nusselt number (Nu). The experimentally measured Nusselt is about 2, which agrees well with the numerical simulation that is being conducted to supplement the experiment. Since the radial flow is suppressed by the Coriolis force, in some tests we place partitions in the container to retard the azimuthal flow and to increase the heat transfer rate. It is shown that Nu more than doubles when the partitions are used.

In the heat transfer experiment we generate bubbles by water electrolysis. Both oxygen (at the anode) and hydrogen (at the cathode) are generated. The bubbles move toward the container axis. A cylindrical post is placed along the container axis with a special filter so that only the bubbles are removed through the center post. The bubble behaviors are observed by a CCD camera. The camera is either stationary or rotates with the container. Along the cold (hot) wall, the liquid flow is opposed (aided) by the bubble flow. In normal gravity, the bubbles tend to move nearly upward near the bottom wall after they are generated, while they move along the top wall forming a so-called bubble layer. Thus, there exist three boundary layers, thermal, Ekman

and bubble layers along the top wall. The top wall situation somewhat resembles that in microgravity. The bubbles could affect the centrifugal buoyancy and Coriolis forces significantly. The present experiment covers from the thermal buoyancy dominant situation to the bubble buoyancy dominant situation. The amount of bubble generation is controlled by the electrical potential applied to the cell. The flow fields and heat transfer data taken under various conditions are presented.

We have also conducted normal gravity experiments on the gas evolution effect on mass transfer in a rotating electrochemical cell. In this experiment, we are in the so-called centrifugal buoyancy regime so that the Coriolis force has relatively weak influence on the mass transfer. It is found that in normal gravity the cell current is basically controlled by the kinetic reaction at the electrode. Thus the current is independent of the rotation speed unless the rotation speed is very high.

A test apparatus for parabolic flight tests is being designed. The basic concept is similar to the ground-based work. Since the time for each test is limited during parabolic flights, we just focus on the bubble behavior in a rotating system without heat transfer, in particular we are interested in the bubble layer characteristics in reduced gravity. We have already conducted preliminary student experiments during parabolic flights on the bubble behavior. Some results from the tests are presented.

GAS EVOLUTION IN ROTATING ELECTROCHEMICAL SYSTEMS UNDER MICROGRAVITY CONDITION

Principal Investigator : Y. Kamotani
Graduate Assistant : T. Boonpongmanee

Case Western Reserve University

OBJECTIVES

- Investigation of effect of gas evolution on heat and mass transfer in a rotating electrochemical cell

- Construction of a prediction model for heat and mass transfer

Motivation

Electrochemical system to support HEDS require gas bubble removal from electrodes.

Rotation of electrochemical cells is an efficient way to remove bubbles as well as increase efficiency

Approach

Ground-based work on effect of gas evolution on heat and mass transfer

Parabolic flight tests on bubble evolution

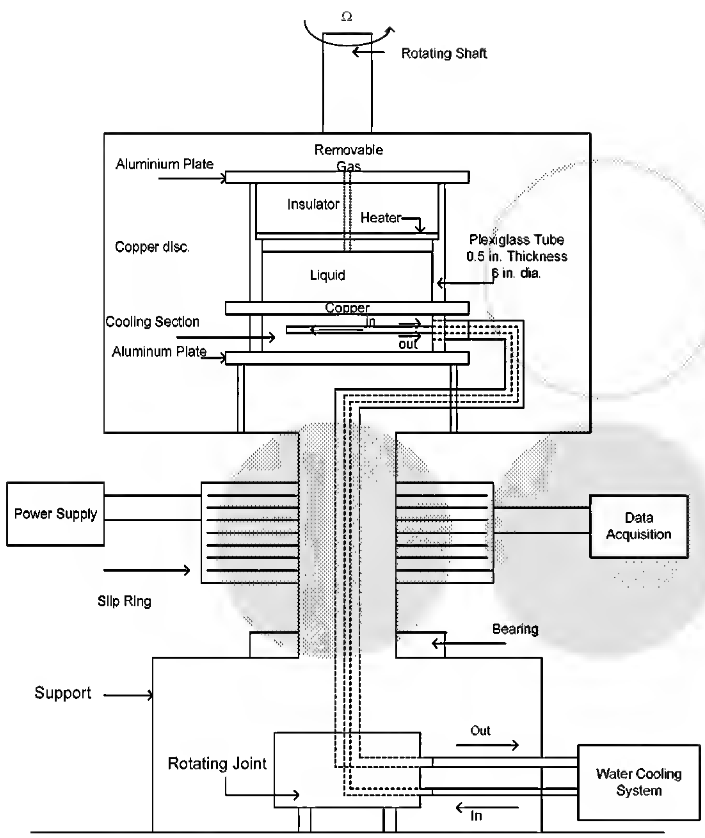

Experimental arrangement

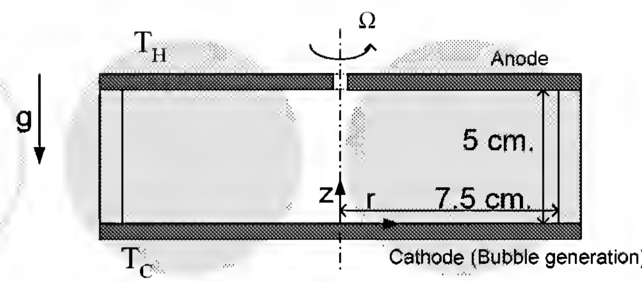

Sketch of rotating cell with heat transfer and gas generation

Ekman suction driven convection

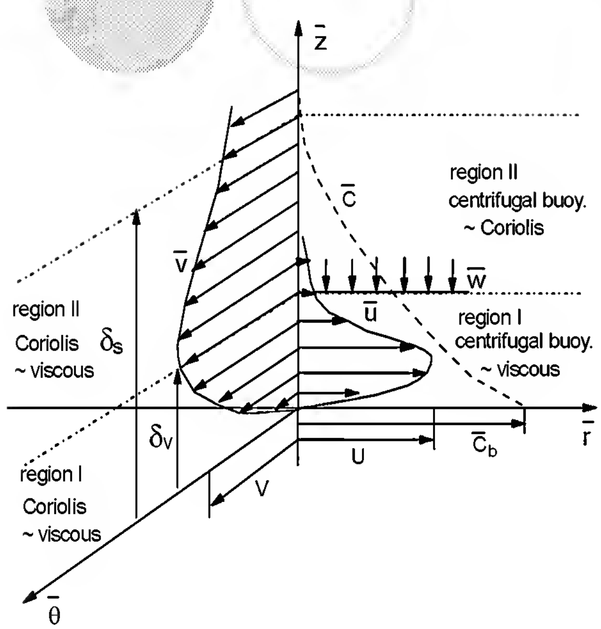

Ekman suction driven convection

$\delta_V \ll \delta_S$ ($ScRo_S \ll 1$) for solutal convection

$\delta_V \ll \delta_T$ ($PrRo_T \ll 1$) for thermal convection

Dimensionless parameters for thermal convection

$$Ac = g/\Omega^2 R$$
$$Ar = H/R$$
$$Ek = \nu/\Omega H^2$$
$$Pr = \nu/\alpha$$
$$Ro_T = \beta \Delta T$$

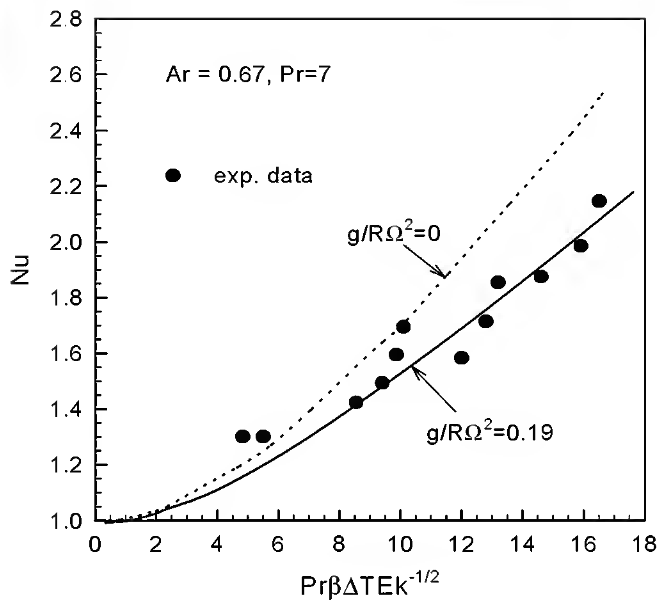

Comparison of computed and experimental
Nusselt numbers

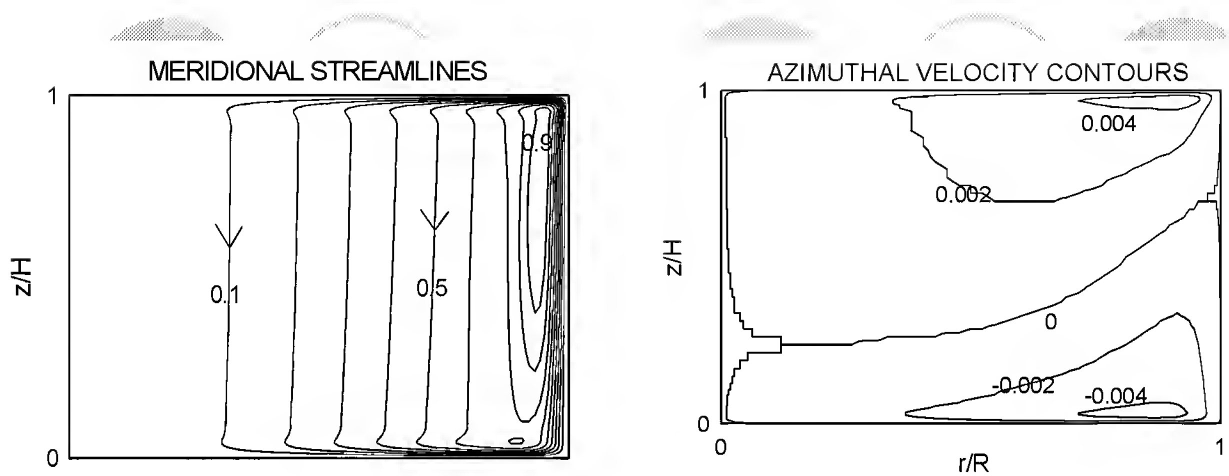

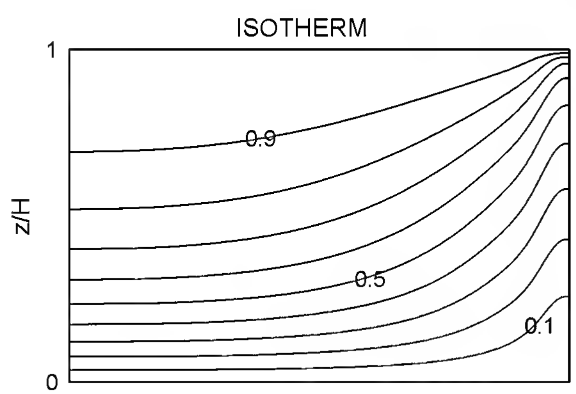

Contour plots in meridional plane (Ek = 2.0×10^{-4}, Ro_T = 0.026, Pr = 7, Ar = 0.67, Ac=0.19).

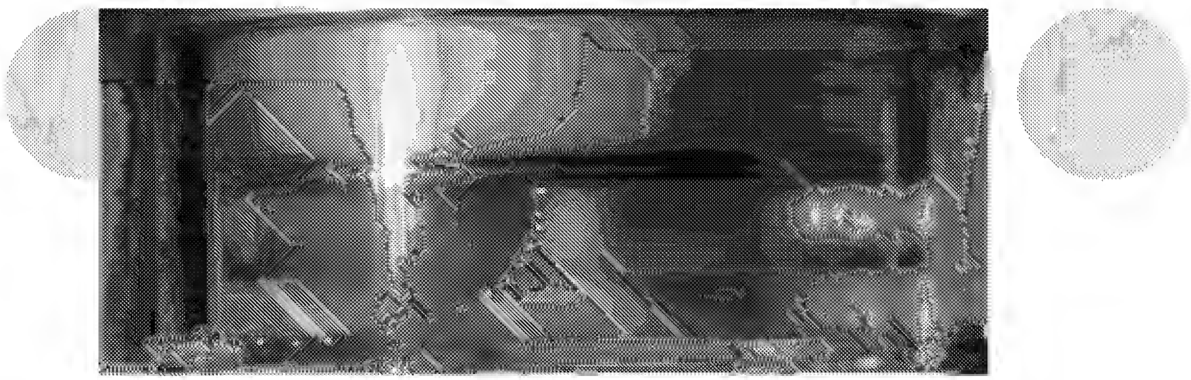

Photograph showing bubble region boundary

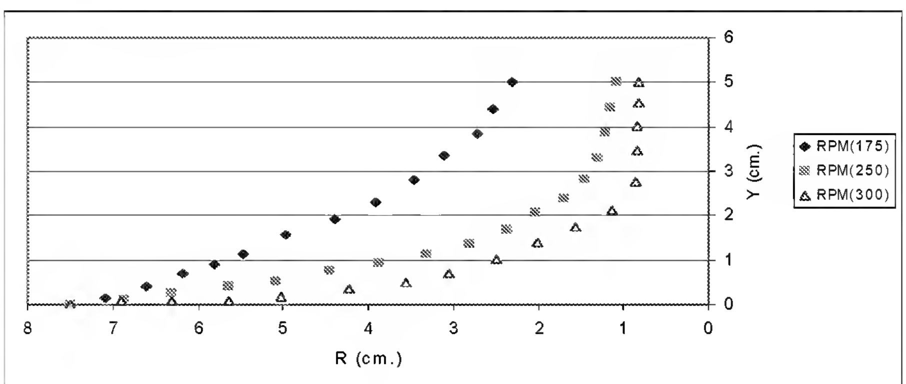

Locations of bubble boundary for different rotation rates

Oscillation Phenomenon (without bubble evolution)

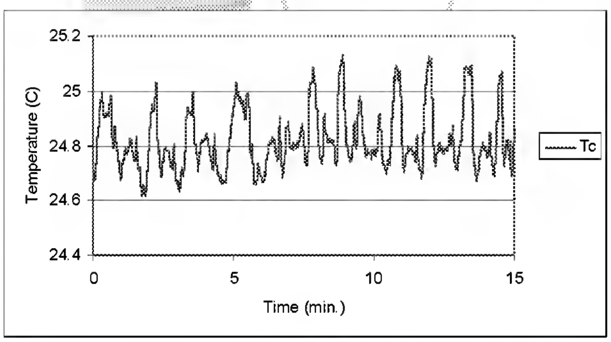

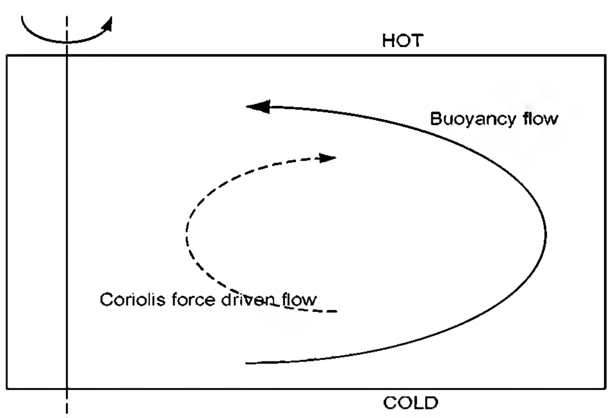

higher rotation rate → larger oscillation

Effect of bubble generation on oscillations

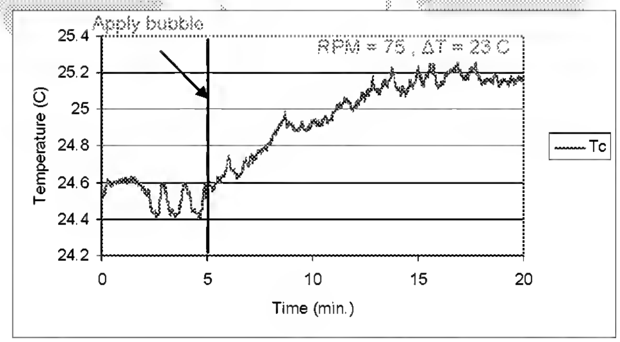

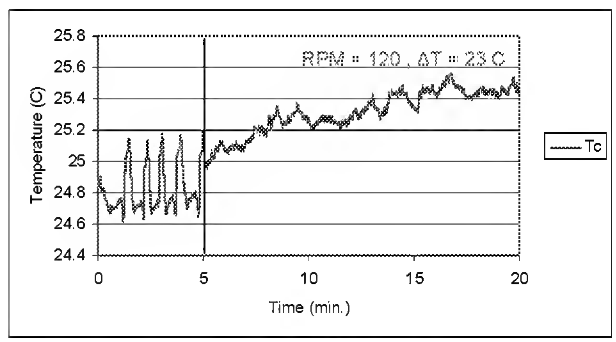

Bubble generation suppresses oscillations

Effect of gas generation on heat transfer with rotation

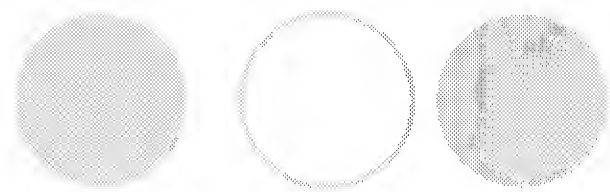

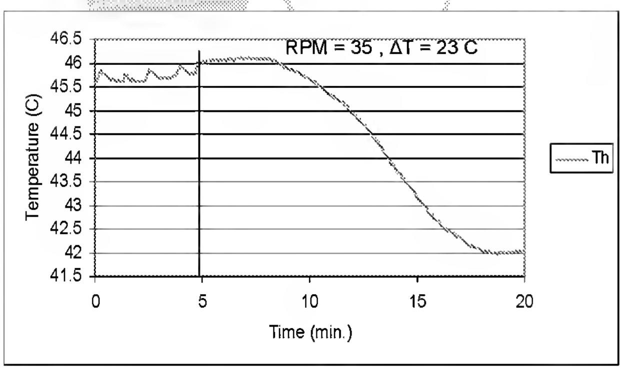

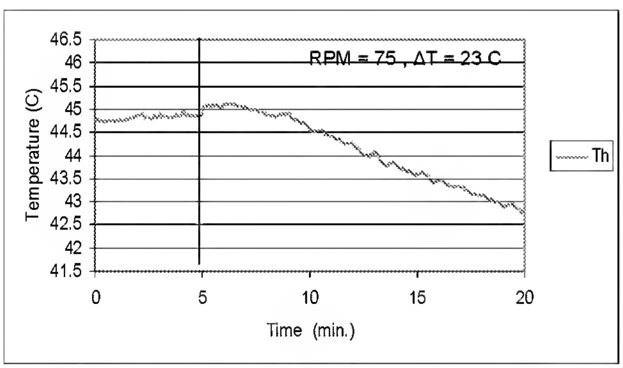

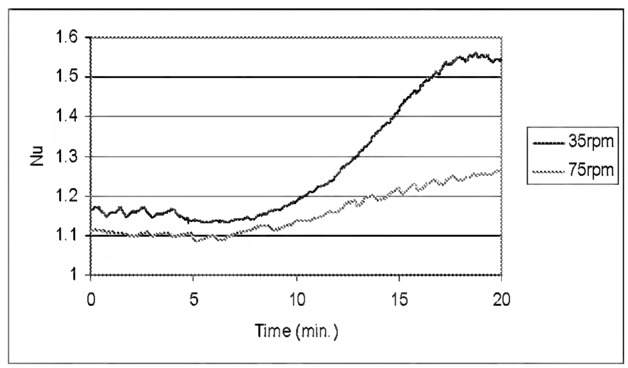

Smaller rotation rate ⟶ larger heat transfer augmentation

ADSORPTION EQUILIBRIUM FOR SEPARATION OF CARBON MONOXIDE AND CARBON DIOXIDE FOR MARS ISRU

Krista S. Walton and M. Douglas LeVan
Department of Chemical Engineering, Vanderbilt University
VU Station B 351604, Nashville, TN 37235
krista.s.walton@vanderbilt.edu m.douglas.levan@vanderbilt.edu
Ph: (615) 322-2441 Fax: (615) 343-7951

ABSTRACT

The overall goal of this part of our research is to determine experimentally the adsorption equilibrium data that will enable efficient design of a separation process to remove carbon dioxide from a CO/CO_2 mixture. An effective separation process will depend on the adsorbent capacity for both the strongly and weakly adsorbed components at the desired operating temperature and pressure ranges, as well as regeneration requirements.

Pure component and binary adsorption isotherms are used to determine the most CO_2-selective adsorbent. A quick uptake of pure CO_2 on a given adsorbent at low pressures compared to the uptake of pure CO on the same adsorbent indicates that CO_2 molecules have a much stronger interaction with the adsorbent surface than CO. This is a necessary property for successful separation by adsorption. Adsorption isotherms are widely available in the literature for many pure components on various adsorbents. Pure component isotherms can be found in various publications and data handbooks for CO and CO_2 on activated carbon and many zeolites [1]. However, the pressure range seldom extends beyond 300 kPa, and the temperature is usually limited as well. Binary adsorption data are much less abundant and are more difficult to measure experimentally [2]. There are models that can predict binary adsorption from the pure component isotherms, but such models rarely provide the desired accuracy. Hence it is necessary to determine both pure component and binary adsorption isotherms to accurately design the separation system [3].

A gravimetric apparatus was used to measure pure adsorption isotherms. This is a desirable method for adsorbent screening due to its ability to provide quick measurements with acceptable accuracy. A sample pan is suspended from a highly sensitive microbalance and is enclosed by a glass tube that is equipped with a water jacket for isothermal experiments. The glassware also contains a coil of nichrome wire that is located around the sample pan and is used to regenerate the adsorbent. During regeneration helium is used to purge impurities from the system as it flows in from the bottom of the glassware and is vacuumed out the top. After regeneration, the system is placed under vacuum, and a data acquisition program is used to record the weight change of the adsorbent with time as the adsorbate is introduced into the system. Equilibrium is reached when the weight of the adsorbent remains constant. The balance can detect weight changes of 10^{-6} grams. CO_2 adsorption isotherms were measured on many adsorbents including

activated carbon and various zeolites. CO adsorption isotherms were measured for the adsorbents with the highest capacity for CO_2. These data are shown in Figure 1.

A volumetric apparatus has been constructed inside an environmental chamber to allow measurement of high-pressure pure component data and binary adsorption data at various temperatures. This apparatus consists of a closed loop containing a circulation pump and a fixed bed packed with adsorbent. The loop is equipped with a pressure transducer to monitor system pressure. A sample cylinder with a pressure transducer is connected to the loop to inject known amounts of gas. After injection, the pump is used to circulate the gas through the fixed bed. An injector and switching valve are used to take 100 μL samples from the loop and inject them into a gas chromatograph. A thermal conductivity detector is used to analyze the composition of the gas after adsorption equilibrium has been reached. Initial moles injected into the loop and final moles remaining in the gas phase at equilibrium are used to calculate the loadings from a material balance. This apparatus has been used to measure adsorption isotherms for pure CO_2 on NaY at 25, 75 and 125°C. These are shown in Figure 2. Mixture data have also been measured to determine the best adsorbent for our application.

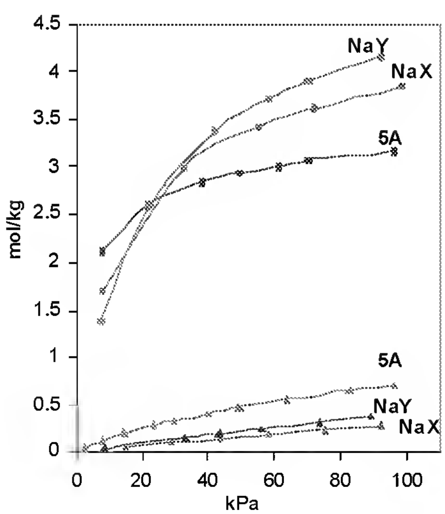

Figure 1. Adsorption equilibria of CO_2 (top three curves) and CO at 25°C.

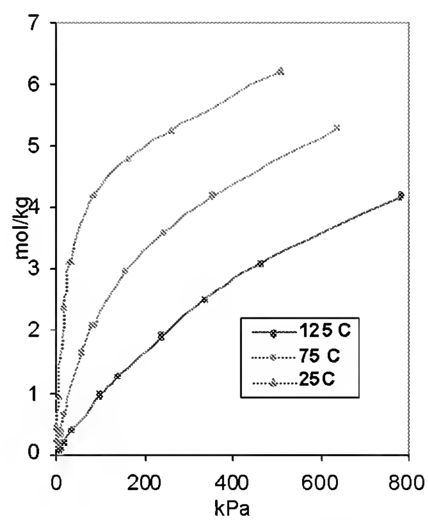

Figure 2. Adsorption equilibria of CO_2 on NaY zeolite using volumetric method.

References:

1. Valenzuela, D. P.; A. L. Myers. *Adsorption Equilibrium Data Handbook.* Prentice-Hall, Inc., Englewood Cliffs, NJ (1989).
2. Vansant, E. F.; G. Peters, I. Michelena. *J. Chem. Res.-S.*, **3**, 90-91 (1978).
3. Talu, O. *Adv. Colloid. Interfac. Sci.*, **76-77**, 227, (1998).

NASA/CP—2002-211212/VOL2

Adsorption Equilibrium for Separation of Carbon Monoxide and Carbon Dioxide for Mars ISRU

Krista S. Walton and M. Douglas LeVan
Vanderbilt University
Nashville, TN

Introduction

Designing an efficient adsorption process for gas separation requires in-depth knowledge of the adsorption equilibrium of each component and their mixtures on the selected adsorbent. It is imperative that the adsorbent have a high capacity for the strongly adsorbed component while maintaining the ability to be easily regenerated.

In our research, we have determined experimentally the adsorption equilibria of CO_2 on various adsorbents. Adsorption equilibria were measured for CO on the adsorbents with highest capacities for CO_2, and a top candidate was chosen for binary adsorption measurements. Thermodynamic and mathematical modeling of the adsorption isotherm data provides the solid foundation for the development of the separation device.

Gravimetric Method for Adsorption Measurement

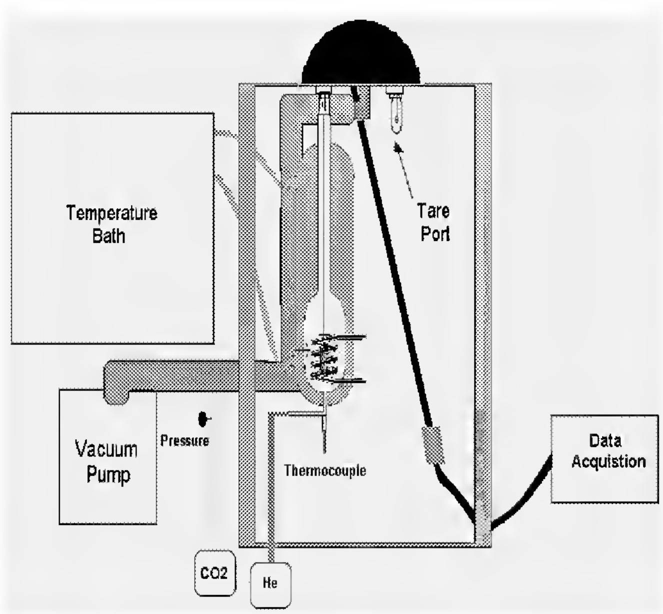

A gravimetric apparatus is a desirable method for screening adsorbents due to its ability to provide quick measurement of pure component adsorption isotherms with acceptable accuracy.

Adsorbent is placed in a sample pan suspended from a microbalance. Uptake is determined directly through measurement of adsorbent weight gain at specified time intervals after a certain pressure of gas is injected into the evacuated system. The glassware is equipped with a nichrome wire coil that can be heated to regenerate the adsorbent. Additionally, a water jacket surrounds the entire sample area to maintain constant temperature during adsorption measurements.

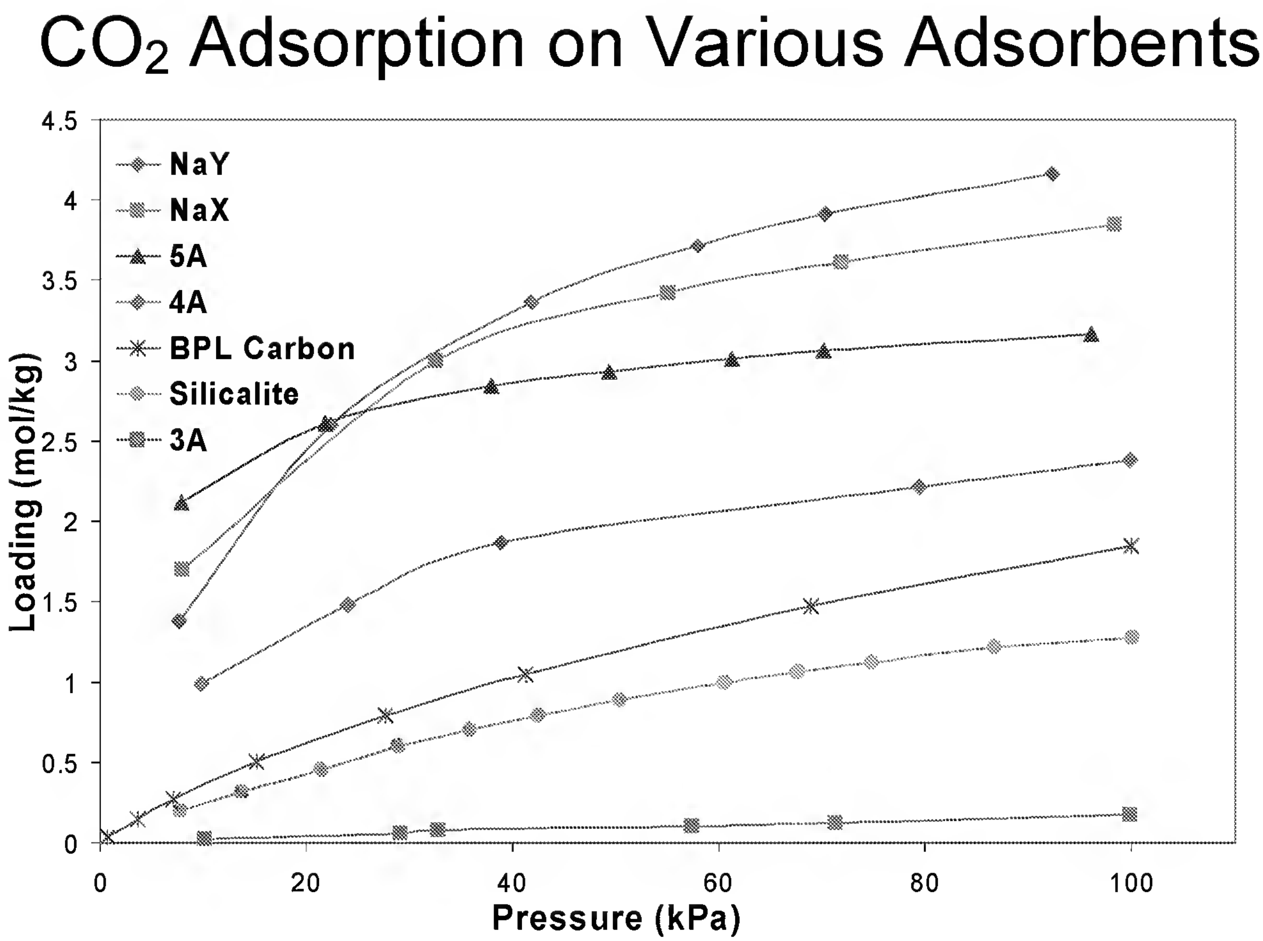

CO_2 Adsorption on Various Adsorbents
NaY
NaX
5A
4A
BPL Carbon
Silicalite
3A
Loading (mol/kg)
Pressure (kPa)
0
0.5
1
1.5
2
2.5
3
3.5
4
4.5
0
20
40
60
80
100

Adsorbent Candidates for Separation Device

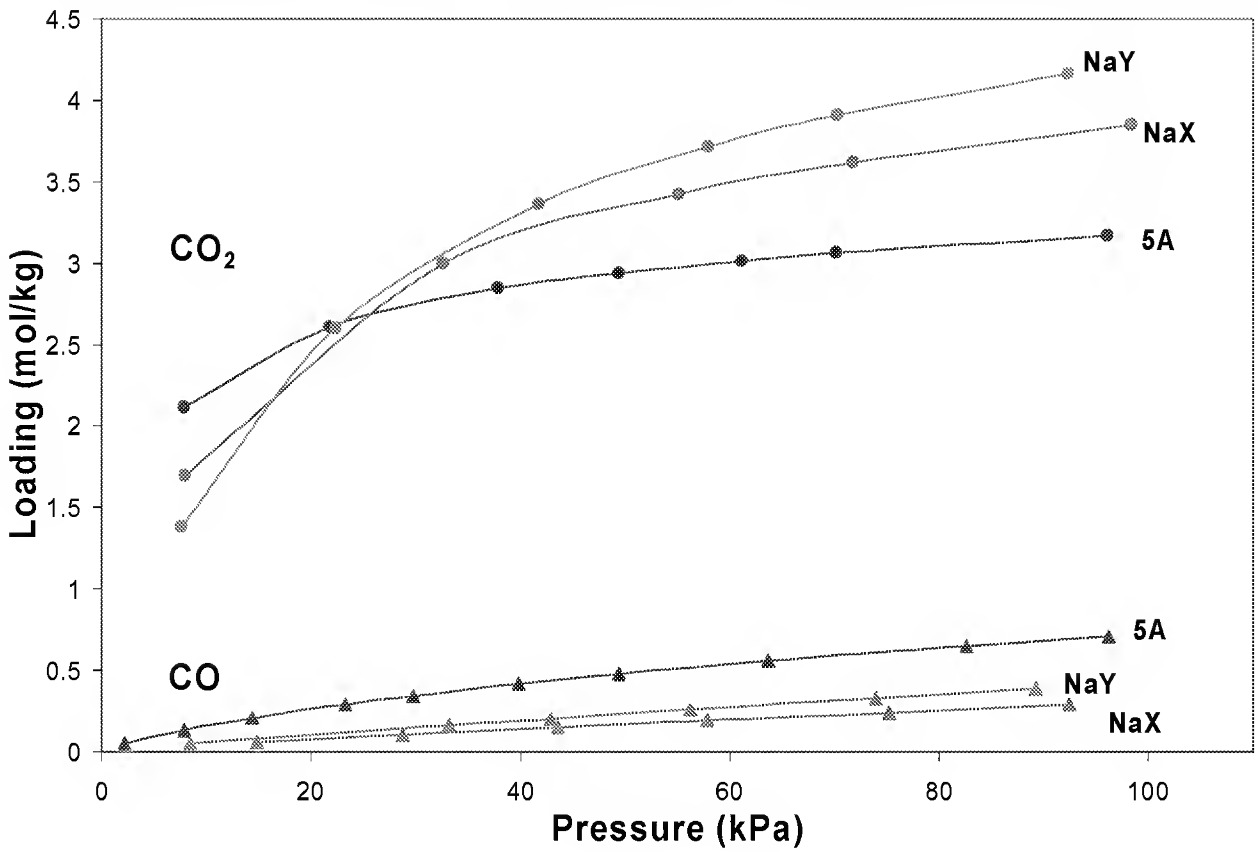

Volumetric Method for Adsorption Measurement

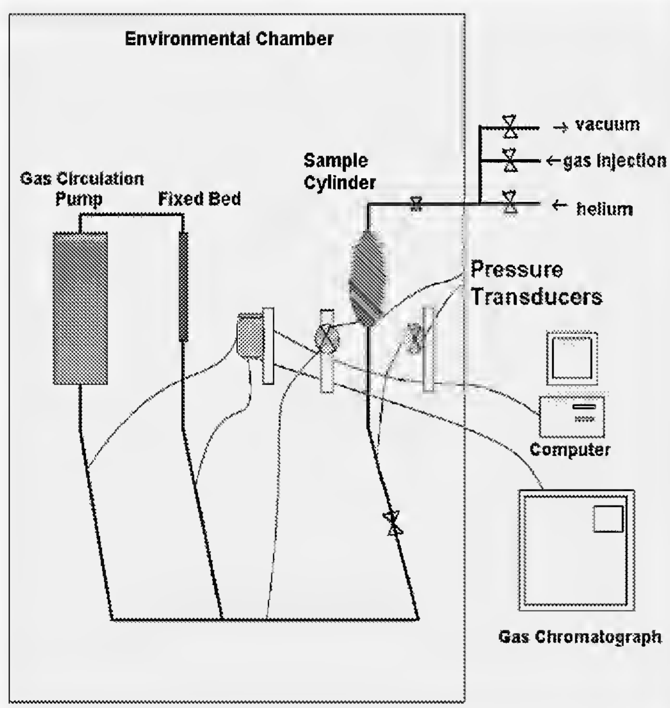

A volumetric apparatus is used to measure pure component and multi-component adsorption equilibria.

A gas of known amount and composition is injected into a closed loop and circulated through a fixed bed. A gas sampling valve takes automatic samples from the loop at specified intervals and injects them into a gas chromatograph. A thermal conductivity detector and appropriate column are used to analyze the gas phase composition.

The initial amount injected less the amount of gas left in the loop gives the amount adsorbed in the fixed bed.

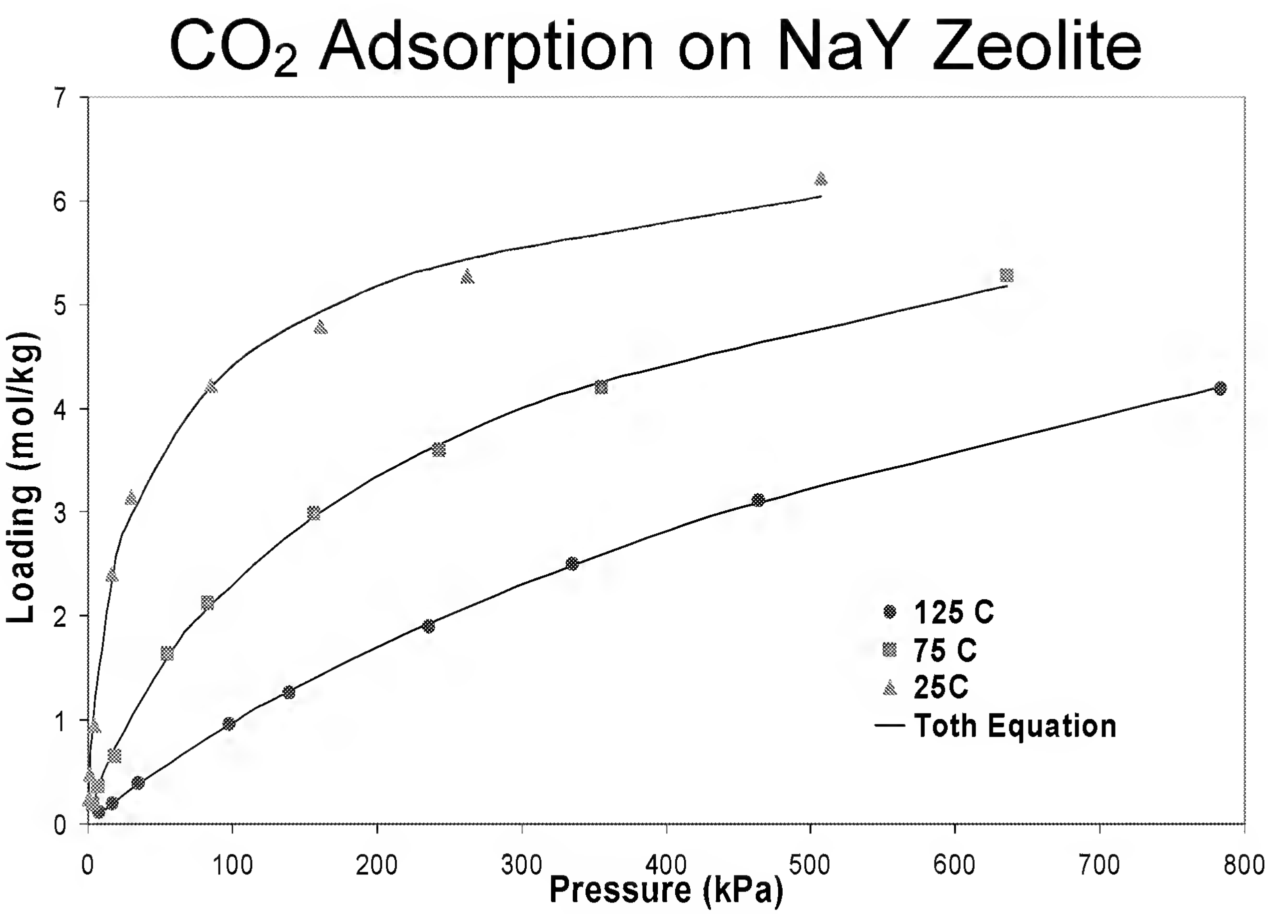
CO2 Adsorption on NaY Zeolite
Loading (mol/kg)
Pressure (kPa)
0
1
2
3
4
5
6
7
0
100
200
300
400
500
600
700
800
125 C
75 C
25C
Toth Equation

Ideal Adsorbed Solution Theory

The IAST[†] provides a reliable method for predicting the adsorption equilibria for components in a gaseous mixture. The only data required for the calculations are pure-component adsorption equilibria for the same temperature and adsorbent of interest.

(1) $y_i P = x_i P_i^o(\pi, T)$ Equation (1) describes the equilibrium relationship between gas phase composition and adsorbed phase composition for an ideal adsorbed solution of components, *i*. P_i^o is the pure component vapor pressure of component *i* at the temperature T and spreading pressure π of the mixture. x_i is the adsorbed phase mole fraction, and $y_i P$ is the known gas phase composition.

(2) $\frac{\pi A}{RT} = \int_0^{P_i^o} \frac{n_i}{P_i} dP_i$ Guess πA and calculate P_i^o from eqn (2) for each component, where n_i is the loading given by the Toth equation shown in eqn (3). Eqn (1) is then used to calculate x_i, and if the sum is not equal to 1, a new guess is made for the spreading pressure. The calculations continue until the sum of the mole fractions is 1. Eqns (4) and (5) are then used to calculate the loadings for each component.

(3) $n_i = \frac{abP_i}{\left[1+(bP_i)^c\right]^{1/c}}$ (4) $\frac{1}{n_T} = \sum_1^i \frac{x_i}{n_i^o}$ (5) $n_i = x_i n_T$

[†]Myers, A.L., and Prausnitz, J.M., "Thermodynamics of Mixed-Gas Adsorption", *AIChE J.*, **11**, 121-127 (1965).

CO/CO$_2$ Adsorption on NaY

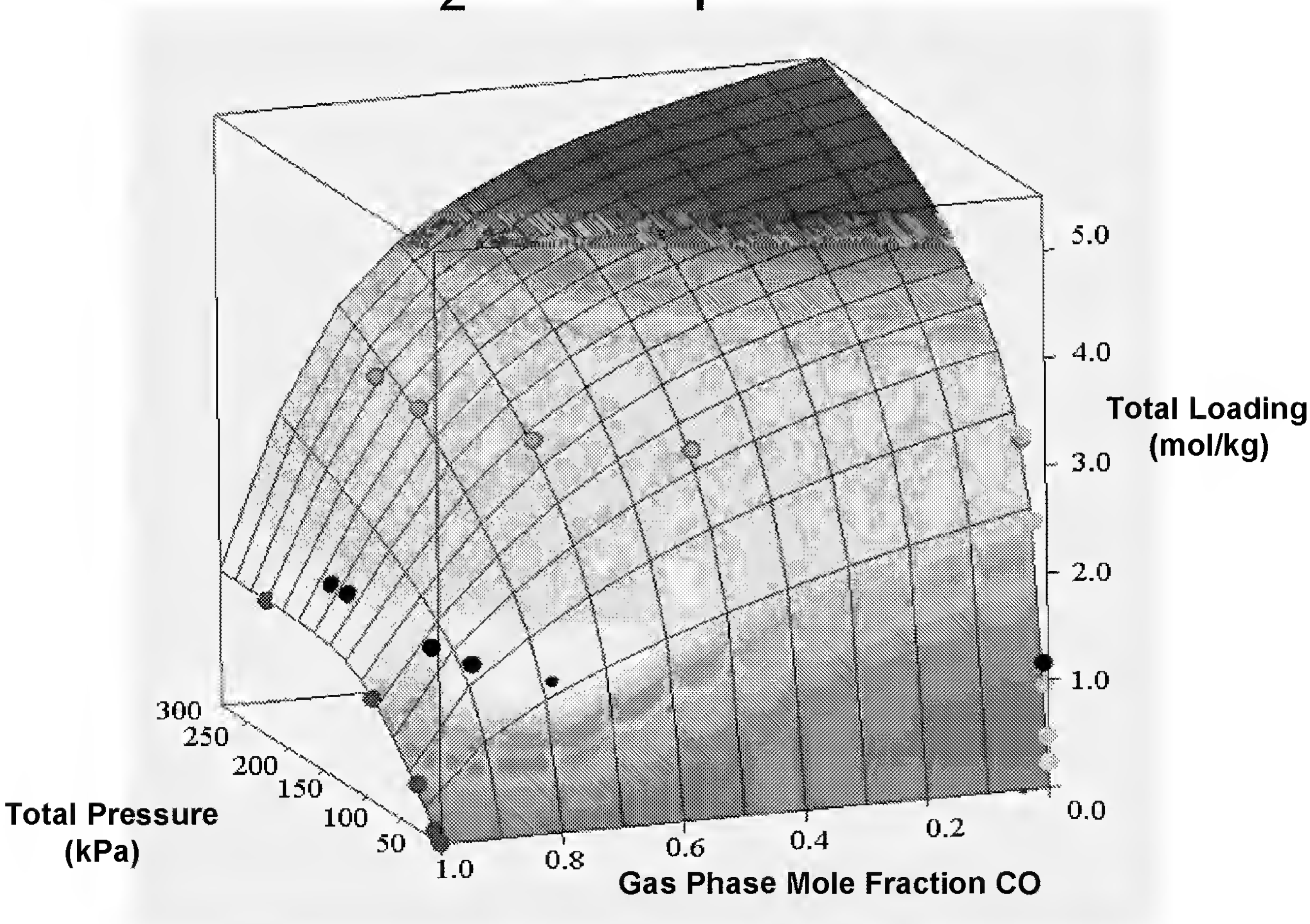

Conclusions

Our experimental results show that NaY zeolite is the best candidate for use in a separation device to produce pure CO from a CO/CO_2 mixture. Pure-component data show that NaY has a high capacity for CO_2 with very little adsorption of CO at the same temperatures. Additionally, NaY exhibits a quick uptake of CO_2 at relatively low pressures, indicating a strong interaction of CO_2 molecules with the adsorbent surface. The Toth equation was used to describe the pure-component adsorption equilibria for both pure components.

Binary adsorption measurements for CO/CO_2 mixtures on NaY at 298K were made using the volumetric apparatus. The Ideal Adsorbed Solution Theory was used to generate a three-dimensional surface of total loading, total pressure, and mole fraction of CO in the gas phase. The experimental data fit the IAST with an average error of 6.6% and 2.5% for low and high total loadings, respectively.

Our separation device is currently under construction. With a predictive model for binary adsorption equilibria, computer simulations are now being performed to model heat and mass transfer effects for proposed PSA/TSA cycles.

ON THE MOTION OF AN ANNULAR FILM IN MICROGRAVITY GAS-LIQUID FLOW

John B. McQuillen
Microgravity Fluid Physics Branch
NASA Glenn Research Center
21000 Brookpark Road,
Cleveland, OH 44135
PH (216)433-2876
FAX (216)433-8050
j.mcquillen@grc.nasa.gov

ABSTRACT

Three flow regimes have been identified for gas-liquid flow in a microgravity environment: Bubble, Slug, and Annular. For the slug and annular flow regimes, the behavior observed in vertical upflow in normal gravity is similar to microgravity flow with a thin, symmetrical annular film wetting the tube wall. However, the motion and behavior of this film is significantly different between the normal and low gravity cases. Specifically, the liquid film will slow and come to a stop during low frequency wave motion or slugging. In normal gravity vertical upflow, the film has been observed to slow, stop, and actually reverse direction until it meets the next slug or wave.

Using the unit slug approach, as seen in Figure 1, a quick estimate for the film thickness can be derived by the following relationship:

$$\alpha = 1 - \left(\frac{2h}{D}\right)^2$$

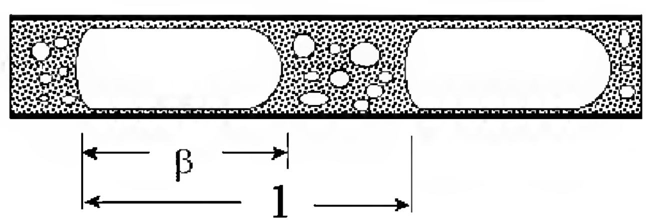

Figure 1: Unit Slug Concept

Combined with the following from the drift flux model:

$$\alpha = \frac{\frac{\rho_L}{\rho_G}\frac{x}{1-x}}{C_0\left(1+\frac{\rho_L}{\rho_G}\frac{x}{1-x}\right)}$$

Rearranging yields the film thickness, however, this estimate assumes that the vapor and liquid phases are either distributed in an annular flow with very thin liquid slugs separating annular pockets or with significant gas entrainment in the liquid slugs.

A minimum film thickness can be attained by assuming that most of the gas is contained in the Taylor bubble. Therefore, if one slug unit consists of both a liquid slug and a Taylor bubble and assuming that the void fraction is zero in the slug, a mass balance performed on the Taylor bubble portion of the slug unit will obtain the following:

$$\alpha_B V + (1-\alpha_B) U_{LB} = j_L + j_G$$

By rearrangment, the void fraction in the Taylor bubbles is given by:

$$\alpha_B = 1 - \frac{V - (j_G + j_L)}{V - U_{LB}}$$

where V is the velocity of the Taylor bubble and U_{LB} is the velocity of the liquid film. Within the Taylor bubble, the film thickness decreases from the nose to the tail. Far from the nose, it reaches its fully developed thickness. This thickness may be found directly by noting that there is no driving force acting on the film except for the interfacial shear stress. By disregarding this effect, the film does not experience a driving force and its velocity must be zero with respect to the standing frame (U_{LB}=0). This has been experimentally confirmed by watching small bubbles that are entrained in the thin liquid film around the Taylor bubble and gives the minimum film thickness in these bubbles:

$$h_{min} = \frac{D}{4}\frac{V - (j_G + j_L)}{V}$$

If $V \approx C_0(U_{LS} + U_{GS})$, then

$$h_{\min} = \frac{C_0 - 1}{C_0}\frac{D}{4}$$

For values of C_0=1.2, the minimum film thickness is approximately 0.8 mm, which is significantly smaller than the values found using the drift flux model.

Data obtained for air-water, air-water and glycerine mixture (50 w/o and viscosity @), and an air-water and surfactant mixture (Zonyl FSP™, 1 w/o and surface tension of 20 dynes/cm) was obtained at in a 1.27 cm ID tube at low gravity[1]. 16 mm movie film data was obtained at 400 frames per second. Bubbles located within the thin liquid annular film were tracked for their position as a function of time and analyzed as a measure of the liquid axial velocity relative to the passage of slugs or annular roll waves. It was found that there was always a slowing of the thin liquid film or substrate until the next slug or roll wave accelerated the film again.

Liquid film thickness data was obtained at 1000 Hz from thin wire conductivity probes. Their accuracy was about 0.02 mm. A histogram analysis was used to obtain a truncated film thickness, by excluding values greater than 1.5 mm film thickness, the mode, and a minimum film thickness. These are compared with an average value that includes wave heights or slugs. In several cases, for both when the liquid film motion stopped or even just significantly slowed, it was found that, for obvious reasons, that the truncated averaged film thickness was less than the average film thickness, the mode value was less than both of the averages and that the "minimum" experimental film thickness was typically less than half of the both averages.

---

1 Bousman, W. S., "Studies of Two-Phase Gas-Liquid Flow in Microgravity," *NASA Contractor Report 195434*, 1995.

In Normal Gravity Vertical Upflow, Liquid Film reverses Direction Between Slugs, Churns and/or Roll Waves

Visual Observations of Microgravity Gas-Liquid Flow Data Reveal that Liquid Substrate slows significantly between Liquid Slugs or Roll Waves.

Film Velocity as a Function of Entrained Gas Bubbles

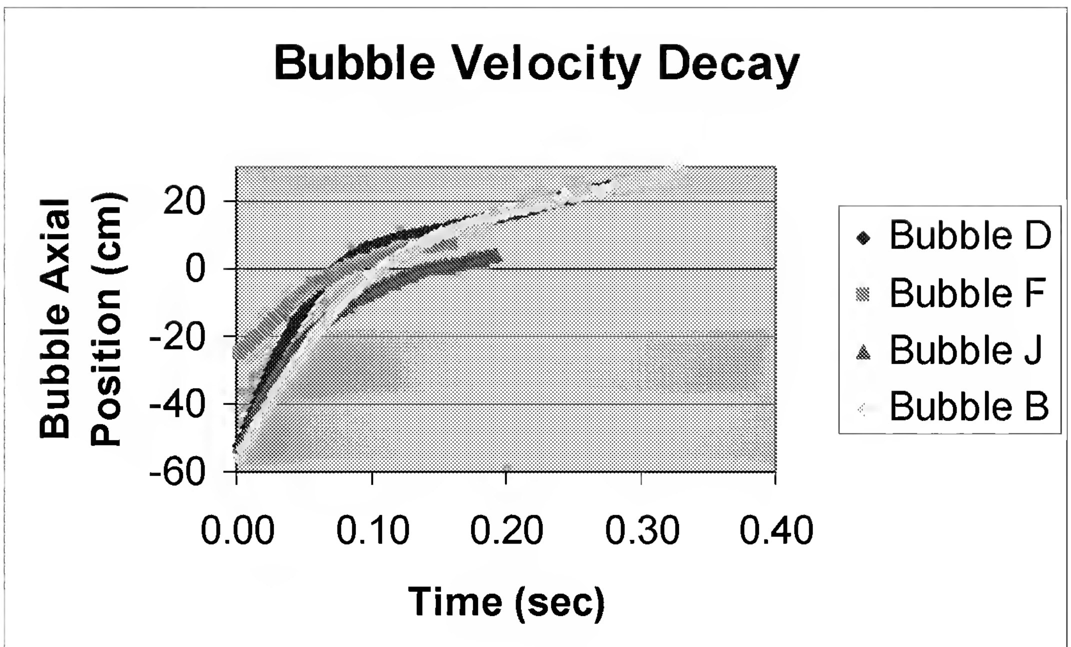

Test Section Layout

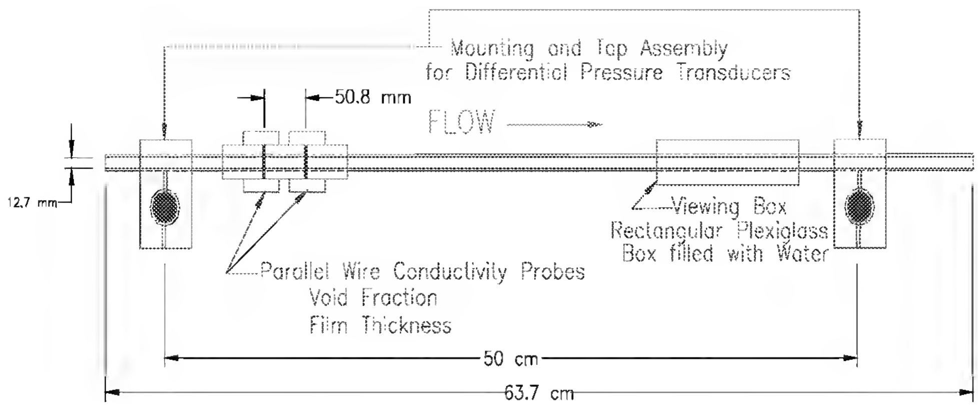

Cross-sectional View of Conductivity Probes

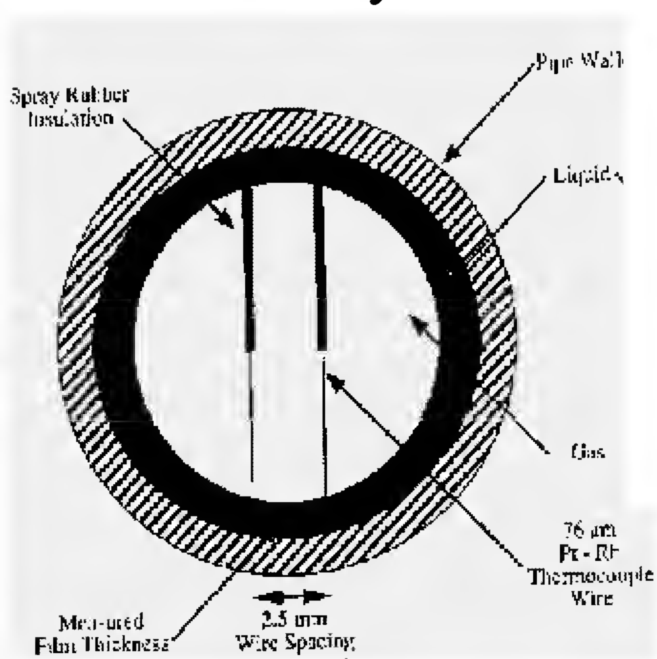

Unit Slug Concept

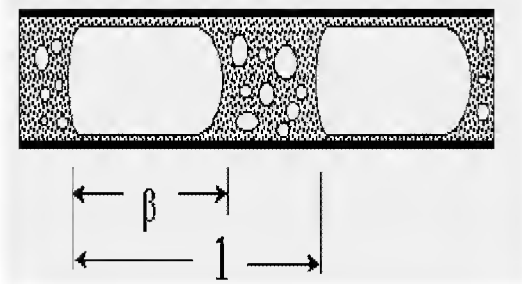

Film Thickness and Void Fraction Relationship

$$\alpha = 1 - \left(\frac{2h}{D}\right)^2$$

From Drift Flux Model

$$\alpha = \frac{\frac{\rho_L}{\rho_G}\frac{x}{1-x}}{C_0\left(1 + \frac{\rho_L}{\rho_G}\frac{x}{1-x}\right)}$$

Mass Balance on Taylor Bubble Portion of Unit Slug

$$\alpha_B V + (1-\alpha_B)U_{LB} = j_L + j_G$$

Only Force on Film is Interfacial Shear ~ 0 based on Bubble motion

Minimum Film Thickness

$$h_{min} = \frac{D}{4}\frac{V - (j_G + j_L)}{V}$$

If $V \approx C_0(U_{LS} + U_{GS})$

$$h_{\min} = \frac{C_0 - 1}{C_0}\frac{D}{4}$$

For values of C_0=1.2 , h_{min} =0.8 mm.

Film Thickness Time Traces

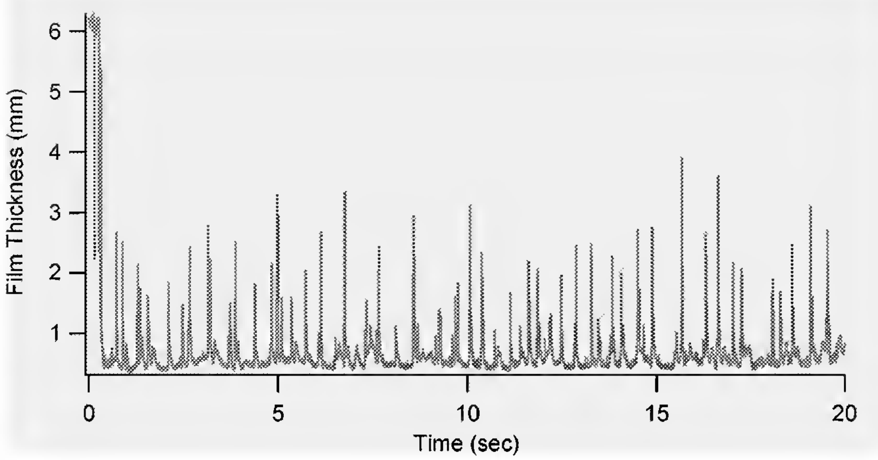

Slug

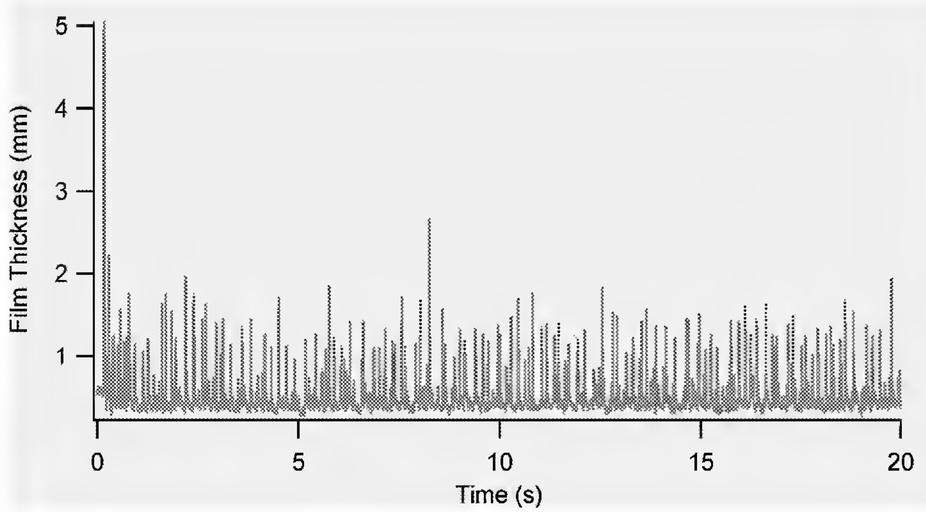

Annular

Histogram Plots

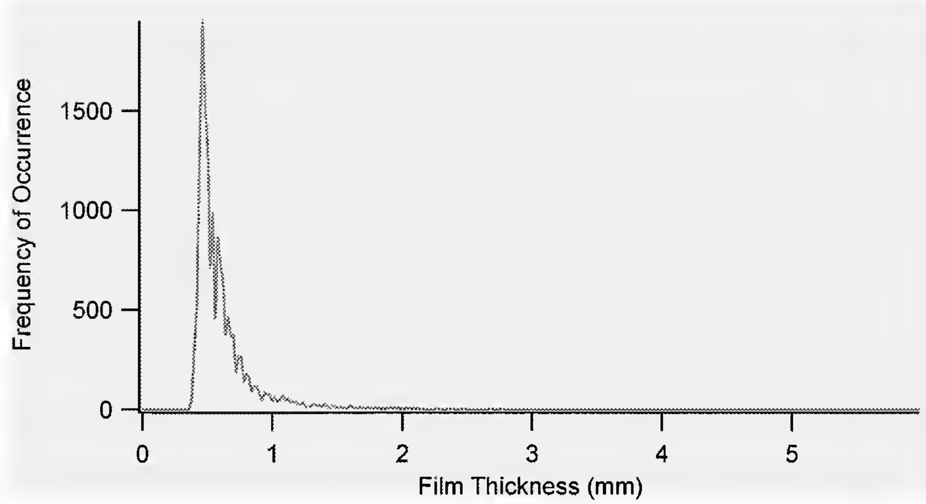

Slug

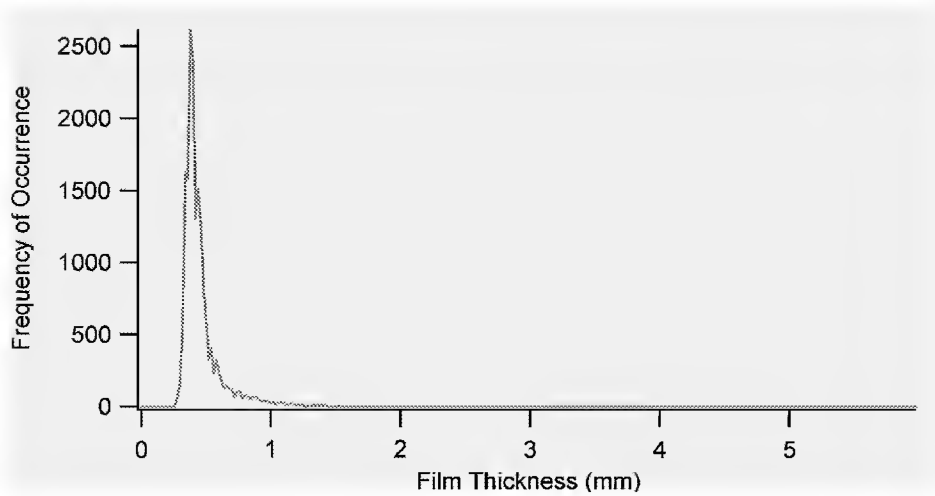

Annular

Comparison of “Film Thicknesses”

Test	Film Thickness Average	Film Thickness Standard Deviation	Average Liquid Substrate Thickness	Liquid Substrate Thickness Standard Deviation	Film Thickness Mode	Minimum Film Thickness
82t1	0.51	0.23	0.49	0.09	0.42	0.24
82t2	1.03	0.74	0.72	0.28	0.62	0.28
83t1	0.90	0.38	0.71	0.21	0.74	0.50
93t1	1.13	0.73	0.79	0.31	0.74	0.58
93t2	1.43	1.34	0.74	0.21	0.84	0.50
96t1	1.05	0.24	0.98	0.24	0.80	0.48
99t12	1.08	0.49	0.96	0.18	0.86	0.38
99t22	1.18	0.68	1.07	0.39	0.86	0.52
101t12	0.46	0.16	0.46	0.15	0.38	0.26
102t12	0.61	0.22	0.43	0.11	0.46	0.36
103t13	0.46	0.24	0.45	0.21	0.34	0.22
103t22	0.75	0.32	0.70	0.16	0.60	0.28

Summary

- Liquid Film Substrate Motion Slows Between Slugs and Roll Waves Based on Liquid Properties and Slugging Frequency(taylor Bubble Length)
- Liquid Film Substrate Based on Unit Slug Concept
  - Independent of Fluid Properties
  - Agrees Well With "Average Film Thickness Measurements for Slug and Annular Flow
  - Histogram Analysis Reveals That Mode and Actual Minimum Film Thickness

MIXING OF CONCENTRATED OIL-IN-WATER EMULSIONS MEASURED BY NUCLEAR MAGNETIC RESONANCE IMAGING (NMRI)

M.A. d'Avila, N.C. Shapley, J.H. Walton*, S.R. Dungan, R.J. Phillips and R.L. Powell
Department of Chemical Engineering and Materials Science,
University of California, Davis
*** NMR Facility, University of California, Davis**

In most emulsions, a density difference between the dispersed and the continuous phases leads to separation of the components by gravity, known as "creaming." Typically, a uniform emulsion is desirable, and hence it is important to examine the kinetics and mechanism of emulsion mixing required to achieve this uniform state. In addition, previous mixing research has focused on the impact of known flow fields on the microstructure of the system, where the microstructures do not modify the flow field in the process. In contrast, in the case of concentrated emulsions, it is shown here that the evolution of the nonuniform droplet concentration profile has a major impact on the observed flow field.

Mixing of concentrated oil-in-water emulsions in a horizontal, concentric-cylinder geometry was studied using nuclear magnetic resonance imaging (NMRI). The NMRI technique provides droplet concentration and velocity profiles noninvasively and *in situ* within a flowing, concentrated emulsion of isooctane and water stabilized with nonionic surfactant. An initial nonuniform concentration profile is established by creaming of a homogeneous emulsion. We then measure the time-dependent effect of slow shear flow on the concentration and velocity profiles. Time-of-flight and chemical shift imaging methods were used to measure velocity profiles and concentration maps during the mixing process, respectively.

The results obtained show detailed information about the mixing process in concentrated emulsions. It was found that the thickness of the cream layer remains constant during mixing while the concentration in that layer decays exponentially as a function of time. It was also observed that while mixing occurs, most of the emulsion is quiescent, the only detectable motion being in a thin moving layer close to the rotating outer cylinder wall. A simple model is introduced that is able to give a reasonable explanation of these experimental observations. These results indicate that the mixing mechanism and kinetics in concentrated emulsions are significantly different from those in single-phase liquids.

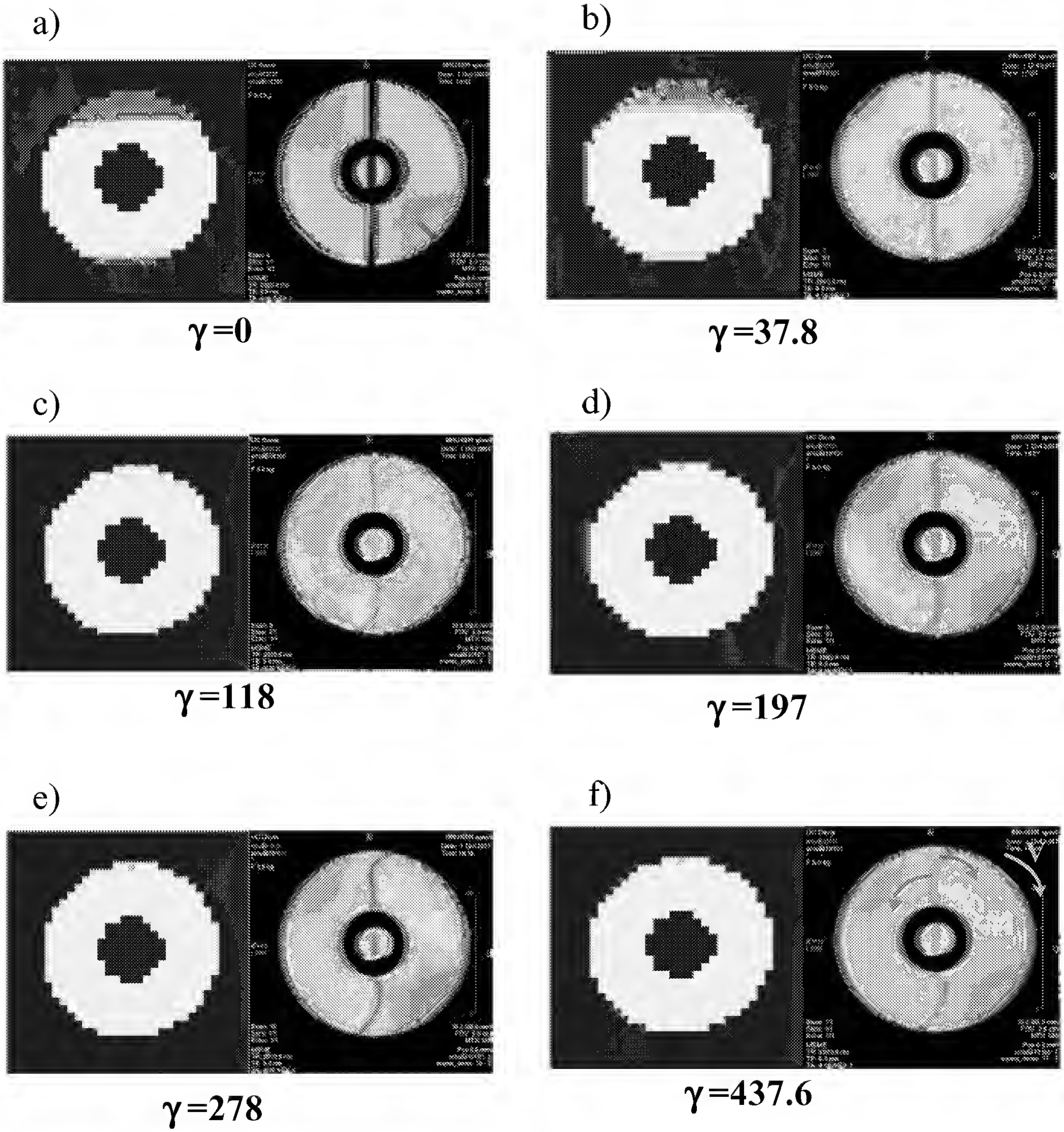

Side by side oil concentration maps and time-of-flight images for an emulsion with $\phi = 0.5$ and $V = 0.05$ cm/s, after 3 hours of creaming. The series of images shows the progression of mixing as the strain increases from a) γ=0, b) γ=37.8 , c) γ=118, d) γ=197, e) γ=278, to f) γ=437.6.

Marcos A. d'Avila, Nina C. Shapley, Jeffrey H. Walton, Stephanie R. Dungan, Ronald J. Phillips and Robert L. Powell

University of California, Davis

Introduction

Study mixing in initially creamed, concentrated emulsion

- **Important in cosmetics, pharmaceuticals, foods**
- **30-50 vol.% isooctane-in-water**
- **0.5 wt% nonionic surfactant (Tween 20)**
- $\eta(\phi=40\%) = 1.8$ cP
- $\rho_{isooctane} = 0.69$ g/cm^3

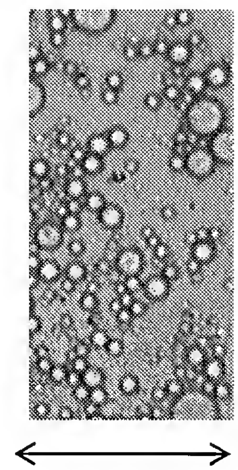

Log-normal droplet size distribution

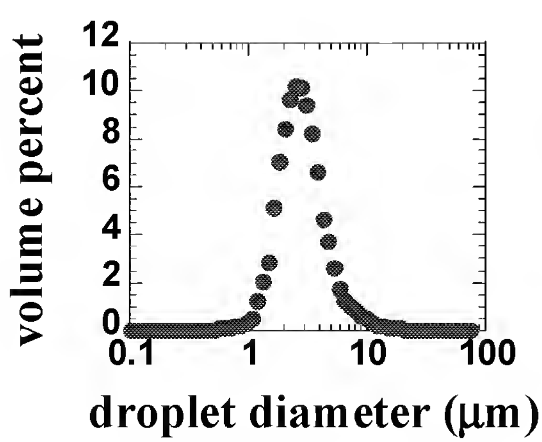

Mean diameter = 3.2 μm

Probe

- Flow in concentric cylinder device
- $(R_o - R_i) / R_i = 1.75$
- Length/Gap = 40
- Outer cylinder rotates

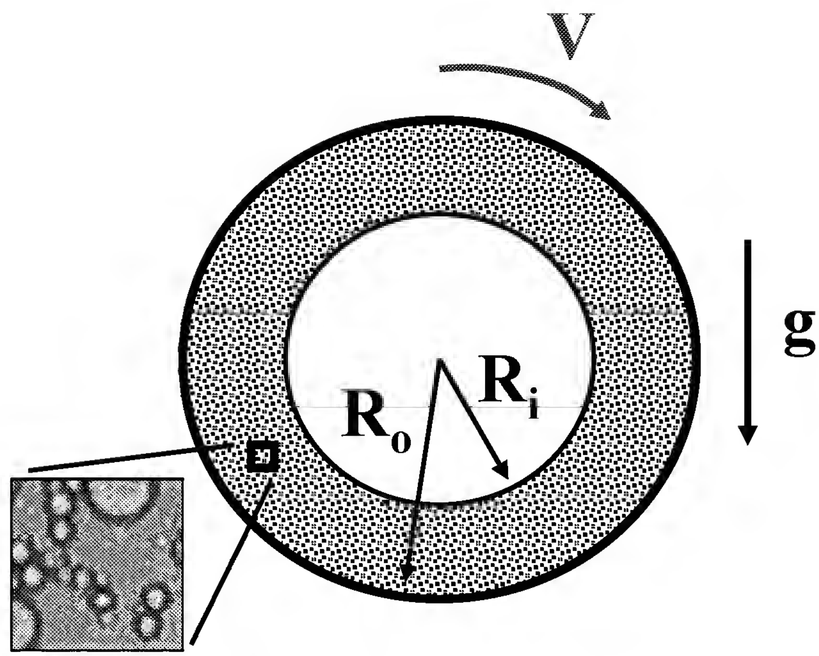

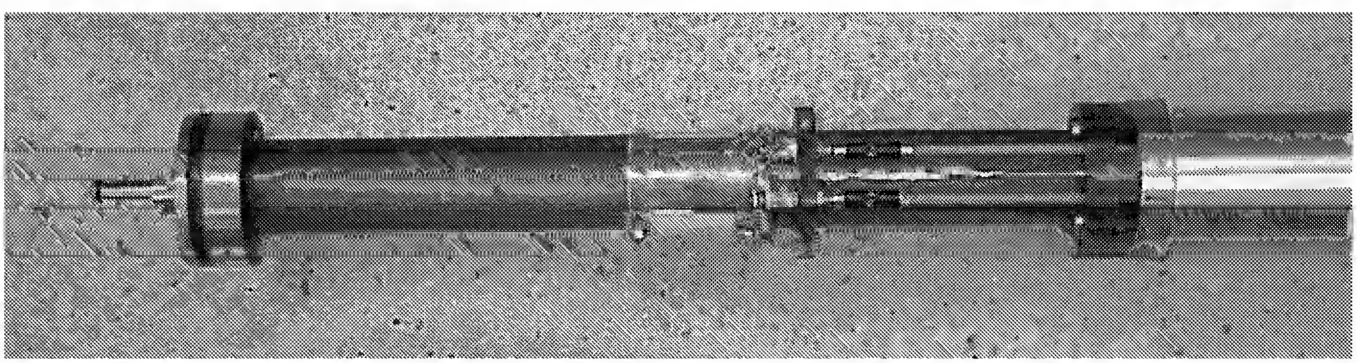

- Custom-built 300 MHz Alderman-Grant RF coil
- Imaging system: 7 T magnet, maximum gradients of 95 G/cm

NMR Flow Imaging Methods

• **Noninvasive techniques for measuring velocity**

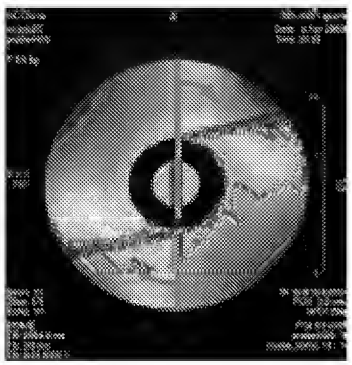

= 0.3 rev/s

• **Time-of-Flight Velocimetry**

Displacement of marked material indicates velocity.

Velocity profile visualization

• **Phase Encoding Imaging**

Phase of NMR signal is proportional to velocity.

2-D velocity maps

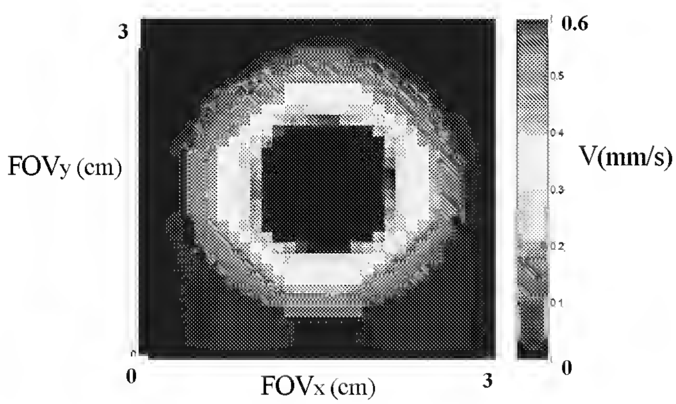

Chemical Shift Imaging

- **Noninvasively measure oil concentration**

<u>Chemical shift imaging</u>
Measure NMR spectrum in each pixel
Peak area α vol. fraction

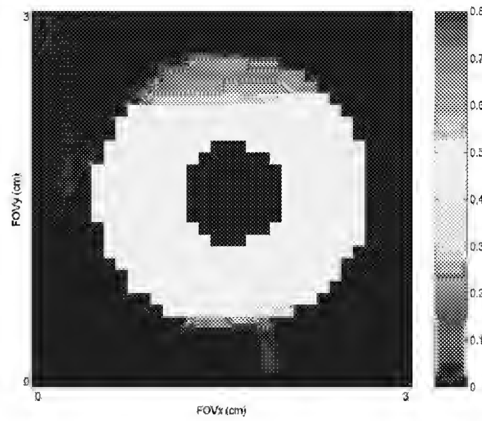

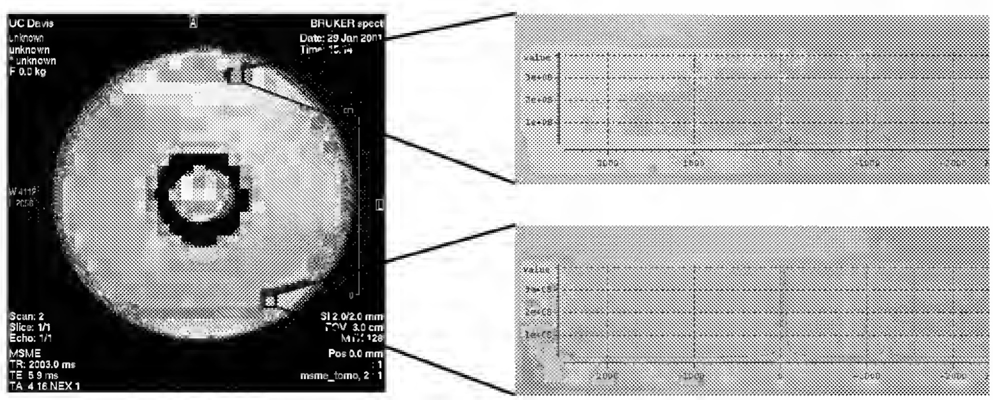

<u>Image calibration</u> - eliminates artifacts

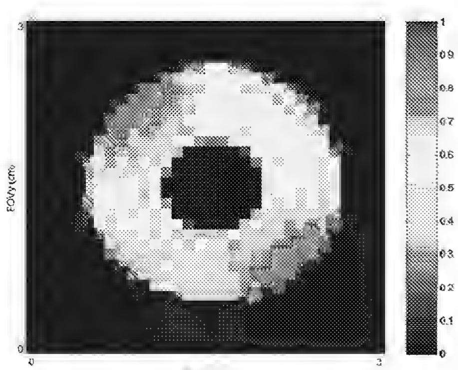

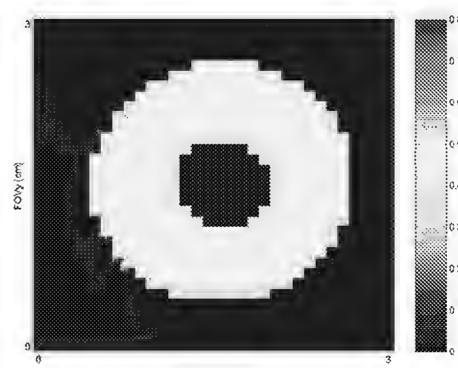

Results: $\phi_{bulk} = 0.5$, V = 0.05 cm/s

average strain, $$\gamma = \frac{V}{R_o - R_i} t$$

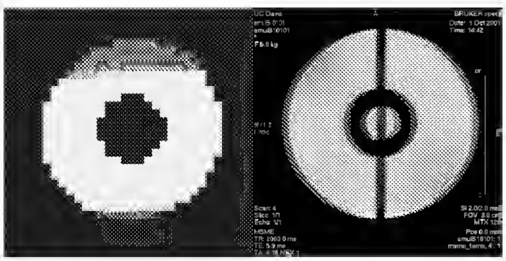

$\gamma = 0$

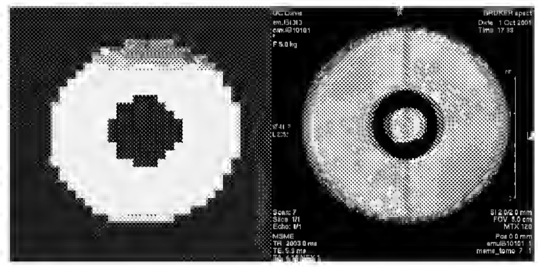

$\gamma = 37.8$

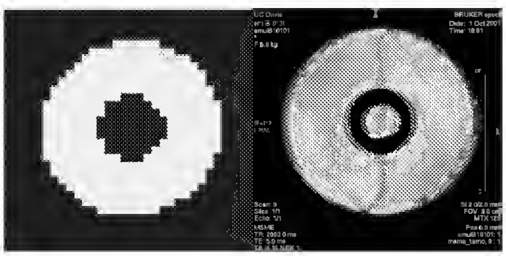

$\gamma = 118$

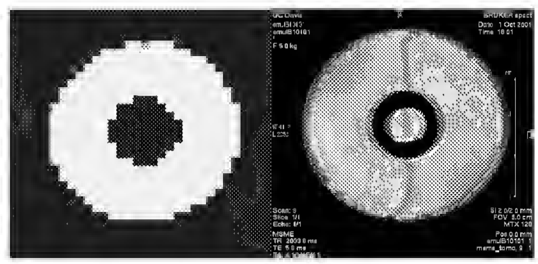

$\gamma = 197$

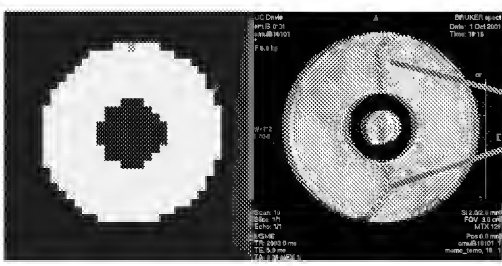

Profiles are not symmetric

$\gamma = 278$

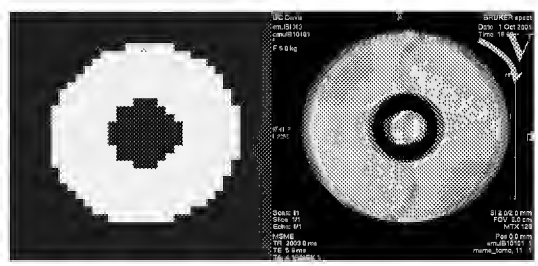

$\gamma = 437.6$

Counter-rotating flow due to buoyancy effects.

Concentration Profiles and Kinetics

Creamed layer thickness does not change

$\phi_{bulk} = 0.4$

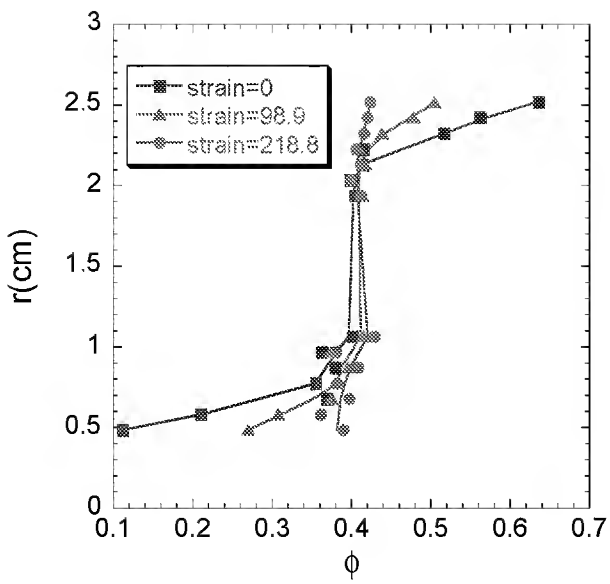

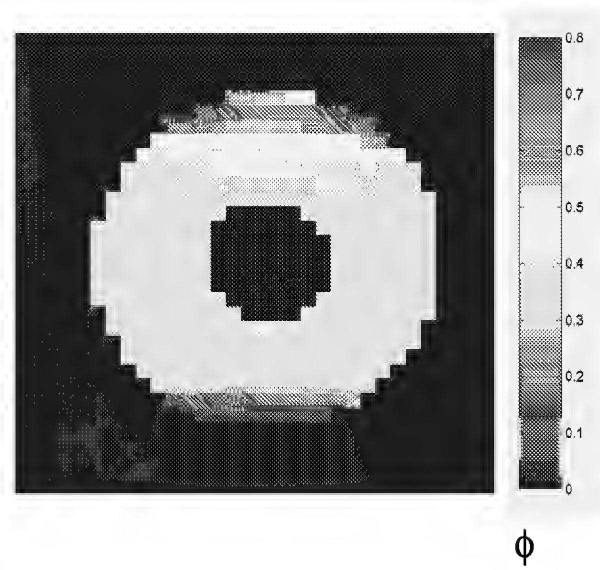

$$\varphi = \frac{\phi - \phi_{bulk}}{\phi_{bulk}}$$

$$\varphi(\underline{r}, t) = f(\underline{r})\, g(t)$$
$$= f(\underline{r}) \exp(-\lambda\gamma)$$

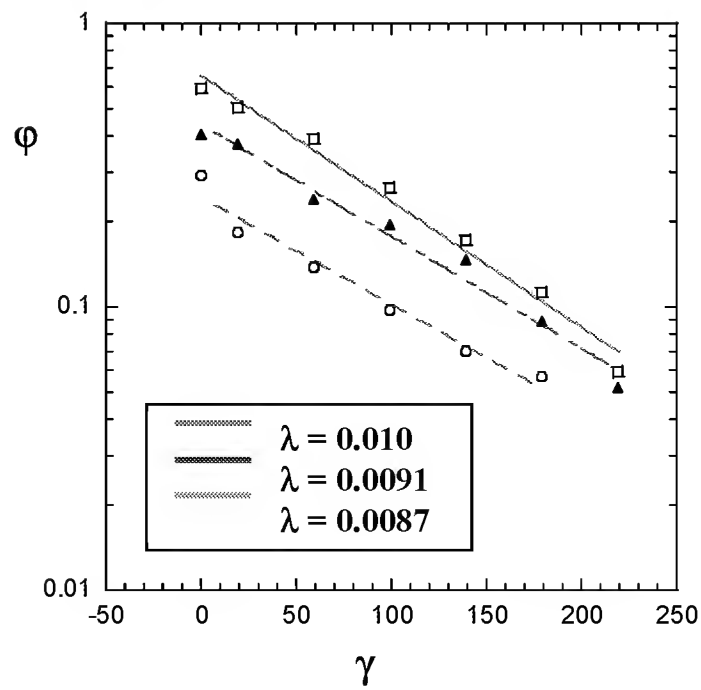

Average decay rate :
$\lambda = 0.00933 \pm 0.0008$

Velocity Profiles

Velocity profile develops once emulsion is well-mixed.

Upper, vertical center line, V = 0.05 cm/s

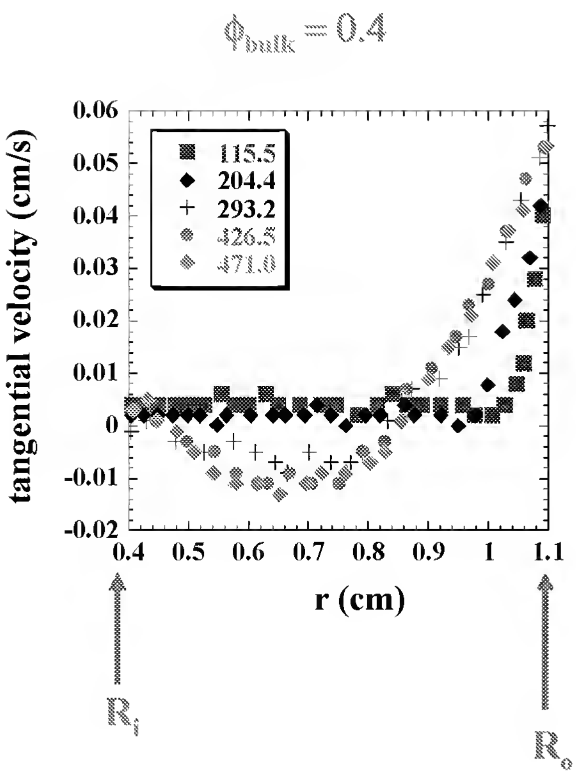

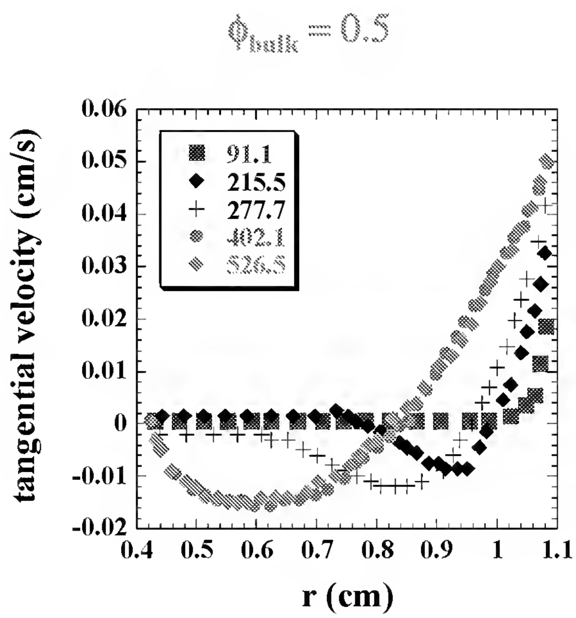

Boundary Layer Transport

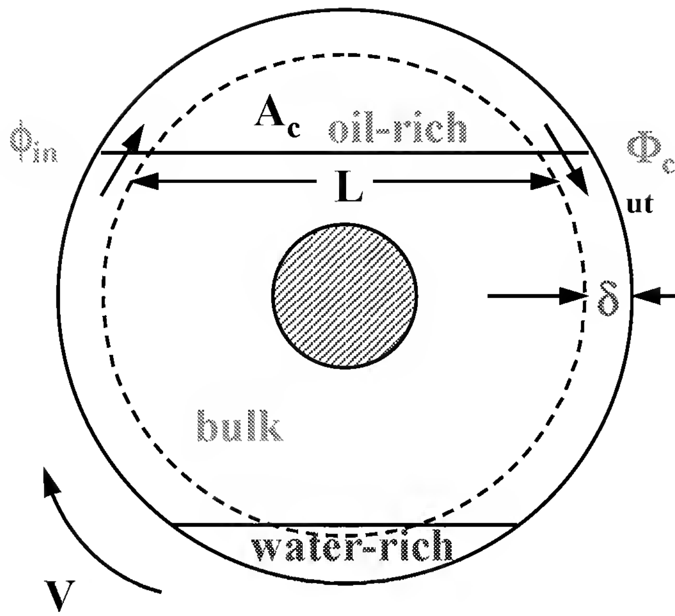

Macroscopic Balance

$$\delta \sim \frac{\lambda A_c}{V} \sim O\,(0.1\ \text{mm})$$

Estimate comparable to experimental observations

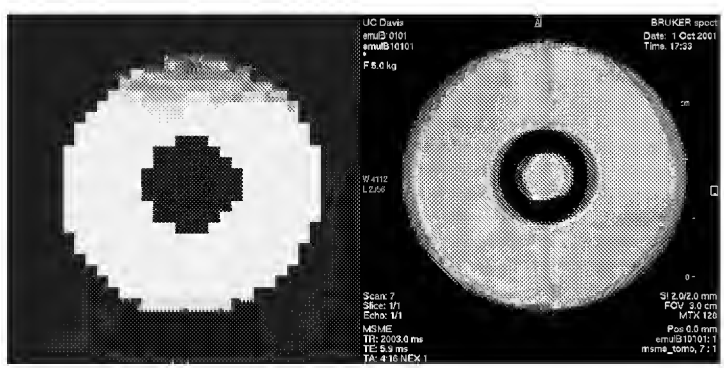

Mixing Mechanism

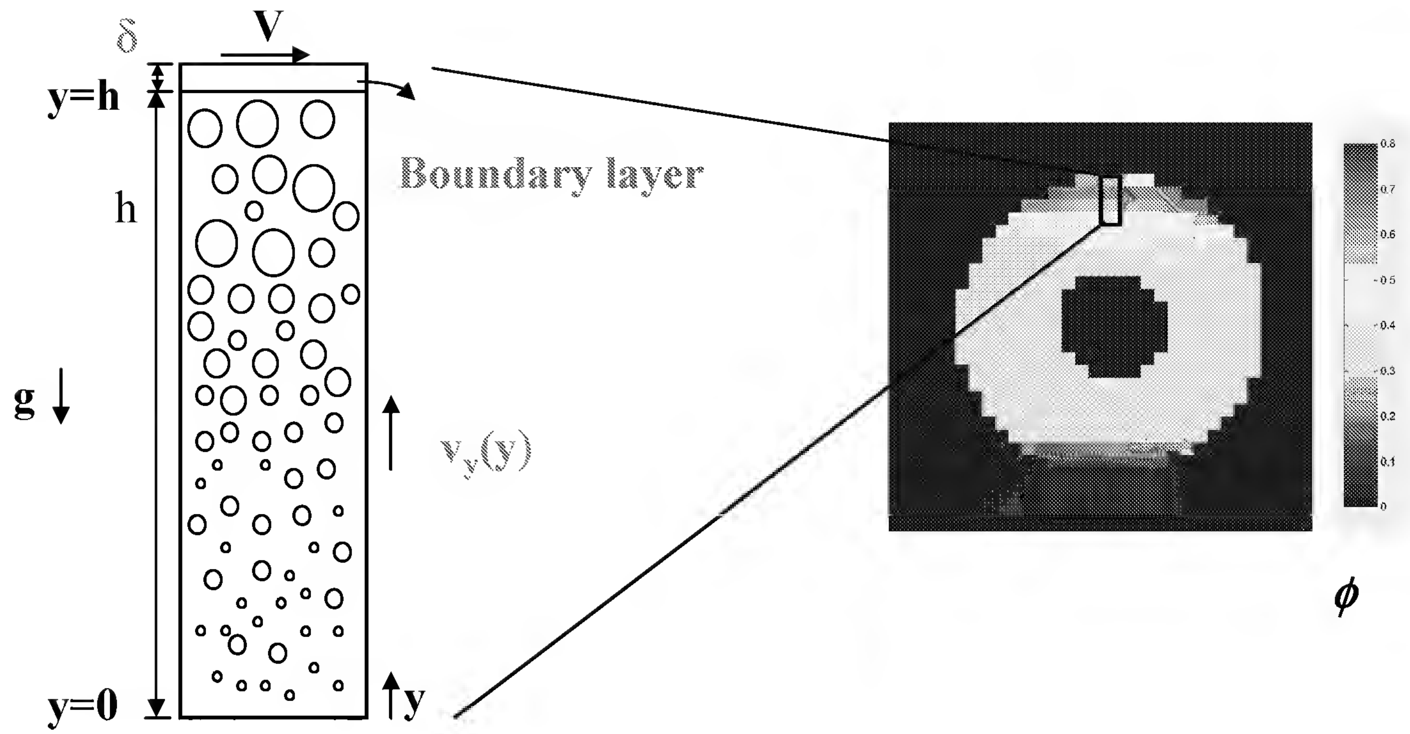

ϕ_{bulk}=0.4, V=0.05 cm/s

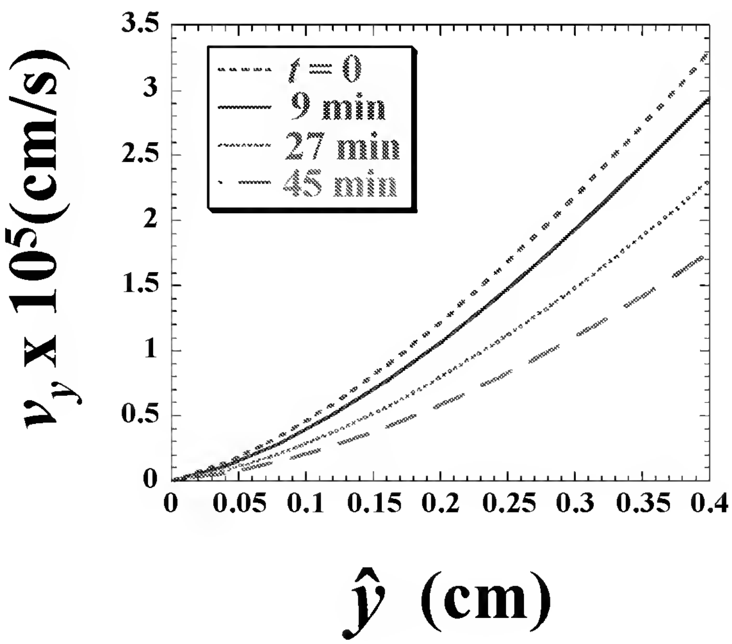

Hindered creaming velocity
$U \sim 10^{-5}$ cm/s

Comparable to v_y

Solve for v_y :

$$\frac{\partial \phi}{\partial t} + \frac{\partial}{\partial y}\left(\phi\, v_y\right) = 0$$

Conclusions and Microgravity Applications

- **Emulsion mixes by** creaming **and** boundary layer convection.
  → Different mechanism from single-phase fluid mixing.

- Droplet buoyancy **has profound effect on emulsion flow and mixing:** what happens in microgravity?

- Model system on Earth for bubbly flows.

- Food and pharmaceutical storage and processing during long-term space flight.

  e.g. Mixing after density separation during launch

A NUMERICAL METHOD FOR GAS-LIQUID FLOWS

Y. Hao and A. Prosperetti
Department of Mechanical Engineering, The Johns Hopkins University
Baltimore MD 21218

The numerical simulation of two-phase flow processes with heat transfer and phase change requires an accurate representation of the flow and temperature fields near gas-liquid (or vapor-liquid) interfaces. This circumstance renders rather problematic the use of several existing methods in which the interface is smeared over a few cells. The present method avoids this shortcoming by maintaining the interface sharp by means of a suitably modified front-tracking approach. In addition, the compressibility of the gas or vapor field can be accounted for, and realistic density ratios can be used. For the time being, the method has been developed and tested for three-dimensional adiabatic calculations. It has been found to perform very well, and its extension to the energy equation is planned for the near future.

The salient aspects of the method are the following:

1. We use a fixed Cartesian three-dimensional grid over which the interface moves. We follow the approach of Tryggvason and co-workers (see e.g. Ref. [1]) in discretizing the free surface by means of triangular finite elements the vertices of which are Lagrangian points. These points are advected normally to the interface with a velocity calculated from

$$\mathbf{v}(\mathbf{x},t) = \int d^3y \; \delta(\mathbf{x}-\mathbf{y})\, \mathbf{u}(\mathbf{y},t) \tag{1}$$

where $\mathbf{u}$ is the liquid velocity. The delta distribution $\delta(\mathbf{x}-\mathbf{y})$ is approximated by a standard regularized form.

Again as in Tryggvason's work, the liquid region is distinguished from the gas region by solving a Poisson equation for the indicator function I which equals +1 in the liquid and -1 in the gas:

$$\nabla^2 I = \boldsymbol{\nabla} \cdot \left(2 \int_S dS_y \; \hat{\mathbf{n}} \; \delta(\mathbf{x}-\mathbf{y}) \right) , \tag{2}$$

in which again the delta distribution is regularized. The solution of this equation gives a smooth approximation to I, but the interface can be maintained sharp by focusing on the line where the function changes sign.

2. In order to be able to use standard differentiation formulae near the interface, the liquid velocity field is extrapolated into the gas region by extending to three dimensions an idea of Popinet & Zaleski [2]. Specifically, the velocity field near an interface point $\mathbf{y}$ is approximated by a linear distribution, $\mathbf{u}(\mathbf{x},t) \simeq \mathbf{u}_0 + \mathsf{T} \cdot (\mathbf{x}-\mathbf{y})$, and the quantities $\mathbf{u}_0$, T are found by a least squares fit incorporating the condition of vanishing tangential stress by means of of a Lagrange multiplier.

3. The liquid flow field is calculated by means of a first-order projection method. In order to facilitate the solution of the Poisson equation for the pressure, the liquid pressure is extended into the gas region by using an idea similar to the one used in the Ghost Fluid method [3]: a fictitious pressure is defined in the gas nodes by using the actual gas pressure and the jump in the normal stresses caused by surface tension.

The figures demonstrate the performance of the method in a few cases. In particular the last example shows the "swimming" of a bubble in microgravity under the action of a modulated liquid velocity including the natural frequency of the $n = 2$ and $n = 3$ shape modes.

References

1. G. Tryggvason, B. Bunner, A. Esmaeeli, D. Juric, N. Al-Rawahi, W. Tauber, J. Han, S. Nas, and Y.-J. Jan. *J. Comput. Phys.*, **169**, 708, (2001).
2. S. Popinet and S. Zaleski. in press, *J. Fluid Mech.*, (2002).
3. X.-D. Liu, R. Fedkiw and M. Kang. *J. Comput. Phys.*, **160**, 151, (2000).

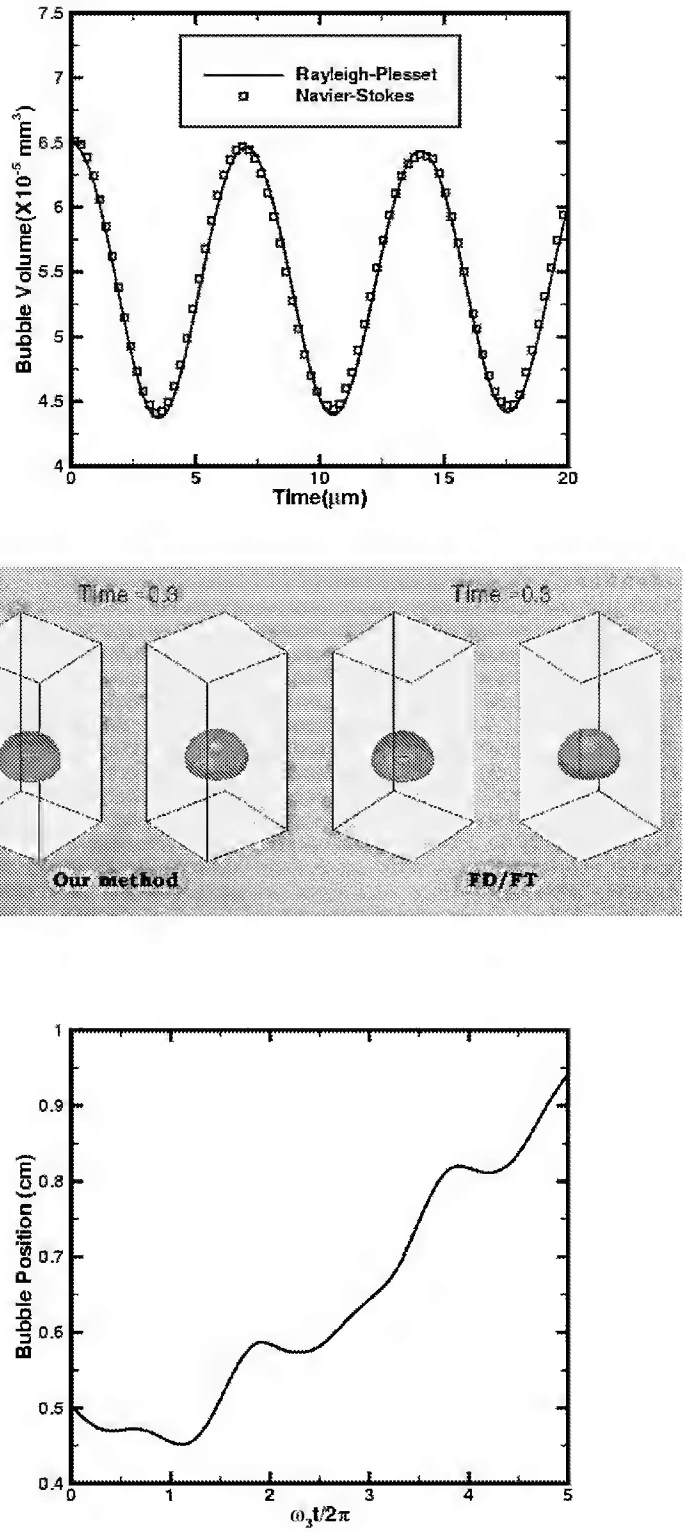

Figure 1: TOP: Comparison of the present results (squares) with the numerical solution of the Rayleigh-Plesset equation for a spherical gas bubble with an equilibrium radius of 23.75 μm released at time 0 from a radius of 25 μm.
MIDDLE: Comparison of the present results with those of the front-tracking code of Tryggvason et al. for a bubble rising under buoyancy; The Eötvös number is 3.57 and the Morton number 3×10^{-7}.
BOTTOM: Position of the center of a bubble in a square tube with a modulated liquid velocity and zero gravity; the modulation includes the natural frequency of the $n = 2$ and $n = 3$ shape modes and causes the bubble to "swim".

A Numerical Method for Gas-Liquid Flows

Yue Hao and Andrea Prosperetti

Department of Mechanical Engineering
The Johns Hopkins University
Baltimore, MD 21218

Supported by NASA
Thanks to Prof. G. Tryggvason

Governing Equations (Liquid/Gas System)

In Liquid Domain

- **Momentum (conservative form N-S equations)**

$$\frac{\partial(\rho \mathbf{u})}{\partial t} + \nabla \cdot (\rho \mathbf{u}\mathbf{u}) = \nabla p + \rho \mathbf{g} + \nabla \cdot \boldsymbol{\tau} \qquad \boldsymbol{\tau} = \mu[\nabla \mathbf{u} + (\nabla \mathbf{u})^T]$$

- **Mass conservation (incompressible flow region)**

$$\nabla \cdot \mathbf{u} = 0$$

In Gas Domain

- **Polytropic model for compressible gas**

$$p_g = p_0 \left(\frac{V_0}{V} \right)^{\gamma}$$

Our numerical method

'Hybrid' based on finite-difference formulation with a fixed grid

- **Interface front-tracking technique for three-dimensional two-phase flow**
  - Same as in the front-tracking method of Tryggvason, et al. 1992
- **Ghost Fluid Method (GFM) approach to solve pressure Poisson equation in the liquid domain**
  - Used by Fedkiw et al. (1999) with the level-set method
- **Velocity extrapolation near the interface by a Lagrange multiplier method**
  - Same as in the volume of fluid method of Zaleski, et al. 2001

Identifying liquid/gas domains

We adopt the idea of the indicator function from Tryggvason's front-tracking method

$$I(\mathbf{x},t) = 1 - 2\int_{V_{gas}(t)} d^3y\,\delta^{(3)}(\mathbf{x}-\mathbf{y})$$

from which we obtain

$$\nabla^2 I = \nabla \cdot \left(2\oint_{\Gamma(t)} ds\,\mathbf{n}\,\delta^{(3)}(\mathbf{x}-\mathbf{y}) \right)$$

Approximation of interface singular terms

$$\int_{\Gamma(t)} ds\,\mathbf{n}\,\delta^{(3)}(\mathbf{x}-\mathbf{y}) = \sum^{l} D^l_{ijk}\,\mathbf{n}_e \Delta s_e$$

D^l_{ijk} weight of grid node (i,j,k) with respect to element l is written as $D^l_{ijk}(\mathbf{y}_p) = d(x_p - ih)\,d(y_p - jh)\,d(z_p - kh)$

$\mathbf{y}_p = (x_p, y_p, z_p)$ geometric center of element l

Identifying liquid/gas domains (cont.)

$d(r)$ is taken as (Peskin, et al. 1977)

$$d(r)=\begin{cases}(1/2\xi h)[1+\cos(\pi r/\xi h)], & |r|<\xi h,\\ 0, & |r|\geq \xi h.\end{cases}$$

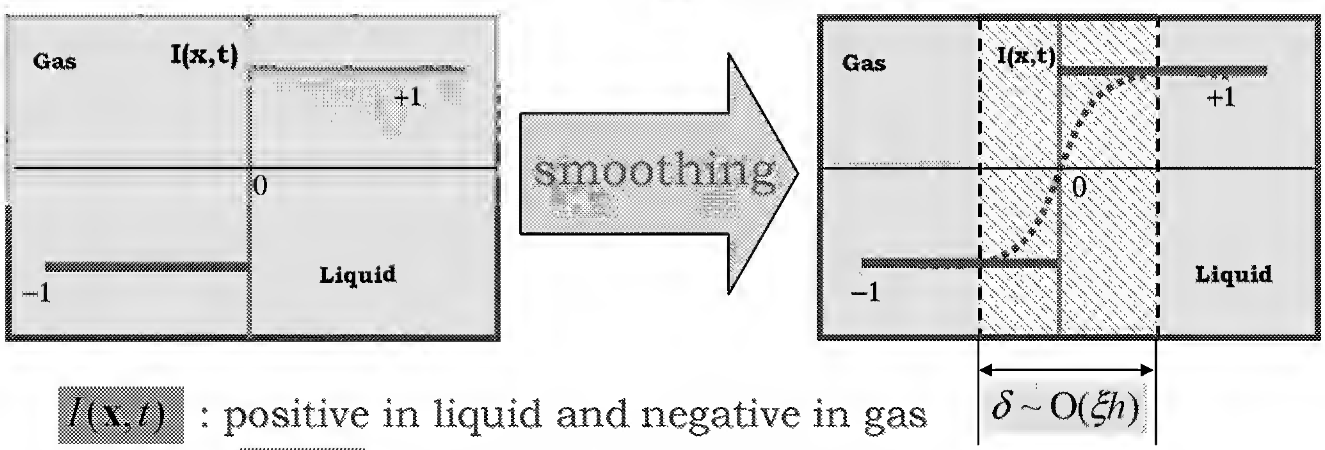

$I(\mathbf{x},t)$: positive in liquid and negative in gas

Also use $I(\mathbf{x},t)$ to calculate the unit normal

Validation test I

❑ Stationary bubble free oscillation

Comparison with the results by Rayleigh-Plesset equation

$$R\ddot{R}+\frac{3}{2}\dot{R}^2=\frac{1}{\rho_L}\left(p_g-P_\infty-\frac{2\sigma}{R}-4\mu\frac{\dot{R}}{R}\right)$$

Air bubble in water

μ=0.001 kg/m s

σ=0.07 N/m

γ=1.4 P_∞ = 1 atm

Bubble initial radius

Ri = 25 μm Ri/Ro =1.06

L=X=Y=Z/Di = 12

Resolution 360X360X360

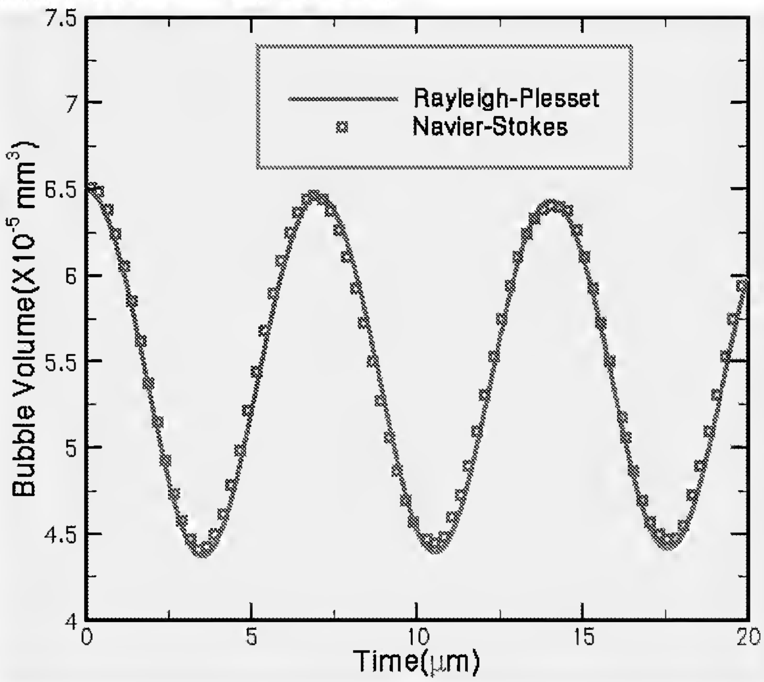

Validation test II

- Bubble rising under gravity

Comparison with the results obtained by FD/FT method (finite difference/front-tracking, Tryggvason, et al. 1992)

$$\text{Eötvös number} = \frac{\rho_L g D^2}{\sigma} = 3.57 \qquad \text{Morton number} = \frac{g\mu_L^4}{\rho_L \sigma^3} = 3\times10^{-7}$$

$$X = Y \quad Z = 2.5X \quad D_i/X = 0.5 \quad \text{Resolution}: 60\times60\times150$$

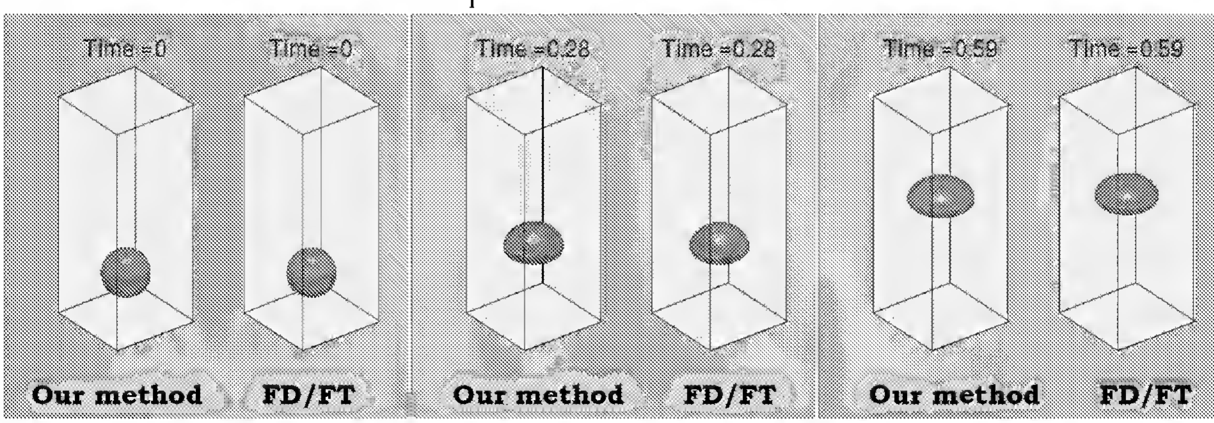

Bubble translation and oscillation under sinusoidal inflow

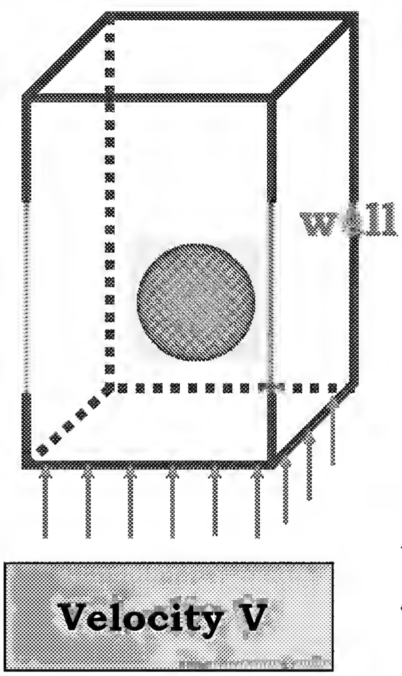

Air bubble in water (no gravity): initial radius Ri = 0.25 cm Computational domain X=Y=1 cm, Z=2 cm 40x40x80 nodes

$$V = -V_{\max}\left[\cos(\omega_3 t) + \sin(\omega_2 t)\right] \qquad V_{\max} = 1\,\mathrm{mm/s}$$

Resonant frequency for shape oscillation

$$\omega_n^2 = \frac{(n-1)(n+1)(n+2)\sigma}{\rho_L R_i^3}$$

$$\omega_2 / 2\pi = 37\,\mathrm{Hz} \qquad \omega_3 / 2\pi = 67\,\mathrm{Hz}$$

(See "Self-propulsion of asymmetrically vibrating bubbles", T. B. Benjamin & A. T. Ellis, *J.Fluid Mech.* **212**, p65-80, 1990)

Bubble translation and oscillation under sinusoidal inflow

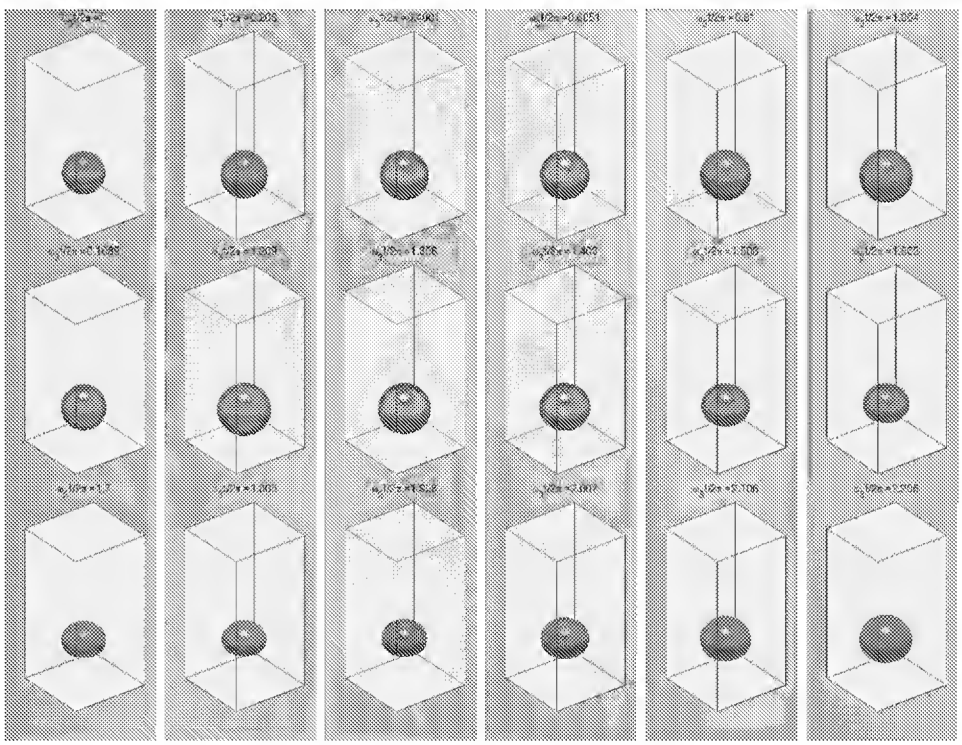

Bubble translation and oscillation under sinusoidal inflow

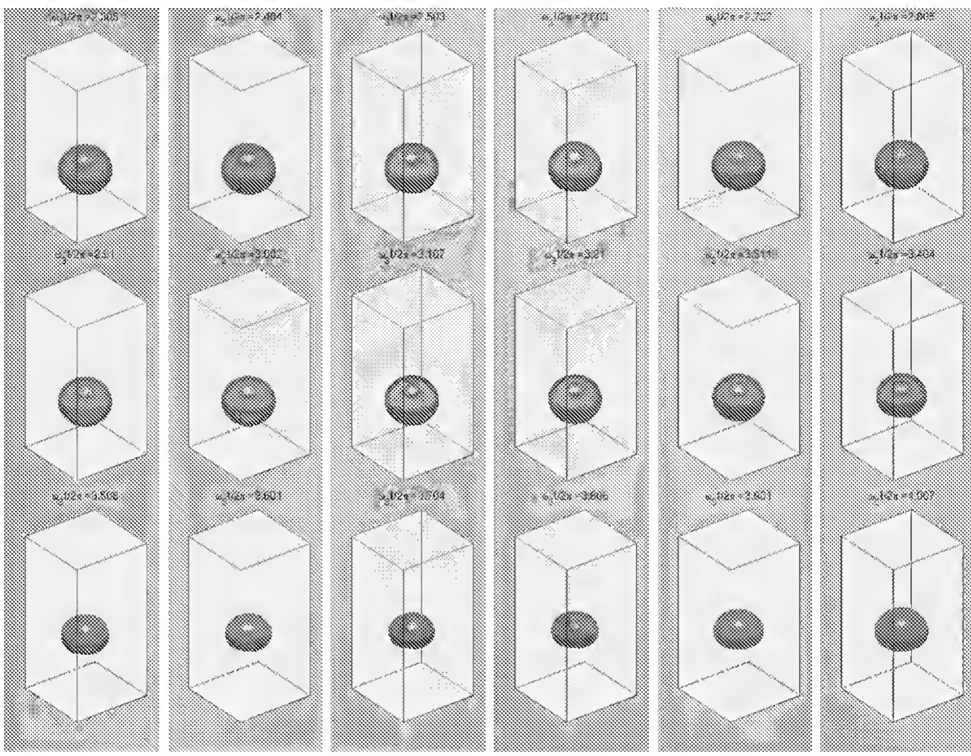

STUDY OF CO-CURRENT AND COUNTER-CURRENT GAS-LIQUID TWO-PHASE FLOW THROUGH PACKED BED IN MICROGRAVITY

Shripad T. Revankar
School of Nuclear Engineering, Purdue University, West Lafayette, IN 47907

ABSTRACT

The main goal of the project is to obtain new experimental data and development of models on the co-current and counter-current gas-liquid two-phase flow through a packed bed in microgravity and characterize the flow regime transition, pressure drop, void and interfacial area distribution, and liquid hold up. Experimental data will be obtained for earth gravity and microgravity conditions. Models will be developed for the prediction of flow regime transition, void fraction distribution and interfacial area concentration, which are key parameters to characterize the packed bed performance. Thus the specific objectives of the proposed research are to: (1) Develop experiments for the study of the gas liquid two-phase flow through the packed bed with three different flow combinations: co-current down flow, co-current upflow and counter current flow. (2) Develop pore scale and bed scale two-phase instrumentation for measurement of flow regime transition, void distribution and gas-liquid interfacial area concentration in the packed bed. (3) Obtain database on flow regime transition, pressure drop, void distribution, interfacial area concentration and liquid hold up as a function of bed characteristics such as bed particle size, porosity, and liquid properties such as viscosity and surface tension. (4) Develop mathematical model for flow regime transition, void fraction distribution and interfacial area concentration for co-current gas-liquid flow through the porous bed in gravity and micro gravity conditions.(4) Develop mathematical model for the flooding phenomena in counter-current gas-liquid flow through the porous bed in gravity and micro gravity conditions.

The present proposal addresses the most important topic of HEDS-specific microgravity fluid physics research identified by NASA 's one of the strategic enterprises, OBPR Enterprise. The proposed project is well defined and makes efficient use of the ground-based parabolic flight research aircraft facility. The project spans for four years. The first two years are devoted to ground based flight definition experimental and modeling program. During the next two years microgravity flight tests are carried out using the ground-based parabolic flight research aircraft.

The experimental program consists of a design of a packed bed loop using a scaling analysis, performing experiments for various parameters: bed diameter, packing size, liquid surface tension, and liquid viscosity. Figure 1 shows the schematic of the test loop. A packed bed sections of 15 cm diameter and 10 cm diameter are designed with sphere packing particles of diameter, 6 mm and 3 mm. The fluid combination used are : 1)water, air, (2) alcohol-water mixture (50%, 80% methanol) and air, and (3) glycerol-water mixture and air (50%, and 64% glycerol weight percent). The loop is instrumented to provide detailed measurement at pore and bed level parameters.

The data analysis involves: (1) generating maps of global mode of operation such as flow regime maps and pressure drop characteristics, (2) identification of the active and passive pores, (3) identification of void fraction in pores, (4) local void and interfacial area distribution, and (5) bed liquid holdup.

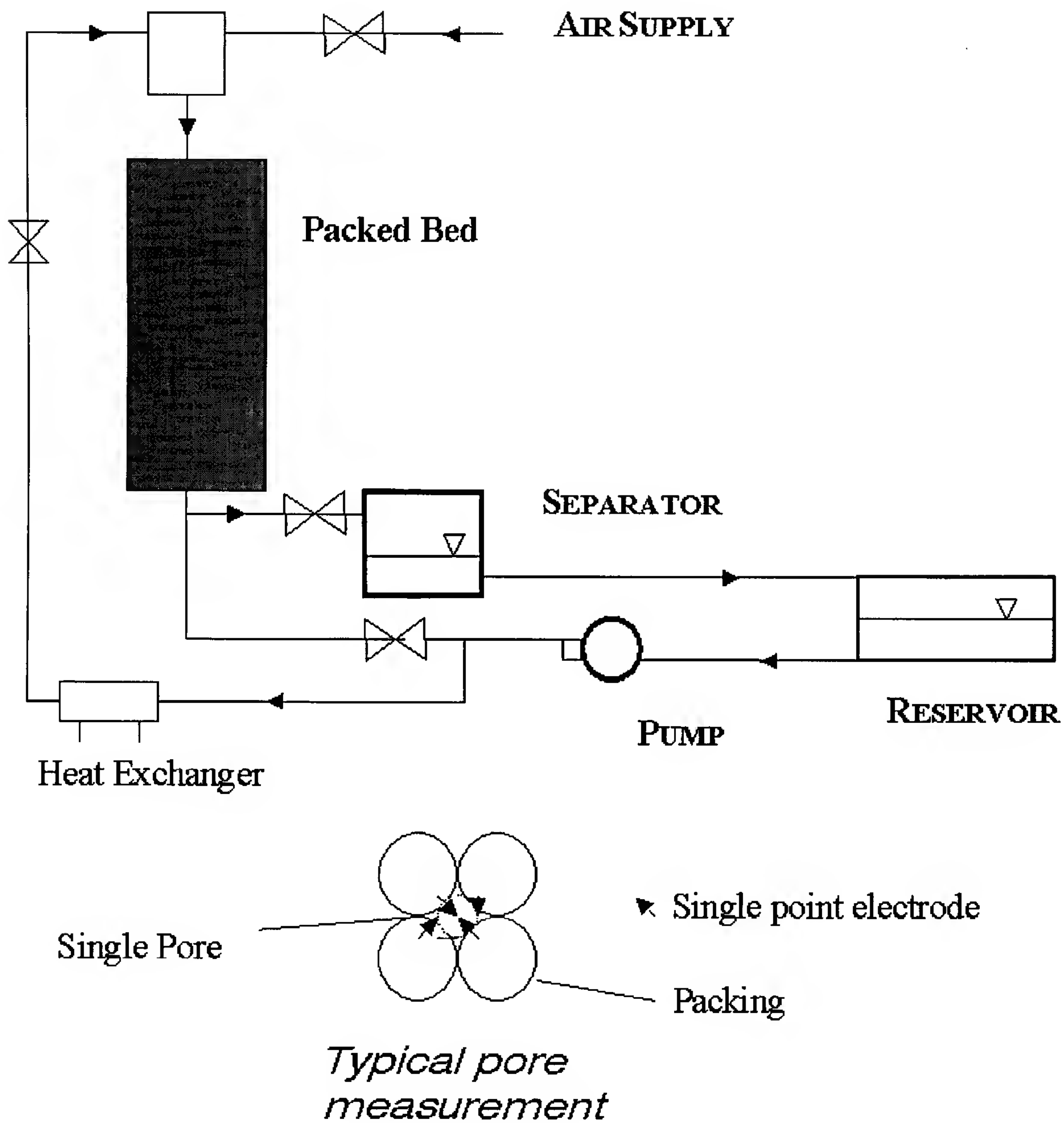

Figure 1. Schematic of the packed bed test loop.

STUDY OF CO-CURRENT AND COUNTER-CURRENT GAS-LIQUID TWO-PHASE FLOW THROUGH PACKED BED IN MICROGRAVITY

SHRIPAD T. REVANKAR

Multiphase Flow Research Laboratory
School of Nuclear Engineering
Purdue University
West Lafayette, IN 47907
shripad@ecn.purdue.edu

Project Goal

Obtain new experimental data and development of models on the co-current and counter-current gas-liquid two-phase flow through a packed bed in microgravity

Objectives

1. Develop experiments for three different flow combinations: co-current down flow, co-current upflow and counter current flow.

2. Develop pore scale and bed scale two-phase instrumentation for measurement of flow regime transition, void distribution and gas-liquid interfacial area concentration.

3. Obtain database on flow regime transition, pressure drop, void distribution, interfacial area concentration and liquid hold up as a function of bed characteristics.

4. Develop mathematical models

5. Train graduate and undergraduate students in instrumentation and measurement methods with particular emphasis on two-phase flow through packed beds.

Literature on Two-Phase Flow in Microgravity

Duct and Tubes

- Drop Tower Studies (Fujii et al 1998),
- NASA Lewis DC-9 microgravity aircraft (Lowe and Rezkallah 1999), NASA's KC-135 zero-gravity aircraft (Elkow and Rezkallah 1996, 1997, Bousman et al 1996, Rite and Rezkallah 1994, 1995, Reinarts et al 1993, 1995),
- NASA Learjet (Reinarts 1995, Colin et al 1991),
- European Space Agency's STS60 aircraft (Delil 1995).

Data on the two-phase pressure drop, film thickness, void fraction and flow regime transition boundaries.
The techniques used in the measurement are flow visualization through photography, void conductivity probes, and capacitance probes for bubbly, slug, churn and annular flows. Weber number has been used in flow regime maps.
Few models have been advanced to predict the flow regime transition in microgravity (Zhao JF. Hu WR 2000, Reinarts et al 1993, Doojeong et al1991, Dukler et al 1988).

Packed Bed

The Volatile Removal Assembly Flight Experiment (VRAFE) (Holder and Parker 2000)

Data on Catalytic Oxidation process

Two-Phase Cocurrent Flow in Packed Column in STPFE Loop (Motil et al 2000 and 2001)

Data on Flow Regime, Pressure Drop will be obtained.

Research Significance

- NASA's one of five core Strategic Enterprises, the Office of Biological and Physical Research (OBPR) Enterprise → affordable Human Exploration and Development of Space (HEDS).

- The Space Studies Board of the National Research Council → power generation and storage, space propulsion, life support, hazard control, material production and storage, and fabrication and maintenance.

- Topic of characterization of gas-liquid two-phase flow through packed beds in variable gravity environments such as for chemical processing and for the flow of nutrients and gases in soils used for plant cultivation in space

- Literature survey shows there is almost no published work on the study of gas-liquid two-phase flow through porous beds in microgravity.

Pore Level Study

- Limited data on the liquid residence time distribution (Iliuta et al. 1996), and local flow regime and void fraction at pore level (Zun et al. 1997).

- Data is very useful in the modeling of transport processes at the phase interface.

- The local flow regime identification at pore level provides insight into the mechanism governing the transition to flow transitions.

- The data of the carrying gas fraction provides information on the specific surface area and breakthrough capillary pressure.

Table. Instrument List

Data	*Instrument*
Air Flow Rate, Global	Rotameter
Liquid Flow Rate, Global	Magnetic Flow Meter/ Rotameter
Local Void Fraction, pore scale	Single Point Conductivity Probe
Local Interfacial Area Concentration, intermediate	Two Point Conductivity Probe
Volume Average Void Fraction, Global/intermediate	Impedance/Capacitance Meter
Bed Pressure Drop and Gage Pressure, Global	Pressure Transducer
Temperature	Thermocouples
Bed Void Fraction/Liquid Holdup, Global	Quick Acting Valve
Flow Visualization, Global	Video Camera; Normal and high Speed
Flow Visualization, Pore scale	Endoscope with LCD Camera

Technical Approach

Experimental Program

Parameters for the Experiments:

- Bed diameter: 7.6 cm (3”), 2.54 cm (1”)
- Packing size: 3 mm. 6 mm sphere
- Liquid surface tension, and liquid viscosity.

  (1) water, air, (2) alcohol-water mixture (50%, 80% methanol) and air, and (3) glycerol-water mixture and air (50%, and 64% glycerol weight percent).
- Density range in 0.84 gm/cm^3 to 1.17 gm/cm^3 ,
- Dynamic viscosity in the range of 0.57 cp to 5 cp
- Surface tension in the range of 25 dynes/cm to 72 dynes/cm
- Liquids mass flux 0.2 kg/m^2s and 40 kg/m^2s
- Gas mass Flux 0.02 kg/m^2s and 0.5 kg/m^2s.

Data

- Flow regime maps and pressure drop characteristics,
- Identification of the active and passive pores,
- Identification of void fraction in pores,
- Local void and interfacial area distribution
- Bed liquid holdup.

Flow Modeling

- Co-current Flow
- Hydrodynamic model based on pore scale for microgravity condition (Revankar 2001)
- Counter Current Flow
    - Separate channel model.
    - Relative permeability model,

Plan of Study and Test Schedules

For the first two years ground-based definition tests are carried out at Purdue University. The remaining two years effort will concentrate on the carrying out ground based flight tests.

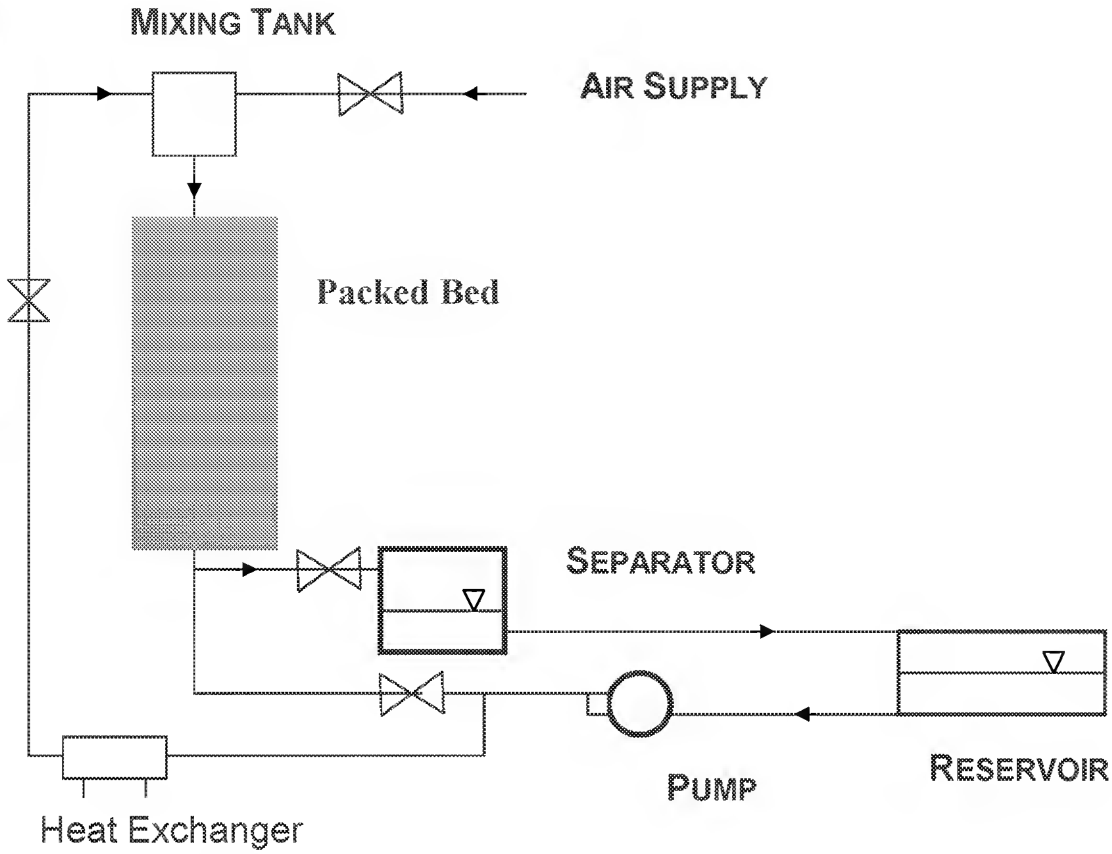

Figure 1. Test loop for two-phase co-current down flow

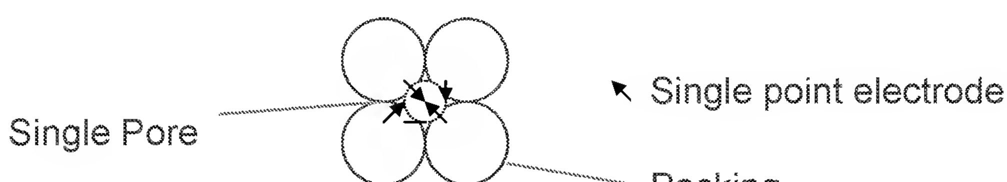

Figure 2. Details of probe arrangement in a single pore

PROJECT STATUS AND FUTURE PLAN

Completed:

- Design of the packed bed column based scaling analysis
- Design and construction of the 7.6 cm diameter packed bed with 6.4 mm spherical packing.
- Design and construction of six sets of circuits each for (i) local conductivity probe, (ii) film thickness probes and (iii) capacitance void meter.

Current Work:

- Installation of the 7.6 cm diameter packed bed loop
- Design and construction of the (i) local conductivity probe, (ii) film thickness probes and (iii) capacitance void meter.

Immediate Future:

- Perform co-current two-phase down flow test
- Plan for KC-135 microgravity flight tests

Table. Project Schedule and Tasks (Revised 8/8/02)

Period	Tasks	Deliverables/Remarks
03/01/02-05/31/02	(1) Project initiation, (2) Scaling and design of the packed bed for co-current downflow experiments at Purdue	Project Startup Discussion with NASA Visit to established lab.
06/01/02-08/31/02	(3) Hardware procurement for co-current downflow experiments at Purdue (4) Construction of the test loop (5) Conductivity probe and impedance probe development	Poster Presentation at Sixth MFPTP Conference
09/01/02-11/30/02	(6) Instrument testing (7) Loop shakedown testing (8) Formal testing and data acquisition	Visit to NASA for test plan presentation and data discussion
12/01/02-02/30/03	(8) Formal testing and data acquisition (Continued) (9) Data Analysis (10) Initial Hydrodynamic modeling of two-phase co-current downflow through packed bed	First Year data/analysis report to NASA
03/01/03-05/31/03	(11) Miniature Conductivity probe development for pore scale measurement and testing (12) Impedance meter development and testing (13) Pore level scale measurement for co-current down flow tests using miniature conductivity probes, endoscope LCD camera, and impedance meter (14) Model complete for two-phase downflow for microgravity	Visit to NASA for model presentation and data discussion
06/01/03-08/31/03	(15) Loop modification for the co-current up flow (16) Co-current upflow two-phase flow data acquisition and data analysis	Visit to NASA for model presentation and data discussion
09/01/03-11/30/03	(16) Co-current upflow two-phase flow data acquisition and data analysis complete (17) Model development for two-phase upflow for microgravity	
12/01/03-02/30/04	(18) Loop Modification fore the counter current flow (19) Counter current two-phase flow data acquisition and data analysis	Second Year data/analysis report to NASA
03/01/04-05/31/04	(19) Counter current two-phase flow data acquisition and data analysis Complete (20) Model development for flooding in packed bed (21) Design of compact packed bed test loop for flight test	Visits to NASA for flight test planning and coordination
06/01/04-08/31/04	(22) Compact test loop construction and testing for flight test	Visits to NASA
09/01/04-11/30/04	(23) 5 ground based flight tests on parabolic flight research aircraft (24) Flight tests data analysis (25) Microgravity two-phase flow through packed bed modeling	Visits to NASA
12/01/04-02/30/05	Tasks (23), (24), (25)	Third Year Report to NASA/Visits to NASA
03/01/05-05/31/05	Tasks (23), (24), (25)	Visits to NASA
06/01/05-08/31/05	Tasks (23), (24), (25)	Visits to NASA
09/01/05-11/30/05	Tasks (23), (24), (25)	Visits to NASA
12/01/05-02/30/06	Tasks (23), (24), (25)	Fourth Year Report to NASA/Visits to NASA

AUGMENTATION OF PERFORMANCE OF A MONOGROOVE HEAT PIPE WITH ELECTROHYDRODYNAMIC CONDUCTION PUMPING

S.I. Jeong
Department of Mechanical Engineering, Texas A&M University
College Station , Texas 77843

J. Seyed-Yagoobi
Department of Mechanical, Materials, and Aerospace Engineering
Illinois Institute of Technology
Chicago, Illinois 60616

The electrohydrodynamic (EHD) phenomena involve the interaction of electric fields and flow fields in a dielectric fluid medium. There are three types of EHD pumps; induction, ion-drag, and conduction. EHD conduction pump is a new concept which has been explored only recently. Net pumping is achieved by properly utilizing the heterocharge layers present in the vicinity of the electrodes.

Several innovative electrode designs have been investigated. This paper presents an electrode design that generates pressure heads on the order of 600 Pa per one electrode pair at 20 kV with less than 0.08 W of electric power. The working fluid is the Refrigerant R-123. An EHD conduction pump consisting of six pairs of electrodes is installed in the liquid line of a mono-grove heat pipe.

The heat transport capacity of the heat pipe is measured in the absence and presence of the EHD conduction pump. Significant enhancements in the heat transport capacity of the heat pipe is achieved with the EHD conduction pump operating. Furthermore, the EHD conduction pump provides immediate recovery from the dry-out condition.

The EHD conduction pump has many advantages, especially in the micro-gravity environment. It is simple in design, non-mechanical, and lightweight. It provides a rapid control of heat transfer in single-phase and two-phase flows. The electric power consumption is minimal with the very low acoustic noise level.

MICROGRAVITY BOILING ENHANCEMENT USING VIBRATION-BASED FLUIDIC TECHNOLOGIES

Marc K. Smith, Ari Glezer, and Samuel N. Heffington
The George W. Woodruff School of Mechanical Engineering,
Georgia Institute of Technology, Atlanta, GA 30332-0405

ABSTRACT

Thermal management is an important subsystem in many devices and technologies used in a microgravity environment. The increased power requirements of new Space technologies and missions mean that the capacity and efficiency of thermal management systems must be improved. The current work addresses this need through the investigation and development of a direct liquid immersion heat transfer cell for microgravity applications. The device is based on boiling heat transfer enhanced by two fluidic technologies developed at Georgia Tech.

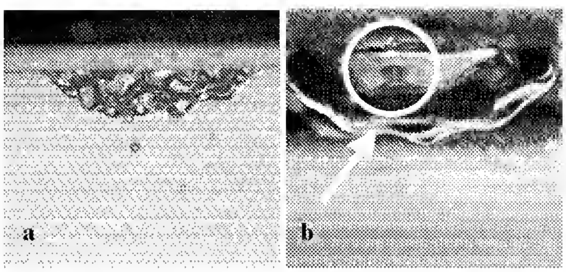

Figure 1. (a) Violent oscillations of a 5 mm air bubble in water driven at 440 Hz. (b) Possible interfacial collapse occurring inside the same gas bubble (white circle and arrow).

The first of these fluidic technologies, called vibration-induced bubble ejection, is shown in Fig. 1. Here, an air bubble in water is held against a vibrating diaphragm by buoyancy. The vibrations at 440 Hz induce violent oscillations of the air/water interface that can result in small bubbles being ejected from the larger air bubble (Fig. 1a) and, simultaneously, the collapse of the air/water interface against the solid surface (Fig. 1b). Both effects would be useful during a heat transfer process. Bubble ejection would force vapor bubbles back into the cooler liquid so that they can condense. Interfacial collapse would tend to keep the hot surface wet thereby increasing liquid evaporation and heat transfer to the bulk liquid.

Figure 2 shows the effect of vibrating the solid surface at 7.6 kHz. Here, small-scale capillary waves appear on the surface of the bubble near the attachment point on the solid surface (the grainy region). The vibration produces a net force on the bubble that pushes it away from the solid surface. As a result, the bubble detaches from the solid and is propelled into the bulk liquid. This force works against buoyancy and so it would be even more effective in a microgravity environment. The benefit of the force in a boiling process would be to push vapor bubbles off the

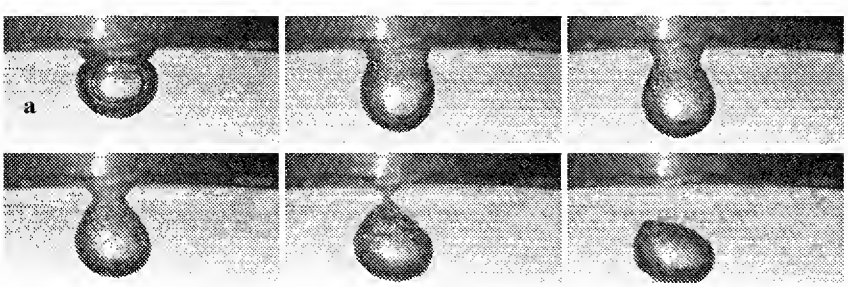

Figure 2. An air bubble in water (5 mm diameter) resting against the underside of a submerged vibrating diaphragm. The upper left image (a) is with no vibration. When the diaphragm vibrates at 7.6 kHz, the image sequence shows the air bubble being pushed away from the surface against the force of buoyancy.

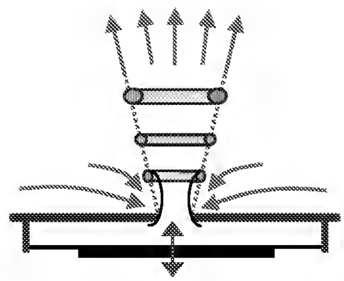

Figure 3. A vibrating diaphragm alternately entrains and expels fluid from a cavity resulting in a synthetic jet.

solid surface, thus helping to keep the solid surface wet and increasing the heat transfer.

The second fluidic technology to be employed in this work is a synthetic jet, shown schematically in Fig. 3. The jet is produced using a small, sealed cavity with a sharp-edged orifice on one side and a vibrating diaphragm on the opposite side. The jet is formed when fluid is alternately sucked into and then expelled from the cavity by the motion of the diaphragm. This alternating motion means that there is no net mass addition to the system. Thus, there is no need for input piping or complex fluidic packaging.

The efficiency of boiling heat transfer is hindered in microgravity because there is no inherent mechanism to remove vapor bubbles from the heated surface (this is the role of buoyancy on Earth). To circumvent this problem, the fluidic technologies described above will be used to develop a nucleate boiling heat transfer cell for efficient, high-flux cooling in microgravity. The cell will be composed of a liquid-filled cavity with one surface attached to the surface to be cooled and with another surface attached to an array of heat transfer fins or some other device that serves to reject the heat to an outside environment. An array of vibration actuators will be designed and fabricated on the hot surface. These actuators will aid nucleate boiling in the cell by vibration-induced bubble ejection from larger vapor bubbles (Fig. 1a), vibration-induced collapse of vapor bubbles against the heated surface (Fig. 1b), and the direct removal of vapor bubbles from contact with the heated surface (Fig. 2). Synthetic jets placed inside the cell (Fig. 3) will produce a flow that will transport vapor bubbles away from the heated surface into the cooler bulk liquid. Since the synthetic jets operate on time scales that are much shorter than the characteristic thermal time scale of the flow, they will also substantially enhance small-scale mixing within the liquid, thus enhancing the condensation of vapor bubbles back into the liquid and the heat transfer out of the cell.

The primary objectives of this research are as follows.

1. Develop, design, and construct a nucleate boiling heat transfer cell based on the vibration-induced bubble ejection and synthetic-jet technologies.
2. Examine the formation, spreading, and detachment of vapor bubbles from a heated surface during boiling in microgravity.
3. Determine the influence of vibration of the heated surface on the spreading, merging, and detachment of vapor bubbles from the surface.
4. Determine the vibration conditions that maximize the interfacial motion of a vapor bubble and that ensure its collapse against the heated surface.
5. Determine the conditions for the effective use of forced convection induced by synthetic jets to remove vapor bubbles from the heated surface.

Both experimental and numerical work will be done during this investigation. If these technologies behave as expected, the simplicity and scalability of the resulting heat transfer cell would make it a very attractive method for thermal management in microgravity. In addition, the technology may also be transferable to Earth-based, boiling applications and provide improved performance over normal pool-boiling technologies.

Using Surfactants to Control Bubble Growth and Coalescence

K. Stebe
Johns Hopkins University

The effects of surfactant adsorption on bubble formation at an orifice are studied numerically at finite Reynolds number. Establishing the hydrodynamics and mass transfer during bubble growth and detachment will improve insight into the nucleate boiling process and aid in developing paradigms for enhancement of the heat transfer coefficient during nucleate boiling. The volume-of-fluid method is employed to solve the two-dimensional axisymmetric Navier-Stokes equations. The interface is tracked using marker points that accurately represent the surface tension forces at the interface. The evolution and detachment of the bubble is examined as a function of the capillary and Bond numbers. At low surface tension, strong deformations of the interface are observed leading to bubbles that assume a mushroom shape. Surfactants change the surface tension according to a non-linear equation of state that takes into account maximum packing at the interface. A variety of behaviors are predicted, depending upon the ratio of the convection rate to the prevailing mass transfer rates. In particular, if these rates are comparable, regions of local surfactant accumulation develop where the surfactant concentration approaches its upper bound, causing the local surface tension to reduce strongly and rendering the interface highly deformable.

USING SURFACTANTS TO CONTROL BUBBLE GROWTH

Nivedita R. Gupta
University of New Hampshire, Durham, NH

R. Balas ubramaniam
NCMR, NASA Glenn Research Center, Cleveland, OH

Kathleen J. Stebe
Johns Hopkins University, Baltimore, MD

ABSTRACT

The effect of surfactant adsorption on bubble formation at an orifice is presented numerically at finite Reynolds number. The volume-of-fluid method is employed to solve the two-dimensional axisymmetric Navier-Stokes equations. The interface is tracked using marker points that accurately represent the surface tension forces at the interface. At low surface tension, strong deformations of the interface are observed leading to bubbles that assume a mushroom shape. Surfactants change the surface tension according to a non-linear equation of state that takes into account maximum packing at the interface. A variety of behaviors are predicted, depending upon the ratio of the convection rate to the prevailing mass transfer rates. In particular, if these rates are comparable, regions of local surfactant accumulation develop where the surfactant concentration approaches its upper bound, causing the local surface tension to reduce strongly and rendering the interface highly deformable.

RAPIDLY EXPANDING BUBBLE

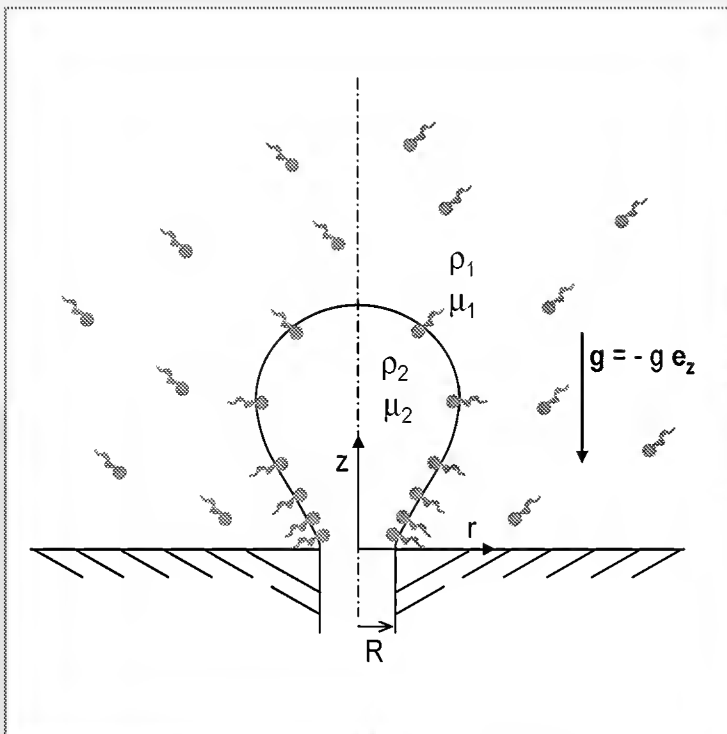

- Incompressible phases
- Constant flow rate
- Isothermal
- Axisymmetric
- Pinned contact line
- Inertial effects important
- Insoluble surfactants
- Soluble surfactant (Adsorption-desorption controlled)

AIM: To handle two-phase flow at finite Re with precise description of interface

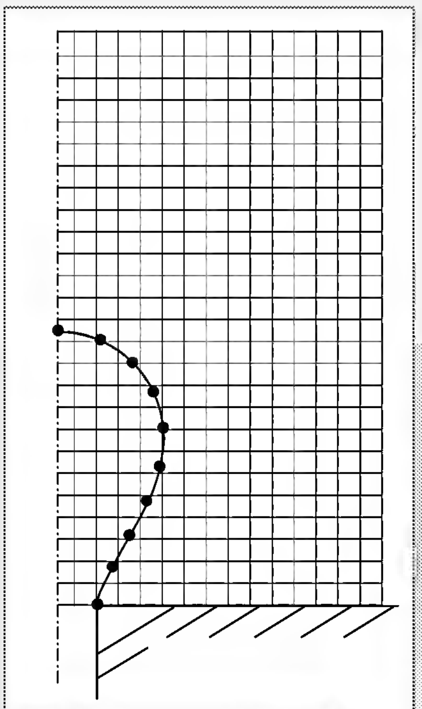

- **VOF for Governing Equations (Eulerian grid)**
  - * Finite volume formulation

$$\iint_{\Omega} \frac{1}{Ca}(\kappa - \mathrm{Bo}\, z)\, \mathbf{n}\, \delta_s dA = \int_{\Sigma} \frac{1}{Ca}(\kappa - \mathrm{Bo}\, z)\, \mathbf{n}\, ds$$

    - – Lagrangian description of interface used to calculate the integral accurately
  - * Time-splitting method
- **Marker particles for interface (Lagrangian grid)**
  - * Bilinear interpolation for marker particle velocities
  - * Update shape, ϕ
- **Marker particles added as area increases**

EVOLUTION OF BUBBLE SHAPE

χ = 0.01, λ = 0.01, Re = 10, Ca = 0.3, Bo = 0.9

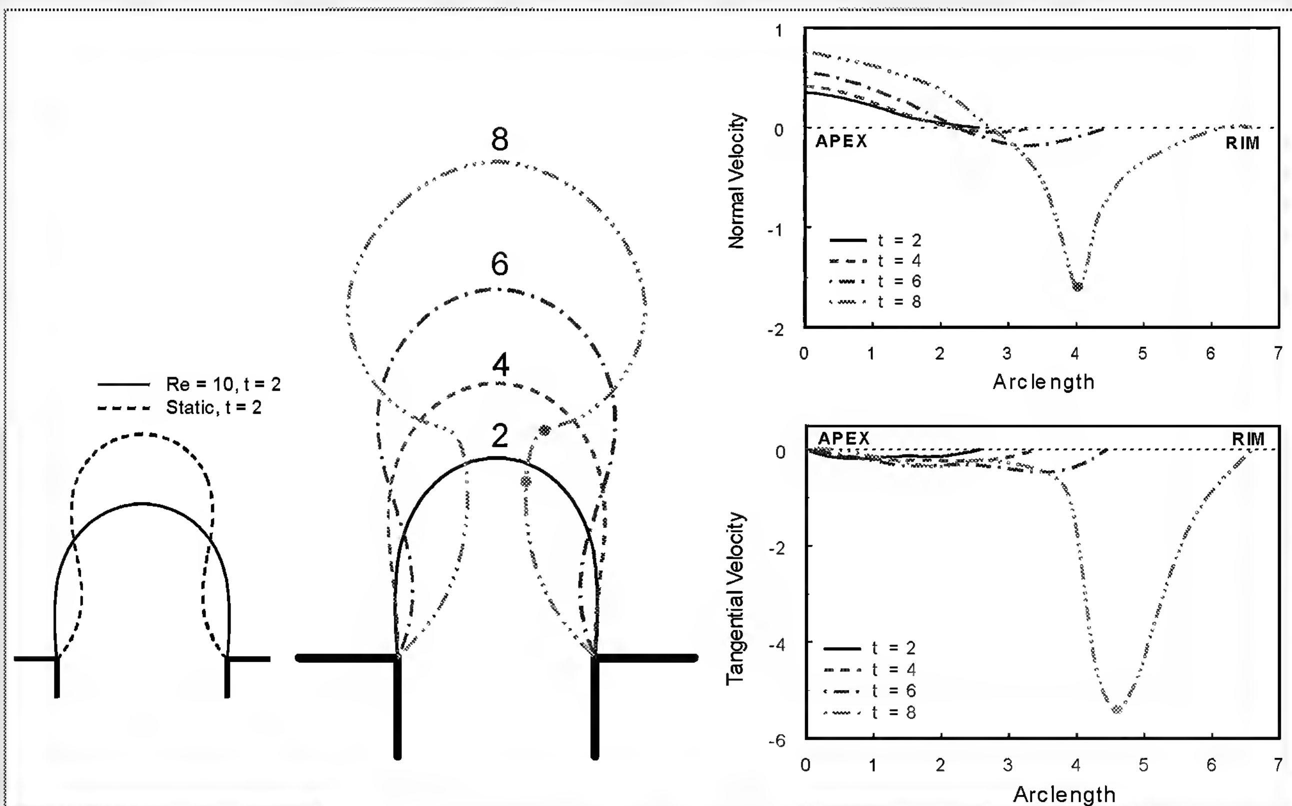

MUSHROOM SHAPE

χ = 0.01, λ = 0.01, Re = 10, Ca = 0.3, Bo = 0.9

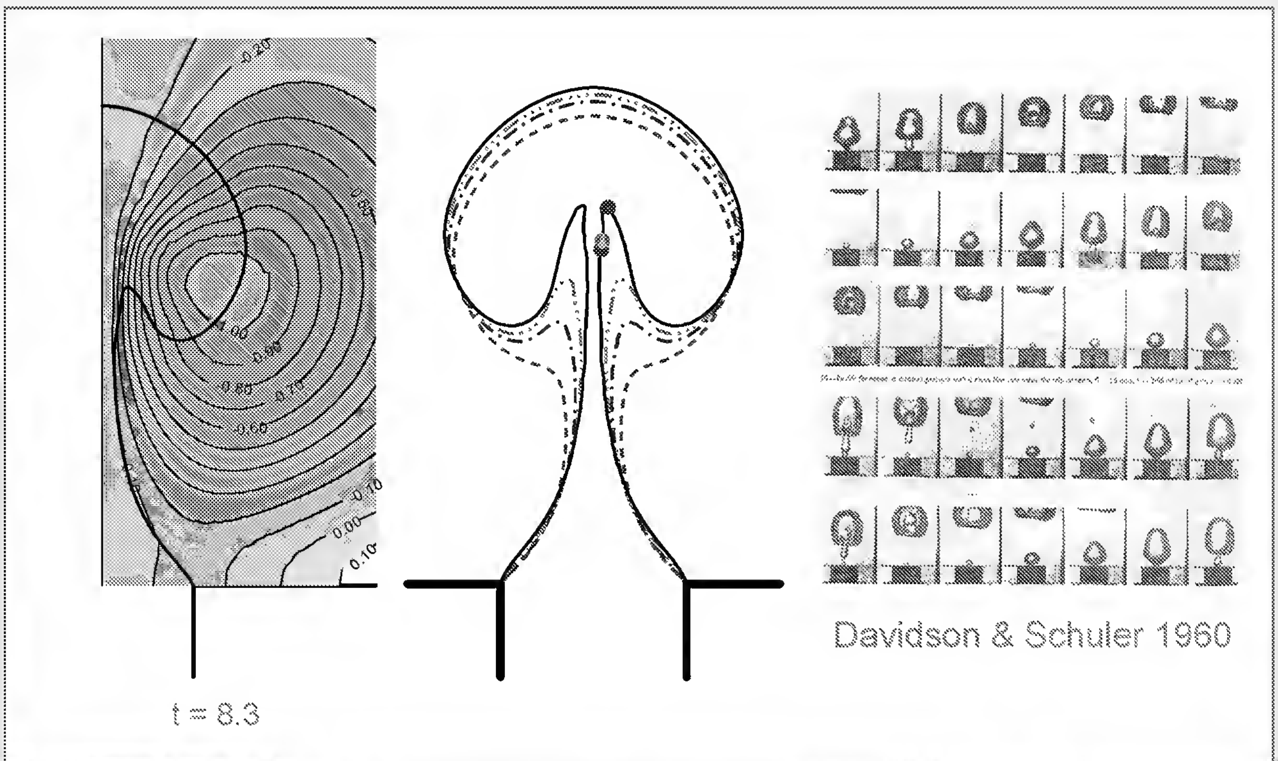

MUSHROOM SHAPE : Interface Velocity

χ = 0.01, λ = 0.01, Re = 10, Ca = 0.3, Bo = 0.9

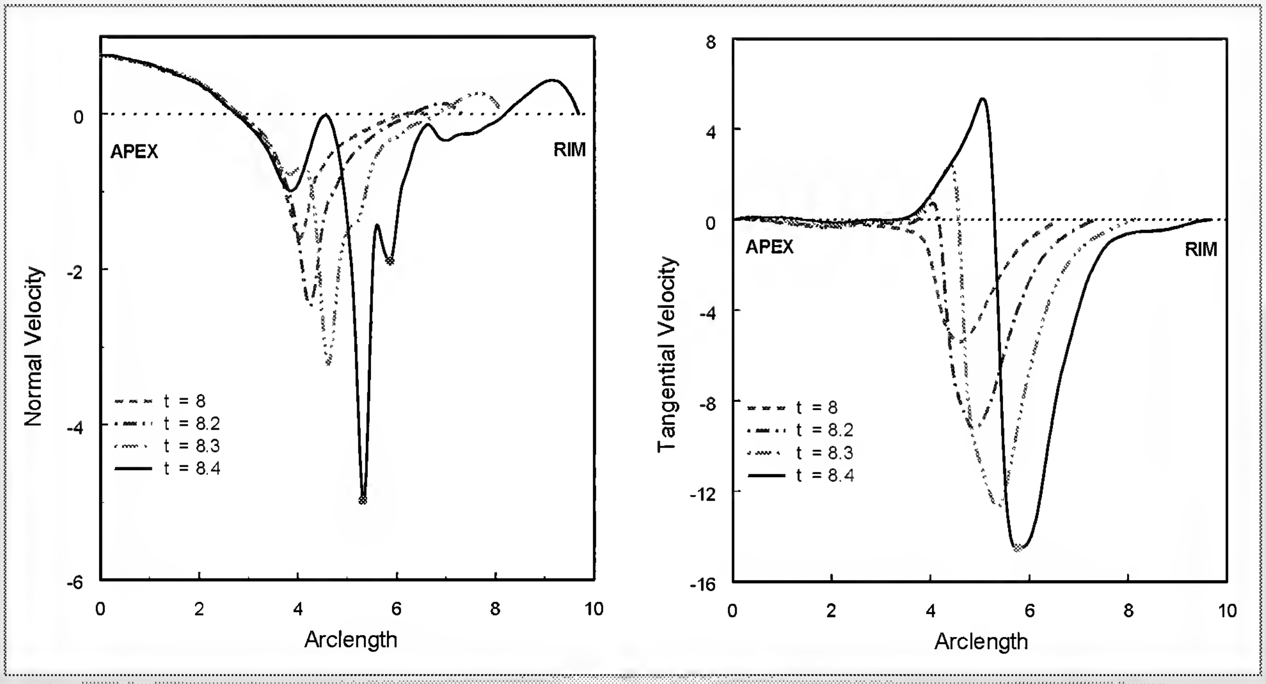

SURFACTANT: Timescales

- $\tau_{MT} << \tau_{conv}$
  - uniform reduction of σ ($\sigma = \sigma_{eq}$)
- $\tau_{MT} >> \tau_{conv}$
  - insoluble surfactant
- $\tau_{MT} \sim \tau_{conv}$
  - adsorption-desorption limited ($\tau_{ads/des} >> \tau_D$)

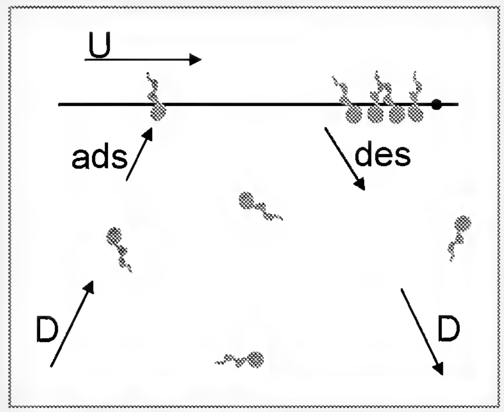

Surface Convection

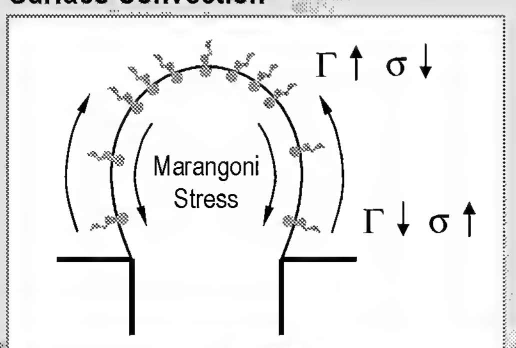

Surface Dilution

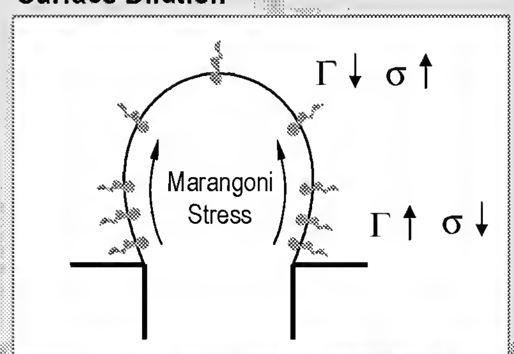

SURFACTANT DYNAMICS

- **Surface Equation of State**

$$\frac{\sigma}{\sigma_c} = 1 + E \ln\left(1 - x\Gamma\right)$$

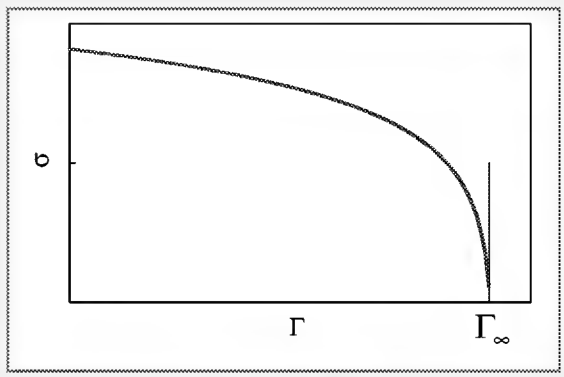

- **Surfactant Mass Balance**

$$\frac{D\Gamma}{Dt} + \left(U_t \cdot \nabla_s \Gamma\right) - \frac{1}{\mathrm{Pe}_s}\nabla_s^2 \Gamma + \Gamma U_n \left(\nabla \cdot \mathbf{n}\right) = \mathrm{Bi}\left(\frac{1}{1-x}\right)\left(1 - \Gamma\right)$$

  - **Insoluble surfactants : Bi = 0**

$$E = \frac{RT\Gamma_\infty}{\sigma_c} \qquad x = \frac{\Gamma_{eq}}{\Gamma_\infty} \qquad Pe_s = \frac{Ru_{max}}{D_s} \qquad \mathrm{Bi} = \frac{\alpha R}{u_{max}}$$

NUMERICAL METHOD TO TRACK SURFACTANTS

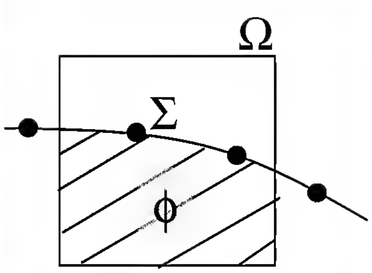

$\rho = 1 + \phi\,(\chi - 1)$

$\mu = 1 + \phi\,(\lambda - 1)$

$\Omega =$ Area

$\Sigma =$ Interface

- **Single fluid VOF formulation**

$$\nabla \cdot \mathbf{v} = 0$$

$$\rho\left[\frac{\partial \mathbf{v}}{\partial t} + \mathbf{v}\cdot\nabla\mathbf{v}\right] = -\nabla P + \mu\nabla^2\mathbf{v} + \mathbf{F}_n + \mathbf{F}_t$$

- **Finite volume formulation**

$$\mathbf{F}_n = \iint_{\Omega} \frac{1}{Ca}(\sigma\kappa - \mathrm{Bo}\,z)\,\mathbf{n}\,\delta_s\,dA$$

$$= \int_{\Sigma} \frac{1}{Ca}(\sigma\kappa - \mathrm{Bo}\,z)\,\mathbf{n}\,ds$$

$$\mathbf{F}_t = \iint_{\Omega} \frac{1}{Ca}\nabla_s\sigma\,\delta_s\,dA = \int_{\Sigma}\frac{1}{Ca}\left(\frac{\partial\sigma}{\partial s}\right)\mathbf{t}\,ds$$

UNIFORM REDUCTION IN SURFACE TENSION

χ = 0.01, λ = 0.01, Re = 10, Bo/Ca = 3

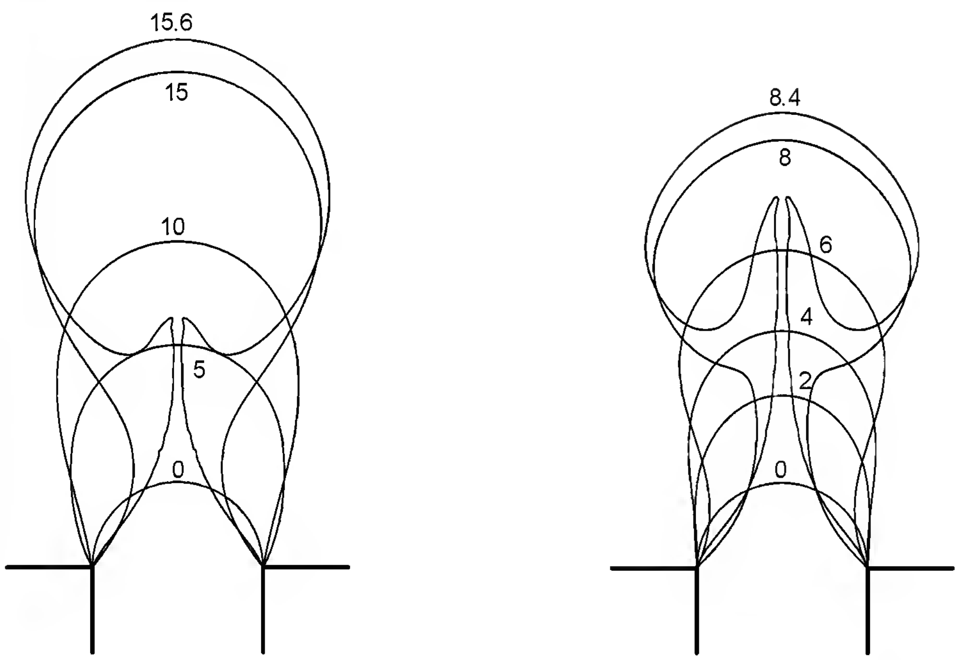

Ca = 0.1, Bo = 0.3 **Ca = 0.3, Bo = 0.9**

INSOLUBLE SURFACTANTS : Γ

χ = 0.01, λ = 0.01, Re = 10, Ca = 0.3, Bo = 0.9, E = 0.175, x=0.5, Pe_s = 10

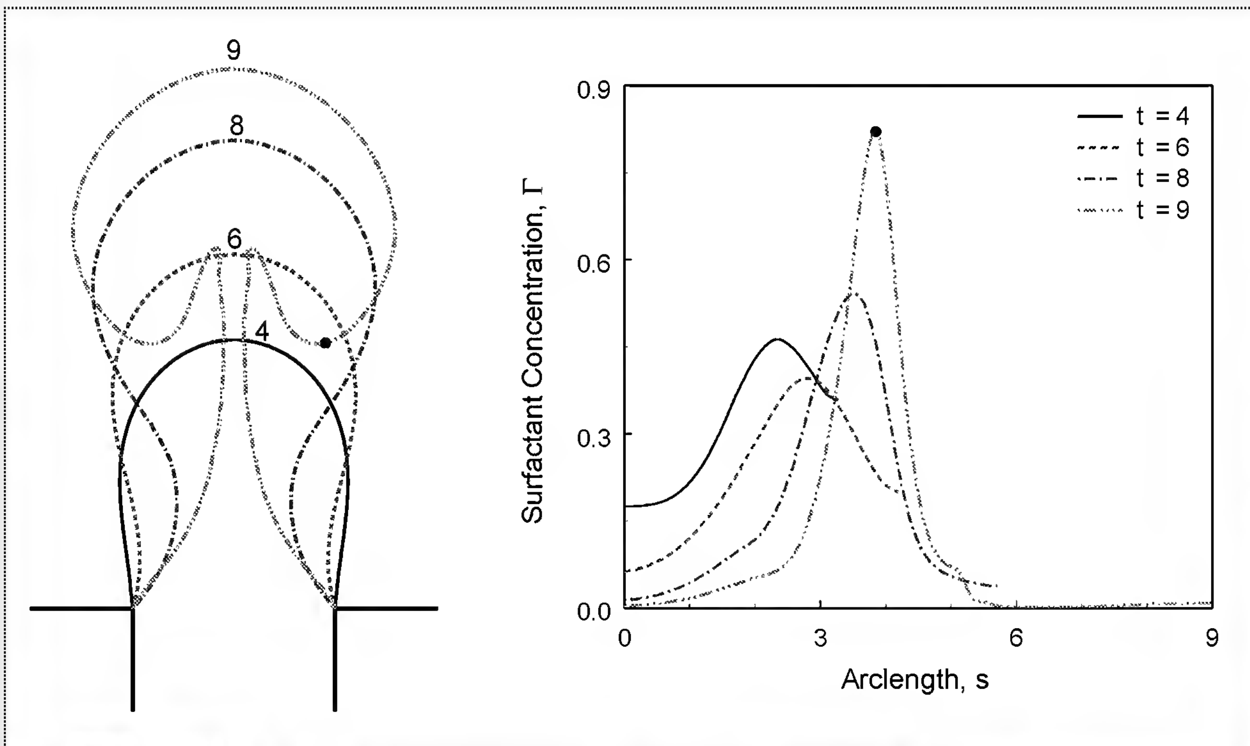

ADSORPTION-DESORPTION LIMIT : Γ

χ = 0.01, λ = 0.01, Re = 10, Ca = 0.3, Bo = 0.9, E = 0.175, x=0.5, Pe_s = 10, Bi = 0.1

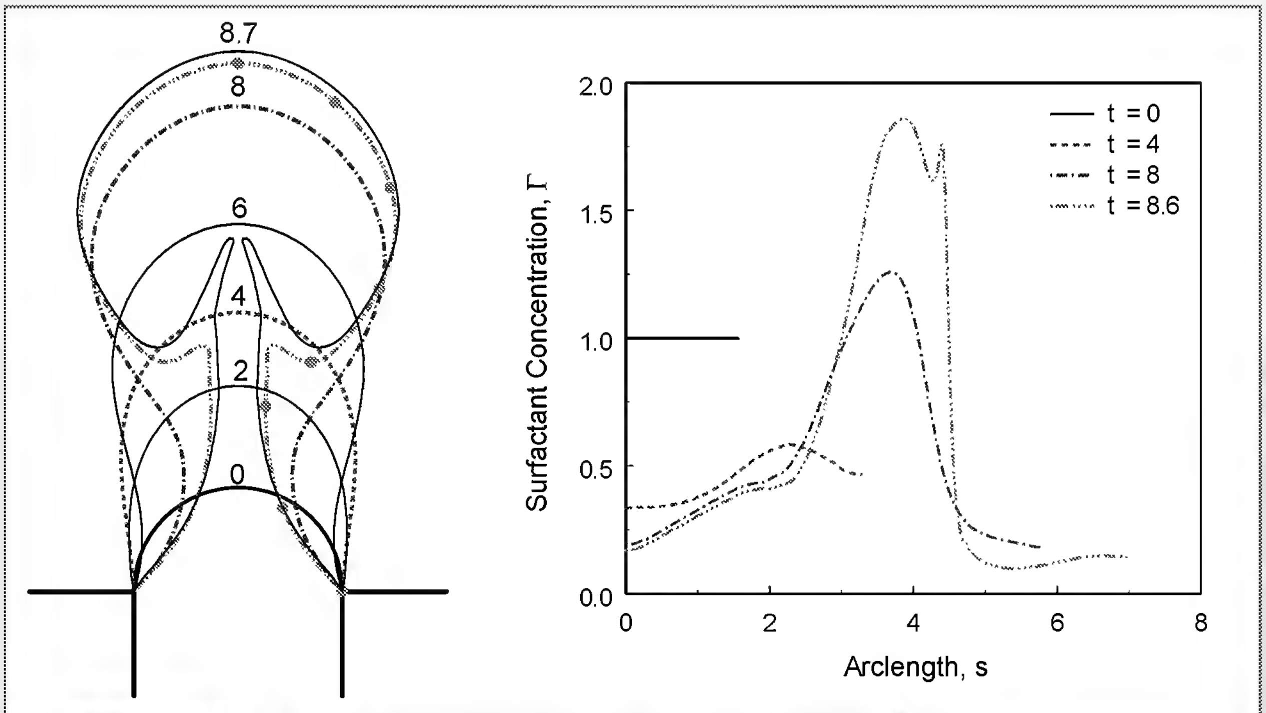

SUMMARY

- **2D Axisymmetric VOF method with an accurate representation of the interface implemented**
- **At low surface tension, bubble evolves into a mushroom shape**
- **In the absence of mass transfer of surfactants to the interface, dilution effect dominates**
- **Transport of surfactants to the interface can lead to a local reduction in surface tension rendering the interface locally highly deformable**

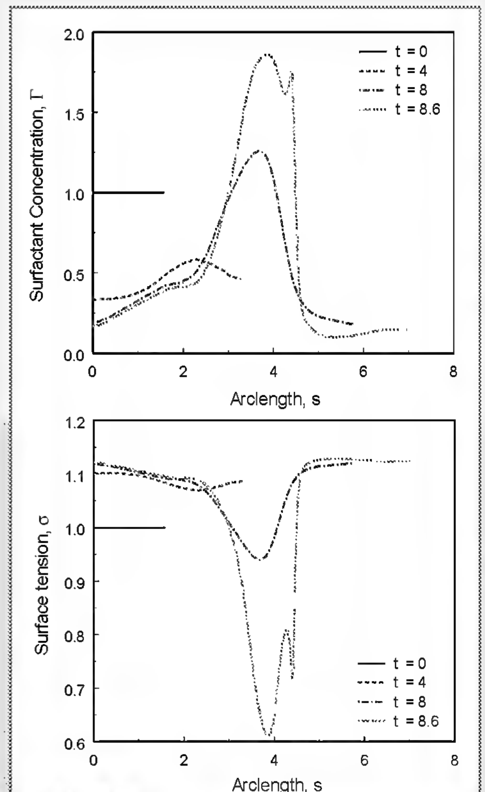

SUPERCRITICAL AND TRANSCRITICAL SHEAR FLOWS IN MICROGRAVITY: EXPERIMENTS AND DIRECT NUMERICAL SIMULATIONS

Doug Talley
Air Force Research Laboratory, AFRL/PRSA, 10 E. Saturn Blvd., Edwards AFB, CA 93524

Josette Bellan
Jet Propulsion Laboratory, 4800 Oak Grove Drive, MS 125-09, Pasadena, CA 91109-8099

Bruce Chehroudi
ERC, Inc., 10 E. Saturn Blvd., Edwards AFB, CA 93524

ABSTRACT

The objective of this research, which began in April 2002, is to develop and experimentally validate a near-critical transcritical and supercritical fluid shear flow model independent of turbulence. We define a supercritical shear flow to be one in which all of the fluid particles remain above their critical temperature and pressure. We define a transcritical shear flow to be one in which at least some of the fluid particles undergo a transition between a subcritical and a supercritical temperature, between a subcritical and a supercritical pressure, or both. The reason it is necessary to validate the fluid model independent of turbulence is that turbulence introduces a large number of additional mechanisms the understanding of which is embryonic at best for near-critical transcritical and supercritical flows. Validating the fluid model without turbulence uncertainties therefore requires laminar flows. However, laminar flows that are not influenced by gravity are difficult to produce in normal gravity due to the large density gradients involved. Therefore, microgravity experiments are necessary.

The co-investigators have considerable experience modeling supercritical mixing and shear layers (JPL), and considerable experience in performing transcritical and supercritical droplet and jet experiments in normal gravity (AFRL/ERC). This experience will be applied to perform a microgravity experiment where the results can be directly compared with direct

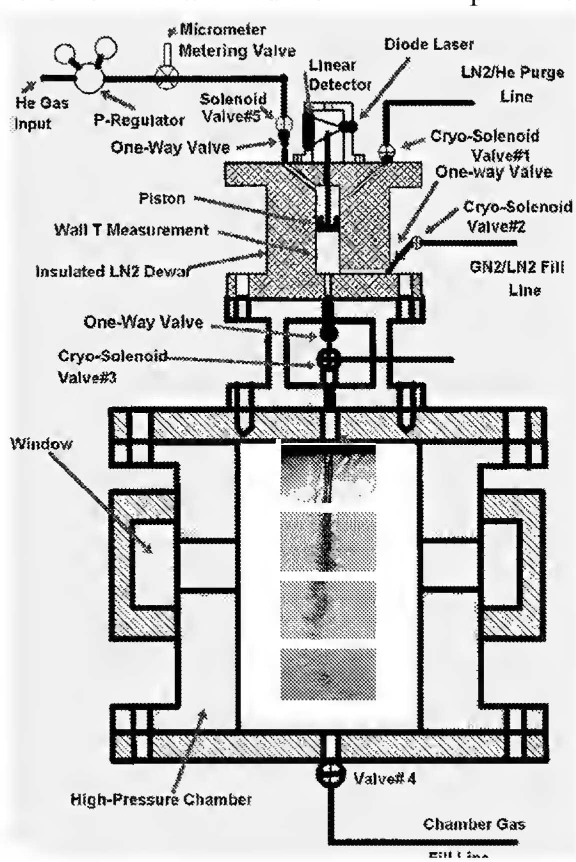

Figure 1. Preliminary Schematic of a Drop Tower Experiment; supercritical jet at 1 g..

numerical simulations. An entry into the related publications of the co-investigators can be found in refs. [1-3].

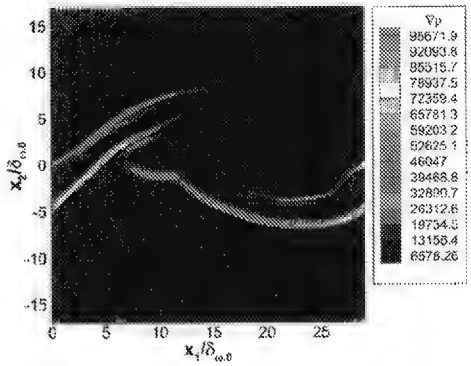

Figure 2. Density gradient magnitude computations in a laminar heptane/nitogen shear layer.

Experimental Approach

Liquid nitrogen (LN_2) initially below the critical temperature will be injected into room temperature gaseous nitrogen (GN_2) and GN_2/He mixtures at various subcritical to supercritical pressures. AFRL/ERC has considerable previous experience with these mixtures under normal gravity, and the substances are inherently safe. A conceptual design of the drop tower rig is illustrated in Fig. 1. Two separate chambers, one for LN_2, and the other for the ambient fluid, are connected through a one-way valve and a cryo-solenoid valve. The LN_2 chamber is an insulated dewar with several inlet and outlet passages as shown. Injection is achieved through pressurized He gas exerted on the upper side of a small piston inside the chamber. Injection initiation is controlled by the Cryo-solenoid-valve #3. The high pressure chamber will be designed to have optical access for flow visualization. The entire setup will be designed to withstand the total stresses caused by internal pressure and decelerating inertia forces. The volumes of the chambers are selected based on the test periods of less than 2.2 seconds and the range of flow rates desired to produce a range of Reynolds numbers, with minimal pressure rise during a test. Several ways to measure the instantaneous flow rates have been discussed, including the method shown in Fig. 1, where piston motion is detected by a diode laser and linear array optical array arrangement. The experimental procedure will be to complete chill down and establish the flow before the drop. Estimates confirm that there should be ample time for the flow to relax from 1 g to μg before the end of the drop.

Theoretical Approach

The theoretical approach includes real-gas equations of state, conservation equations that account for Soret and Dufour effects, and accurate transport properties. This model has already been validated with suspended-drop microgravity data. Preliminary simulations of a forced, laminar heptane/nitrogen mixing layer yielded encouraging results when compared to experimental observations of supercritical jets. An example of the simulation results is depicted in Fig. 2 showing the magnitude of the density gradient, which is pertinent to optical measurements: the finger-like features detected in the simulations qualitatively replicate some features observed experimentally [3]. Further studies will focus on using the same fluids in simulations and experiments, and performing simulations and observations at same conditions.

1. Harstad, K. and Bellan, J., Int. J. of Multiphase Flow, 26(10), 1675-1706, 2000.
2. Chehroudi, B., and Talley, D.G., 40th AIAA Aerospace Sciences Meeting and Exhibit, paper AIAA 2002-0342, Reno, NV, 14-17 January, 2002.
3. Chehroudi, B., Coy, E., and Talley, D.G., Physics of Fluids, 14(2), 850-861, 2002.

THE SCALES SEPARATION PHENOMENON IN HIGH HEAT FLUX POOL BOILING

T.G Theofanous, G.J. Li, J.P. Tu and T.N. Dinh
Center for Risk Studies and Safety
University of California, Santa Barbara
6740 Cortona Drive, Goleta CA 93117
Phone/Fax: (805) 893-4900/4927, theo@crss.ucsb.edu

This is the first progress report on a recently-initiated research project aiming to a basic understanding of Boiling Crisis in forced convection boiling. The work is a continuation and extension of a project that addressed coolability limits in pool boiling carried out over the previous funding cycle. A key result of this previous work was the identification of a scales separation phenomenon, that effectively "isolates" the microhydrodnamics on the heater surface from the chaotic two-phase flow motions away from it. This separation is effected by a persistent very high void fraction region (like a vapor "blanket"), and it is of immense significance in allowing to focus the physics of a long-standing apparently intractable problem (Theofanous et al., 2002a,b).

We expect that such a separation of scales would be present also in convective boiling, especially in the low flow rates regimes that are of interest in space applications, so the subject is pursued as a key component of the present effort as well. In this report we describe our efforts towards a more precise and detailed characterization as needed to elucidate the key mechanisms for both pool and convective boiling geometries.

The region of interest extends from outside the microlayer, undulating on the heater surface (10s of microns), up to a few millimeters away from it. This requires high spatial resolution in the vertical dimension over the whole horizontal macroscopic dimension needed to reveal the pattern (the whole 2.5 cm x 4 cm surface area of the heater), and obviously the measurement must be non-intrusive. Our previous work demonstrated the value and potential of the X-ray radiography technique for this purpose (Theofanous et al., 2002a,b). The point of departure here is consideration of scattered X-rays, associated improvements to our test section and radiography imaging techniques including positioning, collimating, and film/intensifier choice and development. Further, the work included extensive calibrations, especially using "ghosts" of known and similar (but static) material configurations. Of special importance was the replacement of the glass wall of our test section by pieces made of KAPTON material.

Sample results are shown in Figure 1. The radiographs depict projections over the narrow dimension of the test section (2.6 mm) and the gray scales show local (in 2D, heights—width) void fraction distributions and their variation with heat flux. Ensemble averages can be constructed from such images taken repeatedly. The line diagram shows the results of horizontal averaging of these radiographs --- that is, area averages over horizontal planes as function of their distance from the heater. The high void fraction region is seen to be well established at heat flux levels over ~700 kW/m^2. Closer examination can reveal further details on the internal structures of this important region.

References

1. T.G. Theofanous, T.N. Dinh, J.P. Tu, and A.T. Dinh, The boiling crisis phenomenon. Part I: Nucleation and nucleate boiling heat transfer. *Experimental Thermal Fluid Science* (2002a).
2. T.G. Theofanous, T.N. Dinh, J.P. Tu, and A.T. Dinh, The boiling crisis phenomenon. Part II: Dryout dynamics and burnout. *Experimental Thermal Fluid Science* (2002b).

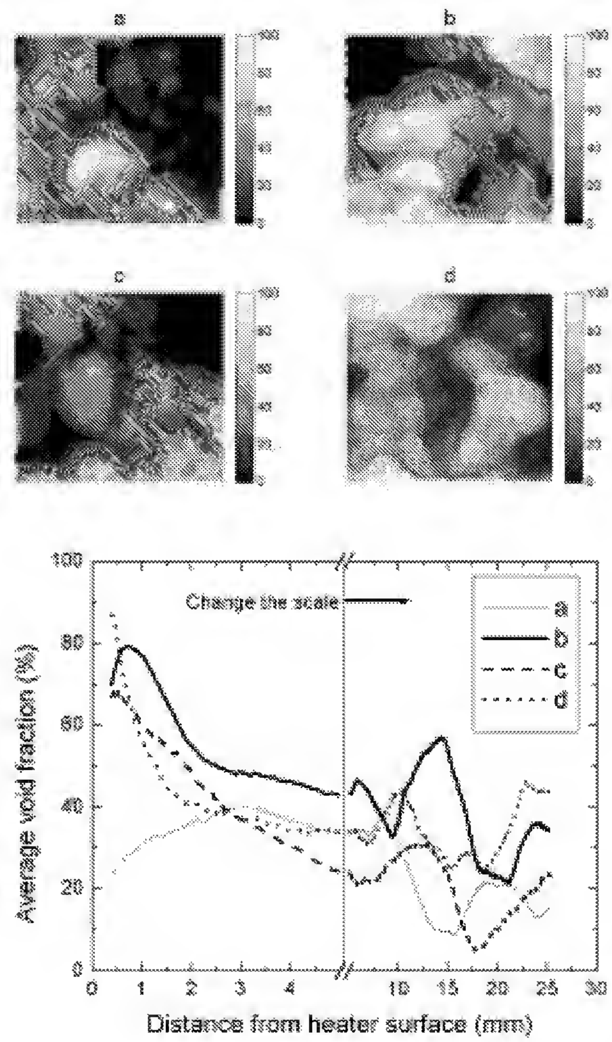

Figure 1. Void fraction distributions in pool boiling as measured by X-ray radiography. (a) 225 kW/m^2, (b) 690 kW/m^2; (c) 1214 kW/m^2; (d) 1656 kW/m^2 (prior to burnout). The bottom figure shows cross-sectional average void fractions.

THE SCALES SEPARATION PHENOMENON IN HIGH HEAT FLUX POOL BOILING

T.G Theofanous, G.J. Li, J.P. Tu and T.N. Dinh

Center for Risk Studies and Safety
University of California, Santa Barbara

This is the first progress report on a recently-initiated research project aiming to a basic understanding of Boiling Crisis in forced convection boiling. The work is a continuation and extension of a project that addressed coolability limits in pool boiling carried out over the previous funding cycle. A key result of this previous work was the identification of a scales separation phenomenon, that effectively "isolates" the microhydrodnamics on the heater surface from the chaotic two-phase flow motions away from it. This separation is effected by a persistent very high void fraction region (like a vapor "blanket"), and it is of immense significance in allowing to focus the physics of a long-standing apparently intractable problem (Theofanous et al., 2002a,b).

We expect that such a separation of scales would be present also in convective boiling, especially in the low flow rate regimes that are of special interest in space applications, so the subject is pursued as a key component of the present effort as well. In this report we describe our efforts towards a more precise and detailed characterization as needed to elucidate the key mechanisms for both the pool and convective boiling situations.

Experimental Arrangement

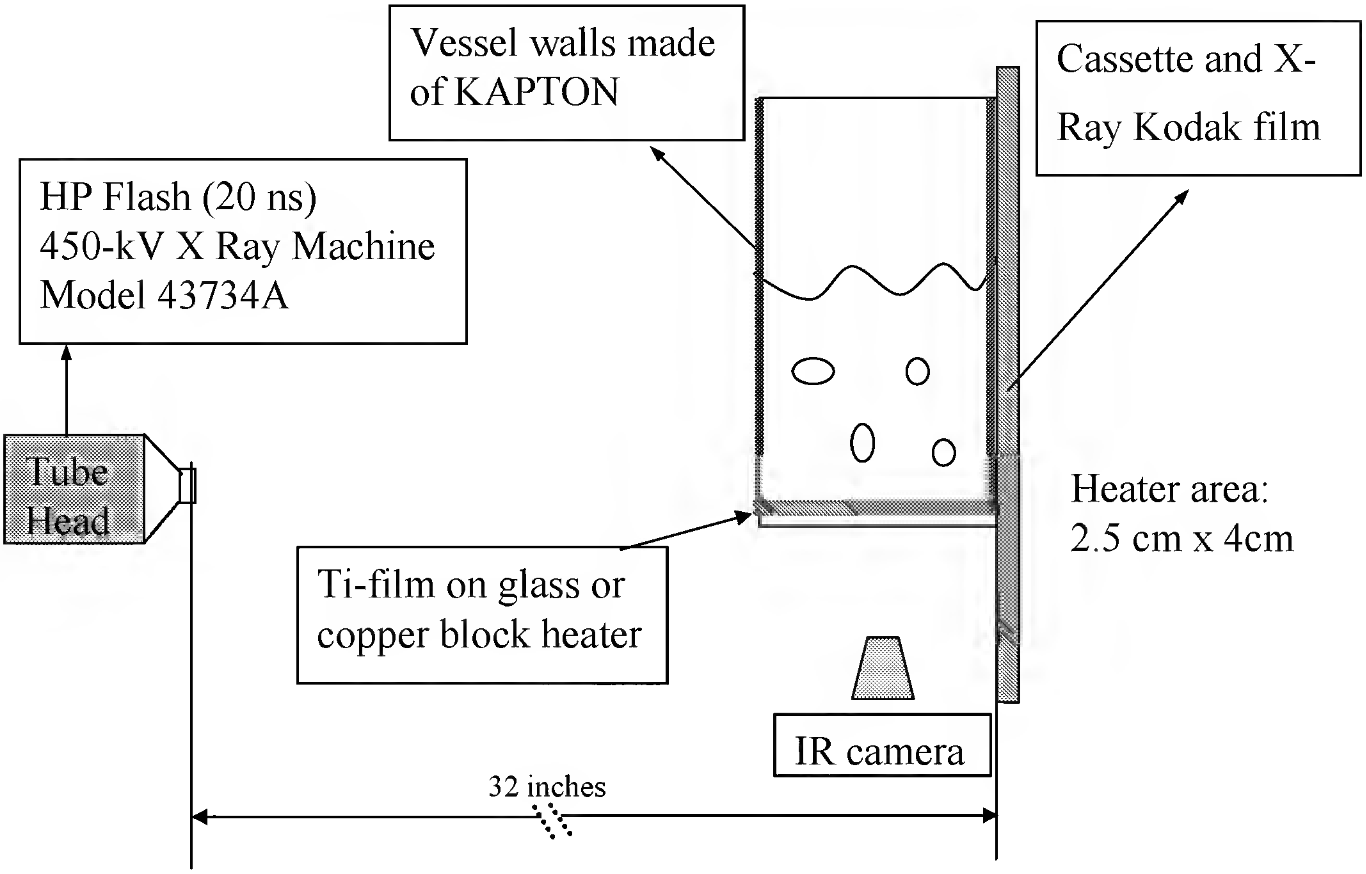

Quantitative X-Ray Radiography: Elements and Calibration

- X-Ray scattering reduction (using special materials for test vessel)

- X-Ray tube head positioning, collimating

- Film/intensifier choice and controlled film development

- Alignment control for individual experiment

- Extensive calibrations ("ghost" subjects, wedge)

Two-Phase Flow Regimes in Pool Boiling

q =102 kW/m²

Original X-ray image

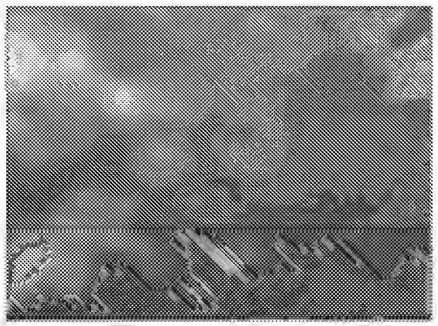

Void Fraction

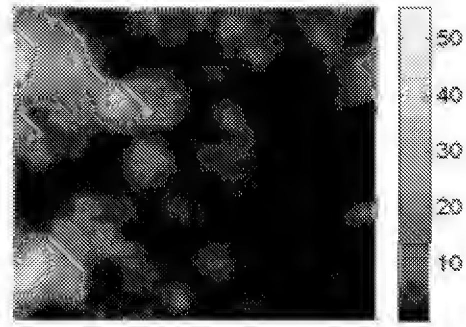

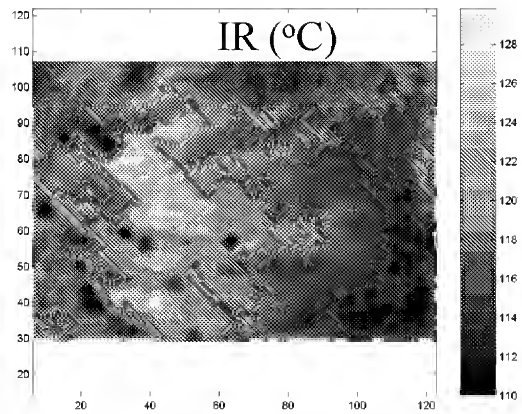

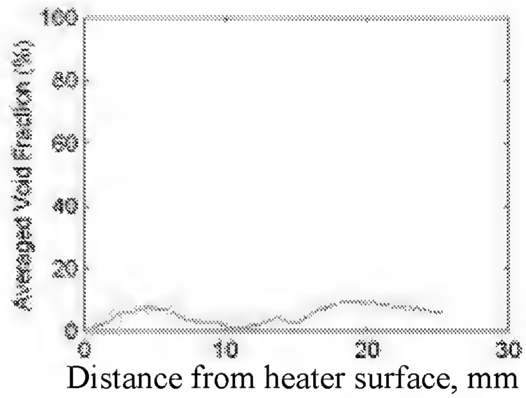

q =225 kW/m²

Original X-ray image

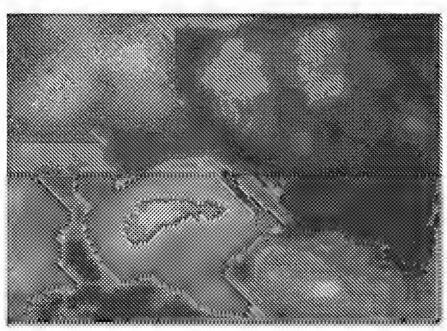

Void Fraction

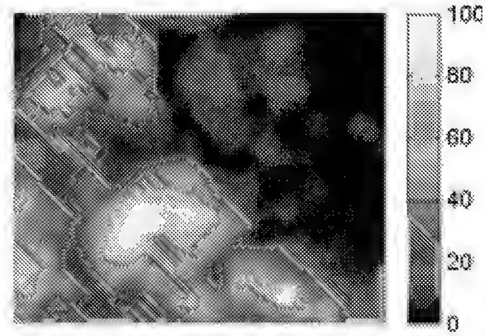

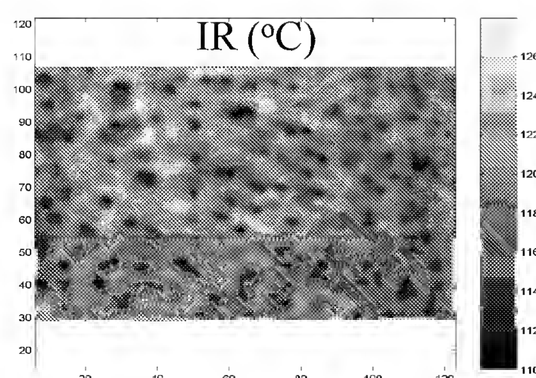

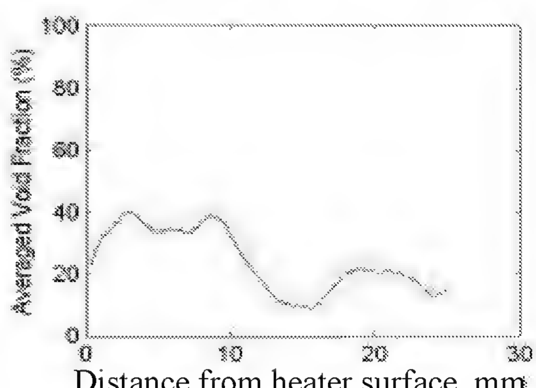

UCSB

Pool Boiling at Intermediate Fluxes

Void Fraction

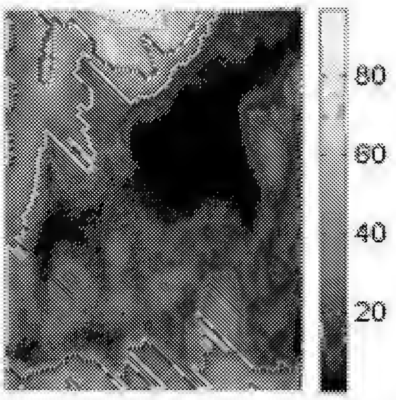

q =500 kW/m^2

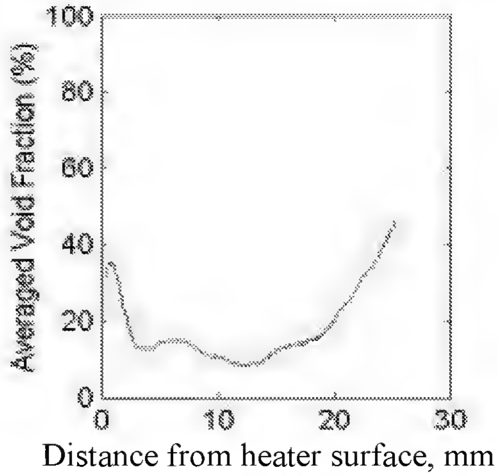

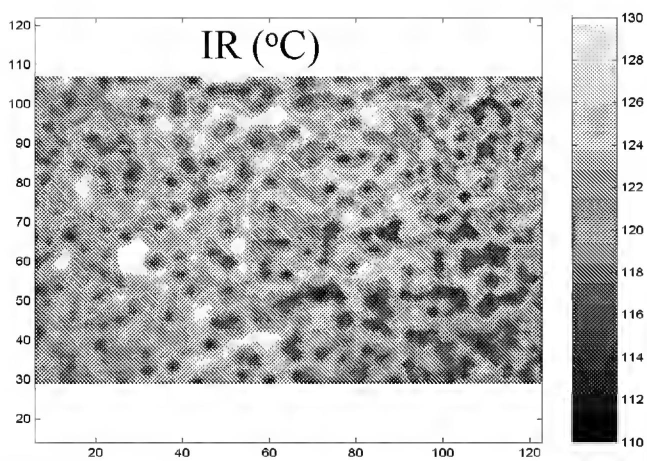

Unstable vapor blanket

Void Fraction

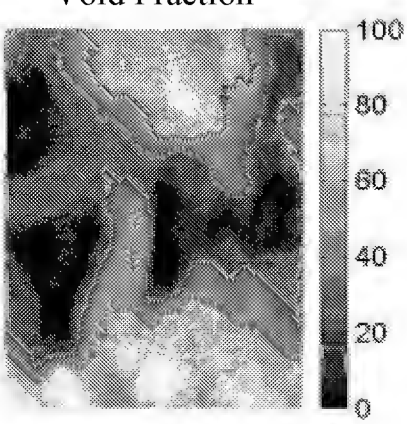

q =500 kW/m^2

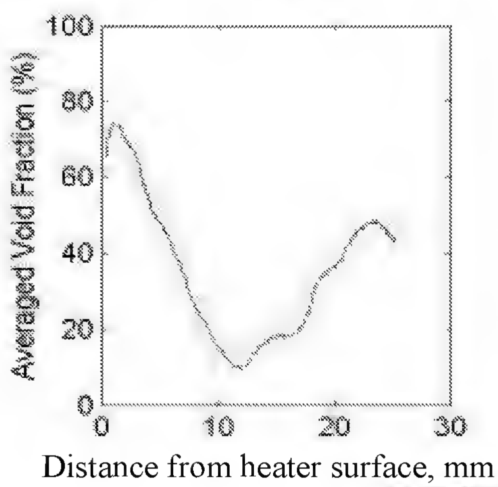

Pool Boiling at High Heat Fluxes

Void Fraction

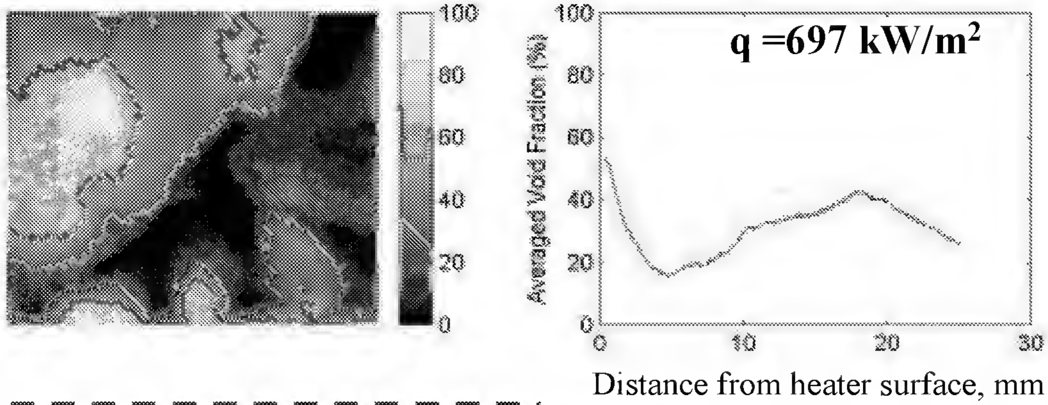

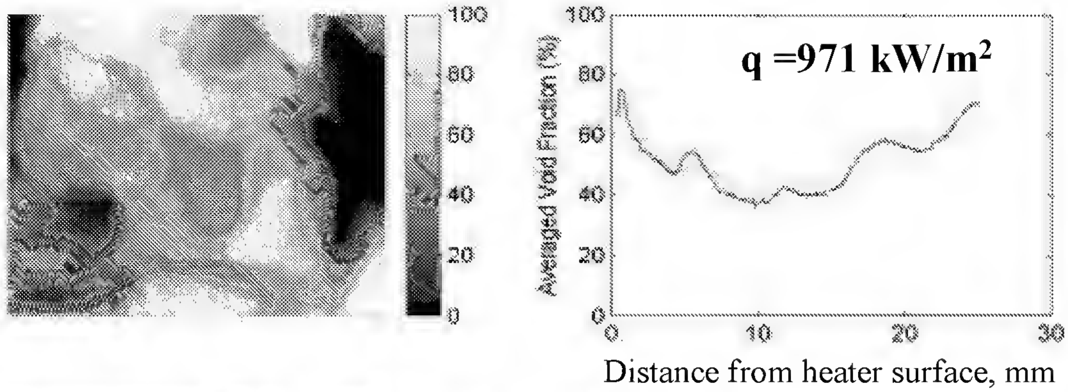

Stable Vapor Blanket

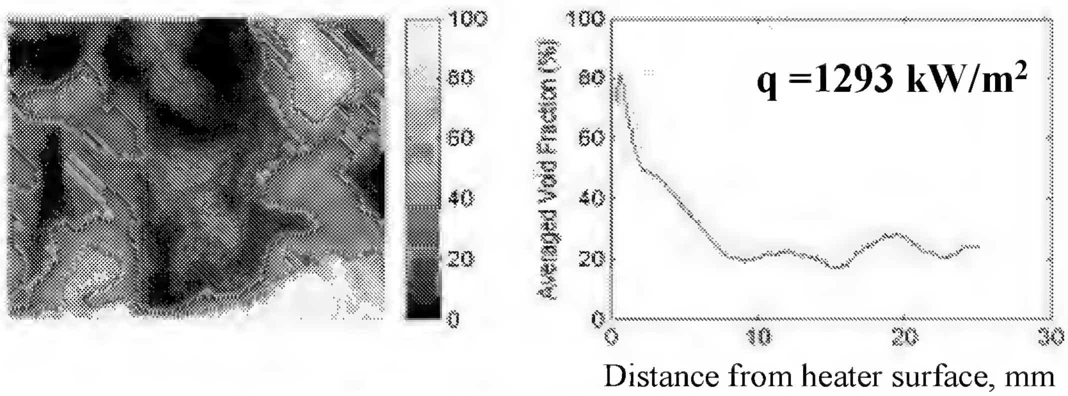

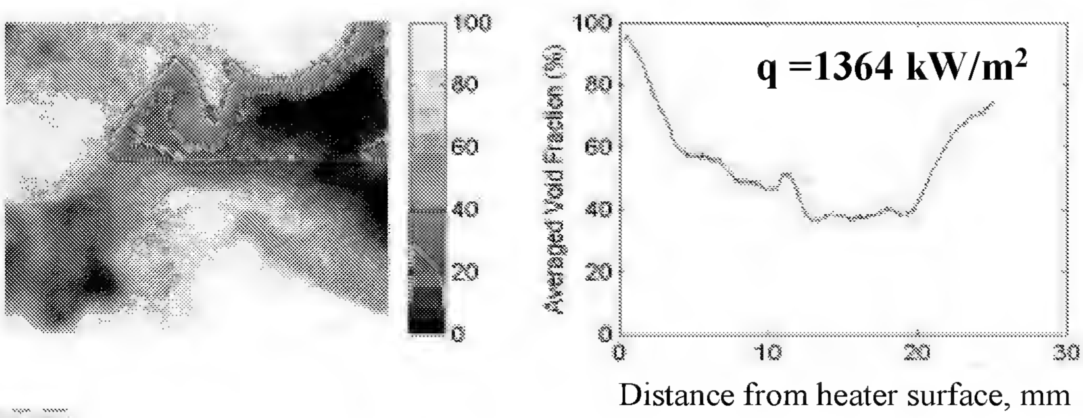

$q = 1440\ kW/m^2$

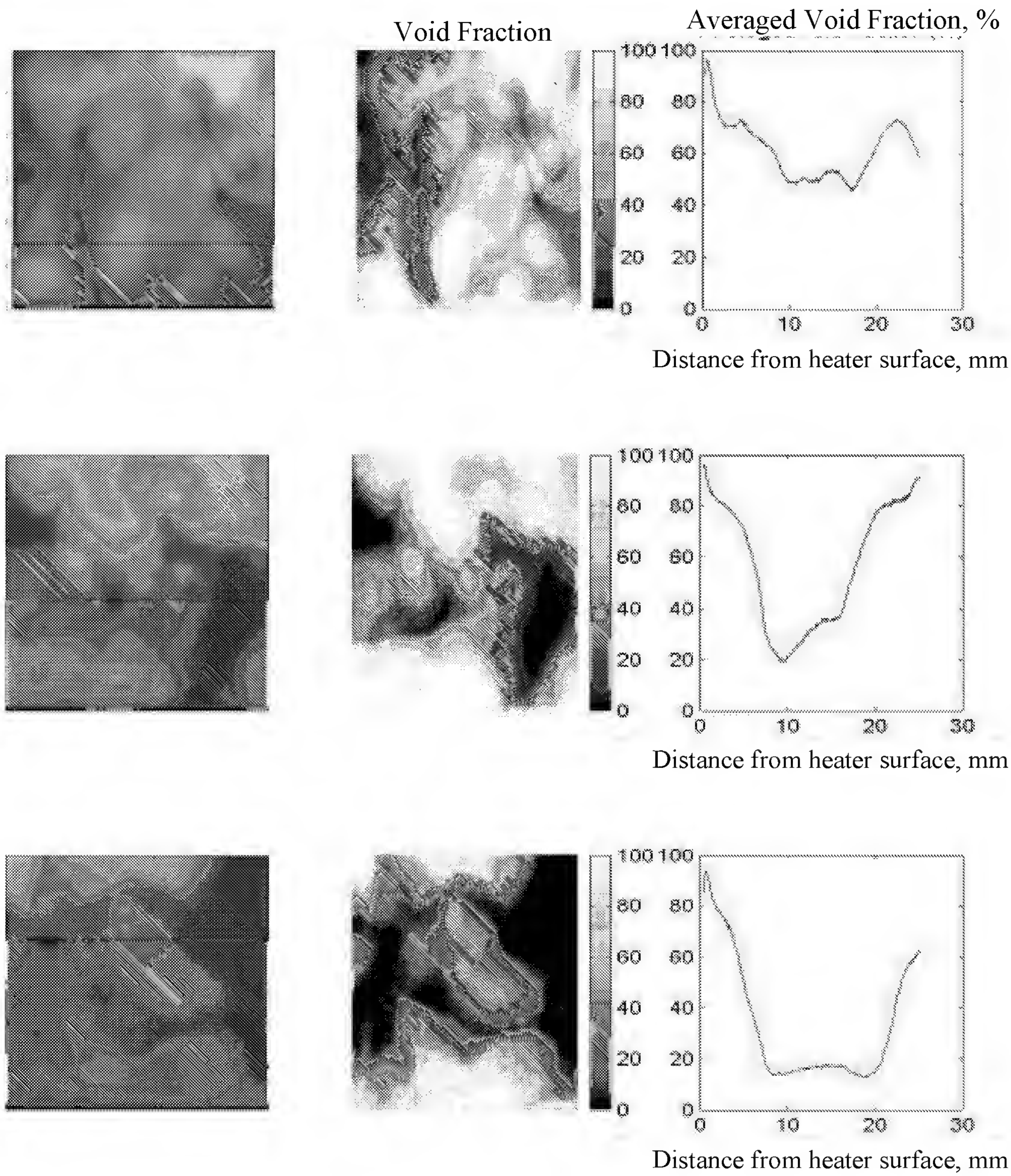

Stable Vapor "Blanket"

Combined Diagnostics: IR and X-Ray

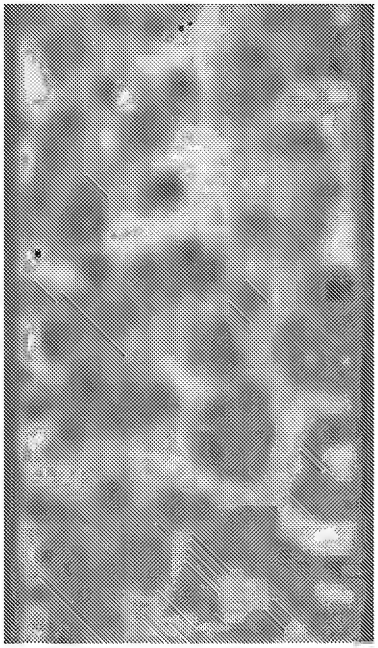

Stable pattern

vs

Chaotic behavior

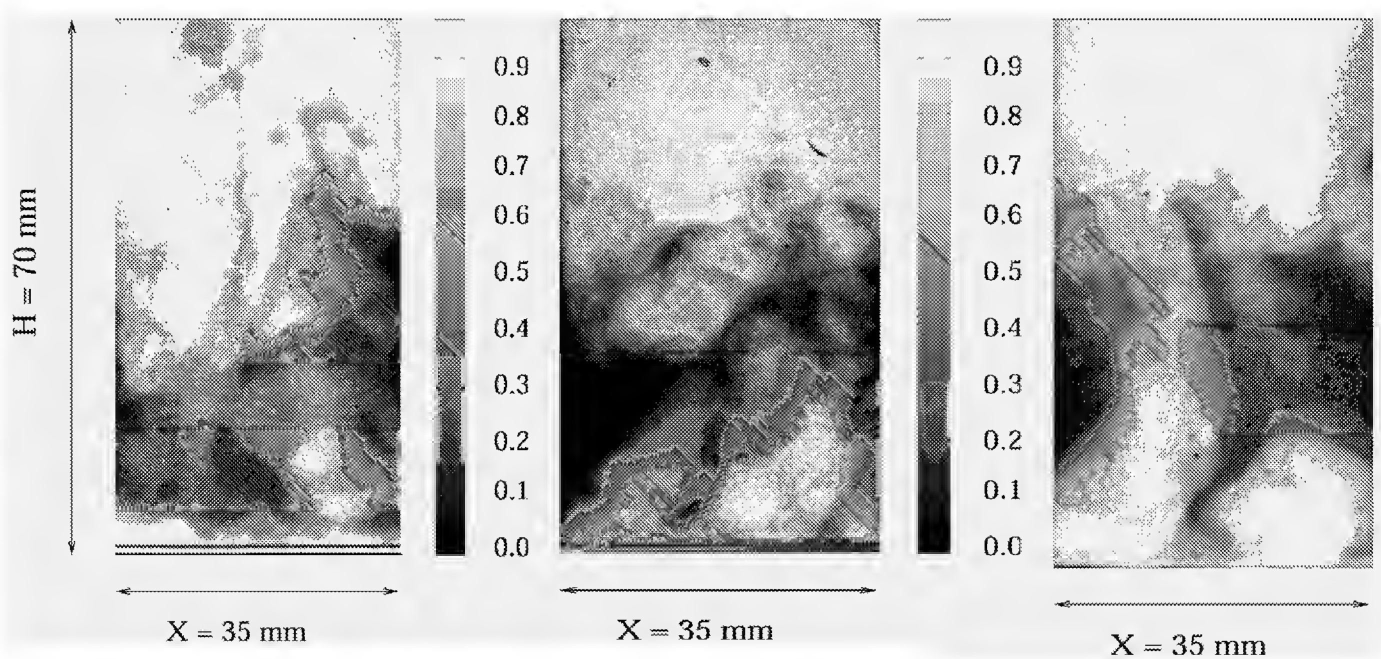

Phenomena and Scales Involved in Pool Boiling

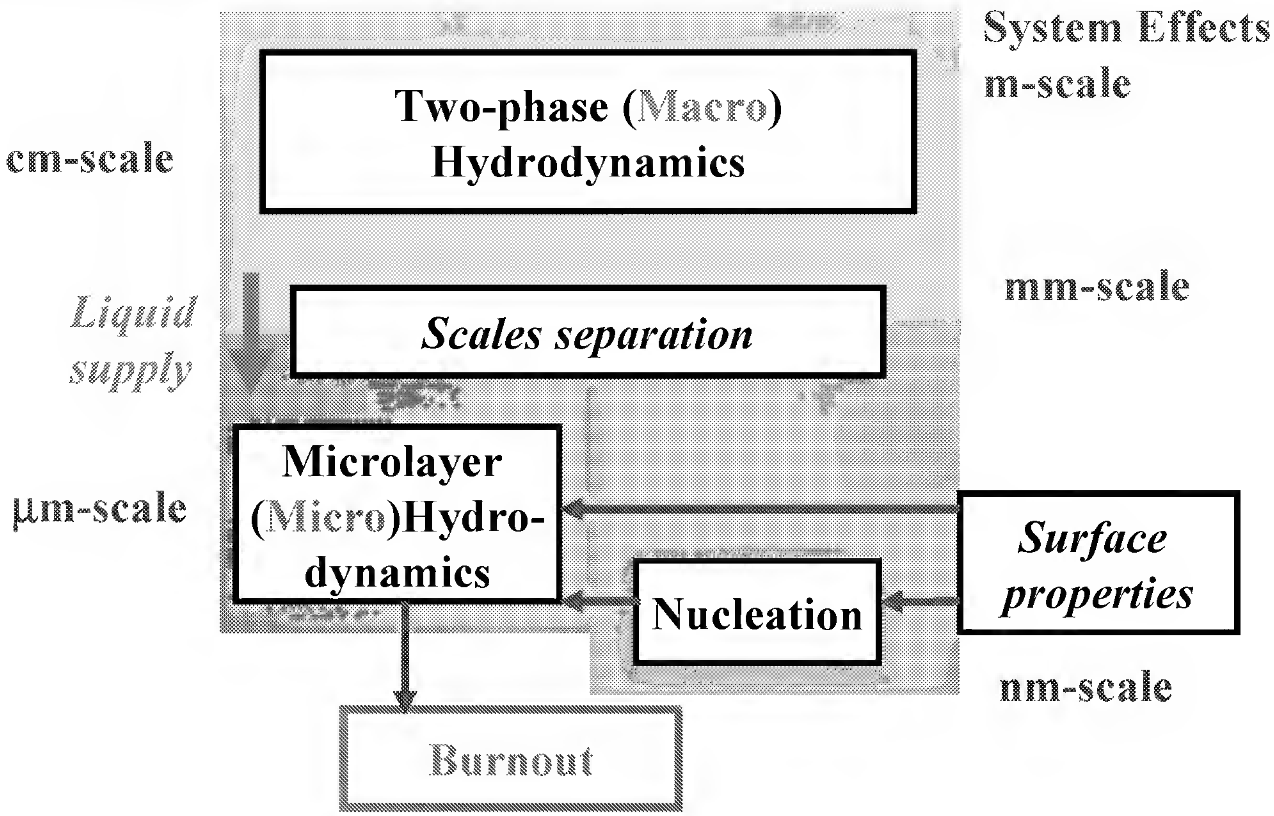

Shifting the focus to **micro-hydrodynamics of thin evaporating liquid film** on heater surface and the role of surface chemistries and nano/micro-morphologies

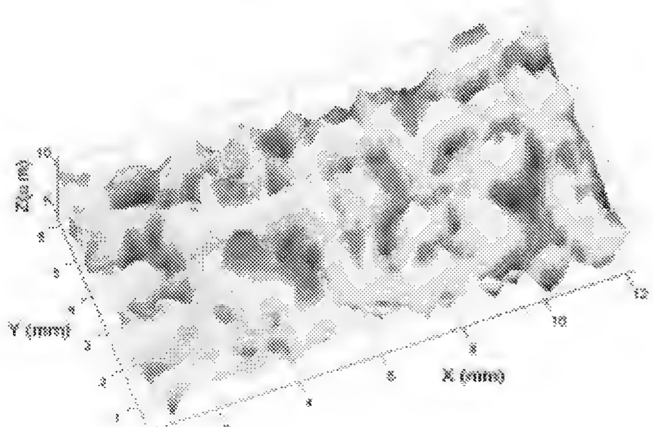

Aged Heater

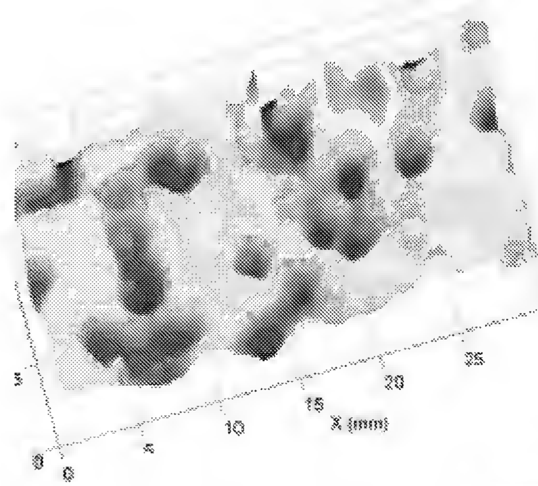

Fresh Heater

NUCLEATION ON NANOSCOPICALLY SMOOTH SURFACES

T.G. Theofanous, J.P. Tu, and T.N. Dinh
Center for Risk Studies and Safety
University of California, Santa Barbara
6740 Cortona Drive, Goleta CA 93117
Phone/Fax: (805) 893-4900/4927, theo@crss.ucsb.edu

This is the first progress report on a recently-initiated research project aiming to a basic understanding and prediction of the Boiling Crisis phenomenon in convective boiling. The work is a continuation and extension of a project that addressed coolability limits in pool boiling and was carried out over the previous funding cycle. A key ingredient of our approach is the use of high speed, high resolution infrared imaging in conjunction with nanofilm (in thickness) heaters of macroscopic dimensions to detect the evolution of thermal patterns at the solid-fluid interface. In particular the configuration allows the detection of bubble nucleation events, and it has permitted the first direct determination of bubble nucleation densities in high heat flux boiling (Theofanous et al, 2002a).

This work established a strong connection of the surface nucleation characteristics and it's resistance to burnout (Theofanous et al 2000b), so nucleation is pursued as a key component of the present effort on convective boiling as well. The point of departure is a further finding of this work that nucleation on nanoscopically smooth (±4 nm rms roughness) surfaces is not consistent with the apparently (and firmly) established preexisting cavity nucleation theory (PEN) as propounded by Zeldovich (1943), Dean (1944),and Bankoff (1958), and elaborated more recently by Wang and Dhir (1993). More specifically our work points to surface nanomorphology and chemistry at the origin of heterogeneous nucleation, thus leading us to question whether there is any role left to "roughness" (as conceived in PEN), even for rough, engineering surfaces. Thus, in this nucleation-focus portion of our project, the domain of interest includes all kinds of surfaces, rough and "dirty" ones as found in traditional engineering equipment, as well as ultrasmooth and "clean" ones as found in new micro scale technologies such as cooling of microelectronic equipment, and operation of micro fluidic devices.

In this report we present the results of our first steps in addressing the potential role of ``roughness". The idea is that this role can be isolated by using nanofilms on preroughened glass substrates. Using precision sandblasting we can create micron-scale roughnesses that resemble those of common engineering surfaces. On the other hand, using metal vapor deposition techniques, we can build films (on these substrates) with chemistries and nanomorphologies precisely similar to those found on our smooth nanofilms of our previous work. All other aspects of the experimental apparatus and diagnostics are also the same. Experiments are conducted either on a pulse-heating mode, where a significant change in heat flux is instantaneously imposed, or in a steady-state mode, where heating is changed by small increments (or decrements).

Sample results are shown on Figures 1 and 2. The gray scales are in degree cemtigrade.

References

1. Bankoff, S.G., Entrapment of gas in the spreading of liquid over a rough surface, AIChE J., 4 (1958) 24-26.
2. Dean, R.B., The formation of bubbles. J.Appl.Phys. 15 (1944) 446-51
3. Theofanous, T.G. , T.N. Dinh, J.P. Tu, and A.T. Dinh, The boiling crisis phenomenon. Part I: Nucleation and nucleate boiling heat transfer. *Experimental Thermal Fluid Science* (2002a).
4. Theofanous, T.G. , T.N. Dinh, J.P. Tu, and A.T. Dinh, The boiling crisis phenomenon. Part II: Dryout dynamics and burnout. *Experimental Thermal Fluid Science* (2002b).
5. Wang, C.H.; Dhir, V.K. On the gas entrapment and nucleation site density during pool boiling of saturated water. ASME Journal of Heat Transfer, vol.115, (3) (1993) 670-9.
6. Zeldovich, Ya.B., On the theory of new phase formation: cavities. Acta Physico. Chim. URSS 18 (1943) 1

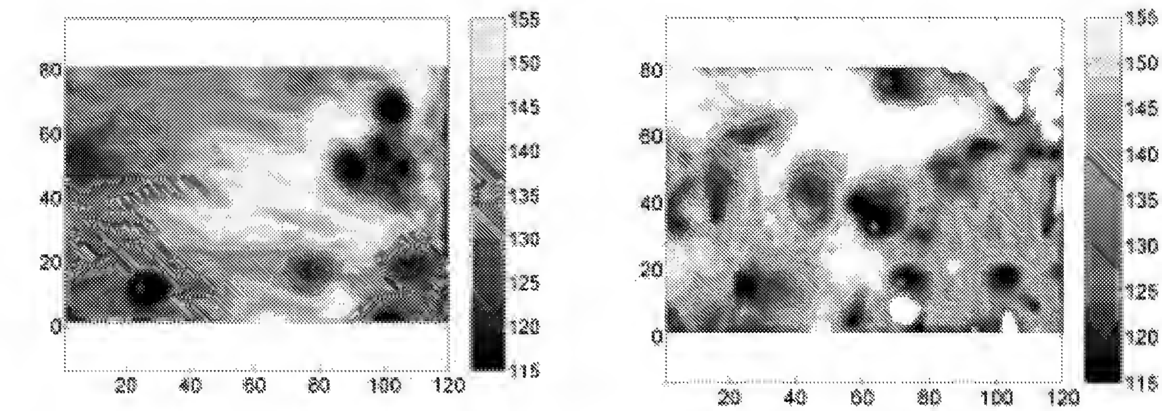

(i) (ii)

Figure 1. IR thermal pattern prior (i) and after (ii) power surge.

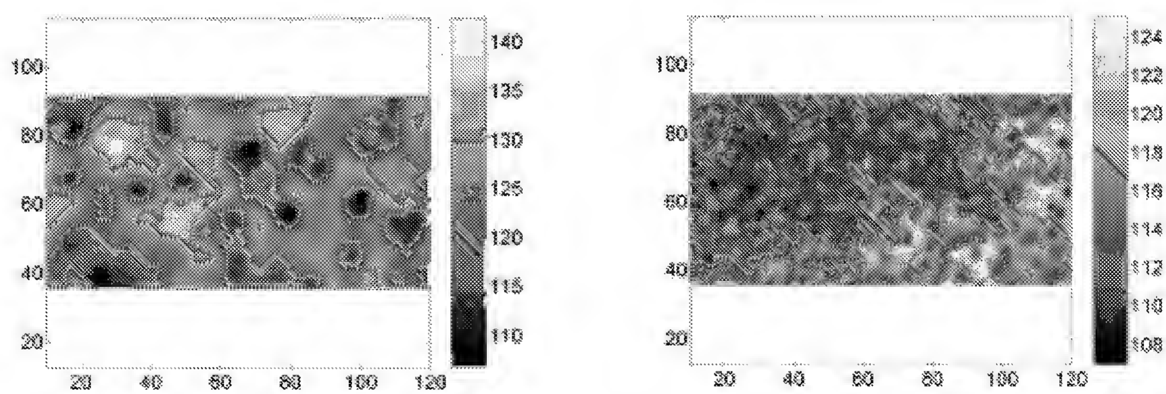

(a) (b)

Figure 2. Infrared thermal imaging of nucleation patterns on,
(a) fresh smooth heater, (b) aged smooth heater at 600 kW/m^2.

NUCLEATION ON NANOSCOPICALLY SMOOTH SURFACES

T.G. Theofanous, J.P. Tu, and T.N. Dinh

Center for Risk Studies and Safety
University of California, Santa Barbara

This is the first progress report on a recently-initiated research project aiming to a basic understanding and prediction of the Boiling Crisis phenomenon in convective boiling. The work is a continuation and extension of a project that addressed coolability limits in pool boiling and was carried out over the previous funding cycle. A key ingredient of our approach is the use of high speed, high resolution infrared imaging in conjunction with nanofilm (in thickness) heaters of macroscopic dimensions to detect the evolution of thermal patterns at the solid-fluid interface. In particular the configuration allows the detection of bubble nucleation events, and it has permitted the first direct determination of bubble nucleation densities in high heat flux boiling (Theofanous et al, 2002a). This work established a strong connection of the surface nucleation characteristics and it's resistance to burnout (Theofanous et al 2000b), so nucleation is pursued as a key component of the present effort on convective boiling as well. The point of departure is a further finding of this work that nucleation on nanoscopically smooth (±4 nm rms roughness) surfaces is not consistent with the apparently (and firmly) established preexisting cavity nucleation theory (PEN) as propounded by Zeldovich (1943), Dean (1944), and Bankoff (1958), and elaborated more recently by Wang and Dhir (1993).

Critical Heat Flux *vs.* Nucleation Site Density

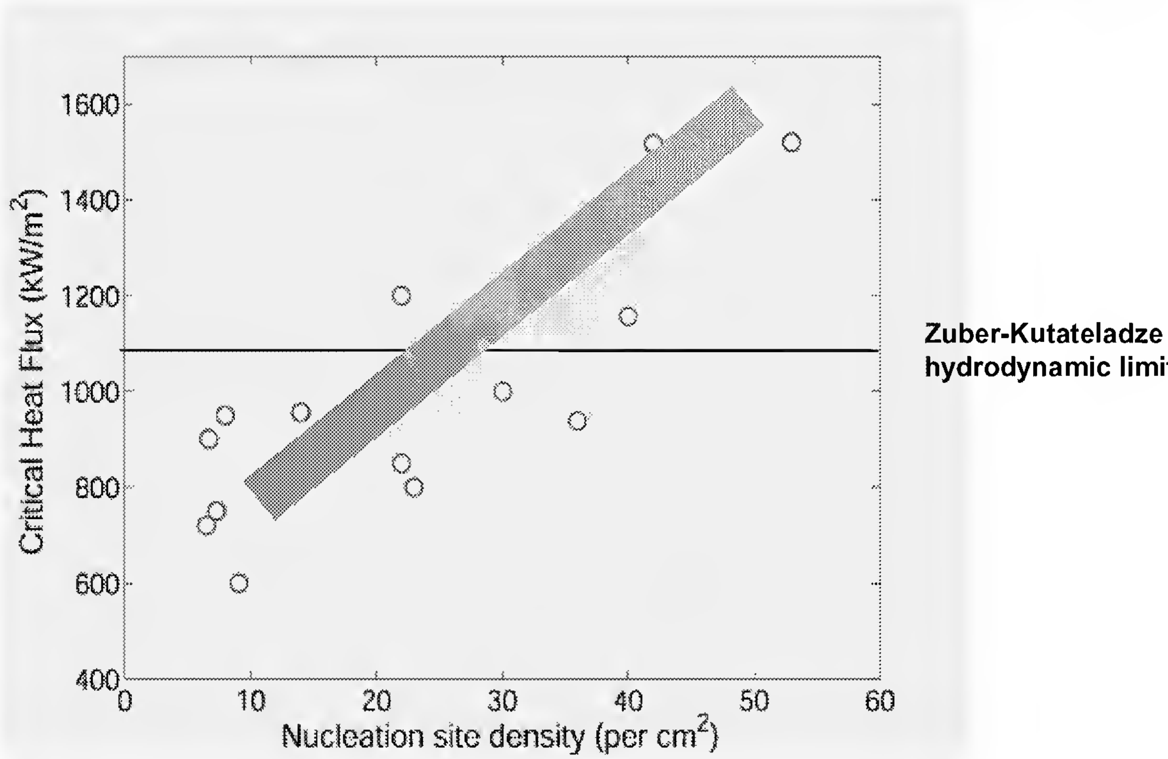

The trend is in the contrary to the current belief that a higher Nucleation Site Density lowers CHF

BETA Experiments:
Boiling on Vapor-Deposited Nano-Film Heaters

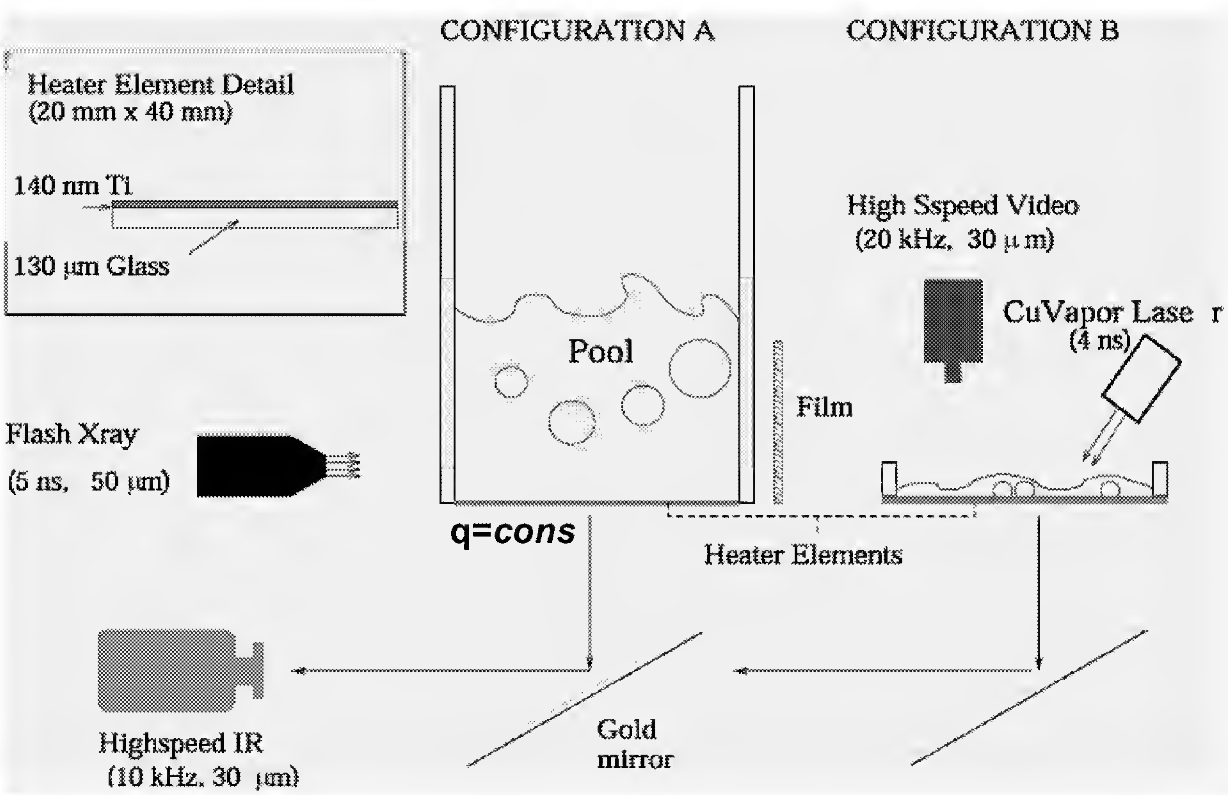

UCSB

Heater aging and surface characterization:
Subject to Strict Experimental Protocol

Fresh heater

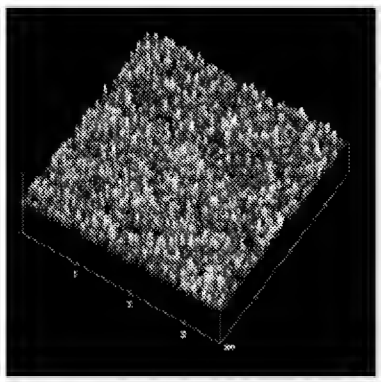

AFM **rms ±4nm**

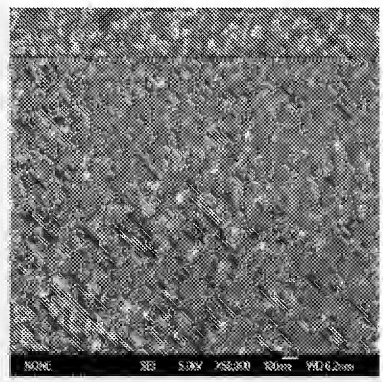

SEM

No μ-cavity !

in BETA heaters

Aged heater

Oxide Island

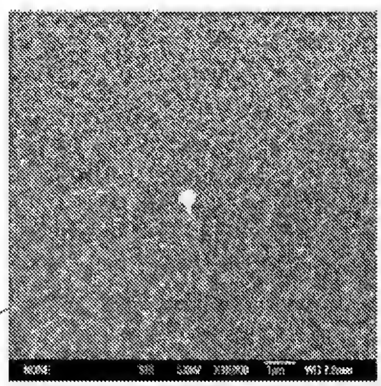

SEM

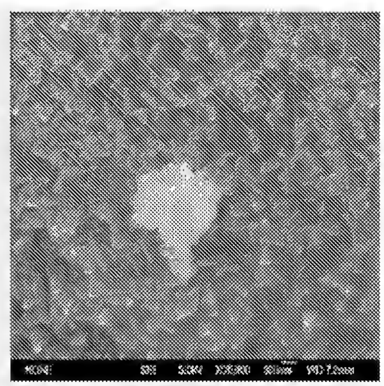

SEM

UCSB

Boiling on Nanoscopically Smooth Surfaces

29 kW/m^2

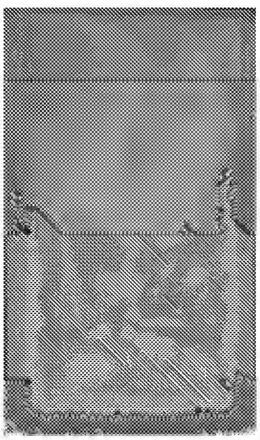

56 kW/m^2

259 kW/m^2

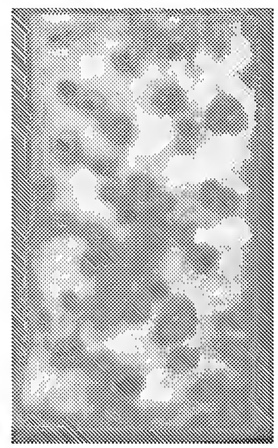

Single-Phase
Natural Convection

Cavity gas entrapment PEN theory

No μ-cavity in BETA heaters, but

Nucleation of Vapor Bubbles occurs at Superheats of 10-15 K

?

Prediction by → Zeldovich (1944)

Dean (1944)

Bankoff (1958)

Wang & Dhir (1993)

Pre-Existed Nuclei (PEN) Theory

	Cavity mouth radii [nm]	Superheat [K]
	700	30
	90	100
BETA - - - -	4	300

↓

Surface Nanomorphology and Chemistry at the Origin of Heterogeneous Nucleation → *Revisit* → Frenkel islands (1943)

Kuni (1996)

UCSB

Footprint of boiling heat transfer

Direct identification of nucleation events

Quantitative measurements of local transient heat transfer

Fresh heater

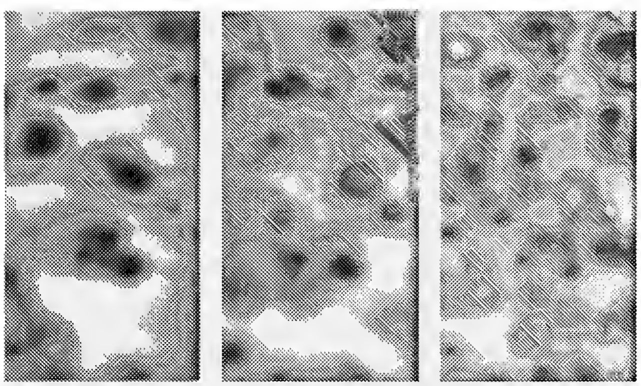

a) b) c)

406 kW/m^2 536 kW/m^2 807 kW/m^2

Aged heater

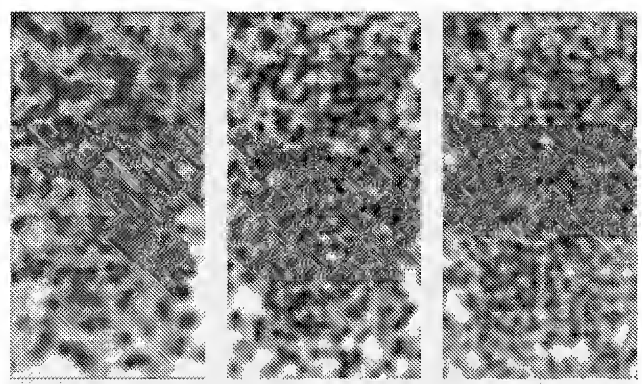

a) b) c)

348 kW/m^2 1051 kW/m^2 1517 kW/m^2

UCSB

Heater Surface Temperature at Active Nucleation Sites

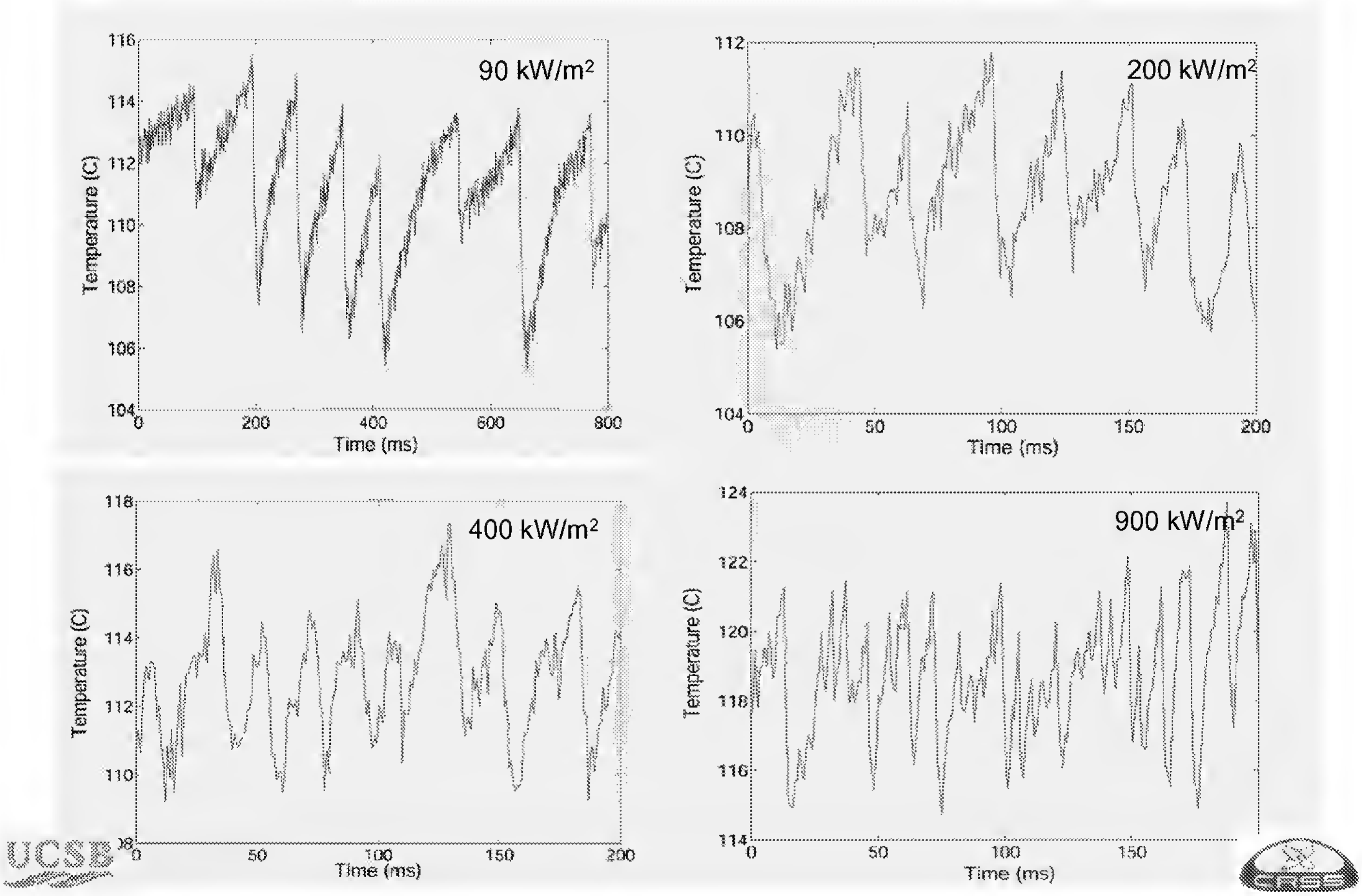

Direct quantification of nucleation events

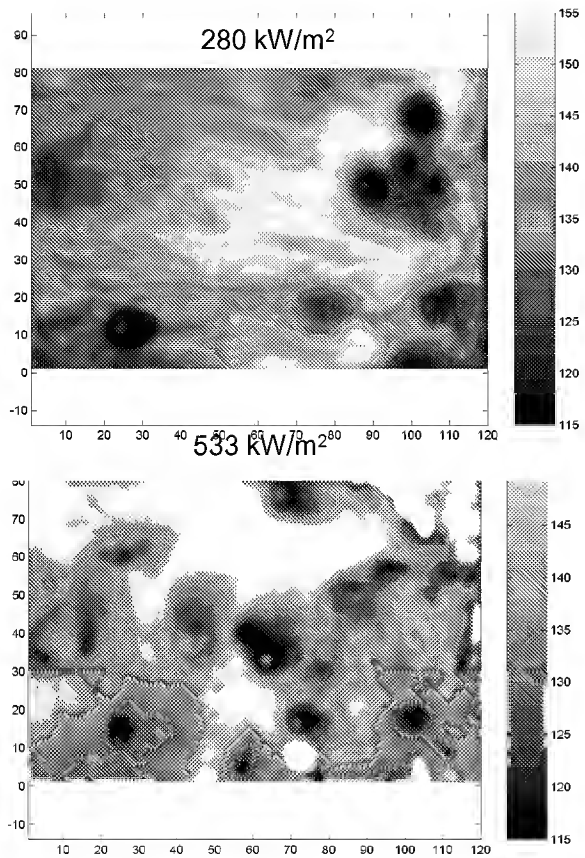

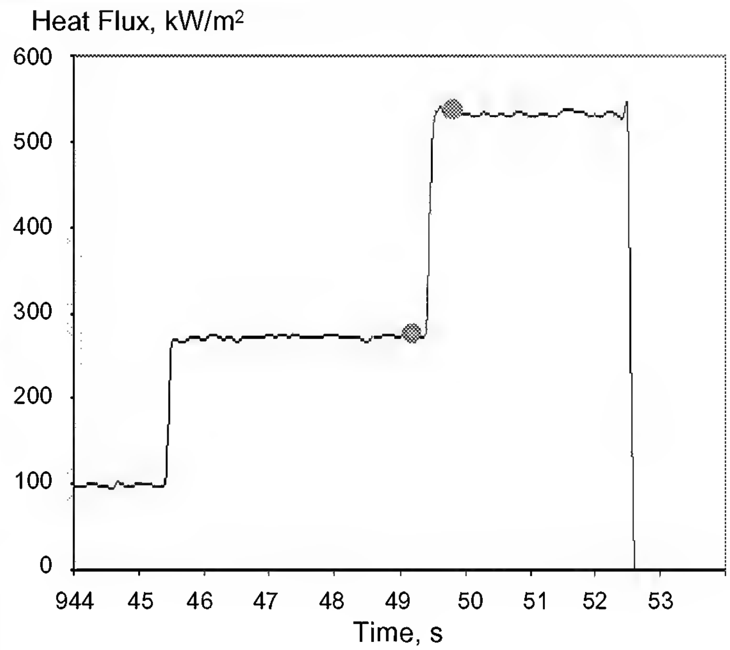

Thermal Pattern Prior and
After the Power Surge

Boiling on pre-roughened heater surfaces

Nucleation behavior on heaters manufactured by

vapor deposition on a sand-blasted glass substrate

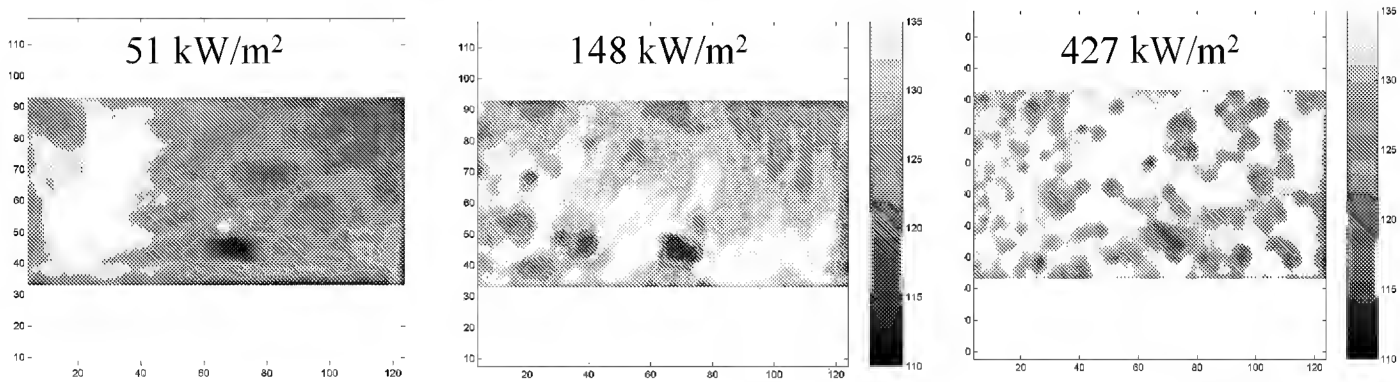

- Below 200 kW/m² nucleation patterns are similar to that of a fresh smooth heater;

- As heat flux increases beyond 300 kW/m² the nucleation patterns approach that of aged heaters.

Further study is in progress

UCSB

ELECTROSTATIC EFFECTS ON DROPLET SUSPENSIONS

Gretar Tryggvason, Arturo Fernandez, and Asghar Esmaeeli
Mechanical Engineering Department
100 Institute Road
Worcester Polytechnic Institute
Worcester, MA 01609-2280
gretar@wpi.edu, Tel.: 508 831-5759, FAX: 508 831-5680

ABSTRACT
Direct numerical simulations are used to examine the effect of electric fields on the behavior of a suspensions of drops in channels. The effect of the electric field is modeled using the "leaky dielectric" model, coupled with the full Navier-Stokes equations. The governing equations are solved using a front-tracking/finite volume technique. The method has been validated by detailed comparison with previous results for the axisymmetric interactions of two drops in Stokes flow.

An extensive set of two-dimensional simulations has allowed us to explore the effect of the conductivity and permittivity ratios in some detail. The interaction of two drops is controlled by two effects. The drops are driven together due to the charge distribution on the surface. Since the net charge of the drops is zero, the drops see each other as dipoles. This dielectrophoretic motion always leads to drops attraction. The second effect is fluid motion driven by tangential stresses at the fluid interface. The fluid motion depends on the relative magnitude of the permittivity and conductivity ratios. When the permittivity ratio is higher than the conductivity ratio, the tangential forces induce flow from the poles of the drops to the equator. If the center of two such drops lies on a line parallel to the electric field, the flow drains from the region between the drops and they attract each other. When the ratios are equal, no tangential motion is induced and the drops attract each other by dielectrophoretic motion. When an electric field is applied to many drops suspended in a channel flow, drops first attract each other pair-wise and some drops move to the wall. If the forces are strong (compared to the fluid shear) the drops can form columns or fibers, spanning the channel and blocking the two-dimensional flow. Electronic "fibration" of suspensions has been observed in a number of systems, including dispersion of milk droplets and red blood cells. If the attractive forces are weak compared to the shear, the columns are immediately broken up. For drops with the permittivity ratio lower than the conductivity ratio, the tangential forces induce flow in the opposite direction (from the equator to the poles of the drops) and if the induced fluid motion is sufficiently strong, the drops repel each other. In two-dimensions, this results in interactions between the drops that are similar to the previous case, except that the attractions take place perpendicular to the electric field. The drops therefore tend to form rows aligned with the flow, or "slugs" where many drops clump together. When the conductivity ratio is much higher than the permittivity ratio, the drops become prolate, expel each other and are spread more uniformly across the channel. Figure 1 shows two frames from one simulation of 36 drops in a channel. The parameters used result in oblate drops and two drops whose centers are on a line parallel to the electric field attract each

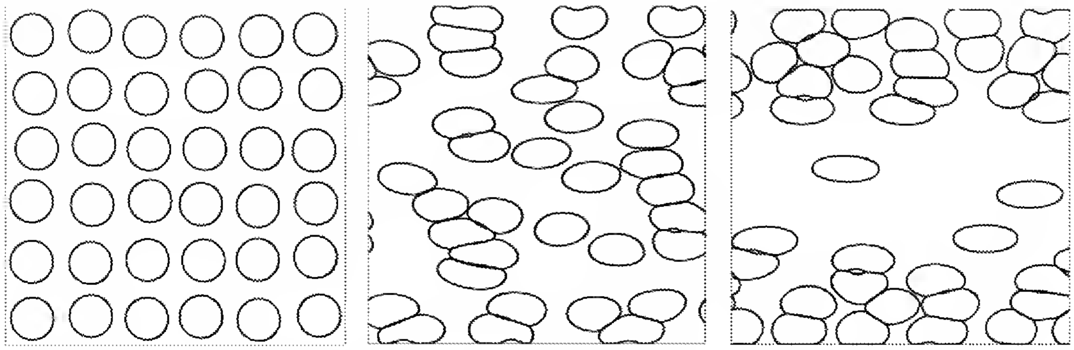

Figure 1. Three frames from a simulation of two-dimensional drops in a channel

other. After the electric field is turned on, the pairwise interactions of drops initially leads to the formation of drop pairs and columns of drops parallel to the field. The drops are also attracted to the walls by the same mechanism that drops are attracted to each other and eventually all the drops migrate to the walls. In this case the drops are not allowed to coalesce, but in reality we would expect the drops to form fluid layers next to the walls.

While the two-dimensional simulations have allowed us to conduct a large number of simulations relatively inexpensively, and explore a large range of conductivity and permittivity ratios, it is clear that fully three-dimensional systems are needed for quantitative predictions. We have developed a fully parallel code to examine three-dimensional systems. Preliminary simulations for oblate drops show that the results are similar to the two-dimensional ones, except that the rate of accumulation at the walls is slower. Large scale computations with many drops, as well as simulations of a wider range of parameters are in progress. Figure 2 show one frame from a simulation of a three-dimensional system. The drops and the electric field is shown after the drops have been deformed by the electric field moved, but before any significant pairwise interaction has taken place.

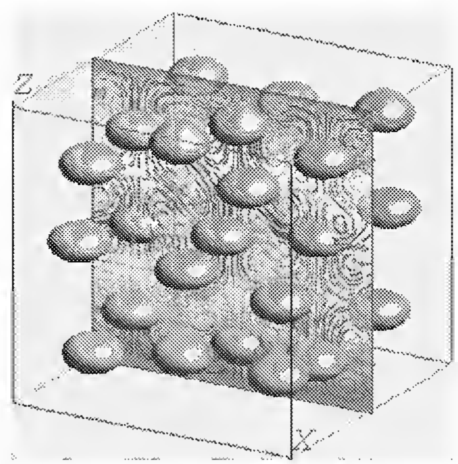

Figure 2. One frame from a three-dimensional simulation.

Our examination of the effect of electric fields on suspensions is still in its early stage and several aspects of the flow remains poorly understood. We have only done a limited number of simulations to examine the effect of the flow, for example. For flows where the drops tend to form fibers across the channel, strong flow (or weaker electric field) breaks up the columns. In some cases this promotes drop accumulation at the walls, but in other case the result is a statistically steady state where drop pairs and short drop chains continuously form and break up.

Electrostatic Effects on Droplet Suspensions

Grétar Tryggvason,
Arturo Fernández, and Asghar Esmaeeli
Worcester Polytechnic Institute

EHD of Droplet Suspension

Introduction

Electric fields can have a dramatic effect on multiphase flows, particularly in microgravity. Electric fields have been used to manipulate suspensions to enhance coalescence, to generate uniform distribution of small drops in sprays, increase heat and mass transfer from drops, to increase boiling efficiency, and to stabilize liquid bridges. While some numerical modeling has been done, it is fairly limited in both the physical assumptions used as well as the generality of the numerical method. Here, we are primarily interested in the use of electrostatic forces to modify the behavior of a suspension of bubbles and drops in channel flow.

EHD of Droplet Suspension

Numerical method

The computations are made possible by a method based on the "one-field" or "weak" formulation of the Navier-Stokes. The flow field is computed on a fixed, rectangular grid where all singular terms due to the interface are treated as generalized functions, approximated on the grid. The interface itself is represented by a lower dimensional "front" to preserve the sharp interface and to allow accurate computation of surface tension.

When the interface between two dielectric fluids is subjected to an external electric field, the dielectric mismatch between the fluids induces a stress at the fluid interface. This stress can be either normal or tangential to the interface, depending on the conduction and dielectric properties of the fluids. The electric field is found using the "leaky dielectric" model of Taylor.

EHD of Droplet Suspension

Deformation of a single drop

Electrostatic deformation of axisymmetric drops are shown in the figure to the right. The steady state is obtained after following the transient motion of an initially spherical drop. For the oblate drop in (a) the electric field induces flow from the poles to the equator, but for the prolate drop in (b) the flow is in the other direction.

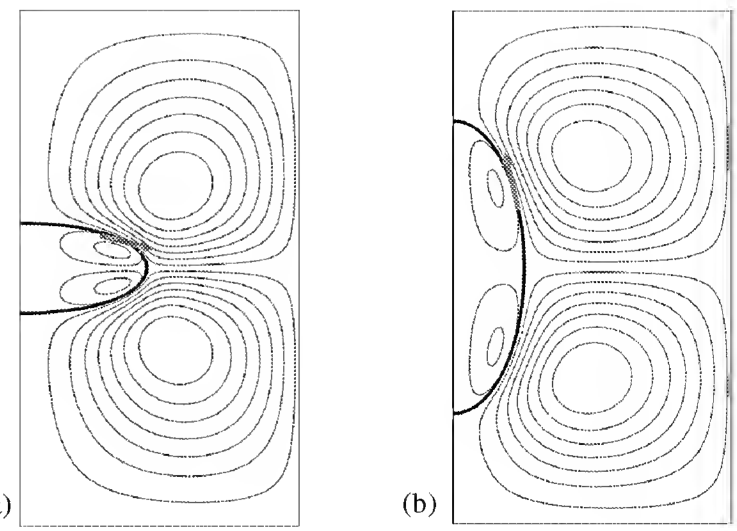

(a) (b)

EHD of Droplet Suspension

Interaction of two drops

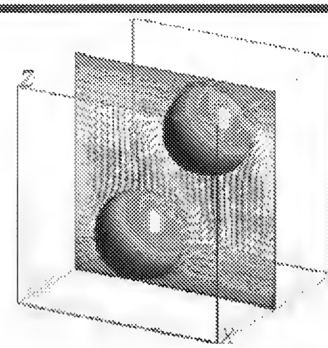

An extensive set of two-dimensional simulations has allowed us to explore the effect of the conductivity and permittivity ratios in some detail. The interaction of two drops is controlled by two effects. The drops are driven together due to the charge distribution on the surface. Since the net charge of the drops is zero, the drops see each other as dipoles. This dielectrophoretic motion always leads to drops attraction. The second effect is fluid motion driven by tangential stresses at the fluid interface. The fluid motion depends on the relative magnitude of the permittivity and conductivity ratios. When the permittivity ratio is higher than the conductivity ratio, the tangential forces induce flow from the poles of the drops to the equator. If the center of two such drops lies on a line parallel to the electric field, the flow drains from the region between the drops and they attract each other. When the ratios are equal, no tangential motion is induced and the drops attract each other by dielectrophoretic motion.

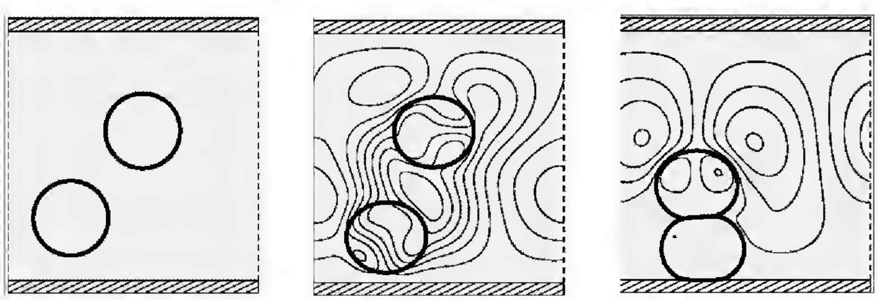

The motion of two oblate drops in a quiescent flow. The drops align with the electric field and attract each other. The drops are also attracted to the wall

EHD of Droplet Suspension

Interaction of many drops

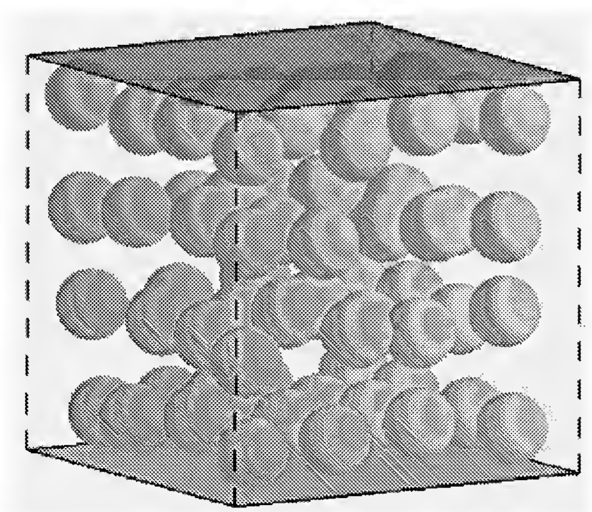

While the two-dimensional simulations have allowed us to conduct a large number of simulations relatively inexpensively, and explore a large range of conductivity and permittivity ratios, they can only provide qualitative insight into the evolution of the flow. The strong droplet interactions, in particular, lead to quantitative differences with three-dimensional drops. To examine the interactions of many three-dimensional drops, large scale computations are being done using a fully parallel version of the code

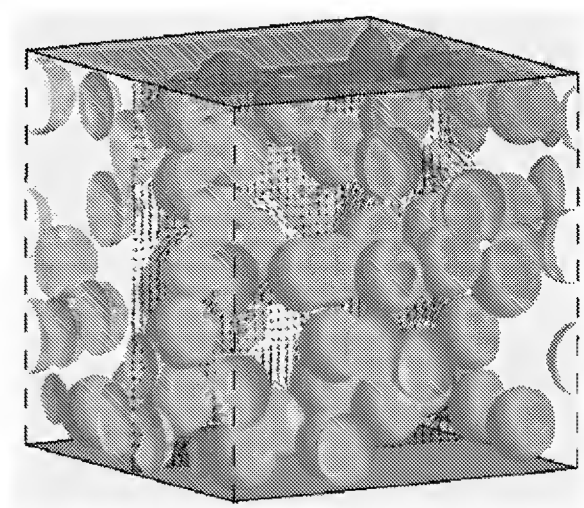

Two frames from a simulation of 64 three dimensional drops in quiescent flow. The drops are initially arranged on a perturbed regular array but as the electric field is turned on, the drops start to align with the electric field. In addition to the drops, the electric potential and the velocity field in a plane cutting through the domain are shown. The results are similar to the two-dimensional ones, except that the rate of accumulation at the walls is slower. The drops here are slightly prolate.

EHD of Droplet Suspension

Interaction of many drops

When an electric field is applied to many drops suspended in a channel flow, drops first attract each other pair-wise and some drops move to the wall. If the forces are strong (compared to the fluid shear) the drops can form columns or fibers, spanning the channel and blocking the two-dimensional flow. Electronic “fibration” of suspensions has been observed in a number of systems, including dispersion of milk droplets and red blood cells. Several simulations have been done to explore the fibrastion of droplets in a quiescent flow. The rate of fibration and the length of the fibers as a function of the parameters of the system, included void fraction has been examined. In the figure below, the dependency of the fiber lengths on the void fraction is examined for a two-dimensional system. The late time distribution for three different void fraction is shown on the right and the fraction of fibers of a given length is plotted on the left.

Fraction of drops in fibers

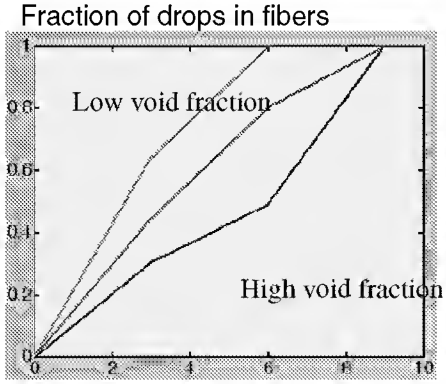

Length of the fibers.

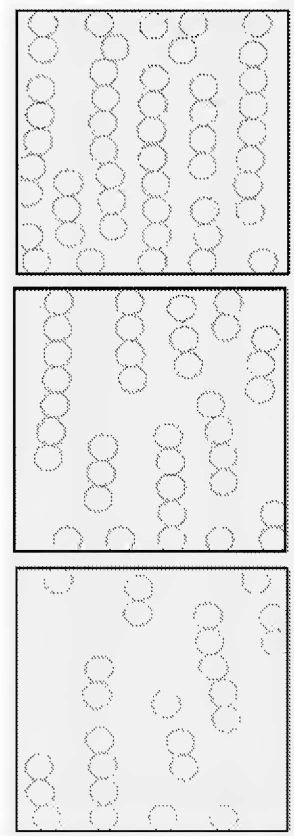

EHD of Droplet Suspension

Effect of flow on the drop distribution

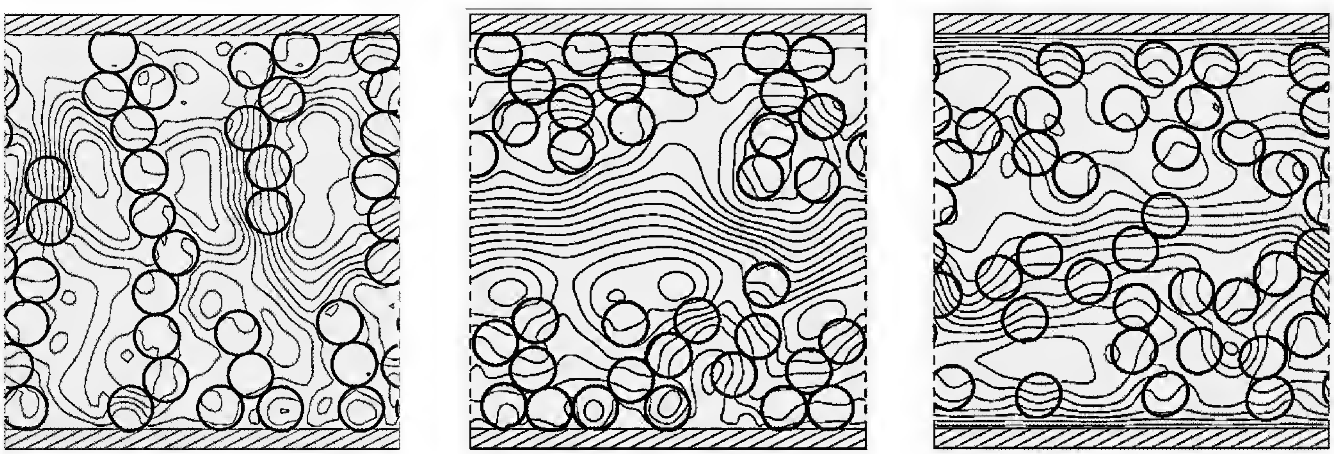

The frames above show the effect of flow rate (Reynolds number) on the drop distribution in a channel flow. The parameters used result in oblate drops and two drops whose centers are on a line parallel to the electric field attract each other. After the electric field is turned on, the pairwise interactions of drops initially leads to the formation of drop pairs and columns of drops parallel to the field. The drops are also attracted to the walls by the same mechanism that drops are attracted to each other. The droplet distribution and a few streamlines are shown after a long time for three different runs. In the first frame the flow is sufficiently weak so the electric forces lead to fibration and the drops block the flow. In the second frame the fluid shear breaks up the fibers and the drops pile up near the walls. In the last row, the fluid shear is sufficiently strong so that the drops resuspend and remain nearly uniformly distributed across the channel. In these simulations the drops are not allowed to coalesce, but in reality we would expect the drops to form fluid layers next to the walls instead of a cluster of drops.

EHD of Droplet Suspension

Effect of flow on the drop distribution

The average nondimensional distance of the drops from the centerline, showing how the drops remain suspended for the highest flow rate and accumulate at the walls for the intermediate flow rate.

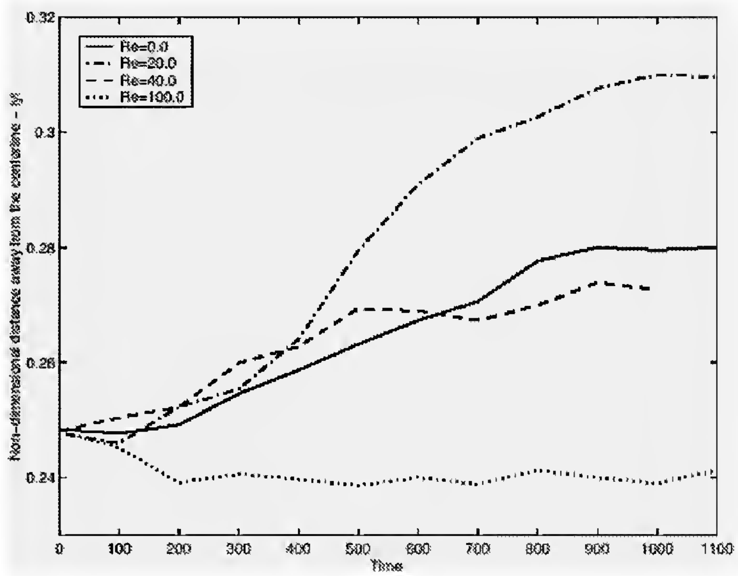

EHD of Droplet Suspension

Effect of flow on the drop distribution

The ratio of the conductivities and the permittivity determine the direction of the flow induced by the electric field. In the figure above, the droplet distribution at long time is plotted for several values of these ratios. The solid line marks the boundaries between oblate and prolate drops. If the attractive forces are weak compared to the shear, the columns are immediately broken up. For drops with the permittivity ratio lower than the conductivity ratio, the tangential forces induce flow in the opposite direction (from the equator to the poles of the drops) and if the induced fluid motion is sufficiently strong, the drops repel each other. In two-dimensions, this results in interactions between the drops that are similar to the previous case, except that the attractions take place perpendicular to the electric field. The drops therefore tend to form rows aligned with the flow, or "slugs" where many drops clump together. When the conductivity ratio is much higher than the permittivity ratio, the drops become prolate, expel each other and are spread more uniformly across the channel.

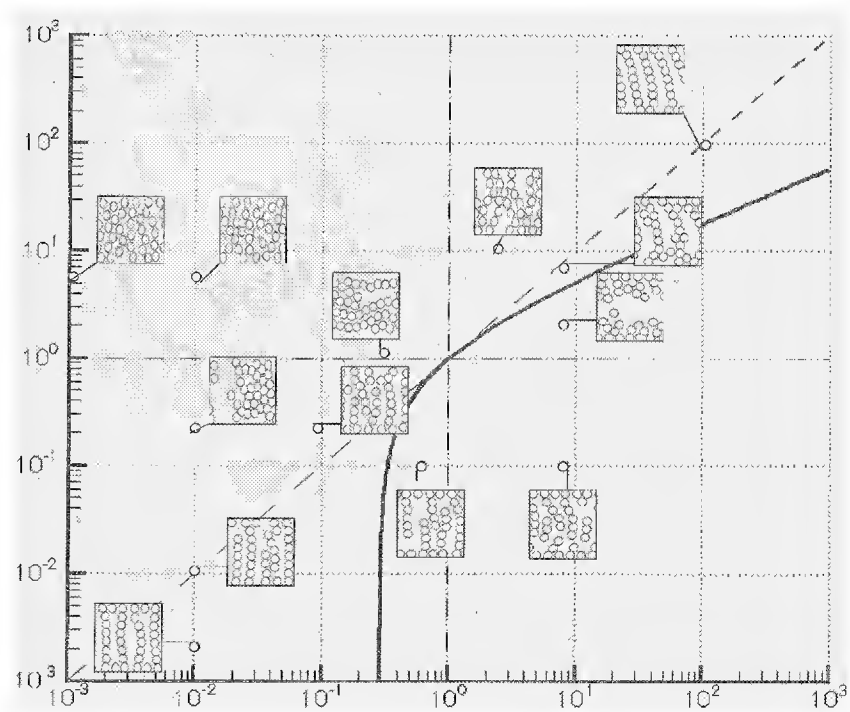

Characteristics of pool boiling on graphite-copper composite surfaces

Nengli Zhang
Ohio Aerospace Institute, Cleveland, OH 44142
David F. Chao
NASA Glenn Research Center, Cleveland, OH 44135
Wen-Jei Yang
ME Department, The University of Michigan, Ann Arbor, MI 44109

ABSTRACT

Nucleate pool boilng performance of different liquids on graphite-copper composite (Gr-Cu) surfaces has been experimentally studied and modeled. Both highly wetting fluids, such as freon-113 and pentane, and a moderately wetting fluid (water) were tested on the Gr-Cu surfaces with different graphite-fiber volume fractions to reveal the enhancement effects of the composite surfaces on the nucleate pool boiling. Results of the experiments show that the graphite-fiber volume fraction has an optimum value. The Gr-Cu composite surface with 25 percent graphite-fiber volume (ϕ=0.25) has a maximum enhancement effect on the nucleate boiling heat transfer comparing to the pure copper surface. For the highly wetting fluid, the nucleate boiling heat transfer is generally enhanced on the Gr- Cu composite surfaces by 3 to 6 times, as shown in Fig.1. In the low heat flux region, the enhancement is over 6 times, but in the high heat flux region, the enhancement is reduced to about 40%. For the moderately wetting fluid (water), stronger enhancement of nucleate boiling heat transfer is achieved on the composite surface. Figure 2 depicts the experimental results in which one observes the nucleate boiling heat transfer enhancement of 5 to 10 times in the low heat flux region and an enhancement of 3 to 5 times in the high heat flux region.

Photographs of bubble departure during the initial stage of nucleate boiling indicate that the bubbles detached from the composite surface are much smaller in diameter than those detached from the pure copper surface. Typical photographs are presented in Fig. 3. It is seen in Fig.3(a) that the bubbles departed from the composite surface have diameters of only O(0.1) mm, while those departed from the pure copper surface have diameters of O(1) mm, as seen in Fig. 3 (b). It is also found that the bubbles depart from the composite surface at a much higher frequency, thus forming vapor columns, as seen in Fig.3 (a). These two phenomena combined with high thermal conductivity of the graphite fiber are considered the mechanisms for such a significant augmentation in nucleate boiling heat transfer on the composite surfaces.

A physical model is developed to describe the phenomenon of bubble departure from the composite surface: The preferred site of bubble nucleation is the fiber tip because of higher tip temperature than the surrounding copper base and poor wettability of the graphite tip compared with that of the base material (copper). The high evaporation rate near the contact line produces the vapor cutback due to the vapor recoil pushing the three-phase line outwards from the fiber tip, and so a neck of the bubble is formed near the bubble bottom. Evaporation and surface tension accelerate the necking process and finally result in the bubble departure while a new small bubble is formed at the tip when the surface tension pushes the three-phase line back to the tip. The process is

schematically shown in Fig. 4. The proposed model is based on and confirmed by experimental results.

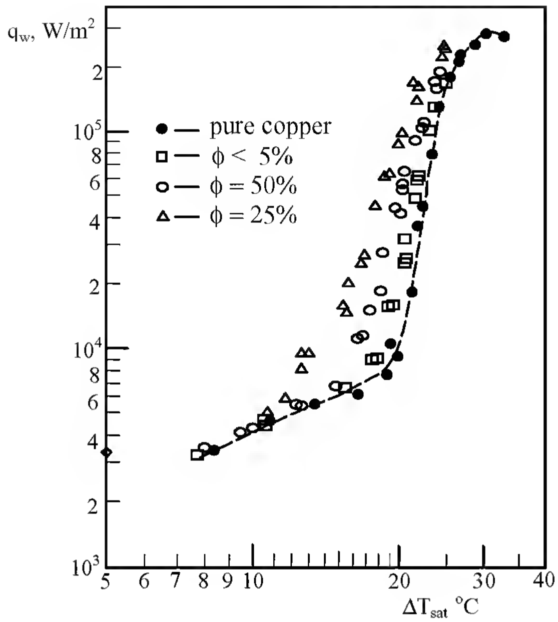

Fig. 1 Experimental data comparison between the Gr-Cu composite surfaces (ϕ < 5%, ϕ=25% and ϕ=25% fiber volume) and the pure copper surface using freon-113.

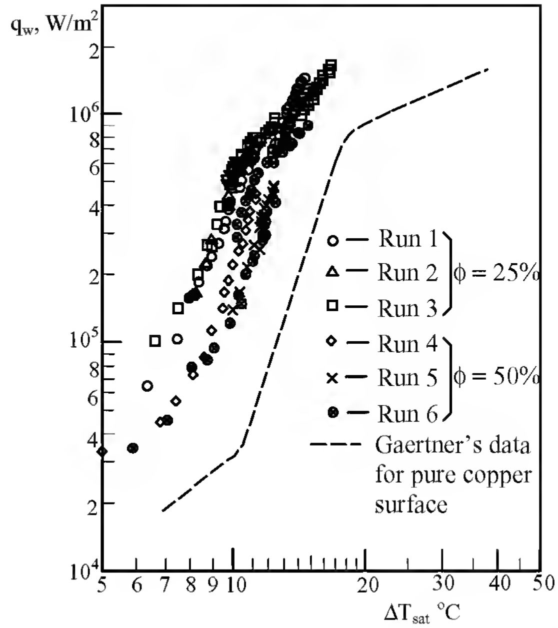

Fig. 2 Experimental data comparison between the Gr-Cu composite surface (25% and 50% fiber volume) and the pure copper surface using water.

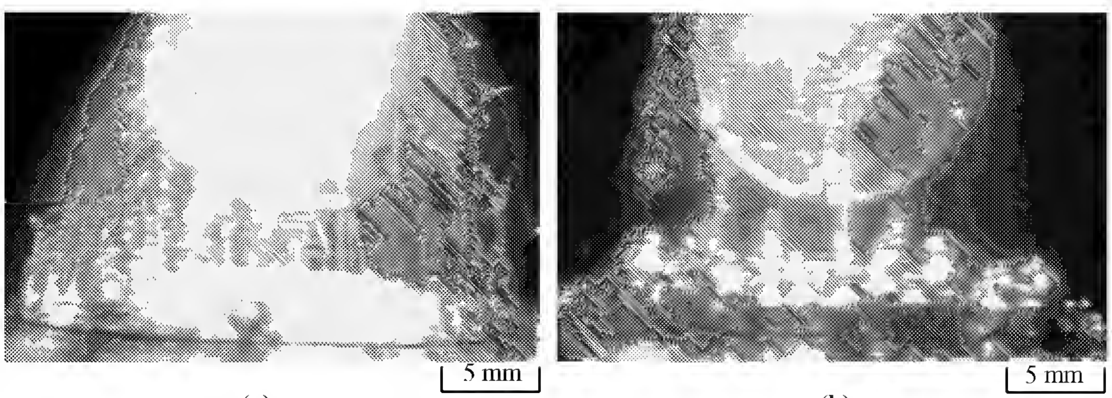

(a) **(b)**

Fig. 3 Photos of water bubble departure during the initial stage of nucleate boiling: (a) on Gr-Cu composite surface (ϕ=0.25); (b) on pure copper surface.

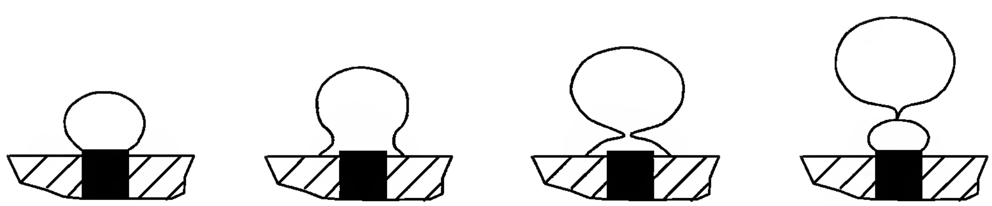

Fig. 4 Bubble necking and departure process.

Exposition Session
Topical Area 5:
Biological Fluid Physics

BLOOD CELL MIGRATION IN PRESSURE-DRIVEN AND ELECTROKINETIC FLOWS

Hsueh-Chia Chang and Paul Takhistov
Department of Chemical Engineering, University of Notre Dame

ABSTRACT

We report our preliminary results on the transverse migration of red blood cells and other particles when they are driven electrokinetically and by pressure-driven flows in micro-channels. The overall objective is to explain the Fahraeus-Lindqvist effect in blood circulation dynamics-blood cells tend to migrate and aggregate at the blood vessel axis and reduce the overall viscous dissipation in the process. At the same hematocrit (blood cell concentration) , blood cell flux at smaller capillaries is higher than in the large ones because of this effect. To avoid blood cell accumulation and depletion, the physiological dynamics maintain the hematocrit for small vessels at a level significantly lower than that in larger ones. However, the migration disappears for capillary radii beyond 250 microns. Hence, hematocrit is uniform within large blood vessels above this cutoff radius. This curious micro-circulation phenomenon has not been satisfactorily explained and is the focus of our research. Once the transverse migration mechanisms for blood cells and other micro-particles are understood, we also intend to exploit the principles to design electrophoretic and flow separation methods for micro-particles, including blood cells.

We drive mouse blood and human blood suspensions in a mm-size capillary and a Hele-Shaw slot with a mm-size gap. They are driven by both a pressure-driven flow applied by a syringe and an electrokinetic flow due to a longitudinal electric field of about 50 V/cm. Significant lateral migration and aggregation are only observed in the former for both concentrated and dilute suspensions. For dilute blood suspensions, the bi-convex doughnut-shaped blood cells form a single file with their axis roughly aligned in the direction of flow. Some precession about this axis is observed in a Hele-Shaw slot. In electrokinetic flow, there is a very thin depleted marginal layer of less than a micron but otherwise no blood cell segregation/migration is observed. Since the electro-osmotic flow field is shear-free away from the Debye layer, we conclude that lateral migration is only possible in the presence of bulk shear.

However, migration is not observed in pressure-driven flow experiments with ion-exchange granules of dimensions similar to blood cells. A preliminary scaling analysis suggests that the migration is only possible with bulk shear, particle deformation and non-spherical geometry. Inertia is ruled out due to the miniscule particle Reynolds number. Without deformation, an ellipsoid is shown to rotate in the vorticity direction but the net lateral hydrodynamic force is zero.

The migration scenario is quite different, however, if an electric field is applied and if the particles are charged. The Maxwell stress can also impart a torque on an asymmetric particle. However, the direction of this torque exerted by the electrokinetic stress depends on the inclination of the ellipsoid whereas that from the bulk hydrodynamic shear depends on the

vorticity of the bulk velocity field. This vorticity changes sign across the capillary axis. Consequently, if electrophoretic motion and hydrodynamic shear are both present, the two torques can balance at a particular equilibrium inclination angle that is not parallel to the flow direction. This angle is also different for different hydrodynamic vorticities. We hence predict a preferred inclination angle for a rigid ellipsoid that is driven electro-phoretically in a pressure-driven flow field. This non-zero angle also implies a net migration even for rigid particles. Preliminary experimental evidence of this new migration mechanism will also be reported. Since blood cells possess significant surface charge, their electrophoretic motion in the presence of a shear flow is quite different from that of a pure pressure-driven flow.

We have also investigated the transport of blood cells by AC dielectrophoresis at hundreds of kilo Hz. A sub-millimeter electrode configuration is designed to produce a non-uniform AC electric field. The blood cells are observed to polarize in the AC field and aggregate along the field lines. They then migrate slowly across the field lines towards regions of low electric fields, as is the case in classical dielectrophoresis. Like all nonlinear electrokinetic phenomena, the dipole formation and the migration are both frequency and particle size dependent. We have exploited these properties to separate large fish blood cells from smaller mouse cells. However, unlike the classical dielectrophoresis, the polarization that occurs in the plasma electrolyte around the blood cell is quite different from that of a dielectric liquid. The high frequency required is expected to be due to the small migration/diffusive time of ions across the blood cell Debye layer. A parallel theory is being pursued to explain this nonlinear AC electrokinetic phenomenon of blood cells. The theory captures the migration of ions within the Debye layer that causes the polarization responsible for aggregation and drift out of the field lines. It extends the classical theories for dielectrophoresis from dielectric liquids to electrolytes.

Total Internal Reflection Tomography (TIRT) for Three-Dimensional Sub-Wavelength Imaging

David G. Fischer
P. Scott Carney

We will present a novel new form of near-field microscopy known as total internal reflection tomography (TIRT), which allows for true three-dimensional sub-wavelength imaging. It is based on recent theoretical advances regarding the fundamental interaction of light with sub-wavelength structures, as well as stable algorithms for the near-field inverse problem. We will discuss its theoretical underpinnings, as well describe current efforts at the NASA Glenn Research Center to implement a TIRT system for biofluid research.

Total Internal Reflection Tomography (TIRT) for Three-Dimensional Sub-Wavelength Imaging

David G. Fischer
NASA Glenn Research Center

P. Scott Carney
University of Illinois

References:

(1) DG Fischer, "The information content of weakly scattered fields: implications for three-dimensional near- field microscopy", *J. Mod. Opt.* **47**, 1359-1374 (2000).

(2) DG. Fischer, "Sub-wavelength depth resolution in near-field microscopy", *Optics Letters* **25**, 1529-1531 (2000)

(3) PS Carney and JC Schotland, "Three-dimensional total internal reflection microscopy", *Optics Letters* **26**, 1072-1074 (2001).

(4) PS Carney, VA Markel, JC Schotland, "Near field tomography without phase retrieval", *Phys. Rev. Lett.* **86**, 5874-5877 (2001).

Introduction

Motivation: Develop an optical imaging device whose resolution exceeds the classical diffraction limit of $\lambda/2$ in all three spatial dimensions.

Implementation: Utilize evanescent (i.e. non-propagating) waves for illumination and novel image reconstruction algorithms.

Microgravity Applications: Interfacial phenomena, cell adhesion, intracellular structure, protein crystal growth.

Classical Inverse Scattering (Imaging)

- Scattering geometry:

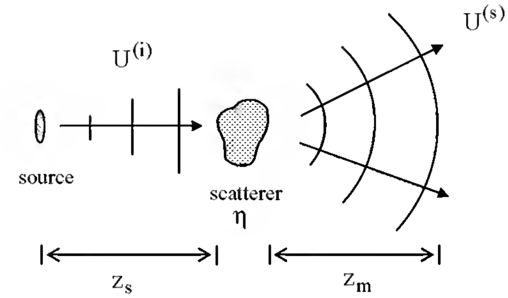

- Inverse scattering / imaging : $U^{(s)} \rightarrow \eta$
- For $z_s, z_m >> \lambda_0 \Rightarrow$ resolution $\approx \lambda_0/2$ (only homogeneous waves used in reconstruction)
- For homogeneous waves, there is a one-to-one mapping between the low frequency Fourier components of the object (i.e. those inside the Ewald sphere) and the scattered field.

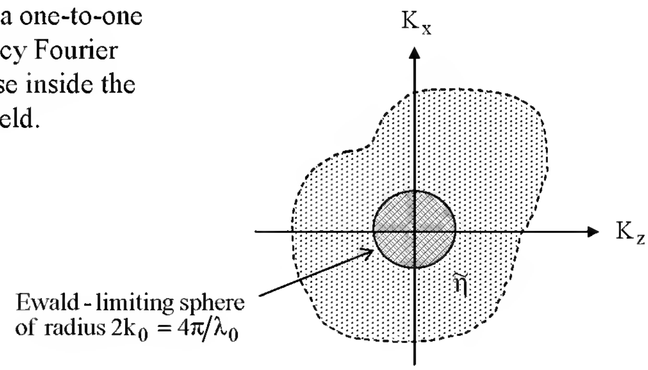

NASA/CP—2002-211212/VOL2

Increased Resolution

- *Option one*: bandlimited extrapolation or analytic continuation (noise problems!)
- *Option two*: utilize the ability of evanescent waves to either *encode* or *carry* sub-wavelength information $\rightarrow$ decrease z_s and/or z_m
- **Evanescent waves ?**

$$U^{(i)}(\mathbf{r}) = \exp[ik(\mathbf{s}_\perp \cdot \boldsymbol{\rho}) + s_z z] \quad \text{where} \quad \mathbf{s}_\perp = (s_x, s_y, 0)$$

$$s_z = \begin{cases} (1 - s_\perp^2)^{1/2} & \text{when } |\mathbf{s}_\perp| \le 1 \quad \leftarrow \quad \text{“homogeneous”} \\ i(s_\perp^2 - 1)^{1/2} & \text{when } |\mathbf{s}_\perp| > 1 \quad \leftarrow \quad \text{“evanescent”} \end{cases}$$

homogeneous wave

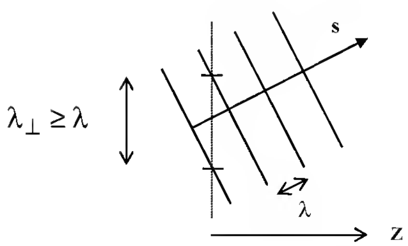

- propagates in direction **s**

$$\boxed{\lambda_\perp = \frac{2\pi}{k_\perp} = \frac{2\pi}{k|\mathbf{s}_\perp|}}$$

evanescent wave

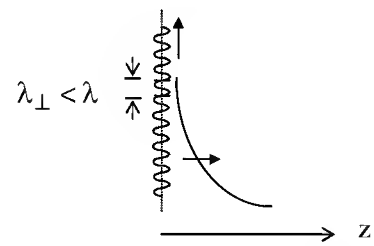

- decays exponentially with increasing z (decay rate $\gamma \propto |\mathbf{s}_\perp|$)

Image Reconstruction

- For **evanescent** illuminating waves and far-field (i.e. homogeneous wave) detection, there is a **many-to-one mapping** between the spatial Fourier components of the object and the scattered field.
- Specifically, a given scattered field measurement is proportional to a weighted line integral (i.e. generalized Radon transform) along the K_z - axis of the Fourier transform of the object. The width of the weighting function is proportional to $|s_\perp|$; consequently, the larger $|s_\perp|$ (i.e. the more evanescent the incident field), the greater the number of spatial Fourier components that contribute to a given scattered field measurement (i.e. the greater the encoded information). However, this additional information is more susceptible to noise in the reconstruction process, since the larger $|s_\perp|$, the greater the evanescent decay and the smaller the incident field amplitude.
- **Reconstruction strategies**:
  - Fourier domain sampling (involving the inversion of the generalized Radon transform)
  - **Singular value decomposition**

$$\Downarrow$$

Lends itself directly to regularization (i.e. stabilization of the inversion procedure in the presence of noise)

Near-Field Microscopy

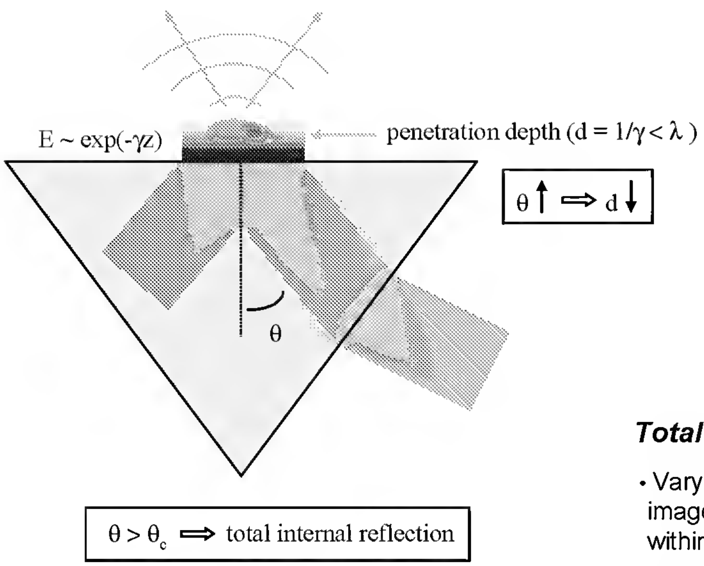

Evanescent Wave Microscopy

- Non-propagating (or evanescent) waves induce coherent or incoherent (i.e. fluorescent) scattering that can easily be measured
- Resulting image is a planar slice through the specimen that is localized to within a wavelength of the prism face (useful for cell membrane and cell adhesion studies)

Total Internal Reflection Tomography (TIRT)

- Varying θ (and hence d) yields two-dimensional images at different "effective" sub-wavelength depths within the specimen
- Synthesizing the scattered field data appropriately for different values of θ allows **three-dimensional sub-wavelength imaging** of specimen structure within a wavelength of the prism face

NASA/CP—2002-211212/VOL2

TIRT Experimental Configuration

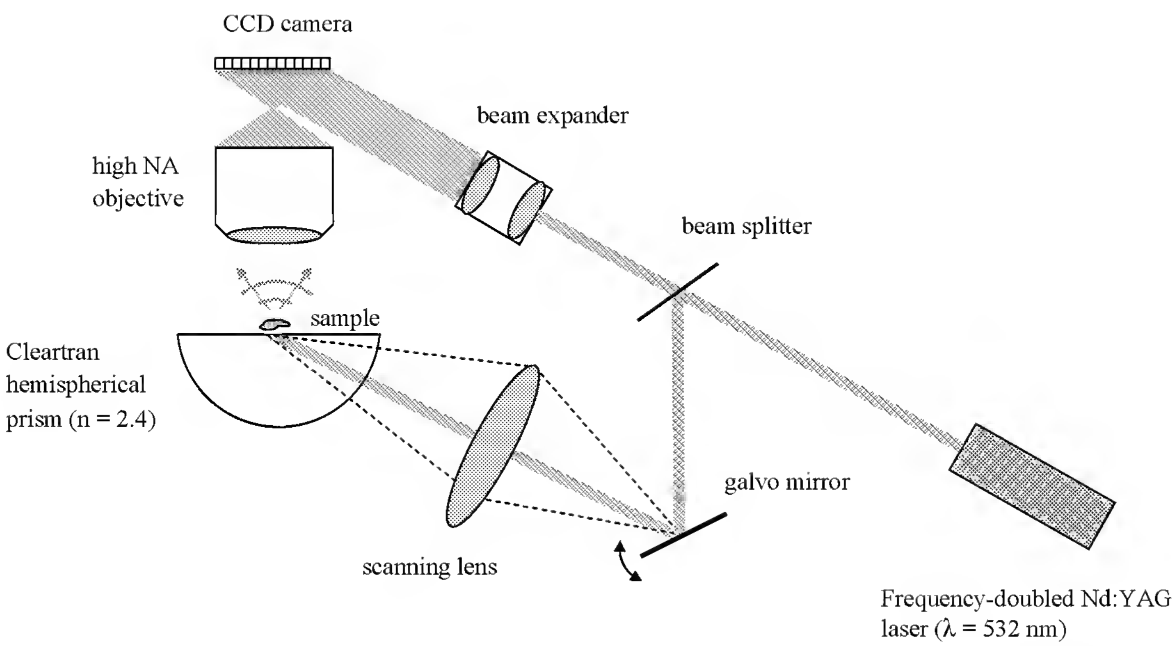

2D Experimental Simulation (object definition)

- Two point scatterers (d = λ/50) separated along the x-axis by λ/4 and the z-axis by λ/10 (the distance along the z-axis between the prism face and the first scatterer is λ/4)

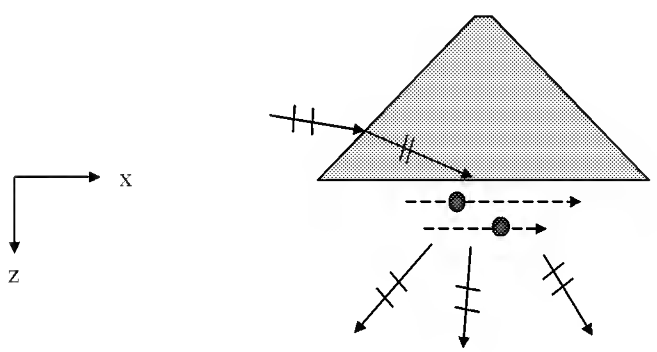

Experimental Simulation (Reconstruction)

- Illustrates sample reconstruction when both homogeneous and evanescent waves are used for illumination (21 equally spaced angles of illumination and angles of detection)

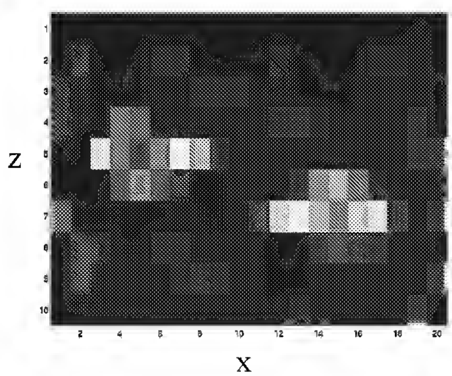

Machine error noise
No regularization

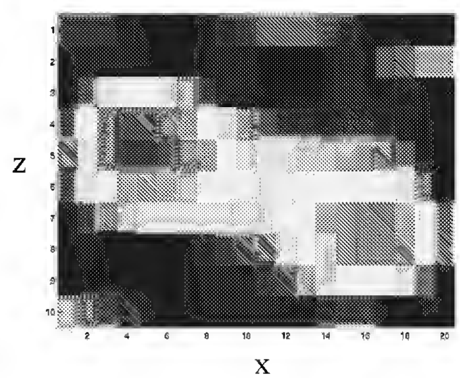

40 dB noise
Regularized

n = 2.4, 21 x 21 data points, FOV: $\lambda/2 \times \lambda/2$

Experimental Simulation with n = 1 (i.e. no prism)

- Illustrates sample reconstruction when only homogeneous waves are used for illumination

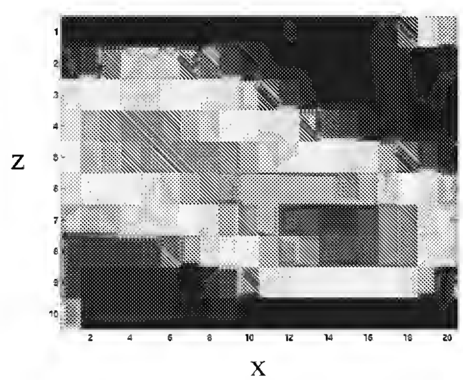

n = 1.0, 21 x 21 data points, FOV: $\lambda/2$ x $\lambda/2$

A CRITERION FOR THE DEVELOPMENT OF BIOCONVECTION INSTABILITY IN A SUSPENSION OF GYROTACTIC MOTILE MICROORGANISMS IN A FLUID SATURATED POROUS MEDIUM

A.V. Kuznetsov
Dept. of Mechanical & Aerospace Engineering, North Carolina State University, Raleigh, NC 27695-7910. E-mail: avkuznet@eos.ncsu.edu

A.A. Avramenko
Institute of Engineering Thermophysics, National Academy of Sciences, Kiev, Ukraine

ABSTRACT

In recent years, there has been increased interest in investigating spontaneous pattern formation in suspensions of motile microorganisms. This phenomenon is called bioconvection. Different from solid particles in traditional multiphase flow systems, motile cells are self-propelled. These microorganisms propel themselves by rotating flagella which are driven by reversible molecular motors that are embedded in the cell wall. They tend to swim in a particular direction in response to certain stimuli such as gravity (gravitaxis), light (phototaxis), or chemical gradients (chemotaxis).

This investigation deals with bioconvection in a suspension of gyrotactic motile microorganisms. Gyrotaxes is a behavior typical for algal suspensions. The direction of swimming of gyrotactic microorganisms is determined by the balance of two torques. The first one is the viscous torque that acts on a body placed in a shear flow. The second torque is generated by gravity because the center of mass of a typical microorganism is displaced from its center of buoyancy. The microorganisms considered in this paper are heavier than water and gyrotactic behavior results in their swimming towards the regions of most rapid downflow. Because of that, the regions of downflow become denser than the regions of upflow. Buoyancy increases the upward velocity in the regions of upflow and downward velocity in the regions of downflow, thus enhancing the velocity fluctuations. The formation of almost regular patterns and gyrotactic plumes in algal suspensions has been documented in numerous experimental papers. This instability is similar to the Rayleigh-Benard convection instability but its development does not require the vertical temperature gradient.

Despite the large number of publications on bioconvection in suspensions of gyrotactic microorganisms, very little has been done to address this type of bioconvection in a fluid saturated porous medium. This phenomenon is important because it may occur in nature (bioconvection in a layer of sand at the floor of a body of water that contains gyrotactic microorganisms) and may also have numerous applications. Upswimming of algal cells can be utilized to concentrate the cells, purify cultures, and separate vigorously swimming subpopulations. For these applications, bioconvection is undesirable, because it would prevent up-swimming cells from concentrating near the surface of the culture. To suppress bioconvection, a porous medium (for example, a surgical cotton wool) can be utilized, which must be sufficiently permeable to allow cells to swim through it but also sufficiently tight to damp out

bioconvection. For practical purposes, it is desirable to have the permeability of the porous medium as high as possible. This would insure that the cells can swim through it without cutting their tails off and this will also maximize the flux of the cells in the upward direction. Numerical results suggest that there is a critical value of the permeability of a porous medium. If permeability is smaller than this critical value, bioconvection does not occur and microorganisms simply swim in the upward direction; if it is larger than the critical value, bioconvection instability develops. The purpose of this research is to obtain the exact expression for the critical permeability based on a full three-dimensional stability analysis.

As a result of this investigation, it is established that an infinite uniform dilute suspension of gyrotactic microorganisms in a fluid saturated porous medium is stable if the permeability of the porous medium is sufficiently small. A critical value of the permeability exists and if a porous medium has larger permeability than this critical value, the suspension is unstable. By performing a liner stability analysis, an analytical expression for the critical permeability of a porous medium is obtained. It is established that increasing the cell diffusivity and fluid viscosity increases critical permeability, while increasing the number density of the cells in the basic state, volume of the cell, density difference, gravitational acceleration, and the average swimming velocity of the cells decreases the critical permeability. This critical permeability value is also presented in terms of a critical Darcy number, which depends only on the cell eccentricity, as

$$\left(Da_{1/\gamma}\right)_{crit} = \begin{cases} 1/(1-\alpha_0) & \text{for } 0 \le \alpha_0 \le 1/3 \\ 8\alpha_0/(1+\alpha_0)^2 & \text{for } 1/3 \le \alpha_0 \le 1 \end{cases} \tag{1}$$

where α_0 is the cell eccentricity.

Tetragonal Lysozyme Nucleation and Crystal Growth: The Role of the Solution Phase.

Marc L. Pusey, Elizabeth Forsythe, John Sumida, Daniel Maxwell, and Sridhar Gorti

Lysozyme, and most particularly the tetragonal form of the protein, has become the default standard protein for use in macromolecule crystal nucleation and growth studies. There is a substantial body of experimental evidence, from this and other laboratories, that strongly suggests this proteins crystal nucleation and growth is by addition of associated species that are preformed by standard reversible concentration-driven self association processes in the bulk solution. The evidence includes high resolution AFM studies of the surface packing and of growth unit size at incorporation, fluorescence resonance energy transfer measurements of intermolecular distances in dilute solution, dialysis kinetics, and modeling of the growth rate data. We have developed a self-association model for the proteins crystal nucleation and growth. The model accounts for the obtained crystal symmetry, explains the observed surface structures, and shows the importance of the symmetry obtained by self-association in solution to the process as a whole. Further, it indicates that nucleation and crystal growth are not distinct mechanistically, but identical, with the primary difference being the probability that the particle will continue to grow or dissolve. This model also offers a possible mechanism for fluid flow effects on the growth process and how microgravity may affect it. While a single lysozyme molecule is relatively small (M.W. = 14,400), a structured octamer in the 4_3 helix configuration (the proposed average sized growth unit) would have a M.W. = 115,000 and dimensions of 5.6 x 5.6 x 7.6 nm. Direct AFM measurements of growth unit incorporation indicate that units as wide as 11.2 nm and as long as 11.4 nm commonly attach to the crystal. These measurements were made at approximately saturation conditions, and they reflect the sizes of species that both added or desorbed from the crystal surface. The larger and less isotropic the associated species the more likely that it will be oriented to some degree in a flowing boundary layer, even at the low flow velocities measured about macromolecule crystals. Flow-driven effects resulting in mis-orientation upon addition to and incorporation into the crystal need only be a small fraction of a percentage to significantly affect the resulting crystal. One Earth, concentration gradient driven flow will maintain a high interfacial concentration, i.e., a high level (essentially that of the bulk solution) of solute association at the interface and higher growth rate. Higher growth rates mean an increased probability that misaligned growth units are trapped by subsequent growth layers before they can be desorbed and try again, or that the desorbing species will be smaller than the adsorbing species. In microgravity the extended diffusive boundary layer will lower the interfacial concentration. This results in a net dissociation of aggregated species that diffuse in from the bulk solution, i.e., smaller associated species, which are more likely able to make multiple attempts to correctly bind, yielding higher quality crystals.

STUDY OF FLUID FLOW CONTROL IN PROTEIN CRYSTALLIZATION USING STRONG MAGNETIC FIELDS

Narayanan Ramachandran[1]
Universities Space Research Association, SD 46, NASA MSFC, Huntsville, AL

Fred Leslie and **Ewa Ciszak**
SD 46, NASA MSFC, Huntsville, AL

ABSTRACT

An important component in biotechnology, particularly in the area of protein engineering and rational drug design is the knowledge of the precise three-dimensional molecular structure of proteins. The quality of structural information obtained from X-ray diffraction methods is directly dependent on the degree of perfection of the protein crystals. As a consequence, the growth of high quality macromolecular crystals for diffraction analyses has been the central focus for biochemists, biologists, and bioengineers.

Macromolecular crystals are obtained from solutions that contain the crystallizing species in equilibrium with higher aggregates, ions, precipitants, other possible phases of the protein, foreign particles, the walls of the container, and a likely host of other impurities. By changing transport modes in general, i.e., reduction of convection and sedimentation, as is achieved in "microgravity", researchers have been able to dramatically affect the movement and distribution of macromolecules in the fluid, and thus their transport, formation of crystal nuclei, and adsorption to the crystal surface. While a limited number of high quality crystals from space flights have been obtained, as the recent National Research Council (NRC) review of the NASA microgravity crystallization program pointed out, the scientific approach and research in crystallization of proteins has been mainly empirical yielding inconclusive results [1].

We postulate that we can reduce convection in ground-based experiments and we can understand the different aspects of convection control through the use of strong magnetic fields and field gradients. Whether this limited convection in a magnetic field will provide the environment for the growth of high quality crystals is still a matter of conjecture that our research will address. The approach exploits the variation of fluid magnetic susceptibility with concentration for this purpose and the convective damping is realized by appropriately positioning the crystal growth cell so that the magnetic susceptibility force counteracts terrestrial gravity.

The general objective is to test the hypothesis of convective control using a strong magnetic field and magnetic field gradient and to understand the nature of the various forces that come into play. Specifically we aim to delineate causative factors and to quantify them through experiments, analysis and numerical modeling. Once the basic understanding is obtained, the study will focus on testing the hypothesis on proteins of pyruvate dehydrogenase complex (PDC),

[1] E-mail address: narayanan.ramachandran@msfc.nasa.gov

proteins E1 and E3. Obtaining high crystal quality of these proteins is of great importance to structural biologists since their structures need to be determined.

Specific goals for the investigation are:

1. To develop an understanding of convection control in diamagnetic fluids with concentration gradients through experimentation and numerical modeling. Specifically solutal buoyancy driven convection due to crystal growth will be considered.
2. To develop predictive measures for successful crystallization in a magnetic field using analyses and numerical modeling for use in future protein crystal growth experiments. This will establish criteria that can be used to estimate the efficacy of magnetic field flow damping on crystallization of candidate proteins.
3. To demonstrate the understanding of convection damping by high magnetic fields to a class of proteins that is of interest and whose structure is as yet not determined.
4. To compare quantitatively, the quality of the grown crystals with and without a magnetic field. X-ray diffraction techniques will be used for the comparative studies.

In a preliminary set of experiments, we studied crystal dissolution effects in a 5 Tesla magnet available at NASA Marshall Space Flight Center (MSFC). Using a Schlieren setup, a 1mm crystal of Alum (Aluminum-Potassium Sulfate) was introduced in a 75% saturated solution and the resulting dissolution plume was observed. The experiment was conducted both in the presence and absence of a magnetic field gradient. The magnet produces a gradient field of ~ 1 Tesla^2/cm. Image analysis of the recorded images indicated an enhanced plume velocity that was of the order of the measurement limit. For this experiment, both the gradient and gravity fields are in the same direction resulting in an enhanced effective gravity that tends to accelerate the observed plume velocity. While the results are not conclusive, pending further tests, it clearly points out the inadequacy of the MSFC magnet for conducting protein crystallization experiments and the need for a stronger magnet. In space-based experiments, however, where the gravitational effects are small, only a weak magnetic field will be required to control or mitigate the effects of convective contamination.

The typical magnetic field – field gradient product required to balance thermal buoyancy for a diamagnetic fluid is given as $B\partial B/\partial z \sim 12.5\ \text{Tesla}^2/\text{cm}$, where B is the magnetic induction and z is the vertical coordinate. The field gradient product required for countering solutal buoyancy is $B\partial B/\partial z \sim 14\ \text{Tesla}^2/\text{cm}$. These fields are realizable in large magnets. We plan to do the first series of experiments to test the flow control hypothesis at the National High Magnet Field Laboratory in Tallahassee, Florida, in Aug. 2002.

1. National Research Council, Space Studies Board, Commission on Physical Sciences, Mathematics and Applications, in Future Biotechnology Research on the International Space Station, national Academy Press, Washington, DC., 2000, 10-16.

SIMULATIONS OF DROP BREAKUP AND DNA DYNAMICS IN FLOW THROUGH ARRAYS OF OBSTACLES

Eric S.G. Shaqfeh
Departments of Chemical and Mechanical Engineering

Prateek Patel, Victor Beck
Department of Chemical Engineering

Stanford University
Stanford, CA 94305-5025

ABSTRACT

The flow through arrays of fixed obstacle beds provides important new methods for creating microstructural dynamics of drops and flexible macromolecules. In the latter instance, new separation techniques for DNA have been suggested based on the mobility change that comes from interactions with obstacles during flow (either electrophoretically driven or hydrodynamically driven motion). Interestingly, the dynamics is so diverse in terms of variation with obstacle concentration, strength of flow driving force, and molecular length, that large-scale simulation can play a very important role in determining where interesting flow parameter regimes are located. In this poster, we will present large-scale simulations of drops and DNA moving through fiber obstacle arrays. We will discuss the breakup mechanisms that are engendered in the former and compare our results to ongoing experiments. In the latter instance we will discuss the efficiency of separation in these arrays and isolate parameter regimes where separation is most efficient.

Two-Photon Fluorescence Correlation Spectroscopy

Gregory A. Zimmerli
David G. Fischer

We will describe a two-photon microscope currently under development at the NASA Glenn Research Center. It is composed of a Coherent Mira 900 tunable, pulsed Titanium:Sapphire laser system, an Olympus Fluoview 300 confocal scanning head, and a Leica DM IRE inverted microscope. It will be used in conjunction with a technique known as fluorescence correlation spectroscopy (FCS) to study intracellular protein dynamics. We will briefly explain the advantages of the two-photon system over a conventional confocal microscope, and provide some preliminary experimental results.

Fluorescence Correlation Spectroscopy using two-photon microscopy

PI's: G. Zimmerli and D. Fischer, NASA Glenn Research Center

Funded through the NASA GRC Strategic Research Fund

Fluorescence Correlation Spectroscopy: Time correlation analysis of a fluorescence signal from a diffraction limited volume.

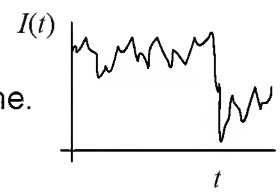

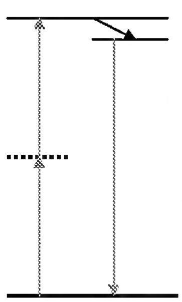

Two-photon microscopy: A confocal microscopy technique which relies on the simultaneous absorption of two photons to produce a fluorescence signal.

Confocal Fluorescence Microscopy

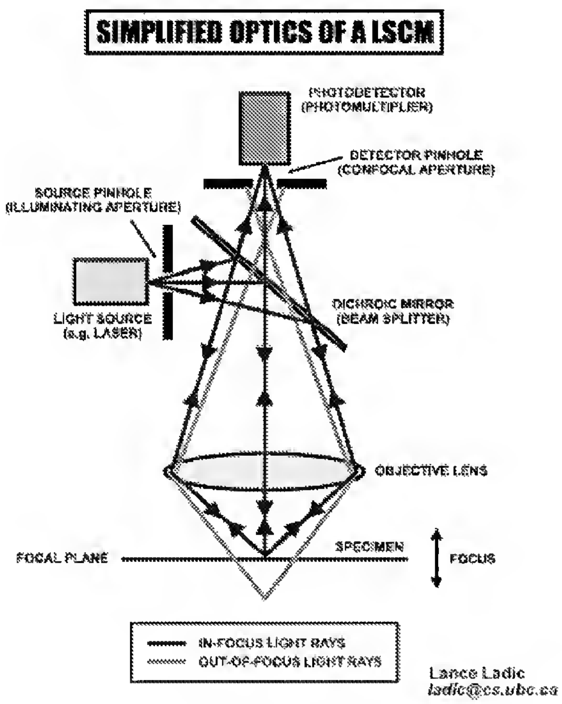

- Confocal microscopy is based on coincident (i.e. confocal) point illumination / point detection. This, in combination with scanning, enables three-dimensional imaging.
- Confocal microscopy provides marginal improvements in lateral and axial resolution. It's real utility, however, lies in the dramatic reduction of out-of-focus light.

Two-photon microscopy

- One limitation of confocal microscopy is that photons are still absorbed everywhere within the beam cross-section and, while not directly imaged, exhaust the available fluorophore population (photobleaching) and contribute somewhat (upon re-emission) to the detected signal, reducing image contrast.
- To circumvent this problem, microscopists are beginning to use higher-order light-matter interactions that have a quadratic dependence on the electric field, thereby localizing the interaction to the region of high electric field strength (I.e. the focus).
- Two such techniques are two-photon fluorescence microscopy (TPFM) and second-harmonic generation microscopy (SHGM).
- **Two-photon fluorescence** is a *radiative absorption event* in which two photons are resonantly coupled to an allowed energy transition of a fluorophore, thereby exciting the fluorophore to a higher energy state. The fluorophore then relaxes back to the ground state with with the incoherent emission (on a nanosecond time scale) of a single photon having nearly twice the energy

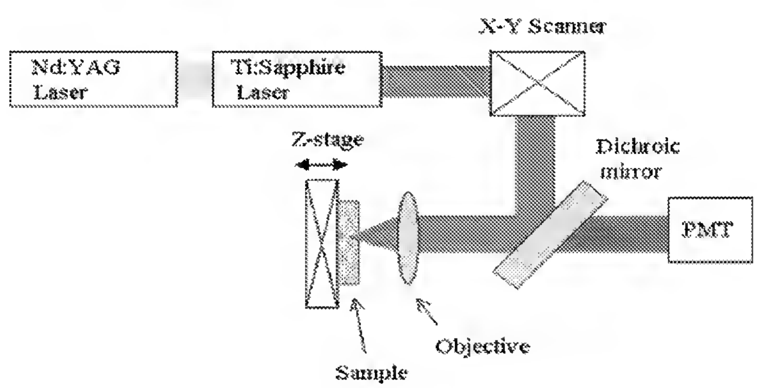

Advantages of two-photon microscopy:

- Increased penetration depth due to the longer excitation wavelength
- Reduced harm to living cells due to the longer (less energetic or ionizing) excitation wavelength
- Reduction of background noise since no excitation outside focal volume

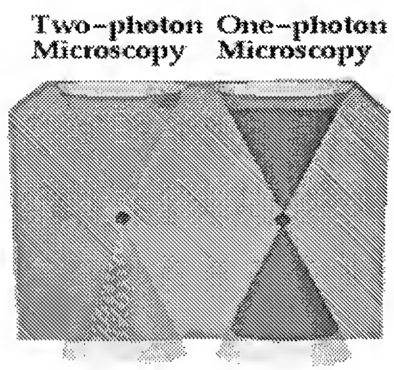

Interaction only occurs where the intensity is high (i.e. the focal region), giving inherent localization.

Fluorescence correlation spectroscopy (FCS) using two-photon microscopy

- Combining two-photon microscopy and correlation spectroscopy allows one to measure the number fluctuations of fluorescent molecules inside a small volume (i.e. the focal volume).

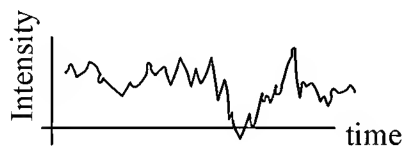

- The intensity autocorrelation function is defined by: $G(\tau) = \left\langle I(t)I(t+\tau) \right\rangle \Big/ \left\langle I^2(t) \right\rangle$

- For translational diffusion $\rightarrow G(\tau) \propto \frac{1}{N}\left(1+\frac{8D\tau}{w_0^2}\right)^{-1}\left(1+\frac{8D\tau}{z_0^2}\right)^{-1/2}$

  where N = number of molecules in detection volume, D = diffusivity, and w_0 and z_0 are the transverse and axial dimensions of the focal volume, respectively.

- One application of two-photon FCS involves the measurement of protein concentration and diffusion rate at multiple cellular sites, as a means of quantify intracellular signaling processes as well as cell membrane transport.

Instrument details: (under construction)

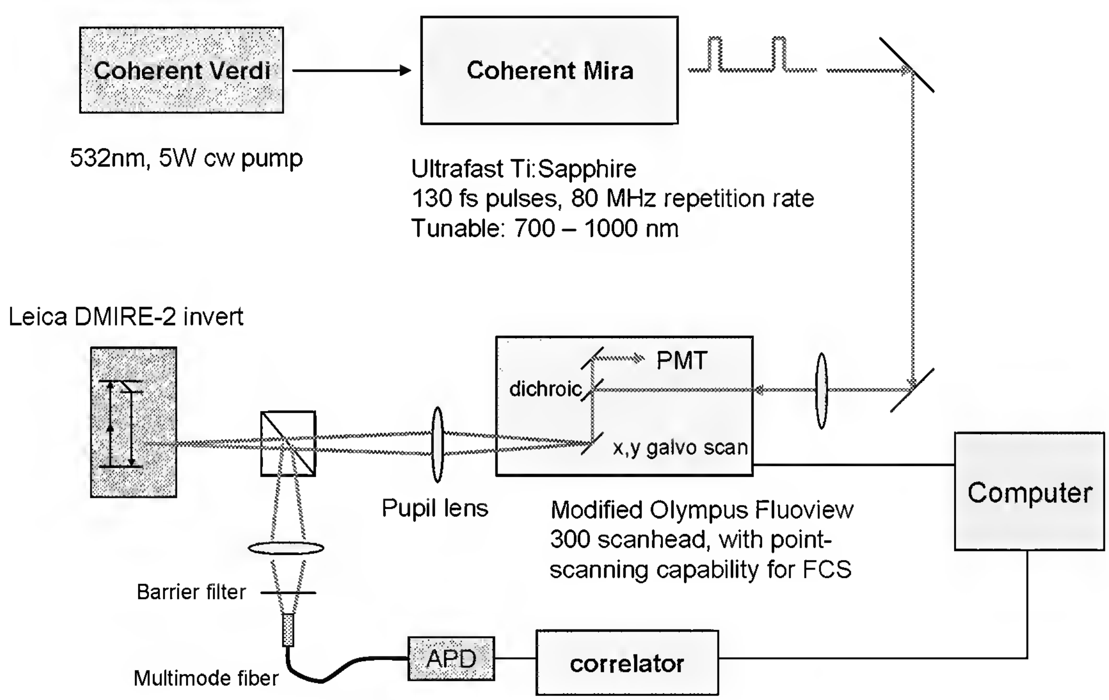

FCS senses fluctuations in the # of fluorescent markers in a sub-femtoliter (< 1μm^3) volume.

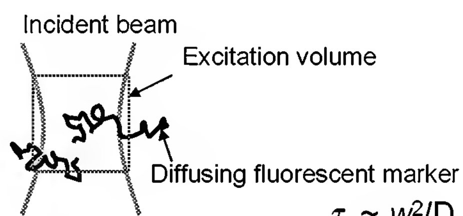

$\tau_D \sim w^2/D \sim 1$ ms

Applications of FCS:

- Single molecule detection (Eigen and Rigler, PNAS 1994)
- Protein associations/dissociations (D. Reisner et al, 1998)
- Protein diffusion inside cells and on cell membranes
  (R. Brock and T. Jovin, N. Petersen, 2001)
- Conformational fluctuations of DNA/proteins (W. Webb et al., 1998)

Exposition Session Topical Area 6: Dynamics and Instabilities

Effect of Gravity on the Near Field Flow Structure of Helium Jet in Air

Ajay K Agrawal[1] **and Ramkumar Parthasarathy**
School of Aerospace and Mechanical Engineering, University of Oklahoma

DeVon Griffin
Microgravity Science Division, NASA Glenn Research Center

ABSTRACT

Experiments have shown that a low-density jet injected into a high-density surrounding medium undergoes periodic oscillations in the near field. Although the flow oscillations in these jets at Richardson numbers about unity are attributed to the buoyancy, the direct physical evidence has not been acquired in the experiments. If the instability were indeed caused by buoyancy, the near-field flow structure would undergo drastic changes upon removal of gravity in the microgravity environment. The present study was conducted to investigate this effect by simulating microgravity environment in the 2.2-second drop tower at the NASA Glenn Research Center. The non-intrusive, rainbow schlieren deflectometry technique was used for quantitative measurements of helium concentrations in buoyant and non-buoyant jets.

Results in a steady jet show that the radial growth of the jet shear layer in Earth gravity is hindered by the buoyant acceleration. The jet in microgravity was 30 to 70 percent wider than that in Earth gravity. The microgravity jet showed typical growth of a constant density jet shear layer. In case of a self-excited helium jet in Earth gravity, the flow oscillations continued as the jet flow adjusted to microgravity conditions in the drop tower. The flow oscillations were however not present at the end of the drop when steady microgravity conditions were reached. The oscillations in Earth gravity were confirmed by a dominant frequency of 12.2 Hz at several jet locations as shown by the power spectra in Fig. 1. In microgravity, a similar analysis was performed using 1.1s of data taken at the beginning and towards the end of the drop to distinguish initial transients from steady conditions in microgravity. The results in Fig. 2 show that no flow oscillations were detected at the end of the drop, thereby, providing direct physical evidence that the flow oscillations in the jet were buoyancy induced. Figure 3 depicts temporal evolution of the jet flow at various axial planes using data from a sequence of schlieren images obtained at 1000Hz. Results clearly demonstrate that buoyancy plays a key role on the near field flow structure of low density jets.

In order to investigate the influence of gravity on the near-injector development of the flow, a linear temporal stability analysis and a spatio-temporal stability analysis of a low-density round jet injected into a high-density ambient gas were performed. The flow was assumed to be isothermal and locally parallel; viscous and diffusive effects were ignored. The variables were represented as the sum of the mean value and a normal-mode small disturbance. An ordinary differential equation governing the amplitude of the pressure disturbance was derived. The velocity and density profiles in the shear layer, and the Froude number (signifying the effects of gravity) were the three important parameters in this equation. Together with the boundary conditions, an eigenvalue problem was formulated. The eigenvalue problem was solved for various values of Froude number; the temporal growth rates and the phase velocity of the disturbances were obtained. It was found that the presence of variable density within the shear

[1] 865 Asp Avenue, Room 212, Norman, OK 73019
Email: aagrawal@ou.edu; Phone: (405) 325-1754, fax: (405) 325-1088

layer resulted in an increase in the temporal amplification rate of the disturbances and an increase in the range of unstable frequencies, accompanied by a reduction in the phase velocities of the disturbances. Also, the temporal growth rates of the disturbances were increased as the Froude number was reduced (i.e. gravitational effects increased), indicating the destabilizing role played by gravity. The spatio-temporal stability analysis was performed to determine the nature of the absolute instability of the jet. The roles of the density ratio, Froude number, Schmidt number, and the lateral shift between the density and velocity profiles on the absolute instability of the jet were determined. The results show that the combination of these variables determines how absolutely unstable the jet will be.

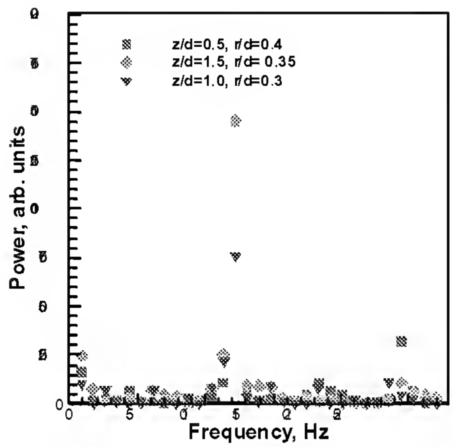

Figure 1. Frequency Power Spectra of an Oscillating Jet in Earth Gravity.

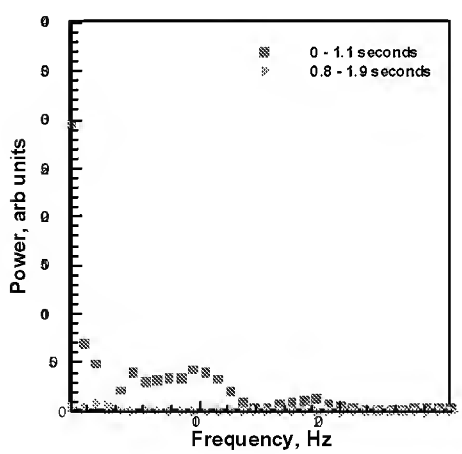

Figure 2. Frequency Power Spectra for two Microgravity Periods at z/d=1.0, r/d=0.6.

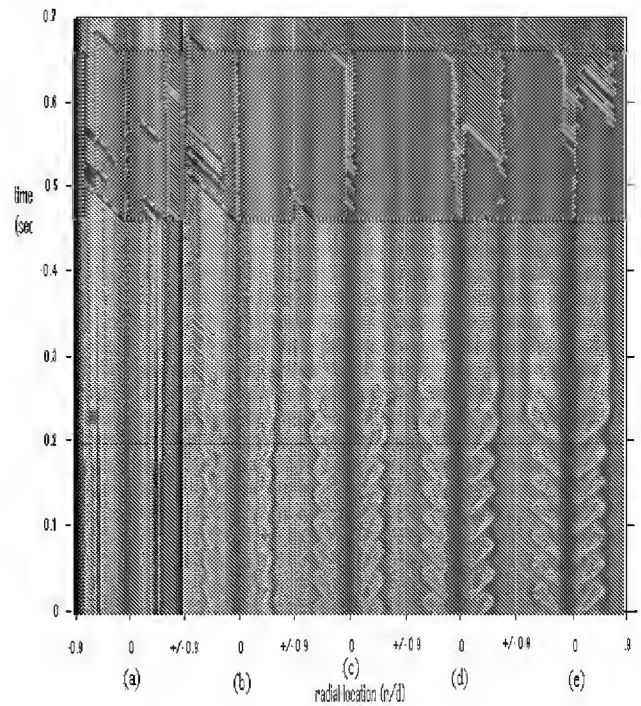

Figure 3. Temporal Evolution of Helium Jet in Microgravity for z/d=0.0, 0.5, 1.0, 1.5, and 2.5 (from left to right). The package is released at time t= 0.2s, as indicated by thin black line.

NASA/CP—2002-211212/VOL2

Effects of Gravity on the Near Field Flow Structure of Helium Jet in Air

Ajay K. Agrawal, Ramkumar Parthasarathy
University of Oklahoma

DeVon Griffin
NASA Glenn Research Center

OBJECTIVES

- Quantify effects of gravity on instability and flow structure of self-excited low-density helium jets.
  - Microgravity environment was simulated using the 2.2-sec drop tower facility.
  - Full field concentrations measurements were obtained using Rainbow Schlieren Deflectometry technique.
- Analytically study buoyancy effects on the absolutely unstable nature of low-density jets

Rainbow schlieren images during an oscillation cycle

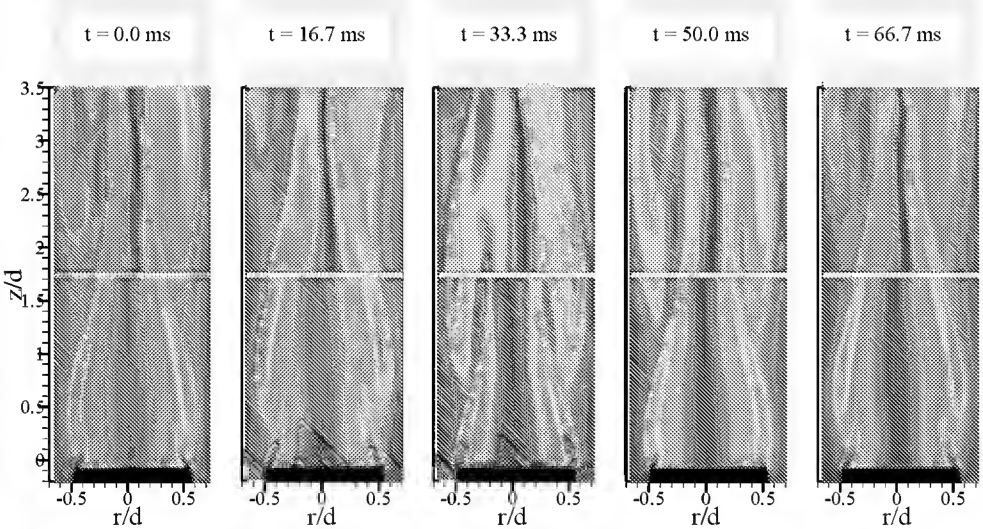

Contours of helium mole percentage during an oscillation cycle

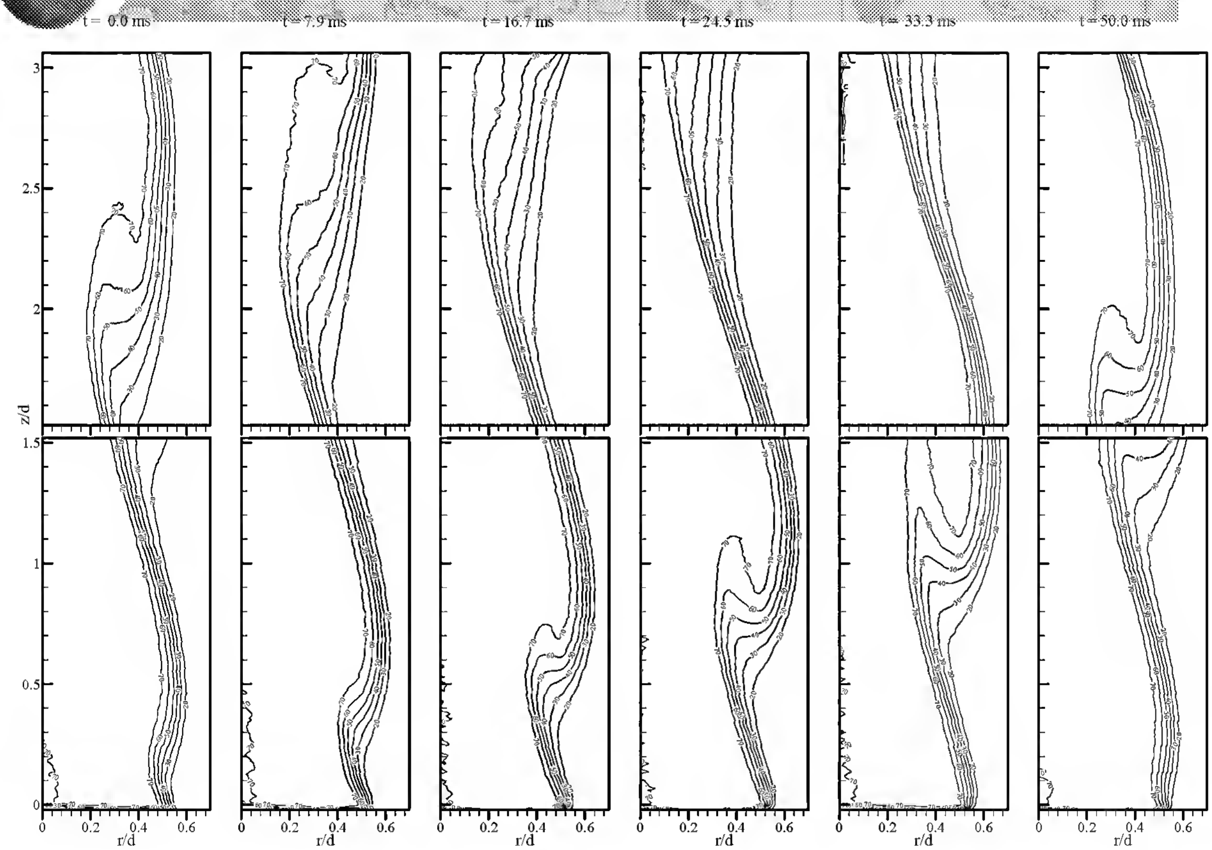

Size, evolution and convection velocity of the vortex

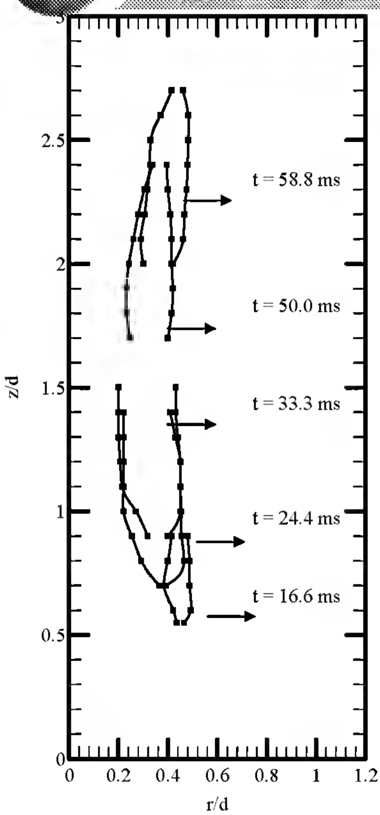

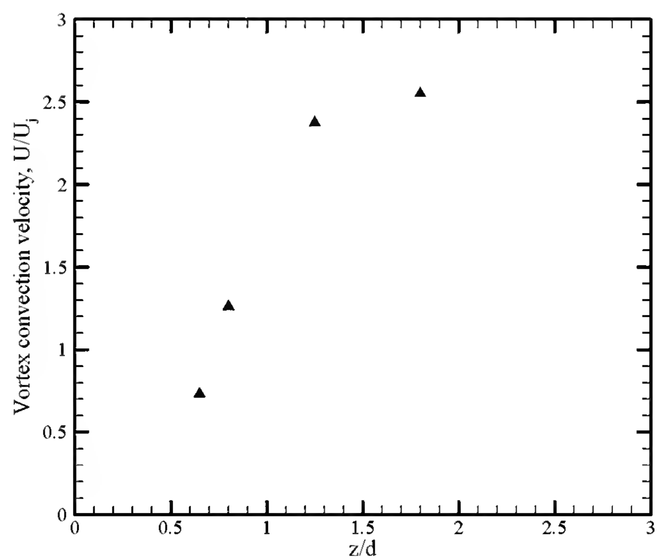

Helium Mole Fraction Contours During the Drop

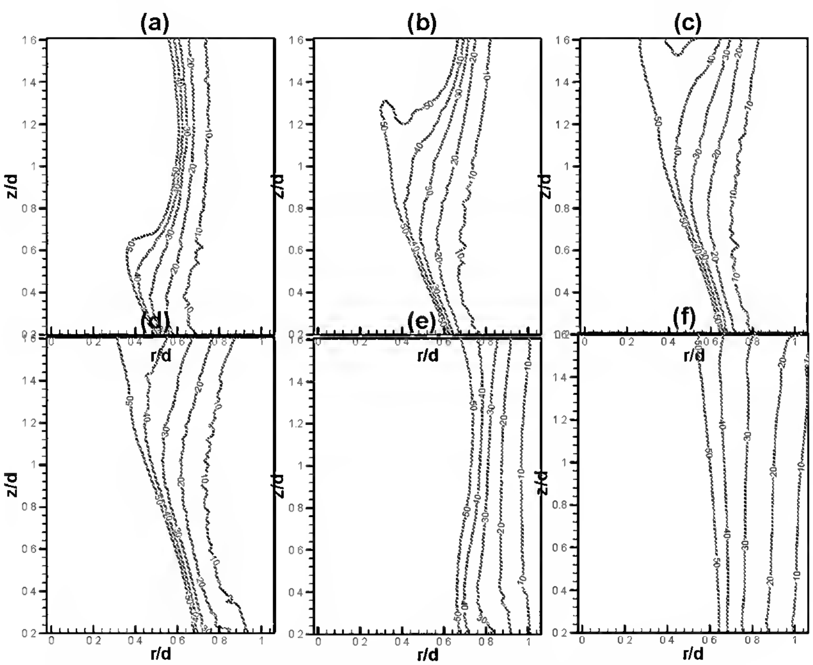

(a) t = 0 sec, (b) t = 1/60 sec, (c) t = 2/60 sec,
(d) t = 3/60 sec, (e) t = 13/60, and (f) t = 2.0 sec.

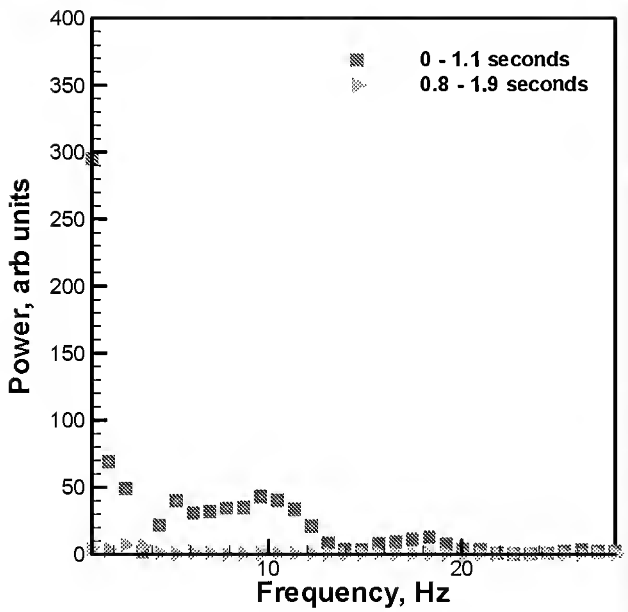

Frequency Spectra

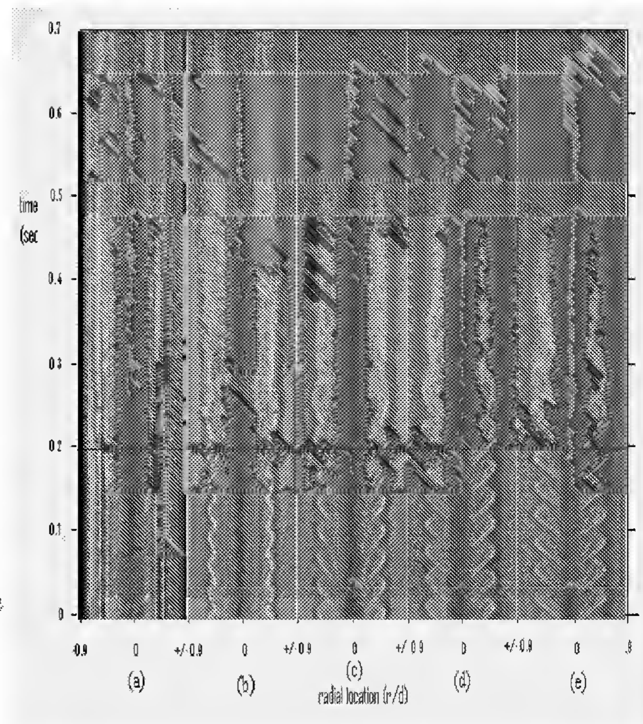

Space-Time Images

Theoretical Analysis

Assuming parallel flow near the injector, linear stability analysis is used to study the effects of buoyancy. Normal disturbances:

$$\left(u', v', w', p', \rho'\right) = \left(\hat{u}(r), \hat{v}(r), \hat{w}(r), \hat{p}(r), \hat{\rho}(r)\right) \exp\left(i(kx-\omega t+m\theta)\right)$$

k is the wavenumber ($2\pi/\lambda$); ω is the frequency; m represents the azimuthal mode.

$$\frac{d^2\hat{p}}{dr^2} + \frac{d\hat{p}}{dr}\left[\frac{1}{r} - \frac{2\frac{d\bar{u}}{dr}}{\left(\bar{u}-\frac{\omega}{k}\right)} - \frac{1}{\bar{\rho}}\frac{d\bar{\rho}}{dr}\left(1+\frac{i\,g}{k\left(\bar{u}-\frac{\omega}{k}\right)^2}\right)\right] - \hat{p}\left(k^2 + \frac{m^2}{r^2}\right) = 0$$

Normalized Growth Rate of Absolutely Unstable Jets

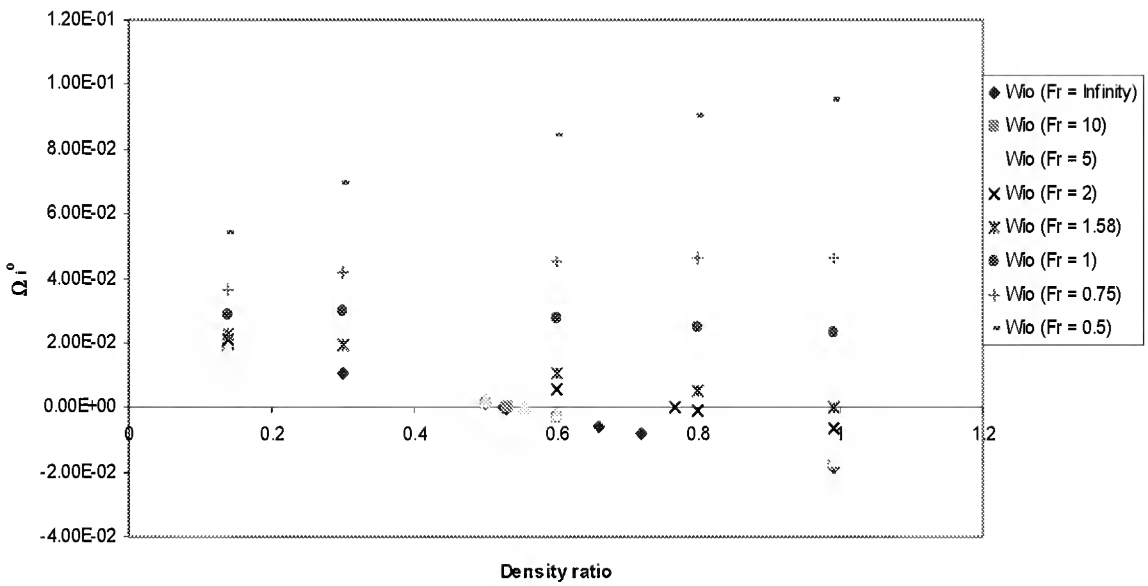

Conclusions and Future Work

- In Earth gravity, the jet oscillated at a constant frequency at locations.
- The flow oscillations diminished towards the end of drop as steady microgravity conditions were reached.
- The flow oscillations were shown to originate by buoyancy.
- Analysis indicated that the low-density jet injected into a high-density gas medium becomes absolutely unstable at a critical density ratio. Further reduction in density ratio caused the jet to become more absolutely unstable.
- Future work will focus on self-excited instability in momentum-dominated jets using high-speed rainbow schlieren deflectometry.

THERMAL IMAGING OF CONVECTING OPAQUE FLUIDS USING ULTRASOUND

Hongzhou Xu, Sean Fife, and C. David Andereck*

Department of Physics, The Ohio State University
174 W. 18th Ave., Columbus, OH 43210
*andereck.1@osu.edu, phone: (614) 292-2360, FAX: (614) 292-7557

ABSTRACT

An ultrasound technique has been developed to non-intrusively image temperature fields in small-scale systems of opaque fluids undergoing convection. Fluids such as molten metals, semiconductors, and polymers are central to many industrial processes, and are often found in situations where natural convection occurs, or where thermal gradients are otherwise important. However, typical thermal and velocimetric diagnostic techniques rely upon transparency of the fluid and container, or require the addition of seed particles, or require mounting probes inside the fluid, all of which either fail altogether in opaque fluids, or necessitate significant invasion of the flow and/or modification of the walls of the container to allow access to the fluid. The idea behind our work is to use the temperature dependence of sound velocity, and the ease of propagation of ultrasound through fluids and solids, to probe the thermal fields of convecting opaque fluids non-intrusively and without the use of seed particles. The technique involves the timing of the return echoes from ultrasound pulses, a variation on an approach used previously in large-scale systems.[1,2]

We initially validated our method by comparing ultrasound measurements with simultaneous visualization using thermochromic liquid crystals suspended in glycerol in a transparent convection cell. As a next step we assembled a linear array of Panametrics M110 ultrasound transducers and calibrated it using the experimentally determined temperature variation of sound speed in mercury. We then used this array to measure temperature profiles in a narrow (2 cm) and shallow (1.3 cm) stainless steel Rayleigh-Bénard convection cell filled with mercury. Figure 1 shows typical data. In this case the array of transducers was aligned with the long dimension of the chamber, and located at mid-height. The data output yields a temperature profile along the chamber, perpendicular to the imposed temperature gradient. The profile clearly reveals the formation of cells driven by natural convection as the temperature difference between the bottom and top plates was slowly increased from 0 to 1.0 °C, the final temperature corresponding to a Rayleigh number (Ra) of 7550.

Figure 2 is a 2D image of the thermal field in convecting mercury for an imposed vertical temperature difference of 5.8 °C (Ra = 43790). This image was obtained by translating one Panametrics V129, under computer control, from location to location across the outside of the chamber. The flow consists of four convection rolls. The warmer, rising plumes are in the middle and at either end, while the cooler, falling plumes are in between.

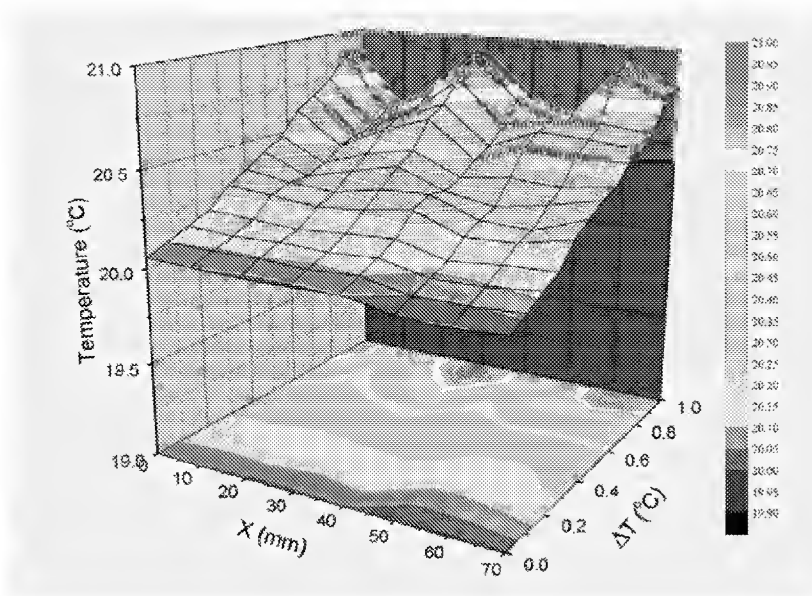

Fig. 1. Temperature profile evolution of Rayleigh-Bénard convection in mercury.

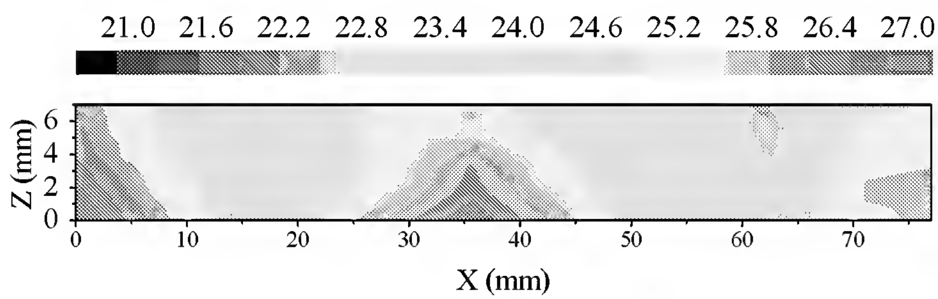

Fig. 2. 2D thermal image of convection in mercury.

Details of our technique, including its limitations and future prospects, will be presented.

This work was supported by NASA Microgravity Fluid Physics Program grant NAG 3-2138.

REFERENCES

[1] Green, S. F., An Acoustic Technique for Rapid Temperature Distribution Measurement, *J. Acoust. Soc. Am.* 77, 759-763 (1985).

[2] Bramanti, M., Salerno, E. A., Tonazzini, A., Pasini, S. and Gray, A., An Acoustic Pyrometer System for Tomographic Thermal Imaging in Power Plant Boilers, *IEEE Trans. Instr. Meas.* 45, 159-167 (1996).

Thermal Imaging of Convecting Opaque Fluids Using Ultrasound

Hongzhou Xu, Sean Fife, and C. David Andereck*

Department of Physics, The Ohio State University
174 W. 18th Ave., Columbus, OH 43210

*andereck.1@osu.edu, phone: (614) 292-2360, FAX: (614) 292-7557

Supported by NASA Grant NAG3-2138

Abstract

We have exploited the temperature dependence of sound velocity to measure the thermal fields in transparent and opaque fluids in a non-intrusive way. A chamber containing Glycerol undergoing Rayleigh-Bénard convection was probed with an ultrasound transducer operating in the pulse-echo mode. The times-of-flight for the ultrasound pulse to traverse the fluid at several transducer locations were converted into a temperature profile that is in qualitative agreement with simultaneous thermochromic liquid crystal visualization of the flow pattern, thereby validating the concept. 2D temperature profiles of a liquid metal (Mercury) filled stainless steel chamber have been obtained for a range of imposed temperature differences. These profiles clearly reveal the convection roll pattern.

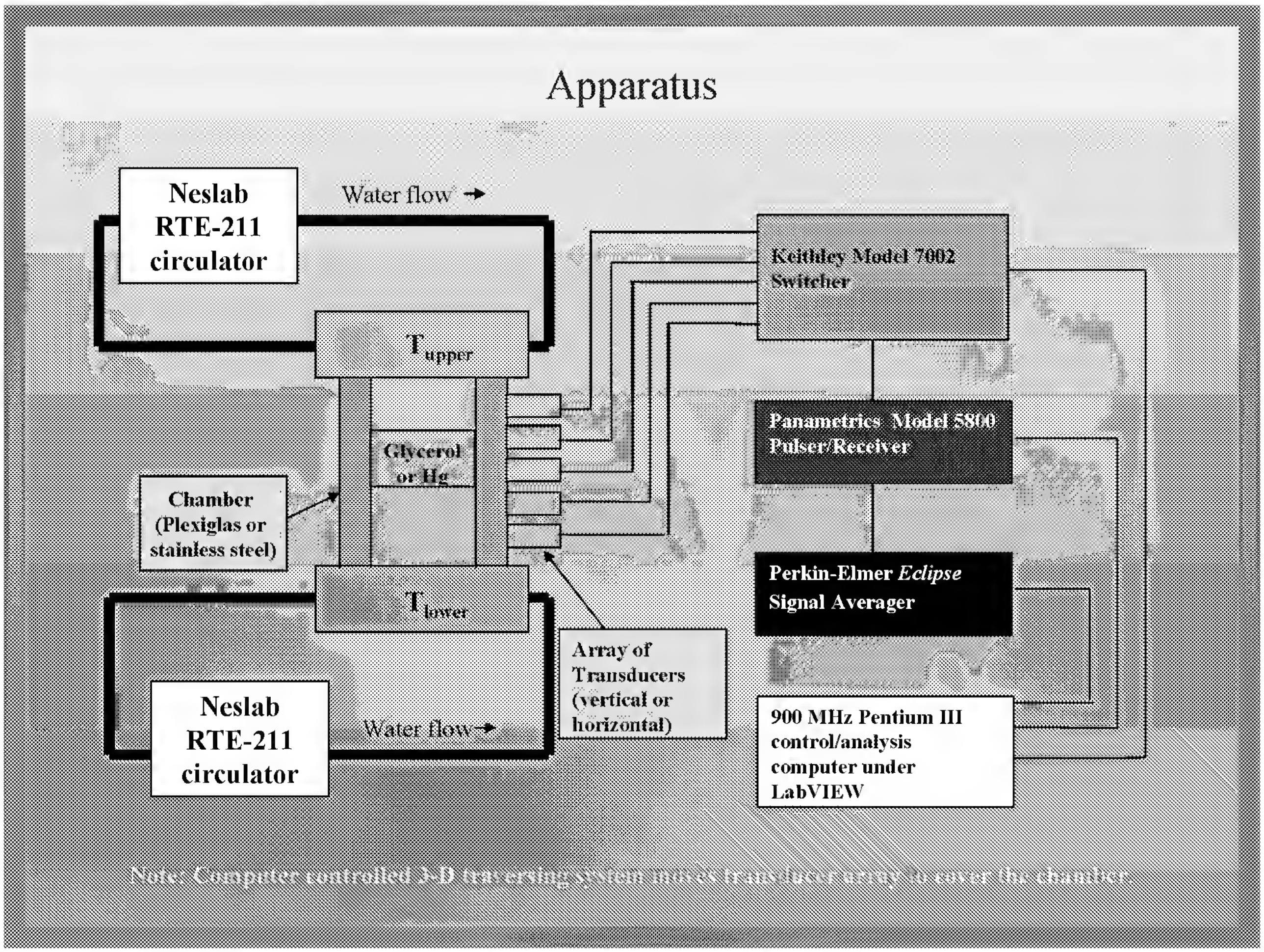
Apparatus
Neslab RTE-211 circulator
Water flow
Keithley Model 7002 Switcher
T upper
Panametrics Model 5800 Pulser/Receiver
Glycerol or Hg
Chamber (Plexiglas or stainless steel)
Perkin-Elmer Eclipse Signal Averager
T lower
Array of Transducers (vertical or horizontal)
Neslab RTE-211 circulator
Water flow
900 MHz Pentium III control/analysis computer under LabVIEW
Note: Computer controlled 3-D traversing system moves transducer array to cover the chamber.

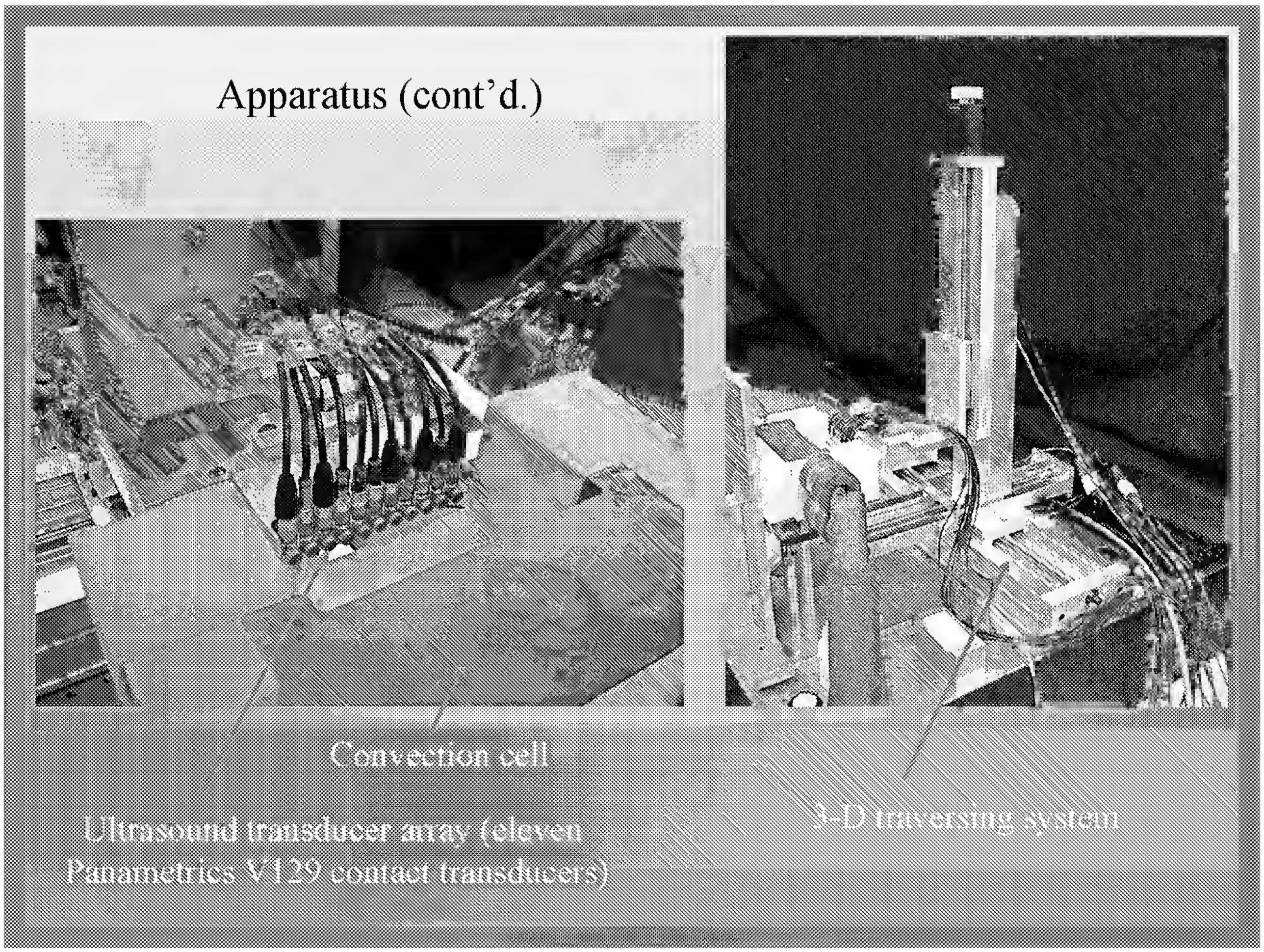
Apparatus (cont'd.)
Convection cell
Ultrasound transducer array (eleven Panametrics V129 contact transducers)
3-D traversing system

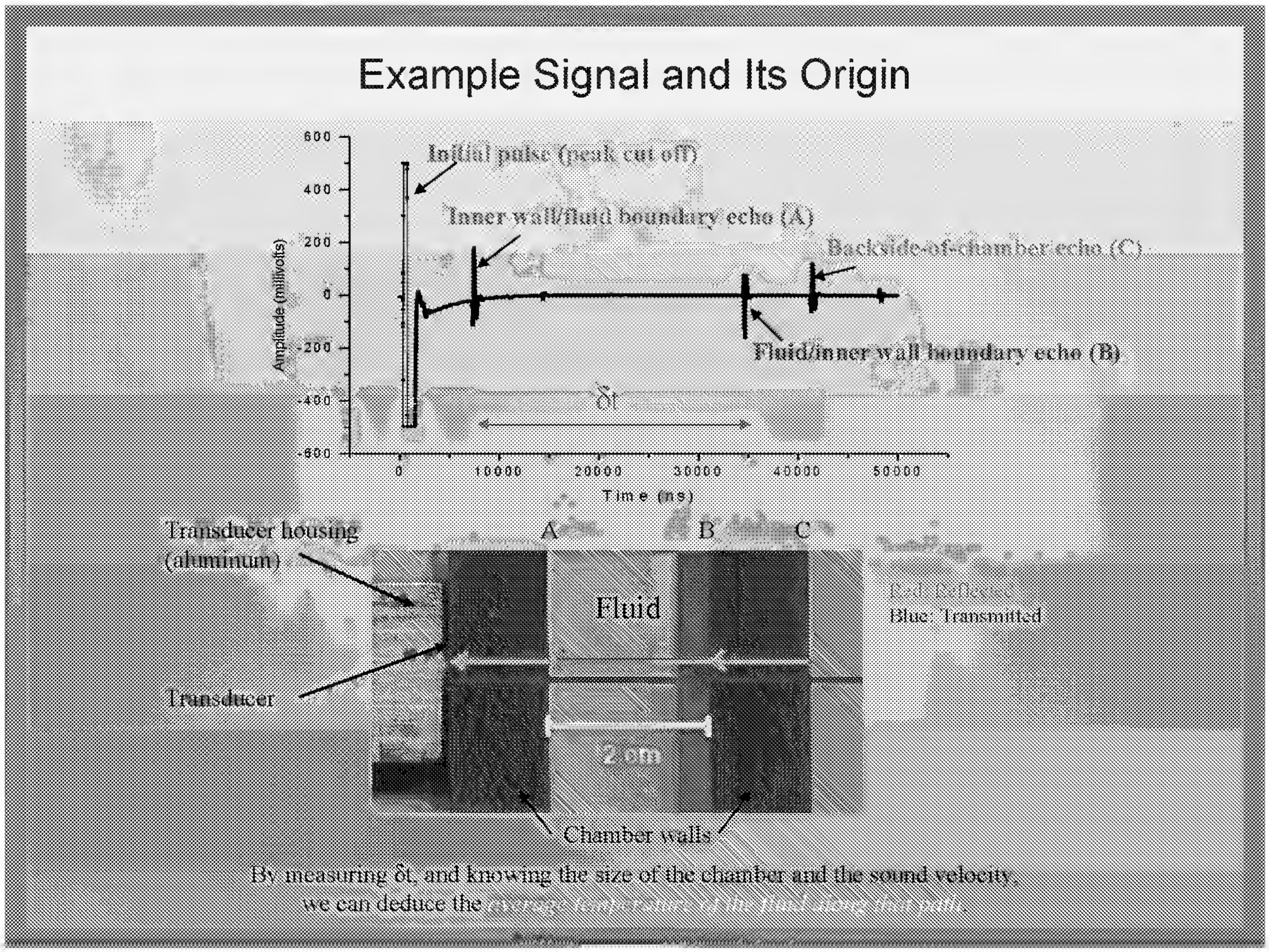
Example Signal and Its Origin
Initial pulse (peak cut off)
Inner wall/fluid boundary echo (A)
Backside-of-chamber echo (C)
Fluid/inner wall boundary echo (B)
δt
Amplitude (millivolts)
600
400
200
0
-200
-400
-600
0
10000
20000
30000
40000
50000
Time (ns)
Transducer housing
(aluminum)
Transducer
A
B
C
Fluid
2 cm
Red: Reflected
Blue: Transmitted
Chamber walls
By measuring δt, and knowing the size of the chamber and the sound velocity,
we can deduce the average temperature of the fluid along that path.

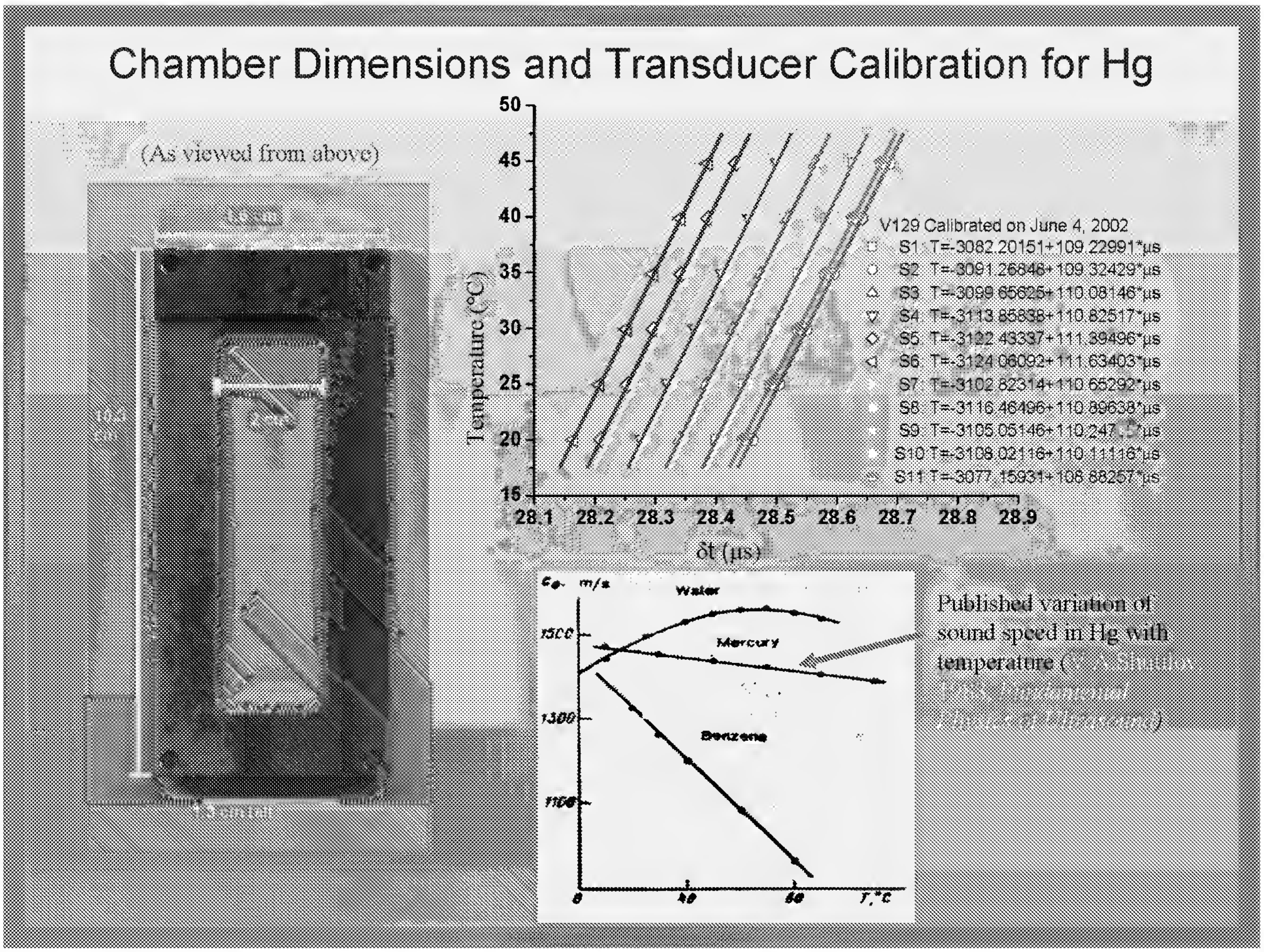
Chamber Dimensions and Transducer Calibration for Hg
(As viewed from above)
V129 Calibrated on June 4, 2002
S1 T=-3082.20151+109.22991*µs
S2 T=-3091.26846+109.32429*µs
S3 T=-3099.65625+110.08146*µs
S4 T=-3113.85838+110.82517*µs
S5 T=-3122.43337+111.39496*µs
S6 T=-3124.06092+111.63403*µs
S7 T=-3102.82314+110.65292*µs
S8 T=-3116.46496+110.89638*µs
S9 T=-3105.05146+110.247
S10 T=-3108.02116+110.11116*µs
S11 T=-3077.15931+108.88257*µs
Temperature (°C)
δt (µs)
Water
Mercury
Benzene
m/s
T, °C
Published variation of sound speed in Hg with temperature

Proof of Concept

We have used a standard visualization technique on a transparent fluid to compare with the ultrasound results.

We seeded glycerol contained in a Plexiglas wall chamber with thermochromic liquid crystals (Hallcrest R29C4W), then heated from below to form Rayleigh-Bénard convection rolls.

We simultaneously obtained ultrasound data from a single transducer moved manually from point to point, showing a strong correlation between the two techniques.

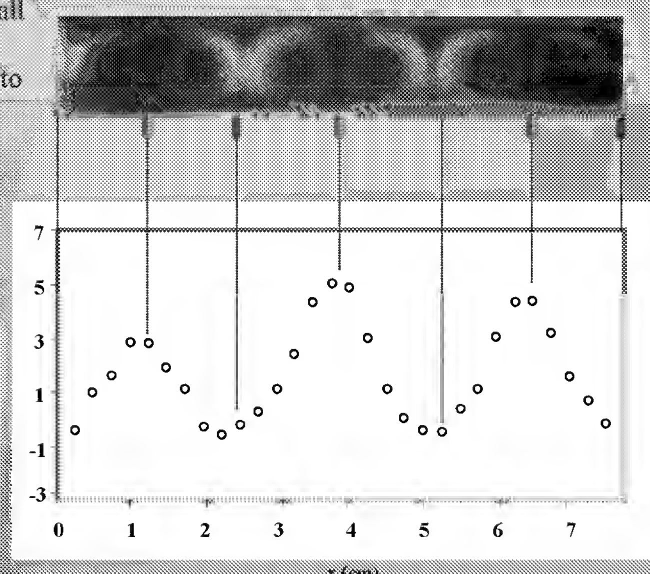

….thus the method is validated.

Temperature Profile Evolution of Rayleigh-Bénard Convection in a Liquid Metal (Hg) With Slowly Ramped ΔT

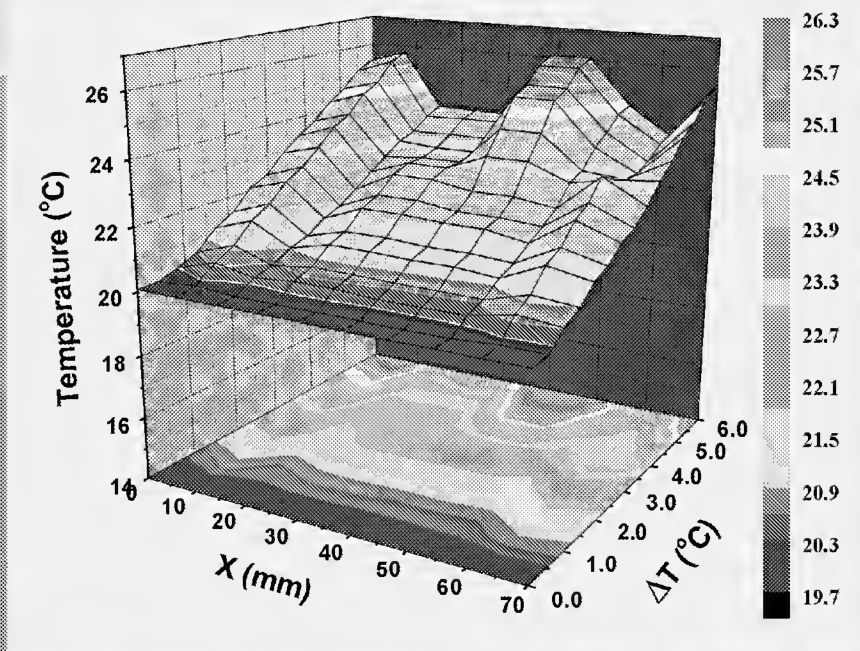

Slowly increasing temperature gradient ΔT (0.005°C/minute). Temperature measured at several locations along the chamber length on a line at mid-depth.

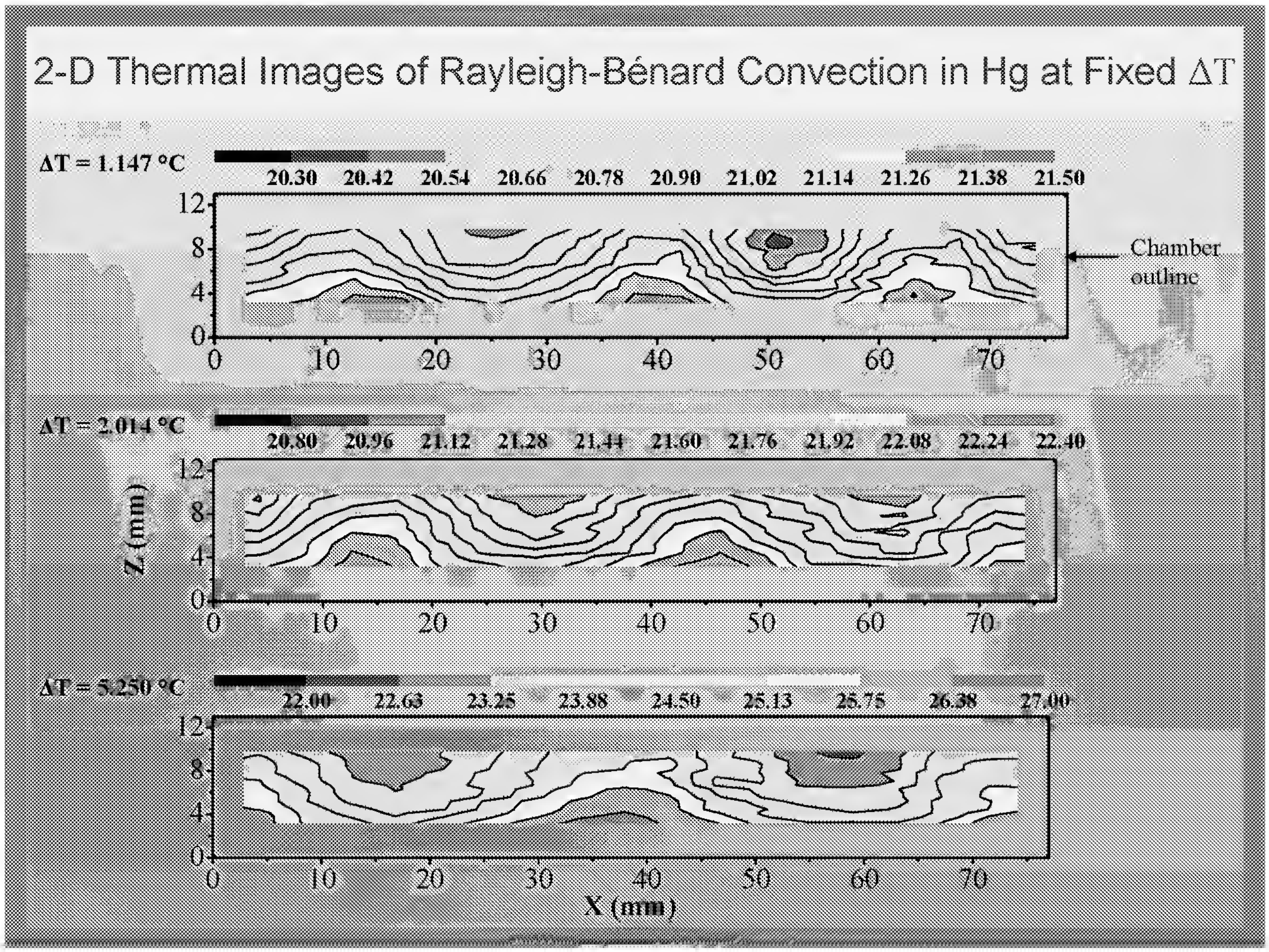
2-D Thermal Images of Rayleigh-Bénard Convection in Hg at Fixed ΔT
ΔT = 1.147 °C
20.30 20.42 20.54 20.66 20.78 20.90 21.02 21.14 21.26 21.38 21.50
Chamber outline
ΔT = 2.014 °C
20.80 20.96 21.12 21.28 21.44 21.60 21.76 21.92 22.08 22.24 22.40
Z (mm)
ΔT = 5.250 °C
22.00 22.63 23.25 23.88 24.50 25.13 25.75 26.38 27.00
X (mm)
0 10 20 30 40 50 60 70
0 4 8 12

Onset of Rayleigh-Bénard Convection in Mercury

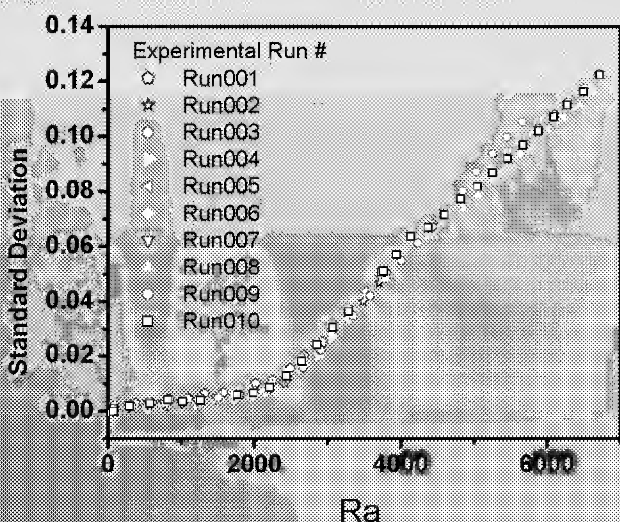

Standard deviation of the temperature profile as a function of Rayleigh number near convection onset.

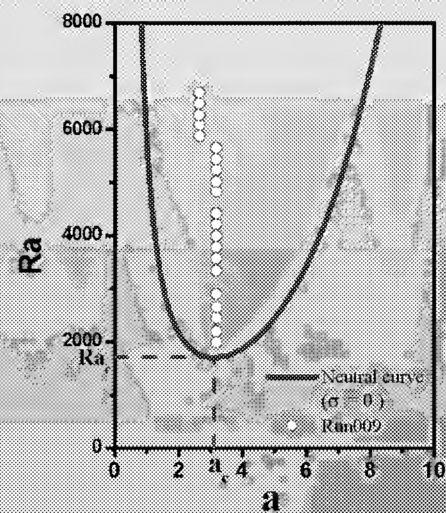

Stability diagram showing the critical Rayleigh number Ra_c, the critical wavenumber a_c, the theoretical neutral curve (Chandrasekhar, S. (1981) *Hydrodynamic and Hydromagnetic Stability*), and measured wavenumbers.

Conclusions and Future Work

- We have successfully demonstrated the use of ultrasound to measure temperature profiles in transparent and opaque fluids in laboratory scale convection with small imposed temperature gradients, and have shown good agreement with predictions and comparison techniques.
- We will use this technique in the future for crystal solidification, ferrofluids, and other physically interesting flows.

Sixth Microgravity Fluids Physics and Transport Phenomena Conference
August 14-16, 2002

TRANSIENT MIXING DRIVEN BY BUOYANCY FLOWS

W.M.B. Duval
NASA Glenn Research Center, Cleveland, Ohio 44135
Email:Walter.M.Duval@grc.nasa.gov, tel 216-433-5023, fax 216-433-5033
C. Batur[+], H. Zhong
University of Akron, Dept. of Mech. Eng., Akron, Ohio 44325

Mixing driven by buoyancy-induced flows is of particular interest to microgravity processes, as the body force that governs the intensity of flow fields can be directly controlled. We consider a model experimental system to explore the dynamics of mixing which employs two miscible liquids inside a cavity separated initially by a divider. The two liquids are oriented vertically inside a rectangular cavity with constant width and height, and varying depths to approach a cubical configuration. The two miscible liquids can be sufficiently diluted and died, for example water and deuterium oxide, such that a distinct interface exists across the divider. The transient mixing characteristic of the two fluids is addressed by following the Lagrangian history of the interface for various aspect ratios in the z-plane (depth variation) as well as a range of pulling velocities of the divider.

The mixing characteristic of the two fluids is quantified from measurement of the length stretch of the interface using image processing techniques. Scaling analysis shows that the length stretch depends on four governing parameters, namely the Grashof number (Gr), Schmidt number (Sc), aspect ratio (Ar), and Reynolds number (Re). We fix the Grashof number as well as the Schmidt number. Thus our problem reduces to a co-dimension two bifurcation in parametric space for Ar and Re.

Our experimental results show that for Gr on the order of 10^6 and a nominal cavity aspect ratio Ar=0.2, the net effect of removal of the divider and the overwhelming buoyancy force causes an overturning motion which stretches and fold the interface to produce an internal breakwave. The structure of the breakwave is similar to the ubiquitous Rayleigh-Taylor instability morphology. The breakwave is dissipated either through internal or wall collision depending on the impulsive velocity of the divider as prescribed by the Reynolds number. The decay of the collision event occurs through sloshing oscillations over a short time scale. The two fluids then become stably stratified with a diffusive band at the interface indicating mass transport.

The local bifurcation of the internal breakwave is investigated as a function of aspect ratio. Results show that for narrow cavities on the order of 2mm (Ar=0.04), folding does not occur the interface only stretches. As the cavity size increases folding occurs through a supercritical bifurcation. Insight into the mechanism of folding is obtained from measurement of the flow field using Particle Imaging Velocimetry. These results show that in the neighborhood of the folding event, there exists hyperbolic points in the flow caused by multiple vortex interactions. The global stretch of the interface as a function of time is nearly Gaussian; calculations of finite-time Lyapunov exponents as well as construction of horseshoe maps indicate the likelihood of a chaotic transient.

Transient Mixing Driven By Buoyancy Flows

W.M.B. Duval*, C. Batur+, H. Zhong+
***NASA Glenn Research Center, Cleveland, Ohio 44135**
+University of Akron, Dept. of Mech. Eng., Akron, Ohio 44325

ABSTRACT

Mixing driven by buoyancy-induced flows is of particular interest to microgravity processes, as the body force that governs the intensity of flow fields can be directly controlled. We consider a model experimental system to explore the dynamics of mixing which employs two miscible liquids inside a cavity separated initially by a divider. The two liquids are oriented vertically inside a rectangular cavity with constant width and height, and varying depths to span the range of a Hele-Shaw cell to a 3-D configuration. The two miscible liquids can be sufficiently diluted and died, for example water and deuterium oxide, such that a distinct interface exists across the divider. The transient mixing characteristic of the two fluids is addressed by following the Lagrangian history of the interface for various aspect ratios in the z-plane (depth variation) as well as a range of pulling velocities of the divider.

The mixing characteristics of the two fluids are quantified from measurement of the length stretch of the interface and its flow field using respectively image processing techniques and Particle Imaging Velocimetry. Scaling analysis shows that the length stretch depends on four governing parameters, namely the Grashof number (Gr), Schmidt number (Sc), aspect ratio (Ar), and Reynolds number (Re). Variation of the Schmidt number is taken into account through thermophysical property variation. Thus our problem reduces to a codimension three bifurcation in parametric space for Gr, Ar, and Re.

Our experimental results show that for Gr on the order of 10^6 and a nominal cavity aspect ratio Ar = 0.2, the net effect of removal of the divider and the overwhelming buoyancy force causes an overturning motion which stretches and folds the interface to produce an internal breakwave. The structure of the breakwave is similar to the ubiquitous Rayleigh-Taylor instability morphology. The breakwave is dissipated either through internal or wall collision depending on the impulsive velocity of the divider as prescribed by the Reynolds number. The decay of the collision event occurs through sloshing oscillations over a short time scale. The two fluids then become stably stratified with a diffusive band at the interface indicating local mass transport.

The local bifurcation of the internal breakwave is investigated as a function of aspect ratio. Results show that for narrow cavities on the order of 2mm (Ar = 0.04) folding does not occur, the interface only stretches. As the cavity size increases folding occurs through a supercritical bifurcation. Insight into the mechanism of folding is obtained from measurement of the flow field which shows that in the neighborhood of the folding event, there exists hyperbolic points caused by multiple vortex interactions. The global length stretch of the interface as a function of time is nearly Gaussian; calculations of finite-time Liapunov exponents as well as construction of horseshoe maps indicate the likelihood of a chaotic transient.

Experimental Set-up to Quantify the Interface Motion

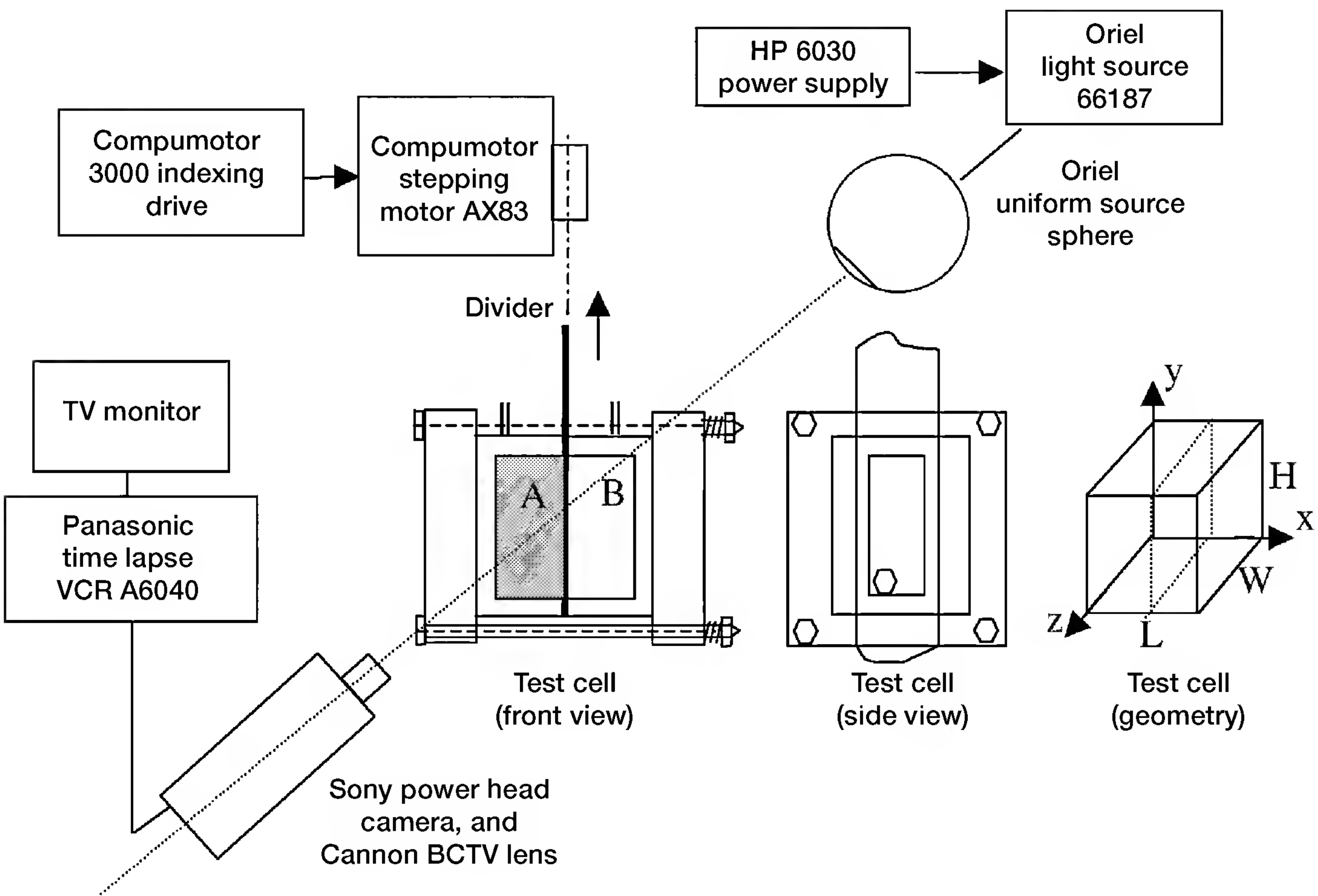

Experimental Set-up for Particle Imaging Velocimetry

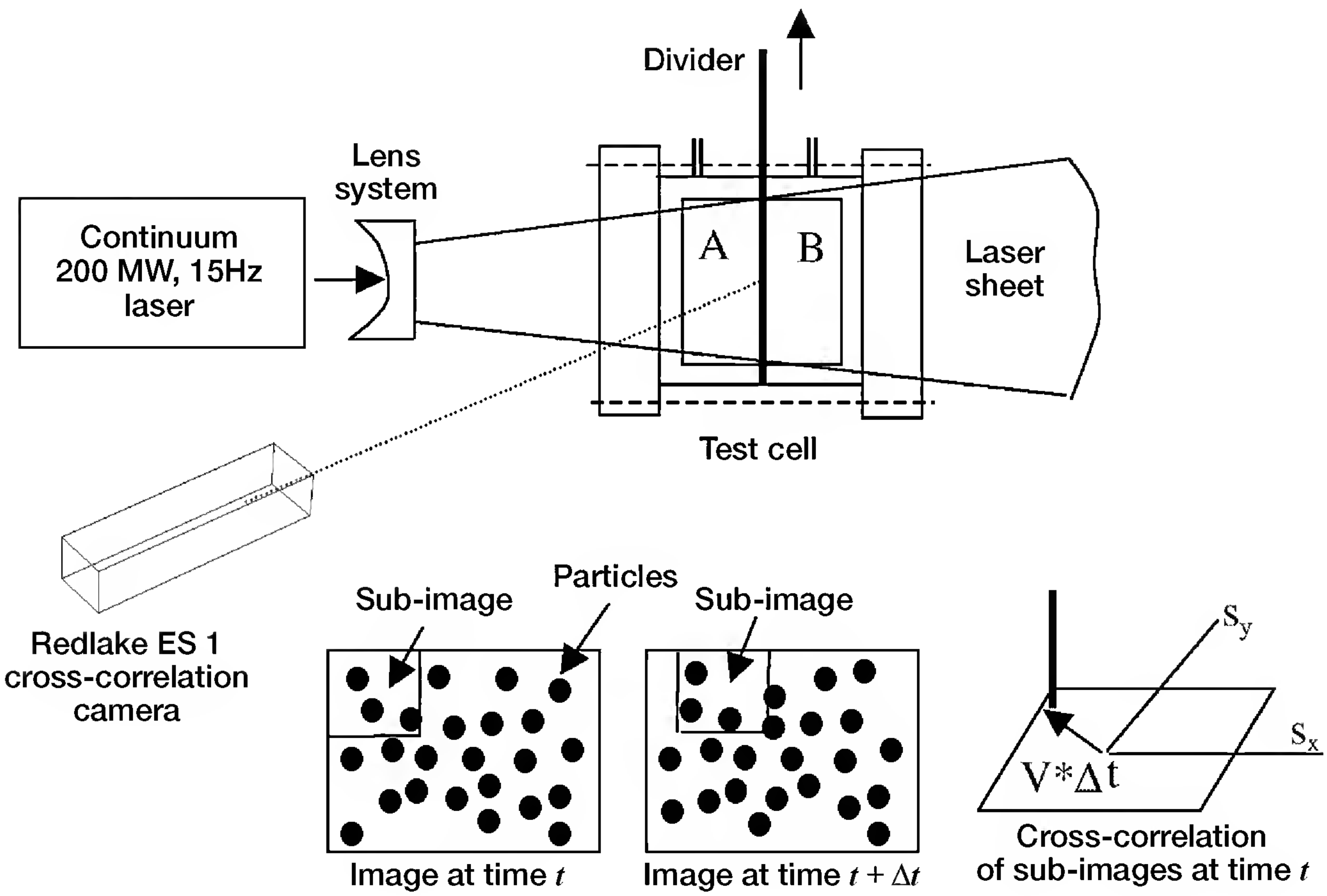

Initial Configuration of Two Fluids at Interface

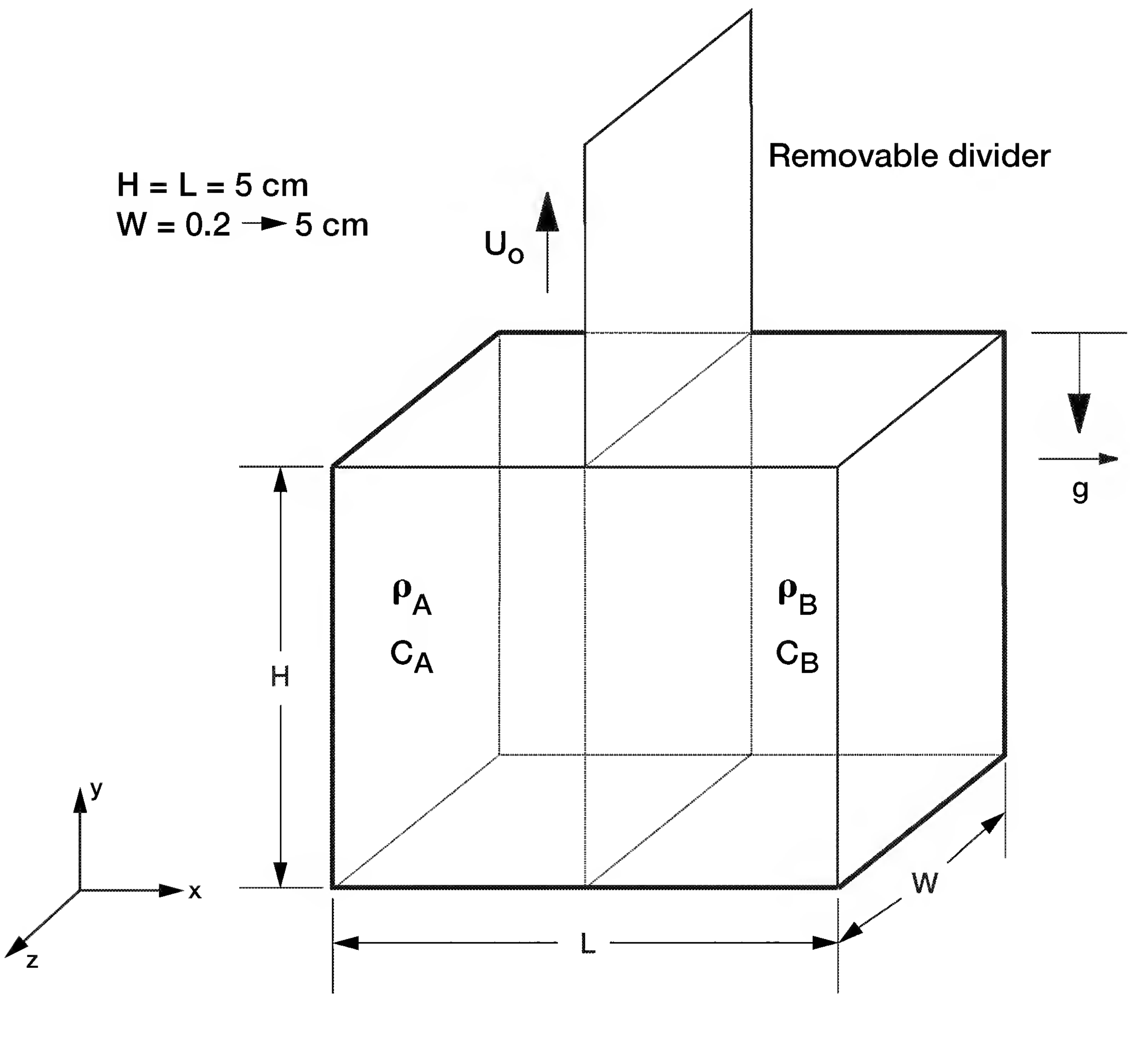

Stretching and Folding of Interface During Mixing by Buoyancy-Induced Flow Field, $Gr = 3.18 \times 10^6$, $Ar = 0.2$

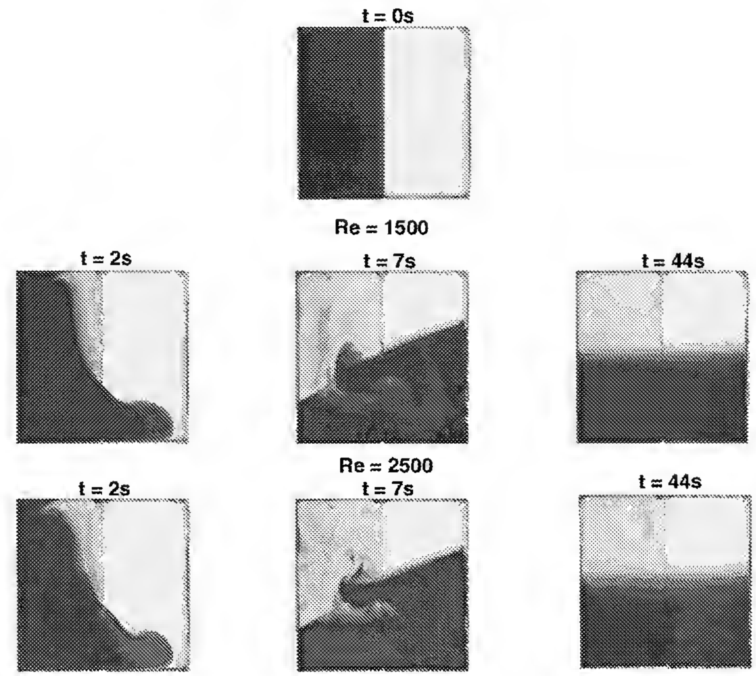

Evolution of Kelvin-Helmholtz Instability Waves During Mixing Due to Impulsive Input Velocity, $Gr = 3.18 \times 10^6$, $Re = 2 \times 10^4$, $Ar = 0.2$

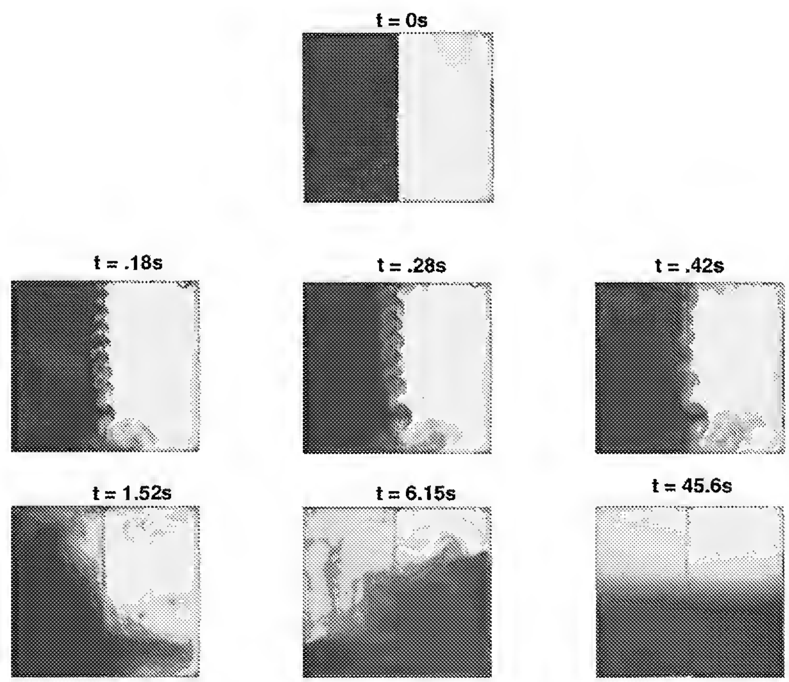

Parametric Range of Experiments

Case	Fluid A	Fluid B	S_A	S_B	ν_A $cm^2/\sec$	ν_B $cm^2/\sec$	$\frac{\Delta\rho}{\bar{\rho}}$	$\frac{\Delta\nu}{\bar{\nu}}$	Gr	Sc
1	H_2O+D_2O	H_2O+D_2O	0.9993	0.99925	0.01	0.01	0.00005	0.00	6.13×10^4	500
2	H_2O+D_2O	H_2O+D_2O	0.99965	0.9994	0.01	0.01	0.00025	0.00	3.06×10^5	500
3*	H_2O+D_2O	H_2O+D_2O	1.0023	0.9997	0.01	0.01	0.00259	0.00	3.18×10^6	500
4*	H_2O+D_2O	H_2O+D_2O	1.0215	0.9993	0.01	0.01	0.02197	0.00	2.69×10^7	500
5	H_2O+D_2O	H_2O+D_2O	1.0525	0.99925	0.01	0.01	0.05191	0.00	6.36×10^7	500
6*	$20\%Et.+H_2O$	$100\%H_2O$	1.026	0.9975	0.01158	0.01	0.02817	0.14643	2.96×10^7	1079
7	$40\%Et.+H_2O$	$100\%H_2O$	1.0505	0.9975	0.01316	0.01	0.05176	0.27288	4.73×10^7	1158
8	$20\%Pp.+H_2O$	$100\%H_2O$	1.013	0.9975	0.08598	0.01	0.01542	1.58325	8.20×10^5	4799
9	$20\%Et.+H_2O$	$20\%Pp.+H_2O$	1.026	1.013	0.01158	0.08598	0.01275	1.52522	6.56×10^5	4878
10	$40\%Pp.+H_2O$	$100\%H_2O$	1.026	0.9975	0.16196	0.01	0.02817	1.76739	4.67×10^5	8598
11	$20\%Et.+H_2O$	$20\%Pp.+H_2O$	1.026	1.0135	0.01158	0.08598	0.01226	1.52522	6.31×10^5	4878
12	$20\%Et.+H_2O$	$100\%H_2O$	1.026	0.9975	0.01158	0.01	0.02817	0.14643	2.96×10^7	1079

Microgravity experiments are denoted by *, Et. and Pp. denote ethylene-glycol and 1,2propylene-glycol

Parametric Space $\Lambda = \Lambda(Gr, Re, Ar, Sc)$

$$Gr = \frac{\Delta\rho}{\rho} \frac{n g_0 H^3}{\bar{\nu}^2}$$

$$Re = \frac{U_0 H}{\bar{\nu}}$$

$$Ar = \frac{W}{H}$$

$$Sc = \frac{\bar{\nu}}{D_{AB}}$$

Length Stretch of Interface
Gr = 3.18×10⁶

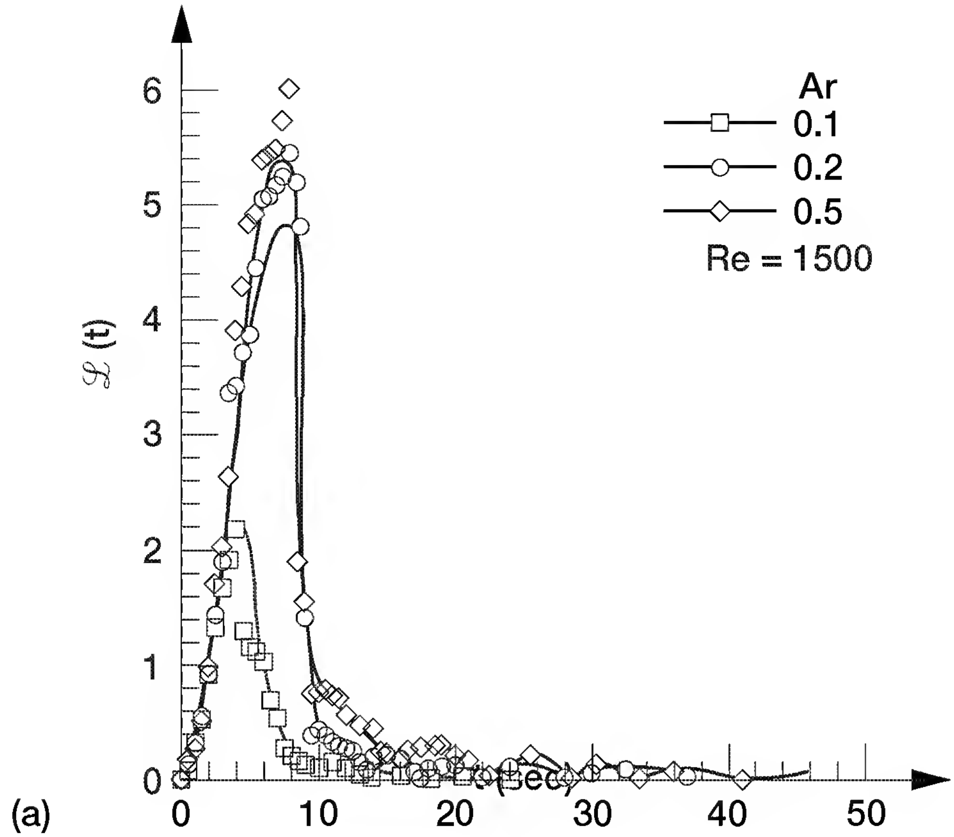

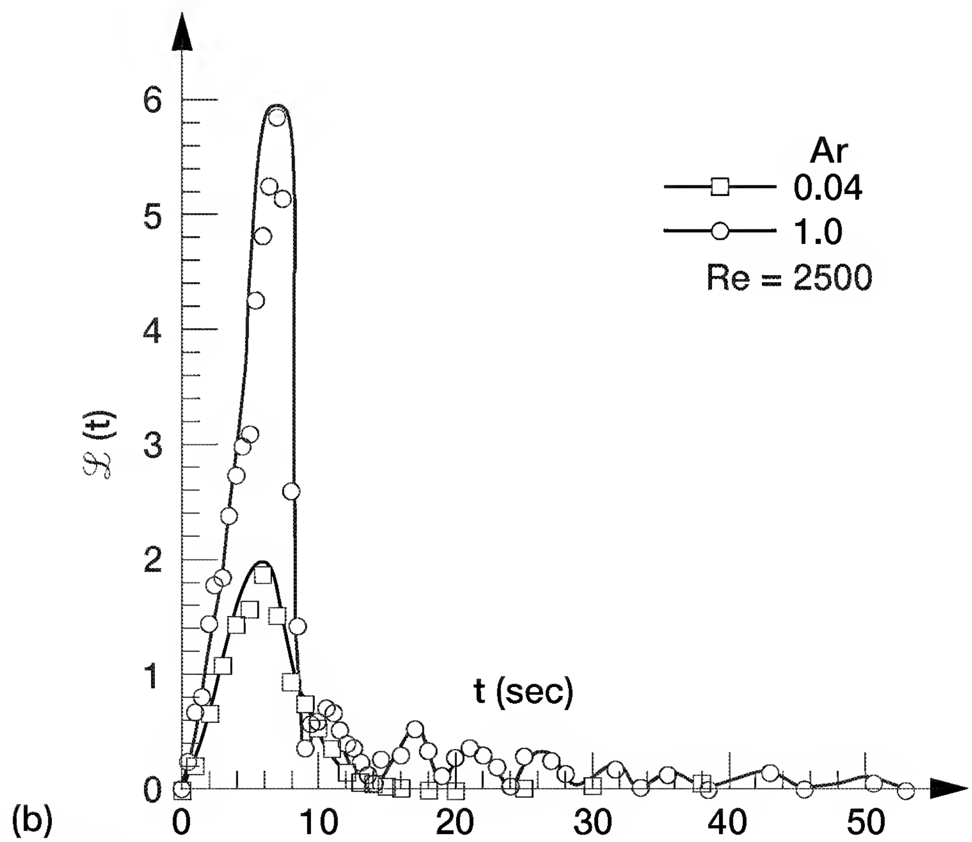

Decay Frequency of Sloshing Oscillations

$Gr = 3.18 \times 10^6$

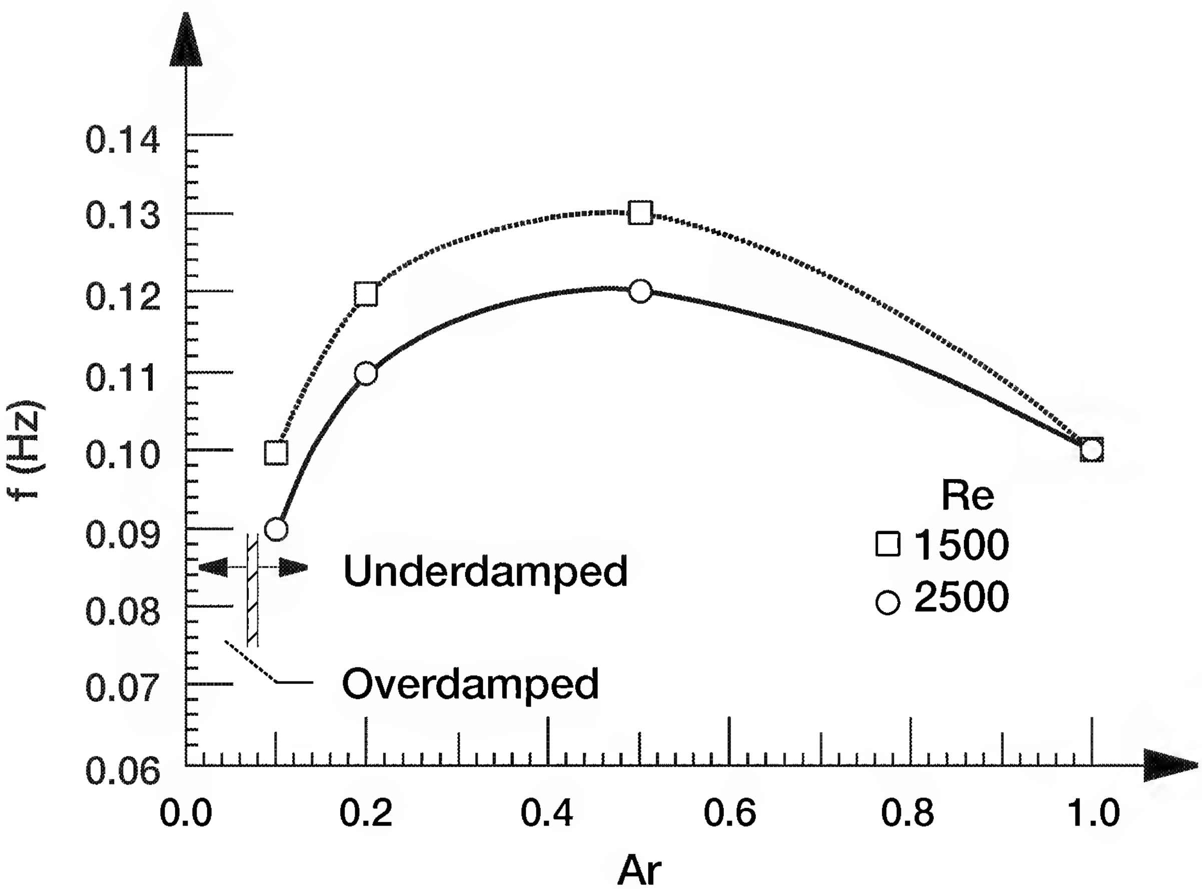

Bifurcation of Interface
Transition from Stretching to Folding

$Gr = 3.18 \times 10^6$

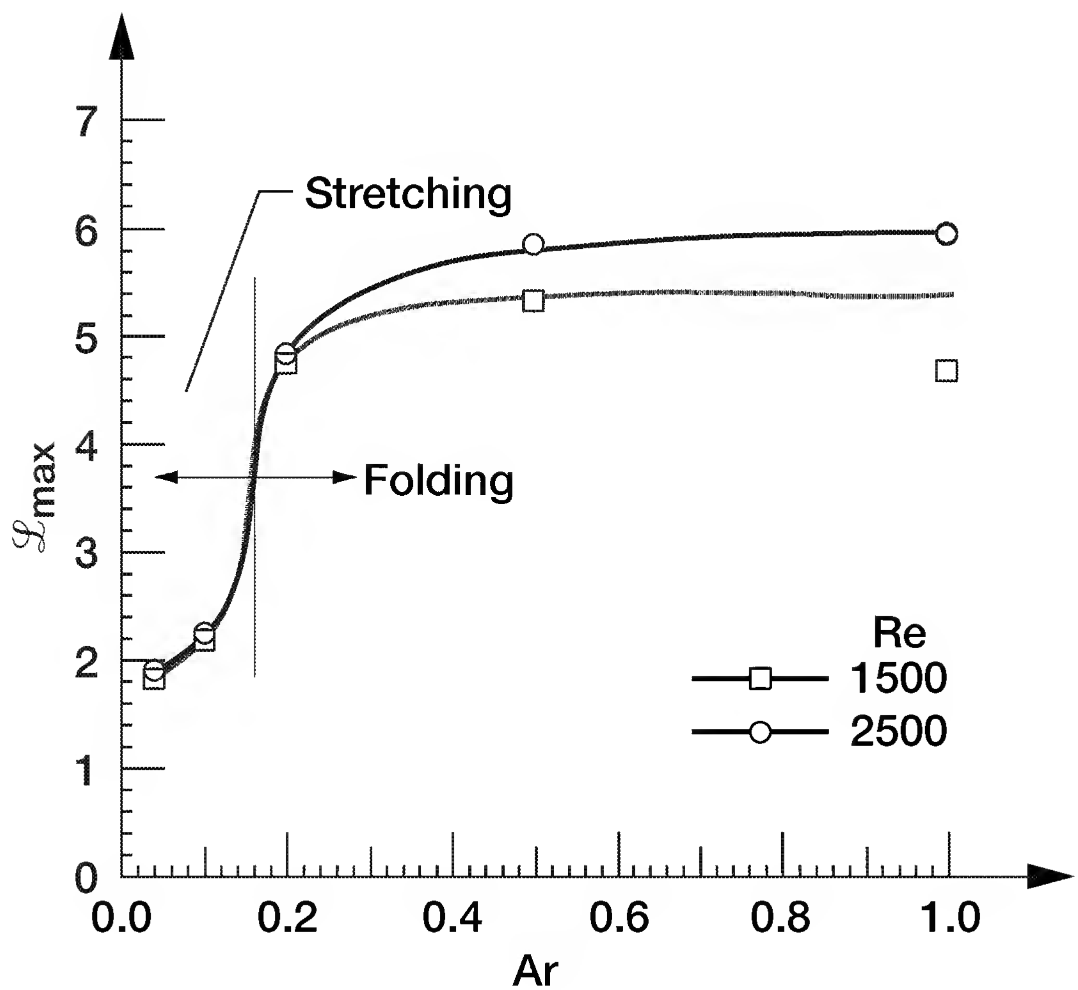

Effect of Impulsive Initial Velocity

$Gr = 3.18 \times 10^6$, $Ar = 0.2$

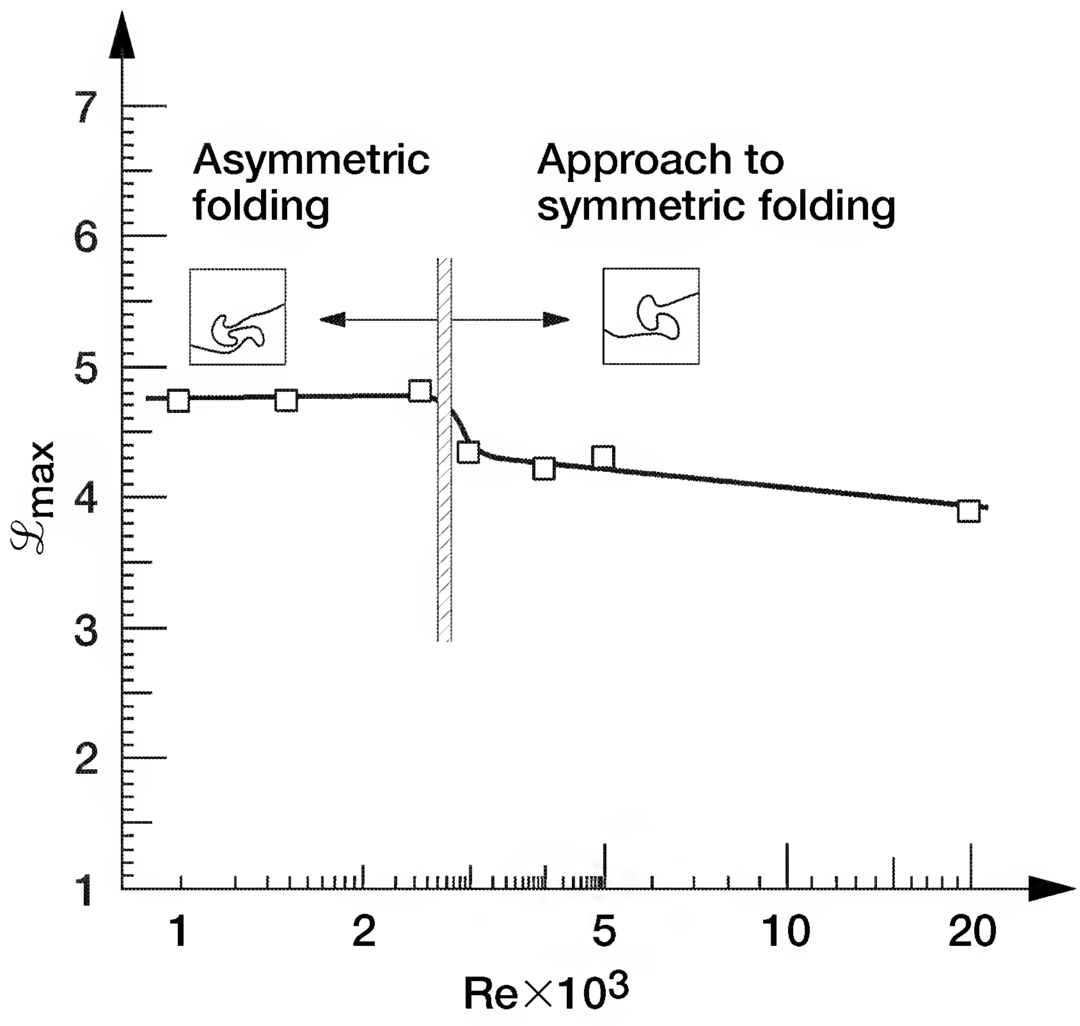

Bifurcation of Interface Due to Buoyancy-Induced Flow

Ar = 0.2, □ U_o = 5 cm/sec, △ U_o = 7 cm/sec

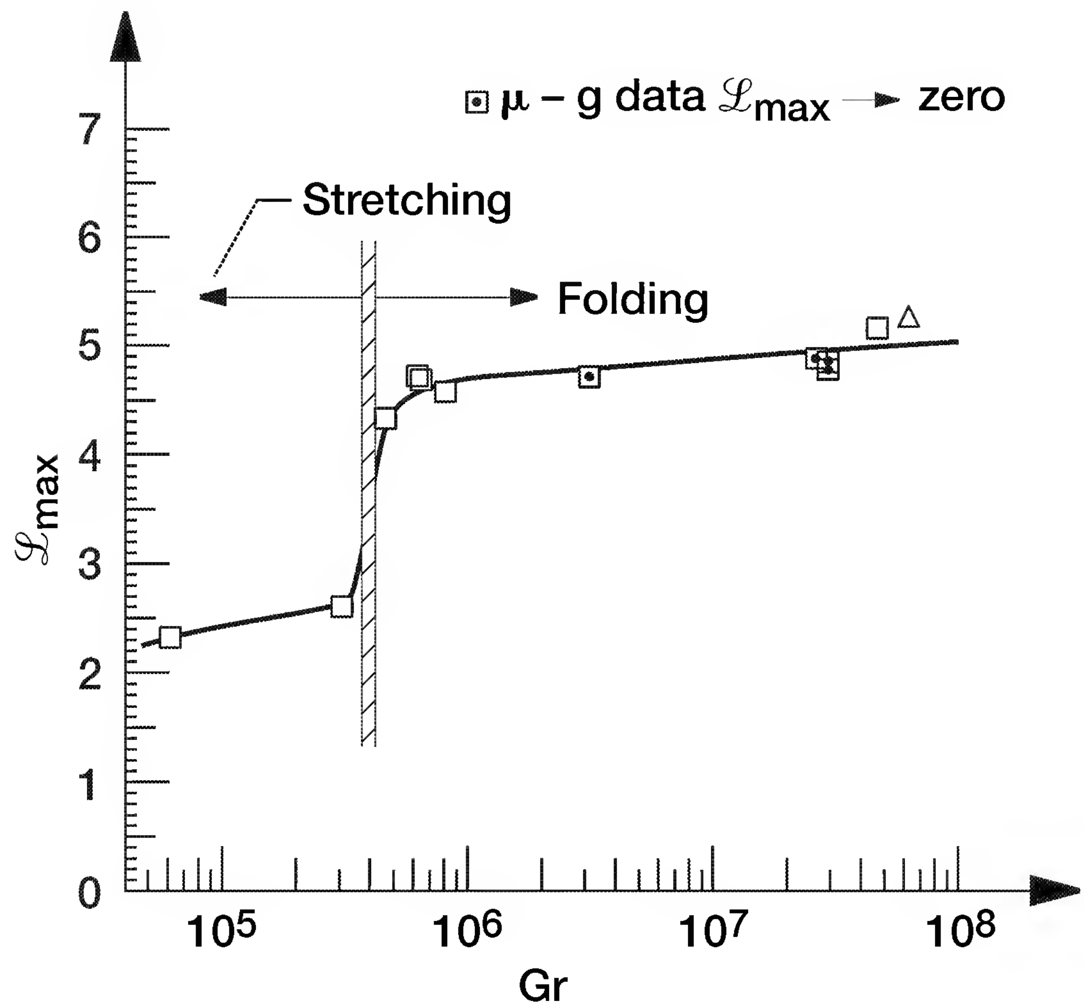

Stability Region of Interface Folding

$Gr = 3.18 \times 10^6$

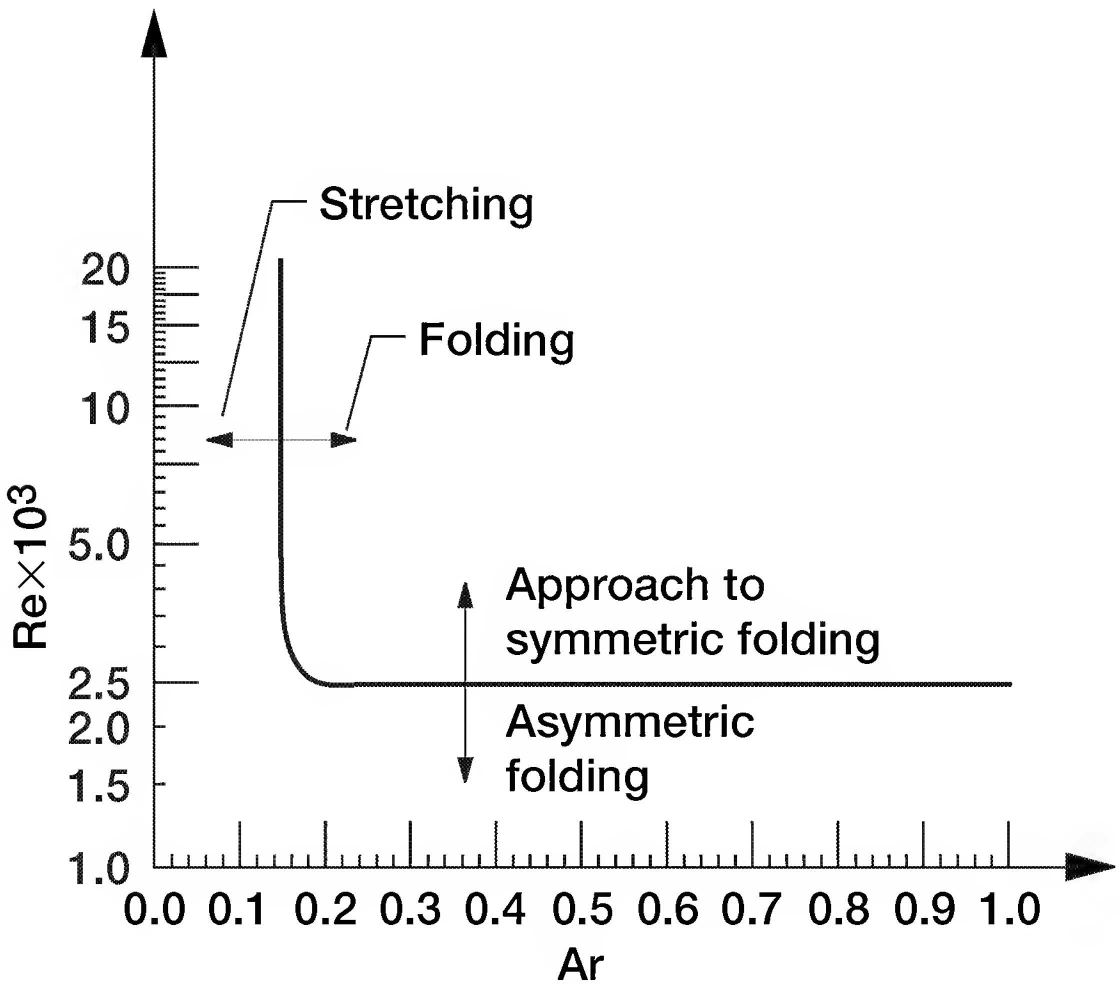

Correlation of Maximum Length
Stretch of Interface

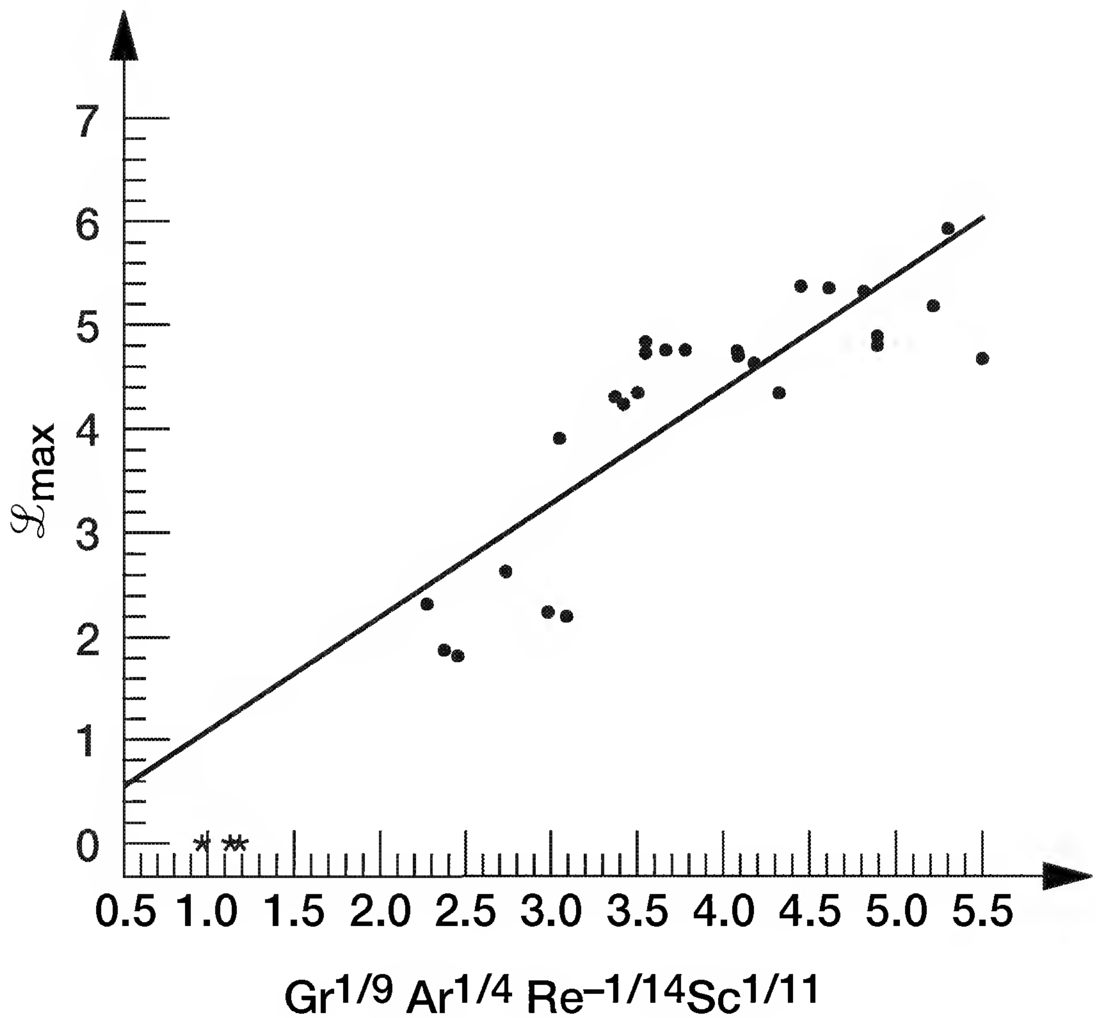

Flow Field Measurement Using Particle Imaging Velocimetry

Gr = 3.18×10^6, Re = 1500, Ar = 0.2

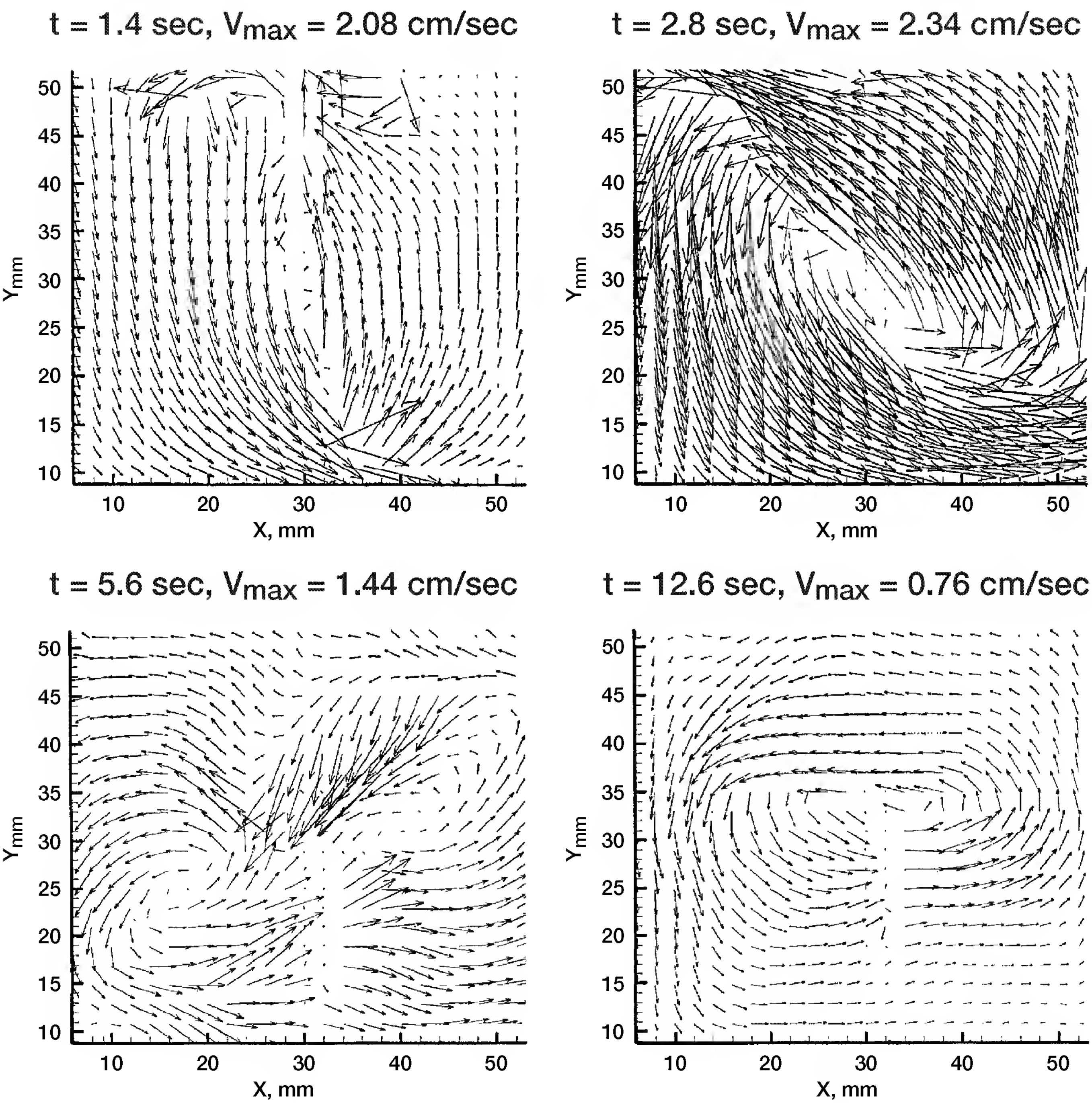

Magnitude of Velocity
Particle Imaging Velocimetry Measurements
Gr = 3.18×10^6, Re = 1500, Ar = 0.2

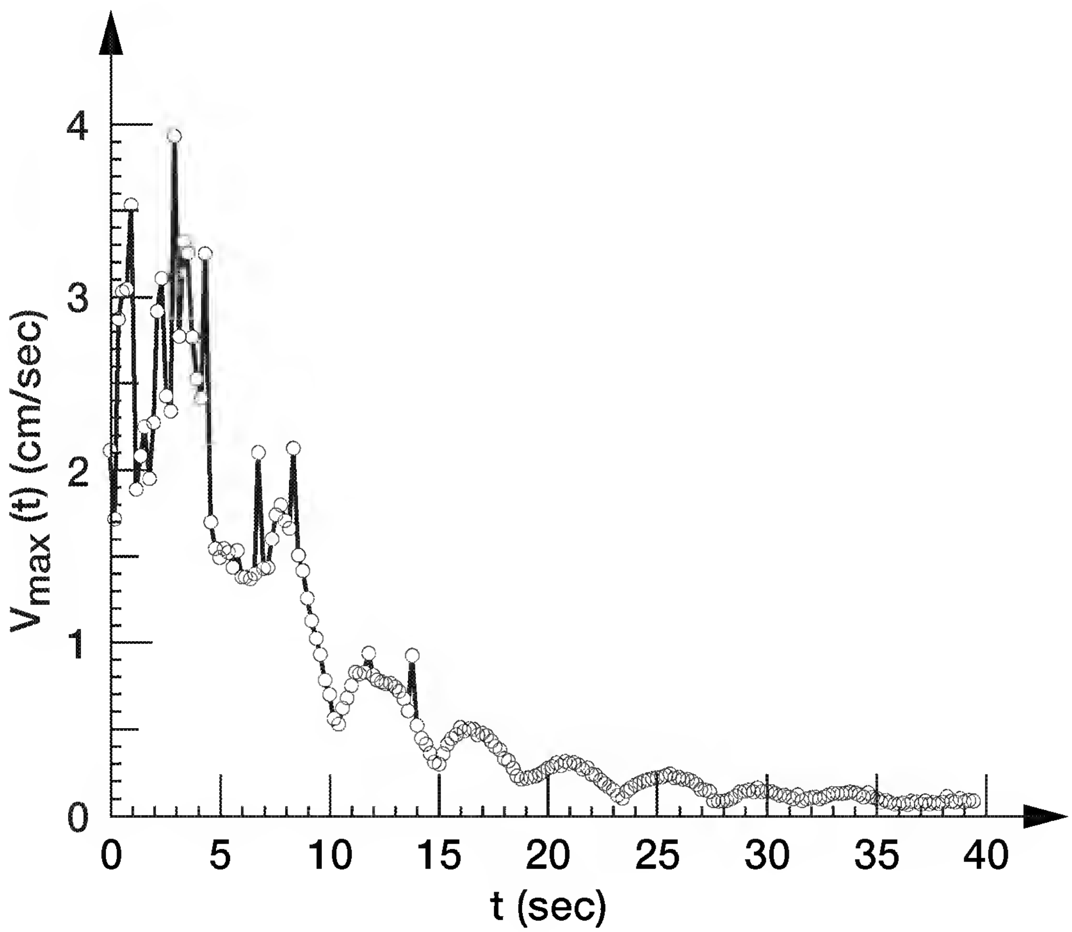

Gaussian Approximation of Length Stretch Ratio

$Gr = 3.18 \times 10^6$

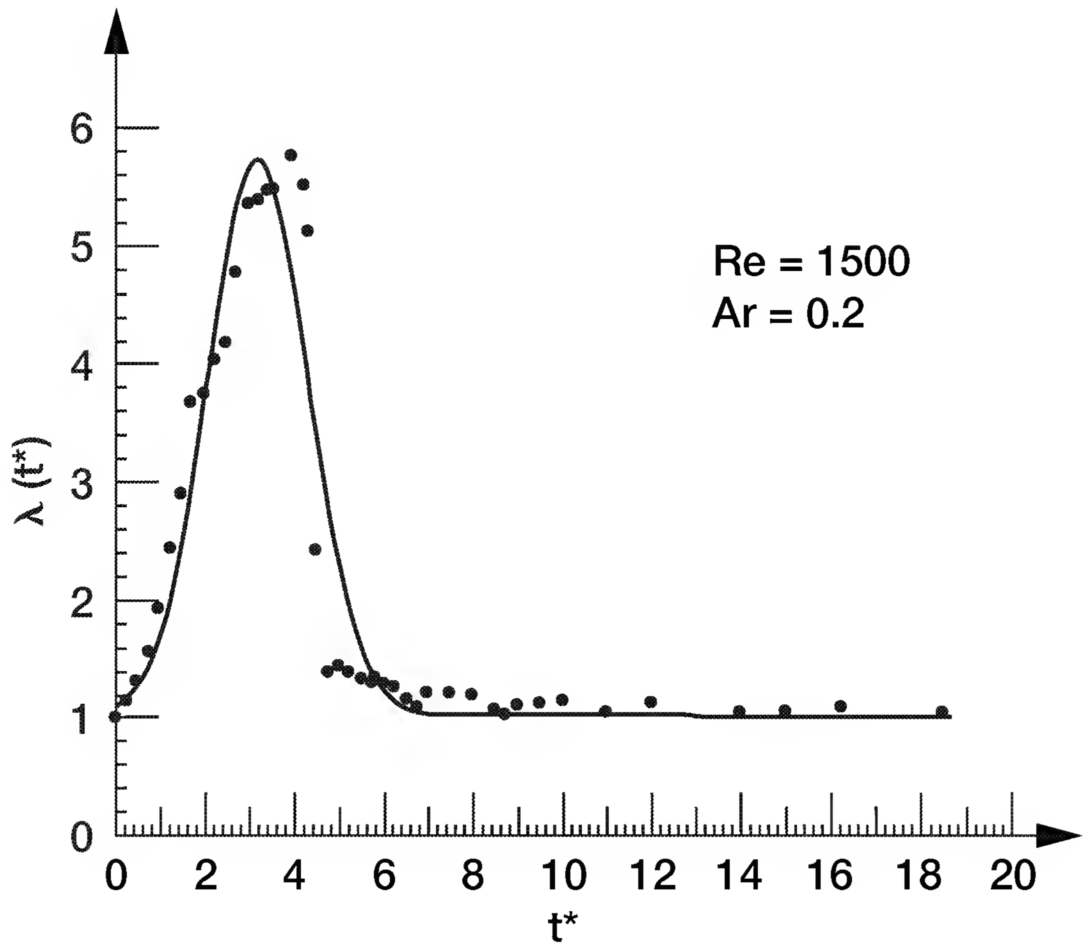

Time History of Liapunov Exponent

$Gr = 3.18 \times 10^6$

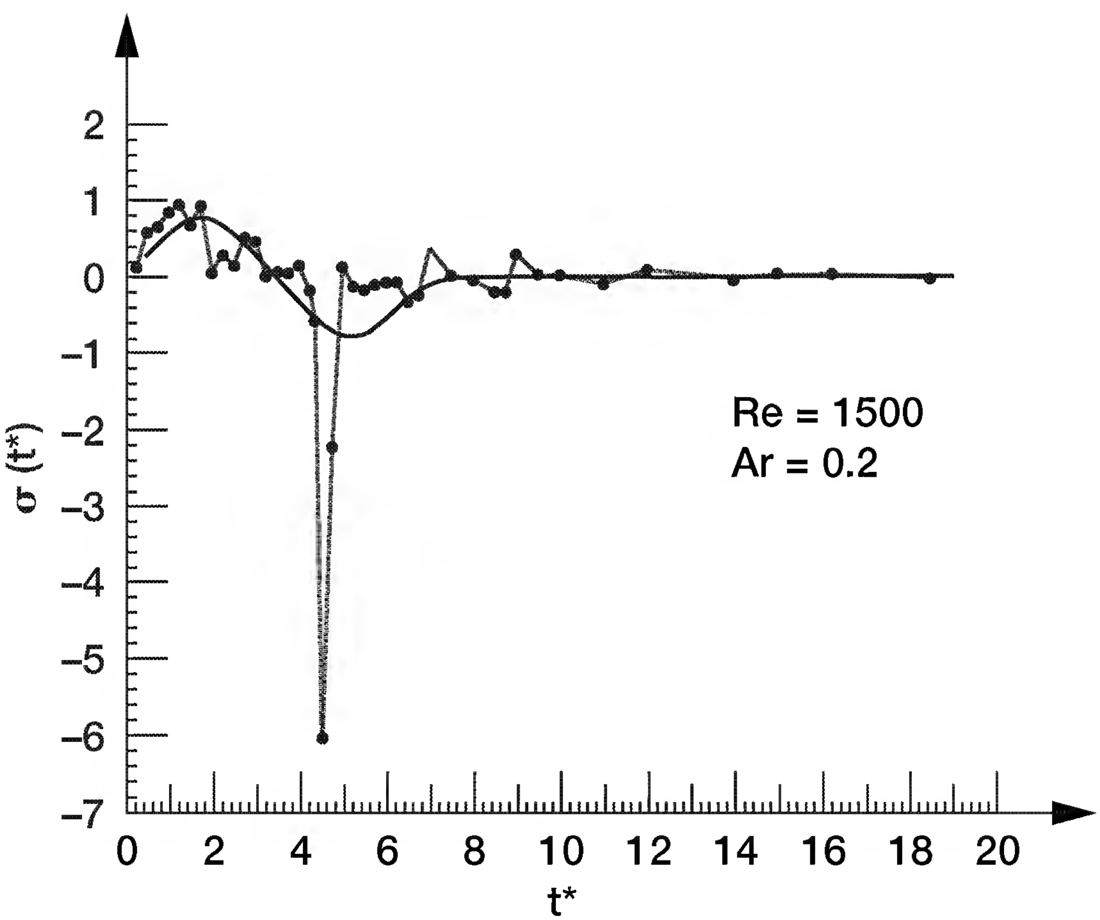

Horseshoe Map of Interface Folding

$Gr = 3.18 \times 10^6$, $Re = 3500$, $Ar = 0.2$, $t = 7.5$ sec

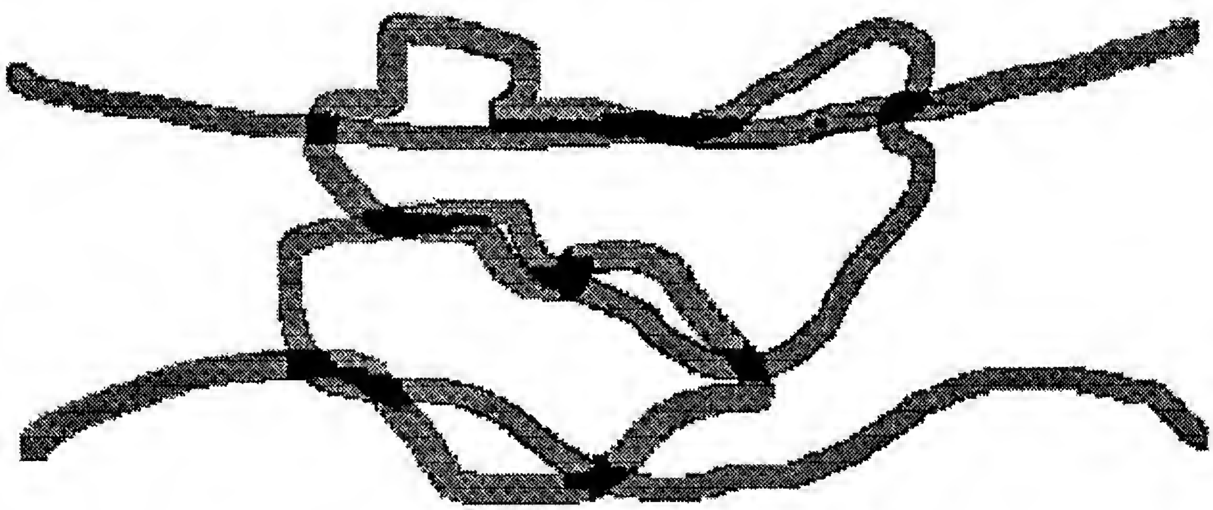

Geophysical flows in spherical geometry from electric fields and near-critical fluids

John Hegseth, Arun Roy, and Ana Oprisan
Department of Physics, University of New Orleans
New Orleans, LA 70148 USA
Telephone: 504-280-6706, FAX: 504-280-6048, E-mail: jhegseth@uno.edu

ABSTRACT

The use of near-critical fluids allows important parameters (e.g., compressibility of supercritical fluids, density of gas and liquid phases, surface tension) to be easily varied by using small changes in temperature. These highly variable properties of near-critical fluids makes it possible to study interesting phenomena when external forces are applied to the fluid. In particular, I plan to study geophysical flows in a spherical capacitor. The spherical capacitor will exert a central polar (di-electrophoretic) force on a supercritical fluid. This creates a central body force on the hyper-compressible fluid with a resultant radial density gradient. Large-scale geophysical flows, analogous to a planetary liquid core, a planetary ocean or atmosphere, etc., could be studied when a Coriolis force is also applied in a rotating frame of reference. In this presentation, I will show experimental results in support of this goal.

In spherical geometry, such as concentric spheres with dielectric fluid between them (a spherical capacitor), an electric field gradient produces a central body force that is similar to the gravitational field of a planet. By using an AC electric field this force is retained and the extraneous effects of free charges are eliminated. Variations in the dielectric constant produce a buoyancy force in the presence of this polarization force, just as variations in mass density produce a buoyancy force in the presence of gravity. We have found, with a sufficiently small capacitor, that this dielectric buoyancy is effective to produce instability near the center electrode in incompressible fluids, on Earth. I will present results of our experiments in this small spherical capacitor that systematically studies this instability when the center sphere is heated. Specifically, we have found upward traveling toroidal or spiral rolls that form along the inner sphere when ΔT (the temperature difference between the spheres) and ΔV (the voltage difference between the spheres) are sufficiently high. These rolls start near the center sphere's equator and travel vertically upward. The onset of this instability depends on both ΔT and ΔV, and these two quantities appear to be related, within the parameter range accessible to our experimental system, by a power law. Measurements of the heat transfer show that these traveling rolls also significantly increase the heat transfer at onset.

In a *compressible* dielectric (near-critical) fluid, the central polarization force present in a spherical capacitor will lead to a density gradient in a manner similar to a compressible fluid in a gravitational field. I have performed experiments on parabolic flights using NASA's KC135A aircraft in a spherical capacitor filled with near-critical fluid. Our attempts to induce a spherical density gradient showed that the 20 seconds of low gravity was insufficient time. The horizontal density gradient from normal gravity never disappears. We did see, however, appreciable density changes in the capacitor in a fluid near the critical point when the field was applied. Our current effort is directed at placing this system in a rotating frame of reference in preparation for a space experiment including: shadowgraph visualization optics appropriate for

a rotating frame, precision temperature control using thermoelectric heat pumps, control and data acquisition in a rotating frame.

Because near-critical fluids are full of novelty when they are driven far-from-equilibrium, it is important to understand near-critical fluid convection so that we can have a reasonable understanding of how such a fluid will respond in the rotating spherical capacitor (RoSCA). To this end we are studying a compressible near-critical fluid in a Rayleigh-Bénard cell (flat fluid layer heated from below). One such novelty that we have discovered is a Rayleigh-Taylor instability, when the top plate is held below the critical temperature in the two-phase regime. A hexagonal droplet pattern forms on the wetted top plate when the bottom is heated. Because the liquid-gas density difference and surface tension become zero as the critical temperature is approached, this is an ideal system to see the effect of thermal fluctuations on pattern formation. By controlling the ambient temperature, the size and periodicity of the droplet pattern is also controlled. As the surface tension gets very small near the critical point the droplets also become very small and randomly positioned (as opposed to the hexagonal pattern). The thin wetting layer is stabilized by the Van der Waal's force from top sapphire plate and the small liquid-gas density difference. On approaching the critical temperature, these droplets decrease in size as the density fluctuations increase in size. Near the critical point, when the forming droplets and the density fluctuations are of the same order of size, we have observed droplets forming in the presence of thermal fluctuations. It appears that the droplets begin to form a pattern that is highly perturbed by fluctuations.

Another novel effect in near critical fluids, that is important for the RoSCA, is the effect of an electric field on the critical temperature. Different theories predict upward or downward shifts in the critical temperature when an electric field is applied. Some experiments have reported a downward shift in the critical temperature for polymers and binary mixtures. These previous experiments have also been criticized for not controlling heating effects and ignoring pressure/density from an external mass reservoir. We have performed an experiment that has avoided these difficulties and I believe resolved this controversy. Using a spherical capacitor of similar dimensions of the RoSCA with near critical fluid between the inner and outer sphere, we have applied an AC field that avoids joule heating. These experiments are performed in a ground-based environment so that a gravitationally induced density gradient assures a small layer of critical fluid somewhere in the capacitor that the light must pass through. In this cell I have found an upward shift in the critical temperature that depends on the electric field, as predicted separately by Landau and Onuki. This shift is repeatable and is found by measuring the average turbidity through the vertical density gradient (monochromatic beam axis is vertical) while slowly ramping the temperature downward through the critical temperature. By measuring the light intensity of a beam that travels through the fluid and varying the ramping rate and voltage, we found a repeatable upward shift of the critical temperature as a function of the applied electric field.

Electric field in a spherical capacitor filled with fluid makes a central force on centrally heated the fluid.

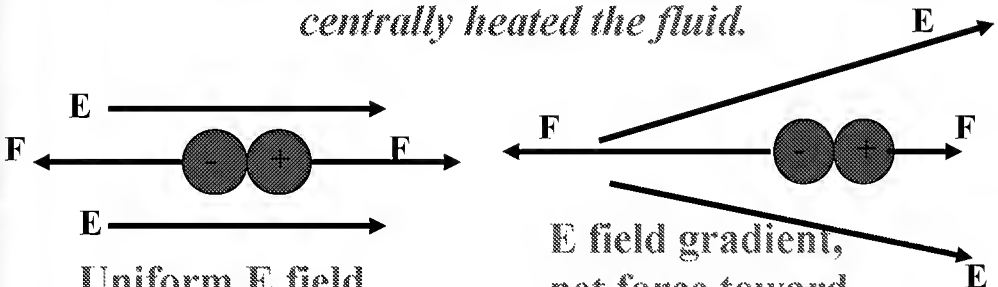

Uniform E field, no force F.

E field gradient, net force toward higher E flux.

This dielectrophoretic force in a heated incompressible fluid generates a buoyancy force from the change in dielectric constant, $\kappa=\kappa_a(1-\gamma\Delta T)$ [this is analogous to the buoyancy from the density change $\rho=\rho_a(1-\beta\Delta T)$]. In the Bousinesq approximation $\mathbf{F}=g_e\gamma\Delta T\mathbf{r}$ [$\mathbf{F}=g\alpha\Delta T\mathbf{r}$ from gravity, g] with g_e given by

$$g_e=\frac{2\kappa\varepsilon_0}{\rho}\left(\frac{\Delta V r_o r_i}{d}\right)^2\frac{1}{r^5}.$$

An AC E-field, with sufficiently high frequency, makes a central buoyancy force when the central sphere is heated.

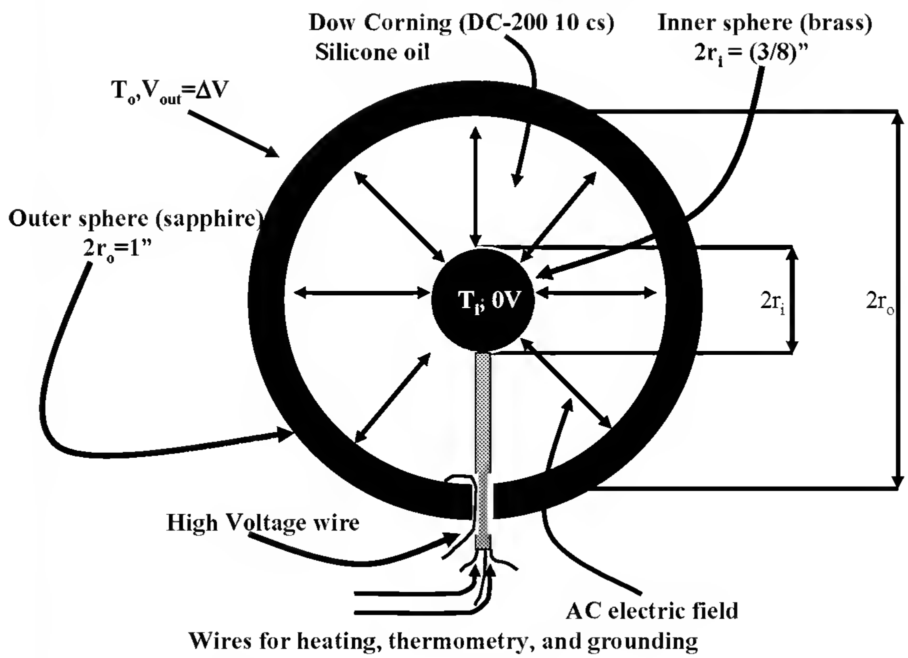

Visualize flow with transmission holographic interferometry and shadowgraph.

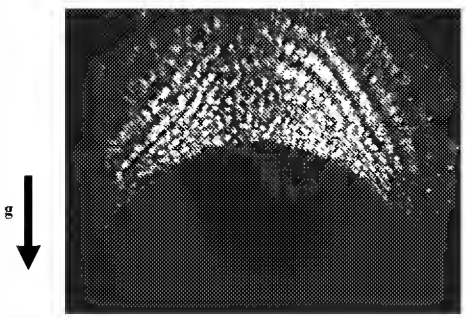

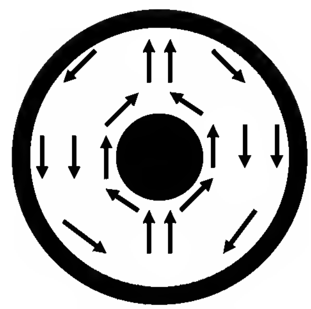

Upward flowing hot fluid makes interference fringes above the inner sphere at $\Delta T = 4^{o}C$. Creates a large axisymmetric "Hadley cell".

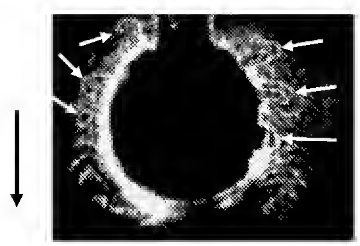

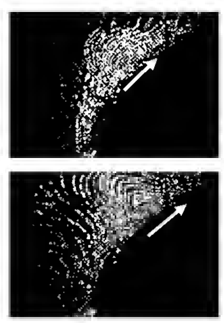

Left image shows a global view of the traveling rolls at $\Delta T = 3.0^{o}C$ with an E-field ($\Delta V = 5000V$). Traveling rolls form near the equator and travel upward along the the inner sphere. Right images show the propagation.

Critical phenomena

- Highly correlated molecular clusters near the critical point have a correlation length, ξ, that diverges as:

$\xi = \xi_0 t^{-\nu}$; ν=0.63, where $t = (T - T_c)/T_c$.

- Other quantities also diverge: $\kappa_T \sim t^{-\gamma}$, $\alpha \sim t^{-\gamma}$, $C_p \sim t^{-\gamma}$; γ=1.2

- Near-critical fluid stratifies under its own weight or the central force.

Ideal radial density gradient for SF_6 in the spherical capacitor.

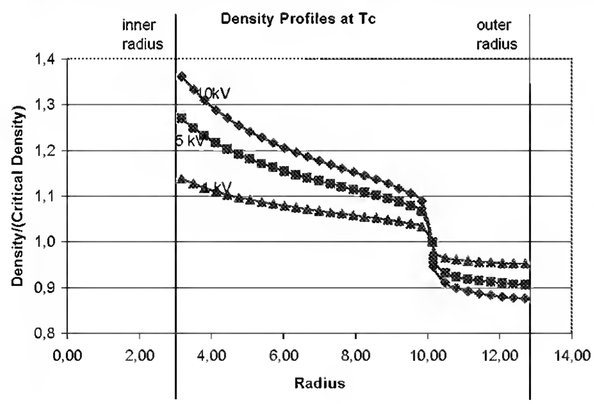

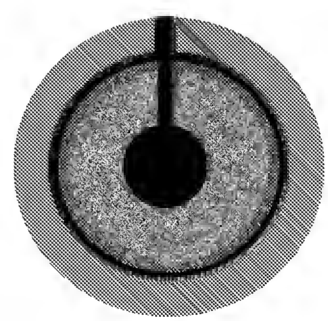

Critical fluid cell, filled with SF_6

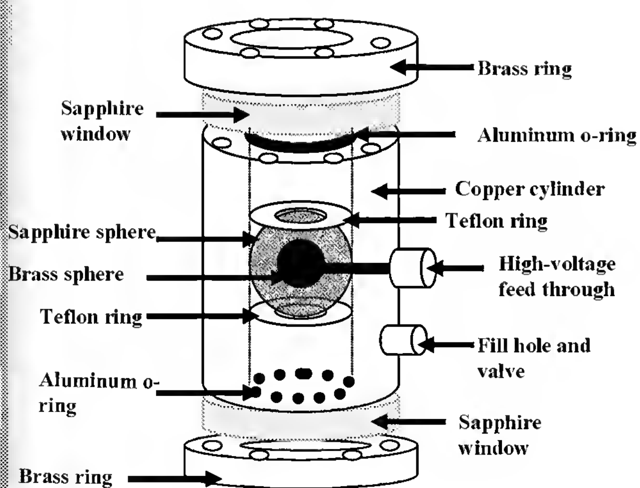

Visualize fluid, horizontally and vertically

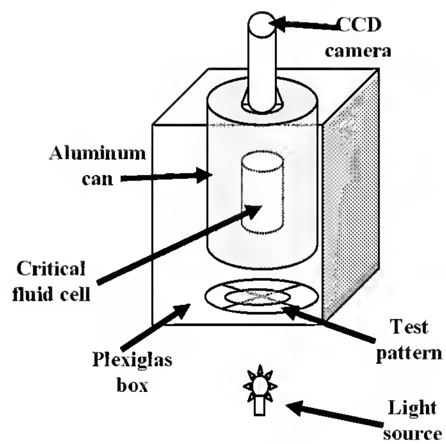

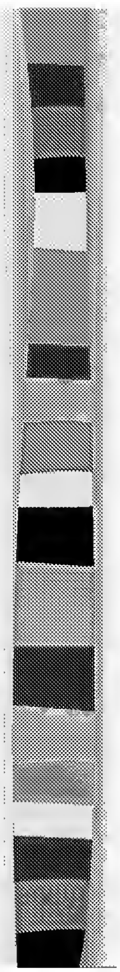

g=9.8m/s²

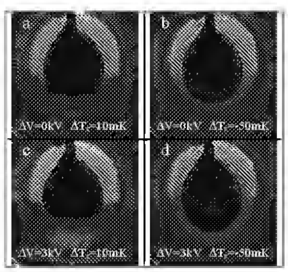

g=0 (parabolic flight) ΔV=3kV and ΔT_c=-100mK
Each image is 0.5 seconds apart and 3kV is applied for one second and then released for a second.

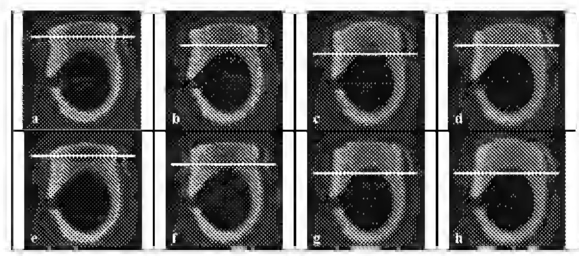

Measured turbidity with cell axis vertical to find Tc shift with applied E-field.

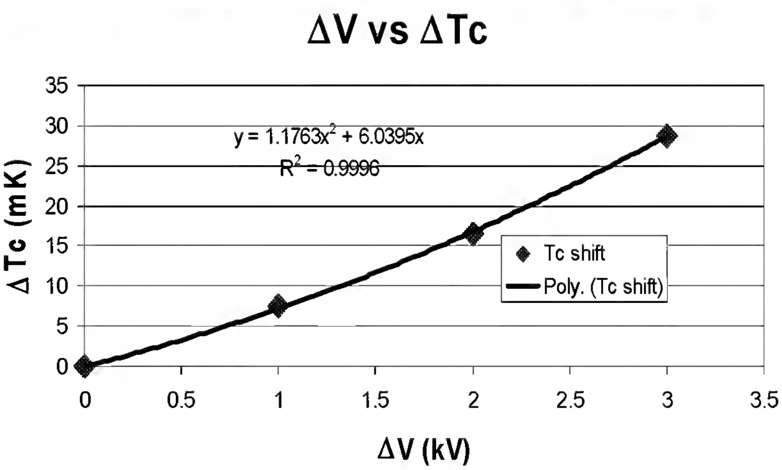

Near critical fluid studies with applied temperature gradient on ground

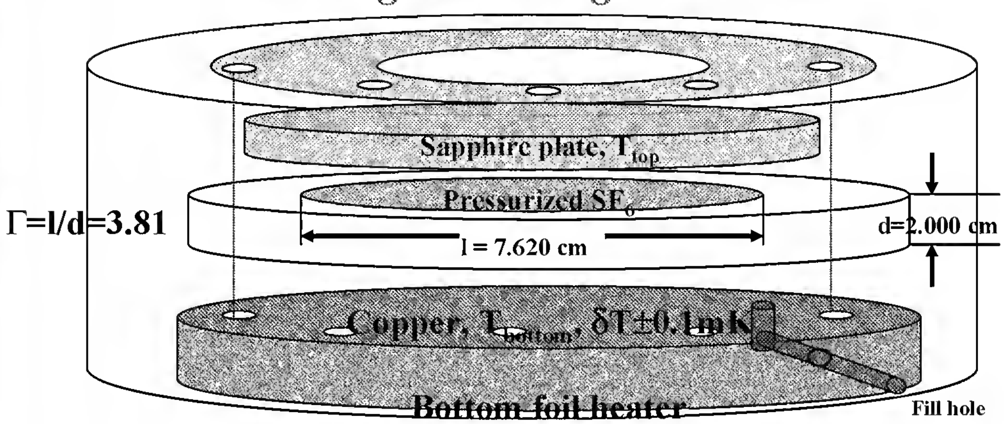

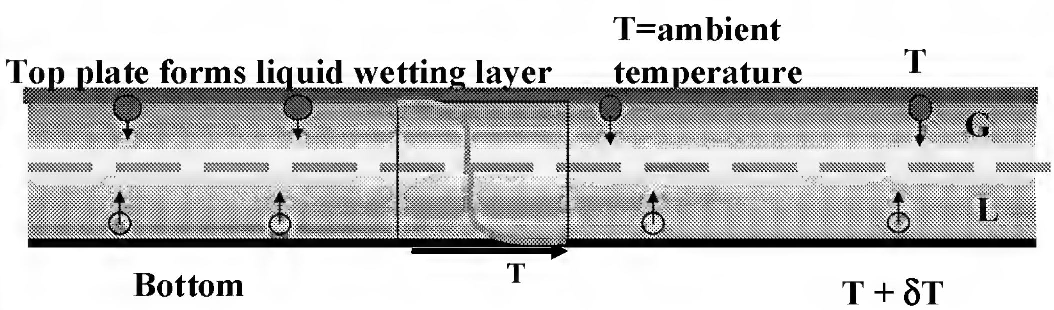

Shadowgraph visualization

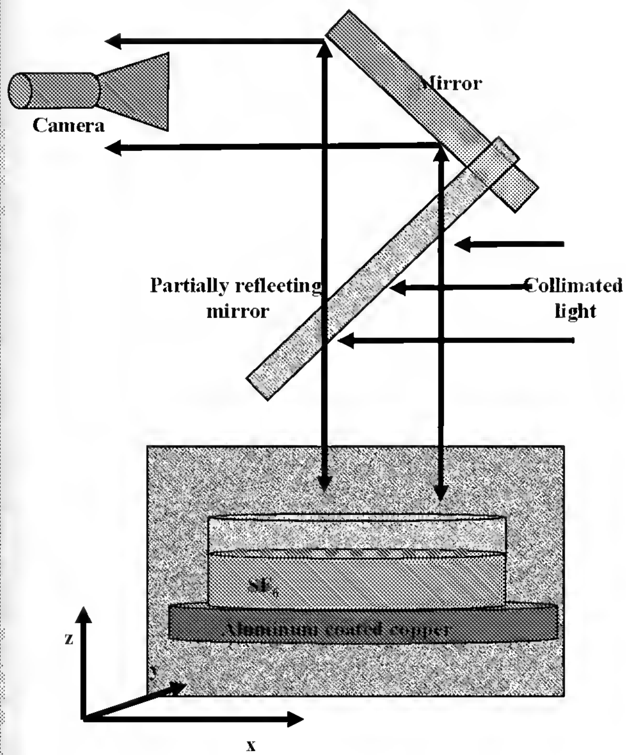

Found an instability threshold.
At $\Delta T = T_c - T_{ambient} = 132$ mK,
droplet pattern forms
when $\delta T = T_{bottom} - T_{top} = 2$mK

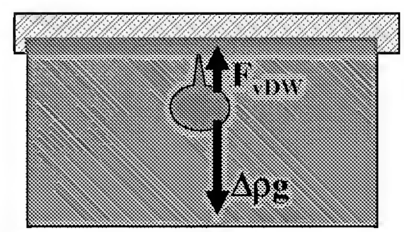

Shadowgraph images of droplets

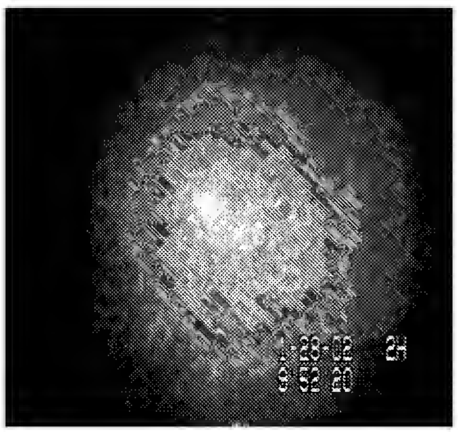

ΔT=137mK
δT=13mK

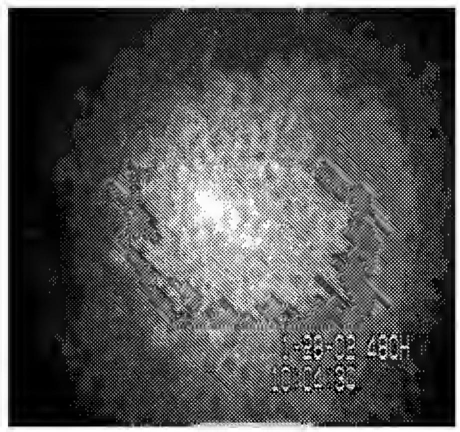

ΔT=144mK
δT=13mK

SONOLUMINESCENCE IN SPACE: THE CRITICAL ROLE OF BUOYANCY IN STABILITY AND EMISSION MECHANISMS

Charles R. Thomas (crt@bu.edu) ,R. Glynn Holt (rgholt@bu.edu) and Ronald A. Roy (ronroy@bu.edu), Boston University, Dept. of Aerospace and Mechanical Engineering, 110 Cummington St, Boston, MA 02215

INTRODUCTION AND MOTIVATION

Sonoluminescence is the term used to describe the emission of light from a violently collapsing bubble. Sonoluminescence ("light from sound") is the result of extremely nonlinear pulsations of gas/vapor bubbles in liquids when subject to sufficiently high amplitude acoustic pressures. In a single collapse, a bubble's volume can be compressed more than a thousand-fold in the span of less than a microsecond. Even the simplest consideration of the thermodynamics yields pressures on the order of 10,000 ATM. and temperatures of at least 10,000K. On the face of things, it is not surprising that light should be emitted from such an extreme process. Since 1990 (the year that Gaitan discovered light from a single bubble) there has been a tremendous amount of experimental and theoretical research in stable, single-bubble sonoluminescence (SBSL), yet there remain at least four unexplained phenomena associated with SBSL in 1g:

- *the light emission mechanism itself,*
- *the existence of anisotropies in the emitted light,*
- *the disappearance of the bubble at some critical acoustic pressure, and*
- *the appearance of quasiperiodic and chaotic oscillations in the flash timing.*

Gravity, in the context of the buoyant force, is implicated in all four of these.

We are developing KC-135 experiments probing the effect of gravity on single bubble sonoluminescence. By determining the stability boundaries experimentally in microgravity, and measuring not only light emission but mechanical bubble response, we will be able to directly test the predictions of existing theories. By exploiting the microgravity environment we will gain new knowledge impossible to obtain in earth-based labs that will enable explanations for the above problems. We will also be in a position to make new discoveries about light-emitting bubbles.

OBJECTIVES

The objectives of the investigation are:

(1) To develop an experimental apparatus to fly on the KC-135 that will monitor cabin pressure, water temperature, bubble position and size, acceleration, emitted light intensity, and acoustic pressure.
(2) To model the hydrodynamic effects of acceleration on bubble dynamics and SBSL in realistic acoustic resonators. The primary Bjerknes force, buoyancy, ambient pressure, drag, mass diffusion, shape stability and (empirically) light emission will be accounted for in the model.
(3) To measure (as a function of acceleration during parabolic flight) a bubble's position, equilibrium radius, maximum radius, oscillatory radius, and spatially and temporally resolved light emission. This will be done for a range of dissolved gas concentrations in order to compare with predictions of our hydrodynamic model.
(4) To measure (as a function of acceleration during parabolic flight) the precise values of acoustic pressure and equilibrium radius that leads to the extinction of a light-emitting bubble, a phenomenon which occurs at a well defined critical acoustic pressure in 1g experiments. This will test theories that postulate either a nonlinear levitation instability, or a Rayleigh-Taylor instability mechanism for the bubble disappearance.

RESULTS

We have completed 3 KC-135 flight campaigns. We attempted to test the prediction of our model [1] that hydrodynamics alone dictate a 5 – 35 % change in SBSL intensity, (depending approximately linearly on the dissolved gas concentration) for the 10^{-4}g to 1.8g swing typical of a K-135 parabolic maneuver. The driving mechanism for this effect is the small change in head pressure experienced by the bubble when the acceleration changes. Figure 1 shows the measured bubble dynamics during a single parabola. The main result [2] is that for nearly 0g, the bubble grows and emits more light, while at 2g the bubble shrinks and emits less light. The results are in rough agreement with our model.

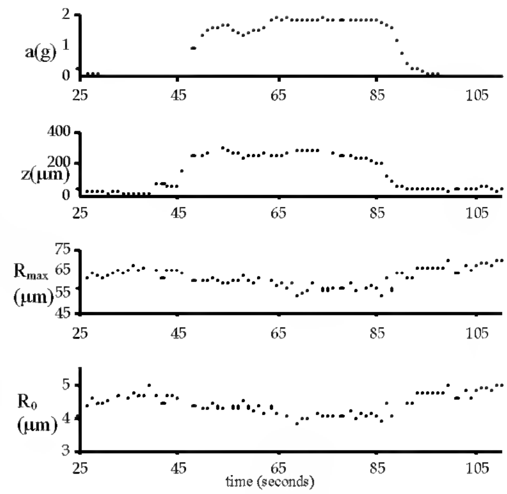

Figure 1. Measured (R_0 inferred) bubble dynamics during KC-135 parabolic maneuver.

We have completely overhauled the data acquisition system to make better use of available computer resources. We have installed a joystick-controlled three axis positioning system, using this system we can better position the cell and track its motion. We have completely replaced the light intensity detection system, including fabrication of a NIM-BIN style gated peak detector. Finally we have divided the apparatus into two equipment racks to facilitate transporting the experiment.

MICROGRAVITY RELEVANCE

SBSL bubbles experience a time-varying buoyancy (quantified by the oscillatory volume ratio V_{max}/V_0, see Fig. 2) which reaches maximal excursions precisely where sonoluminescence is observed. This results in a strong nonlinear coupling between volume and translatory motions. Removing the acceleration of gravity from the system will eliminate buoyancy-driven translatory oscillations of the bubble. This would be a decisive test of light emission mechanisms, and will also shed light on the chemical reaction theory of mass flux for volume stability as well as the resonance-controlled shape oscillation instability. Thus, a microgravity environment will change the geography of the parameter space, and the only hope for a clear understanding of the SBSL phenomenon is to perform experiments which locate light emission within the context of the instability boundaries that exist in the parameter space.

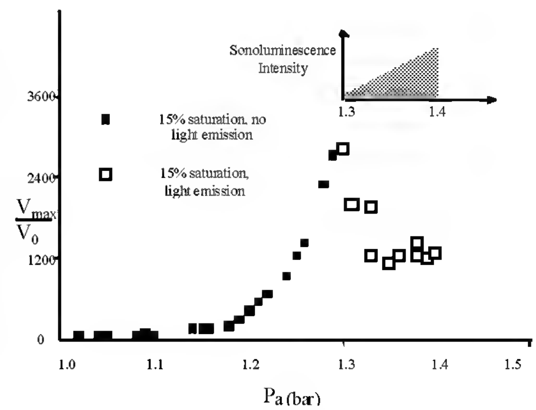

Figure 2. The measured (1g) ratio of V_{max} / V_0 during 1 acoustic cycle as a function of acoustic

REFERENCES

[1] Holt, RG, RA Roy and SC Wyatt, J. Acoust. Soc. Am. 105, No. 2, Pt. 2, p. 960. (Joint EAA/ASA/DAGA meeting, Berlin, 1999)

[2] Thomas, CR, SC Wyatt, RA Roy, R. Glynn Holt, J. Acoust. Soc. Am. 108, No. 5, Pt. 2, p. 2493. (ASA Meeting, Newport Beach, California)

Charles R. Thomas
R. Glynn Holt
Ronald A. Roy

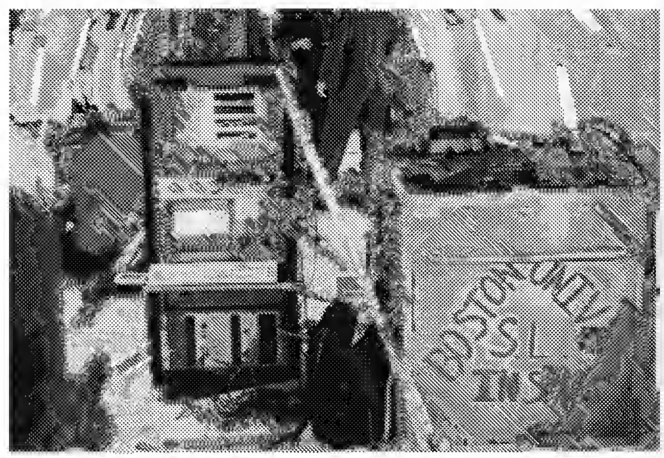

Boston University
Dept. of Aerospace and
Mechanical Engineering
110 Cummington Street
Boston, MA 02215

Sixth Microgravity Fluid Physics and Transport
Phenomena Conference
Cleveland, Ohio
14-16 August, 2002

Work funded by NASA

Objectives

- To develop an experimental apparatus to fly on the KC-135 that will monitor cabin pressure, water temperature, bubble position and size, acceleration, emitted light intensity, and acoustic pressure.
- To model the hydrodynamic effects of acceleration on bubble dynamics and SBSL in realistic acoustic resonators. The primary Bjerknes force, buoyancy, ambient pressure, drag, mass diffusion, shape stability and (empirically) light emission will be accounted for in the model.
- To measure (as a function of acceleration during parabolic flight) a bubble's position, equilibrium radius, maximum radius, oscillatory radius, and emitted light intensity. This will be done for a range of dissolved gas concentrations in order to compare with predictions of our hydrodynamic model.
- To measure (as a function of acceleration during parabolic flight) the precise values of acoustic pressure and equilibrium radius that leads to the extinction of a light-emitting bubble, a phenomenon which occurs at a well defined critical acoustic pressure in 1g experiments. This will test theories which postulate either a nonlinear levitation instability, or a Rayleigh-Taylor instability mechanism for the bubble disappearance.

Bubble Dynamics

$$\left(1-\frac{\dot{R}}{c}\right)R\ddot{R}+\frac{3}{2}\dot{R}^2\left(1-\frac{\dot{R}}{3c}\right)=\left(1-\frac{\dot{R}}{c}\right)\frac{P}{\rho}+\frac{R}{\rho c}\frac{dP}{dt}$$

$$P_{stat} = \rho g h + P_{cabin}$$

$$P\left(R,\dot{R},t\right)=\left(P_{stat}-P_v+\frac{2\sigma}{R_o}\right)\left(\frac{R_o}{R}\right)^{3\kappa}-\frac{2\sigma}{R}-4\mu\frac{\dot{R}}{R}-P_{stat}+P_v-P_a\sin(2\pi\nu t)$$

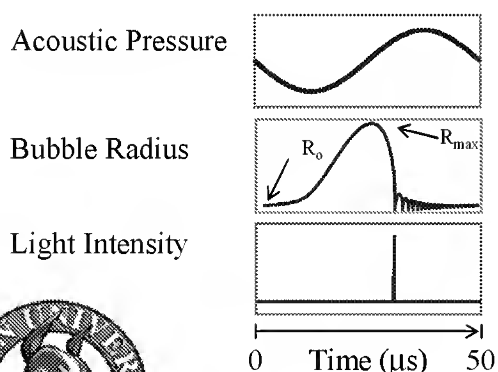

Parameters that can affect the bubble dynamics:

Ambient Acceleration: changes the buoyant force of the bubble, and the hydrostatic force on the bubble

Cabin Pressure in the airplane

Acoustic Pressure

Temperature

Dissolved gas concentration

Quasi-static Model

P_{cabin}, g, h → Compute DGC, P_a, R_o Grid → Compute the levitation height, keeping DGC constant → Gives the levitation height as a function of acceleration. To get bubble trajectory, use this to interpolate from a measured acceleration profile

P_a → Find R_o → Gives R_0 as a function of time

Compute DGC, P_a, R_o Grids → Find R_o

Compute DGC, P_a, R_o Grids → Makes a movie of these to illustrate the idea of moving lines of constant DGC

a, P_{cabin} → Compute DGC, P_a, R_o Grids

- Levitation height, z, found by making buoyant force equal Bjerknes force
- Ro found by requiring the dissolve concentration of AR not to change

$$c_i = kP_{cabin}\left(1+\frac{\rho a h}{P_{cabin}}+\frac{2\sigma}{R_o P_{cabin}}\right)\frac{\left\langle \frac{R}{R_0}\right\rangle}{\left\langle\left(\frac{R}{R_0}\right)^4\right\rangle}$$

- k is Henry's law constant for argon

SL Cell

- Cubical geometry
- Antinode of sound field near center of cube
- Driving frequency is 14.620 kHz
- Ports on top and bottom to fill cell
- Thermocouple in water to record water temperature

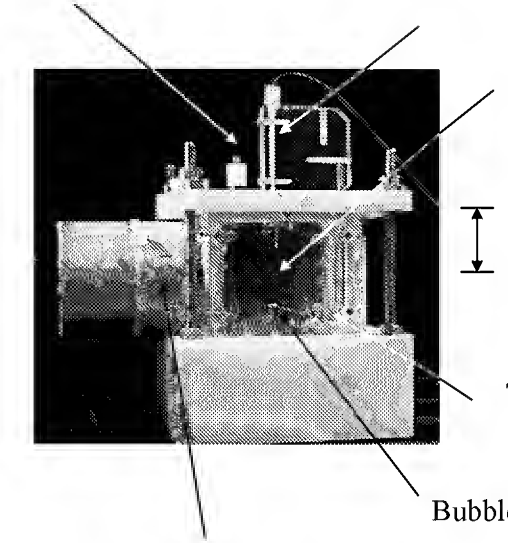

Experimental Schematic

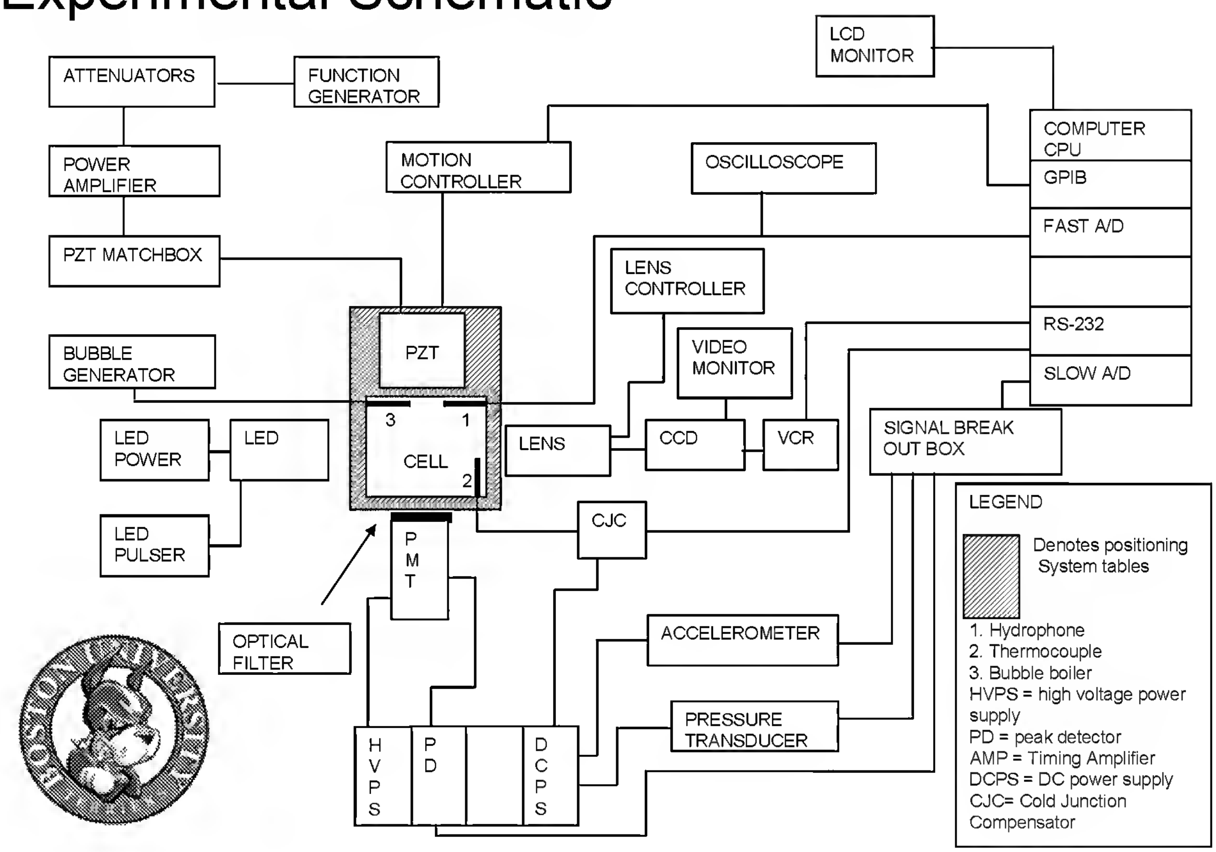

Experimental Apparatus

The experiment is housed in two equipment racks, pictured to the right. The taller one is a modified AMCO engineering equipment rack that holds the data acquisition computer, VCR, NIM-BIN and function generator. The shorter one is a custom built rack with a section that can be made light tight. It is in this section that the cell resides, along with the various transducers used to make the measurements of the bubble dynamics and the light emission.

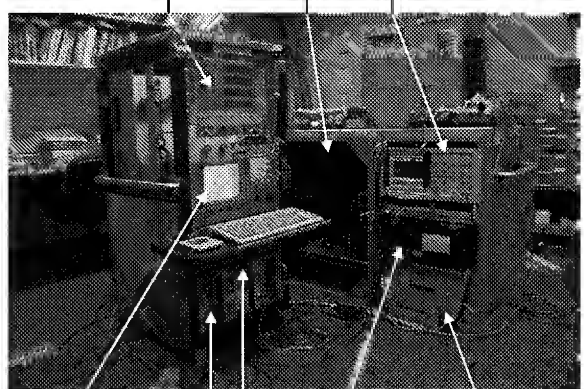

Results: Bubble Images

In 0g the bubble grows larger due to both diffusion and the *reduced* ambient pressure. It also moves toward the antinode of the sound field

In 1.8g, the bubble gets smaller, this time due to both diffusion and *increased* ambient pressure. With an increased buoyant force, the bubble moves further above antinode than in 1g.

As the plots on the slide following illustrate, in addition to growing in size, the light intensity of the bubble also increases during periods of 0g. Conversely, during periods of 1.8g, light intensity emitted by the bubble decreases.

Bubble at 0g Acceleration

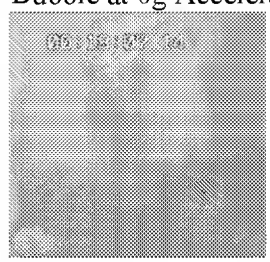

Bubble at 1.8g Acceleration

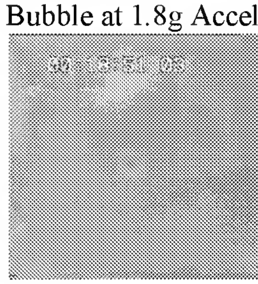

Results: Measured Variables vs Time

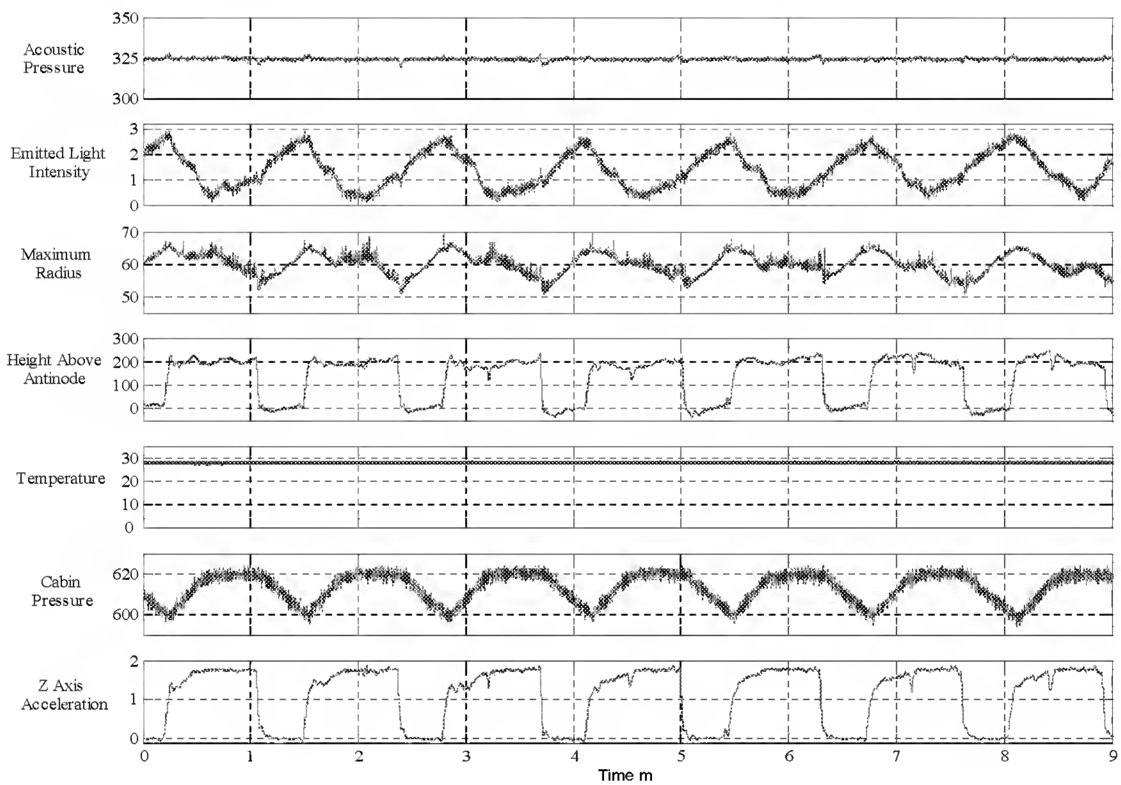

Conclusions and Future Work

Conclusions:

We have successfully completed the first of our objectives – developing an experiment to measure various quantities associated with how the behavior of a bubble changes in a variable acceleration environment.

We have made measurements at two different dissolved gas concentrations during flights on the KC-135, thus partially completing our third objective.

Future Work:

Though a model has been developed (Wyatt Master's Thesis, 00; Thomas, ASA Newport Beach, 99) it needs to be refined to better incorporate changing cabin pressure and effects due to diffusion.

Possibly one more flight on the KC-135 in September 2002 to finish taking data to complete objectives 3 and 4.

THEORY OF MICRO- AND MACRO- ENCAPSULATION

S.P. Lin and J.N. Chen
Department of Mechanical and Aeronautical Engineering,
Clarkson University, Potsdam, NY 13676-5725
Tel: 315-2686584 Fax: 315-2686438
Email: gw02@clarkson.edu

THEORY OF MACRO- AND MICRO- ENCAPSULATION

Macro-capsules are defined to be the capsules whose radii are larger than 100 μm. Micro capsules have radii between 100 μm and 10 μm. Continuum theory is valid for the investigation of macro-capsule and micro-capsules formation is expected to be valid up to the lower range of micro-encapsulation.

Consider the flow in an annular liquid jet of a constant thickness h, a constant inner radius R_i, and a constant outer radius R_0. The jet with density ρ and viscosity μ emanates from an annular nozzle which is coaxial with a circular cylinder of radius R_w. The fluid inside the annular jet has density ρ_i and μ_i. The jet is surrounded by another fluid of density ρ_0 and viscosity μ_0. All three fluids are Newtonian. The governing equations are the Navier-Stokes equations. The corresponding boundary conditions are the dynamic and kinematic boundary conditions at each fluid-fluid interface. And the no-slip conditions at the pipe wall. An exact solution for a steady basic flow which satisfies the governing differential system has been obtained [15]. The relevant flow parameters are: Weber number of the inner interface $We_i = \rho_i U^2 h / S_i$, Weber number of the inner interface $We_0 = \rho_0 U^2 h / S_0$, Reynolds number $\rho U^2 h / \mu$, Froude number $Fr = U^2 / gh$, viscosity ratios $N_i = \mu_i / \mu$, $N_0 = \mu_0 / \mu$, density ratios $Q_i = \rho_i / \rho$, $Q_0 = \rho_0 / \rho$, and radius ratios $r_i = R_i / h$, $r_0 = R_0 / h$, where S_i and S_0 are respectively the surface tension of the inner and the outer interface and U is the liquid jet velocity at $R = (R_i + R_0)/2$, R being the radial distance measured from the axis of the annular. The curve for $Fr^{-1} = 0$ in this figure corresponds to 0-g condition. The other curves correspond to the case of finite gravity.

The onset of instability of this basic flow with respect to temporal and spatial-temporal disturbances has been analyzed by use of a spectra collocation method. Extension of the well tested analytical and numerical method to the present problems is straightforward, but results in a relatively larger system for numerical computation which required a high precision. Extraction of information from the numerical results also becomes more laborious because of the larger number of flow parameters involved. The results we have obtained show that [1] there are two independent interfacial modes of convective instability. Two independent modes of instability were also found in the earlier work for a two dimensional plan liquid sheet as well as an annular jet in an invisid gas, i.e., sinuous and varicose modes [16, 17, 18]. Two interfaces move in phase in the sinuous mode but they move 180° out of phase in the varicose mode. However unlike the plan sheet, there is no surface of symmetry within the annulus, and consequently a completely in-phase or out-of-phase interfacial motion does not exit. Nevertheless the two independent modes of the interfacial motion are actually almost in phase or out of phase. They are call here para-sinuous and para-varicose modes. The emergence of either one of these modes or both of them

depends on the initial condition at the nozzle exit. This fact has an important practical implication in encapsulation applications. The onset of para-varicose mode needs to be suppressed, since it leads to breakup at the thinnest of the annulus and leaves part of the core material unencapsulated as depicted in Fig. 1. On the other hand the onset of para-sinuous mode should be promoted, since it leads to a uniform shell thickness as is also depicted in the same figure. This fact has not been made aware of in the know literature. Fig. 1 also shows the spatial exponential amplification rate k_i as functions of the wave length $\lambda = 2\pi hh/k_r$, k_r being the wave number, for two values of Fr and the rest of parameters specified in the caption. Note that the amplification curves for the two modes for the case of finite g corresponding to $Fr^{-1} = 10000$ intersect at point e. Below the wave number corresponding to point e the para-sinuous mode dominates. Above this wave number the para-varicose mode dominates. Hence if one attempts to produce macro capsules by introducing an external forcing with frequency corresponding to k_r for which the sinuous mode is unstable one will not be able to completely encapsulate the core material, because the para-varicose mode is also present. The same figure also shows that when the finite gravity is reduced to zero, the amplification curves (solid line) for the two modes cease to intersect and the para-varicose mode is absent between the two cutoff wave number f *and* f'. The para-sinuous and para-varicose modes are stable respectively if the wave numbers are larger than that at point f and f' in Fig. 1. Thus in the wave number range between f and f', one may impart a monocramatic external forcing of a frequency corresponding to the selected wave number, and excite a sinuous wave to initiate production of a capsule of desired radius.

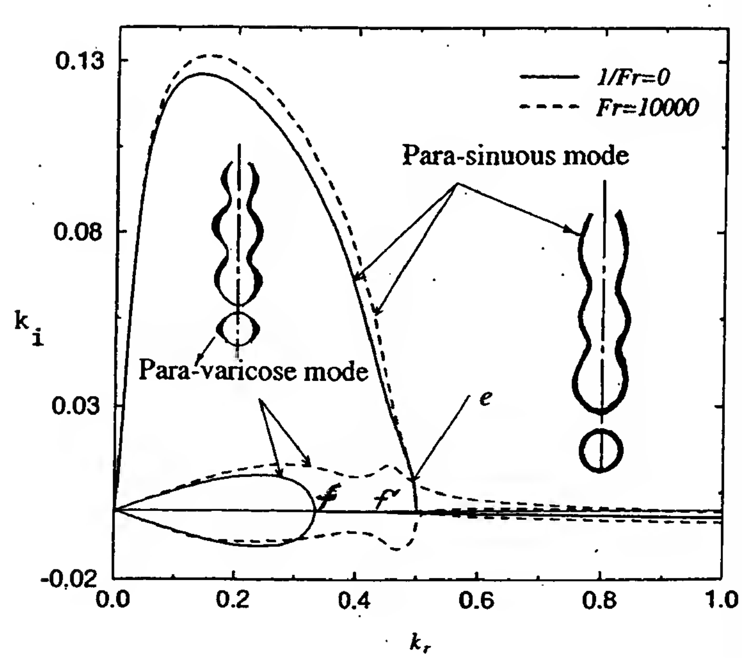

Figure 1. The effects of Froude number on the disturbance growth rate for both modes. Re=1000, We_i=We_o=20.0, Q_i=Q_o=0.0013, N_i=N_o=0.0018, r_i=r_w=13.

Enhancing the Thermocapillary Migration of Bubbles Retarded by the Adsorption of Surfactant Impurities By Using Remobilizing Surfactants

Charles Maldarelli
Levich Institute
Department of Chemical Engineering
City College of New York
Charles@chemail.engr.ccny.cuny.edu
(212)6508160

R. Balasubramaniam
National Center for Microgravity Research
NASA Glenn Research Center

Abstract

Thermocapillary migration is a method for moving bubbles in space in the absence of buoyancy. A temperature gradient is applied to the continuous phase in which a bubble is situated, and the applied gradient impressed on the bubble surface causes one pole of the drop to be cooler than the opposite pole. As the surface tension is a decreasing function of temperature, the cooler pole pulls at the warmer pole, creating a flow which propels the bubble in the direction of the warmer fluid. A major impediment to the practical use of thermocapillarity to direct the movement of bubbles in space is the fact that surfactant impurities which are unavoidably present in the continuous phase can significantly reduce the migration velocity. A surfactant impurity adsorbed onto the bubble interface is swept to the trailing end of the bubble. When bulk concentrations are low (which is the case with an impurity), diffusion of surfactant to the front end is slow relative to convection, and surfactant collects at the back end of the bubble. Collection at the back lowers the surface tension relative to the front end setting up a reverse tension gradient. (This can also be the case if kinetic desorption of surfactant at the back end of the bubble is much slower than convection.) For buoyancy driven bubble motions in the absence of a thermocapillarity, the tension gradient opposes the surface flow, and reduces the surface and terminal velocities (the interface becomes more solid-like and bubbles translate as solid particles). When thermocapillary forces are present, the reverse tension gradient set up by the surfactant accumulation reduces the temperature induced tension gradient, and can decrease to near zero the bubble's thermocapillary velocity.

The objective of our research is to develop a method for enhancing the thermocapillary migration of bubbles which have been retarded by the adsorption onto the bubble surface of a surfactant impurity. Our remobilization theory proposes to use surfactant molecules which kinetically rapidly exchange between the bulk and the surface and are at high bulk concentrations. Because the remobilizing surfactant is present at much higher concentrations than the impurity, it adsorbs to the bubble surface much faster than the impurity when the bubble is formed, and thereby prevents the impurity from adsorbing onto the surface. In addition the rapid kinetic exchange and high bulk concentration maintain a saturated surface with a uniform surface concentrations. This prevents retarding surface tension gradients and keeps the thermocapillary velocity high.

In this report, we detail experimental observations of remobilization for the buoyancy driven motion of air bubbles in a glycerol/water mixture.. Two polyethylene oxide surfactants were studied, $C_{12}E_6$ ($CH_3(CH_2)_{11}(OCH_2CH_2)_6OH$) and $C_{10}E_8$ ($CH_3(CH_2)_9(OCH_2CH_2)_8OH$). Measurements of the kinetic exchange for these surfactants show that the one with the longer hydrophobe chain $C_{12}E_6$ has a lower rate of kinetic exchange. In addition, this surfactant is much less soluble in the glycerol/water mixture because of the shorter ethoxylate chain. As a result, we found that $C_{12}E_6$ had no ability to remobilize rising bubbles because of the limited kinetic exchange and reduced solubility (Fig. 1). However, $C_{10}E_8$, with its higher solubility and more rapid exchange was found to dramatically remobilize rising bubbles (Fig. 2).

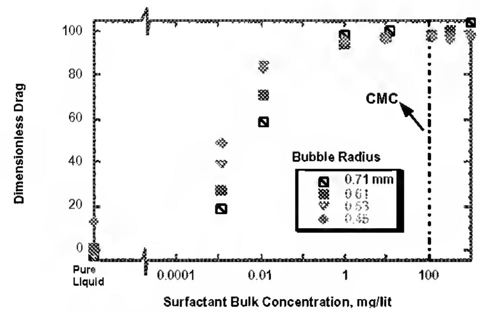

Figure 1: Effect of Addition of $C_{12}E_6$ on the Drag of a Bubble Rising in a 7:3 Glycerol/Water Mixture.

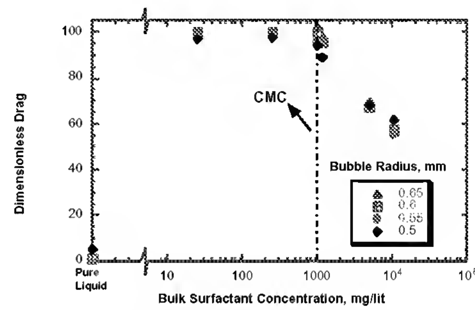

Figure 2: Effect of Addition of $C_{10}E_8$ on the Drag of a Bubble Rising in a 7:3 Glycerol/Water Mixture.

We also report results on describing theoretically the remobilization observed in our ground based buoyancy driven experiments. We construct a model in which a bubble rises steadily by buoyancy in a continuous (Newtonian) viscous fluid containing surfactant with a uniform far field bulk concentration. We account for the effects of inertia as well as viscosity in the flow in the continuous phase caused by the bubble motion (order one Reynolds number), and we assume that the bubble shape remains spherical (viscous and inertial pressure forces are smaller than capillary forces, i.e. small Weber and capillary numbers). The surfactant tension gradients which retard the surface velocity are incorporated by equating the viscous shear stress at the bubble surface to the surface tension gradient created by the surfactant surface concentration distribution. This distribution is calculated by solving the mass transfer equations including convection and diffusion in the bulk, and finite kinetic exchange between the bulk and the surface. Convective effects dominate diffusive mass transfer in the bulk of the liquid (high Peclet numbers) except in a thin boundary layer near the surface. A finite volume method is used to numerically solve the hydrodynamic and mass transfer equations on a staggered grid which accounts specifically for the thin boundary layer. We present the results of the nondimensional drag as a function of the bulk concentration of surfactant for different rates of kinetic exchange, and we compare our theoretical calculations to the experimental measurements of velocity for both the non-remobilizing and remobilizing surfactants, and found excellent agreement.

RIVULET DYNAMICS WITH VARIABLE GRAVITY AND WIND SHEAR

S. Wang, G. McAlister, J.S. Marshall, R. Ettema
IIHR – Hydroscience and Engineering, University of Iowa, Iowa City, IA 52242
jeffrey-marshall@uiowa.edu, FAX (319) 335-5669, phone (319) 335-5817

ABSTRACT

A combined computational and experimental study is conducted of the development of rivulets from a liquid sheet driven by wind shear in different gravitational states. The study concentrates on the effect of the normal component of gravity on rivulet formation and evolution. Understanding of rivulet development in the presence of wind shear is important for a number of coating processes, for modeling development of ice rivulets on aircraft wings and of water motion on vehicle windshields, and for modeling the breakup of annular flow in a tube into a rivulet flow regime. The current study is at the midway point of a four-year project.

The experimental part of the project has focused on the dynamics of gravity- and wind-driven rivulets. The experimental setup comprises a small "rivulet windtunnel", which consists of a flat plate into which a liquid is injected at an upstream location, and through which air flow passes. The entire setup is mounted on a mobile cart that can be tilted to angles varying from 0° to 90°. Preliminary experiments revealed significant differences in rivulet dynamics for gravity-driven and shear-driven cases. Gravity-driven rivulets initially formed as a lobe extending from the liquid source, which flowed for a short distance straight down the base surface and then eventually adopted a meandering form. Shear-driven rivulets start out in a similar manner to gravity-driven rivulets, but instead of extending as a long liquid finger the shear-driven rivulets exhibit an interesting phenomenon that we refer to as "blobbing". Blobbing (illustrated in Fig. 1) is a cyclical process whereby the rivulet progresses by formation of blobs, which enlarge and oscillate in the air flow. After some time a lobe in the blob's downstream side develops and the liquid extends downstream, thus draining the blob. The process then repeats at a downstream location.

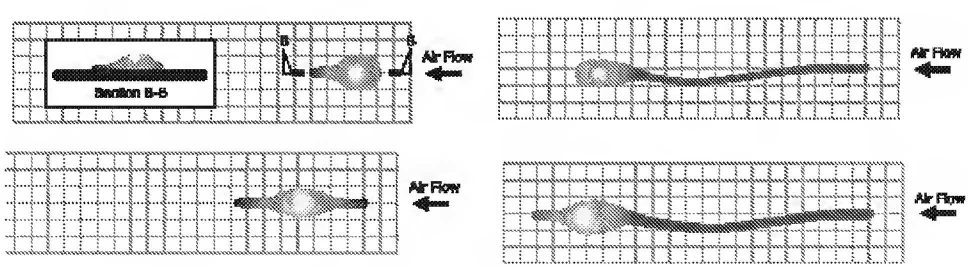

Fig. 1. Blob formation on a shear-driven rivulet.

The computational part of the project uses lubrication theory with a precurser film to remove the contact line singularity and constant surface shear stress. The effect of contact angle is modeled using a disjoining pressure approach. Two-dimensional equilibrium solutions for a shear-driven liquid film front are obtained which show that the ridge of liquid just downstream of the front has layer thickness which decreases with increase in the normal body force to the substrate. A linear stability analysis of the equilibrium liquid front indicates that the decrease in thickness of the front ridge leads to suppression of the fingering instability, and with sufficient normal body force may even eliminate the fingering instability. These results confirm and extend the analysis of Bertozzi and Brenner (*Phys. Fluids* **9**(3), 530-539, 1997) for flow down an inclined plate at different inclination angles. Nonlinear computations are performed using an ADI method which confirm the results cited above. The nonlinear computations (shown in Fig. 2) indicate that rivulet develop in the presence of normal body force proceeds in much the same manner as without body force, only more slowly. We are currently using the numerical computation method to investigate the effect of surface contamination on rivulet formation. In these computations, surface contamination is modeled by driving the liquid front over an array of either droplets or spots of different contact angle. This part of the study is examining the amplification that occurs as a small upstream perturbation passes through the liquid front, and the effect of this amplification on rivulet development for different normal gravity states. Our future computational work will couple a laminar wind flow calculation to the liquid film calculation in order to account for variable shear and pressure on the liquid surface. The wind flow computation will employ a finite-volume approach with moveable mesh, where the bottom boundary condition is set by the liquid layer thickness and velocity.

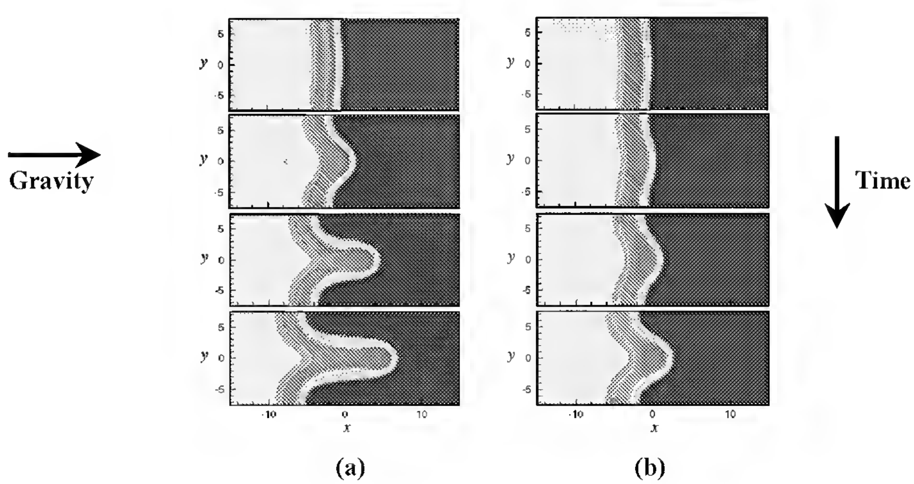

Fig. 2. Contours of liquid layer thickness as the fingering instability leads to rivulet formation, both (a) with no normal body force and (b) with normal body force parameter $P_2 = 0.5$.

Rivulet Dynamics With Variable Gravity and Wind Shear

Investigators

Principal Investigators: J.S. Marshall and R. Ettema
Students: S. Wang and G. McAlister

Department of Mechanical and Industrial Engineering
Department of Civil and Environmental Engineering
IIHR – Hydroscience and Engineering
The University of Iowa

Research Objectives

The objective of the project is to understand the effect of normal gravity on the initiation and development of rivulets in both shear-driven and gravity-driven flows. The computational work has focused on the effect of surface contamination on rivulet initiation. The experimental work has focused on the unique dynamics of shear-driven rivulets and breakup of the rivulets into liquid blobs.

Computations

Approach

Finite-difference computations are performed using an ADI method based on the lubrication-theory equations for a thin liquid layer. The computational model uses the precurser film method to remove the moving contact line singularity, and a disjoining pressure is introduced to account for effects of static contact angle.

Results

The effect of normal body force can be represented by a parameter $P_2 = Bo_V/(Bo_H + S)^{2/3}$, where Bo_H and Bo_V are the horizontal and vertical Bond numbers and $S = 3\tau\, h_\infty / 2\sigma$ is a dimensionless shear stress. The normal body force is found to decrease the thickness of the capillary ridge near a moving contact line and to suppress the fingering instability on a homogeneous surface (Fig. 1).

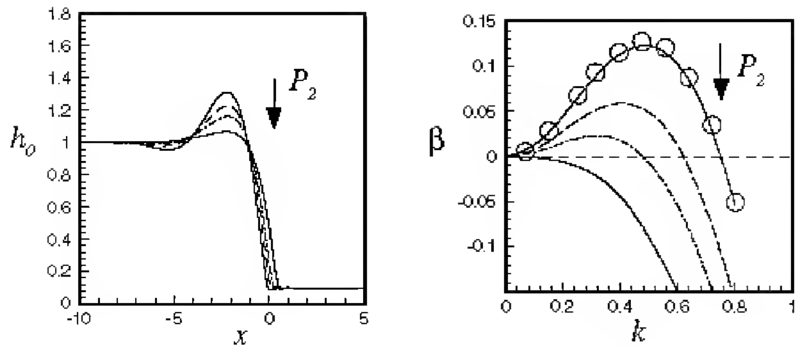

(a) (b)

Fig. 1. Effect of normal gravity parameter P_2 on (a) equilibrium profile and (b) plot of growth rate β versus wavenumber *k*.

A driven liquid layer front is sensitive to small inhomogeneities of the substrate surface, including droplets and variation in static contact angle. Parametric simulations were conducted to evaluate the liquid front's response to different types of surface inhomogeneities and to examine the resulting rivulet growth as the front passes through an array of such inhomogeneities. Examples are shown in Fig. 2. This study suggests that liquid front reaction to surface contamination may often play a larger role in rivulet development on untreated surfaces than does the fingering instability. Application of normal body force suppresses sensitivity of the front to surface imperfections, as shown in Fig. 3.

Liquid Front Impact on Droplet

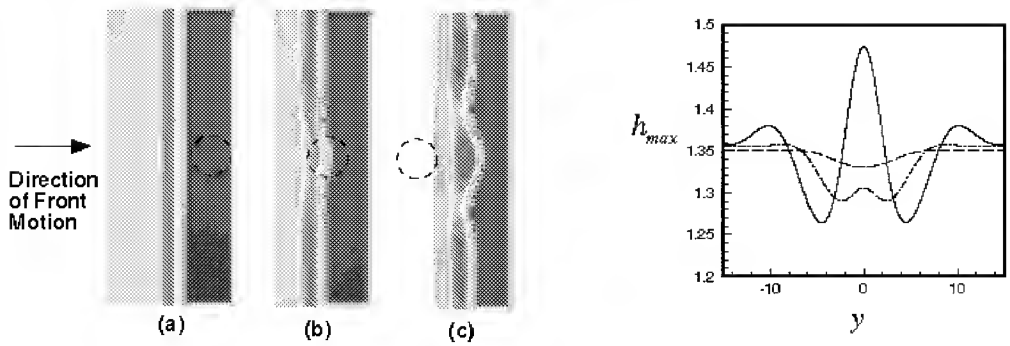

Liquid Front Impact on Spot of Negative Relative Contact Angle $\Delta\theta_E = -0.03$

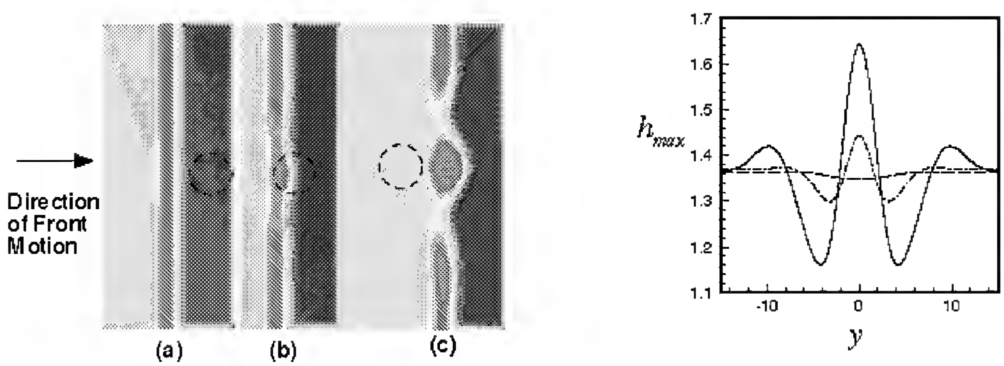

Liquid Front Impact on Spot of Positive Relative Contact Angle $\Delta\theta_E = 0.03$

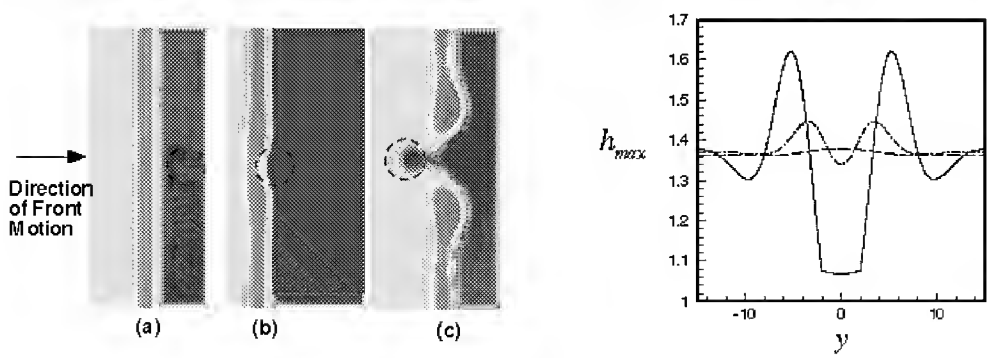

Figure 2. Time series showing impact of a driven liquid layer front on different types of surface inhomogeneities, along with the maximum values of layer thickness on lines $y = \text{const}$ at the same times. The spot/droplet radius and position is indicated by a dashed circle.

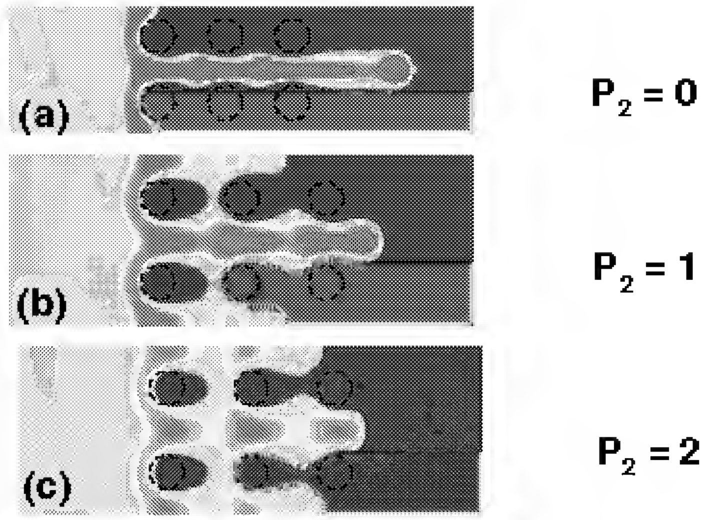

Fig. 3. Growth of rivulets as a driven front passes through an array of negative relative contact-angle spots for three different values of normal body force parameter. For all three cases the liquid front is stable to the fingering instability at the perturbation wavelength.

Experiments

Approach

Experiments with both gravity-driven rivulets (flowing down an inclined plane) and wind shear-driven rivulets have been performed in the laboratory using the device shown in Fig. 4. Microgravity experiments are planned for October, 2002. The wind velocity and plate inclination angle are adjustable.

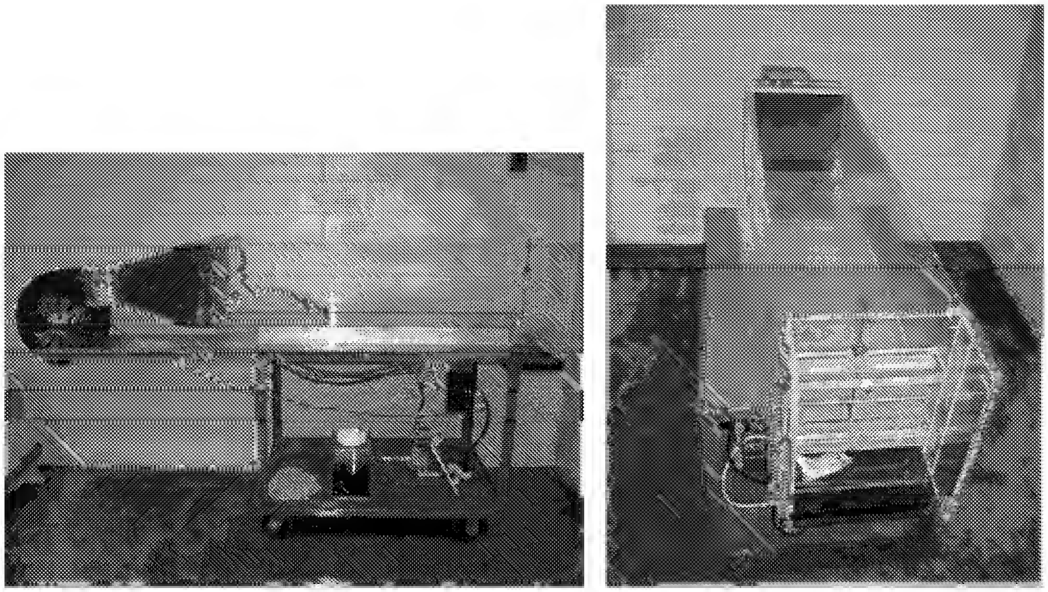

Fig. 4. Photographs of the experimental apparatus.

Results

Whereas the gravity-driven flow exhibits the usual meandering rivulet behavior (which has been recorded numerous times in previous literature), the shear-driven rivulet flow exhibits an entirely different behavior.

In the experiments with wind-driven rivulet flow, a rivulet forms from liquid ejection from a 2-mm opening and progresses downwind along a horizontal smooth Plexiglas plate. The rivulet initially has a nearly uniform cross section, with a slightly larger amount of water at the downstream end (head) of the rivulet. After the rivulet has progressed for a short distance, it is observed to stop and form a blob of liquid at its downstream end, which is fed by the rivulet and continues to increase in size with time. As the blob increases in size and spreads laterally, it experiences an increased aerodynamic load. Eventually the blob grows large enough that the aerodynamic shear force exceeds the retarding surface tension force, leading to detachment of the blob from the rivulet (Fig. 5a). Once the blob has detached, the head of the rivulet generally does not progress downstream. Flow from the rivulet continues to feed the head of the rivulet, leading to formation of a new blob and a periodic repetition of the process described above.

The detached blob reshapes itself in accordance with the airflow pressure distribution and surface tension and bottom shear forces. The blob travels downstream at an approximately constant speed with a characteristic double-lobed shape that is elongated in the cross-stream direction (Fig. 5b). The liquid layer is significantly thicker within the lobes at the ends of the elongated blob than within the center of the blob. Sometimes a blob will bifurcate within its thin middle section, forming two smaller blobs. These

smaller blobs in turn adopt the characteristic elongated double-lobed shape, but they travel much more slowly than the original blob and sometimes stop entirely. There seems to be an optimal size for downstream-propagating blobs, where blobs larger than this optimum break up into two and blobs smaller than this optimum travel slowly and are eventually absorbed into impacting larger blobs.

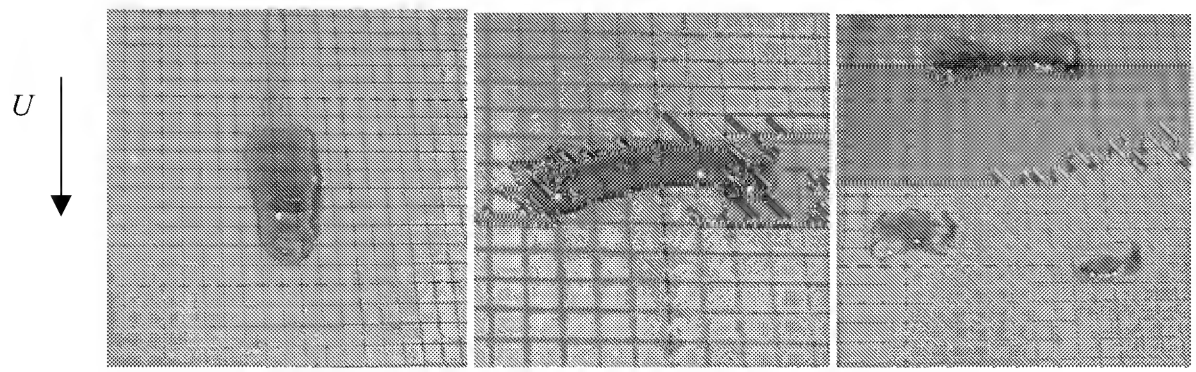

(a) (b) (c)

Fig. 5. Photographs for shear-driven flow showing (a) breakup of rivulet into a blob, (b) close-up view of the elongated double-lobed form of the blob, and (c) a larger blob overtaking two smaller blobs.

On-Going Research

Computations

- Simulation of wind-shear driven flows including pressure variation on liquid –gas interface
- Effect of fluid inertia on liquid front sensitivity to surface inhomogeneities

Experiments

- Effects of microgravity and excess gravity on rivulet breakup and blob motion
- Quantitative measurement of lay thickness using fluorescent imaging

Publications

Wang, S. and Marshall, J.S., "Effect of normal body force on fingering instability of a liquid sheet driven by shear stress or gravity," Joint ASME-European Fluids Engineering Summer Conference, Montreal, July 14-18, 2002.

Wang, S. and Marshall, J.S., "Contact-line receptivity and rivulet formation in the presence of droplets and surface contamination," *Physics of Fluids* (submitted).

Wang, S., " Contact-line receptivity and rivulet initiation in the presence of droplets and surface contamination," M.S. thesis, University of Iowa, Iowa City (2002).

ACOUSTIC EXPERIMENT TO MEASURE THE BULK VISCOSITY OF NEAR-CRITICAL XENON IN MICROGRAVITY

K.A. Gillis, I. Shinder, and M.R. Moldover
National Institute of Standards and Technology, Gaithersburg, MD 20899

G.A. Zimmerli
National Center for Microgravity Research, Cleveland, OH 44135

ABSTRACT

We plan a rigorous test of the theory of dynamic scaling by accurately measuring the bulk viscosity of xenon in microgravity 50 times closer to the critical temperature T_c than previous experiments. The bulk viscosity ζ (or "second viscosity" or "dilational viscosity") will be determined by measuring the attenuation length of sound α_λ and also measuring the frequency-dependence of the speed of sound. For these measurements, we developed a unique Helmholtz resonator and specialized electro-acoustic transducers. We describe the resonator, the transducers, their performance on Earth, and their expected performance in microgravity.

Any fluid very near its liquid-vapor critical point contains highly-correlated density fluctuations characterized by a long relaxation time τ. When $\omega\tau \geq 1$ [where $\omega = 2\pi/$(period of sound wave)] the attenuation of the sound greatly exceeds the attenuation calculated from the shear viscosity and thermal conductivity. The excess sound attenuation is associated with dilatational motion of the fluid and is accounted for by the bulk viscosity. The excess attenuation encountered in monatomic, near-critical, xenon somewhat resembles the excess attenuation encountered in polyatomic molecules that have a long relaxation time characterizing energy exchange between translational and internal degrees of freedom

According to the theory of dynamical scaling, both the attenuation length α_λ and the sound-speed dispersion become universal functions of $\omega\tau$ as the reduced temperature $t \to 0$. [Here $t \equiv (T - T_c)/T_c$.] The best prior tests of the theory were conducted in near-critical xenon and helium [1,2] at frequencies of 0.5 MHz and higher. These tests encountered the condition $\omega\tau = 1$ at $t \approx 10^{-3}$. The experimenters introduced empirical parameters to describe how their $\alpha_\lambda(\omega\tau)$ data might cross over from the experimentally accessible region to the expected asymptotic region at smaller values of t. Even with such parameters, the data disagreed with theory, within combined uncertainties. Because we are using lower frequencies (130 Hz to 1300 Hz) and because we will use microgravity to evade the stratification of near-critical xenon in the Earth's gravity, we expect to encounter $\omega\tau < 1$ at $t \approx 2 \times 10^{-5}$, 50 times closer to T_c.

For these measurements, we designed the acoustic resonator shown in Figs. 1a and 1b. It is composed of two chambers connected by a small tube. The chambers are cylindrical with perpendicular axes. The chambers have nearly equal volumes (~10 cm^3), but very different aspect ratios. One is 48 mm long with a 16 mm ID; the other is 22.2 mm long with a 23.5 mm ID. The connecting tube is 15 mm long with a 4 mm ID. This resonator has two low-frequency acoustic modes that are well separated from each other and all other modes. The lowest-frequency mode is a Helmholtz mode in which the gas oscillates between the chambers through the small tube. In the next mode, the gas oscillates along the length of the longer chamber. For these two modes in microgravity, Figure 2 shows the expected contributions to the acoustic losses Q^{-1} from the bulk

viscosity, the shear viscosity, and the thermal conductivity. On Earth, the stratification of the xenon's density from the top to the bottom of the resonator will prevent accurate measurements of the bulk viscosity closer than 150mK to the critical point ($t < 5 \times 10^{-4}$).

(a) Fig. 1 (b)

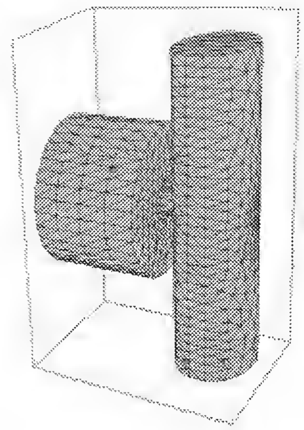

Two types of transducers have been developed to both excite and detect sound. The first type uses piezo-ceramic disks epoxied to the outside of a 2.5mm thick diaphragm at each end of the chambers. Flexure of the diaphragms couples to the radial displacement of the ceramics and, therefore, to the voltages that are applied or detected at the electrodes. The advantages of this technique are (1) electrical feedthroughs are not necessary, (2) no foreign materials come in contact with the xenon, and (3) coupling to the xenon is independent of temperature.

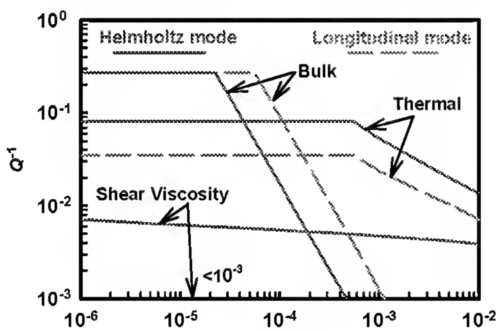

Fig. 2 Fig. 3

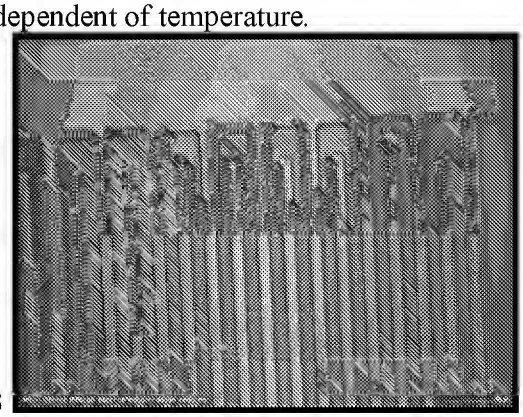

The second type of transducer is immersed in the xenon. It consists of closely-spaced (< 10 µm), interdigitated electrodes deposited on a quartz substrate. (The electrodes are the lighter areas in Fig. 3.) For detecting sound, the electrodes are biased with a DC voltage. An impinging acoustic wave changes the density of the xenon near the electrodes. The resulting change in capacitance generates an AC signal. To generate sound, an AC voltage V at frequency f is applied to the interdigitated electrodes. The resulting electric field creates a pressure (proportional to V^2) that pulls the xenon towards the electrodes at frequency $2f$. This phenomenon is called electrostriction. The advantages of the interdigitated transducers are (1) the frequency response is straight forward to model, (2) low dissipation, (3) no cross talk between drive and detection circuits, and (4) the sensitivity increases with the isothermal compressibility as $t \rightarrow 0$.

[1] Garland, C. W., and R. D. William, 1974, Phys. Rev. **A10**, 1328.
[2] Doiron, T., Gestrich, D., and H. Meyer, 1980, Phys. Rev. **B22**, 3202.

BVX: An Acoustic Experiment to Measure the Bulk Viscosity of Near-critical Xenon in Microgravity

Iosif I. Shinder, Keith A. Gillis (Co-I), Michael R. Moldover (PI)
National Institute of Standards and Technology, Gaithersburg, MD 20899
and Gregory A. Zimmerli (Co-I)
NASA Glenn Research Center, Cleveland, OH 44135

We plan a rigorous test of the theory of dynamic scaling by accurately measuring the bulk viscosity of xenon in microgravity 50 times closer to the critical point than previous experiments. The bulk viscosity ζ (also "second viscosity" or "dilational viscosity") will be determined from measurements of sound attenuation α_λ and dispersion. For these measurements, we have developed a unique acoustic resonator (Greenspan viscometer) and specialized electro-acoustic transducers.

The resonator is an asymmetric double-chamber Helmholtz resonator designed so that the 2 lowest frequency modes are isolated and non-degenerate. The lowest mode is a Helmholtz mode, characterized by alternating gas flow from one chamber to the other through a small connecting tube. This mode has a very long wavelength (0.5m) and low frequency (120 Hz). The next mode is the 1st longitudinal mode of one chamber, which occurs when the wavelength (0.1m) is twice the chamber's length.

With these two modes, we will measure the dissipation and dispersion between t = 1x10^{-3} and 1x10^{-5} in microgravity. Initial ground-based experiments will demonstrate the saturation of thermal boundary layer dissipation. These measurements and others will provide a means to optimize the resonator design so that the most accurate measurements over the widest temperature range will be possible in microgravity.

Motivation

- The attenuation length α_λ and the sound-speed dispersion become universal functions of $\omega\tau$ as $t \to 0$, according to dynamic scaling theory.

- The best prior tests of the theory were conducted on Earth in near-critical xenon and helium at frequencies of 0.5 MHz and higher. These tests encountered the condition $\omega\tau = 1$ at $t \approx 10^{-3}$.

- Empirical parameters were used to describe how their $\alpha_\lambda(\omega\tau)$ data might cross over from the experimentally accessible region to the expected asymptotic region at smaller values of t. The data did not agree with theory within the combined uncertainties.

Our approach

- We use lower frequencies (120 Hz to 1300 Hz) and plan to use microgravity to evade the stratification of near-critical xenon in Earth's gravity. We expect to encounter $\omega\tau < 1$ at $t \approx 2 \times 10^{-5}$, 50 times closer to T_c than previous measurements.

- Initial ground-based experiments will verify the saturation of thermal boundary layer dissipation for $t \leq 5 \times 10^{-4}$. Gravity will limit bulk viscosity measurements for $t \leq 1 \times 10^{-3}$.

- Micro-interdigitated electrode capacitors are being developed as electro-acoustic transducers based on the principle of electrostriction.

The critical point

The critical point is the highest temperature where liquid and vapor can coexist in the same container. For xenon, T_c = 16 °C, P_c = 58 Atm.

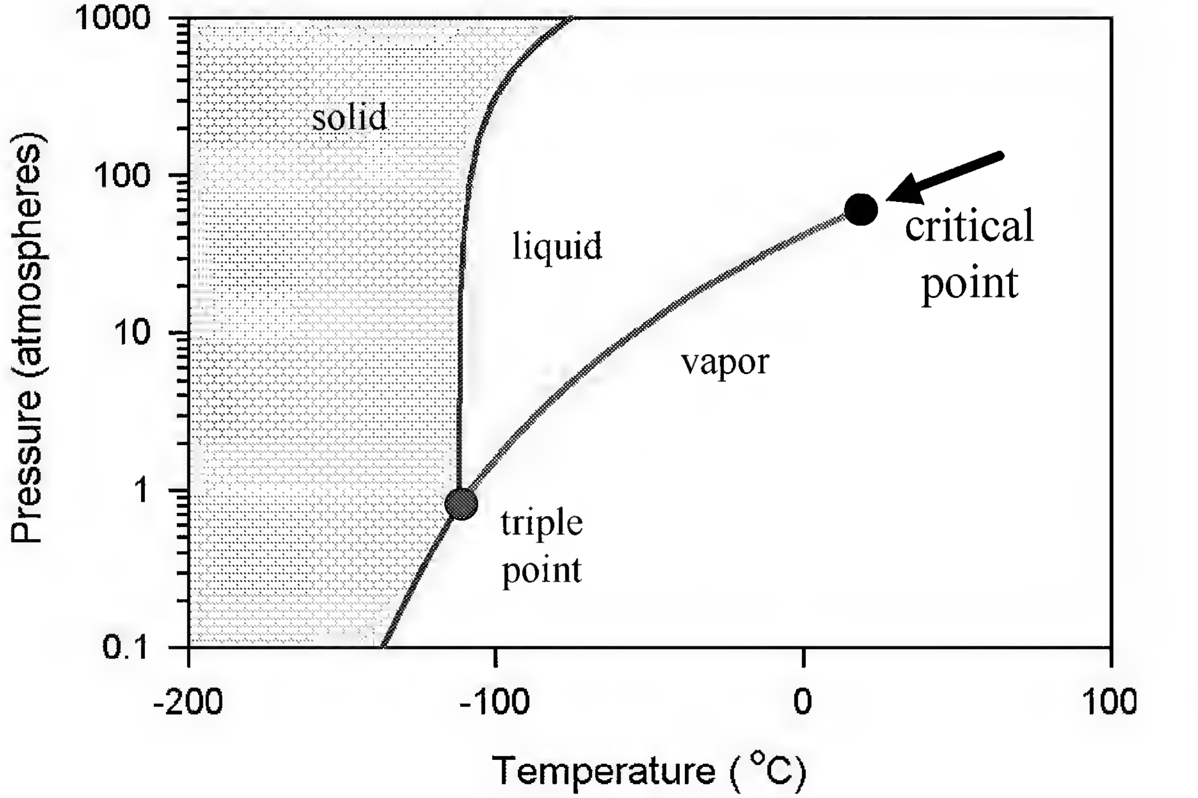

Critical Fluctuations

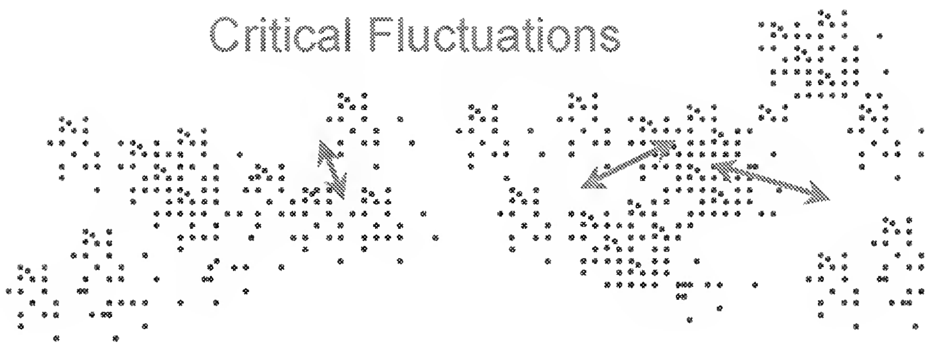

The sizes of the fluctuations are characterized by the correlation length ξ. If the density is exactly the critical density

$$\xi = \xi_0 \left(\frac{T - T_c}{T_c} \right)^{-?} = \xi_0 t^{-?} = 1.84 \times 10^{-10} t^{-0.63} \mathrm{m}$$

Thus, ξ reaches 1.1 μm at $t = 10^{-6}$, corresponding to 0.3 mK above T_c.

Large ξ implies intense light scattering, critical opalescence.

ξ is a natural measure of the distance from the critical point and governs thermodynamic behavior in the critical region.

Bulk Viscosity

- Bulk viscosity ζ of a fluid represents a resistance in the relationship between density and pressure that arises from the conversion of kinetic energy between translational and internal degrees of freedom governed by one or more relaxation times τ_i.

- Sound waves are oscillating pressure/density fields that will exhibit attenuation and dispersion due to bulk viscosity when $2\pi f \tau_i \approx 1$

$$\alpha_\lambda = \frac{\pi\omega}{c^2}\left(\underbrace{(\gamma-1)\frac{\lambda}{\rho C_p}}_{\text{Heat conduction}} + \underbrace{\frac{4}{3}\frac{\eta}{\rho}}_{\text{shear viscosity}} + \underbrace{\frac{\zeta}{\rho}}_{\text{bulk viscosity}} + \underbrace{(\gamma-1)\frac{c^2}{\omega}\frac{C_{\text{relax}}}{C_p}\frac{\omega\tau}{1+(\omega\tau)^2}}_{\text{bulk viscosity from one slowly relaxing mode}} \right)$$

- Important for polyatomic fluids at low densities

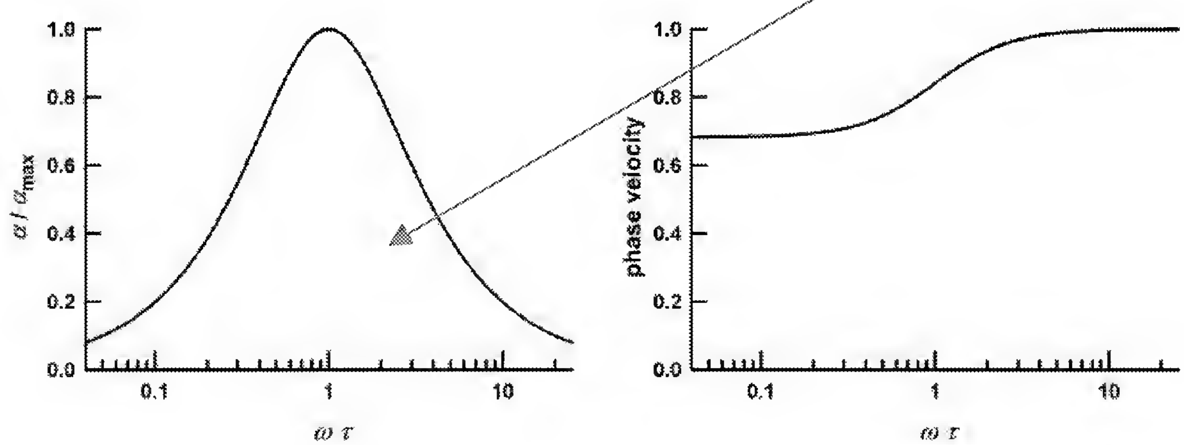

Bulk Viscosity

- Near critical points, monatomic fluids behave like polyatomic fluids with an infinite number of slowly relaxing modes. The distribution of relaxation times is characterized by:

$$\tau \equiv 6\pi\eta\xi^3/\left(k_B T_c\right) = \tau_0 t^{-\nu\left(3+z_\eta\right)} = \tau_0 t^{-1.93}, \qquad t \equiv \left(T - T_c\right)/T_c$$

$$\zeta \approx R_B \tau \rho_c c^2 \propto \xi^{2.89} \propto t^{-1.82}$$

Kogan and Meyer, 1998

Measurements and theory do not agree.
Limitations of high frequency and gravity.

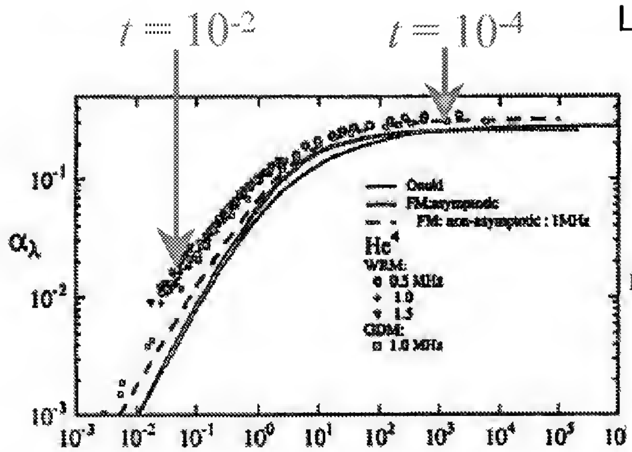

$\omega^* = 2\pi f\, \xi^2 / D_T$

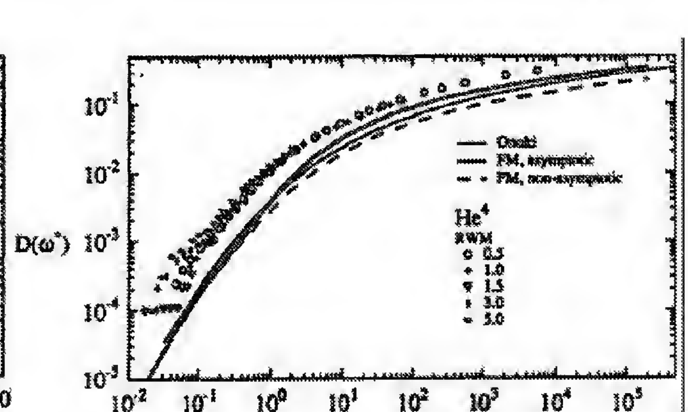

$\omega^* = 2\pi f\, \xi^2 / D_T$

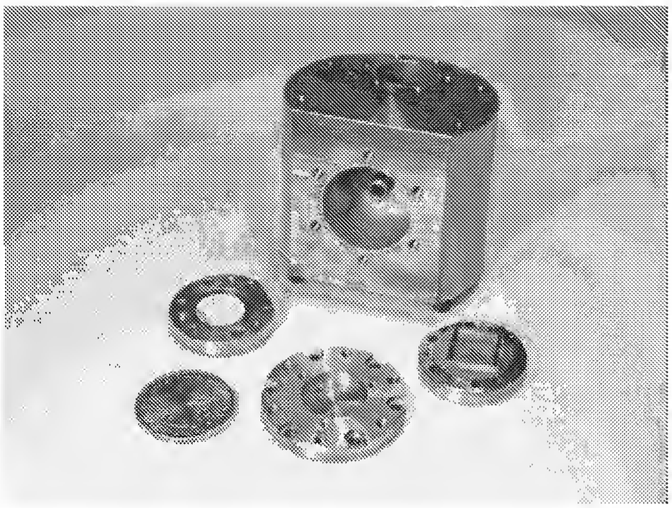

Helmholtz mode

$$f_H \approx \frac{c}{2\pi}\sqrt{\frac{A_d}{L_d}\left(\frac{1}{V_1}+\frac{1}{V_2}\right)} \quad [120-240\text{Hz}]$$

$$Q_H^{-1} = \frac{2g}{f} \approx \frac{\zeta}{\rho c}\sqrt{\frac{A_d}{L_d}\left(\frac{1}{V_1}+\frac{1}{V_2}\right)}$$

$$+(\gamma-1)\frac{\delta_T S_c}{2V_c} \quad [0.01-0.3]$$

Longitudinal mode

$$f_L \approx \frac{c}{2L_1} \qquad [650-1300\text{Hz}]$$

$$Q_L^{-1} \approx (\gamma-1)\left(1+\frac{2r_1}{L_1}\right)\frac{\delta_T}{r_1}+\frac{\pi\zeta}{L_1\rho c}$$

$$[0.01-0.3]$$

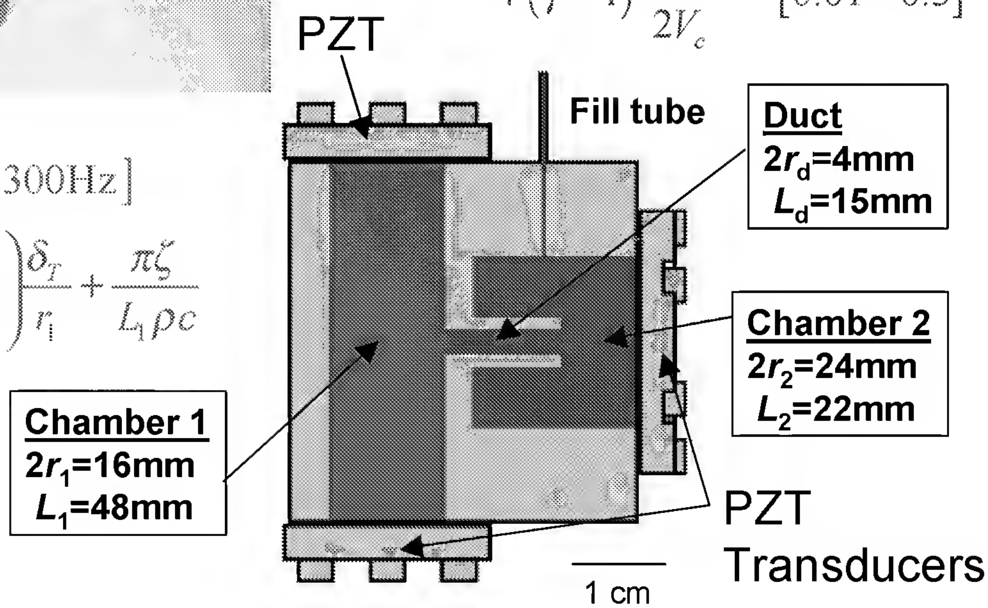

Expected Results

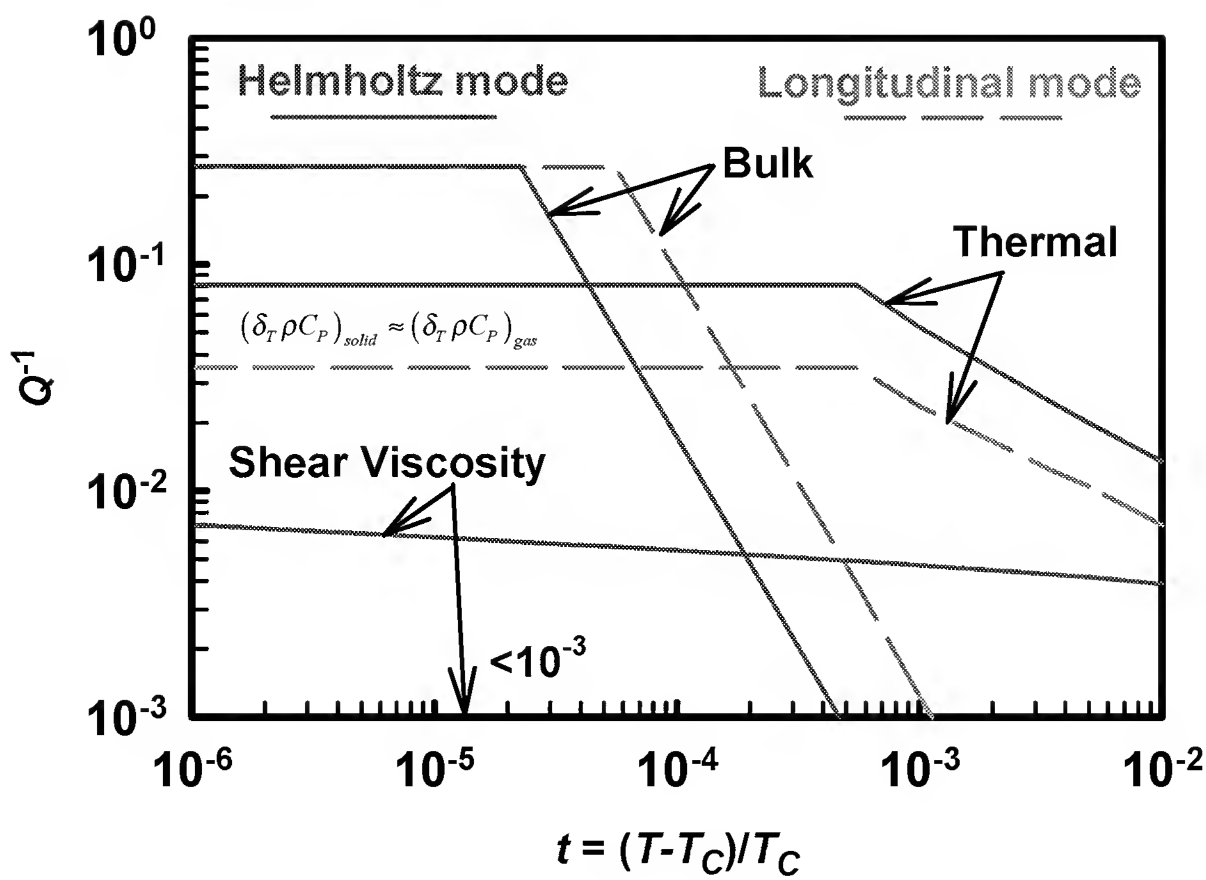

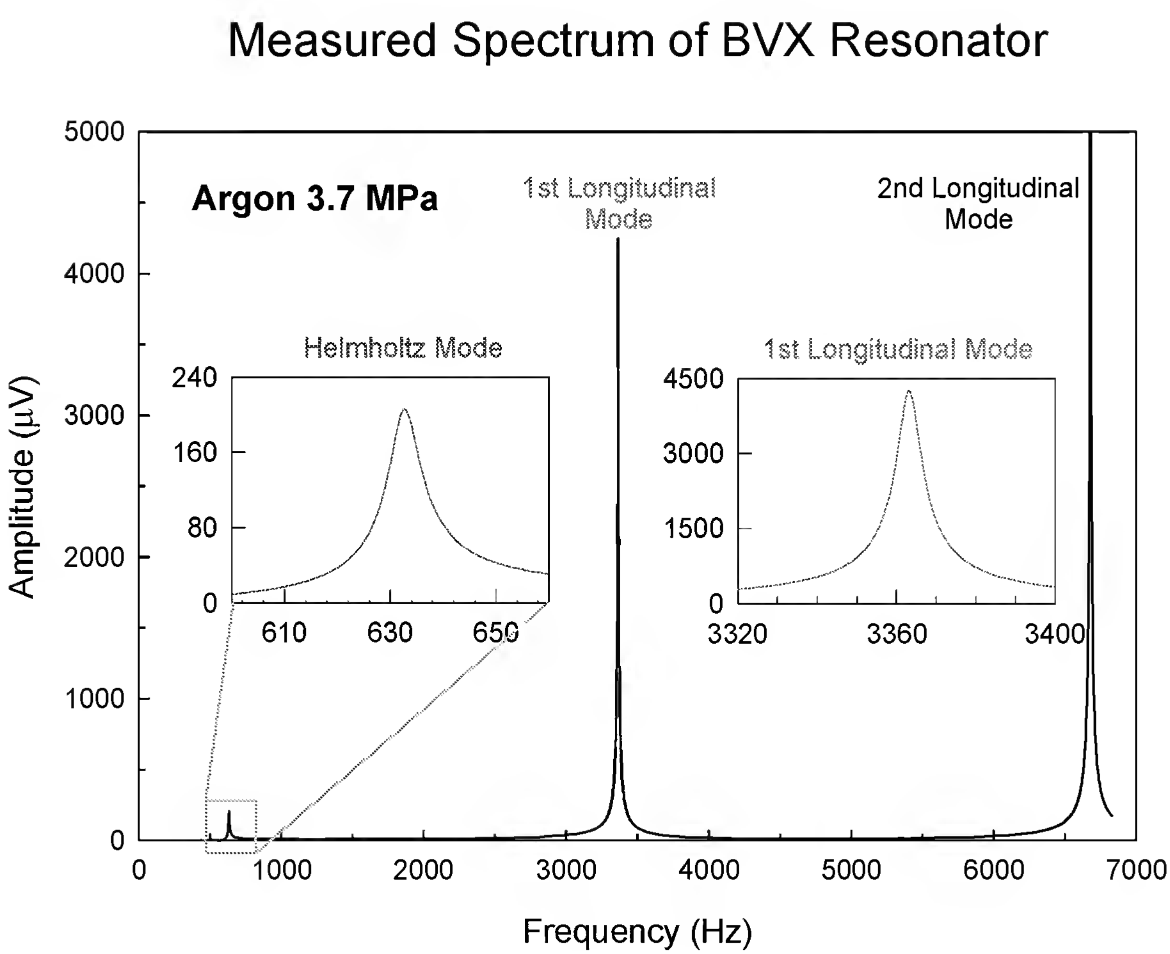
Measured Spectrum of BVX Resonator
Argon 3.7 MPa
1st Longitudinal Mode
2nd Longitudinal Mode
Helmholtz Mode
240
160
80
0
610
630
650
1st Longitudinal Mode
4500
3000
1500
0
3320
3360
3400
5000
4000
3000
2000
1000
0
Amplitude (μV)
0
1000
2000
3000
4000
5000
6000
7000
Frequency (Hz)

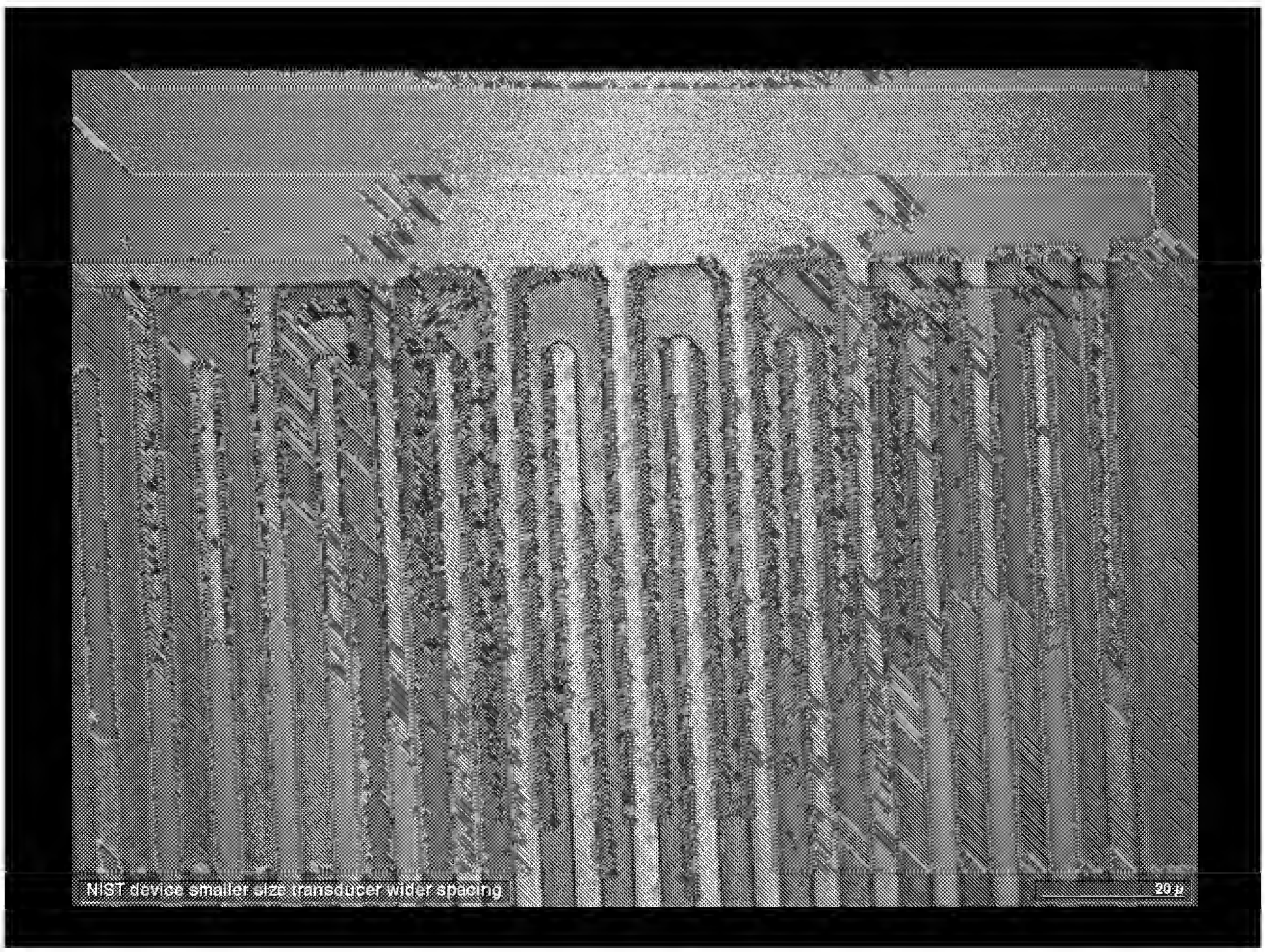
NIST device smaller size transducer wider spacing
20 μ

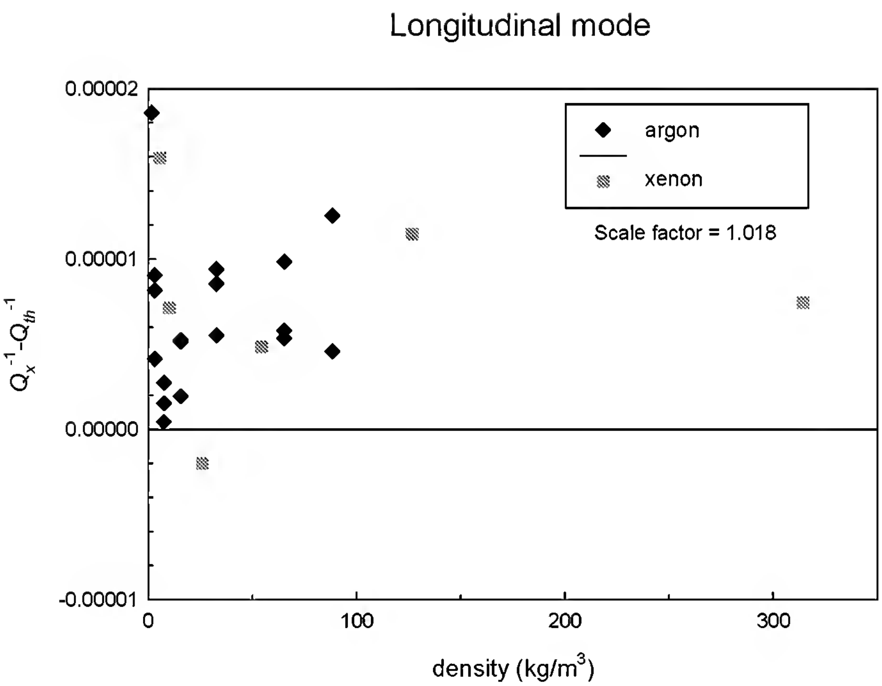
Longitudinal mode
argon
xenon
Scale factor = 1.018
0.00002
0.00001
0.00000
-0.00001
$Q_x^{-1}-Q_{th}^{-1}$
0
100
200
300
density (kg/m^3)

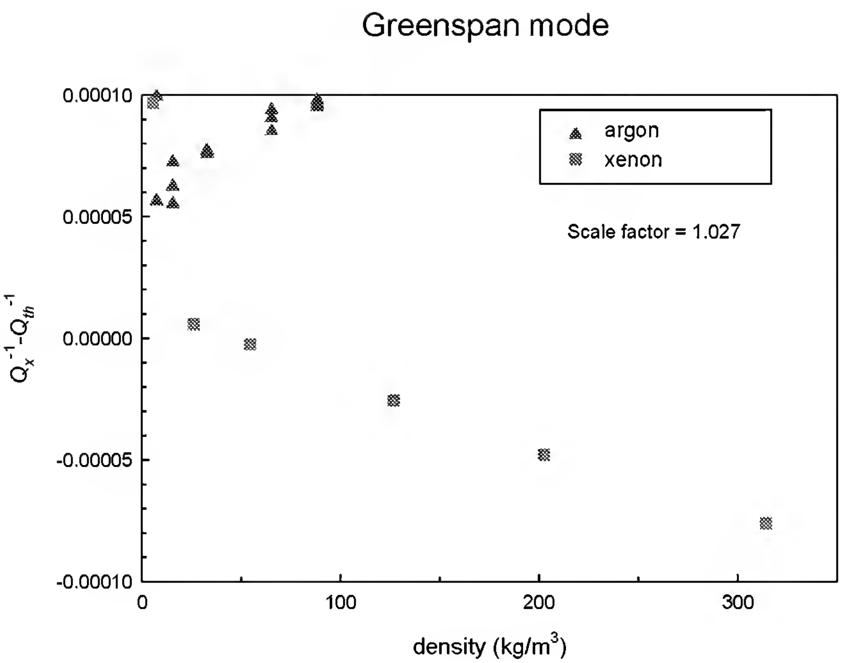
Greenspan mode
0.00010
0.00005
0.00000
-0.00005
-0.00010
Q_x^{-1}-Q_{th}^{-1}
0
100
200
300
density (kg/m^3)
argon
xenon
Scale factor = 1.027

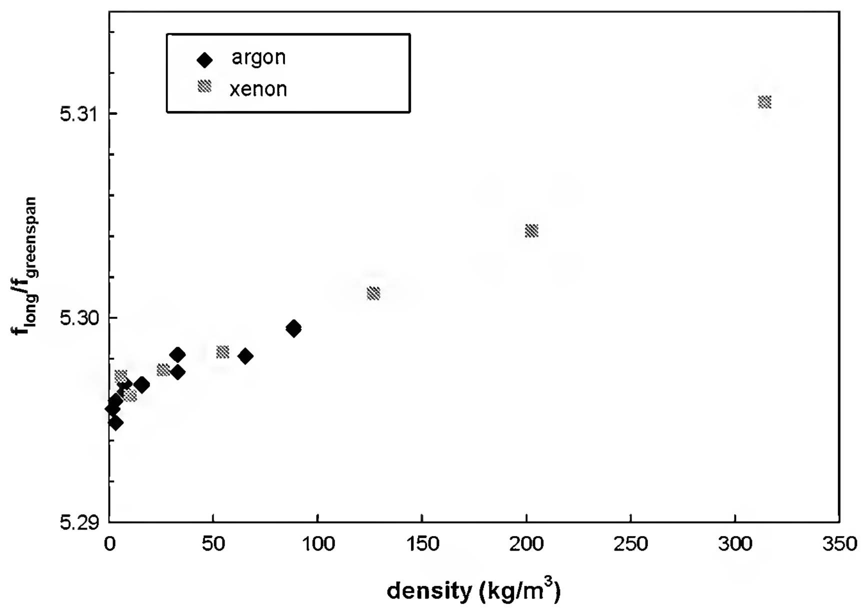
argon
xenon
5.31
5.30
5.29
0
50
100
150
200
250
300
350
density (kg/m3)
flong/fgreenspan

SUBMERGED GAS INJECTION FROM A TUBE IN MICROGRAVITY

J. Carrera, R. N. Parthasarathy, S. R. Gollahalli
School of Aerospace and Mechanical Engineering
The University of Oklahoma
212 Felgar Hall, 865 Asp Avenue
Norman, OK 73019
E-mail: rparthasarathy@ou.edu
Tel: 405-325-1735
Fax: 405-325-1088

ABSTRACT

The effects of buoyancy on the flow regimes, the bubble characteristics, and the bubble detachment mechanisms of submerged gas injection from a free-standing capillary tube were studied. The effects of liquid coflow, reduced surface tension, and increased viscosity were also analyzed. The microgravity experiments were carried out in the 2.2 Second Drop Tower at the NASA Glenn Research Center. The two-phase flow rig (97cm x 41cm x 84 cm) was totally autonomous from the instant of release in the drop tower; photographs of the bubbles were captured by a high-speed camera and stored on the onboard computer. A Lexan rectangular test section with the dimensions: 5cm x 5cm and 41cm in height was used. The injection was vertically upwards from a free-standing tube of 0.51mm in diameter and 150mm in length. The dimensions of the test section ensured that the confinement effects on the bubble formation were minimized for low gas flow rates.

The liquid velocity could be varied from 2 cm/s to 4 cm/s by means of a compressed air system. For all gas and liquid throughputs tested, a pre-flowing procedure of the two phases was followed for an interval of ten seconds before every drop to bring the system to steady state conditions. To reduce the surface tension, a non-ionic surfactant (ChemSurf 90) was added to the deionized water. For the increased liquid viscosity experiments, a mixture of deionized water and glycerin was used. Video images were recorded with a high-speed camera (Kodak EktaPro RO Imager) at a rate of 500 frames/second using backlighting against a reflective white surface. The camera began to record 200ms after the drop was initiated to avoid the transient environment from normal gravity to microgravity conditions. All images were analyzed with a computer image-processing unit.

For the experiments of gas injection into a quiescent liquid, bubble detachment was observed for all the Weber numbers tested (0.28 to 31.12). Also, the bubbles were effectively displaced from the near-injector region. Experiments with liquid coflow (2 cm/s and 4 cm/s), and low gas flow rates indicated faster and more controllable bubble detachment than those injected into a quiescent liquid. For high gas flow rates (We > 10) with the liquid coflow, the bubble sizes were more uniform when compared to injection in a quiescent liquid. Similarly, reduced surface tension (4.2mN/m) decreased detachment times, resulting in smaller and more uniform bubbles.

For the range of Weber numbers tested with the addition of surfactant (0.75 to 81.06), bubble detachment as well as effective bubble displacements was observed for all the conditions tested. An increase in liquid viscosity slowed down the detachment process, resulting in larger bubbles. Bubble detachment was observed for the Weber numbers ranging from 0.74 to 37.12. However,

the bubbles were never effectively displaced from the near injector area for Weber numbers < 4. Bubble formation under quiescent liquid conditions in microgravity is illustrated in Figure 1. The present experimental results highlight the differences observed between bubbles formed in gas injection from free-standing tubes and those formed when the gas is injected from a plate-orifice.

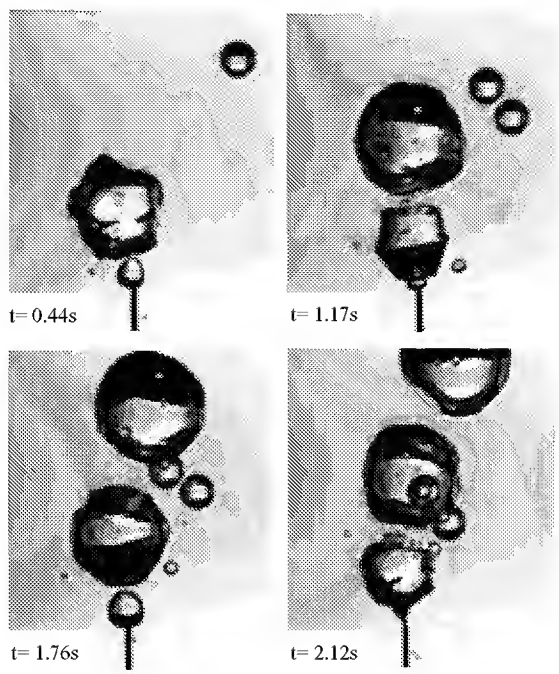

Fig. 1 Bubble formation in quiescent liquid in microgravity, We = 3.02

NASA/CP—2002-211212/VOL2

SUBMERGED GAS INJECTION INTO LIQUID IN MICROGRAVITY

J. Carrera, R.N. Parthasarathy, S.R.Gollahalli
UNIVERSITY OF OKLAHOMA

Acknowledgments:
John McQuillen, Brian Motil
NASA GRC

Fluid Dynamics Laboratory
School of Aerospace and Mechanical Engineering
University of Oklahoma, Norman

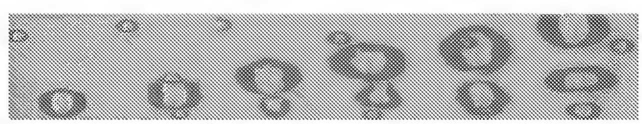

Objectives

- **Bubble formation in Microgravity**
  - Effects of Injector Geometry
  - Reduced Surface Tension
  - Increased Liquid Viscosity
  - Presence of Liquid Coflow

Fluid Dynamics Laboratory
School of Aerospace and Mechanical Engineering
University of Oklahoma, Norman

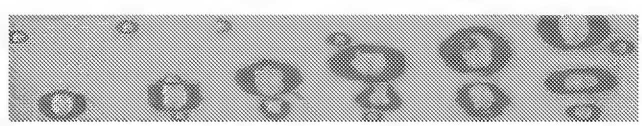

NASA/CP—2002-211212/VOL2

Experimental Set-up

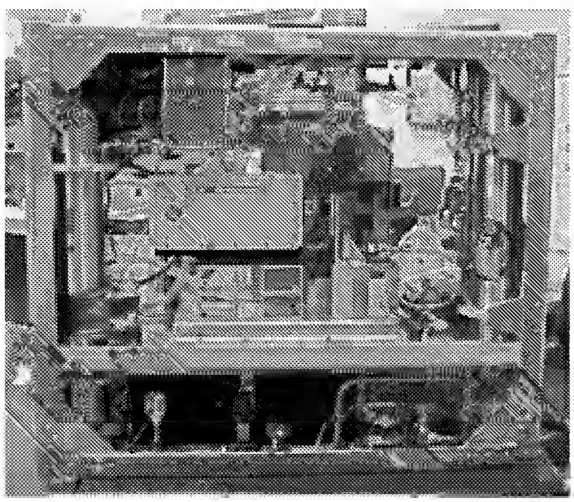

- **TUBE**
  - Diameter = 0.51 mm
  - Length = 150 mm
- **ORIFICE**
  - Diameter = 0.51 mm
  - Chamber Volume = 920 mm^3
- **TEST SECTION**
  - 5 x 5 x 41 cm

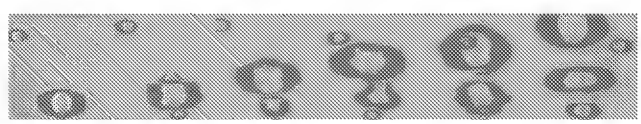

Results

Low Gas Flow Rates

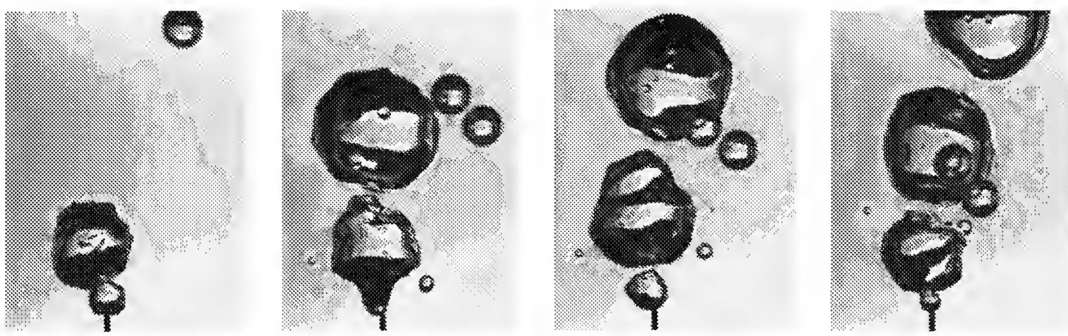

Time = 0.23s | Time = 1.25s | Time = 1.56s | Time = 2.12s

Bubble Formation (We = 3.0) from a Free-Standing Tube in Quiescent Liquid (scale 1: 0.42)

Fluid Dynamics Laboratory
School of Aerospace and Mechanical Engineering
University of Oklahoma, Norman

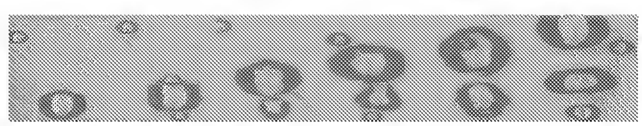

Sixth Microgravity Fluid Physics and Transport Phenomena Conference , 2002

Results

Medium Gas Flow Rates

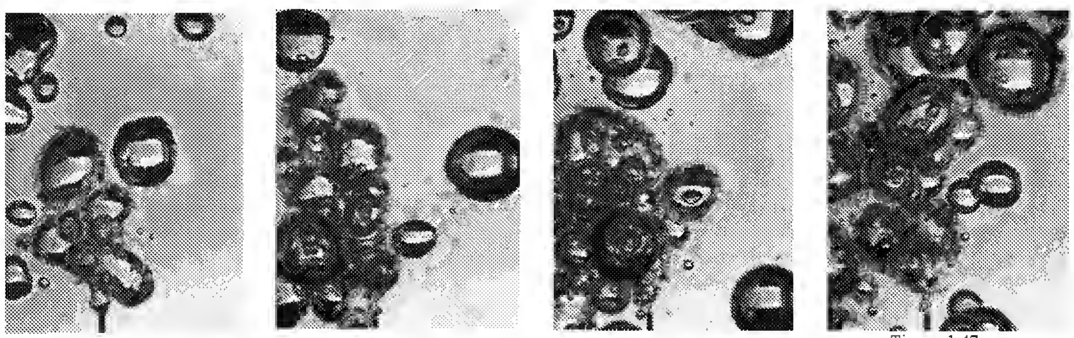

Time = 0.23s Time = 0.73s Time = 1.38s Time = 1.47s

Bubble Formation (We=18.6) from a Free-Standing Tube in a Quiescent Liquid (scale 1: 0.42)

Fluid Dynamics Laboratory
School of Aerospace and Mechanical Engineering
University of Oklahoma, Norman

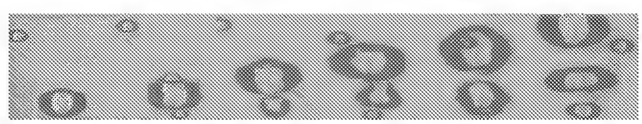

Results

High Gas Flow Rates

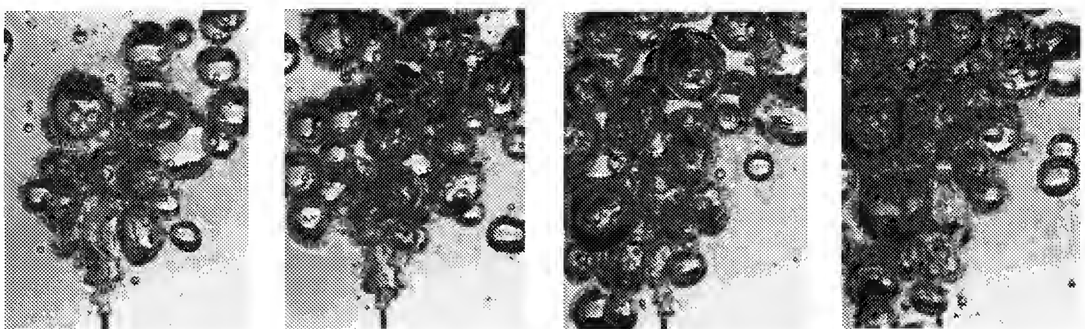

Time = 0.23s Time = 0.55s Time = 1.03s Time = 1.33s

Bubble Formation (We = 28.4) from a Free-standing Tube in a Quiescent Liquid(scale 1: 0.42)

Fluid Dynamics Laboratory
School of Aerospace and Mechanical Engineering
University of Oklahoma, Norman

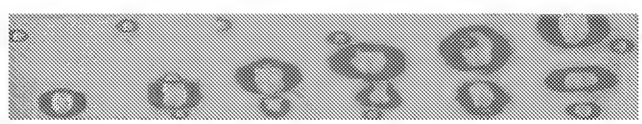

Results

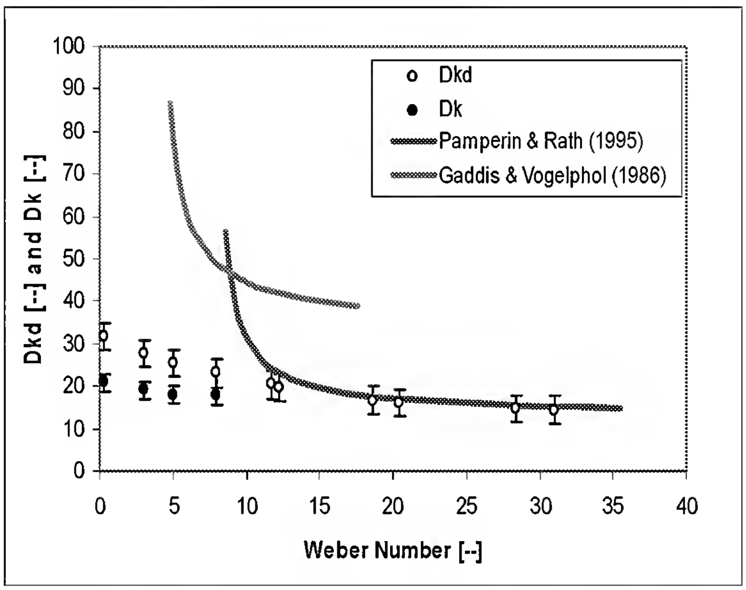

Dispersed and Detached Bubble Diameter (D_{Kd} , D_K) from a Free-Standing Tube in a Quiescent Liquid.

Fluid Dynamics Laboratory
School of Aerospace and Mechanical Engineering
University of Oklahoma, Norman

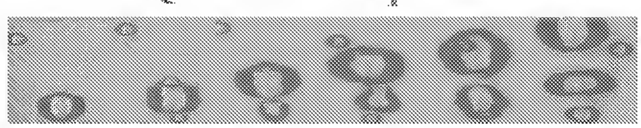

Results

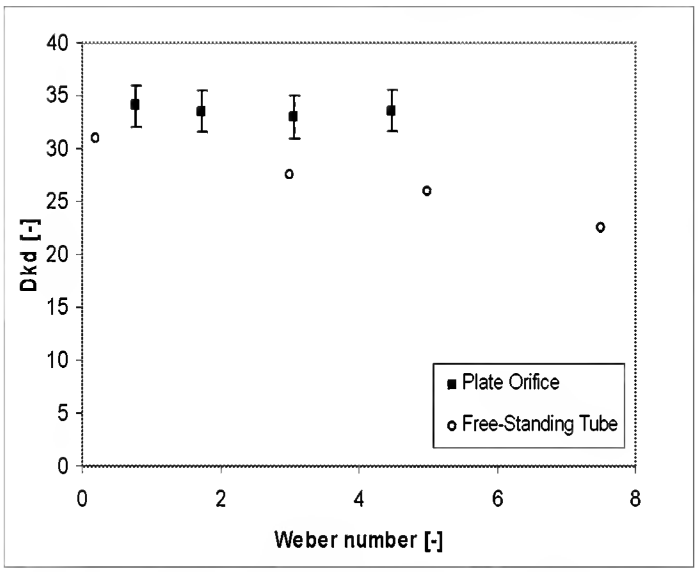

Dispersed Bubble Diameter (D_{Kd}) in a Quiescent Liquid from a Plate Orifice and Free-Standing Tube

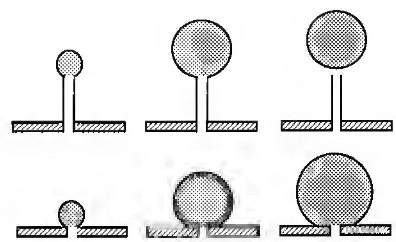

Bubble Formation from Free-Standing Tube (top), and Plate Orifice in Microgravity

Fluid Dynamics Laboratory
School of Aerospace and Mechanical Engineering
University of Oklahoma, Norman

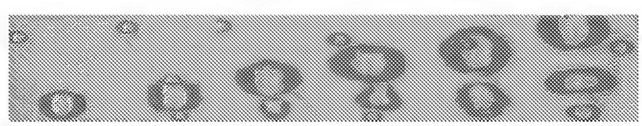

Conclusions

- **Low Gas Flow Rates**
  - Bubble detachment was observed for all conditions.
  - Agreement with theoretical results was not satisfactory.
  - Injector geometry affected bubble formation (bubble base growth and chamber effects caused differences between tube and plate orifice geometries).
  - Low surface tension resulted in smaller bubbles and periodic bubble formation.
- **High Gas Flow Rates**
  - Injector geometry effects were small.
  - Good agreement with theoretical results was observed.

Fluid Dynamics Laboratory
School of Aerospace and Mechanical Engineering
University of Oklahoma, Norman

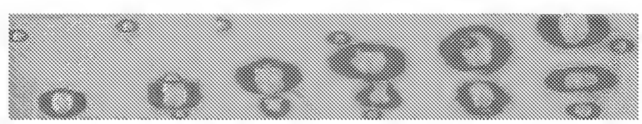

Resonant Interactions, Multi-frequency Forcing, and Faraday Wave Pattern Control

Mary Silber, Jeff Porter, and Chad M. Topaz
Department of Engineering Sciences & Applied Mathematics
Northwestern University
Evanston, IL 60208 USA

ABSTRACT

Standing surface waves form on a layer of fluid when it is subjected to a sufficiently strong periodic acceleration in the vertical direction. There have been numerous theoretical and experimental investigations of pattern formation in this so-called Faraday wave system in the last 15 years or so, in part because it exhibits patterns not seen in other systems (rhombic and triangular patterns, quasipatterns, superlattice patterns, localized structures akin to oscillons, etc.). Hence it provides a versatile framework in which to develop and test our general understanding of the nonlinear pattern formation process in hydrodynamic systems. However, this versatility comes at some cost. Specifically, many of the more exotic patterns are only realized when the periodic forcing function contains more than one frequency component; the introduction of nonsinusoidal periodic forcing functions leads to a large control parameter space that is difficult to fully characterize. For example, there is an increase from 2 parameters (frequency and amplitude) to 5 parameters in the next simplest case of two-frequency forcing (frequencies, amplitudes and relative phase).

We report on research that helps explain the role of each of the forcing function parameters in the pattern formation process. We focus on resonant triad interactions and their contribution to the weakly nonlinear pattern formation process for two-frequency forced parametrically excited surface waves. Our analysis highlights the effects of weakly broken time translation and time reversal symmetries that result in the weak forcing and damping case. We determine scaling laws for the resonant triad interactions with the forcing frequency ratio. We also find that the relative phase of the two forcing terms can have a dramatic effect on the nonlinear interactions. We confirm our predicted scaling by numerically calculating coefficients for the resonant triad amplitude equations from the quasipotential formulation of gravity-capillary waves due to Zhang and Vinals. Our theoretical results explain a number of recent experimental results, in particular the origin of various superlattice patterns. It also suggests how one might design periodic forcing functions to control pattern selection. We present examples showing how we may control nonlinear resonant triad interactions by an appropriate choice of three frequencies, with appropriate phases, for the forcing function.

Progress in Modeling Nonlinear Dendritic Evolution in Two and Three Dimensions, and Its Mathematical Justification

P.I.: S. Tanveer*, Co-PI: M. R. Foster

The Ohio State University
*420 Math Tower
231 W. 18^{th} Ave.
Columbus, Ohio 43210
614 292 5710 (voice), 614 292 1479 (fax)
tanveer@math.ohio-state.edu
foster.9@osu.edu

We report progress in three areas of investigation related to dendritic crystal growth. Those items are noted below.

1. **Selection of tip features dendritic crystal growth**

   It is to be recalled that crystalline anisotropy is essential for prediction of tip-features in microscopic solvability theory[1]. However, the strong dependence of tip-features on surface energy anisotropy in the limit as anisotropy tends to zero is not quite consistent with experimental observations[2]. In some systems (see explicit examples in reference 3) which are nearly structurally unstable, for example dendritic crystal growth and Hele-Shaw flow, small perturbations can cause unexpectedly large effects, and cross-over in the scaling results. Through formal asymptotic calculation, we have investigated[4] the effect of kinetic undercooling in a two-dimensional symmetric model symmetric model of dendritic crystal growth, with surface energy and anisotropy included. We notice that even for small undercooling, there is a lower threshold of surface energy anisotropy beyond which kinetic undercooling effects become important. We are presently considering such effects for three-dimensional models.

2. **Investigation of nonlinear evolution for two-sided model**

   For time evolving dendritic crystal growth, we are investigating how small disturbances on a nearly parabolic interface shape nonlinearly evolve away from the tip. It is to be noted that we have previously considered this problem[5] for one-sided two-dimensional model, and were able to understand the chaotic nature of evolution in terms of complex singularities and related interfacial distortions. We are now generalizing this approach in a way that does not require complexification, but relies on derivation of parameter free-inner nonlinear integro-differential equations that are valid near a spatially localized disturbance[6]. Parametric scaling dependencies have come as bi-products of this approach. Our earlier work made heavy use of conformal mapping[5]. Since it is not restricted to the use of conformal mapping, this current procedure is especially promising for three-dimensional dendrites. We expect that we will be able to determine more precisely the details of the coarsening process for these two-sided models.

3. **Rigorous mathematical justification**

Dendritic crystal growth theory is riven by conflicting claims, so one important aspect of this investigation is rigorous mathematical justification for our procedures. Some investigators seek to justify their mathematics by agreement between theory and experiment, even when the calculations are not based on sound mathematics. For instance, there are scenarios for describing tip-selection based on marginal stability[7] and its variants[8] that are at odds with microscopic solvability.

Therefore, it is necessary to settle some of the mathematical issues once for all. We are in the process of developing tools for rigorous mathematics to accomplish just that. In the first rigorous study of its kind, we have shown[9,10] that the predictions of microscopic solvability are indeed valid for the mathematically related problem of steady fingers in a Hele-Shaw cell. Dendritic crystal growth involves very similar, though more complicated, integro-differential equations. We anticipate similar results for dendritic growth.

Bibliography

1 D.A. Kessler, J. Koplik & H. Levine, *Advances in Physics* **37**, 255 (1988)

2 M.E. Glicksman & S.P. Marsch, *The dendrite*, in Handbook of Crystal Growth, edited by D.T.J. Hurle (Elsevier, New York, 1993), Volume 1.

3 S. Tanveer, *J. Fluid Mechanics* **409**, 273 (2000)

4* S. Tanveer, The effect of kinetic undercooling on tip-selection in 2-D dendritic crystal growth in the small surface energy anisotropy limit, in preparation (2002)

5 M. D. Kunka, M. R. Foster & S. Tanveer, Dendritic crystal growth for weak-undercooling. II. Surface energy effects on nonlinear evolution, *Phys. Rev. E.* **59**, 673 (1999)

6* M. R. Foster & S. Tanveer, Nonlinear evolution of localized disturbances in a 2-D symmetric and 3-D axisymmetric model for dendritic crystal growth, in preparation (2002)

7 S. Langer & H. Muller-Krumbhaar, *Acta Metall.* **26**, 1697 (1978).

8 J.J. Xu, *Eur. J. Appl. Maths* **2**, 105 (1991).

9* X. Xie & S. Tanveer, Rigorous Results in Steady Finger Selection in Viscous Fingering*, *Archives for Rational Mechanics*, to appear (2002)

10* S. Tanveer & X. Xie, Analyticity and Nonexistence of Classical Steady Hele-Shaw Fingers*, *Comm. Pure & Applied Mathematics*, to appear (2002)

* **supported at least in part by NAG3-2700**

Thermal Convection in Two-Dimensional Soap Films

Jie Zhang and X.L.Wu
Department of Physics and Astronomy
University of Pittsburgh, Pittsburgh, PA 15260

Thermal convection in a fluid is a common phenomenon. Due to thermal expansion, the light warm fluid at the bottom tends to rise and the cold, heavier fluid at the top tends to fall. This so-called thermal convection exists in earth atmosphere and in oceans. It is also an important mechanism by which energy is transported in stars. In this study we investigate thermal convection in a vertical soap film. Two aluminum cylinders, one at the top and one at the bottom, separated by about 2 cm are used to control the temperature at two constant values, as shown:

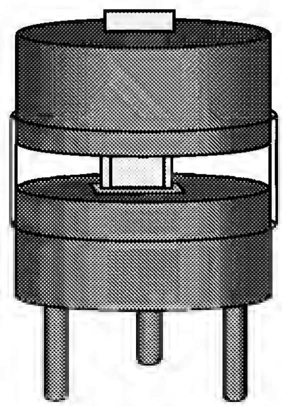

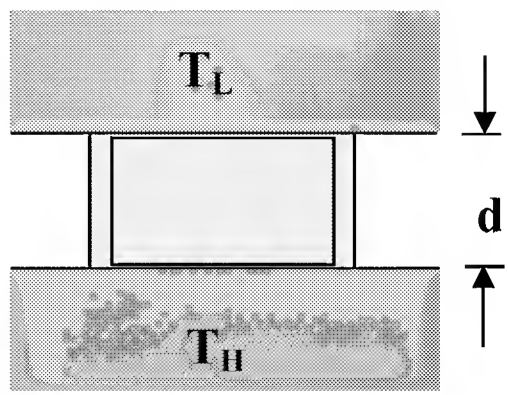

The film is suspended inside a thin metallic frame to improve transverse heat conduction. The aqueous film is made stable by using a small amount of surfactant (1.5 %). At the steady state, the film is typically several microns in thickness, with a uniform thickness gradient due to the gravitational stratification. Thus, thermal convection in the soap film is a double diffusive system, with temperature and 2D mass density forming two diffusive fields.

At a sufficiently large temperature gradient, fluid flow becomes turbulent as delineated below by a shadow graph technique. Here the temperature gradient is about 50 ^{o}C. One observes a frequent emission of thermal plumes at the bottom of the sample along with a large-scale circulation. To study the thermal turbulence quantitatively, power spectra of the temperature field are measured by a thermal radiation detector. This noninvasive technique allows small temperature variations to be measured with a high accuracy and with a time rate of ~100 Hz. Our main observation shows that the temperature

power spectrum scales as a power law $P(f) \sim f^{-\alpha}$, with $\alpha=1.4$ for medium temperature gradients and $\alpha=1.0$ for large temperature gradients, where f is the frequency. The latter case ($\alpha=1.0$) suggests that the temperature field can behave like a passive scalar, similar to dispersion of a dye in a turbulent field. Our preliminary observation seems to suggest that the crossover between the two different behaviors is marked by the onset of the large-scale circulation. Currently we are concentrated on measuring the velocity field simultaneously with the temperature field. These later measurements will shed new light on the intricate interactions between the temperature and velocity fields.

Exposition Session:
Guest Posters

AN OBSERVATION OF FILM THICKNESS AND LOCAL PRESSURE IN UPWARD AND DOWNWARD ANNULAR TWO-PHASE FLOW IN MICROGRAVITY, HYPERGRAVITY AND NORMAL GRAVITY

Kamiel S. Gabriel* and Devon L. Manz
Microgravity Research Group, University of Saskatchewan, Saskatoon, S7N 5A9, Canada

ABSTRACT

The phenomenon of two-phase flow in a near weightless environment (or microgravity) is becoming increasingly important. Two-phase flow loops are used in advanced spacecraft thermal management systems and also occur during the transfer of cryogenic propellants. On earth, two-phase annular flow is common in power plants and many chemical processing plants. The liquid film along the tube wall plays a large role in mass and momentum transfer, featuring a complex wave structure. It is the wave structure phenomenon relating to the pressure and film thickness time trace that is the current interest in this investigation.

Film thickness and local pressure time trace measurements were taken in normal (earth gravity) and microgravity (μ-g) conditions during the 29th and 30th Annual European Space Agency parabolic flight campaign operated by Novespace in Bordeaux, France. A high sampling rate and measurement accuracy are essential for a sufficient representation of the film thickness. The parallel wire conductance probe, initially used by deJong (1999), measures the electrical conductance between two wires stretched across the flow. Annular flow film is highly dynamic and hence the film thickness and associated local pressure fluctuate rapidly. The instruments require high frequency response and minimum damping. The Druck PDCR 900 pressure transducer has a frequency response quoted by the manufacturer to be 0 to 20000 Hz. Local pressure taps were placed in the same horizontal plane as the film thickness probes, perpendicular to the wires. It is essential that the local pressure measurement not interfere with the film phenomena, and as such the measurements were made at the tube wall.

An investigation into upward and downward annular flow at earth's gravity was made by Ariyadasa (2002) in a 9.925 mm diameter tube. The primary interest of this investigation was the relationship between the pressure and the film thickness. An investigation was made by Moe (1991) that examined the film thickness and pressure time traces in a horizontal flow. Moe observed the relationship between pressure peaks and film thickness peaks in a horizontal flow and indicated that the pressure differential might be enough to exert a significant force on the waves. Webb and Hewitt (1975) observed the pressure peaks that accompanied and lagged the film thickness peaks. They concluded that the time delay exists because of interaction with the exit condition of the system.

Based on the time traces of the film thickness and localized pressure obtained from available data, the relationship between the film thickness and the pressure under the wave appear to indicate some correspondence. Comparison of the time traces consisted of considering the film thickness greater than one standard deviation from the mean over the 4 or 8 second window. In

* Formerly K.S. Rezkallah

this region, if the film thickness time trace was increasing or decreasing as the local pressure was increasing or decreasing, the relationship was observed. Classification using nearly 100 microgravity, hypergravity and normal gravity annular flow data points was performed.

A typical film thickness and local pressure time trace for an upward annular flow at normal gravity conditions are featured in figure 1a. The liquid superficial velocity is 0.24 m/s and the gas superficial velocity is 20 m/s. Featured in figure 1b, is a flow image in the same tube diameter.

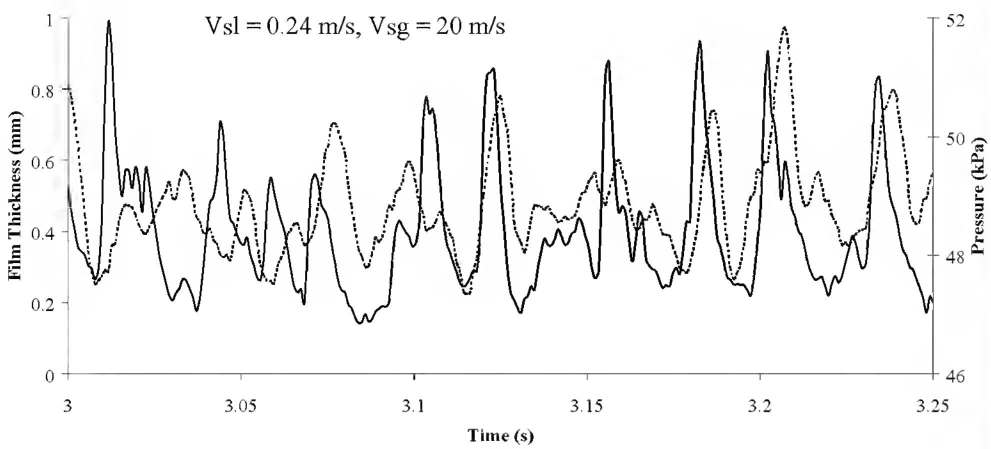

(a)

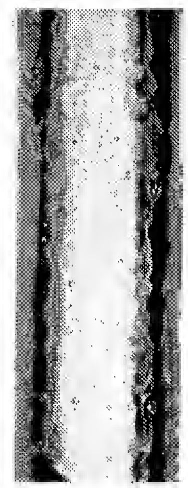

(b)

Figure 1: (a) Film thickness (solid line) and local pressure (broken line) time traces at normal gravity; (b) Annular flow image at normal gravity (Vsl = 0.24 m/s, Vsg = 19.5 m/s, P = 99.3 kPa)

1. Ariyadasa, Umesh (2002). An Investigation of Film Thickness and Pressure in Upward and Downward Annular Two-Phase Flow. M.Sc. Thesis, University of Saskatchewan, Canada.
2. deJong, Pieter (1999). An Investigation of Film Structure and Pressure Drop in Microgravity Annular Flow. M.Sc. Thesis, University of Saskatchewan, Canada.
3. Moe, J. (1991). Long-wave disturbances in stratified two-phase pipe flow, phase-interface phenomena in multiphase flow. In Hewitt, G.F., Mayinger, F., and Riznic, J.R. (Eds.), Phase-interface phenomena in multiphase flow, pp. 58. Hemisphere Publishing Corporation, New York.
4. Webb, D.R., and Hewitt, G.F. (1975). Downward co-current annular flow. Int. J. Multiphase Flow 2, 35.

AN OBSERVATION OF FILM THICKNESS AND LOCAL PRESSURE IN UPWARD AND DOWNWARD ANNULAR TWO-PHASE FLOW IN MICROGRAVITY, HYPERGRAVITY AND NORMAL GRAVITY

Devon L. Manz and Kamiel S. Gabriel*
Microgravity Research Group
University of Saskatchewan
Saskatoon, SK, Canada, S7N 5A9

ABSTRACT

The local pressure and film thickness time traces were observed in an upward two-phase annular flow of air and water in a 9.525 mm inner diameter tube. Superimposed on one another, the film thickness and local pressure time traces appear to follow a similar trend as the work by Ariyadasa (2001) above one standard deviation from the mean film thickness. This was evident in normal gravity (1g), microgravity (~0.05g) and hypergravity (~1.8g) conditions on the Novespace Zero-G aircraft.

INTRODUCTION

Annular flow is a two-phase flow regime where liquid film occupies the outer annulus of a tube as gas passes through the inner core. Two-phase annular flow in microgravity is becoming an increasingly important subject relating to the transfer of cryogenic propellants and heating and cooling systems. Featuring a complex wave structure, the liquid film plays a large role in mass and momentum transfer. It is the wave structure phenomenon that is one of the current interests of the Microgravity Research Group at the University of Saskatchewan, Canada.

An investigation into upward and downward annular flow at earth's gravity was made by Ariyadasa (2001). The primary interest of this investigation was the relationship between the pressure and film thickness. Earlier, an investigation was made by Moe (1991) that examined the film thickness and pressure time traces in a horizontal flow. Moe observed a relationship between pressure peaks and film thickness peaks and indicated that the pressure differential might be enough to exert a significant force on the waves. Webb and Hewitt (1975) observed the pressure peaks that accompanied and lagged the film thickness peaks. They concluded that the time delay existed because of interaction with the exit of the system.

INSTRUMENTATION

Annular flow film is highly dynamic and as such the film fluctuates rapidly. The average film thickness varies from 0.2 mm to 1.0 mm in upward and downward flow. A high sampling rate and measurement accuracy are essential for a sufficient representation of the film thickness. The parallel wire conductance probe, initially used by deJong (1999), measures the electrical conductance between two wires stretched across the flow. A schematic is shown in figure 1a.

* Formerly K.S. Rezkallah

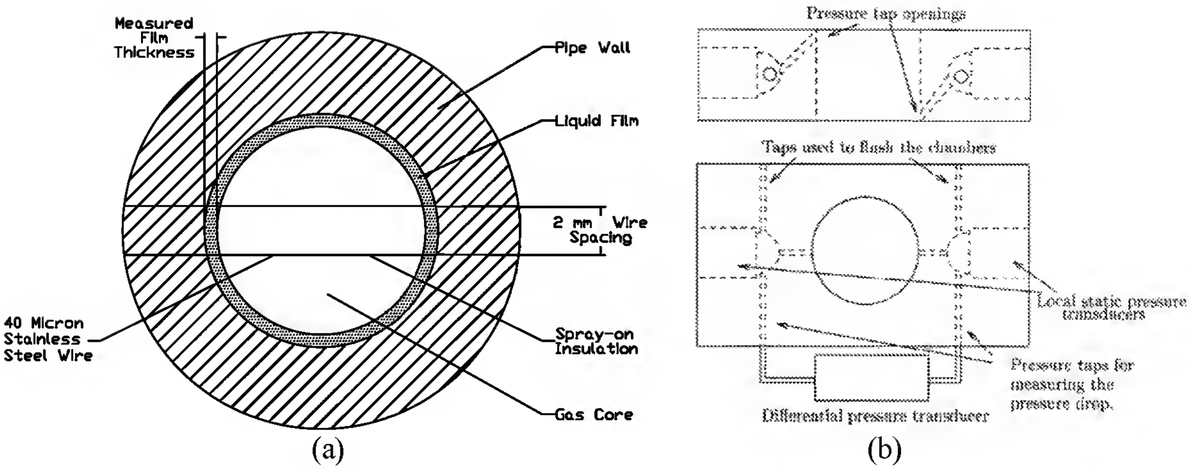

Fig. 1: (a) Film thickness probe; and (b) local pressure block containing pressure taps (Ariyadasa, 2001)

The conductance is measured, representing the proportions of each phase (air-water) at the tube's cross section. Three probes were used to sample the conductance of the flow, with a sampling rate of 1000 Hz. A more detailed explanation of calibration and testing procedure is available from deJong (1999).

The local pressure is highly unsteady, and as such the instrument requires high frequency response and minimum damping. The Druck PDCR 900 pressure transducer has a frequency response quoted by the manufacturer to be 0 to 20000 Hz. Local pressure taps were placed in the same horizontal plane as the film thickness probes, perpendicular to the wires. It is essential that the local pressure measurement not interfere with the film phenomena, and as such the measurements were made at the tube wall. The pressure block, shown in figure 1b is made out of acrylic (19.05 mm in thickness) and placed between two film thickness probes. Two 10 psi piezoelectric transducers were attached to these chambers.

ANALYSIS

The proposed method of analyzing the relationship between the film thickness and local pressure was to consider a region greater than the mean film thickness plus one standard deviation over the four second window of data. A maximum was defined as any peak in the film thickness time trace that was located in a region greater than the mean film thickness by more than one standard deviation. A similar specification was made for the local pressure. If the film thickness and pressure were simultaneously greater than the mean plus one standard deviation, the film thickness and local pressure were well correlated. Further numerical analysis must consider the time response of the data acquisition and instruments.

Alternative methods of analyzing the relationship between the film thickness and local pressure exist. One method is to consider the instantaneous percent change in film thickness and compare the result with the percent change in the local pressure measurement. A second method considers the percent difference between the local pressure and film thickness at each time. A criterion could be established to determine if there is a reasonable agreement between the two measurements.

Ariyadasa (2001) observed that the film thickness characteristics are related to the gas and liquid flow rates. He examined the wave width, frequency, height and volume and came to the following conclusions regarding the local film thickness and pressure:

1. The two film thickness signals are well correlated, while the two local pressure signals are weakly correlated. This suggests that the liquid film undergoes very little change as it moves between the probes, whereas the pressure undergoes a significant change as it moves between the probes.
2. The peaks in the film thickness time trace are usually followed by a peak in the associated pressure time trace. Although previous researchers have stated that this time lag is due to exit effects, no such lag was observed.

A sample film thickness and pressure time trace for upward and downward annular flow is shown in figure 2. In the upward and downward flow examined by Ariyadasa, the local pressure varied by no more than 5 kPa. The maximum film thickness values closely correspond to the local maximum values for the pressure measurements.

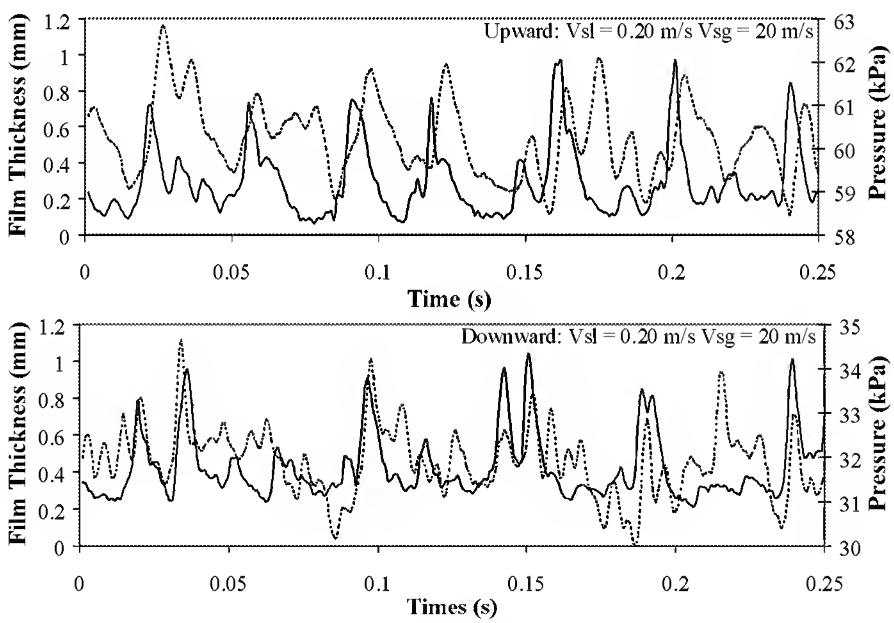

Fig. 2: Instantaneous pressure (broken line) and film thickness (solid line)

An additional consideration regarding the variation in pressure along the cross section of the tube can be made. The local pressure time trace was obtained at the tube wall and may not be representative of the pressure in the gas core. Accurate determination of the pressure in the gas core requires knowledge of the velocity profile, as the local pressure cannot be measured along the interface of the two phases. Based solely upon Bernoulli's principle, a maximum film thickness should result in a minimum pressure in the gas phase. However, the pressure measurement was taken at the tube wall. This suggests that the film velocity profile may be influenced by a pressure gradient across the tube cross section. This also suggests that the

anticipated decrease in pressure in the gas core at maximum values of film thickness cannot be determined solely by the local pressure measurement at the tube wall. Although it seems reasonable to expect a minimum pressure in the gas core when film thickness is a maximum, additional forces act on the liquid film. An interfacial shear stress is exerted on the liquid film, as well as a buoyant force on the fluid particle. Entrained and deposited droplets also influence the velocity distribution in both phases. These additional forces influence the wave shape and liquid film thickness.

The film thickness and local pressure measurements were collected in microgravity (~0.05g) hypergravity (~1.8g) and normal gravity (1g) conditions. These are featured in figure 3 for upward air-water annular flow.

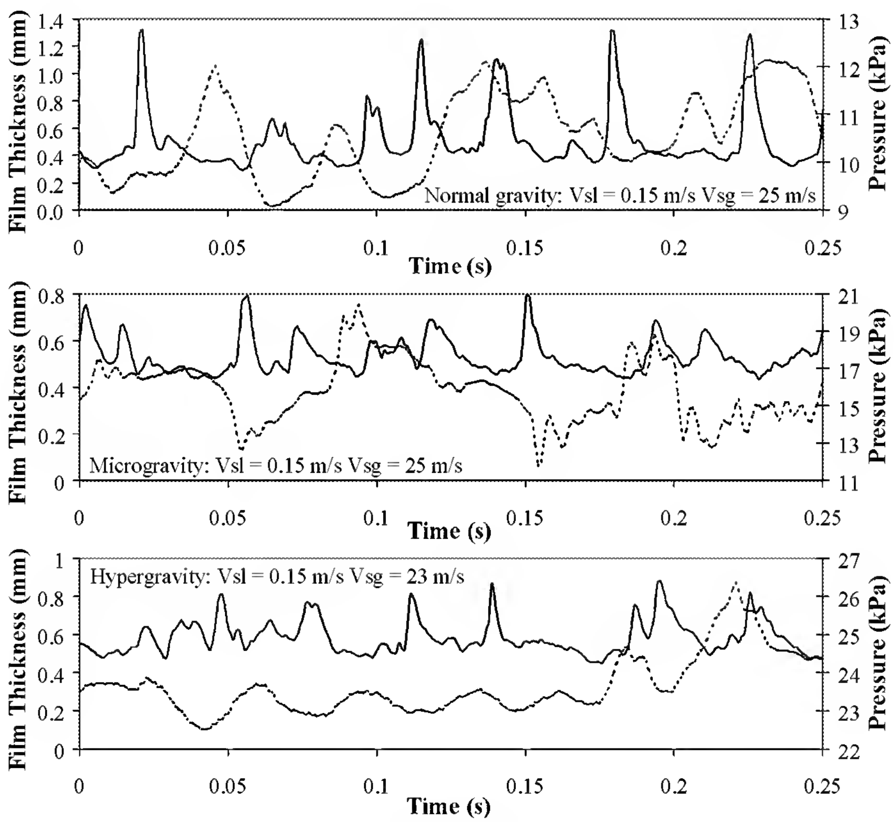

Fig. 3: Instantaneous pressure (broken line) and film thickness (solid line)

All microgravity and hypergravity data were collected during the 30th Annual Parabolic Flight Campaign with the European Space Agency. The results of this flight appear to show less of a correlation between the film thickness and local pressure than the upward and downward flow examined by Ariyadasa (2001). Webb and Hewitt (1975) observed that the exit conditions greatly affected the pressure measurement. The measurements obtained on the flight apparatus are closer to the exit of the system than the apparatus used by Ariyadasa. Also, the delay of the data acquisition on the flight apparatus differed from the apparatus used by Ariyadasa, resulting in a slight misalignment of the film thickness peaks and pressure peaks.

Data at normal gravity were collected in May 2002, on the same apparatus as the hypergravity and microgravity data obtained in May 2001. Again, the correlation between the pressure and the film thickness did not agree as well as the results from Ariyadasa. Images obtained from the digital video camera on the flight apparatus in normal gravity are shown in figure 4.

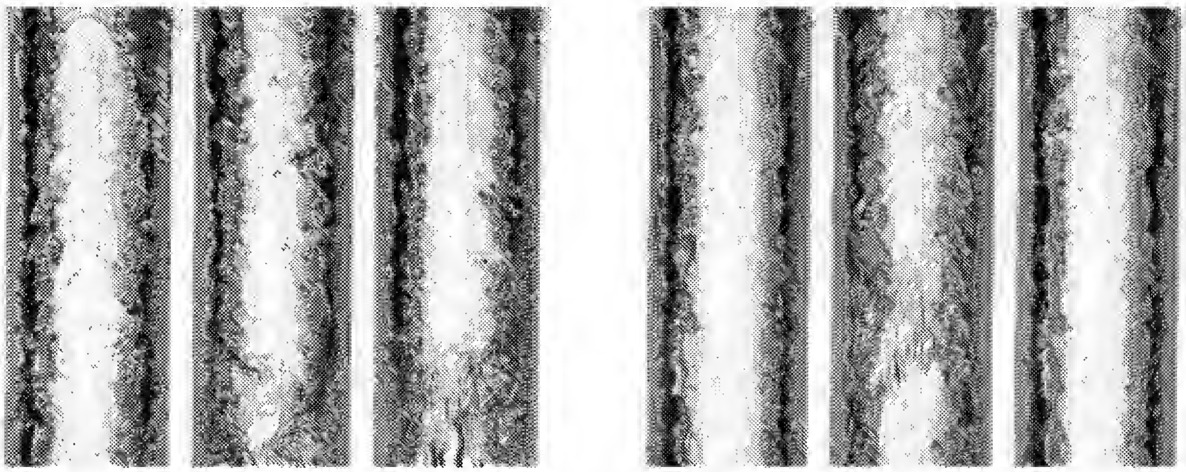

Vsl = 0.12 m/s, Vsg = 29 m/s **Vsl = 0.12 m/s, Vsg = 37 m/s**

Fig. 4: Sample normal gravity flow images of air-water annular two-phase flow

CONCLUSIONS

Although a definite prediction of the pressure at the tube wall cannot be made from knowledge of the film thickness at all times of the trace, the following conclusions and recommendations can be made:

1. Observation of the local pressure and film thickness time traces indicates that the maximum values of film thickness coincide with the maximum local pressure, not accounting for instrument response or data acquisition delay.
2. As the distance from the mean film thickness increases, better agreement between the film thickness and pressure signals is observed.
3. Microgravity, hypergravity and normal gravity data obtained from the flight apparatus may not as clearly illustrate the relationship between the film thickness and local pressure as Ariyadasa (2001), because the location of the test section was closer to the exit of the system.
4. Many methods of analysis exist to determine the relationship between the film thickness and pressure, but presently, the consistency in shape between the two signals above one standard deviation from the mean film thickness indicates reasonable agreement.
5. No correlation appears to exist between the film thickness and the local pressure at film thickness values near the mean, as small pressure and film thickness fluctuations exist, which may be solely due to measurement uncertainty.

REFERENCES

1. Ariyadasa, U. (2001). An Investigation of Film Thickness and Pressure in Upward and Downward Annular Two-Phase Flow. *M.Sc. Thesis, University of Saskatchewan, Canada.*
2. deJong, P. (1999). An Investigation of Film Structure and Pressure Drop in Microgravity Annular Flow. *M.Sc. Thesis, University of Saskatchewan, Canada.*
3. Moe, J. (1991). Long-wave disturbances in stratified two-phase pipe flow, phase-interface phenomena in multiphase flow. *In Hewitt, G. F., Mayinger, F., and Riznic, J. R. (Eds.), Phase-interface phenomena in multiphase flow. pp. 58. Hemisphere Publishing Corporation, New York.*
4. Webb, D. R., and Hewitt, G. F. (1975). Downward Co-current Annular Flow. *Int. J. Multiphase Flow*, **2**, 35.

PHOTOINDUCED CAPILLARY MOTION OF DROPS AND BUBBLES

Bezuglyi B.A., Ivanova N.A.
Tyumen State University, Liquid Microgravity Technology Laboratory
Semakova, 10, Tyumen, 625003, Russia, e-mail: nivanova@utmn.ru

ABSTRACT

Bubbles and drops are inhering in many liquid processes on Earth (microfluidics, MEMS technology, flows through porous media etc.) and in space laboratory under μg conditions (preparation composite materials, degassing of liquefied matter, recycling of waste material). They could have affected these processes significantly. Therefore the study of behavior these capillary objects is necessary in order to develop the efficient methods of manipulation of them in situ.

The best solution of such problem is the use of surface forces, which are aroused when the surface tension locally is departed from its equilibrium value as a result of thermal, concentration or electrical perturbations at interface,

$$\nabla\sigma = \sigma'_T \mid_{C,\varphi} \nabla T + \sigma'_C \mid_{T,\varphi} \nabla C + \sigma'_\varphi \mid_{C,T} \nabla \varphi$$

Among the known methods of control of surface tension the most promising is the thermal one. However, the generation of motion of capillary objects by the thermal gradients imposed in liquid bulk (or along solid substrate) by conduction is a passive method, which requires large amount of energy.

In this paper the new method of generation of motion of bubbles and drops in microchannels or Hele-Show cells are reported. This method based on photoinduced solutocapillary convection discovered by Bezuglyi [1,2].

This motion can be caused through simultaneously acting thermocapillary (TC) and solutocapillary (SC) forces, which are induced by a light beam at the interface of the bubbles and drops. A competition between these two forces takes place. A criterion which measures the importance of surface tension gradient, $(\nabla\sigma)_C = \sigma'_C \nabla C$, related to concentration gradient against surface tension gradient, $(\nabla\sigma)_T = \sigma'_T \nabla T$, caused by thermal gradient is a dimensionless number $CT = (\nabla\sigma)_C / (\nabla\sigma)_T$. If $CT > 1$, then the capillary motion is caused by SC forces. When $CT < 1$, drops and bubbles move due to TC forces.

The behavior of the gas bubble of various diameter in a thin layer (10 – 100 μm) of solution tensioactive substance in a high volatile solvent sandwiched between two glass plates and the growth of drops within bubbles under light radiation have been studied. Continuous and intermittent motions of bubbles for numbers $CT < 1$ and $CT > 1$, respectively, were revealed. First, the division of kidneylike bubble [3] in irradiated region was demonstrated. It was found, that the rate of drop growth within bubble is increased when the diameter of bubble is decreased.

[1] B. Bezuglyi, PhD Thesis. Moscow State University. Moscow 1983.
[2] B. Bezuglyi, Proc. Int. Aerospace Congress, Moscow, Russia. (1995) 261
[3] B. Bezuglyi, A. Fedorets, N. Ivanova, First conference of the International Marangoni Association, Abstracts, Sept. 12-16, Giessen, Germany, (2001) 80.

OBSERVATIONS OF CONFINEMENT OF A PARAMAGNETIC LIQUID IN MODEL PROPELLANT TANKS IN MICROGRAVITY BY THE KELVIN FORCE

John Kuhlman[+], Donald D. Gray[*], Austin Barnard[#], Jennifer Hazelton[#], Matthew Lechliter[#], Andrew Starn[#], Charles Battleson[#], Shannon Glaspell[#], Paul Kreitzer[#], and Michelle Lechliter[#]
West Virginia University, Morgantown, WV 26506

[+]Professor, and [#]Undergraduate Student, Dept. of Mechanical and Aerospace Engineering
[*]Associate Professor, Dept. of Civil and Environmental Engineering

INTRODUCTION

The magnetic Kelvin force has been proposed as an artificial gravity to control the orientation of paramagnetic liquid propellants such as liquid oxygen in a microgravity environment. This paper reports experiments performed in the NASA "Weightless Wonder" KC-135 aircraft, through the Reduced Gravity Student Flight Opportunities Program. The aircraft flies through a series of parabolic arcs providing about 25 s of microgravity in each arc. The experiment was conceived, designed, constructed, and performed by the undergraduate student team and their two faculty advisors.

Two types of tanks were tested: square-base prismatic tanks 5 cm x 5 cm x 8.6 cm and circular cylinders 5 cm in diameter and 8.6 cm tall. The paramagnetic liquid was a 3.3 molar solution of $MnCl_2$ in water. Tests were performed with each type of tank filled to depths of 1 cm and 4 cm. Each test compared a pair of tanks that were identical except that the base of one was a pole face of a 0.6 Tesla permanent magnet. The Kelvin force attracts paramagnetic materials toward regions of higher magnetic field. It was hypothesized that the Kelvin force would hold the liquid in the bottom of the tanks during the periods of microgravity. The tanks were installed in a housing that could slide on rails transverse to the flight direction. By manually shoving the housing, an identical impulse could be provided to each tank at the beginning of each period of microgravity. The resulting fluid motions were videotaped for later analysis.

RESULTS

As summarized in Table 1, positive results (more liquid was confined to the bottom of the magnet tank than in the non-magnet control tank) were obtained in 86 out of 89 tests. For 3 tests with relatively large impulses, the magnetic and non-magnetic results were comparable. No negative results were observed. As expected, the Kelvin force was much more effective in controlling the liquid in the shallower liquid cases.

Table 1. Summary of results.

Case	Tank	Depth	# tests	# positive	# negative	# inconclusive
1	Prism	1 cm	27	27	0	0
2	Cylinder	1 cm	18	18	0	0
3	Prism	4 cm	26	26	0	0
4	Cylinder	4 cm	18	15	0	3
Total			89	86	0	3

In every one of the Case 1 tests, the magnet held the liquid interface essentially flat after the initial sloshing transient quickly damped out. In the control tanks, the liquid quickly moved to the top of the tank in 23 cases. In the remaining 4 tests, the interface tilted 1-6 cm, eventually reaching the top of the tank in 3 tests. Figure 1 shows an example of the Case 1 results. The tank with the magnet is on the left of the image.

Among the Case 2 tests, 6 had no input impulse. In these the magnet held the liquid with an essentially flat interface, while in the control tanks the liquid moved to the top in 3 tests and exhibited a tilting interface in 3 tests. For 1 test in which multiple input impulses set up a swirling motion, the magnet tank showed a smaller amount of the liquid at the top of the tank than the control tank. In 5 tests with impulse, the magnet held the liquid with a flat interface, while the liquid either moved to the top of the tank or tilted significantly from a horizontal position in the control tests. For the remaining 6 tests approximately half of the liquid remained in the bottom of the tank for the magnet tanks, while essentially all of the liquid moved to the top in the control tanks. Figure 2 is a Case 2 image; the magnet is visible below the right hand tank.

In Case 3, there were 17 tests in the which magnet allowed the interface to tilt noticeably, but kept the liquid from reaching the top of the tanks, and 9 in which the tilting was followed by some of the liquid moving to the top of the tank near the test's end. In the control tanks, there were 17 tests in which the bulk of the liquid moved quickly to the top of the tank, and usually moved back down to the bottom of the tank, with the cycle repeating one or more times. In the remaining 9 control tank tests, most of the liquid would move to the top of the tank and stay there for most of the parabola. Figure 3 is a Case 3 image; the magnet is below the right hand tank.

In the Case 4 tests, there were 6 with no input impulse. For 4 of these tests the magnet tank showed a tilted interface that never reached the top of the tank, while for 2 some liquid eventually went to the top of the tank. Of the no-impulse control tank cases, 4 had more liquid go to the top of the tank, while 2 had an interface that tilted more than for the corresponding magnet tanks. For the 3 tests in which multiple input impulses set up a swirling motion, the magnet cases showed a smaller amount of the liquid at the top of the tank than the controls. In 6 additional tests an average of 65% of the liquid was near the tank bottom for the magnet tanks compared with an average of 30% for the controls. In 3 tests there was no significant difference between the magnet and control tanks. Figure 4 is a Case 4 image; the magnet tank is on the left.

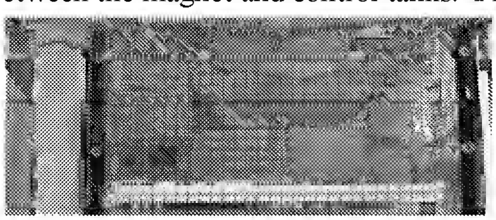

Fig. 1. Sample image for Case 1.

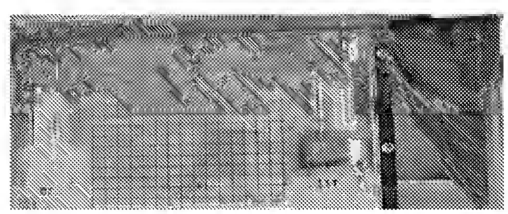

Fig. 2. Sample image for Case 2.

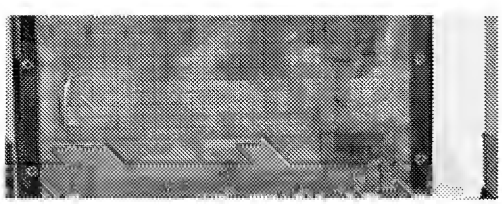

Fig. 3. Sample image for Case 3.

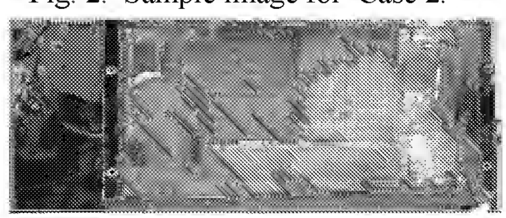

Fig. 4. Sample image for Case 4.

Observations of Confinement of a Paramagnetic Liquid in Model Propellant Tanks in Microgravity by the Kelvin Force

6th Microgravity Fluid Physics and Transport Phenomenon Conference
Cleveland, OH, August 14-16, 2002

John Kuhlman[+], Donald D. Gray[*], Austin Barnard[#], Jennifer Hazelton[#], Matthew Lechliter[#], Andrew Starn[#], Charles Battleson[#], Shannon Glaspell[#], Paul Kreitzer[#], and Michelle Lechliter[#]
West Virginia University, Morgantown, WV 26506

[+]Professor, and [#]Undergraduate Student, Dept. of Mechanical and Aerospace Engineering
[*]Associate Professor, Dept. of Civil and Environmental Engineering

Sponsored by WVU College of Engineering and Mineral Resources,
Depts. of Mechanical and Aerospace Engineering, and Civil and Environmental Engineering,
and WV NASA Space Grant Consortium

Mechanical & Aerospace Engineering

ABSTRACT

The magnetic Kelvin force has been proposed as an artificial gravity to control the orientation of paramagnetic liquid propellants such as liquid oxygen in a microgravity environment. This paper reports experiments performed in the NASA "Weightless Wonder" KC-135 aircraft, through the Reduced Gravity Student Flight Opportunities Program. The aircraft flies through a series of parabolic arcs providing about 25 s of microgravity in each arc. The experiment was conceived, designed, constructed, and performed by the undergraduate student team and their two faculty advisors.

Two types of tanks were tested: square-base prismatic tanks 5 cm x 5 cm x 8.6 cm and circular cylinders 5 cm in diameter and 8.6 cm tall. The paramagnetic liquid was a 4.2 molar solution of $MnCl_2$ in water. Tests were performed with each type of tank filled to depths of 1 cm and 4 cm. Each test compared a pair of tanks that were identical except that the base of one was a pole face of a 0.6 Tesla Neodymium-Iron-Boron permanent magnet. It was hypothesized that the Kelvin force would hold the liquid in the bottom of the tanks during the periods of microgravity. The tanks were installed in a housing that could slide on rails transverse to the flight direction. By manually shoving the housing, an identical impulse could be provided to each tank at the beginning of each period of microgravity. The resulting fluid motions were videotaped for later analysis.

Mechanical & Aerospace Engineering

EXPERIMENTAL CONDITIONS AND PROCEDURE

Two types of tanks were tested: square-base prismatic tanks 5 cm x 5 cm x 8.6 cm, and circular cylindrical tanks 5 cm in diameter and 8.6 cm tall. These tanks are similar in aspect ratio to the NASA MAPO project tanks.

The paramagnetic liquid was a 4.2 molar solution of $MnCl_2$ in water.

Tests were performed with each type of tank filled to depths of 1 cm and 4 cm.

Each test compared pairs of tanks that were identical except that the base of one was a pole face of a 0.6 Tesla Neodymium-Iron-Boron permanent magnet. An identical tank with no magnet served as a control, for comparison.

The tanks were installed in a housing that could slide on rails transverse to the flight direction. By manually shoving the housing, an identical impulse could be provided to each tank.

The resulting fluid motions were videotaped for later analysis. Videotape analyzed for:

1. Fluid velocity (2 m/sec linear motion; 0.3 m/sec max vertical velocity during sloshing)
2. Lateral accelerations; (1-7 g's, or more during impulse) and
3. Evaluation of resulting liquid motions, and evaluation of success of liquid positioning

Mechanical & Aerospace Engineering

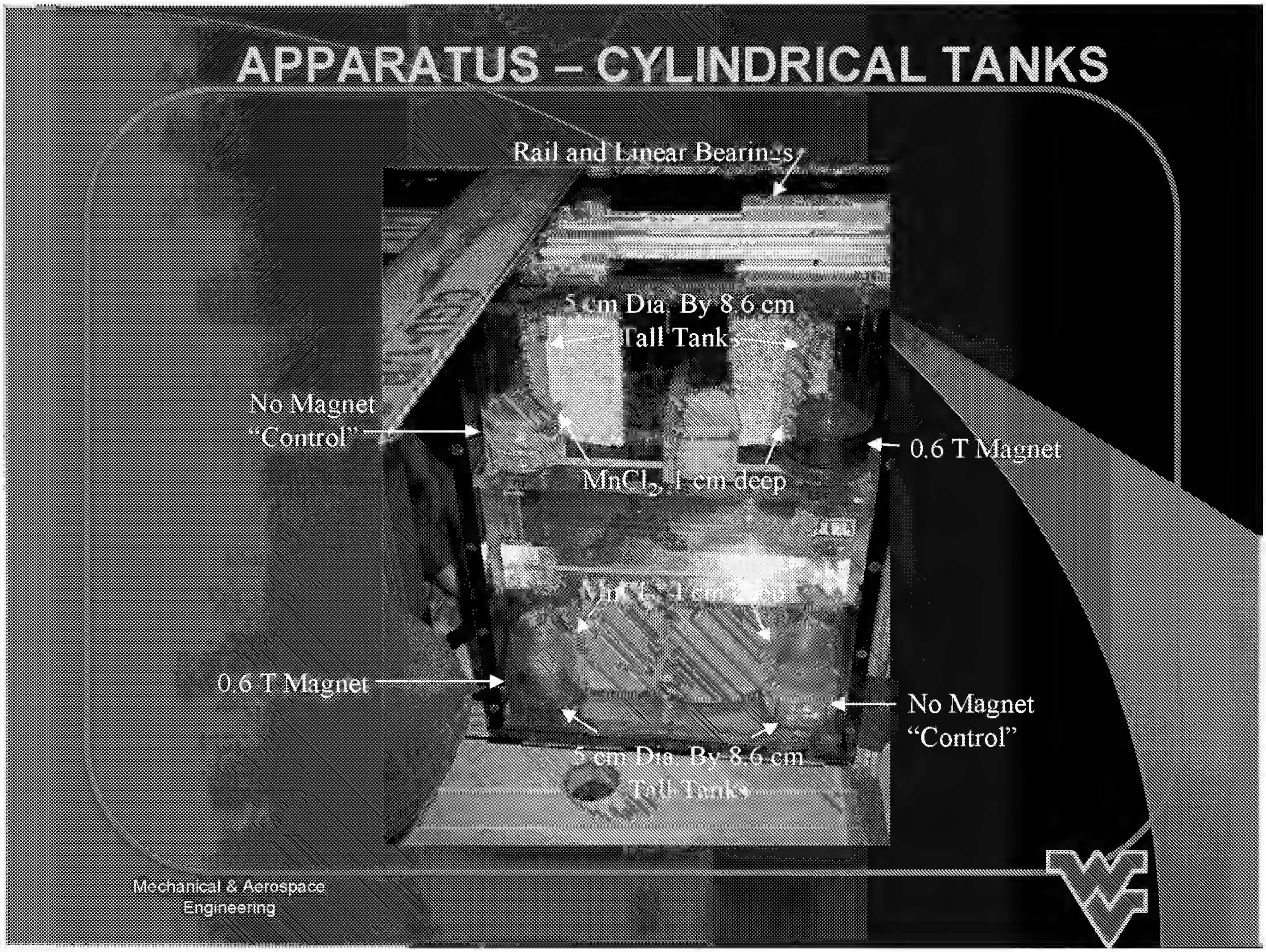
APPARATUS – CYLINDRICAL TANKS
Rail and Linear Bearings
5 cm Dia. By 8.6 cm
Tall Tank
No Magnet
"Control"
0.6 T Magnet
$MnCl_2$, 1 cm deep
0.6 T Magnet
No Magnet
"Control"
5 cm Dia. By 8.6 cm
Tall Tanks
Mechanical & Aerospace
Engineering

NONDIMENSIONAL PARAMETER ESTIMATES

Definitions:

$F_{magnetic} / F_{surface\ tension} = \mu_o \chi H \nabla H L^2 / \sigma = Bo_M$ = Magnetic Bond Number
(See Paper AIAA-2001-0930, by Marchetta, Hochstein, and Sauter)

$F_{inertia} / F_{viscous} = \rho V L / \mu = Re$

$F_{inertia} / F_{magnetic} = \rho V^2 / (\mu_o \chi H \nabla H L) = We / Bo_M$ = Weber / Magnetic Bond

Fluid Properties:

$M = 4.2$ = molarity
$SG = 1.28$
$\mu = 4.48 \times 10^{-03}$ N-s/m = viscosity
$\sigma = 0.16$ N/m = surface tension
$\chi = 7.6 \times 10^{-04}$ = volumetric magnetic susceptibility

Mechanical & Aerospace Engineering

EXPERIMENTAL CONDITIONS

Liquid Depth = 0.01 m

Magnetic Bond # = 2.25
($F_{magnetic}/F_{surface\ tension}$)

$F_{inertia}/\ F_{magnetic} = 27$

$F_{inertia}/\ F_{viscous} = 860$

Liquid Depth = 0.04 m

Magnetic Bond # = 0.76
($F_{magnetic}/F_{surface\ tension}$)

$F_{inertia}/\ F_{magnetic} = 107$

$F_{inertia}/\ F_{viscous} = 3420$

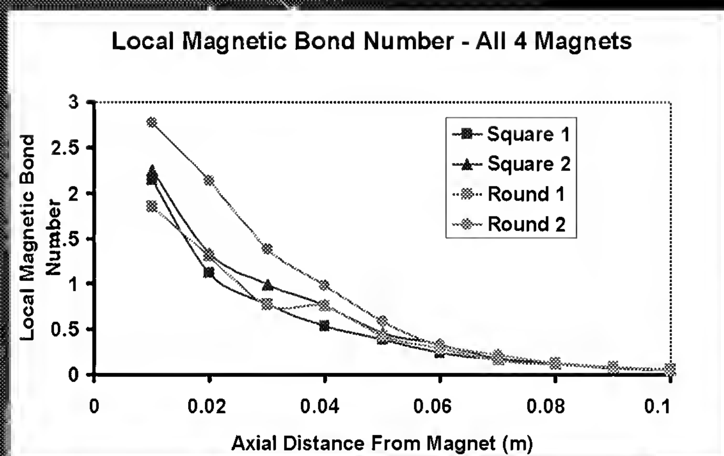

(Inertial forces estimated based on vertical liquid velocities of 0.3 m/sec for "sloshing" motions after impulse was applied, maximum inertial force due to impact is estimated to be an order of magnitude larger.)

Mechanical & Aerospace Engineering

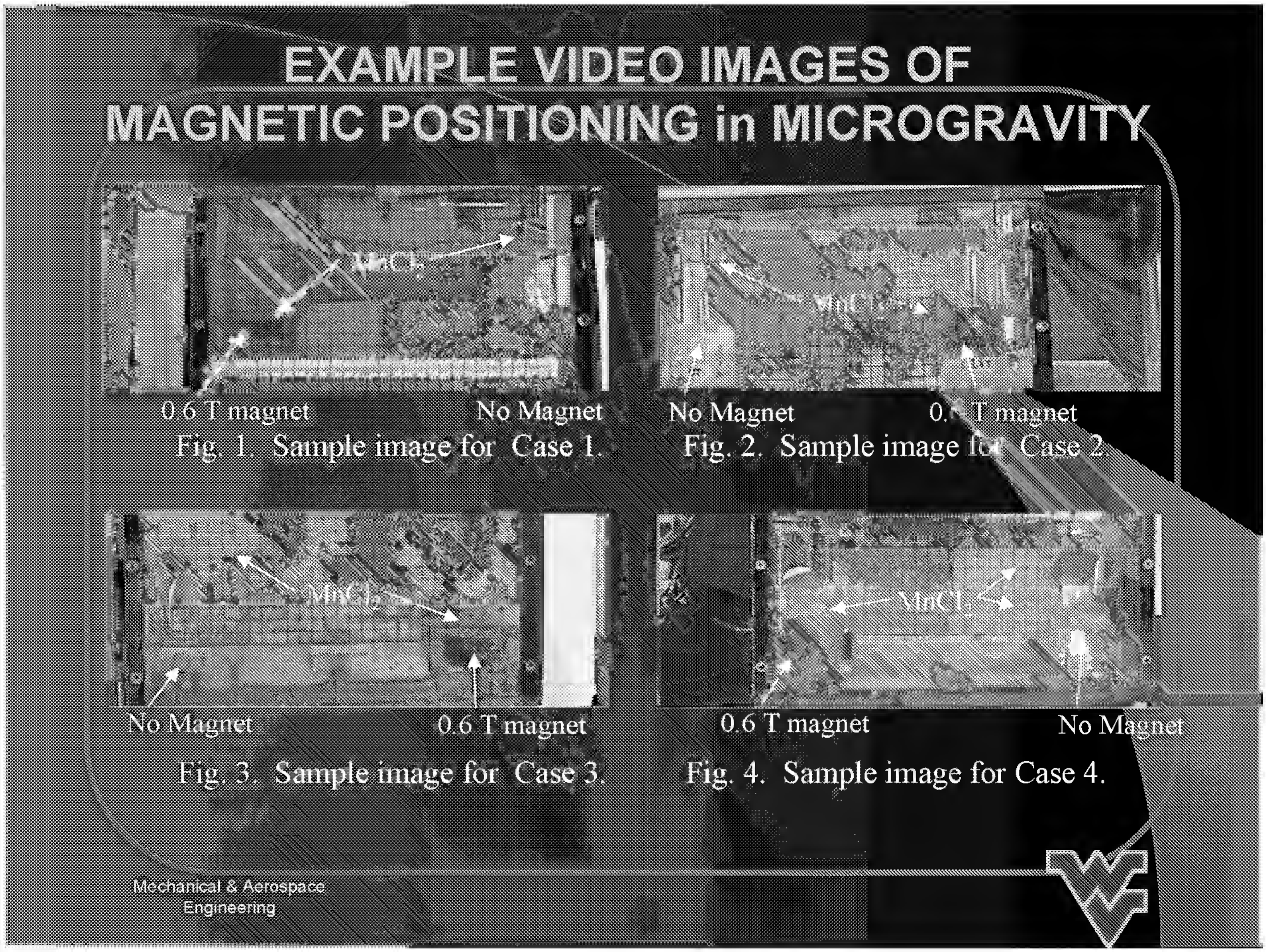
EXAMPLE VIDEO IMAGES OF
MAGNETIC POSITIONING in MICROGRAVITY
MnCl2
0.6 T magnet
No Magnet
Fig. 1. Sample image for Case 1.
MnCl2
No Magnet
0.6 T magnet
Fig. 2. Sample image for Case 2.
MnCl2
No Magnet
0.6 T magnet
Fig. 3. Sample image for Case 3.
MnCl2
0.6 T magnet
No Magnet
Fig. 4. Sample image for Case 4.
Mechanical & Aerospace
Engineering

DESCRIPTION OF RESULTS

In every one of the Case 1 tests, the magnet held the liquid interface essentially flat after the initial sloshing transient quickly damped out. In the control tanks, the liquid quickly moved to the top of the tank in 23 cases. In the remaining 4 tests, the interface tilted 1-6 cm, eventually reaching the top of the tank in 3 tests. Figure 1 (next page) shows an example of the Case 1 results. The tank with the magnet is on the left of the image.

Among the Case 2 tests, 6 had no input impulse. In these the magnet held the liquid with an essentially flat interface, while in the control tanks the liquid moved to the top in 3 tests and exhibited a tilting interface in 3 tests. For 1 test in which multiple input impulses set up a swirling motion, the magnet tank showed a smaller amount of the liquid at the top of the tank than the control tank. In 5 tests with impulse, the magnet held the liquid with a flat interface, while the liquid either moved to the top of the tank or tilted significantly from a horizontal position in the control tests. For the remaining 6 tests approximately half of the liquid remained in the bottom of the tank for the magnet tanks, while essentially all of the liquid moved to the top in the control tanks. Figure 2 is a Case 2 image; the magnet is visible below the right hand tank.

In Case 3, there were 17 tests in the which magnet allowed the interface to tilt noticeably, but kept the liquid from reaching the top of the tanks, and 9 in which the tilting was followed by some of the liquid moving to the top of the tank near the test's end. In the control tanks, there were 17 tests in which the bulk of the liquid moved quickly to the top of the tank, and usually moved back down to the bottom of the tank, with the cycle repeating one or more times. In the remaining 9 control tank tests, most of the liquid would move to the top of the tank and stay there for most of the parabola. Figure 3 is a Case 3 image, the magnet is below the right hand tank.

In the Case 4 tests, there were 6 with no input impulse. For 4 of these tests the magnet tank showed a tilted interface that never reached the top of the tank, while for 2 some liquid eventually went to the top of the tank. Of the no-impulse control tank cases, 4 had more liquid go to the top of the tank, while 2 had an interface that tilted more than for the corresponding magnet tanks. For the 3 tests in which multiple input impulses set up a swirling motion, the magnet cases showed a smaller amount of the liquid at the top of the tank than the controls. In 6 additional tests an average of 65% of the liquid was near the tank bottom for the magnet tanks compared with an average of 30% for the controls. In 3 tests there was no significant difference between the magnet and control tanks. Figure 4 is a Case 4 image; the magnet tank is on the left.

Mechanical & Aerospace Engineering

SUMMARY OF RESULTS

CASE	TANK	Depth	# of tests	# positive	# negative	# inconclusive
1	Prism	1 cm	27	27	0	0
2	Cylinder	1 cm	18	18	0	0
3	Prism	4 cm	26	26	0	0
4	Cylinder	4 cm	18	15	0	3
TOTAL			89	86	0	3

Mechanical & Aerospace Engineering

CONCLUSIONS

1. Magnetic positioning was successful, so long as impulse not so large as to cause liquid to separate into many small droplets.

2. Magnetic positioning was much more successful for shallow fill depth. (11% full, versus 44% full) This is because magnetic Bond number was over 4 times larger for the shallower fill amounts.

3. Magnetic positioning was somewhat more successful for square cross section tanks. (surface tension helps – 4 corners provide flow path between top and bottom of tank.)

4. Need accelerometers to accurately measure accelerations. (30 frames/sec video framing rate inadequate to accurately measure rate of change of velocity)

5. Also, a surfactant could be added, to reduce effects of surface tension.

Mechanical & Aerospace Engineering

Granular Materials Research at NASA-Glenn

NASA Research Members

Juan H. Agui: GRC
Nihad Daidzic: NCMR
Robert D. Green: GRC
Masami Nakagawa: GRC & Colorado School of Mines
Vedha Nayagam: NCMR
Enrique Ramé: NCMR
Allen Wilkinson: GRC
Case Western Granular Research Group

current in-house projects

Impulse Dispersion

Wave Propagation

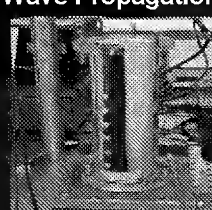

MRI

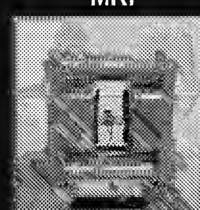

Micro-gravity Hopper

Glenn Research Center

Impulse dispersion of a tapered granular chain

Masami Nakagawa: NASA GRC & CSM(Colorado School of Mines)
Juan H. Agui : NASA GRC

Collaborators: Surajit Sen: SUNY-Buffalo
David Wu: CSM
David Vivanco: CSM Graduate Student

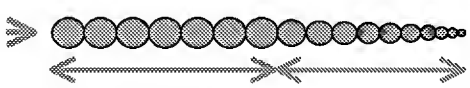

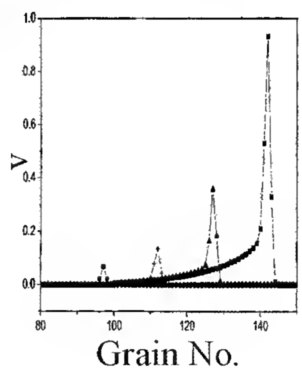

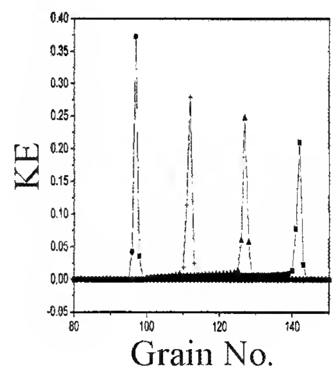

NASA/CP—2002-211212/VOL2

High Speed Digital Images of Tapered Chain Dynamics

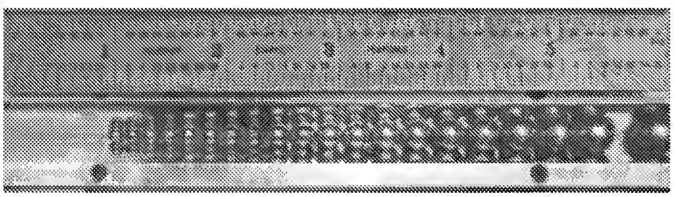

Before Impact

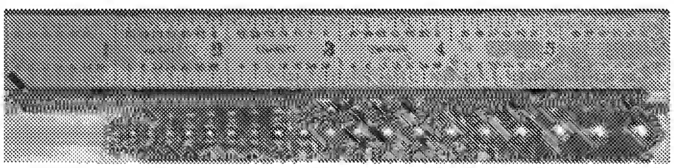

Time of Impact

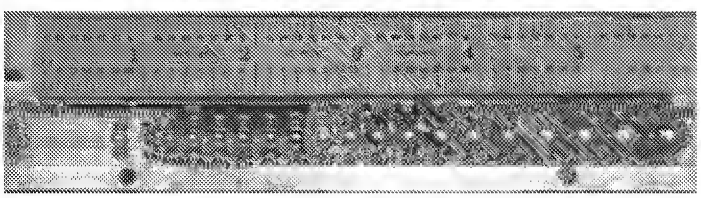

9 ms later
(Notice movement of all the particles)

Glenn Research Center

Microgravity Science Division
Space Directorate

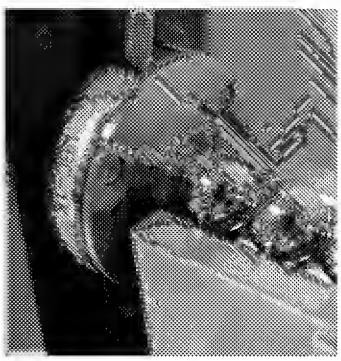

Impact Dispersion

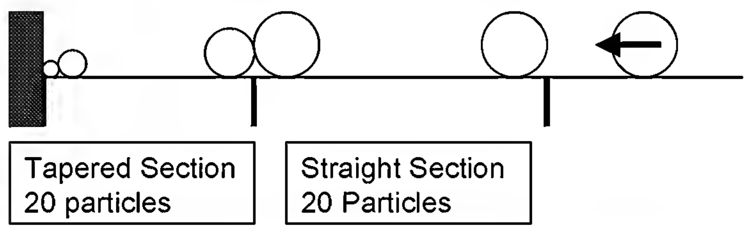

Impact Level	Straight lb	Tapered lb	Tapered/Straight=
			Force in/ Force out
15 v	8.54	4.75	0.557
20 v	15.44	7.196	0.467
25 v	22.02	9.662	0.439
30 v	27.67	11.63	0.42

3-D GRANULAR BED EXPERIMENTAL SETUP

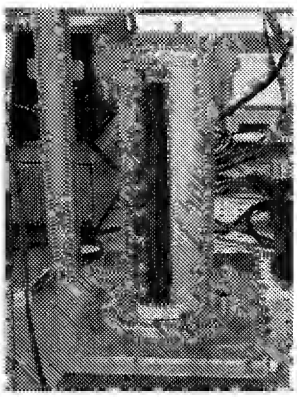

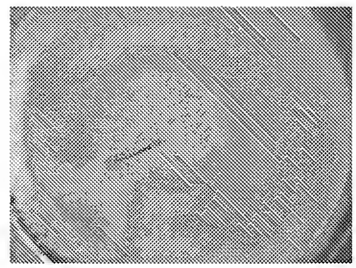

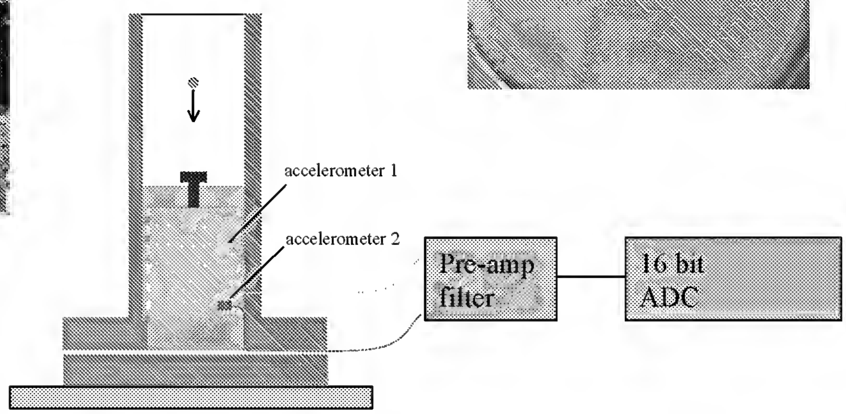

Excitations in granular media are of fundamental importance. Propagation of acoustic waves in granular materials can exhibit rich and complex behavior because of the discrete and non-linear nature of the medium.

Waves in granular beds are studied because of their relevance to bulk granular assemblies such as in hoppers, sand piles, conveyed granular material, etc. A method using a simple drop projectile at a specified height produce an initially localized impulse on the top of the bed. The propagation of this wave is then studied to determine local and global properties of the granular assembly.

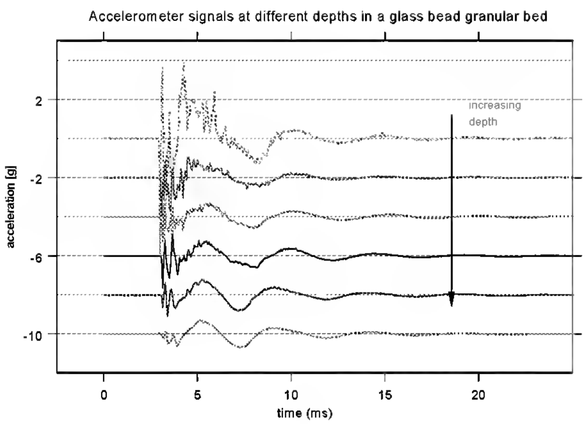

Top: Acceleration signals at different depths of the bed. The shallows depths of the bed, particularly the first probe position, exhibit wild high frequency fluctuations during the initial stage of the wave propagation, followed by resonant decay. At the lower positions the signals show weaker high frequency fluctuations yet little dispersion, indicating that there is a transfer of energy to the lower frequencies.

Bottom: Simultaneous signals from the top and bottom accelerometers placed at a shallow depth (8 mm) and a deep depth (23 mm), with the bottom sensor 25 mm below the top. The shallow depth shows a high degree of incoherence between the two locations, while the deeper sensors show high coherence. There was also an increase in the initial low frequency amplitudes at the lower depths which seem to depend on the position of the probes relative to the total depth of the bed.

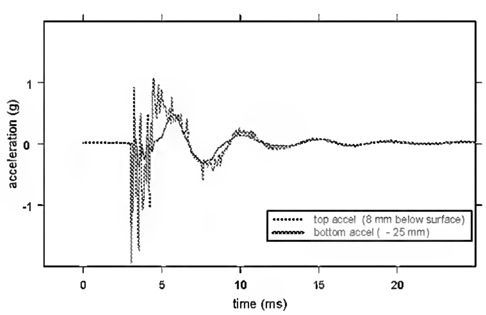

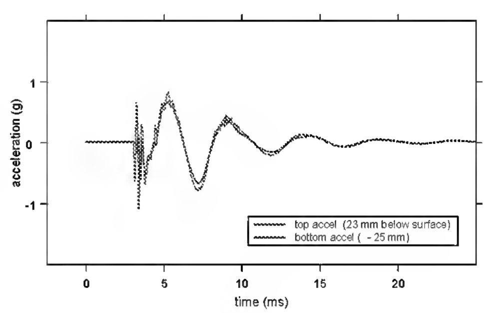

2-D ORDERED PACKING

accelerometers

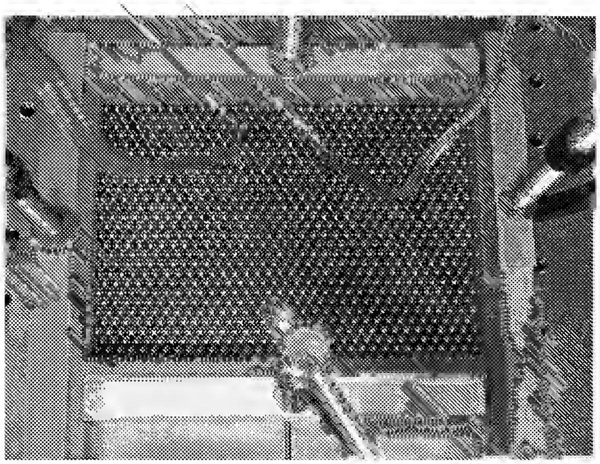

- •hcp using 3.5 mm steel balls
- •Foam padded side walls
- •Light tapping (solenoid)
- •Correlation data

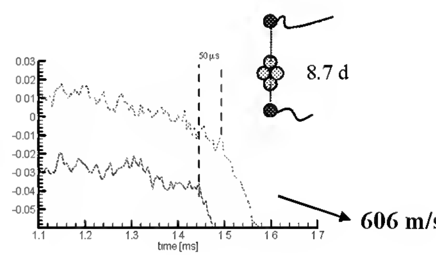

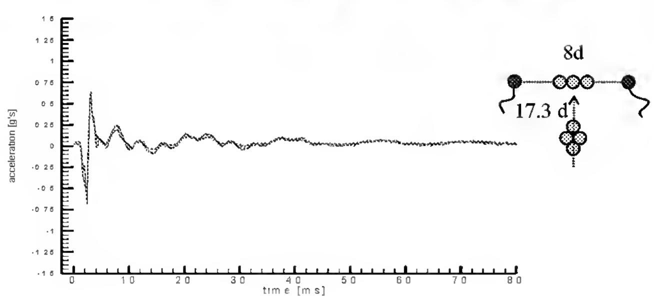

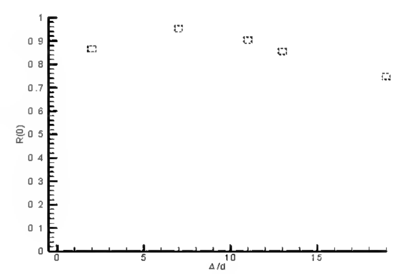

Glenn Research Center

National Center for Microgravity Research on Fluids and Combustion

NCMR fluids&combustion

Magnetic Resonance Imaging of Fluid Flow in Porous Media

Dr. Nihad E. Daidzic

National Center for Microgravity Research (NCMR) @ NASA John H. Glenn Research Center, Cleveland, OH, U.S.A.

Magnetic Resonance Imaging

1. **(Nuclear) Magnetic Resonance Imaging is a map of a weak magnetization of atomic nuclei. The nuclear magnetization M is proportional to the sum of all nuclear magnetic dipole moments of the sample.**
2. **A strong static magnetic field B_0 is applied to polarize the nuclear magnetic moments. Time-dependant magnetic *rf* fields $B_{rf} << B_0$ are used to stimulate the spectroscopic response. Magnetic field gradients $(G \cdot r) << B_0$ are needed to obtain spatial resolution.**
3. **The nuclear magnetization precesses around the direction of the static magnetic field B_0 with the *Larmor* frequency $\varpi = \gamma B_0$ (γ is nuclear gyromagnetic ratio).**
4. **The *chemical shift* or *magnetic shielding* 🕓 gives linear shift of the frequency $\varpi = \gamma (1- 🕓)B_0$ The description of proton NMR (in simple fluids without coupling) is analogous to that of a spinning top with angular momentum in a gravitational field. NMR is a *fingerprint* of the molecular structure.**

NASA/CP—2002-211212/VOL2

Glenn Research Center

National Center for Microgravity Research on Fluids and Combustion

Magnetic Resonance Imaging test rig

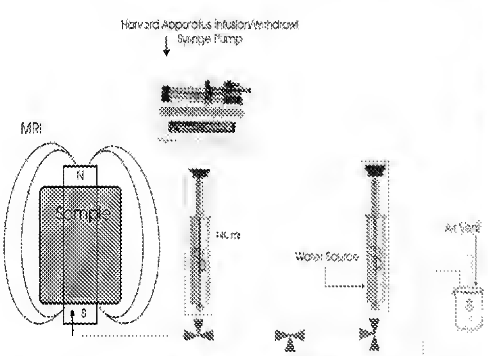

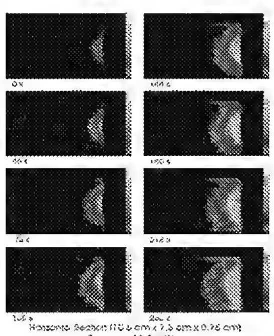

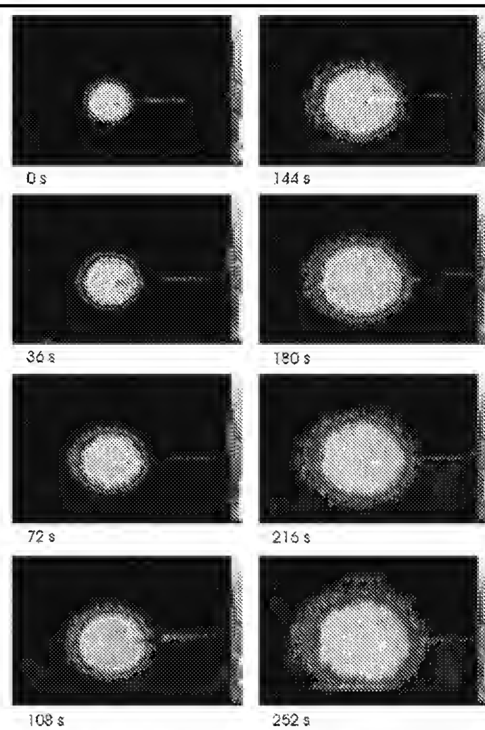

Horizontal Section (10.5 cm x 7.5 cm x 0.75 cm)
Flow from top center. Flow rate: 11.9 ml/min

On the left side the MRI test rig is shown schematically and below it are the images of water infiltration in a horizontal thin section. The porous material is Aquafoam™ with very high porosity (90-95%). The percolation of the front and the saturation level is clearly visible. Specific images are given with the time coordinate in seconds.

On the right-hand side we show the case when water was introduced at the center of the thin and horizontally positioned Aquafoam™ sample in a 1.9T super-conductive MRI scanner. Clearly the porous material is isotropic as the spreading of the front shows.

National Center for Microgravity Research on Fluids and Combustion

Glenn Research Center

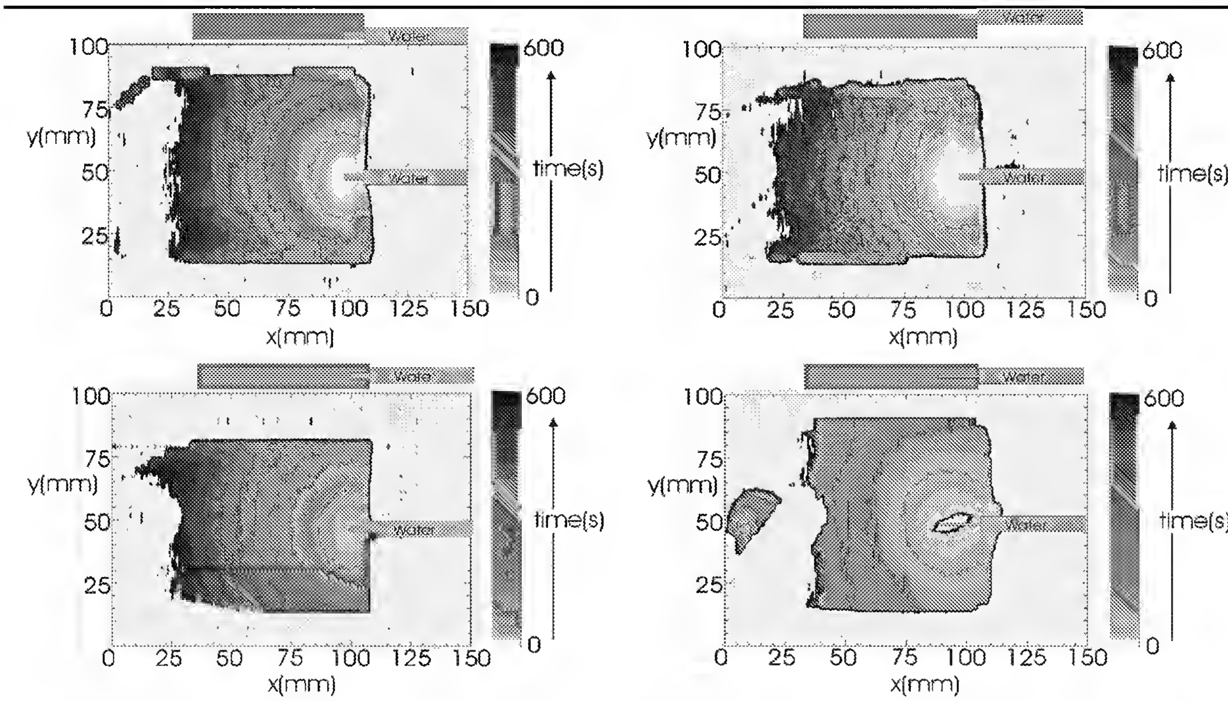

On the following slides the isochrones represent the wetting front of the liquid infiltrating the thin Aquafoam™ sample. On top of each slide a vertical position of the water delivery needle is shown. Note the percolation of the infiltrating front.

Net Charge on Granular Materials (NCharG)

Objectives:

- Develop experimental and data reduction methods for a novel method to measure net charge on granular particles which utilizes Milikan's oil drop technique in a microgravity environment [μg conditions provided by NASA GRC 2.2 sec drop tower].
- Demonstrate the ability to measure net charge on granular materials with particle diameters of 100+ μm. [Previous work using this technique in 1g measured charge on particles with diameters < 10 μm (Kunkel, Cross)].

Applications:

- Provide fundamental understanding of electrostatic force contribution to adhesion forces between particles.
- Industrial applications include electrostatic dust filters (e.g. 3M Filtrete® A/C and heating filters), dust mitigation in clean rooms, ink jet and laser printing.
- NASA applications include reducing dust contamination of lunar or Mars landing craft, habitat, and solar arrays; development of soil-processing equipment for ISRU technologies.

NCharG Experimental Apparatus

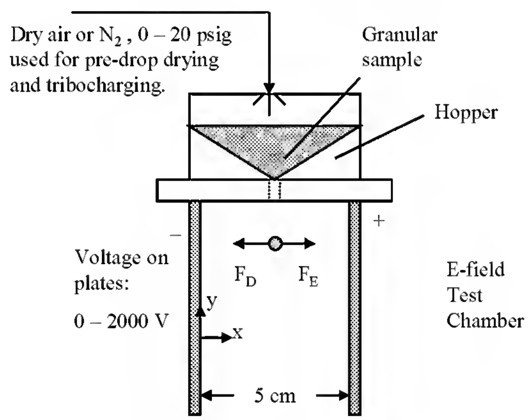

Basic Theory:

- NCharG uses a modified form of Milikan's oil drop technique. ie.

  $F_E = qE = 6\pi\mu r v_x = F_D$
- Absence of gravity allows larger particle displacements in e-field force direction.

Space Program at Glenn Research Center

Microgravity Science Division
Space Directorate

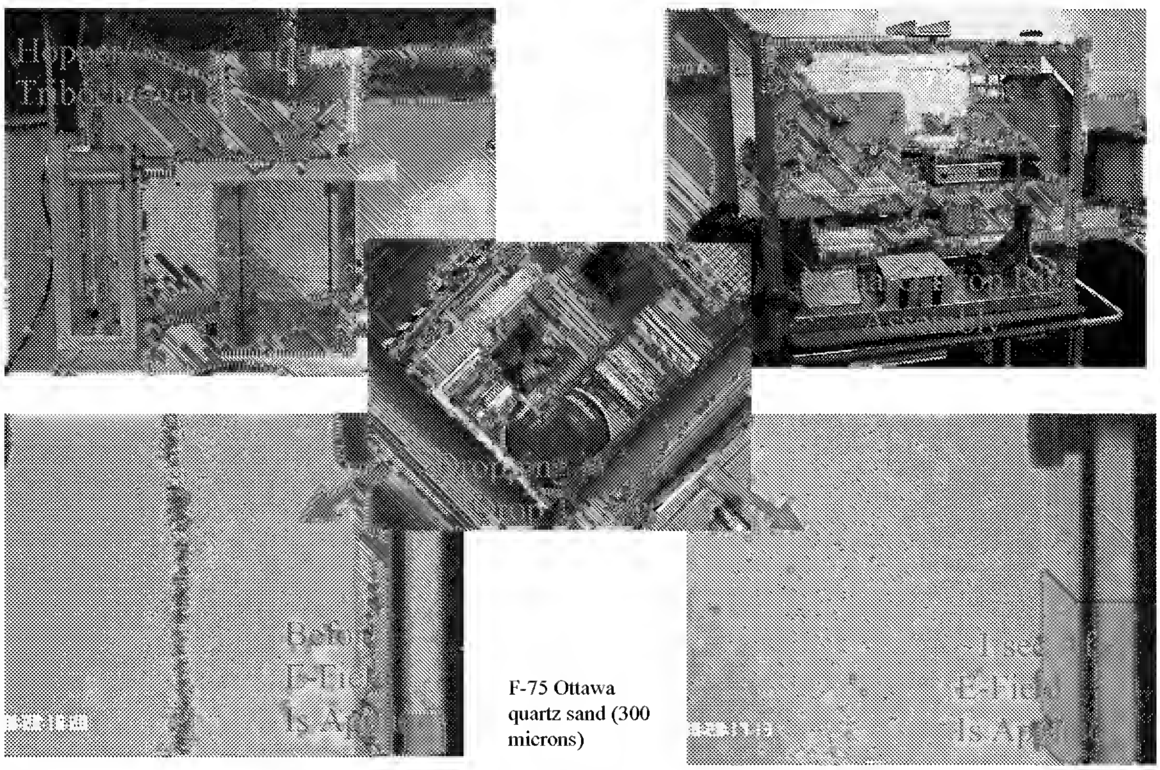

F-75 Ottawa quartz sand (300 microns)

Space Program at Glenn Research Center

Microgravity Science Division
Space Directorate

Net Charge on Granular Materials (NCharG)

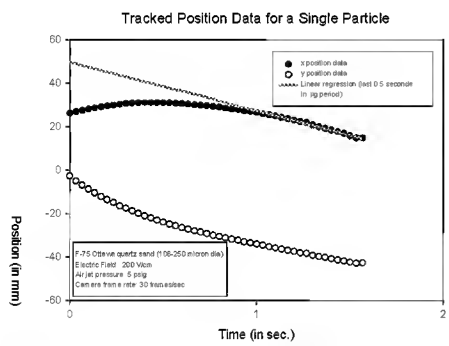

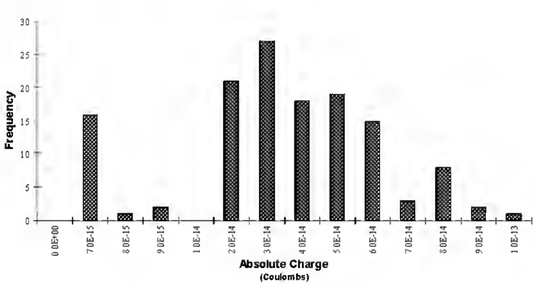

Results and Conclusions:

- To date, 23 drops of F-75 Ottawa quartz sand were made with 150 micron and 300 micron size particles.
- Particles were tracked using GRC in-house software (SpotLight). Position data of last 0.5-1.0 sec of Og period show linear regression fits > 98%, indicating particles reach a constant velocity.
- Preliminary results indicate charge levels of 10^{-15} to 10^{-13} C on these particles with the highest frequency in the 10^{-14} C range. Distribution of charge levels appears to be Gaussian.

Future work:

- Measure charge on additional granular materials such as glass beads and mustard seeds (for MRI granular flow work).
- Provide drop tower rig as a facility for other microgravity researchers in ground or flight-based programs who desire charge measurements on other granular materials or aerosol particles.

Acknowledgements:

- Bonnie Hansen, summer intern, for making drops and reducing data.
- OBPR for providing initial funding for this work.

Author Index

REPORT DOCUMENTATION PAGE

Form Approved
OMB No. 0704-0188

1. AGENCY USE ONLY (*Leave blank*)	2. REPORT DATE	3. REPORT TYPE AND DATES COVERED
	November 2002	Conference Publication

4. TITLE AND SUBTITLE

Sixth Microgravity Fluid Physics and Transport Phenomena Conference
Exposition Topical Areas 1–6

5. FUNDING NUMBERS

WU–101–43–0B–00

6. AUTHOR(S)

Bhim Singh, compiler

7. PERFORMING ORGANIZATION NAME(S) AND ADDRESS(ES)

National Aeronautics and Space Administration
John H. Glenn Research Center at Lewis Field
Cleveland, Ohio 44135–3191

8. PERFORMING ORGANIZATION REPORT NUMBER

E–13064–1

9. SPONSORING/MONITORING AGENCY NAME(S) AND ADDRESS(ES)

National Aeronautics and Space Administration
Washington, DC 20546–0001

10. SPONSORING/MONITORING AGENCY REPORT NUMBER

NASA CP—2002-211212-VOL2

11. SUPPLEMENTARY NOTES

Exposition topical areas 1–6 posters of a conference cosponsored by the NASA Office of Life and Microgravity Sciences and Applications and the Fluid Physics and Transport Phenomena Discipline Working Group and hosted by NASA Glenn Research Center and the National Center for Microgravity Research on Fluids and Combustion, Cleveland, Ohio, August 14–16, 2002. Responsible person, Bhim Singh, organization code 6712, 216–433–5396.

12a. DISTRIBUTION/AVAILABILITY STATEMENT

Unclassified - Unlimited
Subject Category: 34 Distribution: Nonstandard

Available electronically at http://gltrs.grc.nasa.gov

This publication is available from the NASA Center for AeroSpace Information, 301–621–0390.

12b. DISTRIBUTION CODE

13. ABSTRACT ***(Maximum 200 words)***

The Sixth Microgravity Fluid Physics and Transport Phenomena Conference provides the scientific community the opportunity to view the current scope of the Microgravity Fluid Physics and Transport Phenomena Program, current research opportunities, and plans for the near future. The conference focuses not only on fundamental research but also on applications of this knowledge towards enabling future space exploration missions. A whole session dedicated to biological fluid physics shows increased emphasis that the program has placed on interdisciplinary research. The conference includes invited plenary talks, technical paper presentations, poster presentations, and exhibits. This CP is a compilation of the abstracts, presentations, and posters presented at the conference.

14. SUBJECT TERMS

Fluid dynamics; Fluid physics; Fluid mechanics; Microgravity; Reduced-gravity; Heat transfer; Multiphase flow; Complex fluids

15. NUMBER OF PAGES

639

16. PRICE CODE

17. SECURITY CLASSIFICATION OF REPORT	18. SECURITY CLASSIFICATION OF THIS PAGE	19. SECURITY CLASSIFICATION OF ABSTRACT	20. LIMITATION OF ABSTRACT
Unclassified	Unclassified	Unclassified	